

Seeing Below the Surface of Mars

Volatile sublimation in the martian regolith

Narissa Patel (MSci)

A thesis submitted for the degree of
Doctor of Philosophy in Planetary Science

School of Physical Sciences

The Open University

UK

January 2022

Declaration

I confirm that this thesis is my own work, and that I have indicated where data or information has been derived from other sources

Narissa Patel

January 2022

Abstract

The discovery of buried carbon dioxide (CO_2) ice between water (H_2O) ice layers within the martian south polar layered deposits has renewed interest in subsurface CO_2 ice. In this thesis, subsurface CO_2 ice stability is explored using a 1-D thermal and vapour diffusion numerical model that simulates three phases of H_2O , two phases of CO_2 , and adsorption of both for the first time.

Numerical experiments were run to examine how these two ices influence one another, under a variety of ice-layer configurations that are expected to be valid for Mars. The results demonstrate that an overlying near-surface H_2O ice-filled regolith layer increases subsurface CO_2 ice stability by an order of magnitude. This stability increases further with the addition of an underlying H_2O ice-filled regolith layer. The initial porosity and geological materials used to represent the subsurface also have a large influence on CO_2 ice stability. The porosity limits the vapour diffusion rate, while the geological materials influence thermal conductivity and, therefore, subsurface temperatures.

Simulations at different orbital obliquities demonstrate that CO_2 ice stability in the polar regions is greatest at low obliquities and smallest at high obliquities. The reverse is true for the equatorial regions. At higher obliquities ($>45^\circ$) and atmospheric pressures, the results suggest subsurface CO_2 ice deposition could occur in the equatorial region.

The model results suggest that a 0.7–27 km CO_2 ice layer could sublimate away while 1 m of low-porosity H_2O ice forms (in 14–550 kyr depending on method) in the south polar layered deposits. The results also suggest CO_2 ice sublimation is dependent on obliquity: ~ 0.15 km sublimates at low obliquity and ~ 1.9 km sublimates at high obliquity over 100 kyr.

The subsurface model is a useful tool for future investigations into the historical behaviour of ices on Mars, particularly during the Noachian period when the CO_2 frost-point temperature was higher.

Acknowledgements

Throughout the writing of this thesis, I have received a great deal of support and assistance. I would first like to thank my supervisors Prof. Stephen Lewis, Prof. Axel Hagermann and Prof. Matt Balme who have guided and supported me throughout the PhD process. Without their insightful suggestions and invaluable advice, this thesis would not exist. I would like to thank STFC for funding this project.

Thanks also to my co-postgraduate students for their friendship, encouragement and for making the last few years enjoyable. While there are many who have made this time memorable, a special thanks is reserved for Megan, David and Rachael for the countless conversations over tea which both sparked many ideas and allowed me to vent about coding frustrations. A special thanks also goes to James, Paul and Lori-Ann for their valuable advice, patience and support with understanding and fixing the MGCM.

I would also like to thank my family for their continual support. Finally, a special thanks to my partner Patrick, who has been a constant companion throughout this work, providing never-ending support and encouragement.

Contents

I	List of Figures	xv
II	List of Tables	xix
III	Glossary	xxiii
IV	List of Acronyms	xxv
IV.I	Missions and Instruments	xxvi
V	List of Symbols	xxix
VI	List of Publications	xxxiii
VI.I	Publications in peer reviewed journals	xxxiii
VI.II	Conference Abstracts	xxxiii
VII	List of Simulations and MSSM Versions	xxxv
VII.I	MSSM Versions	xxxv
VII.II	Ice Layer Configurations	xxxvi
VII.III	MSSM Simulations List	xxxvii
VII.IV	Schematics of the Different Initial Ice Layer Configurations	xl
1	Introduction	1
1.1	Research Questions	4
1.2	Thesis Structure	4
2	Water and Carbon Dioxide on Mars	7
2.1	The Surface and Subsurface	8
2.1.1	Surface Geology	9
2.1.2	Water in the Subsurface	13
2.1.3	Carbon Dioxide in the Subsurface	14
2.1.4	Carbon Dioxide Clathrate Hydrates	15
2.1.5	Influences on Subsurface Temperature and Ice Deposition . .	16
2.1.5.1	Solar Insolation	17
2.1.5.2	Thermal Inertia	17
2.1.5.3	Thermal Conductivity	18
2.1.5.4	Albedo	20
2.1.5.5	Geothermal Flux	21
2.2	Surface Ice	22

2.2.1	Polar Caps	23
2.2.2	Seasonal Frost	24
2.3	Subsurface Water Ice	26
2.3.1	Observations of Water Ice Distribution	28
2.3.2	Simulations of Water Ice Distribution	30
2.3.3	Mid-latitude Water Ice	31
2.3.4	Polar Layered Deposits	32
2.4	Subsurface Carbon Dioxide Ice	34
2.4.1	Carbon Dioxide Ice in the South Polar Layered Deposits . .	35
2.5	Liquid Water	37
2.6	Climate	38
2.6.1	Planetary Boundary Layer	40
2.6.2	Carbon Dioxide Cycle	41
2.6.3	Water Cycle	42
2.7	Orbital Parameters	44
2.7.1	Obliquity	45
2.7.1.1	High Obliquity	47
2.7.1.2	Low Obliquity	48
2.7.2	Longitude of Perihelion and Eccentricity	49
2.8	Planetary History	50
2.8.1	Distribution of Carbon Dioxide Ice Early in Martian History?	52
2.9	Summary and Remaining Questions	55
3	The Martian Subsurface Model	57
3.1	Grid Stretch	58
3.2	Thermal Scheme	68
3.2.1	Thermal Conductivity of Regolith	72
3.2.2	Effective Thermal Conductivity	74
3.2.2.1	Hertz Factor	74
3.2.3	Testing the Thermal Scheme	76
3.3	Water Scheme	77
3.3.1	Vapour Diffusion through the Regolith	78
3.3.1.1	Diffusion Coefficient	80
3.3.1.2	Tortuosity	82
3.3.2	Distribution of water (H ₂ O) through the Regolith	84
3.3.2.1	Conditions Below the Triple Point Pressure	86
3.3.2.2	Conditions Above the Triple Point Pressure	87
3.3.2.3	Adsorption	88
3.3.2.4	Thermal Conductivity of H ₂ O Ice	93
3.4	Carbon Dioxide Scheme	95
3.4.1	Thermal Conductivity of CO ₂ Ice	95
3.4.2	Vapour Diffusion	96

3.4.2.1	Diffusion Coefficient	97
3.4.3	Phase Distribution of CO ₂	97
3.4.3.1	Saturation Vapour Pressure Over Ice	99
3.4.3.2	Adsorption	100
3.4.4	Density of CO ₂ ice	101
3.5	Surface Flux	101
3.6	Sublimation and Accumulation Rates	102
3.7	The LMD-UK Mars global circulation model	103
3.7.1	Atmospheric Profiles from MGCM Simulations	104
3.8	Summary	109
4	How do CO₂ ice and H₂O ice interact within the regolith?	111
4.1	Initial Conditions	112
4.1.1	Zonal Latitudes and Individual Locations	117
4.2	Simulations with Only One Ice Present	118
4.2.1	H ₂ O Ice	123
4.2.2	CO ₂ Ice	126
4.3	Simulations with Both Ices	130
4.3.1	CO ₂ Ice Filled Regolith over H ₂ O Ice Filled Regolith	130
4.3.2	H ₂ O Ice Filled Regolith over CO ₂ Ice Filled Regolith	132
4.3.2.1	Time Taken To Fully Sublimate CO ₂ Ice When Under H ₂ O Ice	140
4.3.2.2	Zonal Latitudes vs Longitudes	145
4.3.2.3	Effect on the Behaviour of H ₂ O Ice	147
4.4	Alternate Assumptions within the MSSM	154
4.4.1	Maximum Sublimation Rate	154
4.4.2	Atmospheric Source	155
4.5	Discussion and Summary	156
5	What role do subsurface properties and ice layer configurations play in the stability of CO₂ ice?	161
5.1	Initial Ice Porosity	163
5.2	Geological Properties	170
5.2.1	Varying the Regolith Unit Materials	174
5.2.2	Inclusion of a Basalt Basement Unit	181
5.3	Simulations with Multiple Ice-Layers	189
5.4	Summary	199
6	How does Mars' orbital obliquity change the stability of CO₂ ice and H₂O ice within the subsurface?	203
6.1	Atmospheric Profiles	204
6.2	Subsurface Ice Profiles	210

6.3	Obliquity = 15°	214
6.4	Obliquity = 35°	219
6.5	Obliquity = 45°	224
6.6	Discussion	227
	6.6.1 Insights into the CO ₂ Deposits within the SPLD	231
6.7	Summary	239
7	Conclusions and Future Work	241
7.1	Summary and Conclusions	241
	7.1.1 Responses to Research Questions	244
7.2	Future Work	249
	7.2.1 Future Work with the MSSM	250
	7.2.2 Future Work with the Combined MGCM and MSSM Model	252
	7.2.3 Future Mars Missions and Observations	253
	7.2.4 Future Experimental Work	254
8	References	257
A	Detailed Description of Diffusion Methods	285
A.1	Derivation of the Discretisation of the Heat Conduction Equation	285
	A.1.1 Boundary Conditions	287
	A.1.1.1 Surface	287
	A.1.1.2 Base	287
A.2	Derivation of the Finite Volume Method for Diffusion of Vapour	288
	A.2.1 Boundary Conditions	290
	A.2.1.1 Surface	290
	A.2.1.2 Base	291
B	The LMD-UK Mars global circulation model	293
B.1	Input Files	293
	B.1.1 model.input	293
	B.1.2 callphys.def	296
B.2	Integration of the Martian Subsurface Model (MSSM) into the LMD-UK Mars global circulation model (MGCM)	301
	B.2.1 Surface Flux in the MGCM	301
B.3	The Steele et al. (2017a) subsurface water scheme in the MGCM	302
	B.3.1 Water Scheme Description	302
	B.3.2 Testing of the Steele et al. (2017a) model	304
	B.3.2.1 Vapour Diffusion Assumptions	305
	B.3.2.2 Conservation Properties	306
	B.3.3 Derivation of the Finite Difference Method for Vapour Dif- fusion used in Steele et al. (2017a)	307

C	Sublimation Rates	315
C.1	CO ₂ Sublimation Rate at all latitudes	315
	C.1.1 Regional Average CO ₂ Sublimation Rates	323
C.2	H ₂ O Sublimation Rate	327
	C.2.1 Regional Average H ₂ O Sublimation Rates	345

I | List of Figures

VII.1	Initial subsurface profiles for all ice layer configurations.	xl
2.1	The topography of Mars from MOLA observations. Figure from Smith et al. (2001b).	10
2.2	Thermal inertia of Mars. Figure from Putzig et al. (2005).	10
2.3	Map of the thermal inertia and albedo units derived by Putzig et al. (2005)	13
2.4	Seasonal variations of the North Polar Cap	23
2.5	Examples of surface frost.	25
2.6	Observations of subsurface H ₂ O ice.	27
2.7	WEH content of H ₂ O bearing soils derived from MONS data. Figure from Feldman et al. (2004).	29
2.8	A martian glacier from HiRISE data.	32
2.9	Images of the polar layered deposits.	33
2.10	Schematic of the CO ₂ layers within the South Polar Layered Deposits (SPLD).	36
2.11	Schematic overview of the martian water (H ₂ O) cycle	43
2.12	Obliquity, eccentricity and longitude of perihelion variations over the last 20 million years. Plotted using data from Laskar et al. (2004) . . .	45
2.13	Zonal CO ₂ ice depth over time for the 15° obliquity simulations from Soto et al. (2015)	54
2.14	Seasonal distribution of carbon dioxide (CO ₂) ice from simulations by Nakamura and Tajika (2003)	54
3.1	Comparison of Subsurface Grid Stretches	59
3.2	Initial conditions for top-hat tracer distribution experiments	64
3.3	Top-hat experiment results	66
3.4	Grid used for TDMA	68
3.5	Subsurface thermal profile at 60° N 180° E and $L_S = 90^\circ$	70
3.6	Thermal conductivity of the empty regolith matrix	73
3.7	The effect of variable thermal conductivity on temperature	75
3.8	Schematic of the contact area between two grains	76
3.9	Thermal scheme comparison with analytical solution	77
3.10	H ₂ O phase diagram	85
3.11	Comparison of H ₂ O saturation vapour pressure over ice equations . .	87
3.12	Comparison of H ₂ O adsorption experimental results	90

3.13	Thermal conductivity of matrix with the pore space filled with H ₂ O ice	95
3.14	Phase diagram for CO ₂	98
3.15	Comparison of experimental CO ₂ adsorption studies	100
3.16	Annual atmospheric profiles from the obliquity = 25° MGCM simulation	106
3.17	Surface ice from the obliquity = 25° MGCM simulation	107
3.18	Annual atmospheric profiles in the equatorial region from the obliquity = 25° MGCM simulation	108
4.1	Map of MSSM individual locations	117
4.2	Surface flux of H ₂ O vapour for S01	120
4.3	Surface flux of CO ₂ vapour for S01	121
4.4	Column density of H ₂ O ice for H ₂ O ice only simulations (S29, S31, S12)	124
4.5	Column density of CO ₂ for simulations S09 and S30	127
4.6	Annual average CO ₂ surface flux for simulation S30	129
4.7	Column density of CO ₂ ice for simulation S03	130
4.8	Annual average CO ₂ surface flux for simulation S03	132
4.9	Column density of CO ₂ ice for simulations S05, S06 and S07	133
4.10	Annual average CO ₂ surface flux for simulation S06	134
4.11	Average subsurface temperature for simulation S06	136
4.12	Column density of H ₂ O ice in the equatorial region of simulation S06	138
4.13	Number of years for CO ₂ ice to fully sublimate in S05, S06 and S07	139
4.14	Annual sublimation rate of CO ₂ ice for simulation S06	140
4.15	CO ₂ ice density with depth at latitude 7°S from S06.	141
4.16	Number of years for CO ₂ ice to fully sublimate in S06, S09, S30	143
4.17	Column density of CO ₂ ice for 1000MY simulation of S06	144
4.18	Number of years for CO ₂ ice to fully sublimate in 50, 200 and 1000MY simulations of S06	145
4.19	Column density of CO ₂ at different locations across latitude 17° in simulation S06	147
4.20	Column density of CO ₂ ice at different locations across latitude 42.5°S in simulation S06	148
4.21	Column density of H ₂ O ice in simulations S31, S29 and S06	149
4.22	H ₂ O diffusion coefficient with depth at 17°S for simulations S31	150
4.23	Average subsurface temperature in the equatorial region for simulations S06, S29 and S31	153
4.24	Column density of CO ₂ ice for the no sublimation routine simulation (NS01)	155
4.25	Phase diagram for CO ₂ showing pressure and temperature ranges for present-day and the Noachian	159
5.1	Column density of CO ₂ ice for simulation S06	164

5.2	Column density of CO ₂ ice for the $\phi_{\text{ice ini}} = 0$ and $\phi_{\text{ice ini}} = 0.0001$ simulations	165
5.3	Column density of H ₂ O ice for the $\phi_{\text{ice ini}} = 0$ and $\phi_{\text{ice ini}} = 0.0001$ simulations	168
5.4	Column density of CO ₂ for the $\phi_{\text{ice ini}} = 0.01$ and $\phi_{\text{ice ini}} = 0.1$ simulations	169
5.5	Number of years that CO ₂ ice survives for the varying initial ice porosity simulations	170
5.6	Density, porosity and thermal conductivity profiles for the simulations using different stratigraphic profiles	176
5.7	Column density of CO ₂ ice over time for the scenarios with different regolith unit subsurface structures	177
5.8	Comparison of CO ₂ ice sublimation rate for the different subsurface structures without a basement unit	179
5.9	Difference in average temperature across the subsurface between simulations S06 and CDS-SS	180
5.10	Number of years taken to fully sublimate CO ₂ ice for the different subsurface structures without a basement unit	180
5.11	Column density of CO ₂ ice for the different subsurface structure simulations with a basalt basement	182
5.12	Difference in average subsurface temperature between the UR-CDS-B structure and the CDS-SS-B structure sets of simulations	183
5.13	Column density of H ₂ O ice for the UR-CDS-B and CDS-SS-B sets of simulations	185
5.14	Subsurface temperature with depth over time at 12°S for the UR-CDS-B scenario	187
5.15	Comparison of the number of years it takes to fully sublimate CO ₂ ice and the sublimation rate for the different subsurface structures with a basement unit	188
5.16	Initial subsurface profiles for scenarios S33, S34, S35 and S36	189
5.17	Column density of CO ₂ ice for scenarios S33, S35, S36 and S48	193
5.18	CO ₂ diffusion coefficient at 77°S for scenarios S33, S34, S35 and S36	195
5.19	Thermal conductivity profiles for the multiple-ice-layer scenarios	196
5.20	Comparison of the number of years that CO ₂ ice survives for the multiple-layer scenarios	198
6.1	The four obliquities investigated and the effect on surface temperature.	204
6.2	Annual atmospheric profiles from the obliquity = 15° MGCM simulation	206
6.3	Surface CO ₂ ice from the 15° and 45° obliquity MGCM simulations	207
6.4	Annual atmospheric profiles from the obliquity = 35° MGCM simulation	208
6.5	Annual atmospheric profiles from the obliquity = 45° MGCM simulation	209
6.6	Initial subsurface profiles for the four scenarios used for the obliquity simulations	212

6.7	Column density of H ₂ O ice for the <i>IF</i> scenarios at different obliquities	213
6.8	Column density of CO ₂ ice at an obliquity of 15° for scenarios S15, S37 and S40	216
6.9	Column density of CO ₂ ice at an obliquity of 15° for scenarios S16 and S43	217
6.10	Comparison of the number of years that CO ₂ ice survives for the 15° obliquity simulations	218
6.11	Column density of CO ₂ ice at an obliquity of 35° for scenarios S19, S38, S41 and S44	220
6.12	Difference in diurnal average surface temperature between the 25° and 35° obliquity atmospheric profiles	222
6.13	Comparison of the number of years that CO ₂ ice survives for the 35° obliquity simulations	224
6.14	Column density of CO ₂ ice at an obliquity of 45° for scenarios S23, S39, S42 and S45	225
6.15	Comparison of the number of years that CO ₂ ice survives for the 45° obliquity simulations	227
6.16	Comparison of the number of years that CO ₂ ice survives between the different obliquity simulations	228
6.17	Annual average surface temperature with latitude at obliquities 15° to 65°	229
A.1	Grid used for TDMA	286
B.1	An example of the model.input file	293
B.2	An example of a callphys.def file	300
B.3	Flowchart showing the links between the files edited to integrate the MSSM into the MGCM.	301

II | List of Tables

VII.I	MSSM Versions	xxxv
VII.II	Different subsurface structure versions of the MSSM	xxxvi
VII.III	List of all simulations run with the baseline version of the MSSM at present day obliquity (25°). The initial ice conditions use the acronyms from Ice Layer Configurations List	xxxvii
VII.IV	List of the simulations run with different versions of the MSSM.	xxxviii
VII.V	List of all simulations run at 15°, 35° or 45° obliquity with the baseline version of the MSSM.	xxxix
2.1	The thermal inertia and albedo units derived by Putzig et al. (2005)	11
3.1	Skin depths for the timescales relevant to Mars	62
3.2	Comparison of the details of the grid stretches	63
3.3	Conservation of the finite volume discretisation	65
3.4	Thermal conductivity of water (H ₂ O) ice	94
4.1	Amount of ice if pore space is filled	114
4.2	Potential locations on Mars where the two-ice-layer configurations could occur	116
5.1	Properties of the geological materials used across the different subsur- face structures.	173
5.2	Amount of ice if pore space is filled for the different subsurface structures	178
5.3	Locations on Mars where the multiple ice-layer configurations could be found	190
6.1	The estimated thickness of carbon dioxide (CO ₂) ice sublimated during the time taken for each process involved in the formation of a 1 m H ₂ O ice-layer	234
B.1	Description of the dynamics parameters in the model.input file for the MGCM and the range of values used.	294
B.2	Description of the physics parameters in the model.input file and the range of values used.	295
B.3	Testing the effect of using \sqrt{n} instead of $n^{0.51}$ in Equation B.18a for the expected range of conditions	306
B.4	Checking whether $\frac{4m\phi}{F^4}$ is smaller than 1 for the expected range of conditions	307

B.5	Checking whether the scheme is conservative on the grid structures investigated in Section 3.1.	307
C.1	Annual CO ₂ sublimation rates for all latitudes in the S02 to S19 baseline simulations	315
C.2	Annual CO ₂ sublimation rates for all latitudes in the S20 to S42 baseline simulations	317
C.3	Annual CO ₂ sublimation rates for all latitudes in the S43 to S51 baseline simulations	318
C.4	Annual CO ₂ sublimation rates for all latitudes in the different initial ice porosity simulations	320
C.5	Annual CO ₂ sublimation rates for all latitudes in the different subsurface structure simulations	321
C.6	Regional average CO ₂ sublimation rates for each baseline scenario . .	323
C.7	Regional average CO ₂ sublimation rates for the variable initial ice porosity scenarios	325
C.8	Regional average CO ₂ sublimation rates for the scenarios with different subsurface structures	326
C.9	Average annual H ₂ O sublimation rates for all latitudes in the S01 to S14 baseline simulations	327
C.10	Average annual H ₂ O sublimation rates for all latitudes in the S15 to S28 baseline simulations	328
C.11	Average annual H ₂ O sublimation rates for all latitudes in the S29 to S43 baseline simulations	330
C.12	Average annual H ₂ O sublimation rates for all latitudes in the S29 to S43 baseline simulations	331
C.13	Average annual H ₂ O sublimation rates (excluding first year) for all latitudes in the S01 to S11 baseline simulations	333
C.14	Average annual H ₂ O sublimation rates (excluding first year) for all latitudes in the S12 to S22 baseline simulations	335
C.15	Average annual H ₂ O sublimation rates (excluding first year) for all latitudes in the S23 to S33 baseline simulations	336
C.16	Average annual H ₂ O sublimation rates (excluding first year) for all latitudes in the S35 to S45 baseline simulations	338
C.17	Average annual H ₂ O sublimation rates (excluding first year) for all latitudes in the S48 to S51 baseline simulations	340
C.18	Average annual H ₂ O sublimation rates for all latitudes in the different initial ice porosity simulations	341
C.19	Average annual H ₂ O sublimation rates for all latitudes in the different subsurface structure simulations	343
C.20	Regional average H ₂ O sublimation rates for each baseline scenario . .	345

C.21	Regional average H ₂ O sublimation rates for each different initial ice porosity scenario	347
C.22	Regional average H ₂ O sublimation rates for each different subsurface structure scenario	348

III | Glossary

albedo Property of a material that indicates how well a surface reflects solar energy

aphelion Point in the orbit when Mars is furthest from the Sun

epoch A period of time in history. On Mars these are split into the Noachian, Hesperian and Amazonian (present day).

perennial Continuous or surviving between years

perihelion Point in the orbit when Mars is closest to the Sun

permafrost A subsurface layer of soil that remains frozen throughout the year

permeability Property of a rock that indicates how easily fluids (or gas) can flow through it

spin-up A run of the MGCM that starts with no initial climate state and is run until the climate equilibrates

thermal inertia Property of a material that expresses how quickly its temperature reaches that of the environment

IV | List of Acronyms

1-D one dimensional

1-D GCM 1-D version of the LMD-UK Mars General Circulation Model

3-D three dimensional

CCSR/NIES AGCM Center for Climate System Research, University of Tokyo and National Institute for Environmental Studies, Japan atmospheric general circulation model

CO₂ carbon dioxide

GCM global circulation model

GEL global equivalent layer

GEM-Mars GCM global environmental multiscale Mars general circulation model

GFDL Geophysical Fluid Dynamic Laboratory

Gyr billion years

H₂O water

IAA Instituto de Astrofísica de Andalucía

LDA Lobate Debris Apron

LDM Latitude Dependent Mantle

LMD Laboratoire de Météorologie Dynamique

MAOAM Mars atmosphere observation and modelling project

MCD Mars Climate Database

MEPAG Mars Exploration Program Analysis Group

MGCM LMD-UK Mars global circulation model

MSSM Martian Subsurface Model

MTGCM University of Arizona's Mars thermospheric general circulation model

MY Mars Year

Mars-GRAM Mars global reference atmospheric model

MarsWRF GCM Mars weather research and forecasting global circulation model

Myr million years

NASA National Aeronautics and Space Administration

NPLD North Polar Layered Deposits

OU The Open University

PBL planetary boundary layer

PLD polar layered deposits

SPLD South Polar Layered Deposits

SPRC South Polar Residual Cap

TDMA tri-diagonal matrix algorithm

VFF viscous flow feature

WEH water equivalent hydrogen

kyr thousand years

pr μm precipitable micrometres

IV.I Missions and Instruments

Curiosity

DAN Dynamic Albedo of Neutrons

REMS Rover Environmental Monitoring System

InSight Lander

HP³ Heat Flow and Physical Properties Package

MGS Mars Global Surveyor

MOLA Mars Orbiter Laser Altimeter

TES Thermal Emission Spectrometer

MRO Mars Reconnaissance Orbiter

CRISM Compact Reconnaissance Imaging Spectrometer for Mars

CTX Context Camera

HiRISE High Resolution Imaging Science Experiment

MCS Mars Climate Sounder

SHARAD Shallow Radar

Mars Express

OMEGA Observatoire pour la Minéralogie, l'Eau, les Glaces et l'Activité

Mars Odyssey

GRS Mars Odyssey Gamma Ray Spectrometer

HEND High Energy Neutron Detector

MONS Mars Odyssey Neutron Spectrometer

THERMIS Thermal Emission Spectrometer

Phoenix Lander

LIDAR Light Detection and Ranging

Viking Orbiter

MAWD Mars Atmospheric Water Detector

i-MIM international Mars Ice Mapper

V | List of Symbols

General	Description	Unit
A	Area	m^2
D	Diffusion coefficient	$\text{m}^2 \text{s}^{-1}$
f	Flux from the regolith to the atmosphere	$\text{kg m}^{-1} \text{s}^{-1}$
k_{eff}	Thermal conductivity of entire regolith	$\text{W m}^{-1} \text{K}^{-1}$
q_{atm}	Mass mixing ratio in the atmosphere	kg kg^{-1}
R	Ideal gas constant	$\text{J mol}^{-1} \text{K}^{-1}$
t	Time	s
t_p	Time period of a cycle	s
V	Volume	m^3
z	Depth	m
κ	Thermal diffusivity	$\text{m}^2 \text{s}^{-1}$
ρ_{eff}	Density of the entire regolith	kg m^{-3}
ϕ	Total porosity	
ϕ_{ice}	Ice porosity	
$\phi_{\text{ice ini}}$	Minimum Ice Porosity	
ϕ_{tot}	Total porosity	

Temperature	Description	Unit
c_p	Specific Heat Capacity	J K^{-1}
k	Thermal conductivity	$\text{W m}^{-1} \text{K}^{-1}$
k_{∞}	Thermal conductivity of the regolith at an infinite depth	$\text{W m}^{-1} \text{K}^{-1}$
k_0	Thermal conductivity of the regolith at the surface	$\text{W m}^{-1} \text{K}^{-1}$
k_r	Thermal conductivity of the regolith matrix	$\text{W m}^{-1} \text{K}^{-1}$
T	Temperature	K

z^*	Thermal Skin Depth	m
ρ	Density	kg m ⁻³
ρ_∞	Density at an infinite depth	kg m ⁻³
ρ_0	Density at the surface	kg m ⁻³
ρ_r	Density of the regolith matrix	kg m ⁻³
ω	Angular frequency	rad s ⁻¹
ϕ_r	Regolith matrix porosity	

Water	Description	Unit
$D_{\text{H}_2\text{O}}$	Diffusion coefficient for water	m ² s ⁻¹
D_K	Knudsen diffusion coefficient for water	m ² s ⁻¹
D_N	Fickian diffusion coefficient for water	m ² s ⁻¹
$E_{s_{\text{H}_2\text{O}}}$	Sublimation rate of water ice	m s ⁻¹
$f_{\text{H}_2\text{O}}$	Flux from the regolith to the atmosphere	m ⁻³
$h_{\text{H}_2\text{O}}$	Hertz factor for water ice	
$k_{\text{H}_2\text{O}}$	Thermal conductivity of water ice	W m ⁻¹ K ⁻¹
$n_{\text{H}_2\text{O}}$	Water vapour density	kg m ⁻³
$P_{\text{H}_2\text{O}}$	Water vapour partial pressure	Pa
$P_{sat_{\text{H}_2\text{O}}}$	Water saturation vapour pressure	Pa
$\alpha_{\text{H}_2\text{O}}$	Amount of adsorbed water	kg m ⁻³
$\zeta_{\text{H}_2\text{O}}$	Amount of water ice	kg m ⁻³
$\rho_{\text{H}_2\text{O}}$	Density of water ice	kg m ⁻³
$\sigma_{\text{H}_2\text{O}}$	Total amount of water	kg m ⁻³
τ	Tortuosity	
$\epsilon_{\text{H}_2\text{O}}$	Amount of liquid water	kg m ⁻³

CO₂	Description	Unit
D_{CO_2}	Diffusion coefficient for CO ₂	m ² s ⁻¹
$E_{s_{\text{CO}_2}}$	Sublimation rate of CO ₂ ice	m s ⁻¹
h_{CO_2}	Hertz factor for CO ₂ ice	

k_{CO_2}	Thermal conductivity of CO ₂ ice	W m ⁻¹ K ⁻¹
n_{CO_2}	CO ₂ vapour density	kg m ⁻³
P_{satCO_2}	CO ₂ saturation vapour pressure	Pa
α_{CO_2}	Amount of adsorbed CO ₂	kg m ⁻³
ζ_{CO_2}	Amount of CO ₂ ice	kg m ⁻³
ρ_{CO_2}	Density of CO ₂ ice	kg m ⁻³
σ_{CO_2}	Total amount of CO ₂	kg m ⁻³

VI | List of Publications

VI.I Publications in peer reviewed journals

Patel, N., Lewis, S. R., Hagermann, A., and Balme, M., Simulations of the stability of CO₂ ice in the martian subsurface, *In Preparation*

Patel, N., Lewis, S. R., Hagermann, A., and Balme, M., Sublimation of CO₂ ice in the martian subsurface over the obliquity cycle using 1-D modelling, *In Preparation*

Attree, N., Patel, N., Hagermann, A., Grott, M., Spohn, T., and Siegler, M., Potential effects of atmospheric collapse on Martian heat flow and application to the InSight measurements, *Planetary and Space Science*, Elsevier BV, 180, 104778 , 2020. doi: 10.1016/j.pss.2019.104778

Collins, G. S., Patel, N., Davison, T. M., Rae, A. S. P., Morgan, J. V., Gulick, S. P. S., IODP-ICDP Expedition 364 Science Party, and Third-Party Scientists, A steeply-inclined trajectory for the Chicxulub impact, *Nature Communications*, Springer Science and Business Media LLC, 2020, 11

VI.II Conference Abstracts

Patel, N., Lewis, S. R., Hagermann, A., and Balme, M., Simulations of Subsurface Carbon Dioxide Ice and Implications for the Polar Regions of Mars, *CryoMars Workshop*, 2021

Patel, N., Lewis, S. R., Hagermann, A., and Balme, M., Stability of Subsurface Carbon Dioxide Ice over the Obliquity Cycle, In *Seventh International Conference on Mars Polar Science and Exploration*, 2020

Patel, N., Lewis, S. R., Hagermann, A., and Balme, M., Carbon Dioxide Ice within the Subsurface of Mars, In *American Geophysical Union Fall Meeting*, 2019, P51D-3399

Patel, N., Lewis, S. R., Hagermann, A., Balme, M., and Kaufmann, E., Modelling Martian Subsurface Ice Distribution, *Mars Glacier Meeting*, 2018

Patel, N., Hagermann, A., Lewis, S. R., Kaufmann, E., and Balme, M., Subsurface Volatile Deposition on Mars, In *European Planetary Science Congress*, 2018, 13

VII | List of Simulations and MSSM Versions

A summary of all of the versions of the Martian Subsurface Model (MSSM), the acronyms used to define the different ice layer configurations and of all of the simulations referred to throughout the thesis for reference.

VII.I MSSM Versions

Table VII.I: List of the versions of the MSSM used for this thesis with the baseline subsurface structure. The simulation prefix is the letters used in front of the simulation set number, as the number was reset for each of the versions used.

Version	Description of version	Simulation prefix
Baseline	The version described in Chapter 3 with all features enabled and an annual cycle (1 sol timesteps)	S
Diurnal	Uses the diurnal cycle (1 hour timesteps) instead of the annual cycle	D
No sublimation	The sublimation rate feature is turned off. The amount that sublimates is determined by the difference between vapour pressure and saturation vapour pressure	NS
No flux	The flux from the atmosphere to the subsurface is turned off. There is still a flux of vapour from the subsurface to the atmosphere	NF
Variable ice porosity	The initial ice porosity of a completely ice-filled regolith is set to a different value. In the Baseline it is set to 0.001	PM

Table VII.II: List of the different subsurface structure versions of the MSSM used for this thesis. Each one is composed of a regolith unit and some have a basement unit. To define the regolith unit, values for a surface and a compacted material are input into the equations from Grott et al. (2007) (Equations 3.9a, 3.9b and 3.11; Section 3.2). The simulation prefix is the letters used in front of the simulation set number, as the number was reset for each of the versions used.

Regolith Unit		Basement Unit Material	Simulation Prefix
Surface Material	Compacted Material		
Unconsolidated regolith	Coarse dry sand	None	S
Unconsolidated regolith	Fine dry sand	None	UR-FDS
Fine dry sand	Coarse dry sand	None	FDS-CDS
Coarse dry sand	Sandstone	None	CDS-SS
Unconsolidated regolith	Coarse dry sand	Basalt	UR-CDS-B
Coarse dry sand	Sandstone	Basalt	CDS-SS-B

VII.II Ice Layer Configurations

This is a list of the acronyms used for the initial ice layer configurations.

Alternate Layers Alternate Model layers of H₂O ice and CO₂ ice-filled regolith

C CO₂ Ice-filled Regolith across the entire subsurface

C-IF CO₂ Ice-filled Regolith Over Ice-free Regolith

C-W CO₂ Ice-filled Regolith Over H₂O Ice-filled Regolith

IF ice-free regolith across the entire subsurface

IF-C Ice-free Regolith over CO₂ Ice-filled Regolith

IF-W Ice-free Regolith over H₂O Ice-filled Regolith

IF-W-C Ice-free Regolith Over H₂O Ice-filled Regolith Over CO₂ Ice-filled Regolith

Mixed Layer H₂O Ice-filled Regolith Over CO₂ Ice-filled Regolith With A Mixed Layer

W H₂O Ice-filled Regolith across the entire subsurface

W-C H₂O Ice-filled Regolith Over CO₂ Ice-filled Regolith

W-C-W H₂O Ice-filled Regolith Over CO₂ Ice-filled Regolith Over H₂O Ice-filled Regolith

W-IF H₂O Ice-filled Regolith over Ice-free Regolith

VII.III MSSM Simulations List

Table VII.III: List of all simulations run with the baseline version of the MSSM at present day obliquity (25°). The initial ice conditions use the acronyms from Ice Layer Configurations List

Run	Obliquity	Initial ice layer configuration
S01	25	<i>IF</i>
S02	25	<i>C-W</i> with the boundary at 0.5 m
S03	25	<i>C-W</i> with the boundary at 1 m
S04	25	<i>C-W</i> with the boundary at 2 m
S05	25	<i>W-C</i> with the boundary at 0.5 m
S06	25	<i>W-C</i> with the boundary at 1 m
S07	25	<i>W-C</i> with the boundary at 2 m
S08	25	<i>IF-C</i> with the boundary at 0.5 m
S09	25	<i>IF-C</i> with the boundary at 1 m
S10	25	<i>IF-C</i> with the boundary at 2 m
S11	25	<i>IF-W</i> with the boundary at 0.5 m
S12	25	<i>IF-W</i> with the boundary at 1 m
S13	25	<i>IF-W</i> with the boundary at 2 m
S29	25	<i>W</i>
S30	25	<i>C</i>
S31	25	<i>W-IF</i> with the boundary at 1 m
S33	25	<i>Alternate Layers</i>
S35	25	<i>W-C-W</i>
S36	25	<i>IF-W-C</i>
S48	25	<i>Mixed Layer</i>

Table VII.IV: List of the simulations run with different versions of the MSSM. All of the minimum porosity and different geological layering simulations have been run with the initial scenario *W-C* with the boundary at 1 m (Figure VII.1b).

Run	Obliquity	Initial ice layer configuration	Version of the MSSM
NS01	25	<i>W-C</i> with the boundary at 1 m	No Sublimation
NF01	25	<i>C-W</i> with the boundary at 1 m	No Flux
NF02	25	<i>W-C</i> with the boundary at 1 m	No Flux
NF03	25	H ₂ O ice-filled regolith only	No Flux
Run	Obliquity	Initial Ice Porosity	Version of the MSSM
PM01	25	$\phi_{\text{ice ini}} = 0$	Variable ice porosity
PM02	25	$\phi_{\text{ice ini}} = 0.01$	Variable ice porosity
PM03	25	$\phi_{\text{ice ini}} = 0.1$	Variable ice porosity
PM04	25	$\phi_{\text{ice ini}} = 0.0001$	Variable ice porosity
Run	Obliquity	Description of geological layering	Version of the MSSM
UR-FDS	25	Unconsolidated regolith to fine dry sand	UR-FDS
FDS-CDS	25	Fine dry sand to coarse dry sand	FDS-CDS
CDS-SS	25	Coarse dry sand to sandstone	CDS-SS
UR-CDS-B	25	Unconsolidated regolith to fine dry sand with basalt below 10 m	UR-CDS-B
CDS-SS-B	25	Coarse dry sand to sandstone with basalt below 10 m	CDS-SS-B

Table VII.V: List of all simulations run at 15°, 35° or 45° obliquity with the baseline version of the MSSM.

Run	Obliquity	Initial ice layer configuration
S14	15	<i>C-W</i> with the boundary at 1 m
S15	15	<i>W-C</i> with the boundary at 1 m
S16	15	<i>IF-C</i> with the boundary at 1 m
S17	15	<i>IF-W</i> with the boundary at 1 m
S18	35	<i>C-W</i> with the boundary at 1 m
S19	35	<i>W-C</i> with the boundary at 1 m
S20	35	<i>IF-C</i> with the boundary at 1 m
S21	35	<i>IF-W</i> with the boundary at 1 m
S22	45	<i>C-W</i> with the boundary at 1 m
S23	45	<i>W-C</i> with the boundary at 1 m
S24	45	<i>IF-C</i> with the boundary at 1 m
S25	45	<i>IF-W</i> with the boundary at 1 m
S26	15	<i>IF</i>
S27	35	<i>IF</i>
S28	45	<i>IF</i>
S37	15	<i>Alternate Layers</i>
S38	35	<i>Alternate Layers</i>
S39	45	<i>Alternate Layers</i>
S40	15	<i>W-C-W</i>
S41	35	<i>W-C-W</i>
S42	45	<i>W-C-W</i>
S43	15	<i>IF-W-C</i>
S44	35	<i>IF-W-C</i>
S45	45	<i>IF-W-C</i>
S49	15	<i>Mixed Layer</i>
S50	35	<i>Mixed Layer</i>
S51	45	<i>Mixed Layer</i>

VII.IV Schematics of the Different Initial Ice Layer Configurations

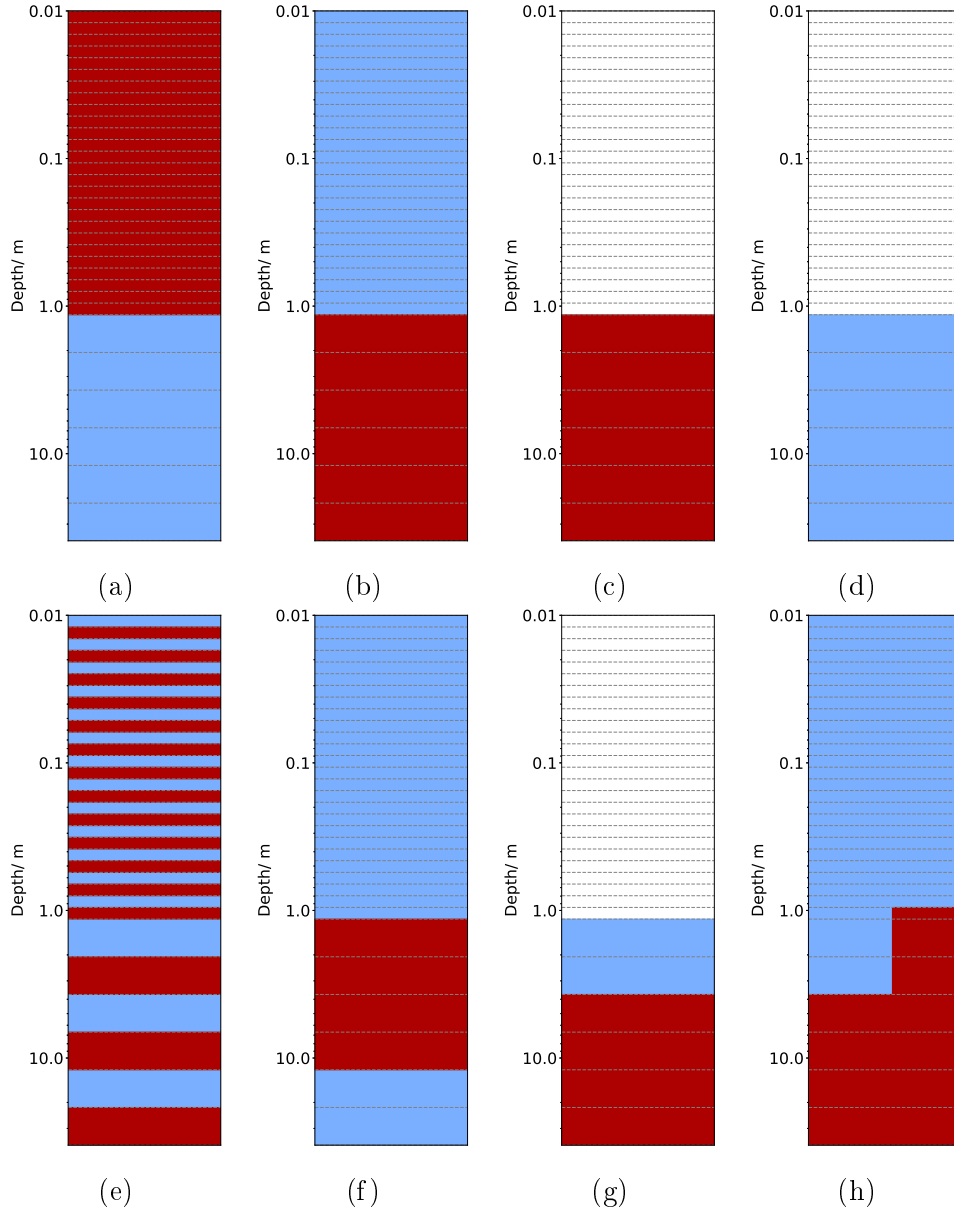


Figure VII.1: Initial subsurface profiles showing the distribution of H₂O ice and CO₂ ice for the two-ice-layer configurations with the boundary at 1 m and all multiple-ice-layer configurations. (a) *C-W*, (b) *W-C*, (c) *IF-C*, (d) *IF-W*, (e) *Alternate Layers*, (f) *W-C-W*, (g) *IF-W-C*, and (h) *Mixed Layer*. White represents an ice-free regolith, blue represents a H₂O ice-filled regolith and red represents a CO₂ ice-filled regolith. The dashed grey lines represent the boundary between model layers.

1 | Introduction

Carbon dioxide (CO_2) ice and water (H_2O) ice have been observed across the martian surface and H_2O ice has also been observed within the subsurface. The martian polar ice caps have been observed telescopically from Earth since at least the 16th century by William Herschel and were determined to be composed of predominantly CO_2 ice at the surface through spacecraft observation (e.g. Hess et al., 1977; Leovy, 1966). Surface H_2O ice frost has been observed by the Viking landers (e.g., Christensen and Zurek, 1984; Clark, 1980), while subsurface H_2O ice was discovered in a trench dug by the Phoenix lander (Mellon et al., 2009). Over time, the distribution of ices has been observed in more detail. As a result, the surface reservoirs of CO_2 ice and H_2O ice, and the subsurface reservoirs of H_2O ice are currently well characterised.

The polar regions host the largest ice reservoirs, with permanent polar caps that are seasonally covered in CO_2 ice (Aharonson et al., 2004; Hansen, 1999). The permanent polar cap in the northern hemisphere is composed only of H_2O ice, whereas the southern polar cap is composed of a H_2O ice layer overlain by a CO_2 ice layer (Thomas et al., 2000). Both permanent polar ice caps overlie a series of layered deposits composed of H_2O ice and dust mixtures that are known as the polar layered deposits (PLD). Outside of the polar regions, subsurface H_2O ice is found across the mid-latitudes in the form of an extensive ice-rich layer known as the Latitude Dependent Mantle (LDM; Mustard et al., 2001). Alongside the LDM, many glacial-like surface features such as Lobate Debris Aprons (LDAs) and viscous flow features (VFFs) are thought to contain ice (Holt et al., 2008; Plaut et al., 2009).

Studies investigating the distribution of H_2O ice and CO_2 ice have shown that the present-day distribution is a mixture of the current stable distribution and of remnants from previous periods in Mars' history that are not in direct contact with the atmosphere and so take longer to sublimate away. One such example of a remnant deposit is the LDM (Laskar et al., 2004; Levrard et al., 2004). The distribution of

subsurface ices is primarily dependent on the obliquity cycle, which alters the distribution of solar insolation across the surface (Laskar et al., 2004). During periods of low obliquity ($<15^\circ$), large permanent polar caps form, composed of both H_2O ice and CO_2 ice. During periods of higher obliquity ($>45^\circ$), these permanent polar caps become unstable and sublimate away, with only seasonal polar caps forming. At these high obliquities, temperatures in the mid-latitudes are reduced enough that H_2O ice becomes stable and the H_2O ice sublimating from the polar regions is redeposited in the mid-latitudes, forming features such as the LDM. This cycling of H_2O ice between the polar regions and mid-latitudes also forms the PLD that are observed in both polar regions (Kreslavsky and Head, 2002; Laskar et al., 2002).

The formation of the PLD has been studied using both observations and numerical modelling (e.g., Lasue et al., 2012; Phillips et al., 2008). Most studies have assumed the layers are composed of H_2O ice with a small dust content and that any CO_2 ice that formed during a period of low obliquity would have fully sublimated away during a period of high obliquity before the next CO_2 ice layer was deposited in the next low obliquity period (e.g., Kreslavsky and Head, 2002). However, recent observations have since shown that there are massive CO_2 ice deposits within the South Polar Layered Deposits (SPLD) and recent efforts have been made towards modelling the formation and persistence of these CO_2 ice deposits (Biersen et al., 2016; Buhler et al., 2019; Manning et al., 2019). The existence of these buried CO_2 ice deposits suggests that modelling of CO_2 ice needs to be expanded to include the subsurface processes (such as the reduced sublimation rate with depth) that have already been demonstrated to influence the distribution and stability of subsurface H_2O ice (e.g., Mellon and Jakosky, 1993; Schorghofer and Aharonson, 2005). The record of these subsurface CO_2 ice deposits and the processes related to their formation have been identified as one of the main goals for future martian ice studies by the Mars Exploration Program Analysis Group (MEPAG; Banfield, 2020; Diniega and Putzig, 2019). These goals also include investigating the interactions between the H_2O and CO_2 cycles during sublimation/condensation; the influences of these interactions on the distribution of ices at seasonal and multi-annual timescales; and constraining the processes by which volatiles exchange between the subsurface and the atmosphere (Banfield, 2020; Diniega

and Putzig, 2019).

The purpose of this thesis is, therefore, to begin the investigation into the impacts of subsurface CO₂ ice processes on CO₂ ice persistence and on the rest of the martian system, through the development of a detailed subsurface model (the Martian Subsurface Model, ‘MSSM’). The MSSM is a one dimensional (1-D) thermal and vapour diffusion model that determines the partitioning of H₂O and CO₂ between the vapour, ice and adsorbate phases (as well as the liquid phase for H₂O). The subsurface model has been coupled to a fixed annual atmospheric cycle taken from the results of a Mars global circulation model (MGCM) that was jointly designed by the Laboratoire de Météorologie Dynamique (‘LMD’, France), The Open University (‘OU’, UK), Oxford University (UK) and the Instituto de Astrofísica de Andalucía (‘IAA’, Spain) to simulate climatic processes in detail. In future investigations, the MSSM will be integrated into the MGCM, but for the purpose of this thesis, only the fixed annual atmospheric cycles are used, partially due to the computational time required to run the MGCM for 10,400 martian years in total, where each martian year is 669 sols or 360° of solar longitude (L_S) long. The stand-alone MSSM is also used because many experiments are required due to the large regions of parameter space to be explored, as there is currently a lack of constraints on the initial conditions. To date, only the surface CO₂ ice distribution has been observed or modelled (e.g., Aharonson et al., 2004; Titov, 2002; Vincendon et al., 2010). While the surface distribution could be used as an initial indicator of where subsurface CO₂ ice is expected, observations of subsurface H₂O ice in the mid-latitudes have proven that the subsurface ice distribution does not necessarily follow the surface ice distribution (Dundas et al., 2018; Feldman et al., 2004). Therefore, the simulations presented in this thesis have been designed to present initial investigations into the distribution and stability of subsurface CO₂ ice. The chosen scenarios cover a variety of situations expected to describe the martian environment, both in the present-day and under different obliquity conditions, with the aim to investigate the research questions outlined in the next section.

1.1 Research Questions

1. What is the impact of adding CO₂ ice physics on the H₂O ice distribution predicted by models that previously only took H₂O physics into account?
2. How do CO₂ ice and H₂O ice interact in the subsurface of Mars?
3. What impact does layering have on the stability of both subsurface H₂O ice and CO₂ ice?
4. How do changes in the orbital obliquity of Mars change the stability of subsurface CO₂ ice?
5. How important are subsurface properties for the distribution of ices?

1.2 Thesis Structure

In Chapter 2, I give an overview of the behaviour of the states of H₂O and CO₂ (vapour, ice, adsorbate and liquid) that exist on Mars, both in the present-day and throughout Mars' history. The chapter also includes a summary of the influence of climatic processes, orbital parameters and geology on H₂O and CO₂, particularly on their ice phases.

In Chapter 3, I outline the details of the subsurface model I developed for this work to simulate the distribution of subsurface H₂O and CO₂ ice, referred to as the MSSM. This chapter includes both the equations used in the MSSM and the reasoning behind their use over other available equations. The chapter also includes a description of the MGCM and the method used to produce the annual atmospheric cycles for the MSSM from the output of the MGCM.

In Chapters 4 to 6, I present the results of this thesis, starting in Chapter 4 with the use of two-ice-layer scenarios under present-day conditions. These results include a discussion about the ability of the MSSM to reproduce similar subsurface H₂O ice results to previous studies, alongside a discussion on how the presence of both ices influences the stability of each other. Alongside the two-ice-layer scenarios, the results

from a series of simulations using different assumptions within the MSSM are also presented.

Chapter 5 continues the investigation into the effects of assumptions in the MSSM on the stability of both ices, as I present a series of investigations exploring how different initial porosities and subsurface structures influence the outputs. This chapter concludes with a series of multiple-ice-layer scenarios, exploring the influence of thin ice-layers on the stability of both CO₂ ice and H₂O ice.

In Chapter 6, the influence of planetary obliquity on subsurface CO₂ ice and H₂O ice is explored. I present a series of simulations at obliquities of 15°, 35° and 45° for the different ice-layer scenarios presented in Chapters 4 and 5. The chapter concludes with a synthesis of the implications of the results presented in Chapters 4 to 6 for subsurface CO₂ ice.

In Chapter 7, I summarise the results of this thesis, including an explanation of how each of the research questions has been answered by the results presented. I also identify several avenues for future research.

2 | Water and Carbon Dioxide on Mars

The presence of ice on Mars, both at the surface and within the subsurface, is well established (e.g., Anderson et al., 1967; Dundas et al., 2018; Hansen, 1999; Kieffer, 1970; Leovy, 1966; Souness et al., 2012; Warren et al., 1990). This ice is either carbon dioxide (CO_2) ice (at the poles or as seasonal frost) or water (H_2O) ice (at the poles, as seasonal frost or buried in the mid-latitudes). Previous work has investigated the surface distribution of both ices and the subsurface distribution of H_2O ice in the present and throughout Mars' history (e.g., Aharonson et al., 2004; Feldman et al., 2004; Leighton and Murray, 1966). These studies show that the conditions during previous geological periods have influenced both the present-day geology and the present-day distribution of both ices.

On Mars, the geologic history has been split into four main periods based on crater counting and changes in global conditions (e.g., Carr, 2007a; Carr and Head, 2010; Tanaka and Kolb, 2001): pre-Noachian (4.5–4.0 Gyr¹), the Noachian (most heavily cratered surfaces; 4.0–3.7 Gyr), the Hesperian (3.7–3.0 Gyr), and the Amazonian (sparsely cratered; 3.0 Gyr–present-day). The three periods also approximately correspond with significant changes in global conditions from the high atmospheric pressures during the Noachian (estimates of up to 5 bar) to the low atmospheric pressures at present (6 mbar; e.g., Head et al., 2003; Mustard et al., 2001; Nakamura and Tajika, 2001; Wordsworth et al., 2013). These changes in atmospheric conditions have been shown to influence the formation and survival of subsurface H_2O ice and will also influence subsurface CO_2 ice. However, this is an area with limited evidence and, therefore, research. The recent discovery of buried CO_2 ice deposits within the South Polar Layered Deposits ('SPLD'; Phillips et al., 2011) renewed interest in the potential for subsurface CO_2 ice and consequently, subsurface CO_2 ice is the focus of this work.

¹kyr, Myr and Gyr are counted in Earth years rather than martian years and smaller timescales are counted in martian years.

The formation and survival of subsurface CO₂ ice is dependent on many factors that are themselves interdependent. Therefore, in order to study subsurface CO₂ ice distribution an initial understanding of the different forms in which H₂O and CO₂ exists across Mars (e.g. vapour, ice, hydrous minerals and carbonates), alongside the factors that influence their formation and distribution (e.g. climate and surface geology), is needed. An overview of the relevant aspects of Mars research is provided in this chapter, starting with a summary of the surface and subsurface geology (Section 2.1), with a more detailed look at the forms, other than ice, of H₂O (Sections 2.1.2 and 2.1.4) and CO₂ (Sections 2.1.3 and 2.1.4) that exist within the subsurface. This leads to an overview of the distribution of surface ices (Section 2.2), subsurface H₂O ice (Section 2.3) and subsurface CO₂ ice (Section 2.4).

The overview of surface and subsurface ices is followed by an overview of the climate (Section 2.6) including an overview of the processes within the planetary boundary layer ('PBL'; Section 2.6.1) as well as the atmospheric CO₂ (Section 2.6.2) and H₂O (Section 2.6.3) cycles. This is followed by an overview of the orbital parameters and their influences on ice distribution (Section 2.7). The final section discusses the evolution of H₂O and CO₂ over Mars' history (Section 2.8). Each of these topics has been summarised because the interactions between them are what result in the behaviour and distribution of the subsurface ices discussed throughout the remainder of this thesis.

2.1 The Surface and Subsurface

Research concerning the surface of Mars is ongoing as there are still many unknowns but as more observations, of different properties and/or increasing resolution, become available more information is revealed and existing knowledge is constrained further. Current knowledge is limited by what can be determined from remote observations or surface observations by landers and rovers. The instruments that make these observations have a variety of vertical resolutions and depths of penetration below the surface (a few centimetres to several kilometres) and data from them can be synthesised to produce an overall picture of the present-day and past geology of the planet (Sections 2.1.1 and 2.8).

Alongside geological materials, volatiles (H_2O and CO_2) are an important component of the surface and subsurface that are of particular interest for this work. When investigating variations in volatile abundance over both short (10s to 100s martian years) and long (kyr to Gyr) timescales, all possible reservoirs for H_2O and CO_2 on Mars need to be accounted for, as some reservoirs are only relevant at either short or long timescales. The work in this thesis focuses on simulating variations over hundreds of martian years and consequently on the reservoirs that exchange volatiles on short timescales, known as the exchangeable reservoirs (discussed across Sections 2.1.2, 2.1.3 and 2.2 to 2.4).

While the reservoirs that only interact at long timescales (kyr–Gyr; non-exchangeable) are not directly relevant for the simulations discussed here, they need to be considered when interpreting observations and when putting the simulation results into historical context. This is particularly the case for simulations of earlier epochs on Mars, when these reservoirs are expected to have formed. The main non-exchangeable reservoirs for H_2O and CO_2 are carbonates, hydrous minerals, and CO_2 clathrate hydrates (Section 2.1.4). Each of these has been observed in some way on Mars and hydrous minerals in particular must be considered when interpreting observations of hydrogen content within the subsurface, as some instruments cannot differentiate between hydrous minerals, adsorbed H_2O and H_2O ice.

The surface (and subsurface) material (geological and ice) also influences the amount of heat adsorbed and conducted through the subsurface, which impacts both subsurface H_2O and CO_2 ice formation and stability. A summary of the main factors that will influence subsurface temperatures and subsurface ice is therefore given in Section 2.1.5.

2.1.1 Surface Geology

For most of Mars, the geology can only be characterised by remote observations which means most of the current knowledge is from properties that can be determined remotely such as elevation, morphology, and gravity (Carr, 2007a). Figure 2.1 shows the topography of Mars (based on Mars Orbiter Laser Altimeter, ‘MOLA’, data; Smith et al., 1999) and the stark difference in elevation between the northern lowlands and

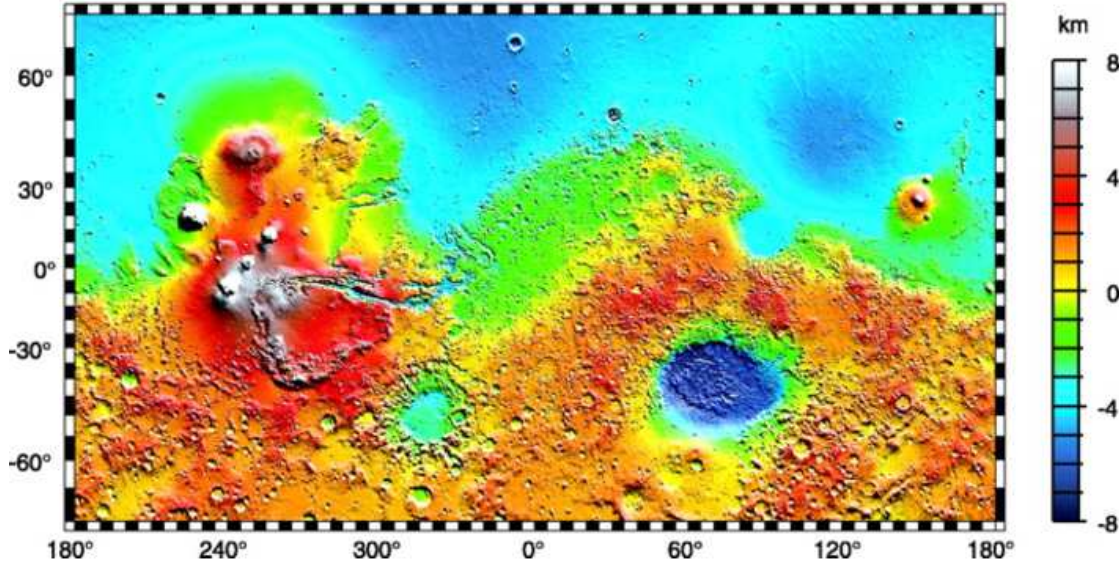


Figure 2.1: The topography of Mars from Mars Orbiter Laser Altimeter (MOLA) observations. Figure from Smith et al. (2001b).

the southern highlands is immediately noticeable. The boundary between these two provinces is mostly transitional across varying distances and can be traced across the surface. In general, this global dichotomy can be summarised by describing the northern regions as sparsely cratered plains underlain by a thin crust, whereas the southern regions are heavily cratered uplands underlain by a thick crust (Carr, 2007b).

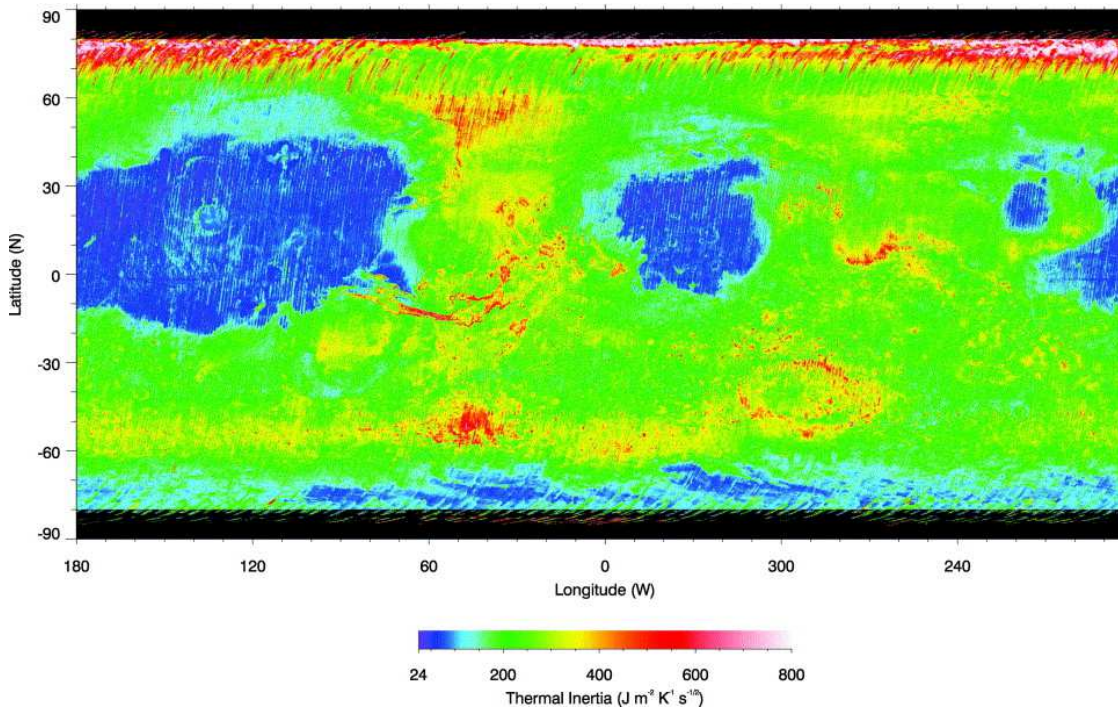


Figure 2.2: Thermal inertia of Mars. Figure from Putzig et al. (2005).

Characterising the geological composition of both provinces requires additional data

sets, such as thermal inertia and albedo observations, to be considered before any characterisations can be made (e.g., Bandfield, 2007; Putzig et al., 2005). Thermal inertia (Equation 2.2 on 18) is an important material property that indicates how quickly a material’s temperature responds to that of its environment (Section 2.1.5.2), while albedo is a material property that indicates how well a surface reflects solar energy (Section 2.1.5.4). Thermal inertia (derived from surface temperature observations by the Thermal Emission Spectrometer, ‘TES’, on Mars Global Surveyor, ‘MGS’) can be used to infer broad-scale surface geological materials on its own. However, each type of material has a large range of thermal inertias. From a map of thermal inertia (Figure 2.2), surfaces can be broadly characterised as either unconsolidated fines (low values); indurated fines or sand-sized particles (intermediate values); and rocks or exposed bedrock or ice (high values). Putzig et al. (2005) then combined this thermal inertia data with albedo data, and split the surface into seven broad thermal inertia-albedo (thermophysical) units (information in Table 2.1 and shown in Figure 2.3).

Table 2.1: The thermal inertia and albedo units derived by Putzig et al. (2005) to characterise the material at the surface of Mars. Data taken from Putzig et al. (2005).

Unit	Thermal Inertia [$\text{J m}^{-2} \text{K}^{-1} \text{s}^{-\frac{1}{2}}$]	Albedo	Interpretation	Percent- age of surface
A	Low (28–135)	High (0.23–0.31)	Surfaces dominated by unconsolidated fines (dust grain sizes $< 40 \mu\text{m}$)	19
B	High (160–355)	Low (0.10–0.19)	Surfaces composed of coarser grained sediments, rocks, bedrock exposures and some duricrust	36
C	High (110–330)	Medium (0.19–0.26)	Surfaces dominated by duricrust with some rocks and/or bedrock exposures	23
D	Low (24 – 170)	Low– medium (0.09–0.24)	Low density mantle or dark dust	2
E	High (140–386)	Very Low (< 0.09)	As B, but little or no fines	0.3
F	Very High (> 386)	All	Rocks, bedrock, duricrust, and polar ice	4
G	Low–high (40–386)	Very high (> 0.23)	As A, thermally thin at higher inertia	0.7

According to these thermophysical units, over half of the surface is covered in units A and B, both of which are interpreted to be composed (at least partially) of sediments with varying grain size and these units may contain enough pore space for ice to form within. However, the regions of unit B are more likely to have surfaces that are a mixture of fines, coarser sand-sized particles, bedrock and ice because high thermal inertia values have non-unique interpretations (Ruff and Christensen, 2002) and only part of this unit will therefore have a subsurface with large enough pores for ice to form within. The possibility of unit B containing unconsolidated sediments is supported by data from the Viking landers and the Pathfinder rover (VL-1, VL-2 and MPF on Figure 2.3), all of which landed within this unit. These ground based observations showed the surface was covered in a fine-textured soil that is compositionally similar to atmospheric dust (Banin, 2005).

Thermal inertia and albedo observations provide information on the grain size and consolidation of the surface geologic material, but do not indicate the composition of this material, which also needs to be considered for subsurface modelling. To determine composition, remote spectral observations (e.g., from the Observatoire pour la Minéralogie, l'Eau, les Glaces et l'Activité, 'OMEGA', on Mars Express, and the Compact Reconnaissance Imaging Spectrometer for Mars, 'CRISM', on Mars Reconnaissance Orbiter, 'MRO') and observations by rovers (e.g. Phoenix, Pathfinder, Opportunity, and Curiosity) are needed (e.g., Banin, 2005; Bell et al., 2000; Bibring et al., 2005; Moore et al., 1982). OMEGA and CRISM observations have revealed that the surface mineralogy is diverse and complex (e.g., Bibring et al., 2005; Ehlmann et al., 2011). These observations have revealed a variety of mafic silicates and hydrated minerals, which indicate magmatic, volcanic and hydrous alteration processes occurred over Mars' history (Ehlmann et al., 2011).

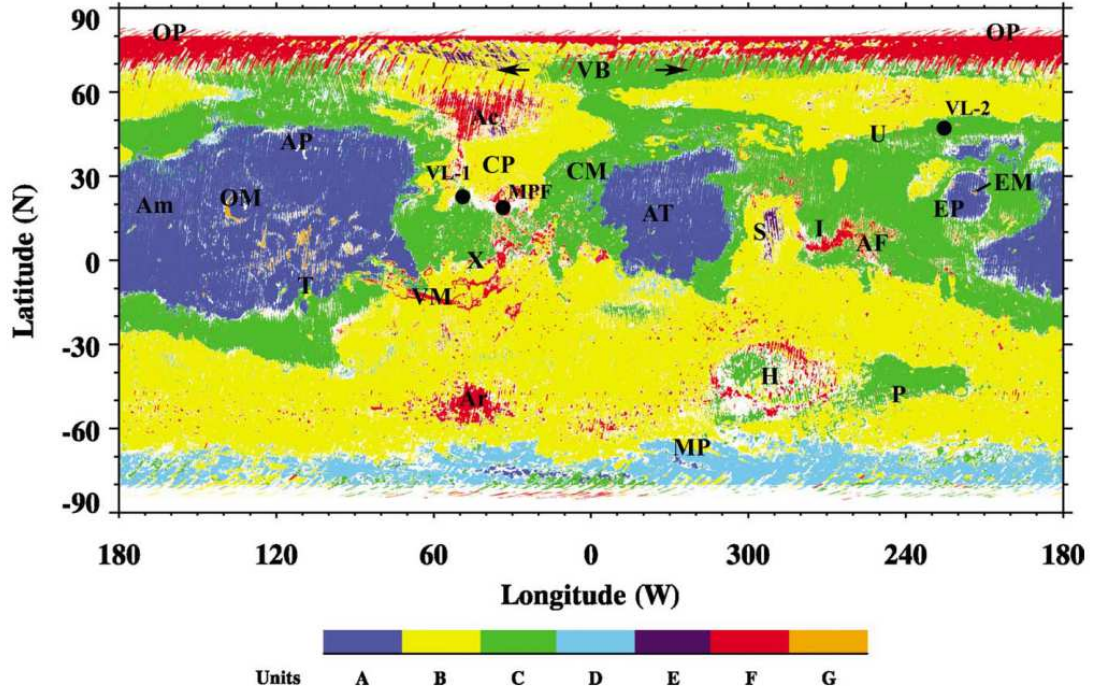


Figure 2.3: Map of the thermal inertia and albedo units derived by Putzig et al. (2005) to characterise the material at the surface of Mars. Lander locations and several key regions for the Putzig et al. (2005) study are noted on the map as follows: VL-1, Viking Lander 1; VL-2, Viking Lander 2; MPF, Mars Pathfinder Lander; Ac, Acidalia; AF, Amenthes Fossae; Am, Amazonis; AP, Alba Patera; Ar, Argyre; AT, Arabia Terra; CP, Chryse Planitia; CM, Cydonia Mensae; EM, Elysium Mons; EP, Elysium Planitia; H, Hellas; I, Isidis; MP, Malea Planum; P, Promethei Terra; OM, Olympus Mons; OP, Olympia Planitia; S, Syrtis Major; T, Tharsis; U, Utopia Planitia; VB, Vastitas Borealis; VM, Valles Marineris; X, Xanthe Terra.

2.1.2 Water in the Subsurface

The exchangeable subsurface reservoir of H_2O is composed primarily of H_2O vapour, H_2O adsorbed onto regolith grains and subsurface H_2O ice (e.g., Farris et al., 2018; Steele et al., 2017a). The phase in which H_2O is present will depend on the subsurface thermal gradient (Section 2.1.5) and local humidity values (Farris et al., 2018; Fischer et al., 2014). H_2O also exists in the form of hydrous minerals where it is chemically bound (observed in Noachian age terrain; e.g., Bibring et al., 2005; Bish et al., 2003; Ehlmann et al., 2011), as CO_2 clathrate hydrates (Section 2.1.4; Buffett, 2000; Kargel et al., 2000) and as liquid H_2O /brines, which have been suggested to form in the deep subsurface and beneath the polar caps (Section 2.5; Clifford and Parker, 2001; Orosei

et al., 2018).

H₂O vapour in the near surface is in diffusive equilibrium with the atmosphere, as long as the subsurface material is porous and responds to changes in the atmospheric H₂O column abundance over short timescales (on the order of hours for the top 1 m of soil; Squyres and Carr, 1986; Williams et al., 2015). This exchange is dependent on the rate of diffusion of vapour through the pore space, which is affected by the presence of ice, the total porosity, and the connected pathways through the pore space (tortuosity; e.g., Bryson et al., 2008; Hudson et al., 2007; Steele et al., 2017a). Vapour diffusion is a key feature of subsurface H₂O models and the theory behind it is discussed in Section 3.3.1.

The vapour pressure within the pore space also responds to changes in the amount of H₂O adsorbed onto regolith grains, which in turn is dependent on the size, composition, and temperature of the regolith material (Fanale and Jakosky, 1982b; Haberle et al., 1994). The regolith material is particularly important for determining the amount of H₂O adsorbed because the adsorptive capacity of clay is significantly higher than the adsorptive capacity of basalt due to its larger specific surface area (e.g., Bryson et al., 2008; Fanale and Cannon, 1971). The absorptive capacity of the martian regolith has been studied many times (discussed further in Section 3.3.2.3; e.g., Böttger et al., 2005; Bryson et al., 2008; Fanale and Cannon, 1971; Pommerol et al., 2009; Zent et al., 1993), showing that adsorption has the largest influence on the diurnal cycle and a smaller influence over long timescales (> tens of martian years; Schorghofer and Aharonson, 2005). The influence of adsorption on the regolith-atmosphere exchange is also dependent on the presence of H₂O ice, since, if present, H₂O ice will be the main control on vapour pressure in the pore space rather than adsorption (Böttger et al., 2005).

2.1.3 Carbon Dioxide in the Subsurface

The exchangeable regolith reservoir of CO₂ is similar to H₂O and comprises CO₂ vapour, CO₂ adsorbed onto regolith grains and CO₂ ice (e.g., Fanale and Cannon, 1974; Phillips et al., 2011). The phase of CO₂ is also dependent on the subsurface thermal gradient and the partial CO₂ vapour pressure. Carbonates (which formed early in

Mars' history when liquid H₂O was available; Bandfield, 2003; Ehlmann et al., 2011; Gooding, 1992) and CO₂ clathrate hydrates (Buffett, 2000; Kargel et al., 2000, see Section 2.1.4) are also expected to have formed from the CO₂ atmosphere. However, these reservoirs are expected to be more stable on short geological timescales and, therefore, are not included in studies of the short-term changes in ice distribution.

While the behaviour of CO₂ within the regolith is similar to that of H₂O, there is much less research on its behaviour: subsurface studies have mainly focussed on subsurface H₂O as this species is more prevalent as ice, easier to observe and has been observed in significant quantities across the planet (e.g., Feldman et al., 2004). Most of the subsurface CO₂ research has focussed on the amount of CO₂ adsorbed in the regolith, since the regolith has been suggested to be a potential reservoir for exchangeable CO₂ that could have stored large amounts when the CO₂ inventory was larger earlier in martian history (Armstrong et al., 2004; Fanale and Jakosky, 1982b; Fanale and Salvail, 1994; Toon et al., 1980). While experiments have shown that large amounts of CO₂ can be adsorbed by the regolith (e.g., Fanale and Cannon, 1971, 1979), later experiments have found that CO₂ molecules spent orders of magnitude longer adsorbed onto the grain surfaces than diffusing through the pore space (Fanale and Jakosky, 1982b). This implies that the exchange between the CO₂ regolith reservoir and the atmosphere is ineffective on seasonal timescales and this has since been supported by observations (Armstrong et al., 2004; Hess et al., 1980; Zent and Quinn, 1995). The seasonal exchange of CO₂ adsorbed in the regolith is also limited by the rate of CO₂ vapour diffusion which is smaller than the diffusion rate of H₂O vapour (Fanale et al., 1982a; Toon et al., 1980). However, while not effective on seasonal timescales, the exchange between the regolith and atmosphere is still expected to be effective on the timescale of an obliquity cycle (10⁵ years) and should therefore be considered as a reservoir for studies over long geological timescales (Fanale and Jakosky, 1982b).

2.1.4 Carbon Dioxide Clathrate Hydrates

Clathrate Hydrates are ice-like solids that have similar structures to pure H₂O ice but the arrangement of H₂O molecules allows for smaller gas molecules to be trapped inside (Buffett, 2000). On Mars, the expected dominant clathrate forming gas is CO₂ (Kargel

et al., 2000). CO₂ clathrate hydrates have the same appearance and spectral signature as H₂O ice, making them difficult to observe remotely (Dobrovolskis and Ingersoll, 1975). There is potential for large amounts to be present in the upper crust and polar deposits (Dobrovolskis and Ingersoll, 1975; Kargel et al., 2000), although the small amount of H₂O in the atmosphere could limit the amount that can form under present atmospheric conditions (Miller and Smythe, 1970).

CO₂ clathrate hydrates form at temperatures around 5 K warmer than CO₂ frost (Ingersoll, 1974; Miller and Smythe, 1970). They can also only exist with either H₂O ice or CO₂ ice present and probably form between layers of pure H₂O ice and pure CO₂ ice (Miller and Smythe, 1970). Some suggested formation mechanisms for CO₂ clathrate hydrate on Mars include: (i) the reaction of permafrost ice with CO₂ vapour; (ii) polar precipitation of H₂O ice reacting with either atmospheric CO₂ vapour or CO₂ ice; (iii) trapping and subsequent burial of atmospheric CO₂ vapour within polar ice deposits that reacts with H₂O ice under pressure; and (iv) direct atmospheric precipitation and accumulation of CO₂ clathrate hydrates from a formerly denser and warmer CO₂ atmosphere (Kargel et al., 2000). While all of these mechanisms are plausible, the existence and amount of CO₂ clathrate hydrates on Mars remains unknown (Titus et al., 2017).

2.1.5 Influences on Subsurface Temperature and Ice Deposition

Surface and subsurface temperatures have been shown to have the largest influence on the stability of H₂O ice. When temperatures are low and atmospheric H₂O vapour partial pressure is equal to or higher than the subsurface saturation vapour pressure of H₂O, subsurface H₂O ice is stable and will not sublime (Chevrier et al., 2007). On the other hand, when temperatures are higher or the atmospheric H₂O partial pressure is lower than the subsurface saturation vapour pressure, H₂O ice will gradually sublime away (Smoluchowski, 1968). Therefore, the main influences on subsurface temperatures need to be understood for subsurface modelling of ices. These include: insolation, radiative heat transfer, geothermal flux, heat conduction into the subsurface, thermal conductivity and thermal inertia variations, albedo variations, the condensation-sublimation cycles of CO₂ and H₂O (Sections 2.2, 2.3 and 2.4), and the

obliquity cycle (Section 2.7). Alongside these factors, it is also important to understand how the presence of either H₂O ice or CO₂ ice will influence subsurface properties and, therefore, their influence on further deposition in that region.

2.1.5.1 Solar Insolation

The amount of solar insolation that reaches the surface varies seasonally, diurnally and latitudinally according to variations in the orbital parameters (Section 2.7; François et al., 1990). The heat adsorbed by the surface is then conducted through the subsurface by radiative heat transfer, which is increasingly damped with depth. The magnitude of this damping is determined by the skin depth, z^* :

$$z^* = \sqrt{\frac{2k}{\omega \rho c_p}}, \quad (2.1)$$

where k is the thermal conductivity [$\text{W m}^{-1} \text{K}^{-1}$], ρ is the density of the regolith [kg m^{-3}], c_p is the specific heat capacity of the regolith [J K^{-1}] and ω is the angular frequency [rad s^{-1}]. Due to the large magnitude of the thermal wave near the surface (where damping is small), variations in the seasonal and diurnal cycles dominate subsurface temperatures. At greater depths, where the thermal wave is mostly damped out, the geothermal heat flux has the largest influence on subsurface temperatures (Section 2.1.5.5; Grott et al., 2007). The seasonal skin depth is around 26 times deeper than the diurnal skin depth, with the diurnal thermal wave damped out after a few centimetres while the seasonal thermal wave is damped out after a few 10s of centimetres (Leighton and Murray, 1966; Schorghofer and Aharonson, 2005). However, it is important to include these cycles in thermal models, because disregarding the seasonal and diurnal cycles in models of the subsurface produces subsurface temperatures that are too high (François et al., 1990).

2.1.5.2 Thermal Inertia

The thermal inertia, I , of the surface has been shown to be one of the main influences on regional H₂O ice distributions (Mellon and Jakosky, 1993), particularly on the

longitudinal variations in H₂O ice stability (Schorghofer and Aharonson, 2005). It is a measure of heat conduction into the subsurface and is calculated by the following equation:

$$I = \sqrt{k \rho c_p} \quad (2.2)$$

These three parameters can also be combined to produce thermal diffusivity, k , a measure of the rate of transfer of heat, and is given by:

$$\kappa = \frac{k}{\rho c_p} \quad (2.3)$$

Although thermal inertia is used more often for characterising surfaces. Of the three parameters, thermal conductivity has the largest range (0.01 to 7 W m⁻¹ K⁻¹; e.g., Grott et al., 2007; Labus and Labus, 2018), and therefore influence, on thermal inertia values (see Section 2.1.5.3 for details). Measured martian thermal inertias range from 30 to 2000 J m⁻² K⁻¹ s^{- $\frac{1}{2}$} (see Figure 2.2; Pilorget et al., 2011; Putzig et al., 2005) depending on the material at the surface, as discussed in Section 2.1.1.

Thermal inertia also has implications for the depth of stability of H₂O ice (Bandfield, 2007). In high thermal inertia regions, the depth to the H₂O ice table should lie deeper and the latitudinal limit closer to the poles than for low thermal inertia regions (Paige, 1992), due to the increased depth of penetration of annual thermal oscillations (Mellon and Jakosky, 1993). As a result, low thermal inertia regions (Figure 2.2) are more favourable for near-surface H₂O ice deposits (Paige, 1992). However, the presence of H₂O ice in these low thermal inertia regions is also dependent on other local surface properties such as albedo and surface slope (Schorghofer and Aharonson, 2005).

2.1.5.3 Thermal Conductivity

Thermal conductivity, k , determines the ability of a material to conduct heat (Hoffman, 2001; Presley and Christensen, 1997a). It varies with material and temperature (e.g. Grott et al., 2007; Mellon and Jakosky, 1993), and has a large influence on the energy balance of a planet. On Mars, large portions of the surface are expected to be covered in a particulate regolith (see Section 2.1.1). The thermal conductivity of these partic-

ulate materials is a function of four components: the conductivity of the solid grains, the solid conductivity at the contact between the grains, the radiative heat transfer between grains through the pores and the interstitial gas conductivity (e.g. Piqueux and Christensen, 2009; Presley and Christensen, 1997a,b). Piqueux and Christensen (2009) showed that the radiative contribution is not significant for most martian surfaces and as a result, this is not included in most thermal models. Consequently, the thermal conductivity increases within increasing atmospheric pressure, particle size and bulk density, and is also dependent on temperature (Presley and Christensen, 1997a,c, 2010).

There is only one martian measurement of thermal conductivity so far, which was taken by the Heat Flow and Physical Properties Package (HP³) instrument on the InSight Lander (Grott et al., 2021). The measurement was taken between depths of 0.03 and 0.37 m, and thermal conductivity was determined to be 0.039 ± 0.002 W m⁻¹ K⁻¹. Using a specific heat capacity of 630 J K⁻¹ kg⁻¹ and the measured soil density (1211 kg m⁻³), Grott et al. (2021) estimated a thermal inertia of 172 J m⁻² K⁻¹ s^{- $\frac{1}{2}$} for this location. This value is consistent with previous thermal inertia measurements (orbital and in-situ) of the landing site (Elysium Planitia), which found thermal inertia to be between 160 and 230 J m⁻² K⁻¹ s^{- $\frac{1}{2}$} , consistent with an unconsolidated regolith (Grott et al., 2021). Soil density at the landing site was also measured (1211 kg m⁻³), indicating a porosity of 0.61, where porosity is the ratio of the volume of pores to the volume of bulk rock. This porosity is also consistent with that of an unconsolidated regolith (Grott et al., 2007, 2021).

Another factor that impacts the thermal conductivity, alongside the geological material, is the presence of H₂O ice within the regolith, which increases the bulk thermal conductivity of the regolith and causes a feedback loop between temperature and the amount of H₂O ice (Paige, 1992; Schorghofer and Forget, 2012; Siegler et al., 2012). The increase in thermal conductivity causes more heat to be conducted deeper and stored during summer, before being released back to the surface during autumn and winter (Paige, 1992; Schorghofer and Forget, 2012). This increased conduction enables H₂O ice to be stable at shallower depths than it would be without the presence of H₂O

ice (e.g. Haberle et al., 2008; Paige, 1992). The increased thermal conductivity also causes higher near-surface winter temperatures and has been shown to reduce CO₂ frost deposition by up to three times the amount that would be deposited if the H₂O ice table is below 1 m (Haberle et al., 2008). This effect is very sensitive to the depth of the H₂O ice layer, and the closer the H₂O ice is to the surface, the less CO₂ ice will be deposited (Schorghofer and Forget, 2012).

2.1.5.4 Albedo

Surface albedo variations have a large impact on surface temperatures (Grott et al., 2007) and, as a result, on the regions of H₂O ice stability (Mellon and Jakosky, 1993; Piqueux et al., 2003). In maps of surface albedo values, regions of high albedo show where H₂O ice is more likely to be stable on the surface (Palluconi and Kieffer, 1981). The surface albedo value therefore influences the geographic boundary of the polar caps and the depth of stability for subsurface ice at all latitudes (Schorghofer and Aharonson, 2005). Lower albedo regions are likely to have a deeper ice table (Bandfield, 2007) and the limit of surface ice stability will be at higher latitudes (Mellon and Jakosky, 1993). While these studies focused on the effects of albedo on subsurface H₂O ice, albedo will have a similar effect on subsurface CO₂ ice.

The high surface albedos are often the result of ice at the surface and variations in ice albedo will also impact the stability of ice. The albedo of the polar caps varies between hemispheres due to the higher dust content of the northern cap during ice formation. This is because the northern cap forms during the time of year when martian dust storms occur (François et al., 1990). Alongside this, the albedo varies within each polar cap and is much brighter within the central region of both polar caps than along the edges (Wood and Griffiths, 2009). The albedo is also impacted by the type of CO₂ ice deposition (either as a translucent slab or snow; e.g., Haberle et al., 1994; Kieffer et al., 2006; Soto et al., 2011). Translucent slab ice has the same low albedo as the underlying regolith (around 0.2), which warms and sublimates the ice from the base and is observed in the southern polar cap (Kieffer et al., 2006). CO₂ snow, on the other hand, has a much higher albedo (ranges from 0.60 to 0.75; Haberle et al., 1994; Mellon and Jakosky,

1993; Soto et al., 2011), causing lower surface and atmospheric temperatures. The lower temperatures enhance the likelihood of condensation, resulting in more ice formation (Jakosky and Carr, 1985b).

2.1.5.5 Geothermal Flux

Geothermal flux, F , is an important parameter for subsurface thermal models because, along with the thermal conductivity, it determines the geothermal gradient, $\frac{\partial T}{\partial z}$, according to Fourier’s law of heat conduction (e.g., Beardsmore and Cull, 2001; Turcotte and Schubert, 2002):

$$F = k \frac{\partial T}{\partial z} \quad (2.4)$$

The geothermal gradient influences the depth at which ice deposition ceases (Mellon and Jakosky, 1993; Wood, 2011). A lower geothermal gradient is produced by a higher thermal conductivity, such as that produced by the presence of H₂O ice in regolith (Mellon and Jakosky, 1993). This increases the depth of the lower ice deposition boundary, increasing the amount of ice that can form within the subsurface (Hoffman, 2001; Mellon and Jakosky, 1993).

Across the surface of Mars, geothermal heat flux is expected to be relatively homogeneous (Grott et al., 2012). However, its value is not well constrained and the values used in models vary greatly. Subsurface studies often use estimated values for the geothermal heat flux from various models of planetary heat evolution (e.g. Dehant et al., 2012). Dehant et al. (2012) presented a summary of heat flow models for Mars, showing that these models suggest a range of 5-50 mW m⁻² and the value depends on the method used to derive the heat flow estimate. Within this range, geographical variations from 17 to 37 mW m⁻² are expected due to factors such as the enrichment of radioactive elements and crustal thickness (e.g., Grott and Breuer, 2010; Neumann et al., 2004; Taylor et al., 2006; Zuber et al., 2000). However, in general estimates of average geothermal flux around 30 mW m⁻² have been used (e.g. Plesa et al., 2016; Soto et al., 2015) and this value is the best estimate until a measurement of geothermal heat flux is made.

2.2 Surface Ice

Surface H_2O and CO_2 ice play a major role in the diurnal, seasonal and annual cycling of both volatiles (e.g., Mischna et al., 2003; Titus et al., 2017). In the present-day, they are found in the polar ice caps (see Section 2.2.1), as seasonal surface frost across the mid-latitudes on pole-facing slopes (see Section 2.2.2) and in the highest altitude regions of Tharsis (Titus et al., 2017).

The accumulation of surface ice is dependent on solar insolation, topography and the thermal inertia of the underlying subsurface (Blackburn et al., 2010; Mischna et al., 2003). H_2O ice is preferentially found in regions with high altitude or high thermal inertia due to the lower surface temperatures (Mischna et al., 2003). However, while CO_2 ice is also preferentially found in regions of high thermal inertia, at high altitudes the decrease in pressure causes a corresponding decrease in the frost point temperature (Vincendon et al., 2010). Another difference is that H_2O ice forms on the surface earlier than CO_2 ice due to its higher frost point temperature ($\sim 195\text{ K}$ for H_2O and $\sim 145\text{ K}$ for CO_2 at average martian pressures; Hardy, 1998; Kasting, 1991) and when temperatures have cooled enough for CO_2 ice to form the atmosphere is generally depleted in H_2O vapour (Leighton and Murray, 1966). The reverse is also the case, as H_2O ice will remain at a surface until all of the overlying CO_2 ice has sublimated away.

Observations have revealed mid-latitude and tropical surface features, such as Lobate Debris Aprons (LDAs) and glacial-related landforms (see Section 2.3.3), that are indicative of long-term (10–100s Myr) stability of surface H_2O ice in the past (e.g., Fastook et al., 2008; Forget et al., 2006; Levrard et al., 2004; Madeleine et al., 2009; Steele et al., 2018). For H_2O ice to be stable at these latitudes, the past climate would have had to be significantly different from that of the present-day, where H_2O ice preferentially deposits at the poles (Chamberlain and Boynton, 2007). Changes in solar insolation distribution and climate caused by variations in orbital parameters have been found to allow H_2O ice to deposit at these lower latitudes (Sections 2.7 and 2.8; e.g., Jakosky, 1985a; Mischna et al., 2003; Richardson and Wilson, 2002).

2.2.1 Polar Caps

In both polar regions, a perennial ice cap underlies the seasonal ice cap that forms each winter and sublimates each summer (e.g., Haberle et al., 2008; Hansen, 1999). The seasonal cap at both poles is mainly composed of CO_2 ice, with small amounts of H_2O ice, and around 30% of the atmospheric CO_2 inventory is condensed to form these seasonal caps each year (Forget et al., 1998).

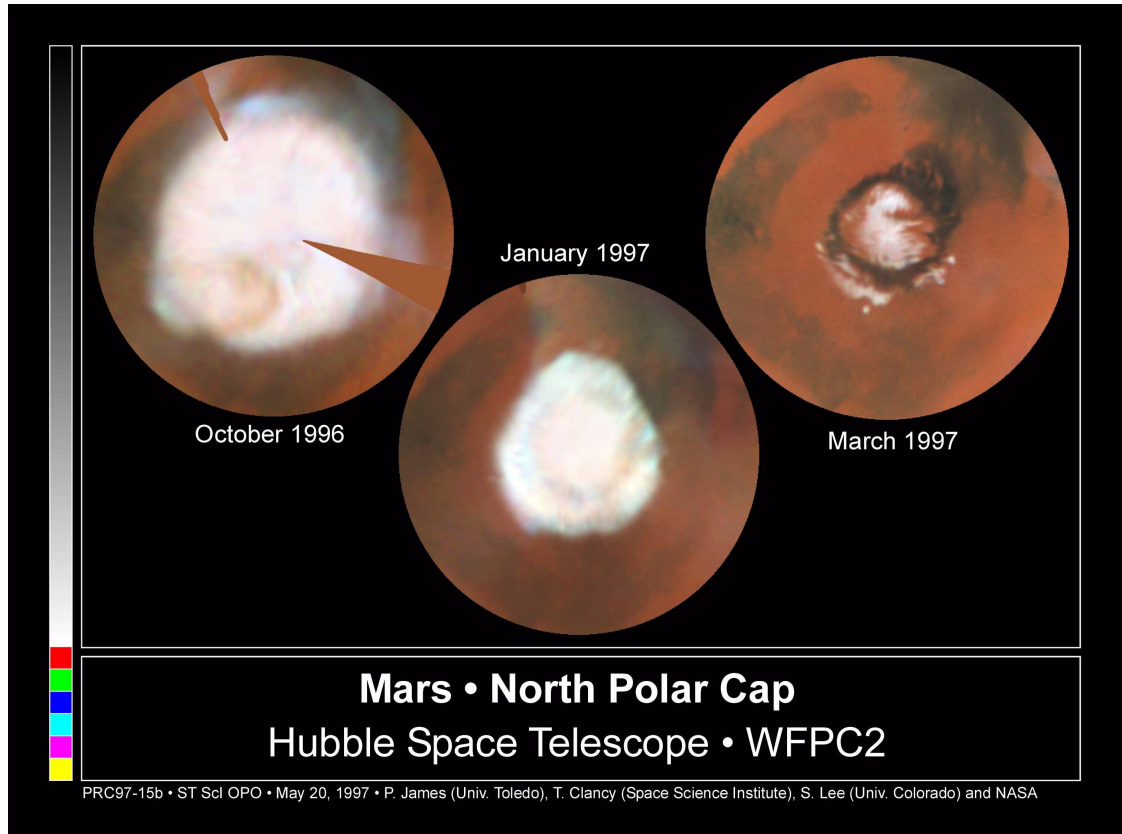


Figure 2.4: Seasonal changes in the North Polar Ice Cap. Credit: JPL/NASA/STScI (1998)

The perennial caps, however, have different compositions in each hemisphere. The northern perennial cap is composed of mostly H_2O ice, whereas the southern perennial cap contains a thin layer of CO_2 ice overlying a layer of H_2O ice (Bibring et al., 2004; Bierson et al., 2016; Thomas et al., 2000). The southern polar cap has a permanent CO_2 ice cap due to the asymmetrical global circulation throughout the martian year (Aharonson et al., 2004; Schorghofer and Edgett, 2006). This is dependent on the eccentricity and the longitude of perihelion, both of which have the largest affect at moderate obliquities ($\sim 25^\circ$) such as at present (Toon et al., 1980), implying that the

northern pole would have had a perennial CO₂ ice cap at some point in Mars' history (Toon et al., 1980).

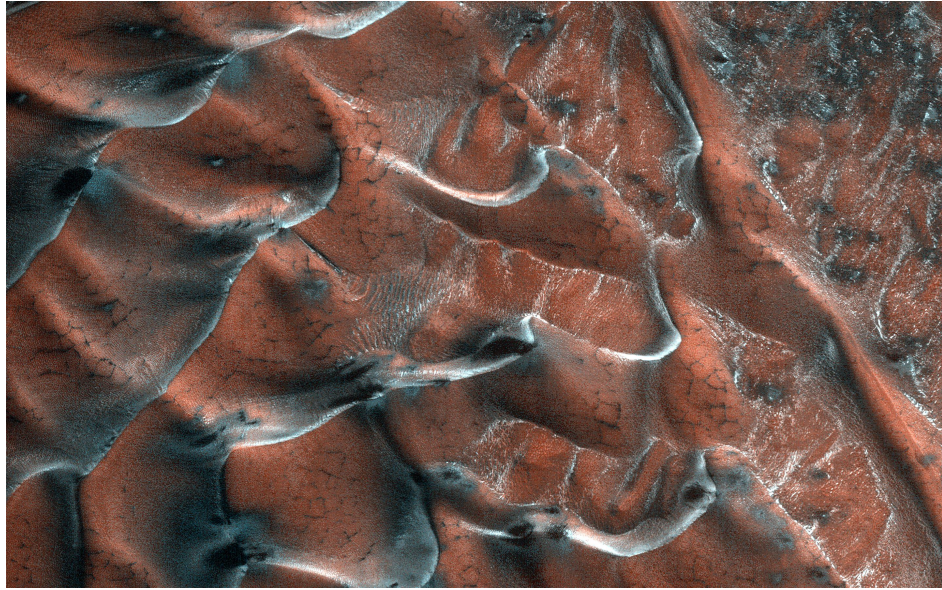
During summer, when the overlying seasonal cap has sublimated away, the perennial caps also start to sublimate and around 0.4 m of CO₂ ice is lost from the southern perennial cap each year (Blackburn et al., 2010). In the northern polar cap, however, the amount of H₂O ice that sublimates (and is transported away from the pole as vapour) during summer is returned to the pole through various transport mechanisms and is redeposited in winter, forming the observed nearly closed H₂O cycle (Forget et al., 2017; Titov, 2002). Both perennial caps also form the top layer of a series of layered deposits (the polar layered deposits, PLD), composed predominantly of H₂O ice, from previous cycles of accumulation and sublimation that occurred throughout Mars history (see Section 2.3.4).

2.2.2 Seasonal Frost

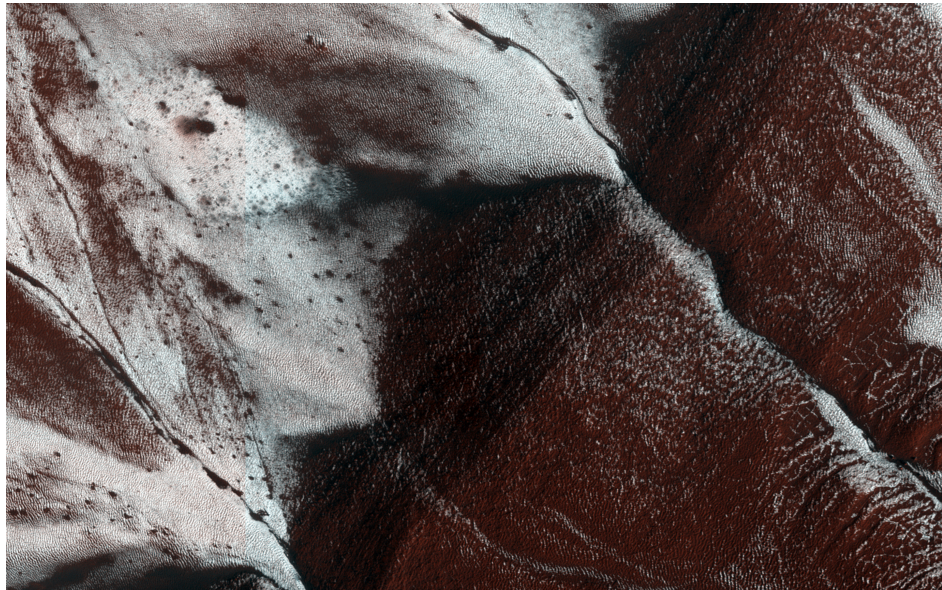
Both H₂O and CO₂ frost have been observed during winter in both hemispheres spanning the poles to the mid-latitudes. In the polar regions, frost forms the seasonal polar caps discussed in the previous section and the thickness of this frost cover decreases with decreasing latitude (Aharonson et al., 2004).

Outside of the polar regions, both types of frost are found either on or near pole-facing slopes during winter. This occurs because these slopes remain shadowed for longer than the surrounding surfaces and temperatures remain lower as a result (Carrozzo et al., 2009; Schorghofer and Edgett, 2006). H₂O frost is more widespread than CO₂ frost because of its higher frost point temperature (Hardy, 1998; Kasting, 1991) and has consequently been observed at lower latitudes. CO₂ frost has only been observed to 38°S (Schorghofer and Edgett, 2006), whereas H₂O frost has been observed down to 15°S (Carrozzo et al., 2009; Schorghofer and Edgett, 2006; Vincendon et al., 2010). In the mid-latitudes, simulations found that buried subsurface H₂O ice (below a dry regolith cover) was needed for CO₂ frost to form on pole-facing slopes as found in observations (Vincendon et al., 2009)

Night-time frost has also been observed by the Opportunity Rover at 2°S, further



(a)



(b)

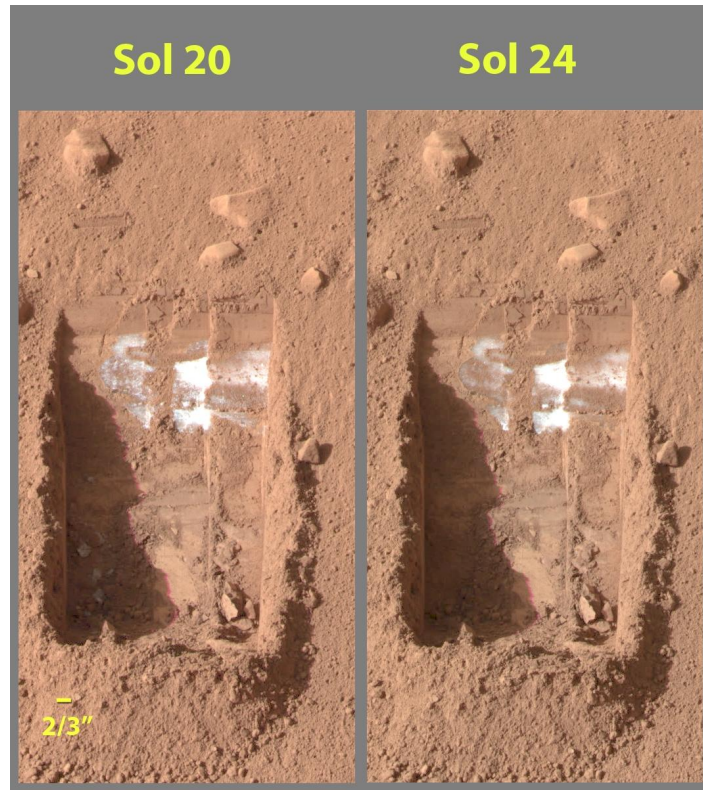
Figure 2.5: Examples of surface frost on (a) sandy dunes in the northern plains and (b) on gullies on a south facing slope within a crater. Credit: (a) NASA/JPL-Caltech/University of Arizona (2021) (b) NASA/JPL-Caltech/University of Arizona (2014).

equatorward than remote observations suggest (Schorghofer and Edgett, 2006). This is because remote observations require reflected light to observe frost which is not available at night (Piqueux et al., 2016). Night-time CO₂ frost has also been inferred from surface temperature observations and it has been suggested that the CO₂ ice crystals form optically thin layers which are not visible in images (Piqueux et al., 2016).

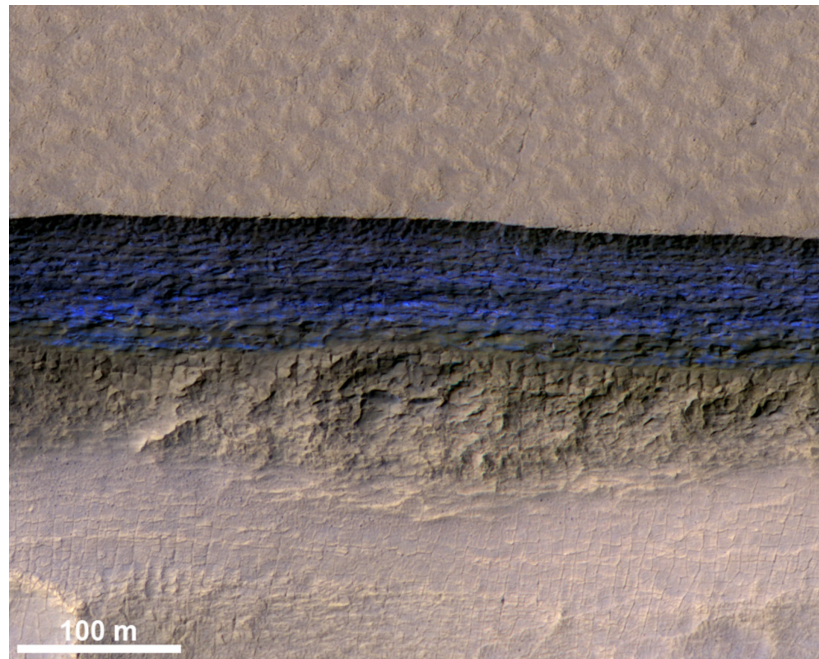
Seasonal frosts are an important consideration for subsurface ice modelling because their presence slows the loss of any underlying subsurface ice by providing a near-surface source of vapour and has been shown to result in shallower ice table depths (Williams et al., 2015). Therefore, surface frost, of both ice types, is likely to impact the persistence of any subsurface ice of the same type.

2.3 Subsurface Water Ice

Subsurface H₂O ice has been predicted (e.g., Leighton and Murray, 1966) and observed (in images, see Figure 2.6 for some examples, and as hydrogen by spectrometers; e.g., Dundas and Byrne, 2010; Feldman et al., 2004; Smith et al., 2009) in the polar and mid-latitude regions. It is found near the surface at high latitudes and the H₂O ice table increases in depth with decreasing latitude (Bandfield, 2007; Squyres et al., 1992). The observed latitudinal distribution of H₂O ice is sensitive to variations in topography (Aharonson and Schorghofer, 2006), surface heterogeneities (such as surface rocks; Sizemore and Mellon, 2006), changes in the global distribution of atmospheric H₂O vapour concentration (Chamberlain and Boynton, 2007) and obliquity variations (discussed in more detail in Section 2.7.1; Fanale et al., 1986; Mellon and Jakosky, 1993). All of these factors increase or decrease the latitudinal limit of H₂O ice stability at different longitudes and comparisons have shown that the modelled effects correspond to the observed effects of these factors (e.g., Bandfield, 2007; Bandfield and Feldman, 2008; Feldman et al., 2004). The stability of H₂O ice is also sensitive to the presence of H₂O ice in the subsurface, as the high thermal conductivity of ice-rich soil results in heat being transported away from the surface and extends the region of ice stability towards the surface (Paige, 1992).



(a)



(b)

Figure 2.6: Observations of subsurface H_2O ice. (a) H_2O ice observed in the trenches dug by Phoenix, (b) Exposed subsurface ice sheet (blue) on a scarp. Credit: (a) NASA/JPL - Caltech/University of Arizona/Texas A&M University (2008) (b) Dundas et al. (2018).

Subsurface H₂O ice can be emplaced by one of two methods (Schorghofer and Forget, 2012) and the type of subsurface ice (pore-filling or excess) can be used to infer which method led to the deposition of the ice (Bramson et al., 2015). Pore ice forms by direct deposition from the vapour phase within the available pore space, whereas excess ice forms from snowfall or direct deposition on the surface forming a layer on the surface that is later buried. Burial of an ice layer can occur either by dust deposition from a change in climatic conditions or by the retreat of ice leaving a protective sublimation lag layer of dust (Schorghofer and Forget, 2012). Pore ice that sublimates can reform due to recharge from atmospheric H₂O vapour, although excess ice that has sublimated is unlikely to be recharged by the atmosphere (Bramson et al., 2015). This is because it is difficult to produce ice volumes that exceed the regolith pore space from vapour diffusion alone (Dundas and Byrne, 2010; Fisher, 2005; Kreslavsky and Head, 2000).

The time that subsurface H₂O ice can survive is dependent on both subsurface temperatures (Section 2.1.5) and on the thickness of the overlying regolith layer, which drastically reduces the rate of sublimation (see Section 3.3.1; e.g., Boynton et al., 2002; Chevrier et al., 2007; Feldman et al., 2004; Hudson et al., 2007). Laboratory experiments and numerical simulations have shown that a 1 m layer of H₂O ice can survive around 800 martian years under a 1 m layer of regolith and up to 400 kyr under a 2 m layer of regolith at 235 K (e.g., Bryson et al., 2008; Chevrier et al., 2007, 2008; Jakosky et al., 2005).

2.3.1 Observations of Water Ice Distribution

Observations from the Mars Odyssey Neutron Spectrometer (MONS) instrument are sensitive to the abundance of hydrogen in the upper metre of the subsurface and vary non-linearly with ice fraction (Aharonson and Schorghofer, 2006; Bandfield and Feldman, 2008; Feldman et al., 2004). Feldman et al. (2004) used this technique to determine a lower limit for the global inventory of water equivalent hydrogen (WEH) within the upper metre of the subsurface, which is shown in Figure 2.7. Their results showed the expected hydrogen-rich deposits (20–100%) at high latitudes where the polar caps are observed and also significant deposits (2–10%) in the mid-latitudes (discussed further in Section 2.3.3). From these observations, they estimate that the lower limit of

the global inventory (for the upper metre of the subsurface) is equivalent to a global H_2O layer 14 cm thick. This is a lower limit because the presence of an overlying dessicated layer can mask an underlying H_2O -rich layer (Feldman et al., 2004).

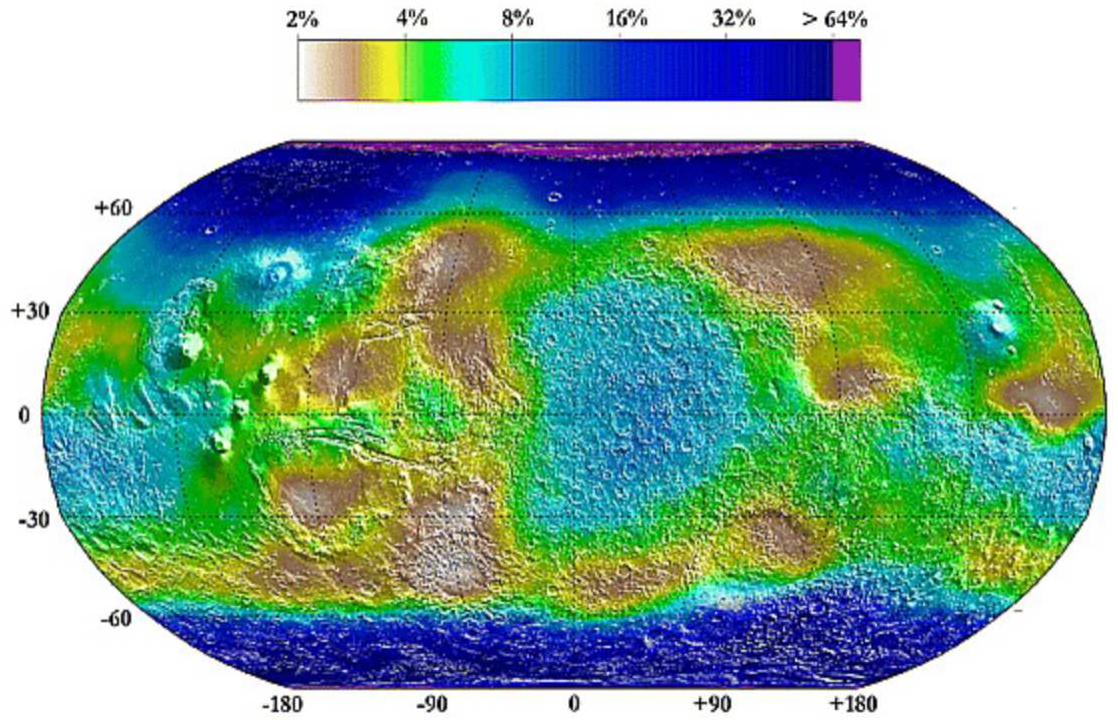


Figure 2.7: Water equivalent hydrogen (WEH) content of H_2O bearing soils derived from Mars Odyssey Neutron Spectrometer (MONS) data. Figure from Feldman et al. (2004).

The permafrost depths derived from the MONS data are consistent with depths derived from TES surface temperature data at high latitudes (Bandfield and Feldman, 2008) and with the high Hydrogen concentrations found in Mars Odyssey Gamma Ray Spectrometer (GRS) detections (e.g., Bandfield, 2007; Boynton et al., 2002; Levrard et al., 2004). The GRS detections showed that H_2O ice is insulated by several centimetres of ground cover that decreases in thickness towards the pole (Bandfield, 2007; Boynton et al., 2002). Subsurface H_2O ice concentrations are also estimated to increase towards the pole (from 70% at 60° latitude to 100% near the poles; Levrard et al., 2004). At these concentrations, ice volume is greater than the available pore space, implying that at least some of the ice is excess ice (Levrard et al., 2004). This has been confirmed in observations by the Phoenix lander, which found both pore ice and excess ice confirming the suggestion that the ground ice detected by Mars Odyssey

is in diffusive equilibrium with the atmosphere (Cull et al., 2010; Mellon and Feldman, 2006; Mellon et al., 2009). The presence of an insulating ground cover layer over a H₂O ice-filled layer has been confirmed by multiple observations, including observations from the High Energy Neutron Detector (HEND) instrument on Mars Odyssey (Mitrofanov et al., 2003) and ice-related features in images from the High Resolution Imaging Science Experiment (HiRISE) on MRO (e.g., Byrne et al., 2009; Dundas et al., 2018; Schon et al., 2009; Viola et al., 2015).

2.3.2 Simulations of Water Ice Distribution

Alongside observations, many numerical simulation studies have predicted present-day or long term subsurface H₂O ice distribution and many different subsurface models have been developed to do this, each incorporating different features of the subsurface according to the purpose of the model. From these simulations, a lower latitudinal limit of 49° (for flat ground) and $\sim 25^\circ$ (for slopes of 30°) for permanent subsurface H₂O ice has been suggested (Schorghofer and Aharonson, 2005; Schorghofer and Edgett, 2006). These limits are consistent with the observed zonally averaged boundaries from Feldman et al. (2004) and correspond with the locations that require subsurface H₂O ice below 1 m to match surface CO₂ frost observations (Vincendon et al., 2010).

Thermal and vapour diffusion models are the main method used to investigate subsurface H₂O ice (e.g., Fanale et al., 1986; Mellon and Jakosky, 1993; Paige, 1992; Schorghofer and Aharonson, 2005) and some have been coupled to GCMs to simulate global changes (e.g., Böttger et al., 2005; Guo et al., 2009; Richardson et al., 2003; Steele et al., 2017a; Wilson and Smith, 2006). The thermal schemes in these models are capable of resolving diurnal and seasonal temperature changes, due to variations in solar insolation, heat conduction and orbital parameters (see Section 2.1.5; e.g., Aharonson and Schorghofer, 2006; Grott et al., 2007; Hapke, 1996; Leighton and Murray, 1966). Many subsurface models also include a vapour diffusion scheme to investigate the stability and evolution of subsurface H₂O ice, alongside the increase in thermal conductivity caused by the presence of H₂O ice (e.g., Fisher, 2005; Mellon and Jakosky, 1993; Paige, 1992; Vincendon et al., 2010). These thermal and vapour diffusion models only simulate pore ice deposition since ice deposition by vapour diffusion

(with no other processes occurring) cannot exceed pore volume, and excess ice can, therefore, only be incorporated into these models as an initial condition (Fisher, 2005; Schorghofer, 2007).

Models that simulate both pore ice and excess ice suggest that the near-surface H₂O ice in the mid-latitudes is mostly pore ice, whereas at high latitudes, there is a three layered depth distribution (a dry layer over a pore ice layer over a zone of excess ice; Schorghofer, 2007). The suggestion of only pore ice in the mid-latitudes implies that the estimates of the latitudinal limits of the near-surface H₂O ice already discussed are unlikely to be impacted by the addition of excess ice into the models. At high latitudes, however, excess ice should be considered when investigating the stability of subsurface ices. In these high latitudes, the excess ice is likely the remanent of an ice sheet that has since been buried either by deposition of an overlying ice layer or by the formation of an overlying dust lag deposit that forms as the ice sheet sublimates away (Schorghofer, 2007, 2010; Schorghofer and Forget, 2012).

2.3.3 Mid-latitude Water Ice

In the mid-latitudes (30° to 60° N/S) observations show the subsurface contains 2% to 10% WEH (Feldman et al., 2004). Further observations have shown the existence of a thick, ice-rich layer (or layers) that drapes the existing topography and has a protective cover of ice-free regolith. This layer becomes thinner at lower latitudes and is known as the Latitude Dependent Mantle (‘LDM’; e.g., Byrne et al., 2009; Dundas et al., 2018; Mustard et al., 2001). It covers more than 23% of Mars’ surface (Holt et al., 2008) and is estimated to be at least metres thick with a high ice content (Conway and Balme, 2014; Dundas et al., 2018; Kreslavsky and Head, 2002). The LDM is proposed to be the remnant of an extensive ice sheet that formed during a previous high obliquity epoch, when ice was stable in the mid-latitudes, and that has since been buried and protected from sublimation by either a sublimation lag or dust cover (e.g Forget et al., 2006; Head et al., 2003; Holt et al., 2008; Mischna et al., 2003; Mustard et al., 2001).

Alongside the buried H₂O ice sheet, features similar to debris-covered glaciers on Earth (known as Lobate Debris Apron, ‘LDAs’, on Mars; Figure 2.8) and other viscous flow features (that have a core of H₂O ice) have been observed (Holt et al., 2008;



Figure 2.8: Image of a martian glacier from HiRISE data. Credit: Grindrod and NASA/JPL-Caltech/University of Arizona/USGS) (2018)

Karlsson et al., 2015; Levy et al., 2014; Plaut et al., 2009; Souness et al., 2012). The observed LDAs consist of multiple lobate flows and are remnants of glaciers that existed at higher obliquities that have been protected from sublimation by overlying debris cover (Brough et al., 2019; Dickson et al., 2008). Other surface features such as eskers (Gallagher and Balme, 2015) and fan shaped deposits (Kadish et al., 2014) in equatorial regions are indicative of glacial flow. These features occur in locations with existing glaciers and in locations with evidence of past glaciers that have since sublimated away, providing further evidence of H_2O ice accumulation closer to the equator in the past (Head and Marchant, 2003; Kadish et al., 2014; Shean et al., 2007).

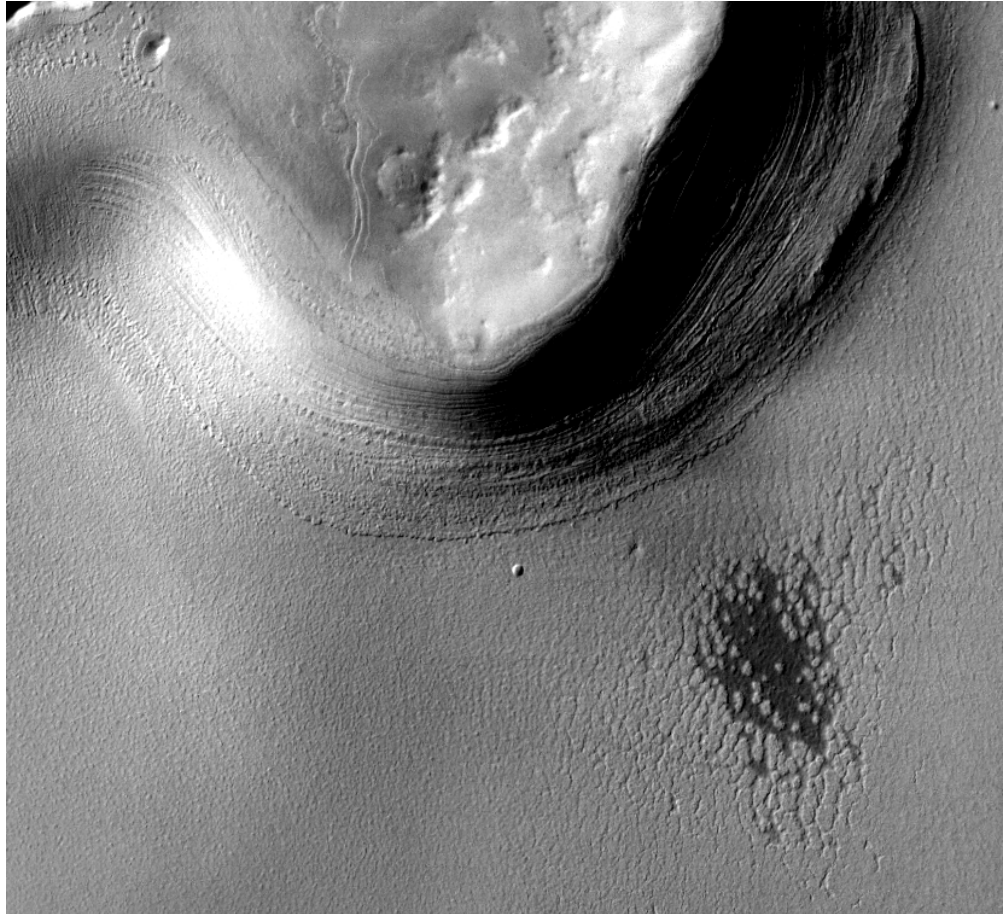
2.3.4 Polar Layered Deposits

The seasonal and perennial polar caps (see Section 2.2.1) form the upper layer of deposits at each pole known as the polar layered deposits (PLD), which are the largest known ice reservoirs on Mars (e.g., Kreslavsky and Head, 2002; Levrard et al., 2007). The exact composition of the layers is not known, but observations show the layers are spatially distinct (at the resolution of HiRISE: 30 cm) and composed of different mixtures of H_2O ice and dust (Lasue et al., 2012). Results from the Shallow Radar (SHARAD) instrument have shown that the North Polar Layered Deposits (NPLD) have a volume fraction of dust around 2%, while the SPLD contain around 10%

(Phillips et al., 2008).



(a)



(b)

Figure 2.9: Images of the (a) North and (b) South Polar Layered Deposits. Credit: (a) NASA/JPL-Caltech/University of Arizona) (2014) and (b) NASA/JPL-CaltechNASA/JPL-Caltech) (2003)

The layering in the PLD is due to variations in orbital parameters altering the latitudes where H₂O ice preferentially deposits on timescales of tens to hundreds of thousands of years (Laskar et al., 2002; Milkovich, 2005; Mischna et al., 2003). The dust content of each layer is also influenced by variations in obliquity since H₂O ice sublimates more during summer at high obliquities, leaving a dust lag and at low obliquities, polar deposition of dust increases, resulting in dust-rich ice layers. Hvidberg et al. (2012) showed this by modelling accumulation of the NPLD using a combination of the insolation record (based on obliquity variations) and these two mechanisms for producing dust-rich layers. Their model produced simulated NPLD with a similar thickness to the observed thickness reported in Phillips et al. (2008) and suggested that formation began 4.2 Ma, corresponding to the age found from LMD-UK Mars global circulation model (MGCM) simulations by Levrard et al. (2007).

The SPLD were formed by the same mechanisms as the NPLD, but the surface of the SPLD is around 2 orders of magnitude older (around 10 Ma) than the NPLD (around 100 ka). Herkenhoff (2000) found that modelled resurfacing rates are 20 times larger in the NPLD compared with the SPLD. From these values, they suggest that the NPLD have been a recent active site for deposition and erosion, whereas the SPLD are expected to have been relatively stable over the last 10 Myr, explaining the difference in their surface ages. Another difference between the NPLD and the SPLD is the recent discovery of CO₂ ice deposits within the SPLD by the SHARAD instrument (Bierson et al., 2016; Manning et al., 2019; Phillips et al., 2011), which is discussed in more detail in Section 2.4.1.

2.4 Subsurface Carbon Dioxide Ice

The existence of subsurface CO₂ ice on present-day Mars has been suggested and debated for many years. CO₂ ice has been considered to be largely non-existent in the near subsurface (e.g., Leighton and Murray, 1966; Mellon, 1996; Tanaka et al., 2001; Ward et al., 1974b) and only expected to be feasible for a CO₂ ice layer completely sealed from the atmosphere by a H₂O ice layer for many years (Ingersoll, 1974; Kargel et al., 2000). In this scenario, CO₂ ice has no influence on surface processes but would have provided a sink for large amounts of CO₂ (Ingersoll, 1974). Observations of the

SPLD have revealed three buried CO₂ ice layers in larger quantities than were thought to be able to remain following obliquity changes (Bierson et al., 2016; Phillips et al., 2011). These deposits and their implications are discussed in detail in the following section.

The presence of subsurface CO₂ ice has also been proposed to have acted as a fluidising agent for the observed debris flows at the edge of the northern plains and for gully formation (e.g., Pilorget and Forget, 2015; Tanaka et al., 2001). This is because CO₂ ice is more volatile than H₂O ice so debris-rich gas buoyancy flows would form more easily and be more energetic if caused by the melting or sublimation of CO₂ ice compared with H₂O ice. Flow of material due to CO₂ ice has also been considered in the context of glaciers and some studies have investigated both glacier-like flow of CO₂ ice and the existence of CO₂ glaciers (e.g., Clark and Mullin, 1976; Smith et al., 2016). These studies ran experiments under martian temperatures and pressures, predicting that CO₂ ice will flow more easily than H₂O ice, especially on the steep flanking slopes of the SPLD topographic basin (Clark and Mullin, 1976; Cross et al., 2020; Nye et al., 2000). Smith et al. (2016) compared observations of the SPLD with simulations of CO₂ glaciers, finding that their simulations provided a plausible scenario for the observed topography. Further evidence for the flow of CO₂ ice includes a series of narrow ridges with lobate planforms on steep west- and northwest-facing slopes of the NPLD that have been suggested to be drop moraines from a CO₂ glacier (Kreslavsky and Head, 2010, 2011).

2.4.1 Carbon Dioxide Ice in the South Polar Layered Deposits

Deposits of buried CO₂ ice were revealed by observations from the MRO SHARAD instrument (Bierson et al., 2016; Phillips et al., 2011). From analyses of these observations, the volume of the CO₂ ice deposits were estimated to be 7700 kg m⁻³ and an extrapolation towards the pole implies that there is 14,800 kg m⁻³ of CO₂ ice across the entire region (Bierson et al., 2016). This extrapolation implies that there is enough buried CO₂ ice within the SPLD to more than double the current atmospheric CO₂ inventory (Bierson et al., 2016).

The regions containing buried CO₂ ice are all sheltered regions of the SPLD and

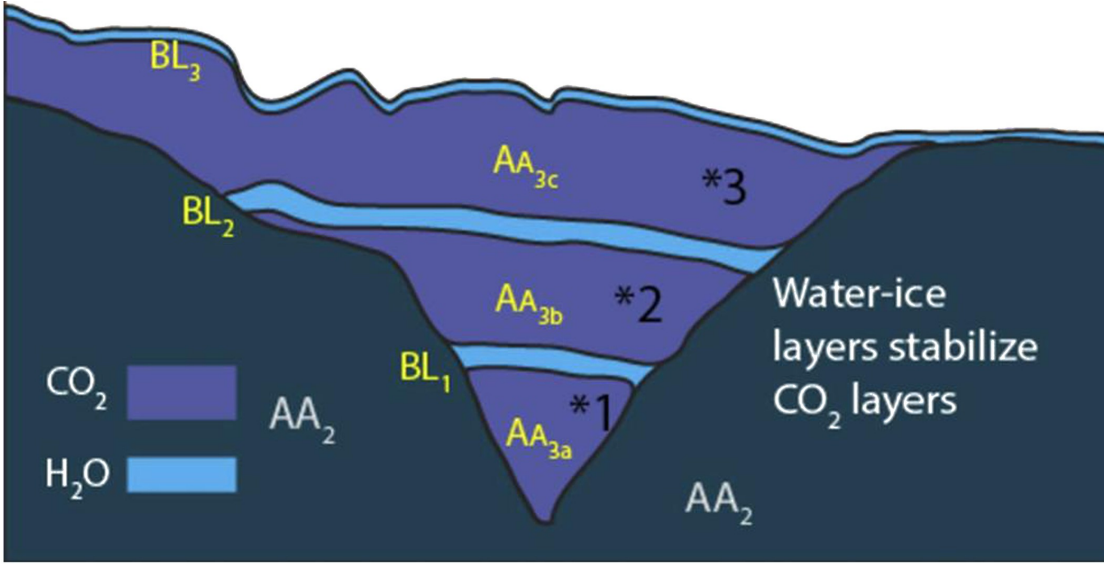


Figure 2.10: A cartoon profile of the CO₂ ice layers within the SPLD. BL refers to the boundary layer number and AA refers to the stratigraphical layers discussed in Bierson et al. (2016). Figure is from Bierson et al. (2016).

amount to around 10% of the SPLD surface area. This suggests that in more exposed regions, CO₂ ice will sublime when obliquity rises (Manning et al., 2019). In their analysis of the SHARAD data, Bierson et al. (2016) observed three distinct CO₂ ice units (Figure 2.10), each capped by a thin, 10–60 m bounding layer of mostly H₂O ice. Simulations of the formation of the SPLD suggest that the three units would have formed during three separate periods and that an overlying H₂O ice layer of 15 to 60 m is sufficient to reduce the sublimation rate of the underlying CO₂ ice layer to near-zero values (Bierson et al., 2016).

For the CO₂ ice deposits to persist, their formation must be followed by the deposition of an insulating layer of porous H₂O ice which can seal in the CO₂ ice (Buhler et al., 2019; Manning et al., 2019). There are currently two main hypotheses for the formation of a H₂O ice layer overlying a CO₂ ice layer proposed by Buhler et al. (2019) and Manning et al. (2019).

The Buhler et al. (2019) hypothesis suggests that H₂O ice and CO₂ ice are simultaneously deposited at low obliquities. Then as obliquity increases and polar temperatures rise, CO₂ ice will sublime away, leaving a H₂O ice lag deposit behind. This H₂O ice lag deposit can then protect the remaining CO₂ ice from rapid sublimation. If the overlying H₂O ice layer is too thin, the CO₂ ice deposit will sublime away fully,

leaving only a H₂O ice lag deposit that combines with the H₂O ice lag deposit from the previous obliquity cycle. This lag deposit would then be re-covered by surface CO₂ ice during the next low obliquity period and the cycle will continue (Buhler et al., 2019).

The Manning et al. (2019) hypothesis uses the idea that the different cadences of the obliquity, eccentricity and longitude of perihelion cycles can result in alternating deposition cycles of CO₂ ice and H₂O ice within a low obliquity excursion, producing the observed layered deposit. This is because eccentricity and timing of perihelion influence which pole accumulates the most ice. When perihelion occurs in northern summer, around 50 m of H₂O ice would be expected to accumulate over 10 kyr. Since the rate and timing of accumulation is dependent on orbital parameters, the ages of the layers within the NPLD and SPLD are expected to be offset by ~ 25 kyr (Manning et al., 2019). The accumulation of the overlying H₂O ice layer would also have been significantly thicker initially, given the 70% porosity of snow, and would have densified over time to densities greater than 800 kg m^{-3} , which is the pore cut off limit. The timescale for this densification process is expected to have accelerated due to an increase in sintering and compression of the lowest parts of the layer as temperatures increase with depth. Manning et al. (2019) suggest the densification process could take ~ 14 kyr, whereas Arthern (2000) suggest it could take between 300–550 kyr.

2.5 Liquid Water

The existence of liquid H₂O on Mars has been the focus of many studies over the years because of its implications for astrobiology. Pure liquid H₂O is not permanently stable at the surface at present because surface conditions are below the triple point of H₂O (Hardy, 1998; Jakosky and Carr, 1985b), however, it has been suggested to be present in the deep subsurface. Liquid brines are more stable near the surface because their melting temperature is significantly lower than pure liquid H₂O (Hoffman, 2001; Martín-Torres et al., 2015). Identification of minerals such as clays/phyllosilicates (e.g., Bibring et al., 2005; Ehlmann et al., 2011), sulphates (e.g., Bibring et al., 2005) and carbonates (e.g., Ehlmann et al., 2008), each of which require liquid H₂O to form, indicates that liquid H₂O was present at some point in Mars’ history (Bibring et al., 2005; Ehlmann et al., 2011).

In the present-day, liquid H_2O has been suggested to form at night by deliquescence, which is a mechanism to form thin films of liquid brines when large amounts of liquid H_2O are unavailable (Martín-Torres et al., 2015; Pál and Kereszturi, 2020). However, the amounts that can form are very small and do not persist throughout the day. Another form of liquid H_2O on present-day Mars has been proposed from analyses of radar observations which suggest there is a stable subsurface body of liquid perchlorate brine under parts of the SPLD either mixed with basal soils or on top of impermeable material as localised brine pools (Lauro et al., 2020; Orosei et al., 2018). This scenario is suggested to be plausible because perchlorates have been observed on the surface elsewhere on the planet and they suppress the freezing point of H_2O to below the temperature estimated for the base of the SPLD (205 K; Lauro et al., 2020; Orosei et al., 2018), although this is still debated.

2.6 Climate

The atmosphere of Mars is mainly composed of CO_2 ($\sim 95\%$), with smaller amounts of argon, nitrogen, and other trace gases (such as H_2O , oxygen, and carbon monoxide; Read and Lewis, 2004). Seasonal variations in pressure, temperature, CO_2 , dust and H_2O are the key drivers of the climate and subsurface-atmosphere exchanges, while the other components of the atmosphere predominantly respond to changes in these cycles (Toon et al., 1980). Within the atmosphere, three broad layers can be defined: the lower, middle and upper atmosphere (Smith et al., 2017). The lower atmosphere is the region below an altitude of 50 km (containing $\sim 99\%$ of total atmospheric mass; Zurek et al., 2017) and, since the focus of this thesis is the subsurface, only processes within this region will be discussed. Within the lower atmosphere, there is a smaller subregion known as the planetary boundary layer (PBL) where the atmosphere interacts directly with the surface and processes within this region are discussed separately (Section 2.6.1) to processes that occur across the entire lower atmosphere.

Circulation in the lower atmosphere is dominated by two asymmetrical meridional overturning cells (known as Hadley cells), which can extend to over 50 km in the vertical and over 5000 km in latitude, encircling the planet in longitude. These form due to asymmetric seasonal heating between the spring-summer and the autumn-winter

hemispheres (Haberle et al., 1993; Lewis, 2003). The Hadley cells are important for cross-equatorial transport as the near-equinox cells are not completely symmetric about the equator, allowing material to be transported between hemispheres (summarised by Barnes et al., 2017). Around the northern spring equinox ($L_S = 0^\circ\text{--}30^\circ$), the rising branches of both cells are in the northern hemisphere, whereas around the northern autumn equinox ($L_S = 180^\circ\text{--}210^\circ$), the rising branches are centred in the southern hemisphere. When centred in the southern hemisphere, the cells extend further poleward due to a combination of the asymmetry in zonal-mean topography, the stronger thermal forcing (which is related to the thermal structure) and the larger atmospheric dust loading. The final two factors are a consequence of northern autumn occurring closer to perihelion (summarised by Barnes et al., 2017), which is discussed further in Section 2.7.2.

Alongside the longitude of perihelion, the thermal structure of the lower atmosphere is influenced by a combination of surface temperature, seasonal changes, diurnal changes, atmospheric dust distribution and the dynamics of the entire atmosphere (Bandfield, 2007; Smith et al., 2017; Toon et al., 1980). At low latitudes, the longitude of perihelion and degree of orbital eccentricity (Section 2.7.2) are the dominant influence, with warmer temperatures occurring during the perihelion season ($L_S = 180\text{--}360^\circ$ at present) and cooler temperatures during the aphelion season in both hemispheres. At high latitudes, however, the dominant influence is the obliquity, which controls seasonal changes by varying the latitudinal distribution of solar insolation (discussed further in Section 2.7.1; Bandfield, 2007). Surface temperatures are also influenced by surface albedo (Section 2.1.5.4), thermal inertia (Section 2.1.5.2), slope (and subsequent shadowing) and atmospheric opacity (Aharonson and Schorghofer, 2006; Bandfield, 2007; Bandfield and Feldman, 2008; Smith et al., 2017). These properties also affect the lowest region of the atmosphere (the PBL; <10 km) which has temperatures that correspond to surface temperatures.

Atmospheric pressures are influenced by the same processes as the thermal structure. However, for pressure, another main influence is the ‘freezing out’ of around 30% of the atmospheric CO_2 to form the seasonal polar caps (Sections 2.2.1 and 2.6.2),

which is partially responsible for the observed semi-annual cycle in atmospheric pressures (Hourdin et al., 1995; Leighton and Murray, 1966; Mischna et al., 2003). Some other main influences on the seasonal pressure cycle include the latitudinal redistribution of atmospheric mass between the hemispheres and variations in mean zonal winds caused by geostrophic balance changes (Hourdin et al., 1995). Surface pressures (6.36 mbar on average) also vary spatially according to surface elevation, with higher pressures at low elevations and vice versa (Smith et al., 2017). This effect also influences atmospheric dynamics: the large difference in mean elevation (1 to 3 km) between the northern and southern hemispheres causes topographically-steered flows (Hourdin et al., 1993).

The presence of dust in the atmosphere plays a major role in the annual climate, specifically through its influence on the atmospheric thermal structure as airborne dust absorbs and scatters radiant energy, resulting in atmospheric heating (Kahre et al., 2017; Smith et al., 2017). Its presence also provides a nucleation site for the formation of both H₂O and CO₂ ice clouds, which are important components of the CO₂ and H₂O cycles (Sections 2.6.2 and 2.6.3; Gooding, 1986; Kahre et al., 2017; Montmessin et al., 2017). The atmospheric dust cycle can be characterised using two overarching seasons, the ‘non-dusty’ season (with low-level atmospheric dust loading; $L_S = 0^\circ$ to 135°) and the ‘dusty’ season (with a higher atmospheric dust loading; $L_S = 135^\circ$ to 360° ; Smith et al., 2017). During the ‘dusty’ season, dust is generally transported from regions that act as dust sources to regions that act as dust sinks. The polar caps are expected to be dust sinks as dust storms tend to deposit rather than remove dust there (Toon et al., 1980) and as a result, the variations in dust storm activity have been suggested to affect the dustiness of the PLD. The dust loading of the atmosphere has also been shown to impact the stability of subsurface H₂O ice, as a dusty atmosphere results in a higher atmospheric H₂O vapour content and consequently reduces the sublimation of any subsurface H₂O ice deposits (Steele et al., 2017a).

2.6.1 Planetary Boundary Layer

The planetary boundary layer (PBL) refers to the lowest region of the atmosphere that interacts directly with the surface (summarised in Read et al., 2017). Observations by

the Phoenix lander and from orbital measurements have shown that the PBL is well mixed. It is in this region that short and long term exchanges of heat, H_2O , CO_2 , dust, and other chemical tracers are exchanged between the surface/subsurface and atmospheric reservoirs (Read et al., 2017; Whiteway et al., 2009).

The height of the PBL varies between 1 and 10 km depending on the time of day and interactions with local surface topography (Read et al., 2017). During the day, intense surface heating-driven convection occurs, increasing the height of the PBL to 10 km in some locations. This leads to efficient mixing and vertical transport of quantities such as heat, dust, and moisture from the atmosphere directly above the surface to greater heights, where the global circulation is likely to pick them up and distribute them around the rest of the planet (Jakosky et al., 1997; Read et al., 2017; Tillman et al., 1994). The vertical transport of quantities such as H_2O vapour into the upper atmosphere suggests that any H_2O vapour lost from the subsurface during the day may be quickly transported upwards and into the global circulation and any local vapour concentration increase will not persist for long.

At night, however, convection with the upper portions of the atmosphere is inhibited and radiative cooling results in a stably stratified layer. During this period, the PBL is forced by mechanical turbulence at the bottom of the stable layer and the maximum height is reduced to around 1 km (Read et al., 2017). Any vapour lost from the atmosphere during the night will remain in the near surface, increasing the near surface vapour concentration and impacting the flux of vapour between the subsurface and atmosphere.

2.6.2 Carbon Dioxide Cycle

The atmospheric CO_2 seasonal cycle is controlled by the polar energy budget which is highly dependent on both the albedo of the polar cap and orbital parameters (Section 2.7; Toon et al., 1980). CO_2 vapour is transported from the subliming to the condensing pole by the global circulations described in the earlier sections. The presence of dust and H_2O ice clouds in the atmosphere influence the rate of CO_2 condensation and sublimation in the polar regions as discussed earlier.

CO₂ clouds also influence the rate of surface CO₂ ice formation. CO₂ clouds form when the atmosphere is supersaturated and dust or H₂O ice is available for nucleation to occur (Hu et al., 2012). In remote observations, CO₂ clouds are difficult to distinguish from surface CO₂ frosts, since they have the same spectral signature and altitude is needed to distinguish them. They have been observed over the poles in vertical atmospheric profiles determined using a combination of MGS, Mars Climate Sounder (MCS) on MRO and MOLA data (Hayne et al., 2012; Hu et al., 2012; Titus et al., 2017). Most observed clouds appear to extend down to the surface and cloud opacity increases towards the pole. The most persistent and densest clouds are observed over the South Polar Residual Cap (SPRC) where a 500 km diameter cloud was observed to persist throughout winter (Hayne et al., 2012).

The presence of CO₂ ice clouds reduces net accumulation of surface CO₂ ice, and consequently subsurface CO₂ ice, via the low emissivities of the clouds themselves and the low emissivity of the resulting CO₂ snowfall. The low emissivity snow on the surface causes backscattering of incoming radiation (Hayne et al., 2012; Wood and Paige, 1992), whereas CO₂ ice deposits that have directly condensed on the ground, or have undergone sintering, are more likely to act as black-body emitters (Forget et al., 1998). This means that the presence of clouds and snow on the ground will increase temperatures resulting in a smaller net accumulation of surface CO₂ ice. The reduction of surface ice accumulation due to the presence of clouds also applies to surface H₂O ice accumulation when H₂O ice clouds form at high altitudes.

2.6.3 Water Cycle

The atmospheric H₂O cycle is governed by interactions between the atmosphere and H₂O ice exposed at the northern polar cap during northern summer (Chamberlain and Boynton, 2007; Forget et al., 2017; Titov, 2002). Figure 2.11 shows a schematic overview of the main events within the annual H₂O cycle (from Montmessin et al., 2004). The highest H₂O column abundances occur in the north polar region during northern summer, when the overlying seasonal CO₂ polar cap has sublimated and the underlying H₂O ice cap is exposed (85% of all H₂O vapour is in the northern hemisphere during northern summer; Chamberlain and Boynton, 2007; Montmessin et al., 2017;

Titov, 2002). A small peak in H_2O vapour column abundance also occurs over the south pole during southern summer (Chamberlain and Boynton, 2007), with only 60% of all H_2O vapour in the southern hemisphere at this time of year (Montmessin et al., 2017). The southern peak is smaller because the southern perennial polar cap is mostly CO_2 ice, with few locations of exposed H_2O ice (as shown by OMEGA observations; Bibring et al., 2004, ; Section 2.2.1), as well as due to asymmetries in global transport due to southern summer occurring in perihelion (Montmessin et al., 2004).

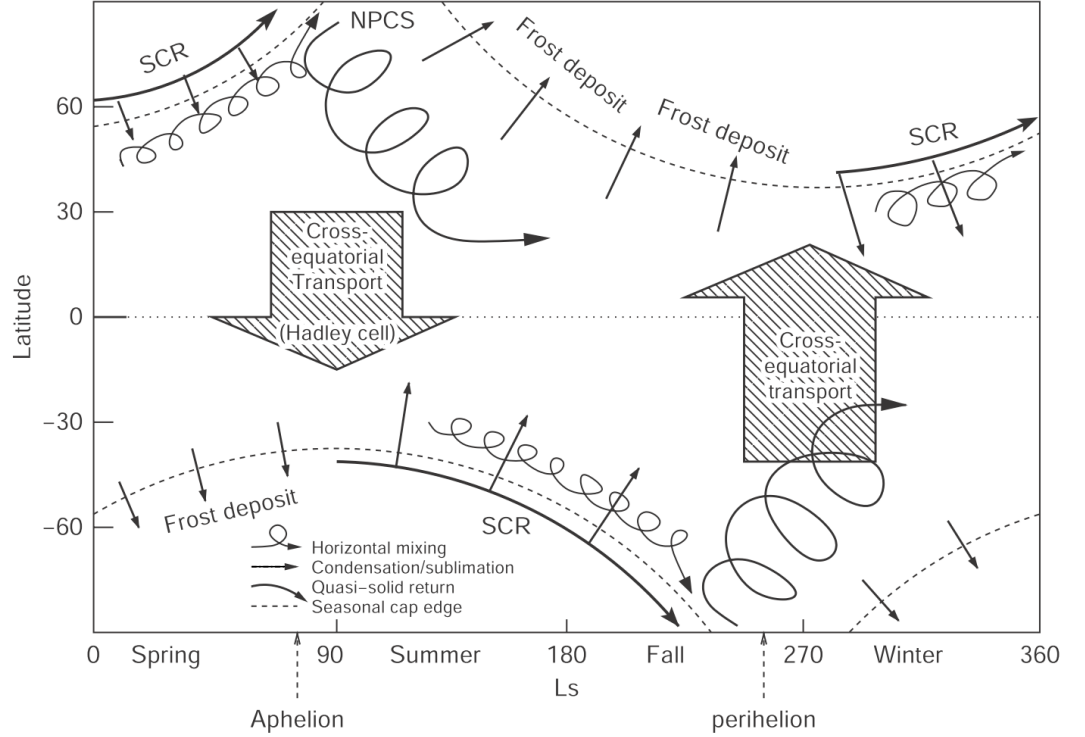


Figure 2.11: Schematic overview of the key processes that affect the martian H_2O cycle over a year. NPCS stands for north polar cap sublimation and SCR stands for seasonal cap recession. Figure from Montmessin et al. (2004).

At lower latitudes, seasonal variations in H_2O vapour column abundance are smaller in magnitude than at either pole (Chamberlain and Boynton, 2007). This is because the non-polar H_2O ice sources, such as the LDM (see Sections 2.2 and 2.3), respond to polar atmospheric H_2O vapour variations (Chamberlain and Boynton, 2007; Jakosky, 1983) which are transported by meridional circulations to the rest of the planet (Forget et al., 2017; Steele et al., 2017a). This means that the strength and direction of the Hadley cells play a more important role in the H_2O vapour abundances of the mid- and equatorial latitudes than the presence of H_2O ice at these latitudes (Montmessin

and Lefèvre, 2013; Montmessin et al., 2017). The non-polar H₂O ice sources become more important for atmospheric H₂O when the orbital parameters are different from the present-day (see Section 2.7).

The vertical distribution of H₂O vapour throughout the year is an important consideration for subsurface models since the abundance can be strongly inhomogeneous across a vertical profile through the atmosphere (Titov, 2002). This vertical distribution is the result of a combination of advection and convection in the atmosphere as well as regolith-atmosphere exchanges (Böttger et al., 2005b; Titov, 2002).

2.7 Orbital Parameters

The orbital parameters of Mars (obliquity, degree of orbital eccentricity and areocentric longitude of perihelion) have a large influence on solar insolation and therefore on the climate of Mars (Toon et al., 1980). The obliquity is the tilt of the axis of rotation with respect to a line normal to the plane of Mars’ orbit around the Sun, the degree of orbital eccentricity is a measure of the ellipticity of Mars’ orbit around the Sun, and the longitude of perihelion is the solar longitude (L_S) at which Mars is closest to the Sun in its orbit (Laskar et al., 2004; Toon et al., 1980). Variations in the longitude of perihelion and changes in the orientation of Mars’ spin axis about the vertical plane are known as apsidal precession and axial precession respectively. Over the course of these precession cycles, the relative times of perihelion and seasons change, influencing the strength of seasons in each hemisphere (discussed further in Section 2.7.2). All three orbital parameters undergo large dynamical variations due to perturbations from other bodies in the solar system (Toon et al., 1980; Touma and Wisdom, 1993; Ward, 1974a; Ward et al., 1974b, 1979). These perturbations are stronger than those experienced by the Earth due to a resonance overlap in the orbit of Mars and nearby bodies in the Solar System (Bills, 1990; Bills and Keane, 2019; Forget et al., 2017). These resonances cause the obliquity cycle to be strongly chaotic, whereas the eccentricity and longitude of perihelion cycles are relatively predictable (Laskar et al., 2004, as shown in Figure 2.12).

Obliquity has the largest influence on the climate because it controls the latitudinal

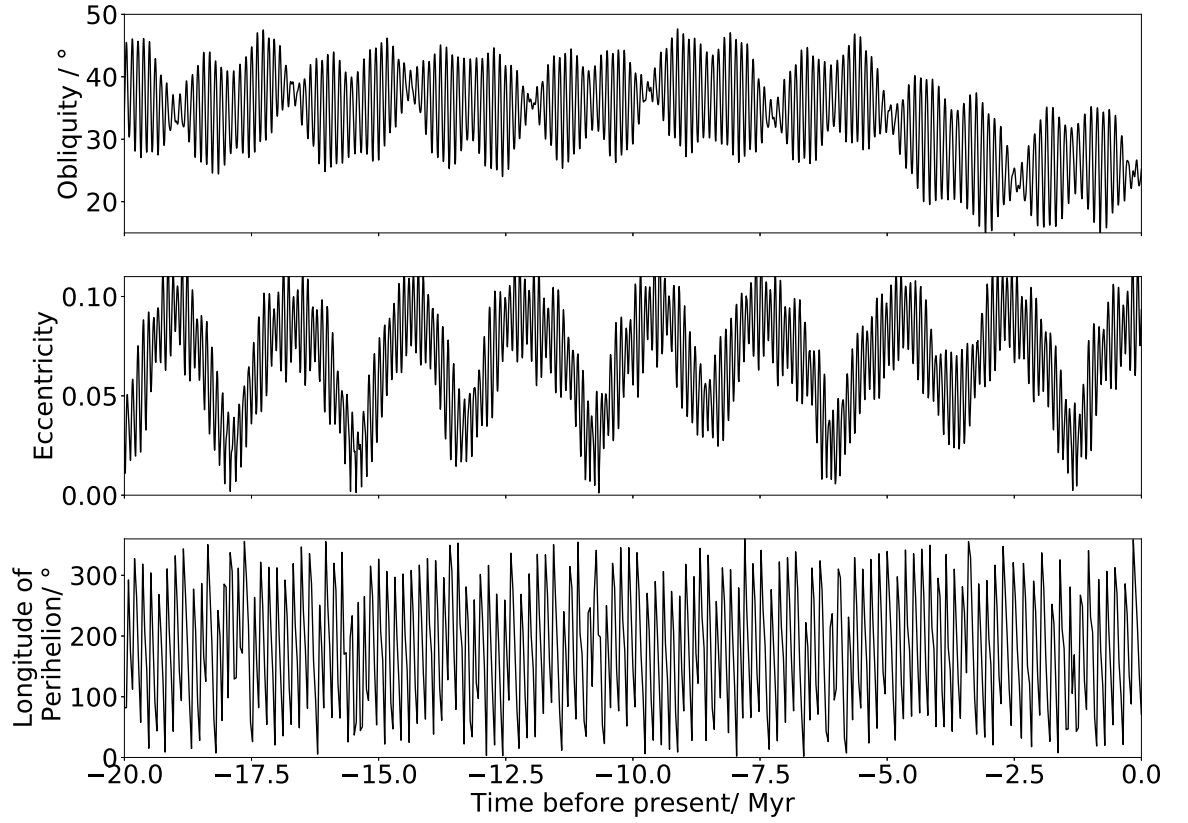


Figure 2.12: Obliquity, eccentricity and longitude of perihelion variations over the last 20 million years. Plotted using data from Laskar et al. (2004)

distribution of solar insolation directly (e.g., Mischna et al., 2003; Schorghofer, 2008). Eccentricity and longitude of perihelion are not significant individually, but combined they determine which season (summer or winter) is longer (Mischna et al., 2003). This in turn influences the size of the atmospheric and surface volatile inventories (Mischna et al., 2003).

2.7.1 Obliquity

The current martian obliquity is 25.19° and this value oscillates between 10° and 35° with a period of $\sim 120,000$ years (Fanale et al., 1982a; Laskar et al., 2002; Ward et al., 1979). The period of the cycle is controlled by the differential between the spin axis and orbital plane precession rates, which have stronger resonances than on Earth resulting in larger amplitude oscillations (Forget et al., 2017). This cycle is modulated by a longer (~ 1.3 Myr) cycle from the slow oscillations in the inclination of the martian orbital plane (Forget et al., 2017). Laskar et al. (2004) showed that the most probable obliquity over the last 4 Gyr is 41.8° and Figure 2.12 shows their best solution for obliquity over

the last 20 Myr, which is commonly used in studies of the effect of obliquity on the martian atmosphere (e.g., Forget et al., 2006; Levrard et al., 2004; Read et al., 2015; Steele et al., 2017a). The solution for the obliquity cycle is only reliable for the past 10 Myr because the obliquity cycle is strongly chaotic and the present understanding of the rotational state of Mars is only reliable for this period. The Laskar et al. (2004) obliquity solution in Figure 2.12 shows a distinct transition around 5 Myr ago between a high mean obliquity regime ($\sim 35^\circ$) and a low mean obliquity regime ($\sim 25^\circ$), which was a robust solution for the range of parameters in their study. This transition was also found in the obliquity model of Touma and Wisdom (1993). After this transition, the lower mean obliquity results in a decrease in the summer insolation around the north pole, therefore changing the distribution of surface ices (Laskar et al., 2002).

Obliquity variations impact the latitudinal distribution of solar insolation and significantly impact the peak radiative heating of the polar regions, since the polar energy supply over summer increases with obliquity (Mischna et al., 2003; Toon et al., 1980). Estimates of surface temperature for obliquities between 10° and 40° have suggested that annual mean regolith temperatures change by 4 K at equatorial latitudes, 15 K in the mid-latitudes and by as much as 45 K at polar latitudes (Mellon and Jakosky, 1993). For obliquities greater than 50° , which are expected to have occurred during the Hesperian (3.7–3.0 Gyr; Laskar et al., 2004), the polar regions receive more insolation on average than the tropics (Forget et al., 2017). These surface temperature variations impact both atmospheric circulation and the redistribution of volatiles across the surface.

Volatile redistribution takes 10 kyr to 1 Myr to respond to the variations in surface temperature caused by obliquity variations (Levrard et al., 2004). This is similar to on Earth, where the obliquity cycles control the oscillations between glacial (at low obliquities) and interglacial (at high obliquities) periods, that are characterised by the transfer of H_2O between ice sheets (glacial) and oceans (interglacial; Levrard et al., 2004). On Mars, the obliquity cycle is also the dominant factor that controls subsurface ice distributions and the partitioning of CO_2 between phases (Schorghofer and Forget, 2012). However, the larger amplitude of obliquity oscillations results in a very different

redistribution of surface ice from that seen on Earth. On Mars, during periods of high obliquity ($>30^\circ$), the equatorward transport of atmospheric H_2O vapour is enhanced, producing the observed mid-latitude ice deposits (and only seasonal polar caps form; discussed further in Section 2.7.1.1), whereas at low obliquities, ice accumulates at the poles (see Section 2.7.1.2; e.g., Forget et al., 2017; Head et al., 2003; Jakosky and Carr, 1984; Mischna et al., 2003). There is a transition period between these two scenarios, which typically occurs at moderate obliquities (such as at present) where the climate system changes from hosting permanent polar caps (low obliquity) to hosting only seasonal polar caps and permanent mid-latitude ice deposits (high obliquity; Nakamura and Tajika, 2003).

2.7.1.1 High Obliquity

During periods of high obliquity ($>35^\circ$), variations in solar insolation are larger across the year, particularly in the polar regions which experience the largest temperature variations ($>150\text{ K}$ at 60° obliquity; Mischna et al., 2003). Consequently, the seasonal cycles discussed earlier become more extreme. Over the winter season, polar temperatures are cooler than at present and are low enough for large seasonal CO_2 ice caps to form. These seasonal CO_2 ice caps extend further equatorward than at present and therefore cause a larger annual pressure cycle (Mischna et al., 2003; Toon et al., 1980).

The summer season shows the largest difference from the present-day as insolation at the poles increases by up to 75%, increasing temperatures to as high as 273 K. At these high temperatures, both CO_2 and H_2O ice are unstable and the permanent polar CO_2 ice caps will sublime away (Toon et al., 1980). This exposes the underlying H_2O ice cap at both poles (rather than just the northern pole) and, since temperatures are higher than the H_2O frost point, the H_2O ice caps begin to sublime away (Head et al., 2003; Jakosky and Carr, 1984). As much as a few centimetres of H_2O ice sublimates from the poles each year (Forget et al., 2017; Mischna et al., 2003) which is then transported equatorward by the stronger and broader meridional circulation that is the result of the higher solar insolation in the polar regions (Mischna et al., 2003; Newman et al., 2005). Since summer polar temperatures are greater than summer equatorial

temperatures at very high obliquities ($>45^\circ$), the atmosphere in the equatorial regions becomes supersaturated and ice is deposited at the surface (Jakosky, 1985a; Mischna et al., 2003; Richardson and Wilson, 2002). This ice remains trapped in the equatorial region during winter, rather than returning back to the pole, because the influx of H_2O vapour from the other hemisphere keeps atmospheric H_2O vapour concentration high (Jakosky and Carr, 1984; Mischna et al., 2003). At mid to high obliquities ($\sim 35^\circ$), however, the coldest regions are in the mid-latitudes and ice is deposited there instead of in the equatorial region, resulting in the formation of the mid-latitude glaciers that are still observed today (see Section 2.3.3; e.g., Holt et al., 2008; Mischna et al., 2003).

2.7.1.2 Low Obliquity

When obliquity is low ($<20^\circ$), the polar regions become colder, the equatorial regions become warmer, and the amplitude of the annual temperature cycle decreases (Toon et al., 1980). Seasonal variations are also much smaller than at moderate ($\sim 25^\circ$) or high obliquities ($>35^\circ$) and the mean overturning circulation of the atmosphere becomes weaker (Forget et al., 2017; Newman et al., 2005).

The colder temperatures in the polar regions result in the formation of thick permanent polar ice caps, which extend further equatorward than the present-day permanent caps but not as far as the seasonal polar caps at high obliquities. The fall in atmospheric pressure caused by the growth of the polar caps has implications for the subsurface reservoirs of CO_2 and H_2O (Toon et al., 1980; Wood and Griffiths, 2007a). Simulations suggest that mean surface pressure would fall to below 1 mbar and perhaps even as low as 0.3 mbar (Toon et al., 1980; Wood and Griffiths, 2007a,b). At such low pressures, the thermal conductivity (see Section 2.1.5.3) of porous regolith is reduced, which causes near surface temperatures to increase (by up to 20–30 K in regions where subsurface H_2O ice is expected at present-day; Wood and Griffiths, 2007b), which would reduce the stability of any existing subsurface ice (Presley and Christensen, 1997b; Toon et al., 1980; Wood and Griffiths, 2007a). This will have a larger influence on the H_2O ice distribution in the tropics and mid-latitudes than any changes in the eccentricity or longitude of perihelion, but still not be as large an influence as the change in obliquity

(Steele et al., 2017a).

The extent of the equatorward expansion of the polar caps at low obliquities is dependent on the size of the initial CO₂ inventory (Forget et al., 2013; Kahre et al., 2013; Soto et al., 2011, 2015). During the Noachian (4.0–3.7 Gyr ago; see Section 2.8), the CO₂ inventory is estimated to have been larger than in the present-day, which would impact the size of the polar caps and the climatic response to their formation. Simulations suggest that permanent CO₂ polar caps only form at low obliquities when pressure is higher than 3 bar or lower than 1 bar (Forget et al., 2013). It has also been suggested that larger CO₂ inventories result in permanent CO₂ ice caps forming at higher obliquities than for the present-day atmosphere (Soto et al., 2015).

2.7.2 Longitude of Perihelion and Eccentricity

The eccentricity of Mars’ orbit oscillates with a period of 95 kyr with a modulating period of 2.4 Myr due to resonances with other bodies in the solar system (Laskar et al., 2002, 2004; Toon et al., 1980). Over the last 10 Myr the degree of orbital eccentricity has varied between 0 and 0.12 and over the last 4 Gyr, the most probable value for eccentricity is 0.068 (Laskar et al., 2004). Changes in the degree of orbital eccentricity alter the amount of energy received seasonally by varying the length of the seasons (Mischna et al., 2003; Toon et al., 1980). At the present eccentricity (0.093; Jakosky et al., 1995; Newman et al., 2005), Mars receives around one third less sunlight during the aphelion season (when Mars is furthest from the Sun) than the perihelion season (when Mars is nearest to the Sun; Forget et al., 2017). As eccentricity increases, the length of the season at aphelion increases, while the season during perihelion decreases (Mischna et al., 2003). The winter season at aphelion is, therefore, longer and colder than the winter season at perihelion. The hemisphere with the winter season at perihelion is dependent on the longitude of perihelion, which at present is at $L_S = 251^\circ$ (late northern fall), resulting in southern winter being longer and colder than northern winter (Mischna et al., 2003). As eccentricity decreases, the importance of the longitude of perihelion also decreases as the length and amount of solar insolation during the seasons become more symmetrical (Newman et al., 2005). In general, the influence of eccentricity and longitude of perihelion is greatest at moderate

obliquities ($\sim 25^\circ$; Pollack and Toon, 1982; Toon et al., 1980) when the influence of obliquity is at its weakest.

The timing of the areocentric longitude, L_S , of perihelion is related to the precession of the spin axis which oscillates with a period of 51 kyr (Forget et al., 2017; Schorghofer, 2008). Areocentric longitude of perihelion has the largest influence around latitude $\pm 60^\circ$ where annual surface temperatures are not closely related to annual mean insolation (Schorghofer, 2008; Schorghofer and Forget, 2012). This region where longitude of perihelion dominates also corresponds to the margins of the ice-rich layers in each hemisphere. Across the rest of Mars, the mean annual surface temperature is controlled by the obliquity cycle (Schorghofer, 2008), as discussed earlier. When perihelion occurs during northern autumn, such as at present, it minimises the H_2O ice loss from the northern cap since heating rates are lower (Forget et al., 2017; Mischna et al., 2003). The opposite is true when perihelion occurs during northern spring/summer, as H_2O ice becomes unstable at the north pole and accumulates at the south pole instead (Forget et al., 2017). When this happens atmospheric H_2O vapour concentrations can be an order of magnitude greater at perihelion than at aphelion (Clancy et al., 1996).

2.8 Planetary History

The above sections provide an overview of the state of Mars during the Amazonian (the most recent geological period). However, this recent atmospheric state is the result of the processes that Mars has undergone over its history and so knowledge of the historical evolution is needed to place the observations and predictions into context. This is particularly important for volatile related features (such as valley networks and glaciers) as many are the result of conditions different from the present, such as variations in orbital parameters and climate conditions throughout history (such as increased atmospheric pressure, lower solar luminosity and increased impact rates; e.g., Kahre et al., 2012; Kasting, 1991; Wordsworth et al., 2013). The main changes in conditions can be understood using three of the geological periods: the Noachian (4.0–3.7 Gyr), the Hesperian (3.7–3.0 Gyr) and the Amazonian (3.0 Gyr – present-day; Carr, 2007a).

The Noachian period (4.0–3.7 Gyr ago) is characterised by high impact and erosion rates, higher surface pressures and a lower solar luminosity (Carr and Head, 2010; Golombek and Bridges, 2000; Tanaka, 1986). Surface pressures are estimated to have been significantly higher during this period based on estimates of the amount of CO₂ that would have been lost to space, trapped in carbonates, or trapped in ice (or clathrate) deposits (Section 2.4; Ehlmann et al., 2011). Estimates of the initial atmospheric inventory range from 0.1–10 bar depending on the method used to find the estimate (e.g., Haberle et al., 1994; Kahn, 1985; Kite et al., 2014; Manning et al., 2006; Nakamura and Tajika, 2001). However, an initial inventory much greater than 1 bar is considered unlikely as none of the known mechanisms of atmospheric loss will remove more than 1 bar (Forget et al., 2013).

Higher atmospheric pressures in the Noachian would have meant the climate was very different from the present-day and features within Noachian terrains (such as dendritic valley networks and the presence of hydrated minerals) show evidence of liquid H₂O related processes occurring (Carr and Head, 2010; Fassett and Head, 2008; Golombek and Bridges, 2000; Tanaka, 1986). Two end-member scenarios have been proposed to explain the presence of liquid H₂O (e.g., Wordsworth et al., 2015). The ‘warm and wet’ scenario suggests that the global average surface temperature was higher than 273 K and that liquid H₂O was stable across most of the surface for long periods of time during the Noachian (Kasting, 1991; Wordsworth et al., 2015). The ‘cold and icy’ scenario, on the other hand, assumes that surface temperatures remained below the freezing point of H₂O and that liquid H₂O only formed by episodic melting due to a combination of seasonal, volcanic and impact forcing (Wordsworth et al., 2015). Simulations suggest that the ‘cold and icy’ scenario is more likely, while geological evidence suggests the opposite and that the ‘warm and wet’ scenario is more likely. It has been suggested, that the true Noachian climate is most likely to be a combination of both scenarios, with a mostly ‘cold and icy’ climate that periodically becomes ‘warm and wet’ (Wordsworth, 2016). Consequently, it is still debated which of the two scenarios best fits the available evidence for the conditions of Early Mars. Despite the debate on the climate conditions, one common point is that the volume of H₂O during the Noachian was significantly larger than at present and has decreased

over time (Scheller et al., 2021, estimated a decrease of 40–95%).

The Hesperian period (3.7–3.0 Gyr ago) saw the rate of impacts, volcanism and fluvial activity decrease (Carr and Head, 2010; Hoffman, 2000). This led to a decline in the rate of H₂O -related rock alteration processes that formed phyllosilicates and other hydrous minerals, changes in global groundwater chemistry and the formation of sulphate-rich deposits (Carr and Head, 2010; Ehlmann et al., 2011). The change in these processes, alongside the reduced amount of valley formation, indicate that the surface conditions required for liquid H₂O to form were rare during the Hesperian (unlike the Noachian where evidence for liquid H₂O is more widespread) and conditions were closer to the present-day climate. In contrast, some geological evidence, such as the distribution of martian deltas, has been suggested to indicate the potential existence of an ocean in the northern lowlands during the Hesperian (e.g. Clifford and Parker, 2001; Di Achille and Hynek, 2010; Parker et al., 1993). However, the existence of this ocean is heavily debated.

The Amazonian period (3.0 Gyr ago–present) experienced a further slowing of geologic activity, and evidence of processes involving liquid H₂O from this period are rare. Features related to ice and wind processes are more evident, especially for ice related processes in the high and mid-latitudes (Carr and Head, 2010). It is during this period that many of the features observed at the surface, such as the PLD and mid-latitude glaciers, would have formed (Head and Pratt, 2001; Head et al., 2003; Howard, 1981; Kargel and Strom, 1992). These features probably formed as a result of changes in climatic conditions caused by variations in orbital parameters (see Section 2.7) rather than due to global conditions vastly different from the present-day.

2.8.1 Distribution of Carbon Dioxide Ice Early in Martian History?

At the higher atmospheric pressures expected during the Noachian and early Hesperian, the higher CO₂ partial pressures will result in an increased frost point temperature (~ 195 K; Kasting, 1991), expanding the regions of CO₂ ice stability on the surface. Simulations under higher atmospheric pressures indicate that CO₂ ice could have been more

widespread than it is at present (Forget et al., 2013; Nakamura and Tajika, 2003; Soto et al., 2015). However, all of these simulations used the present-day martian topography for the simulations, and volcanic features (such as Olympus Mons) are estimated to have formed at the end of the Noachian and their presence has a large impact on the climate. Therefore, the results of these simulations only relate to the post-Tharsis Mars, when the topography of the present-day had mostly formed. Another issue with these simulations is that the climate during the Noachian and Hesperian is largely unknown and GCMs are based on present-day Mars and Earth.

In most simulations under higher atmospheric pressures (6 mbar–3 bar), the polar caps form as is expected from previous obliquity simulations, with permanent polar caps at low obliquities ($<15^\circ$) and large seasonal caps at high obliquities ($>35^\circ$; see Section 2.7.1 Forget et al., 2013; Soto et al., 2015). The main impact of higher atmospheric pressure in these simulations is that permanent polar caps can form at higher obliquities as pressure increases, as would be expected due to the higher frost point temperature at higher pressures. The other interesting result from these simulations is the formation of CO₂ ice deposits at around 15° latitude when the CO₂ inventory is greater than 300–600 mbar (depending on obliquity; see Figure 2.13 for an example of the zonally averaged results), likely on the flanks of Olympus Mons (Soto et al., 2015). This is much further equatorward than previous work has suggested that surface CO₂ ice could have formed and its presence at these latitudes could have implications for the processes that occurred in the equatorial region during Early Mars.

The formation of CO₂ ice deposits further equatorward than at present and deposits at around 45° latitude were simulated by Nakamura and Tajika (2003) in simulations with a lower solar constant (70% of present-day). In their simulations, they found that when obliquity was lower than 50° , the minimum mean-annual solar incident flux occurred at the poles and the CO₂ ice deposits would form there, which is the case at present and in all other simulations. However, when obliquity was increased to 60° (which would have occurred earlier in Mars’ history; Laskar et al., 2004), the minimum mean-annual solar incident flux now occurred in the mid-latitudes. This resulted in CO₂ ice depositing there and permanent CO₂ ice deposits forming circularly around

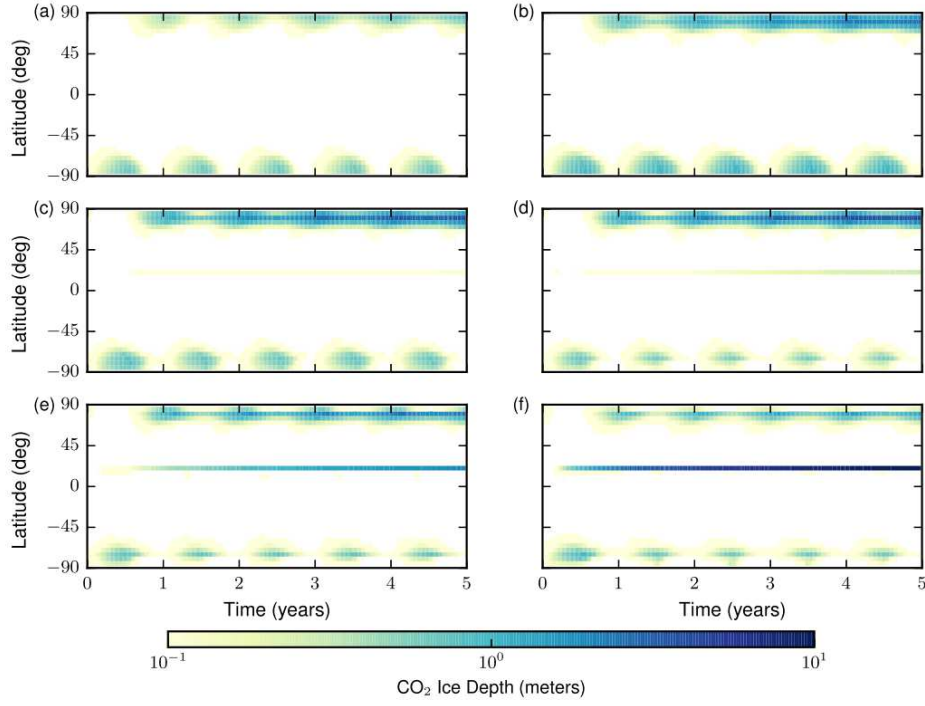


Figure 2.13: Zonal CO₂ ice depth over time for the 15° obliquity simulations from Soto et al. (2015), assuming a CO₂ ice density of 1600 kg m⁻³. The simulations in their study used initial surface pressures of (a) 6 mbar, (b) 60 mbar, (c) 300 mbar, (d) 600 mbar, (e) 1200 mbar and (f) 3000 mbar. Figure from Soto et al. (2015).

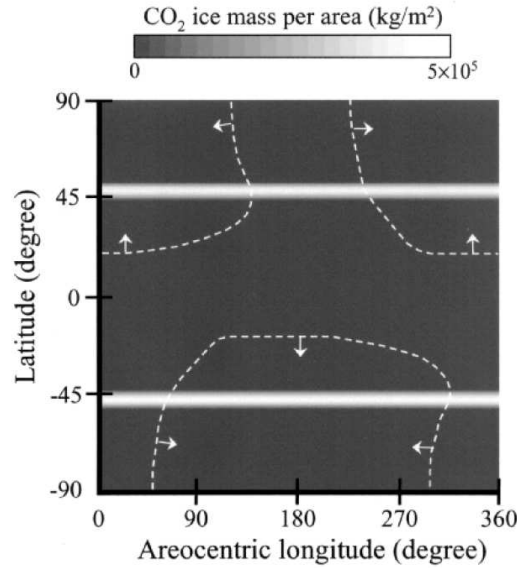


Figure 2.14: Seasonal distribution of CO₂ ice from simulations by Nakamura and Tajika (2003) at an obliquity of 60° and with a solar constant 70% of the present-day value. The white regions represent permanent CO₂ ice and the grey represents an uncovered surface. The dashed white lines represent the areal extent of seasonal CO₂ ice. Figure taken from Nakamura and Tajika (2003)

the mid-latitudes (see Figure 2.14), which could have implications for mid-latitude processes during Early Mars.

2.9 Summary and Remaining Questions

The sections above provide a brief summary of martian research related to H₂O and CO₂ ice to date, focussing primarily on subsurface ices. From the research already done, it can be seen that the distribution of surface ices and subsurface H₂O ice is heavily dependent on climatic conditions and the geological material (at the surface and in the subsurface). While the surface geological material is expected to have remained almost the same throughout the Amazonian, the climate is highly variable according to variations in the orbital parameters. The climate has also changed drastically over time, as atmospheric pressures are expected to have been higher during the Noachian and to have decreased over time until the present-day atmospheric pressures were reached. All of these factors will also impact the distribution of subsurface CO₂ ice. However, subsurface CO₂ ice has only recently been observed in the southern polar region and is not expected outside of the polar regions at the present obliquity. This means its global distribution is an area that is not well studied and there are a lot of questions still remaining about the existence of subsurface CO₂ ice in the present-day and its recent history, including:

- How long does CO₂ ice remain in the subsurface?
- What conditions are needed for CO₂ ice to be buried?
- When and where would CO₂ ice have formed in the subsurface in the recent past?

These questions can be answered using the current understanding of present-day Mars, which has characterised many of the factors that will influence subsurface CO₂ ice. The main remaining unknowns are related to the global distribution of subsurface CO₂ ice, which is difficult to observe and the properties of CO₂ ice when underlying either a dust or H₂O ice layer.

Answering these questions about present-day subsurface CO₂ ice will provide a starting point for future investigations into its distribution earlier in Mars' history when subsurface CO₂ ice was likely more prevalent, particularly during the Noachian

when atmospheric pressures were higher and CO₂ ice could form at higher temperatures. However, in order to study subsurface CO₂ ice during this period, the Noachian climate needs to first be well characterised. Therefore, this work is focused on characterising the behaviour of subsurface CO₂ ice during the Amazonian period at all relevant obliquities.

3 | The Martian Subsurface Model

A stand-alone one dimensional (1-D) subsurface model, hereafter referred to as the Martian Subsurface Model (MSSM), was developed to investigate the distribution of water (H_2O) and carbon dioxide (CO_2) within the subsurface of Mars for this work. The MSSM has been designed to simulate both vapour diffusion and the phase distribution for both H_2O and CO_2 over an annual cycle, using timesteps of one sol. The MSSM is comprised of three main parts: the temperature scheme, the water scheme, and the carbon dioxide scheme, which are all described in this chapter. Each scheme was developed sequentially in the order listed to ensure each was working as expected before incorporating a new scheme.

The main feature of the MSSM is the inclusion of CO_2 in all phases (vapour, ice and adsorbate). In all previous numerical modelling studies of the subsurface of Mars, H_2O has been the only volatile investigated (e.g. Fanale et al., 1982c; Meslin et al., 2008; Schorghofer and Aharonson, 2005; Steele et al., 2017a) and until the recent discovery of CO_2 within the polar layered deposits (PLD; Phillips et al., 2011) it was assumed that CO_2 ice could only be present at the surface in the present-day. The MSSM provides a way to investigate how well CO_2 could survive under present-day martian conditions, as well as at different obliquities and under the conditions expected during the Noachian and early Hesperian. The model is particularly useful for Noachian studies because atmospheric pressures during the Noachian are expected to have been higher (Section 2.8; Hu et al., 2015; Jakosky et al., 2017; Kite et al., 2014), which would allow CO_2 ice to form at higher temperatures and make the build-up of CO_2 ice in the subsurface more likely. Investigating the survival conditions of any CO_2 that could have formed during the Noachian will provide information about where in the subsurface CO_2 ice might have survived for long periods of time.

In this thesis, the MSSM is used as a stand-alone model to allow for many multi-year simulations to be run. However, the MSSM has been designed so that it can

be integrated into the LMD-UK Mars global circulation model (MGCM) to allow for future simulations to be run over the entire surface of Mars with the full 3D climate, which accounts for spatial and temporal variations in all properties. This will be useful for more detailed studies when the diurnal cycle is more important, or when investigating how the H_2O and CO_2 distribution changes on a global scale. The MSSM differs from the subsurface model that is currently included in the MGCM (Steele et al., 2017a) in many ways. These include a different discretisation for the diffusion of H_2O vapour, H_2O equations of state, H_2O thermal conductivity, the thermal scheme, variable regolith density and porosity, and the inclusion of CO_2 vapour, adsorbate and ice. A full description of the subsurface model currently used in the MGCM can be found in Appendix B.3, while the differences between the Steele et al. (2017a) model and the water scheme in the MSSM (and the reasoning behind these differences) are discussed in this chapter. The integration of the MSSM into the MGCM has been started and a description of how the MSSM can be integrated into the MGCM is provided in Appendix B.2 for future reference.

The methods and equations used to develop the rest of the MSSM (and the justifications for them) are also discussed throughout this chapter. Starting with the grid the model has been discretised onto (Section 3.1), followed by the thermal scheme (Section 3.2), water scheme (Section 3.3) and CO_2 scheme (Section 3.4). These sections are followed by a discussion on the methods to calculate surface flux (Section 3.5) and the sublimation and accumulation rates (Section 3.6) since these methods are the same for both H_2O and CO_2 . The final section provides a brief introduction to the MGCM, alongside a description of the atmospheric condition used for the MSSM in this thesis (Section 3.7).

3.1 Grid Stretch

The numerical solution of differential equations requires a mesh (to discretise the domain), a timestep and a numerical method to solve the equation (the finite volume method is used here and is described in Sections 3.2, 3.3.1 and 3.4.2). Since the MSSM is a 1-D model of the subsurface, the mesh is in the form of a series of grid points at different depths, with increasing spacing between them. This is referred to as the

grid stretch and the increasing spacing between grid points with depth accounts for the higher resolution required near the surface (<1 m), where properties, such as temperature, change more rapidly with depth and time than at depths greater than 5 m.

The method used to increase the spacing between the grid points with depth is important since the grid stretch impacts the accuracy of the solution, the conservation of the property, and the time it takes to solve the equations. Therefore, to decide on the grid stretch to be used I compared the grid stretch originally used in the MGCM (Hourdin et al., 1993), the grid stretch currently used (Steele et al., 2017a), a constant grid stretch and a new variable grid stretch. Figure 3.1 shows a comparison of these grid stretches.

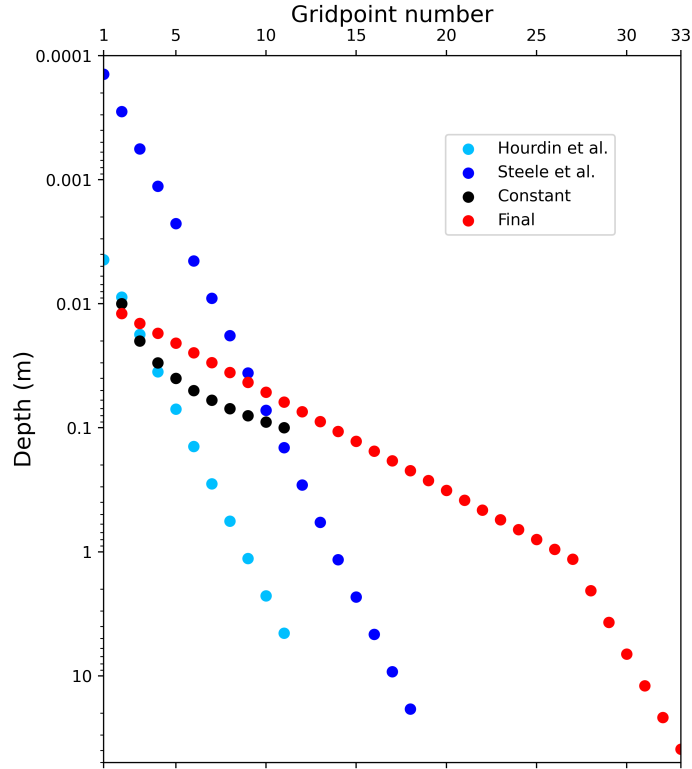


Figure 3.1: Relationship between grid point number and the depth below the surface for the grid stretch by Hourdin et al. (1993) that was originally in the MGCM (light blue), the grid stretch by Steele et al. (2017a) currently in the MGCM (dark blue), the constant grid stretch (black), and the variable grid stretch used in the thesis (red).

The original grid stretch used by the MGCM was developed by Hourdin et al. (1993). In this version of the MGCM an 11-layer soil model was used. This version of the model used the e-folding timescale instead of depths for each layer and the first

layer was at a tenth of the diurnal cycle ($t_{min} = 887.75$ s), and subsequent layers were calculated by

$$z[i] = z_0 \frac{\psi^{i-1}}{\psi - 1} \quad (3.1a)$$

$$z_0 = \sqrt{\frac{t_{min}}{\pi}}, \quad (3.1b)$$

where ψ is the ratio of the depth between two successive layers and is set to 2. This gives the e-folding timescale in seconds, which cannot be directly compared with the depths of the other grid stretches. The equivalent depth for these timescales can be calculated using the skin depth, z^* , for z_0 (see Section 2.1.5.1 and Equation 2.1 for a full description of the equation).

$$z^* = \sqrt{\frac{t_p k}{\pi \rho c_p}} \quad (3.2)$$

For the purpose of comparison, values of k , ρ , c_p and t_p have been chosen based on those used in the MSSM, $0.1 \text{ W m}^{-1} \text{ K}^{-1}$, 1740 kg m^{-3} , $830 \text{ J K}^{-1} \text{ kg}^{-1}$, and 88806.7 s, respectively. This results in a skin depth equal to 0.04 m. Since Equation 3.1b uses a t_{min} of a tenth of the diurnal cycle, one tenth of the skin depth is used as the new z_0 . The grid stretch in metres can then be calculated using Equation 3.1a and the resulting grid stretch is shown in Figure 3.1 in light blue.

The grid stretch currently used in the MGCM was developed by Steele et al. (2017a, dark blue in Figure 3.1) and starts at a set depth and increases by a factor, ψ^{i-1} , where i is the grid point number. The equation calculates depths directly and is an updated version of the equation used in the Hourdin et al. (1993) method which uses timescales:

$$z[i] = z_0 \times \psi^{i-1}, \quad (3.3)$$

where $z_0 = 2e^{-4}$ and $\psi = 2$. The similarity between the Steele et al. (2017a) and Hourdin et al. (1993) grid stretches, seen in Figure 3.1, is expected because they were developed for the same model, but with slightly different aims. The Steele et al. (2017a) work on subsurface H_2O ice needed physical depths and a higher resolution near the surface in order to calculate H_2O vapour diffusion, whereas the Hourdin et al. (1993)

model aimed to calculate subsurface thermal profiles only, for which timescales were sufficient.

For the variable grid, the first grid point is at the surface and subsequent grid points have an increasing grid spacing between them. The initial grid spacing is 0.01 m and this gets multiplied by 1.2 for the first 28 grid points and then by 1.8 for the remaining grid points (Equation 3.4).

$$z[i] = \begin{cases} 0.01 & \text{when } i = 1 \\ z[i - 1] \times 1.2 & \text{if } i < 28 \\ z[i - 1] \times 1.8 & \text{if } i \geq 28 \end{cases} \quad (3.4)$$

This particular grid stretch has a high resolution near the surface and the resolution decreases with depth, while insuring that the resolution at depth is small enough that changes on annual timescales can still be resolved. This is important since only the upper few centimetres are affected by diurnal changes in the surface temperature according to the skin depth at that location (Equation 2.1; e.g.,; see Section 2.1.5.1 for more details). Table 3.1 shows how skin depths vary with the temperature cycle and the geological material that are being considered. On Mars the lowest observed thermal inertias (Equation 2.2) are $24 \text{ J m}^{-2} \text{ K}^{-1} \text{ s}^{-\frac{1}{2}}$ (for unconsolidated regolith), the highest are $>800 \text{ J m}^{-2} \text{ K}^{-1} \text{ s}^{-\frac{1}{2}}$. In general, the observed range of thermal inertias for most martian surfaces is around $200\text{-}300 \text{ J m}^{-2} \text{ K}^{-1} \text{ s}^{-\frac{1}{2}}$ (Putzig et al., 2005). In this range of thermal inertias, the annual skin depth can vary from 0.4 m to >3.6 m. This means a maximum depth of at least 20 m is needed, since the annual thermal cycle will be fully damped within 5 skin depths (Beardsmore and Cull, 2001).

A top-hat tracer distribution experiment was run to compare the grid stretches described above with a constant grid stretch. The constant grid stretch had grid spacing fixed at 0.01 m and was included as a reference to which the results from the other grid stretches could be compared, as ideally the grid stretch would have many small layers. However, this would increase the computational time to unrealistically high values.

Table 3.1: Skin depths for the timescales and materials relevant to Mars, including the values used for each property of the materials to calculate skin depth from Equation 2.1. The material properties for regolith and sandstone are from Grott et al. (2007), the properties for Basalt are from Mellon et al. (2008), the properties for CO₂ ice are from Konstantinov et al. (1988); Maass and Barnes (1926); Mangan et al. (2017) and the properties for H₂O ice are from Cuffey and Paterson (2010); Klinger (1981); Paige (1992). A temperature cycle is fully damped after around 4 skin depths.

Timescale	Period (s)	Skin Depth (m)				
		Regolith	Sandstone	Basalt	CO ₂ Ice	H ₂ O Ice
1 sol	88806.7	0.0185	0.045	0.14	0.107	0.19
1 year	5.93 x 10 ⁷	0.477	1.16	3.63	2.77	4.92
2 years	1.19 x 10 ⁸	0.675	1.64	5.13	3.91	6.96
10 years	5.93 x 10 ⁸	1.51	3.66	11.5	8.75	15.6
100 years	5.93 x 10 ⁹	4.77	11.6	36.3	27.7	49.2
1000 years	5.93 x 10 ¹⁰	15.1	36.6	115	87.5	155
10,000 years	5.93 x 10 ¹¹	47.7	115	362	276	492
124,000 years (Obliquity cycle)	7.36 x 10 ¹²	167	407	1278	974	1732
Parameters Used to Calculate Skin Depth						
Property	Unit	Regolith	Sandstone	Basalt	CO ₂ Ice	H ₂ O Ice
Thermal conductivity, k	W m ⁻¹ K ⁻¹	0.01	0.1	1.75	0.627	2.5
Density, ρ	kg m ⁻³	1000	1700	2900	1600	930
Specific heat capacity, c_p	J K ⁻¹ kg ⁻¹	830	830	865	967	2097
Thermal inertia	J m ⁻² K ⁻¹ s ^{-$\frac{1}{2}$}	91	375	2095	984	2208

The top-hat tracer distribution experiment involved starting with an initial amount of vapour concentrated in a small portion of the grid and allowing it to diffuse through the grid. The tests were done using the H₂O vapour diffusion scheme described in Section 3.3.1 and were run until the vapour was fully diffused through all grid stretches. The aim of the tests was to understand the effectiveness of each grid stretch both for conserving the amount of vapour and the time taken to reach equilibrium. This is a common type of test for a diffusion scheme and has been used in other studies (e.g Devkota and Imberger, 2009; Scheepbouwer et al., 2008).

An initial concentration of vapour of 1 kg m^{-3} was assumed only in the region between 0.02 m and 0.15 m for the Hourdin et al. (1993) and Steele et al. (2017a) grid stretches, and between 0.02 m and 0.17 m for the constant and variable grid stretches. The initial vapour region was extended for the constant and variable grid stretches to keep the total amount of vapour considered in each simulated test nearly equal. There is still a slight difference between the total amount of vapour in the grids despite the extended region considered, which affects the final equilibrium values. The experiments were initialised with no flux at the upper and lower boundaries, and the model was run for 10 minutes to allow the system to reach equilibrium. Figure 3.2 shows the initial vapour profiles and the grid for each grid stretch tested. The maximum depth of all four of the grid stretches used for the test reached around 30 cm because the upper 30 cm of the subsurface experience the largest changes in temperature across diurnal and annual cycles and therefore will experience the largest vapour fluxes. A summary of the four grid stretches used in these tests is shown in Table 3.2.

Table 3.2: The details of the grid stretches used for the top-hat tracer distribution tests. In the equations shown, dz is the grid spacing, z is the depth of the grid points, z_0 is the initial grid depth, and i is the grid point number. The initial grid step size used for Hourdin et al. (1993) is 0.1 times the skin depth (0.044 m), and $\psi = 2$ to represent the grid depth doubling with each grid point.

	Constant	Variable	Steele et al. (2017a)	Hourdin et al. (1993)
Initial grid depth [m]	0.01	0.01	0.0001	0.0044
Grid stretch	$dz[i] = 0.01$	$z[i] = z[i - 1] \times 1.2$	$z[i] = 2e^{-4} \times 2^{i-0.5}$	$z[i] = z_0 \frac{\psi^{i-1}}{\psi-1}$
No. grid layers	31	19	12	7
Final depth (m)	0.31	0.31	0.29	0.28

The results of these tests (Figure 3.3) show that the four grid stretches equilibrated within 5 minutes and produced similar final equilibrium values, with slight differences due to their slightly different initial total amount of vapour. All four grid stretches equilibrate at the same rate, which means that the time for the MSSM to equilibrate would be unaffected by the grid stretch. In Figure 3.3, the Steele et al. (2017a) and Hourdin et al. (1993) grid stretches appear to have an equilibrated value, in each

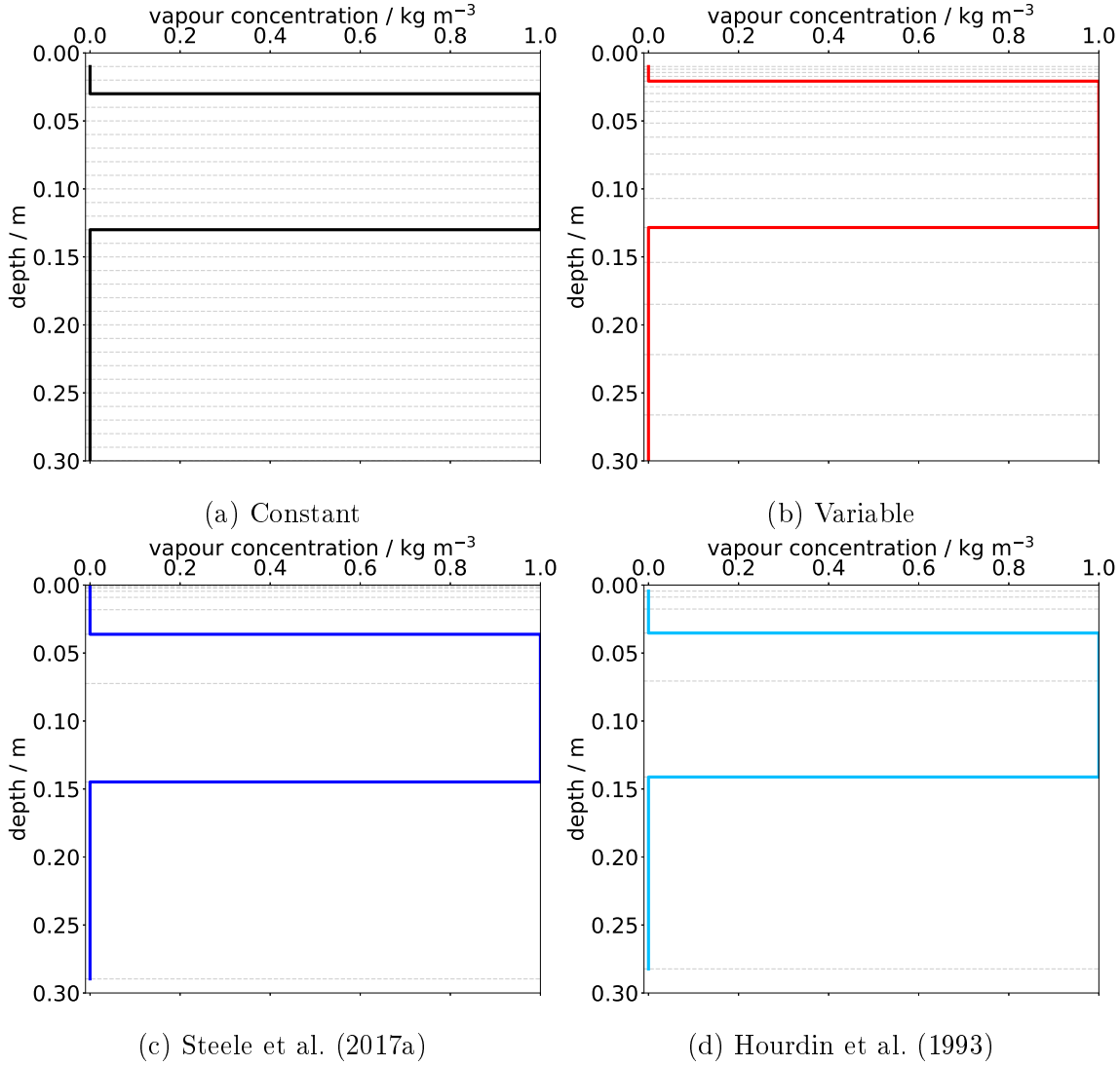


Figure 3.2: Top-hat tracer distribution experiment initial condition over the grid stretch used for (a) the constant grid stretch, (b) the variable grid stretch, (c) the Steele et al. (2017a) grid stretch and (d) the Hourdin et al. (1993) grid stretch. The location of the grid points is shown in light grey and the colours correspond to the colours used for each grid stretch in Figures 3.1 and 3.3 for comparison.

numerical layer, that is closer to the constant stretch’s equilibrated value than the variable grid stretch. However, the total amount of vapour is smaller in the Steele et al. (2017a) and Hourdin et al. (1993) grid stretches than in the variable grid stretch, and the observed difference in the figure is due to the differing grid stretches and boundaries of the grid stretches.

Since the four grid stretches produce similar equilibrated values, the conservation of the grid stretch is the next most important factor to consider. Table 3.3 shows the initial total amount of vapour, the final total amount of vapour and the percentage loss of vapour over the time period for all four grid stretches. While the constant grid stretch conserves the amount of vapour the best, using a constant grid stretch would be computationally infeasible. The next best grid stretch is the variable grid stretch, which conserves the total amount of vapour better than both the Steele et al. (2017a) and Hourdin et al. (1993) grid stretches.

Table 3.3: Checking whether the finite volume discretisation is conservative for four grid stretches, see Table 3.2 for details on the stretches and Section 3.1 for details on the tests

	Constant	Variable	Steele et al. (2017a)	Hourdin et al. (1993)
Initial total [kg m ⁻³]	0.1355	0.1340	0.1334	0.1276
Final total [kg m ⁻³]	0.1354	0.1325	0.1266	0.1215
Percentage Loss over entire time [%]	0.07	1.12	5.09	4.78

These diffusion tests were also run with the Steele et al. (2017a) H₂O vapour diffusion method (Section B.3.1) and using their method, the system was still equilibrating after 4000 simulated minutes, whereas for the H₂O vapour diffusion scheme used in the MSSM, the system equilibrated within 5 simulated minutes for all grid stretches. This showed that the new vapour diffusion scheme is more efficient than that used by Steele et al. (2017a). The tests also showed that vapour in the variable grid stretch was equilibrating to similar values to the constant grid stretch and at a faster rate than in the Steele et al. (2017a) or Hourdin et al. (1993) grid stretches.

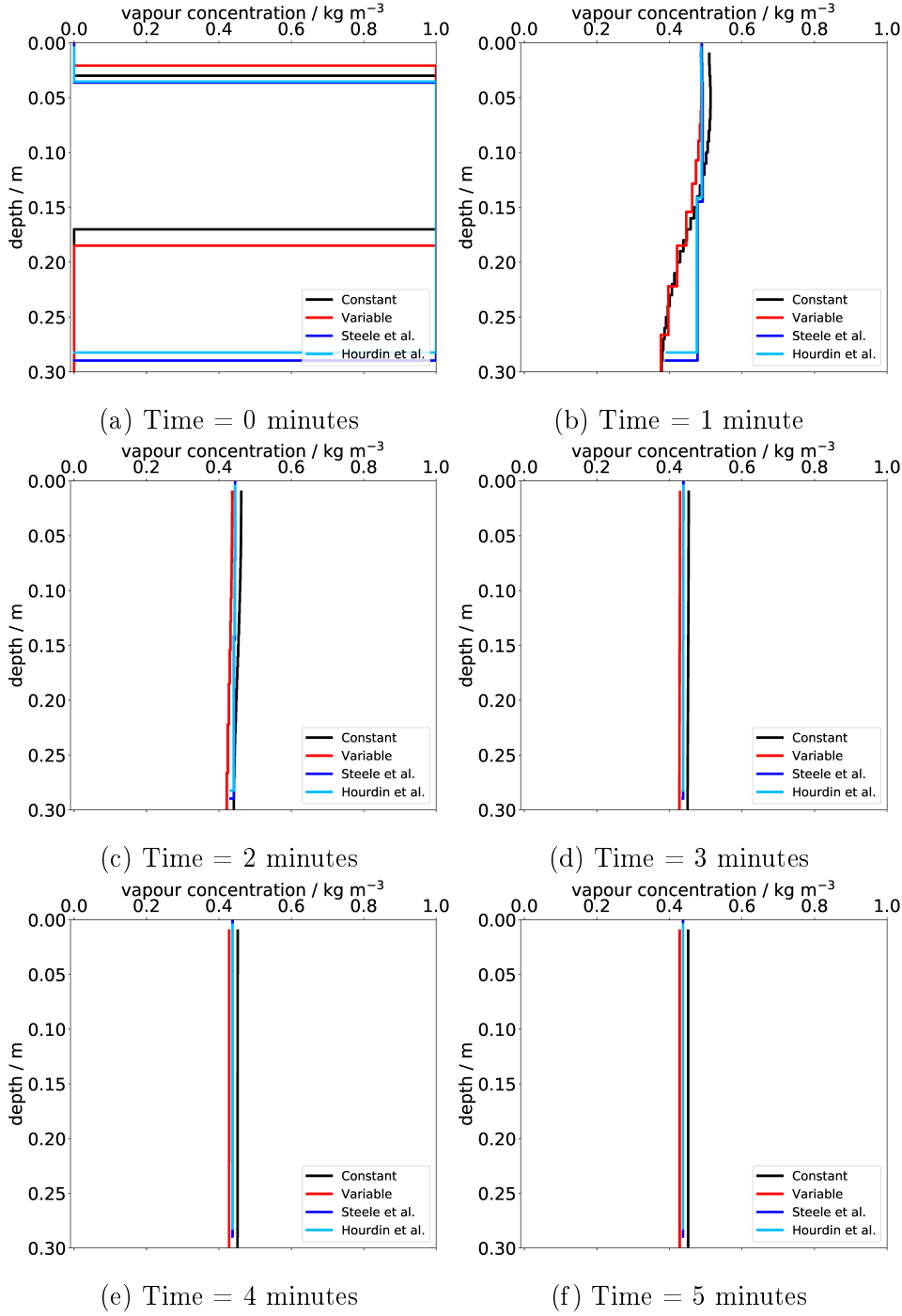


Figure 3.3: Top-hat experiment results to test different grid stretches. (a) An initial 'top hat' profile was applied at the beginning of each run and left to diffuse through the regolith. The rest of the plots show how these profiles changed after (b) 1 minute, (c) 2 minutes, (d) 5 minutes, (e) 20 minutes, (f) 70 minutes. Each line represents a different grid stretch, with black representing the constant grid stretch, red representing the final grid stretch and blue representing the grid stretch of Steele et al. (2017a, see Table 3.2 for more details).

Overall, the Hourdin et al. (1993) and Steele et al. (2017a) grid stretches, which were originally and currently used in the MGCM respectively, have a resolution that is too low for depths greater than 5 cm for the MSSM and a constant grid would require too many layers to be computationally realistic. The variable grid stretch is also nearly as conservative as the constant grid stretch, which is desirable for the MSSM since the amount of vapour in the subsurface should be controlled by the initial condition and fluxes at the boundaries. Therefore, I decided that the variable grid stretch would be the most appropriate for the MSSM as this type of grid ensures a high resolution in the upper 4 m, where the greatest temperature changes occur, and a slightly lower resolution at depths where subsurface temperatures become stable across diurnal and annual cycles in regolith and sandstone materials (>4 m). The resolution at these depths is also still high enough for the diffusion scheme to work effectively.

Since the MSSM is being used for 200 martian year runs, the maximum depth of the model was determined by the depth needed for the annual cycle to be fully damped at the base of the model for all materials being considered. Compact H_2O ice has the largest thermal diffusivity (Equation 2.3) and therefore has the greatest skin depth of the materials used (annual skin depth of H_2O ice is 5 m compared with 0.5 m for regolith; see Table 3.1). As a result, Equation 3.4 is used with 33 grid points to generate a maximum depth of 38 m, which is sufficient for the annual cycle to be damped when the pore space is filled with H_2O ice.

3.2 Thermal Scheme

The thermal scheme was developed before the water and carbon dioxide schemes because subsurface temperature is one of the controlling factors for the diffusion of vapour through a porous soil and because the saturation vapour pressure over an ice or adsorbate surface is exponentially dependent on temperature (Mellon and Jakosky, 1993).

The scheme uses the steady state 1-D heat conduction equation (Equation 3.5) which governs heat transport through the subsurface.

$$\rho(z)c_p \frac{\partial T}{\partial t} = \frac{\partial}{\partial z} \left(k(z) \frac{\partial T}{\partial z} \right), \quad (3.5)$$

where T is the temperature [K] at a depth z [m] and time t [s], k is the thermal conductivity [$\text{W m}^{-1} \text{K}^{-1}$], ρ is the density [kg m^{-3}] and c_p is the specific heat capacity [$\text{J K}^{-1} \text{kg}^{-1}$]. In the MSSM a surface boundary of surface temperatures (from the MGCM) and a base boundary of geothermal heat flux (30 mW m^{-2} ; see Section 2.1.5.5) is used. This equation is discretised (onto the grid shown in Figure 3.4) using the finite control volume method described by Patankar (1980) and Versteeg and Malalasekera (2007) producing Equation 3.6. The discretisation (Equation 3.6) assumes that the value of temperature, T , suddenly changes from T^0 to T^1 over a timestep and then stays at T^1 for the entire timestep.

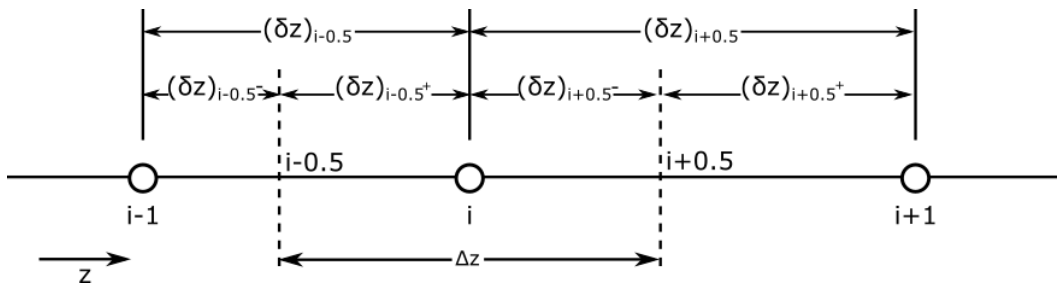


Figure 3.4: Grid used for tri-diagonal matrix algorithm (TDMA), where i is the midpoint of the layer at which the value is currently being calculated, $i - 1$ is the midpoint of the layer before and $i + 1$ is the midpoint of the layer after. $\delta z_{i-0.5}$ and $\delta z_{i+0.5}$ represent the distance between the midpoints of the layers before and after the current layer with the current layer's midpoint, i . Δz is the distance between the interface of layer $i - 1$ (interface $i - 0.5$) and layer $i + 1$ (interface $i + 0.5$), i.e. the thickness of layer i . Figure is adapted from Patankar (1980).

$$\rho c_p \frac{\Delta z}{\Delta t} (T_i - T_i^0) = \frac{k_{i+0.5}(T_{i+1} - T_i)}{(\delta z)_{i+0.5}} - \frac{k_{i-0.5}(T_i - T_{i-1})}{(\delta z)_{i-0.5}}, \quad (3.6)$$

where the superscript 0 represents the value from the previous timestep and the subscripts i , $i - 1$ and $i + 1$ represent the values at the current, previous and next grid point respectively. In these equations $(\delta z)_{i-0.5}$ represents the distance between mid-points and Δz represents the thickness of each layer. The subscripts $i - 0.5$ and $i + 0.5$ represent the values at the interface between the grid points, as shown in Figure 3.4. The values at the interface are calculated assuming the value is constant within one layer and changes instantly at the interface, which is not midway between the grid points since the layers have different thicknesses. Thermal conductivity at the interface is calculated using a weighted harmonic mean to account for the different layer thicknesses:

$$k_{i-0.5} = \left(\frac{1 - f_{i-0.5}}{k_{i-1}} + \frac{f_{i-0.5}}{k_i} \right)^{-1} \quad (3.7a)$$

where

$$f_{i-0.5} = \frac{(\delta z)_{i-0.5+}}{(\delta z)_{i-0.5}} \quad (3.7b)$$

To numerically solve Equation 3.6, it is rearranged into the form of a fully implicit tri-diagonal matrix algorithm ('TDMA'; Equation 3.8), which is time efficient to solve computationally. The implicit version of the TDMA method is used because it allows for the use of substantially larger timesteps than an explicit method. This was an important consideration because the MSSM is used to model an annual cycle with the diurnal cycle smoothed out. If an explicit model was used, a much smaller timestep would be required (~ 1 minute), increasing the number of timesteps for one martian year from 669 (for 1 sol timesteps) to 963,360 (for 1 minute timesteps). This would increase the actual time to run the long multi-year simulations from hours to months and is therefore computationally infeasible in the course of this project.

$$a_i^t T_i = b_i^t T_{i+1} + c_i^t T_{i-1} + d_i^t \quad (3.8a)$$

where

$$a_i^t = \frac{\rho c_p \Delta z}{\Delta t} + \frac{k_{i+0.5}}{(\delta z)_{i+0.5}} + \frac{k_{i-0.5}}{(\delta z)_{i-0.5}} \quad (3.8b)$$

$$b_i^t = \frac{k_{i+0.5}}{(\delta z)_{i+0.5}} \quad (3.8c)$$

$$c_i^t = \frac{k_{i-0.5}}{(\delta z)_{i-0.5}} \quad (3.8d)$$

$$d_i^t = \frac{\rho c_p \Delta z}{\Delta t} T_i^0 \quad (3.8e)$$

For a full overview of the method used to discretise and numerically solve the heat conduction equation see Appendix A.1. Figure 3.5 shows an example of the thermal profiles over a diurnal cycle using Equation 3.8.

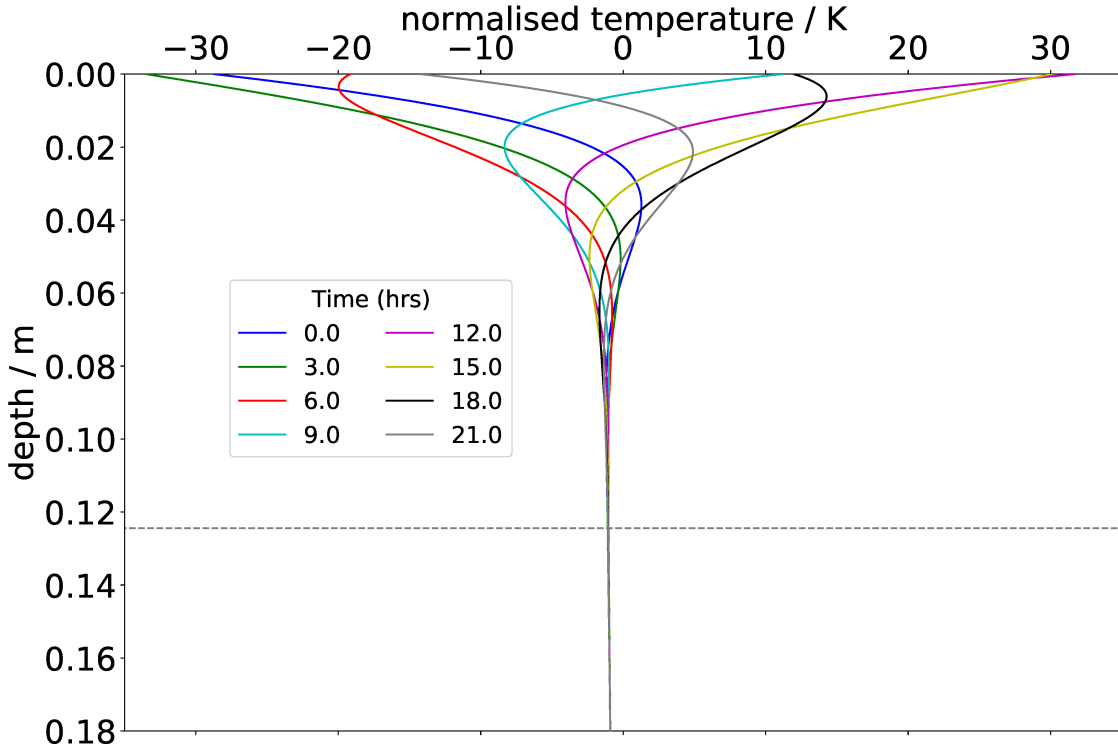


Figure 3.5: Thermal profile of the subsurface at 60° N 180° E and $L_S = 90^\circ$. The surface temperatures are taken from the Mars Climate Database (MCD), geothermal heat flux is 30 mW m^{-2} , and average temperature is 230.3 K . The grey dashed line represents 5 diurnal skin depths.

The value used for specific heat capacity, $c_p = 830 \text{ J K}^{-1} \text{ kg}^{-1}$, is kept constant with depth, and is the value used by both Siegler et al. (2012) and Cornwall (2014) for unconsolidated regolith. The regolith matrix density, ρ_r is varied with depth (Equation 3.9a), using the method of Grott et al. (2007), to account for unconsolidated regolith at the surface that is then compacted with depth. The constants c_3 and c_4 in Equation 3.9a are calculated using the conditions $\rho(z = 0) = \rho_0$ and $\rho(z = 10\text{m}) = 0.95\rho_\infty$, where ρ_0 is the density at the surface and ρ_∞ is the density of the final compacted

material. The regolith porosity, ϕ_r , is then determined from the density difference between the regolith matrix density, $\rho_r(z)$, and the grain material density (assumed to be 2730 kg m^{-3}), using Equation 3.9b (Hütter et al., 2008).

$$\rho_r(z) = \rho_\infty \frac{z + c_3}{z + c_4} \quad (3.9a)$$

$$\phi_r = 1 - \frac{\rho(z)}{2730 \text{ kg m}^{-3}} \quad (3.9b)$$

In the model, ρ_0 and ρ_∞ are assumed to be 1000 kg m^{-3} and 1750 kg m^{-3} , respectively, assuming an unconsolidated regolith at the surface and that the geological material at depth is a coarse sandstone (Grott et al., 2007). The surface density ($\rho_0 = 1000 \text{ kg m}^{-3}$) corresponds to a very low surface porosity ($\approx 63\%$), which is consistent with the estimated porosity of regolith by Demidov et al. (2015) and the lower end of the measurements from the Viking landing site 1, which had an estimated bulk density ranging from 1000 to 1600 kg m^{-3} (Shorthill et al., 1976). This low value of porosity has also been supported by the recent measurements by Heat Flow and Physical Properties Package (HP³) on the InSight Lander, which measured a porosity of 61% between depths of 0.03 and 0.37 m (Grott et al., 2021). A very low porosity has also been interpreted in regions with extremely low thermal inertia as the result of atmospherically sedimented dust (Presley and Christensen, 1997b).

The density of the bulk regolith, ρ_{eff} , and the bulk porosity, ϕ , in the model will also increase with the amount of H_2O ice or CO_2 ice present within the pore space.

$$\rho_{\text{eff}} = \rho_r + \zeta_{\text{H}_2\text{O}} + \zeta_{\text{CO}_2} \quad (3.10a)$$

$$\phi = \phi_r \times \left[1 - \left(\frac{\zeta_{\text{H}_2\text{O}}}{\phi_r \times \rho_{\text{H}_2\text{O}}} \right) \left(\frac{\zeta_{\text{CO}_2}}{\phi_r \times \rho_{\text{CO}_2}} \right) \right], \quad (3.10b)$$

where $\zeta_{\text{H}_2\text{O}}$ and ζ_{CO_2} are the concentration of H_2O ice and CO_2 ice in the pore space. Both of the density of the bulk regolith and the bulk porosity are dependent on the amount of ice that fills the pore space. Pure H_2O ice is assumed to have a constant density, $\rho_{\text{H}_2\text{O}}$, of 920 kg m^{-3} at martian temperatures (Mellon, 1996), whereas, the density of pure CO_2 ice, ρ_{CO_2} , is highly dependent on temperature, as discussed in

Section 3.4.4.

The method to calculate the effective thermal conductivity of the bulk regolith, k_{eff} , is more complex, since it needs to account for conduction through the bulk solid, conduction via pore spaces, and radiative conduction through the pore space since the bulk regolith is porous (Presley and Christensen, 1997a; Siegler et al., 2012). The method used to account for all of these in the model is discussed in the following sections.

3.2.1 Thermal Conductivity of Regolith

The method used for thermal conductivity of the regolith in this model is different from the method currently used in the original subsurface model of the MGCM (Böttger et al., 2005b; Steele et al., 2017a) because the original method assumes that thermal conductivity of the regolith is constant with depth. This assumption is insufficient to describe subsurface thermal properties because thermal conductivity will increase with depth as density increases and porosity decreases (Grott et al., 2007; Presley and Christensen, 1997c) and the method described here accounts for this increase.

The thermal conductivity of the regolith matrix varies with depth and remains constant throughout a single simulation (see Figure 3.6). It is calculated using the following equation from Grott et al. (2007):

$$k_r(z) = k_\infty \frac{z + c_1}{z + c_2} \quad (3.11)$$

The constants c_1 and c_2 are calculated using the conditions $k_r(z=0) = k_0$ and $k_r(z=10m) = 0.95k_\infty$, where k_0 is the thermal conductivity at the surface and k_∞ is the thermal conductivity at depth. The increasing thermal conductivity with depth correlates with the increasing regolith matrix density, ρ_r , and decreasing porosity, ϕ_r , that also occurs with depth, which was found from measurements of the lunar regolith (Heiken et al., 1991). Grott et al. (2007) use the assumption that there is a fine dust layer above the martian regolith, and that heat conduction in the gas filled pores dominates its thermal conductivity at the surface. The surface thermal conductivity (k_0) is therefore the thermal conductivity of CO₂ gas at martian pressures and tempera-

tures, $0.01 \text{ W m}^{-1} \text{ K}^{-1}$. Their model also used two end member values of k_∞ for fine ($0.02 \text{ W m}^{-1} \text{ K}^{-1}$) and coarse ($0.1 \text{ W m}^{-1} \text{ K}^{-1}$) dry sand. In the baseline version of the MSSM used in this work, the compacted geological material is assumed to be coarse dry sand in order to simulate the compaction from an unconsolidated surface layer to a coarse dry sand layer.

The regolith matrix that is used in the baseline version of the MSSM is a simple distribution that captures some of the complexity of the regolith surface (see Section 2.1.1), but it is only representative of some locations on Mars. In reality, the surface material varies with location and is likely to contain several smaller layers of different sedimentary materials, due to redistribution of surface materials over time. Alongside layers of sedimentary materials, a massive basaltic bedrock is expected to underlie the regolith layer and in some locations this bedrock is exposed at the surface. To account for these differences, a series of simulations have been run using different configurations of the regolith matrix, including with a basement layer (see Section 5.2).

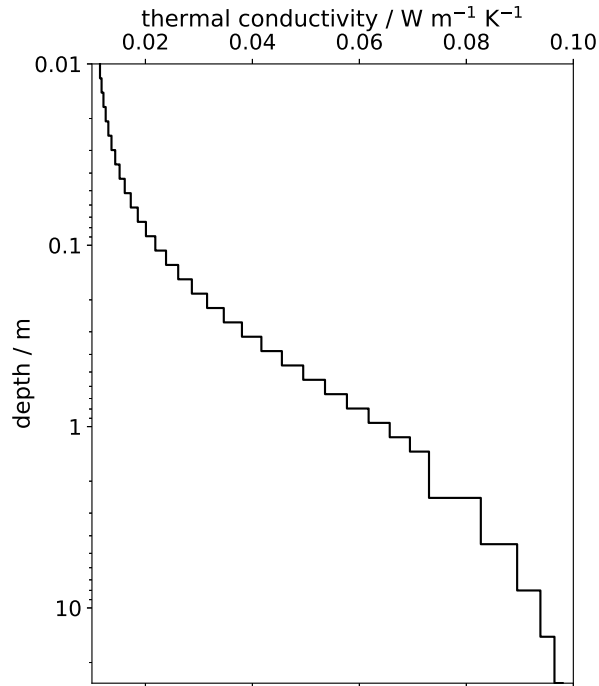


Figure 3.6: Thermal conductivity of the regolith matrix with no ice in the pore space. Calculated using Equation 3.11 and $k_0 = 0.01 \text{ W m}^{-1} \text{ K}^{-1}$ and $k_\infty = 0.02 \text{ W m}^{-1} \text{ K}^{-1}$.

3.2.2 Effective Thermal Conductivity

The effective thermal conductivity is needed in the thermal scheme, but instead of only using the matrix thermal conductivity (k_r), the new model takes into account the presence of ice (either H₂O or CO₂) which changes the thermal conductivity enough that the temperature is significantly affected (e.g., Paige, 1992). This can be seen in Figure 3.7, which shows the seasonal temperature cycle for a subsurface with no ice in the pore space (Figure 3.7a) and a layer of H₂O ice in the upper 1 m and a layer of CO₂ ice below the H₂O ice (Figure 3.7b). As can be seen in the two plots, the presence of H₂O and CO₂ ice significantly increases the annual skin depth (the depth scale over which the temperature cycle is damped) and the temperature profile extends deeper into the subsurface. This will impact the timescales of stability for both H₂O and CO₂ ice which are dependent on temperature.

When calculating the effective thermal conductivity, k_{eff} , of the subsurface, changes in porosity and contact area of the solid materials need to be considered, as heat is conducted through either the contact points between the regolith grains of the matrix or within void spaces. Both the increased contact area of the regolith grains and decreasing porosity of the regolith with depth are intrinsically accounted for within the equation for the thermal conductivity of the regolith, k_r , (Equation 3.11), and do not need to be accounted for in the calculation for the effective thermal conductivity. However, the increase in thermal conductivity due to the increased contact area with increasing ice content is accounted for by the Hertz factor, h (see Section 3.2.2.1). The values used for the thermal conductivity of both H₂O ice, $k_{\text{H}_2\text{O}}$, and CO₂ ice, k_{CO_2} , are discussed in more detail in sections 3.3.2.4 and 3.4.1, respectively.

$$k_{\text{eff}} = k_r + h_{\text{H}_2\text{O}} k_{\text{H}_2\text{O}} + h_{\text{CO}_2} k_{\text{CO}_2} \quad (3.12)$$

3.2.2.1 Hertz Factor

The Hertz factor, h , is defined as the ratio of contact area, A_{cont} , to total area, A_{tot} , if the medium is cut along an arbitrary plane (Shoshany et al., 2002), as shown in

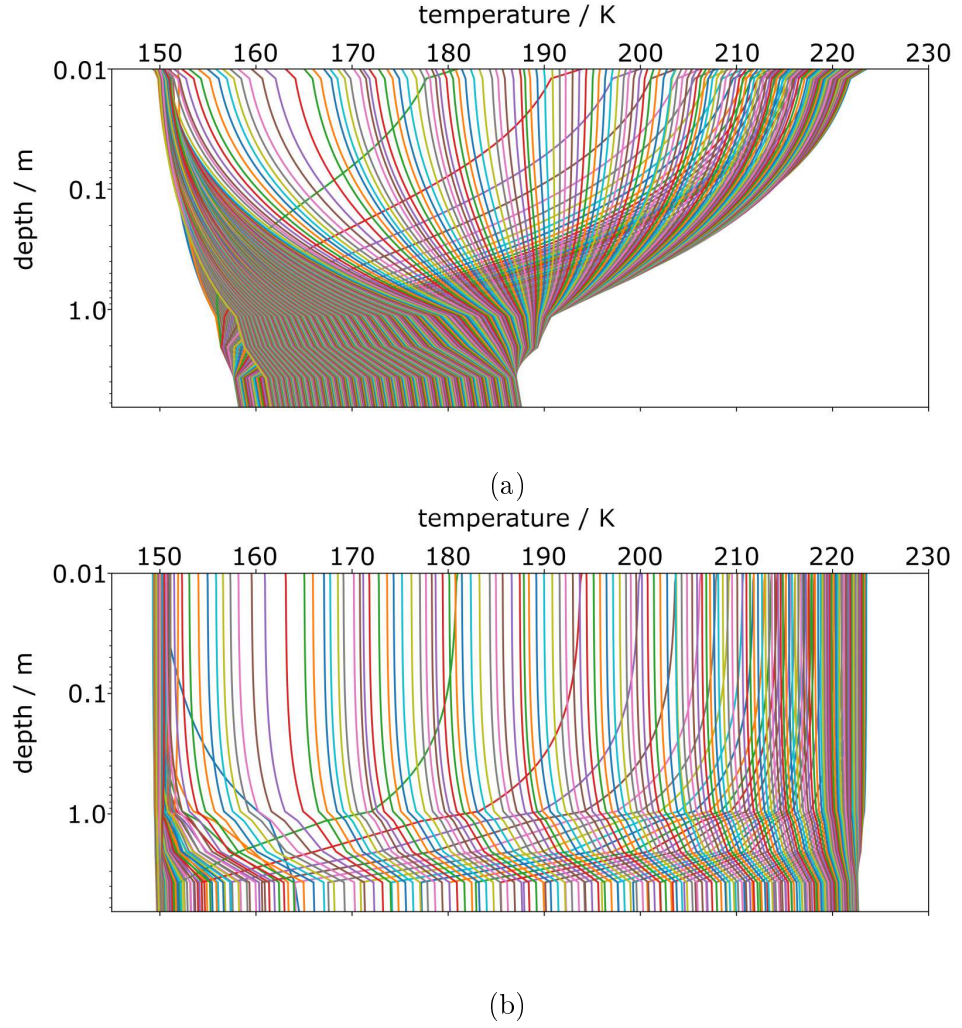


Figure 3.7: The seasonal temperature cycle at 82°N and 104°W with depth using a) only the matrix thermal conductivity and b) the effective thermal conductivity when there is a H₂O ice layer to a depth of 1 m, and a CO₂ ice layer from 1 m to the base. Each line in the plot represents the average diurnal temperature profile for 1 individual sol and all lines together show the variations over an entire year (669 sols).

Equation 3.13.

$$h = \frac{A_{cont}}{A_{tot}} \quad (3.13)$$

It is used to calculate the effective thermal conductivity (Equation 3.12) of the icy regolith (Seiferlin et al., 1996), because the ice contact area will have a large influence on the solid state conduction via grain contact points (Steiner et al., 1991).

The arrangement of the regolith grains to produce each porosity is needed to calculate the Hertz factor. This can be quite difficult to estimate due to the non-uniqueness of packing arrangements that can produce different porosities. To account for this,

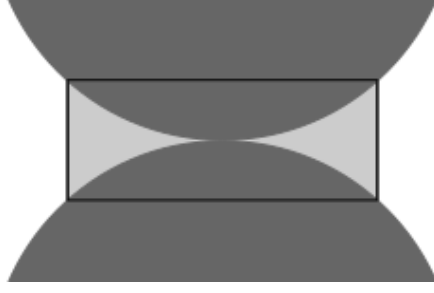


Figure 3.8: Schematic of the contact area between two grains (dark grey) with ice (light grey) forming at the neck shown by the black box.

I have assumed that the regolith is composed of uniform spherical grains and that they are arranged in the simple cubic structure suggested by Piqueux and Christensen (2009). This structure is shown in Figure 3.8 and produces a regolith with a porosity of 47.6%. This structure was then used to calculate ice volumes as a percentage of pore space and the contact area of the ice for a range of grain sizes typical for Martian regolith (from $17\text{ }\mu\text{m}$ to 0.4 cm , as determined from thermal inertia values by Palluconi and Kieffer, 1981).

The range of Hertz factors calculated using Equation 3.13 is only applicable for a porosity of 47.6%, due to the arrangement of grains used to calculate A_{cont} and A_{tot} , and the model uses a variable porosity with depth (Grott et al., 2007, Equation 3.9b). As a result, the calculation for the Hertz factor must also account for the variable initial porosity and I achieved this by applying a scaling law (Equation 3.14) to the Hertz factor value calculated from the initial porosity of 47.6% (h_{47}). The scaling law accounts for the increase in contact area between grains as porosity decreases and the matrix becomes more compacted.

$$h = h_{47} \frac{1 - \phi_0}{1 - 0.47} \quad (3.14)$$

3.2.3 Testing the Thermal Scheme

To ensure that the thermal scheme was calculating an accurate thermal profile with depth, continuous testing was done during development. Testing involved comparing the results from the thermal scheme with analytical solutions for the same problems. The initial thermal scheme (with no grid stretching, layering or basal heat flux) was

tested against Equation 3.15 for a diurnal cycle (Buntebarth, 1984).

$$T(z, t) = T_0 \exp\left(-z\sqrt{\omega/(2\kappa)}\right) \cos\left(\omega t - z\sqrt{\omega/(2\kappa)}\right), \quad (3.15)$$

where κ is the thermal diffusivity (Equation 2.3). This equation is a well-accepted analytical solution for heat conduction into the subsurface with depth, which makes it ideal for testing the thermal scheme. The resulting plots for a normalised temperature cycle (Figure 3.9) are near identical showing that the thermal scheme works as expected.

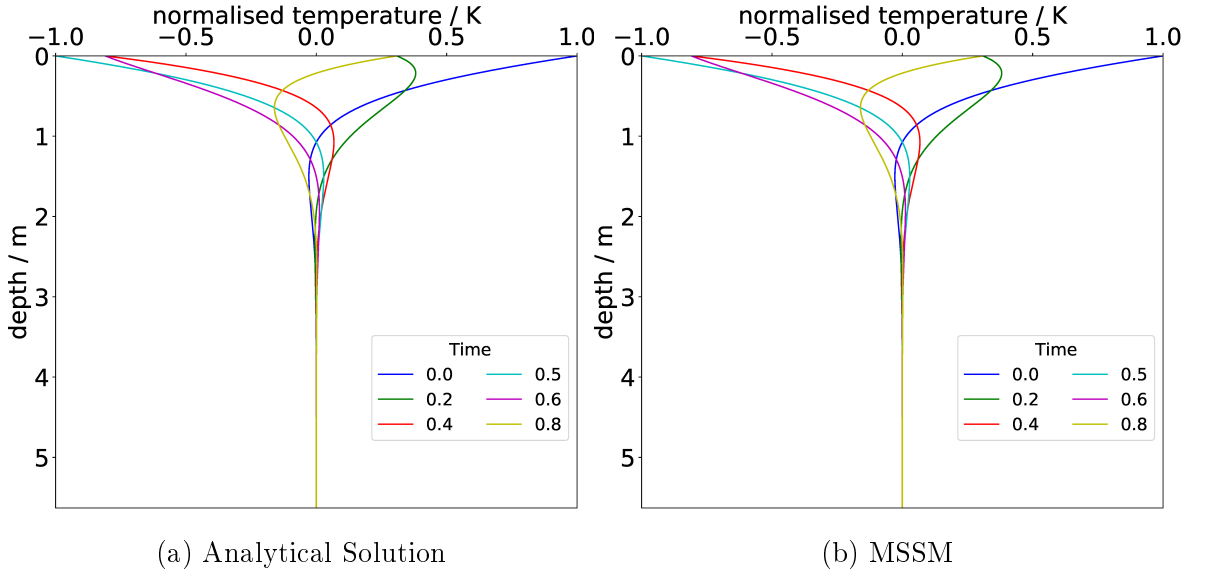


Figure 3.9: The thermal profiles produced by (a) the analytical solution (Equation 3.15) and (b) the MSSM using a normalised temperature range

Each successive feature of the regolith that was implemented (variable grid steps, a multi-layered regolith, constant surface temperatures and a heat flux from the base) was tested against several of the analytical models in Carslaw and Jaeger (1959). This testing ensured that all aspects of the scheme were working as expected.

3.3 Water Scheme

Water is assumed to exist in one of four states: vapour (n), adsorbate (α), pore ice (ζ) and liquid H_2O (ϵ), and the model determines the total H_2O content using:

$$\sigma_{\text{H}_2\text{O}} = n_{\text{H}_2\text{O}} + \alpha_{\text{H}_2\text{O}} + \zeta_{\text{H}_2\text{O}} + \epsilon_{\text{H}_2\text{O}}, \quad (3.16)$$

where $\sigma_{\text{H}_2\text{O}}$ is the total amount of H_2O [kg m^{-3}], $n_{\text{H}_2\text{O}}$ is the density of H_2O vapour per unit volume of regolith [kg m^{-3}], $\alpha_{\text{H}_2\text{O}}$ is the density of adsorbed H_2O [kg m^{-3}], $\zeta_{\text{H}_2\text{O}}$ is the density of subsurface H_2O ice [kg m^{-3}], and $\epsilon_{\text{H}_2\text{O}}$ is the density of subsurface liquid H_2O [kg m^{-3}]. This equation is based on the water scheme that is currently included in the MGCM (see Appendix B.3 for details on the current model; Böttger et al., 2005b; Steele et al., 2017a; Zent et al., 1993). The amount of H_2O vapour is calculated using a vapour diffusion scheme (Section 3.3.1), alongside a scheme to determine the partitioning of H_2O between the vapour, liquid and ice phases (Section 3.3.2). All of the properties that need to be calculated for vapour diffusion and the partitioning of H_2O are described in the following sections, and where possible equations and values from the current subsurface model in the MGCM (Steele et al., 2017a) have been used for consistency with previous work.

For the purpose of this study, a constant adsorption value has been included to simplify the overall model, and because the studies of H_2O adsorption on Mars for a variety of geological materials show a very large distribution of values (discussed in more detail in Section 3.3.2.3). I also decided a constant adsorption value would be used because there are a limited number of studies on the adsorption of CO_2 in the martian regolith (Section 3.4.3.2) and I have only included features that could be added for both H_2O and CO_2 since I am primarily investigating subsurface CO_2 ice. This decision limited the overall complexity, which proved useful since there has not been a similar study into subsurface CO_2 to compare the results of this work with and there is a limited understanding of what processes will impact subsurface CO_2 ice in the literature.

3.3.1 Vapour Diffusion through the Regolith

The process by which H_2O vapour is transported through the regolith is controlled by the unsteady diffusion equation (Fick's 1st law), which is expressed as follows in 1-D:

$$f_{\text{H}_2\text{O}} = D_{\text{H}_2\text{O}} \frac{\partial n_{\text{H}_2\text{O}}}{\partial z}, \quad (3.17)$$

where $f_{\text{H}_2\text{O}}$ is the H_2O vapour flux [$\text{kg m}^{-1}\text{s}^{-1}$], $D_{\text{H}_2\text{O}}$ is the H_2O diffusion coefficient [m^2s^{-1}] (see Section 3.3.1.1), and $n_{\text{H}_2\text{O}}$ the H_2O vapour concentration [kg m^{-3}]. This is combined with the relation $\frac{\partial n_{\text{H}_2\text{O}}}{\partial t} = \frac{\partial f_{\text{H}_2\text{O}}}{\partial z}$ to form the diffusion equation that needs to be solved:

$$\frac{\partial n_{\text{H}_2\text{O}}}{\partial t} = \frac{\partial}{\partial z} \left(D_{\text{H}_2\text{O}} \frac{\partial n_{\text{H}_2\text{O}}}{\partial z} \right) \quad (3.18)$$

The base boundary has no flux and there is a positive flux towards the atmosphere from the subsurface (see Section 3.5 for details) in the MSSM.

The discretised form is calculated by integrating Equation 3.18 over a finite timestep, δt , and control volume, cv (Equation 3.19; Patankar, 1980; Versteeg and Malalasekera, 2007), following the same method used for the thermal scheme (Equations 3.6-3.8). To make the following equations easier to read n and D have been used instead of $n_{\text{H}_2\text{O}}$ and $D_{\text{H}_2\text{O}}$ since in this case all the variables relate to H_2O vapour. The superscripts relate to time (where t represents the current timestep) and the subscripts relate to the grid point (where i represents the current grid point).

$$\int_{cv} \int_t^{t+\delta t} \left(\frac{\partial n}{\partial t} dt \right) dV = \int_t^{t+\delta t} \int_{cv} \left(\frac{\partial D \frac{\partial n}{\partial z}}{\partial z} dV \right) dt \quad (3.19)$$

The discretised form of this equation (Equation 3.20a) can be divided by $A \Delta t$ to produce Equation 3.20b, which is in the same form as the discretised form of the heat conduction equation (Equation 3.6)

$$\left(\Delta V + \frac{D_{i+0.5}^t A_i \delta t}{\delta z_i} + \frac{D_{i-0.5}^t A_{i-1} \delta t}{\delta z_{i-1}} \right) n_i^t - \frac{D_{i+0.5}^t A_i \delta t}{\delta z_i} n_{i+1}^t - \frac{D_{i-0.5}^t A_{i-1} \delta t}{\delta z_{i-1}} n_{i-1}^t = \Delta V n_i^{t-\delta t} \quad (3.20a)$$

$$\left(\frac{\Delta z}{\Delta t} + \frac{D_{i+0.5}^t}{\delta z_i} + \frac{D_{i-0.5}^t}{\delta z_{i-1}} \right) n_i^t - \frac{D_{i+0.5}^t}{\delta z_i} n_{i+1}^t - \frac{D_{i-0.5}^t}{\delta z_{i-1}} n_{i-1}^t = \frac{\Delta z}{\Delta t} n_i^{t-\delta t} \quad (3.20b)$$

The matrix from this equation is diagonally dominant and is now in the correct form to be numerically solved with a fully implicit TDMA, similar to the thermal scheme. The implicit version of the TDMA is required for vapour diffusion because using an explicit scheme would require a timestep of less than 2 milliseconds for stability according to the Courant-Fredric-Lewy condition for stability. This timestep is much smaller than the timestep of 1 sol being used in this study, whereas an implicit method allows for a

large timestep to be used, which is required for the stand-alone MSSM.

Equations 3.21a-e show the rearrangement of Equation 3.20b for a TDMA. For a detailed derivation of the equations used for the diffusion scheme see Appendix A.2.

$$a_i^t n_i = b_i^t n_{i+1} + c_i^t n_{i-1} + d_i^t \quad (3.21a)$$

where

$$a_i^t = \frac{\Delta z}{\Delta t} + \frac{D_{i+0.5}^t}{\delta z_i} + \frac{D_{i-0.5}^t}{\delta z_{i-1}} \quad (3.21b)$$

$$b_i^t = \frac{D_{i+0.5}^t}{\delta z_i} \quad (3.21c)$$

$$c_i^t = \frac{D_{i-0.5}^t}{\delta z_{i-1}} \quad (3.21d)$$

$$d_i^t = \frac{\Delta z}{\Delta t} n_i^{t-\delta t} \quad (3.21e)$$

3.3.1.1 Diffusion Coefficient

In the MSSM I have used the diffusion coefficient experimentally determined by Hudson et al. (2007) (also used in the current subsurface model of the MSSM; Steele et al., 2017a), which considers the effects of both normal (D_N) and Knudsen Diffusion (D_K), with the coefficients for each type of diffusion described by Equations 3.22a and 3.22b respectively. The two types of diffusion describe whether the molecules are colliding predominantly with each other (normal or molecular diffusion), or predominantly with the walls of the pores (Knudsen diffusion). The type of diffusion that occurs within the pore space depends on the ratio between the pore size and the mean free path of the molecules, λ . If the ratio is much greater than 1 then diffusion is occurring in the normal regime, if it is much less than 1 then diffusion is occurring in the Knudsen regime. In the transition region between these two regimes, where collisions with pore walls and with other molecules occur frequently, a combined or effective diffusion coefficient is needed (Equations 3.22c and 3.22d). For H₂O diffusing in a 6 mbar dry CO₂ atmosphere, the mean free path of H₂O vapour is roughly 9 μm (Hudson et al., 2007). In this model, it is assumed that the pore radius is 50 μm , with a ratio of ~ 5.5 ,

and therefore diffusion is always occurring in the transition region.

$$D_N = 0.1654 \text{ cm}^2 \text{ s}^{-1} \phi_r^{4/3} \frac{P_{\text{ref}}}{P(z)} \left(1 - \frac{\zeta}{\rho_{\text{H}_2\text{O}} \phi_r}\right)^2 \left[\frac{T(z)}{T_{\text{ref}}}\right]^{\frac{3}{2}} \quad (3.22a)$$

$$D_K = \frac{\pi}{8 + \pi} \frac{\phi}{1 - \phi} \frac{\bar{v} \bar{r}}{\tau} \quad (3.22b)$$

$$D_{N_{\text{new}}} = \frac{\phi}{\tau} D_N \quad (3.22c)$$

$$D_{\text{H}_2\text{O}} = \left(\frac{1}{D_{N_{\text{new}}}} + \frac{1}{D_K} \right)^{-1} \quad (3.22d)$$

In Equations 3.22a to 3.22d: D_N is the normal diffusion coefficient [$\text{m}^2 \text{ s}^{-1}$], ϕ_r is the ice-free porosity, T_{ref} is the reference temperature ($T_{\text{ref}} = 273.15 \text{ K}$), P_{ref} is the reference pressure ($P_{\text{ref}} = 1013 \text{ mbar}$), $P(z)$ is the pressure at depth z [mbar], D_K is the Knudsen diffusion coefficient [$\text{m}^2 \text{ s}^{-1}$], ϕ is the porosity, \bar{v} ($= (8k_B T / \pi m_w)^{1/2}$) is the mean velocity of the diffusing molecules (where m_w is the mass of one molecule of H_2O and k_B is the Boltzmann constant), \bar{r} is the average pore size in the regolith [m], τ is the tortuosity (see Section 3.3.1.2), $D_{N_{\text{new}}}$ is the updated normal diffusion coefficient that accounts for porosity and tortuosity [$\text{m}^2 \text{ s}^{-1}$], and $D_{\text{H}_2\text{O}}$ is the final diffusion coefficient [$\text{m}^2 \text{ s}^{-1}$] that is used in the MSSM.

Hudson and Aharonson (2008) presented an improved method for the diffusion coefficient, using Equations 3.23a-3.23c.

$$D_N = 0.1654 \text{ cm}^2 \text{ s}^{-1} \phi_0^{4/3} \frac{p_{\text{ref}}}{p(z)} \left[\frac{T(z)}{T_{\text{ref}}}\right]^{\frac{3}{2}} \quad (3.23a)$$

$$D_K = \frac{1}{3} \langle l_p \rangle \langle v \rangle \left[\frac{\langle l_p^2 \rangle}{2 \langle l_p \rangle^2 - \beta} \right] \quad (3.23b)$$

$$D_{\text{Hudson08}} = \frac{\phi}{\tau} \left(\frac{1}{D_F} + \frac{1}{D_K} \right)^{-1} \quad (3.23c)$$

where $\langle l_p \rangle$ is the first moment of the chord length distribution (Levitz, 1993), β is a series sum of cosine angles between sequential trajectory segments that are separated by wall collisions. The chord length distribution, l_p , is the range of distances that a vapour particle can travel before hitting a pore wall, assuming random trajectories, and the first moment, $\langle l_p \rangle$, represents the most likely distance that a particle will

travel. It is determined using the method of Zalc et al. (2004) and can be estimated by $\langle l_p \rangle_{estimated} = \frac{4\phi}{S_v}$, where S_v is the surface area per unit volume. Zalc et al. (2004) and Hudson and Aharonson (2008) have shown that $\beta \approx 4/3 = 0.3077$. The porosity, ϕ , is dependent on ice content and is calculated using the method described in Section 3.2.2.1 and Equation 3.9b.

This method uses a more realistic Knudsen diffusion equation (Equation 3.23b), which accounts for variable pore sizes throughout the regolith using a theoretical pore size distribution. Another difference between the methods is the way the final diffusion coefficient, D , is calculated, using Equation 3.23c. The method of Hudson and Aharonson (2008) uses the average of the diffusion coefficients before accounting for the effect of porosity and tortuosity, whereas the method of Hudson et al. (2007) accounts for the effect of porosity and tortuosity on normal and Knudsen diffusion individually before calculating the average. While this is an improved version of the diffusion coefficient equations of Hudson et al. (2007), these equations are not used in the MSSM due to uncertainties in the calculations of $\langle l_p \rangle$, S_v and β .

3.3.1.2 Tortuosity

In porous media, the interconnectedness of pores and the sinuosity between them will impact the transport of vapour through them (also known as the permeability; Clennell, 1997; Smoluchowski, 1968; Toon et al., 1980), and this is accounted for by the tortuosity factor. The tortuosity is a structural property of a porous medium that is independent of diffusive regime (Sizemore and Mellon, 2008) and encompasses the effects of all geometrical and chemical interactions that could impact diffusion of vapour through the pore space (Clennell, 1997). In general, porosity effects are excluded from the tortuosity factor (as they are accounted for elsewhere), and the tortuosity only accounts for the effects of sinuosity and dead-end pore space (Clennell, 1997). Tortuosity can be defined as the ratio of the shortest available path to the straight line between two connected pores (Clennell, 1997).

The value for tortuosity is not well constrained as it cannot be directly measured and its value varies depending on the method used. There is also no unique relationship

between the porosity and tortuosity that can be applied to all porous materials, but previous studies show an inverse relationship between the two (Currie, 1960; Sizemore and Mellon, 2008; Smoluchowski, 1968). In a study by Sizemore and Mellon (2008), the value of tortuosity was determined from a combination of experimental measurements of flux, porosity, pore size and martian environmental conditions. They found that measured values of tortuosity for glass spheres range from 1.33 to 1.62, which is consistent with previous measurements by Currie (1960). They used the empirical relationship that is often used for beds of unconsolidated particles:

$$\tau = \frac{1}{(\phi - C)^n}, \quad (3.24)$$

where τ is the tortuosity, ϕ is the porosity, n is typically a value between 0.3 and 0.5, and C is a constant related to the range of porosities for a given particulate material. They found that when using $n = 0.3$ and $C=0$, the empirical relationship fit their data well. For JSC Mars-1 (an analog for martian regolith), Sizemore and Mellon (2008) determined that tortuosity ranges from 1.77 to 2.31 for porosities between 0.5 and 0.8, and these results also fit Equation 3.24 when $C = 0.2$ and $n = 0.5$. Similar tortuosity values to those for JSC Mars-1 were also found for soil samples from the Antarctic Dry Valleys (Sizemore and Mellon, 2008). These values were at the lower end of tortuosities reported in previous work (between 1 and 16; Satterfield, 1970) and two to three times lower than the values that are generally used in theoretical studies of martian diffusion (Hudson and Aharonson, 2008; Hudson et al., 2007; Mellon and Jakosky, 1993; Smoluchowski, 1968; Titov, 2002). These previous martian studies all used the values of Smoluchowski (1968), who state tortuosity values of 1, 2 and 10 for porosities of 0.8, 0.5 and less than 0.5, respectively. Smoluchowski (1968) concludes that there is a rough upper limit of 2.5 on the tortuosity of unconsolidated dry soils, with values typically between 1.5 and 2.

Ideally a different value of tortuosity would be used depending on both the material and the porosity based on the literature described above. This is not possible since porosity and tortuosity are related but not dependent on each other, and therefore there is no unique relationship between them that can be used for all porous mate-

rials (Sizemore and Mellon, 2008). The relationship described above (Equation 3.24; Sizemore and Mellon, 2008) is also only applicable for unconsolidated dry soils, while the values for porosity in the MSSM assume that the regolith is compacted with depth from an unconsolidated regolith (Equation 3.9b). This compaction with depth will cause a corresponding increase in the tortuosity value as the lower porosity will reduce the number of available pathways between pores. Since the equation discussed for tortuosity is only applicable for an unconsolidated regolith, it is not suitable for this work. As a result, the MSSM uses a constant tortuosity of 1.5, which is the lower limit of the range found by Sizemore and Mellon (2008) under martian conditions, and is applicable for high porosities which is the case for the near-surface empty regolith used here.

The presence of ice within the subsurface will also have an impact on the tortuosity, because it will reduce the number of free pathways for vapour to travel through. Therefore, when ice is present within the subsurface, the tortuosity value will be expected to increase. This increase in tortuosity value will cause a reduction in the diffusion coefficient (e.g. Equation 3.23c) and will result vapour taking longer to diffuse out of the subsurface. This in turn would cause ice (either H_2O or CO_2) to survive even longer when buried beneath an overlying porous layer. However, the effect of the presence of ice on the tortuosity value is unknown and since the regolith tortuosity value is uncertain, I have decided to not incorporate the impact of a variable tortuosity with ice content into the MSSM because of this uncertainty, and investigating the impact of tortuosity will be an area for future work.

3.3.2 Distribution of H_2O through the Regolith

The presence of H_2O vapour, ice and liquid is dependent on where in the phase diagram (Figure 3.10) the pressure and temperature conditions fall. H_2O ice forms at all pressures as long as the temperature is below the frost point temperature, but the equation for frost point temperature is different above and below the triple point pressure of H_2O (6.11 mbar; Hardy, 1998). To account for this, different equations of state are used for above and below the triple point, as shown in the phase diagram in Figure 3.10 and described in the following sections. For the temperatures and pressures expected in

Mars' shallow subsurface, H_2O ice is assumed to have a density of 920 kg m^{-3} , since the density of H_2O ice does not vary with temperature as much as the density of CO_2 ice does (Cuffey and Paterson, 2010; Mangan et al., 2017). The change in density due to high pressures, such as at the base of glaciers, is not considered in this work, since H_2O ice is assumed to form as pore ice, with very little overburden pressure.

The presence of liquid H_2O on Mars, on the other hand, is only possible if the partial pressure of H_2O rises above the triple point. While the presence of liquid H_2O is not expected at the surface in the present-day (e.g., Hoffman, 2001), the inclusion of it in the water scheme allows for this theory to be tested and for future studies to test its formation under the higher H_2O partial pressure conditions expected during the Noachian (such studies have already been done for surface H_2O ice; e.g., Wordsworth et al., 2013).

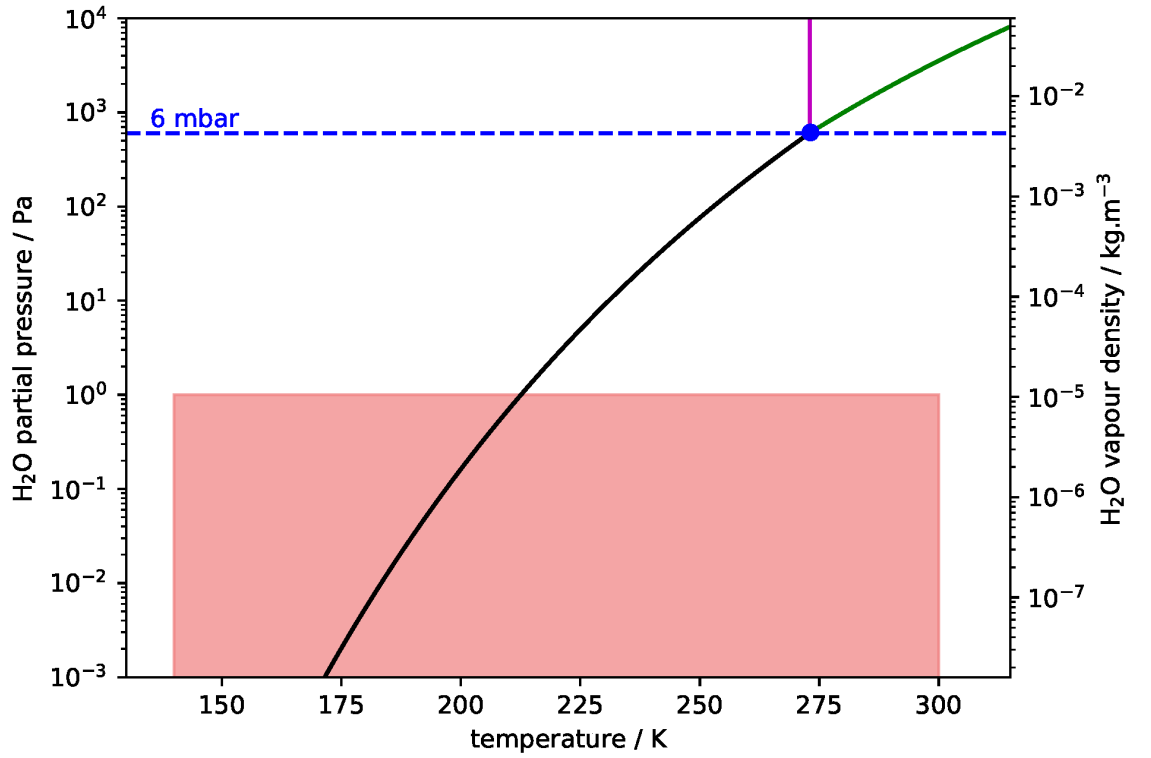


Figure 3.10: Phase diagram for H_2O from the equations incorporated into the model. The blue dot represents the triple point at 273.16 K and 6.11 mbar (Hardy, 1998). The saturation vapour pressure over ice (black line) is Equation 3.28, the saturation vapour pressure over liquid H_2O (green line) is Equation 3.29 and the melting point curve (pink line) is constant with pressure at 273.16 K. The conditions appropriate to Mars (red box) show the range of partial pressures expected in the atmosphere and does not represent regions of localised higher partial pressure such as at the base of glaciers.

3.3.2.1 Conditions Below the Triple Point Pressure

In general, conditions on Mars are below the triple point pressure of H₂O (e.g., Jakosky, 1985a). Consequently, the main phase transition that needs to be considered is between vapour and ice. This occurs when the saturation vapour pressure over ice is reached (Hardy, 1998).

Several equations have been used to calculate the saturation vapour pressure over ice, at a temperature T , in martian studies including those in Steele et al. (2017a); Stevens et al. (2001), and Bryson et al. (2008): Equations 3.25-3.27 respectively.

$$P_{Steele} = 611 \exp \left(22.5 \times \frac{1 - 273.16}{T} \right) \quad (3.25)$$

$$P_{Stevens} = \exp \left(28.868 - \frac{6132.935}{T} \right) \quad (3.26)$$

$$P_{Bryson} = 10^{7.551 - \frac{2666}{T}} * 100000 \quad (3.27)$$

Another equation for the saturation vapour pressure over ice is given by Hardy (1998, Equation 3.28), and is the generally accepted equation for saturation vapour pressure over ice. It is only valid below the triple point of H₂O (273.16 K and 6.11 mbar; Jakosky, 1985a) and is therefore appropriate for martian conditions. A comparison of the four equations (Figure 3.11) shows that the equations only differ slightly near the triple point and the variation is quite small. From this comparison, Equation 3.28 was chosen to be used in the water scheme because it is widely accepted as the standard equation for the vapour pressure of H₂O over ice.

$$\ln(P_{sat_{H_2O}}) = \frac{k_0}{T} + k_1 + k_2 T + k_3 T^2 + k_4 T^3 + k_5 \ln(T), \quad k_0 = -5866.6426 \quad (3.28a)$$

$$k_1 = 22.32870244 \quad (3.28b)$$

$$k_2 = 0.0139387003 \quad (3.28c)$$

$$k_3 = -3.4262402 \times 10^{-5} \quad (3.28d)$$

$$k_4 = 2.7040955 \times 10^{-8} \quad (3.28e)$$

$$k_5 = 0.67063522 \quad (3.28f)$$

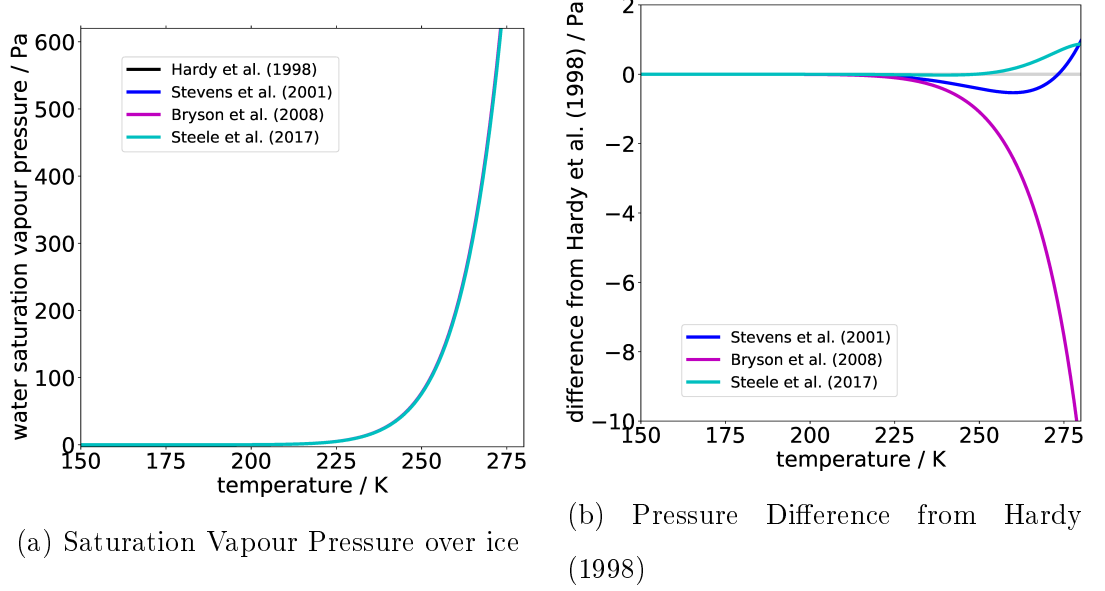


Figure 3.11: (a) Comparison of different equations for saturation vapour pressure over ice (b) The difference in saturation vapour pressure between Equations 3.25-3.27 and Equation 3.28 which is used in the final water scheme (Bryson et al., 2008; Hardy, 1998; Steele et al., 2017a; Stevens et al., 2001).

3.3.2.2 Conditions Above the Triple Point Pressure

Above the triple point pressure, liquid H_2O becomes stable and a different set of equations of state are needed to determine the state of H_2O . In this region, the saturation vapour pressure is found over liquid H_2O rather than H_2O ice, and Equation 3.29 is the accepted equation for this (Hardy, 1998).

$$\ln(P_{sat_{\text{H}_2\text{O}}}) = \frac{g_0}{T^2} + \frac{g_1}{T} + g_2 + g_3 T + g_4 T^2 + g_5 T^3 + g_6 T^4 + g_7 \ln(T), \quad (3.29a)$$

where

$$g_0 = -2836.5744 \quad (3.29b)$$

$$g_1 = -6028.076559 \quad (3.29c)$$

$$g_2 = 19.54263612 \quad (3.29d)$$

$$g_3 = -0.02737830188 \quad (3.29e)$$

$$g_4 = 1.6261698 \times 10^{-5} \quad (3.29f)$$

$$g_5 = 7.0229056 \times 10^{-10} \quad (3.29g)$$

$$g_6 = -1.8680009 \times 10^{-13} \quad (3.29h)$$

$$g_7 = 2.7150305 \quad (3.29i)$$

The phase transition from liquid H₂O to ice is different from the phase transition from vapour to liquid, as the freezing temperature remains near enough constant at 273.16 K with increasing pressure up to pressures of around 10 MPa (Sanz et al., 2004). Using this constant temperature condition for the phase change from liquid H₂O to ice is applicable for the MSSM, as H₂O partial pressures are not expected to reach 10 MPa near the martian surface at any point in Mars' history.

3.3.2.3 Adsorption

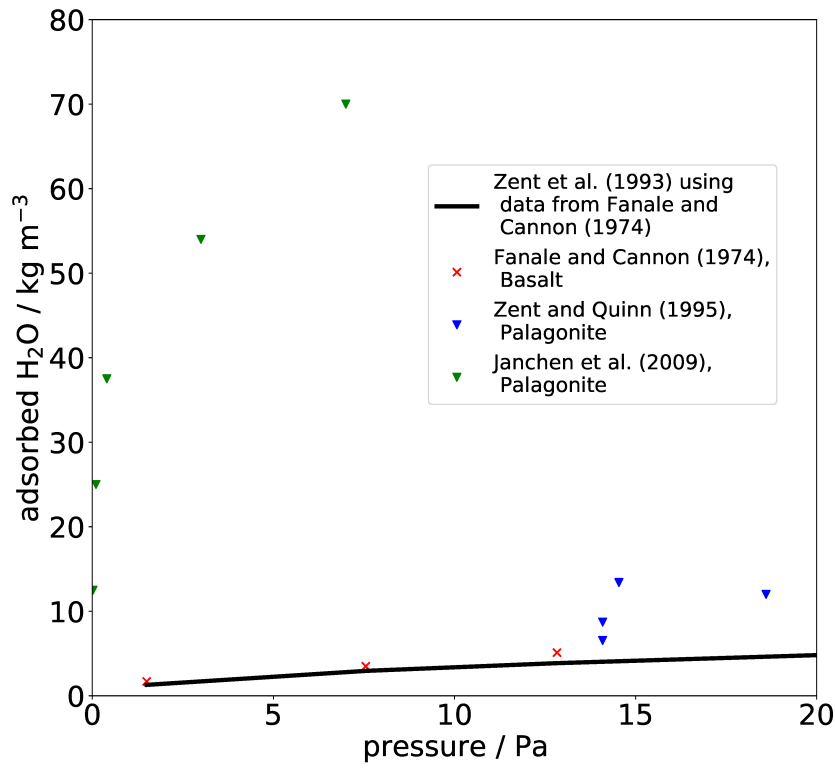
The adsorption of H₂O onto regolith grains is a complex topic that has been studied many times experimentally under martian conditions (e.g., Fanale and Cannon, 1974; Jänchen et al., 2006; Zent and Quinn, 1995). However, the results from these studies use a variety of different geological materials and show variations greater than an order of magnitude in the amount adsorbed between the different geological materials used. The experimental study of Fanale and Cannon (1974) on basalt grains (and the equation to fit these data points from Zent et al., 1993) have been well cited in previous studies (e.g., Blackburn et al., 2010; Schorghofer and Forget, 2012; Steele et al., 2017a). Steele et al. (2017a) incorporated this isotherm into their vapour diffusion scheme, which was found to be not conservative, and the assumptions used to simplify the adsorption equation for the diffusion scheme resulted in values that greatly differed from those

produced by the original equation (see Appendix B.3.2 for details on the testing done on the Steele et al., 2017a, scheme). This led to the decision that the adsorption equation should no longer be incorporated into the diffusion scheme, and this is one reason why the diffusion equation I used for the MSSM differs from the one currently used in the MGCM. The decision to not incorporate the adsorption isotherm into the diffusion scheme resulted in a detailed study of adsorption studies for Mars to ensure that the most appropriate representation of adsorption was used.

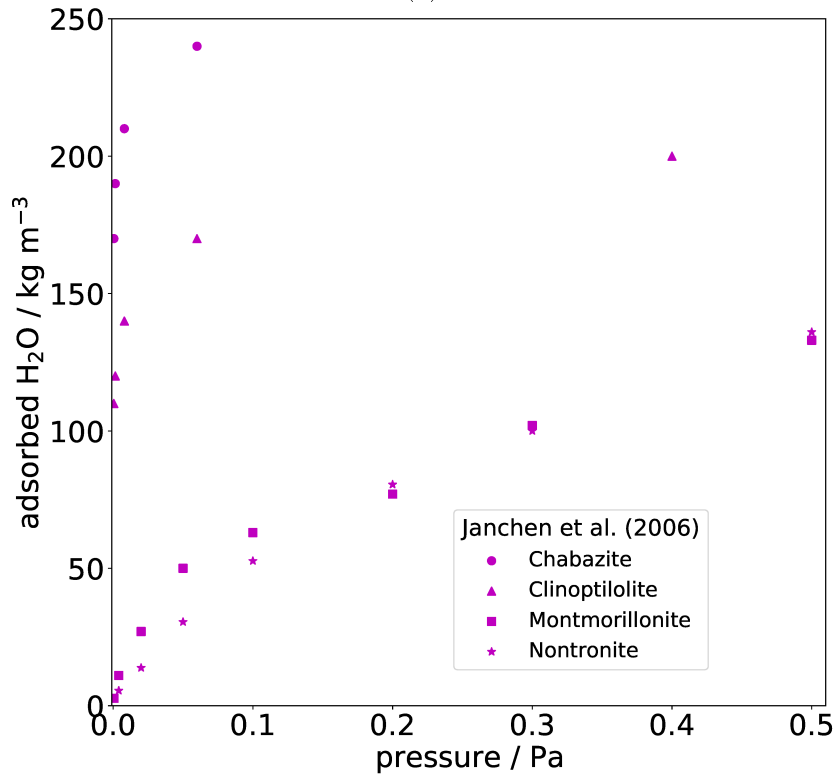
The amount of H₂O that is adsorbed onto a regolith grain is heavily dependent on the adsorptive capacity of the grain and the conditions (temperature and pressure) of the system (Möhlmann, 2002). Basalt is a common geological material across the surface of Mars (alongside its weathering products) and is often used as a representative for the entire surface, but it is not very adsorptive (e.g., Fanale and Cannon, 1971). Clay minerals (e.g. montmorillonite and nontronite), on the other hand, are around twice as adsorptive as basalts and occur in several locations across Mars (Jänchen et al., 2006). Different geological materials therefore have a large influence on the amount of H₂O that is adsorbed and will also affect the diffusion of H₂O through the regolith. Consequently, a comparison of the experimental work on the amount of H₂O adsorbed by these materials under martian conditions was undertaken.

Figure 3.12 shows the wide range of values for the amount of adsorbed H₂O that have been measured across various geological materials (including basalt, palagonite, zeolitic minerals and clay minerals) under martian conditions (Fanale and Cannon, 1974; Jänchen et al., 2006, 2009; Zent and Quinn, 1995). The results from several studies (Bryson et al., 2008; Farris et al., 2018; Nikolakakos and Whiteway, 2018; Pommerol et al., 2009) are not shown in Figure 3.12 because the units¹ used to present their results are not compatible for conversion to kg m⁻³, the units used in this work, and therefore are not comparable to the results shown in the figure. Consequently, the values in the excluded studies (Bryson et al., 2008; Farris et al., 2018; Nikolakakos and Whiteway, 2018; Pommerol et al., 2009) were not considered for use in the MSSM.

¹Results were presented in H₂O content (Farris et al., 2018; Pommerol et al., 2009), ramen signal (Nikolakakos and Whiteway, 2018; Pommerol et al., 2009) or as BET coefficients (Bryson et al., 2008; Farris et al., 2018)



(a)



(b)

Figure 3.12: H_2O adsorption results from the experimental studies of (a) Fanale and Cannon (1974), Zent and Quinn (1995), Jänchen et al. (2009) and (b) Jänchen et al. (2006). The results have been split according to the differences in pressures used for the experiments.

The experimental studies included in Figure 3.12 show the importance of the geological material being considered: the basaltic materials (basalt and palagonite; Figure 3.12a) adsorb a significantly smaller amount of H₂O than the rest of the geological materials considered (Figure 3.12b) which are all strongly adsorbing due to their larger specific surface areas (Zent and Quinn, 1997). The large difference in adsorptive capacity for different geological materials is the main issue with using one method to describe adsorption in the regolith across the entirety of Mars. In their paper, Bryson et al. (2008) compared their results with those of Fanale and Cannon (1971) and Zent and Quinn (1997), correcting for the differences in conditions between the studies, and found that the clay in their study adsorbed 1.3 to 7 times more H₂O than the Fanale and Cannon (1971) and Zent and Quinn (1997) studies. They concluded that more work would be needed to resolve the discrepancy, which is supported by the comparison of results shown in Figure 3.12.

An alternative method for determining the adsorption of H₂O in the martian regolith for low to mid latitudes is outlined by Möhlmann (2002) and is further expanded in Möhlmann (2003, 2004, 2005). The Möhlmann (2002) model determines the number of adsorption layers, n , on a grain according to the relative pressure, x (where x = pressure over saturation pressure), using Equation 3.30 which was originally published by Mikhail and Robens (1983).

$$n(x) = (1.03 + (1.9 + (-1 + (3.33 + (-1.21 \times 10^{-13} + (16.66 + (-55.55 + 213.29(-0.8 + x))(-0.6 + x))(-0.5 + x))(-0.4 + x))(-0.3 + x))(-0.2 + x))(-0.1 + x)) \quad (3.30)$$

The number of monolayers is then converted into a mass density of adsorbed H₂O, ρ_a , using Equation 3.31.

$$\rho_a = \rho_s n S_A \Sigma, \quad (3.31)$$

where ρ_s is the soil mean mass density (1300 kg m⁻³) and Σ is the surface mass density of a monolayer of H₂O molecules (2.84 × 10⁻⁷ kg m⁻²). S_A is the specific surface area and a value of 1.7 × 10⁴ m² kg⁻¹ was used, corresponding to the value measured at the Viking 1 lander site (Ballou et al., 1978). Using these values, a monolayer of adsorbed

H₂O is equivalent to a mass density of 6.3 kg m^{-3} . If an adsorbed H₂O content of 1 wt% is assumed in the martian crust, with the specific surface area value mentioned above, then the equivalent number of adsorption layers is 2, which is equivalent to an adsorption mass density of 12.6 kg m^{-3} .

Mars Odyssey observations have shown regionally high subsurface H₂O contents of up to 9 wt% in the equatorial regions (Feldman et al., 2004). This could be in the form of either H₂O ice, liquid H₂O, adsorbed H₂O, or hydrated minerals. Möhlmann (2002, 2003) suggests that the existence of two layers of adsorbed H₂O (on average) could be used to explain the H₂O content in the upper martian surface observed by Mars Odyssey. This suggestion assumes that the specific surface area was the only property that would change between locations across the surface. If a value of $S_A = 1.5 \times 10^5 \text{ m}^2 \text{ kg}^{-1}$ is used instead of the measured Viking value mentioned earlier, then two layers of adsorbed H₂O would correspond to a subsurface H₂O content of 9 wt%.

Möhlmann (2004) uses the assumption of two monolayers of adsorbed H₂O to give maximum estimates for specific surface area for the range of H₂O contents measured by Feldman et al. (2004). The H₂O content ranged from 2 wt% to 10 wt%, which corresponded to specific surface areas in the range from $3.3 \times 10^4 \text{ m}^2 \text{ kg}^{-1}$ to $1.66 \times 10^5 \text{ m}^2 \text{ kg}^{-1}$ assuming the entire H₂O content was adsorbed H₂O. These values are comparable to the measured values of terrestrial materials (Van Olphen and Fripiat, 1979) and shows the applicability of the model of Möhlmann (2002, 2003, 2004, 2005).

After comparing all of the available experimental data and models for adsorbed H₂O within the martian subsurface, I decided that a constant value would be the best option for the MSSM, because the aim is to investigate the long-term ice distribution. This decision was supported by the study of Schorghofer and Aharonson (2005) which compared the net accumulation of ice with and without adsorption over a period of 35 martian years. The results of this study showed that, while adsorption can inhibit diffusion and ice formation over short time periods (a few martian years), it has a negligible effect on the long-term (>30 martian years) amount of ice accumulated. This is because adsorption impacts the transient diffusion and overall mass balance of the subsurface, but will not impact the stationary diffusion between the air and

ground ice, which is governed by the difference between the mean vapour densities at the surface of the ice and the air in contact with ice (Schorghofer and Aharonson, 2005).

An adsorption concentration of 12.6 kg m^{-3} is, therefore, used for the entire sub-surface based on the work of Möhlmann (2004). This value is equivalent to 2 layers of adsorbed H_2O when using the value for specific surface area from Ballou et al. (1978). It is used because it is currently the only published value for the specific surface area of martian soil, even though it is still uncertain whether this local measurement for a specific surface area can be used as an approximation for the global value. The value chosen for the amount of adsorbed H_2O is also within a similar range to the measured values of adsorbed H_2O found from experimental studies on basalt and some of the palagonite studies (Figure 3.12; Fanale and Cannon, 1974; Jänchen et al., 2009; Zent and Quinn, 1995). Basalt (and palagonite, which is an altered form of basalt) is considered to be one of the geological materials that is an important constituent of the martian surface (Bryson et al., 2008; Christensen et al., 2004). The Thermal Emission Spectrometer (TES) found that over 8% of the planet is covered by at least 30% concentrations of basalt (Bryson et al., 2008) and values for basalt are often used as representative for the entire surface in martian adsorption studies because it represents the lower end of adsorption capability. Future work will be required to update the way adsorption is calculated to better represent the range of materials found at the surface. However, for investigating long term subsurface ice distribution, the constant value is sufficient.

3.3.2.4 Thermal Conductivity of H_2O Ice

The thermal conductivity of H_2O ice varies with temperature and ice content. The variation in thermal conductivity with temperature is accounted for using the model of Klinger (1981) shown in Equation 3.32a. However, many other studies use the equation of Hobbs (1974) instead (Equation 3.32b), including the subsurface thermal

model currently in the MGCM (Steele et al., 2017a).

$$k_{\text{H}_2\text{O}} = \frac{567}{T} \quad (3.32a)$$

$$k_{\text{H}_2\text{O}}_{\text{Hobbs}} = \frac{488.19}{T} + 0.4685 \quad (3.32b)$$

Both equations produce similar values for the range of Martian temperatures, as shown in Table 3.4. For the purpose of my thermal model, Equation 3.32a (Klinger, 1981) is more appropriate because it was developed for cometary ices and other low pressure environments such as Mars (e.g Kossacki et al., 1994), whereas Equation 3.32b was developed for environments with Earth like pressures (Hobbs, 1974).

Table 3.4: Values for the thermal conductivity [$\text{W m}^{-1} \text{K}^{-1}$] of H_2O ice appropriate for Martian temperatures [K] using the equation by Hobbs (1974) and Klinger (1981).

Temperature	$k_{\text{H}_2\text{O}}$ (Hobbs, 1974)	$k_{\text{H}_2\text{O}}$ (Klinger, 1981)
149	3.7449	3.8053
214	2.7497	2.6495

The method used here to account for the increase in effective thermal conductivity, k_{eff} with H_2O ice content also differs from that in the Steele et al. (2017a) model, which uses the method of Siegler et al. (2012) rather than a Hertz factor ($h_{\text{H}_2\text{O}}$; Section 3.2.2.1). Siegler et al. (2012) use the fraction of the pore space filled with ice, rather than the contact area to determine the effect of H_2O ice within the pores, and account for the change in porosity of the regolith from the formation of H_2O ice explicitly when determining the effective thermal conductivity, as shown in their equation:

$$k_{\text{eff}} = k_r + \phi_r k_{\text{H}_2\text{O}} F \quad (3.33)$$

where F is the fraction of the pore space filled with ice. The method used in the MSSM (Grott et al., 2007, see Section 3.2.1) accounts for the change in porosity within the calculation of the effective thermal conductivity, using the Hertz factor. The decrease in porosity of the regolith matrix with depth is also accounted for in this model and is not included in the method of Siegler et al. (2012). Figure 3.13 shows the effect of a diurnal temperature cycle on the thermal conductivity if the pore space is filled with

H₂O ice and the Hertz factor is used to determine the subsequent increase in thermal conductivity.

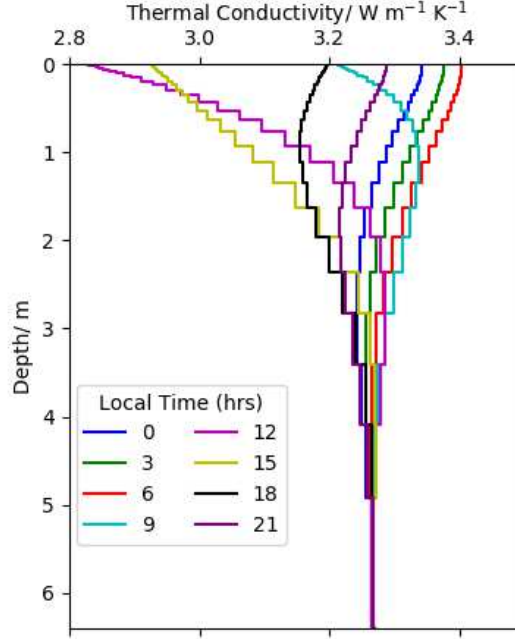


Figure 3.13: Thermal conductivity of the regolith matrix with the pore space filled with H₂O ice over one sol. Calculated using Equation 3.11 and using the diurnal temperature cycle at 40°N, 120°E and $L_S = 270^\circ$ from the MCD. The parameters for the matrix are the same as those in Figure 3.6.

3.4 Carbon Dioxide Scheme

The carbon dioxide scheme shares many of the same elements as the water scheme, with the same method used for vapour diffusion and phase distribution. The main differences between the two schemes are the equations that are dependent on the species being considered, in this case CO₂. A description of the equations used for CO₂ are presented in the following sections.

3.4.1 Thermal Conductivity of CO₂ Ice

The thermal conductivity of CO₂ ice does not have as much of an impact on the total thermal conductivity of the regolith as that of H₂O ice. However, it does still have an influence and therefore a temperature dependent thermal conductivity of CO₂ ice is used in the MSSM (Equation 3.34; Ross and Kargel, 1998). The equation is derived

from the experimental data of Konstantinov et al. (1988).

$$\log_{10}(k_{\text{CO}_2}) = -5.39941 + 5.45894 \log_{10}(T) - 1.41326 \log_{10}(T^2) \quad (3.34)$$

An alternative thermal conductivity equation (Equation 3.4.1) is used by Manning et al. (2019) from the work of Kravchenko and Krupskii (1986). This equation is also used in the work of Mellon (1996), Wiczorek (2008), Stewart and Nimmo (2002), and Heldmann and Mellon (2004). However, it was not possible to follow the derivation for this equation through the literature, which is the reason Equation 3.34 was used instead.

$$k_{\text{CO}_2}(T) = \frac{93.4}{T} W m^{-1} K^{-1} \quad (3.35)$$

3.4.2 Vapour Diffusion

The diffusion scheme for CO₂ vapour is similar to the scheme used for H₂O vapour diffusion. The scheme uses the same equations and finite volume method, because the overall process of vapour diffusion is insensitive to the species that is diffused. The final equation for the CO₂ vapour diffusion scheme (Equation 3.36a) is identical to the one for H₂O vapour diffusion, apart from the fact that in this case n and D represent n_{CO_2} and D_{CO_2} , respectively.

$$a_i^t n_i = b_i^t n_{i+1} + c_i^t n_{i-1} + d_i^t \quad (3.36a)$$

where

$$a_i^t = \frac{\Delta z}{\Delta t} + \frac{D_{i+0.5}^t}{\delta z_i} + \frac{D_{i-0.5}^t}{\delta z_{i-1}} \quad (3.36b)$$

$$b_i^t = \frac{D_{i+0.5}^t}{\delta z_i} \quad (3.36c)$$

$$c_i^t = \frac{D_{i-0.5}^t}{\delta z_{i-1}} \quad (3.36d)$$

$$d_i^t = \frac{\Delta z}{\Delta t} n_i^{t-\delta t} \quad (3.36e)$$

3.4.2.1 Diffusion Coefficient

The diffusion of CO₂ into martian regolith is a complex topic that has a limited amount of literature. Fanale et al. (1982a) ran experiments to measure diffusion and give the following diffusion coefficient:

$$D = \phi \tau D_p, \quad (3.37)$$

where D is the gas diffusivity [$\text{m}^2 \text{s}^{-1}$], ϕ is the porosity, τ is the tortuosity and D_p is the diffusivity of a single pore ($\text{m}^2 \text{s}^{-1}$, Equation 3.38; Fanale et al., 1982a).

$$D_p = \frac{4r}{3} \left(\frac{2RT}{\pi M_{\text{CO}_2}} \right)^{\frac{1}{2}}, \quad (3.38)$$

where r is the pore radius [μm], T is the temperature, R is the ideal gas constant [$\text{m}^3 \text{Pa K}^{-1} \text{mol}^{-1}$] and M is the molecular mass (kg; Fanale et al., 1982a). The combined equation (Equation 3.39) is used for the diffusion coefficient in the carbon dioxide scheme.

$$D_{\text{CO}_2} = \phi \tau \frac{4r}{3} \left(\frac{2RT}{\pi M_{\text{CO}_2}} \right)^{\frac{1}{2}} \quad (3.39)$$

3.4.3 Phase Distribution of CO₂

Similar to H₂O, CO₂ forms as either vapour, adsorbate or ice within the subsurface (Equation 3.40). Liquid CO₂ is not stable under any expected conditions on Mars and is therefore not included. Figure 3.14 shows the CO₂ phase diagram (using the equations used in the MSSM) and shows that the saturation vapour pressure over ice equation is the only relevant part of the phase diagram for the temperatures and pressures that are relevant on Mars (red box on Figure 3.14).

$$\sigma_{\text{CO}_2} = n_{\text{CO}_2} + \alpha_{\text{CO}_2} + \zeta_{\text{CO}_2}, \quad (3.40)$$

where σ_{CO_2} is the total amount of CO₂ [kg m^{-3}], n_{CO_2} is the concentration of CO₂ vapour per unit volume of regolith [kg m^{-3}], α_{CO_2} is the concentration of adsorbed CO₂ [kg m^{-3}] and ζ_{CO_2} is the concentration of subsurface CO₂ ice [kg m^{-3}].

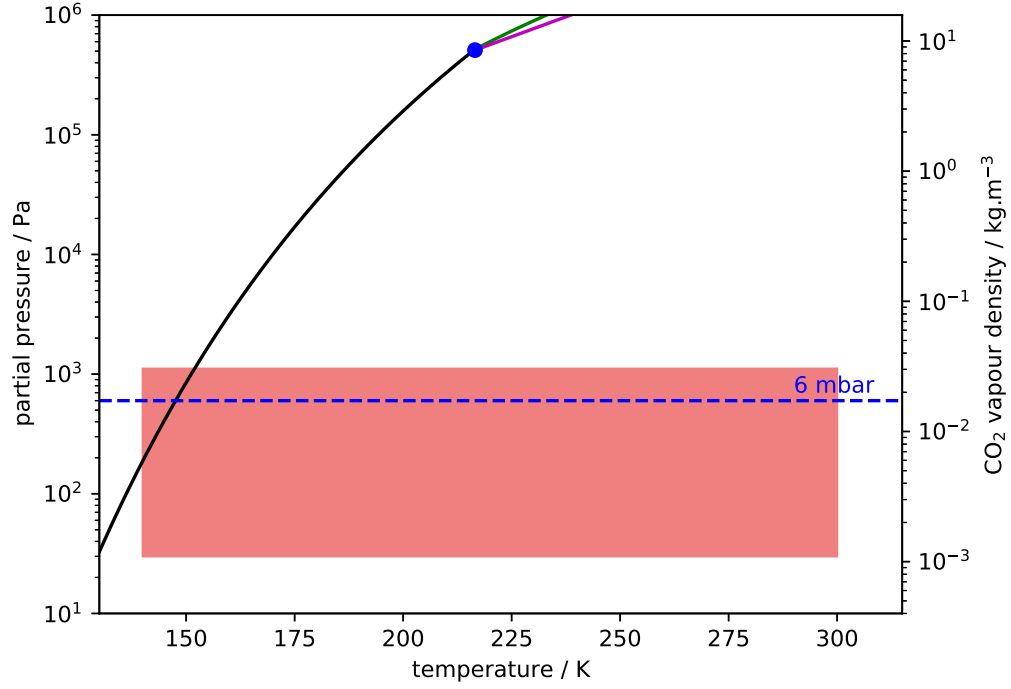


Figure 3.14: Phase diagram for CO_2 from the equations incorporated into the model. The blue dot represents the triple point at 216.56 K and 5100 mbar. The saturation vapour pressure over ice (black line) is Equation 3.41b, the saturation vapour pressure over liquid CO_2 (green line) is Equation 3.41a and the melting point curve was determined using the phase diagram in Witkowski et al. (2014). The conditions appropriate to Mars (red box) are all far below the triple point (216.56 K and 5100 mbar), which means that only the saturation vapour pressure over ice equation is relevant for this work.

3.4.3.1 Saturation Vapour Pressure Over Ice

The equation for saturation vapour pressure over CO₂ ice (also known as frost point pressure) used is from Kasting (1991). Their study included equations for above (Equation 3.41a) and below (Equation 3.41b) the triple point temperature of CO₂ (216.56 K), and as shown by the red box in Figure 3.14, the equation for above the triple point is not relevant for Mars conditions. The equation for below the triple point is used in several Mars studies including Hu et al. (2012), which makes it an appropriate equation to use for this study.

$$\log_{10}(P_{sat_{CO_2}}(\text{atm})) = 3.128082 - \frac{867.2124}{T} + 18.65612 \times 10^{-3} T - 72.48820 \times 10^{-6} T^2 + 93 \times 10^{-9} T^3 \quad (3.41a)$$

$$\log_{10}(P_{sat_{CO_2}}(\text{atm})) = 6.760956 - \frac{1284.07}{T - 4.718} + 1.256 \times 10^4 (T - 143.15) \quad (3.41b)$$

Other studies have used different equations for frost point pressure which are only used within the cited study (e.g., Hourdin et al., 1993; Miller and Smythe, 1970; Span and Wagner, 1996, Equations 3.42a-c respectively) and were therefore not considered appropriate for this work.

$$T_{CO_2} = 149.2 + 6.48 \ln(P), \quad (3.42a)$$

where T_{CO_2} is in kelvin and P is in hectopascals.

$$\log_{10}(P(\text{mb})) = 11.3450 - \frac{1470.2}{T} - 4.1024 \times 10^{-3} T \quad (3.42b)$$

$$\ln\left(\frac{P_{sub}}{P_t}\right) = \frac{T_t}{T} \left[a_1 \left(1 - \frac{T}{T_t}\right) + a_2 \left(1 - \frac{T}{T_t}\right)^{1.9} + a_3 \left(1 - \frac{T}{T_t}\right)^{2.9} \right], \quad (3.42c)$$

where $T_t = 216.592$ K, $P_t = 0.51795$ MPa, $a_1 = -14.740846$, $a_2 = 2.4327015$, and $a_3 = -5.3061778$.

3.4.3.2 Adsorption

A detailed investigation of experimental studies on the adsorption of CO₂ under martian conditions was also undertaken to find the most appropriate value or equation to use. Figure 3.15 shows the results from all experimental studies of CO₂ adsorption (Fanale and Cannon, 1971; Jänchen et al., 2006; Zent and Quinn, 1995; Zent et al., 1987). These were all completed using either basalt (Fanale and Cannon, 1971) or palagonite, a weathering product of basalt (Jänchen et al., 2009; Zent and Quinn, 1995; Zent et al., 1987). It shows that for a range of Mars-relevant temperatures and pressures, the amount of CO₂ that can be adsorbed has a wide spread. There is very little correlation between the data sets (despite each data set showing individual correlation) making it difficult to define a CO₂ adsorption isotherm, which led to the decision to also use a constant value for CO₂ adsorption. A value of 10.7 kg m⁻² was chosen because this is the average value across all experiments in the pressure range shown in Figure 3.15 (0 to 1050 Pa).

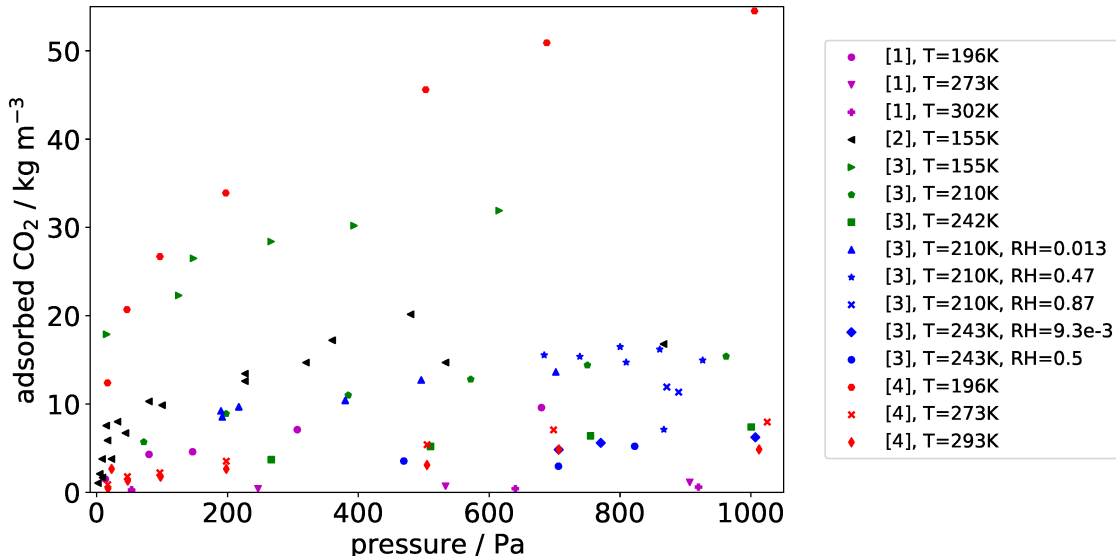


Figure 3.15: Results from experimental studies of CO₂ adsorption. The studies shown in this figure are [1] Fanale and Cannon (1971), [2] Zent et al. (1987), [3] Zent and Quinn (1995) and [4] Jänchen et al. (2006). All experiments (apart from those indicated in the legend) were done under a relative humidity (RH) of 0, i.e. no H₂O in the system. The experimental study of [1] Fanale and Cannon (1971) was done on basalt, whereas all of the other studies in the figure used palagonite

3.4.4 Density of CO₂ ice

CO₂ ice density is more heavily dependent on temperature than that of H₂O ice (Mangan et al., 2017). As a result, the temperature dependent equation for CO₂ density of Mangan et al. (2017) is used in this work (Equation 3.43). They developed this equation from a combination of their own experimental data at Mars-relevant conditions and previous experimental data in the literature, making it appropriate for use in this study.

$$\rho_{CO_2} = 1.7239 - 2.53 \times 10^{-4} T - 2.87 \times 10^{-6} T^2 \quad (3.43)$$

3.5 Surface Flux

In the MSSM, a fixed atmospheric annual cycle is used for the atmospheric boundary. The annual cycles used are taken from one of four baseline MGCM simulations (Section 3.7), one at each obliquity considered (15°, 25°, 35°, and 45°). The details of these baseline runs can be found in Section 3.7.1. The atmospheric values for H₂O and CO₂ vapour density are then used to calculate the regolith-to-atmosphere flux of each volatile using Fick's 1st law (Equation 3.17), which can be written as:

$$f = D \frac{n_{surf} - n_{atm}}{z_{0.5}}, \quad (3.44a)$$

where

$$n_{atm} = \rho_{atm} \times q_{atm}. \quad (3.44b)$$

Here, f is the surface flux from the regolith to the atmosphere [kg m⁻¹ s⁻¹], D is the diffusion coefficient [m² s⁻¹], n_{surf} is the vapour concentration in the top layer of the subsurface [kg m⁻³], n_{atm} is the vapour concentration in the lowest layer of the atmosphere [kg m⁻³] and $z_{0.5}$ is the depth to the midpoint of the first regolith layer [m]. n_{atm} is not calculated directly by the MGCM, which is used to provide the atmospheric inputs, and has to be calculated from the density of the atmosphere in the lowest atmospheric layer, ρ_{atm} [kg m⁻³], and the mass mixing ratio for the volatile

being considered, q_{atm} . The same equation is used for H_2O and CO_2 , but the values used for D , n_{surf} , ρ_{atm} and n_{surf} are those appropriate for the volatile being considered.

3.6 Sublimation and Accumulation Rates

The sublimation rate of ice is included because temperature changes can drastically change the saturation vapour pressure for both H_2O and CO_2 ice. When the saturation vapour pressure is much higher than in the previous timestep, and if there is enough ice to increase the amount of vapour in the pore space to the amount needed to be at saturation vapour pressure, then all of the ice that would need to sublimate for that to occur would sublimate instantaneously. In reality, this process would be gradual and several studies investigating the change in sublimation rate when a H_2O ice layer is overlain by a porous regolith on Mars have shown that sublimation rate is inversely proportional to the depth of the layer (Bryson et al., 2008; Chevrier et al., 2007, 2008; Dundas and Byrne, 2010; Soare et al., 2008). Consequently, I have included the experimental equation for H_2O ice sublimation rate, E_{sw} of Chevrier et al. (2008, Equation 3.45), which takes into account the depth of the ice layer and the difference in vapour pressure between the subsurface pore space and the atmosphere.

$$E_{s_{H_2O}} = \frac{D_{H_2O} M_{H_2O} P_{sat_{H_2O}}}{L R T_s \rho_{H_2O}} \left[1 - \frac{T_s P_{atm}}{T_{atm} P_{sat_{H_2O}}} \right], \quad (3.45)$$

where D_{H_2O} is the H_2O diffusion coefficient [$m^2 s^{-1}$], M_{H_2O} is the molecular weight of H_2O [kg], $P_{sat_{H_2O}}$ is the saturation pressure [Pa] of H_2O ice at temperature T_s [K], L is the thickness of the regolith layer [m], R is the ideal gas constant [$m^3 Pa K^{-1} mol^{-1}$], ρ_{H_2O} is the density of H_2O ice [$kg m^{-3}$], P_{atm} is the H_2O vapour pressure [Pa] in the atmosphere and T_{atm} is the temperature [K] in the atmosphere (Chevrier et al., 2008). I have adapted this for use within the MSSM by using the vapour pressure and temperature in the overlying model layer rather than the atmosphere, and the thickness of the current layer, rather than the thickness of the entire subsurface for layers below the surface layer. This allows for a unique sublimation rate to be calculated in each layer and a more accurate estimation of the rate of H_2O ice loss within the subsurface.

There have been a few experimental studies to determine the sublimation rate of

CO₂ ice, $E_{s_{\text{CO}_2}}$. The sublimate rate determined by Blackburn et al. (2010) was found to be most appropriate for the MSSM after an investigation into the other studies showed the sublimation rate values were either measured under standard Earth pressure and temperature conditions (Aylward et al., 2019) or were calculated to determine an expected gas flux rate (Cedillo-Flores et al., 2011). In the experiments done by Blackburn et al. (2010) sublimation rate was measured from pure CO₂ ice under simulated martian conditions, although there was no consideration of the effect of either dust within the ice or an overlying regolith/water ice layer, both of which would impact the sublimation rate. Despite this, their value for the average sublimation rate of CO₂ ice, 1.2 mm h⁻¹, is used since it is the most appropriate of the experimental values.

Ideally an accumulation/deposition rate for both H₂O and CO₂ ice would be included in the model alongside the sublimation rate. However, there is no known value for the accumulation rates within regolith for Mars. There are values for the accumulation rate of the PLD; for example Banks et al. (2010) found an average accumulation rate of 0.5 mm MY⁻¹ from resurfacing rates of the North Polar Layered Deposits (NPLD). These values, however, are only applicable for surface accumulation and more work is needed to understand subsurface accumulation. Consequently, I have assumed that any amount of vapour above the saturation vapour concentration is converted into ice instantaneously, which is the method used in many studies (e.g., Schorghofer and Aharonson, 2005; Steele et al., 2017a). This is likely an overestimation of the amount of ice that will accumulate within a timestep, but should provide a good first approximation for deposition of ice within the regolith for simulations longer than 20 martian years.

3.7 The LMD-UK Mars global circulation model

The Mars global circulation model that has been co-developed between the Laboratoire de Météorologie Dynamique (LMD) du Centre National de la Recherche Scientifique in Paris, The Open University (OU) and Oxford University in the UK, and the Instituto de Astrofísica de Andalucía (IAA) in Granada (referred to as the MGCM; Forget et al., 1999; Lewis et al., 1999) is used to generate the annual atmospheric cycles (of surface temperature, pressure, H₂O vapour density and CO₂ vapour density) that are surface

inputs for the MSSM. The MGCM uses the physical parametrisations from the LMD global circulation model (GCM; Forget et al., 1999) coupled with a UK-only spectral dynamical core and a semi-Lagrangian advection scheme for tracers (dust and H₂O ; Holmes et al., 2018; Newman et al., 2002). It uses topography from Mars Orbiter Laser Altimeter (MOLA) data, a dust scenario that can be prescribed from Mars Global Surveyor (MGS) data, and cloud microphysics for both H₂O and CO₂ (Forget et al., 1998; Holmes et al., 2018; Levrard et al., 2004; Montmessin et al., 2004; Navarro et al., 2014; Steele et al., 2017a).

The MGCM also includes a thermal and water scheme for the subsurface. The original aim of this work was to expand the subsurface water scheme (Steele et al., 2017a) to include all states of CO₂, although on testing of the subsurface water scheme, it was found to not conserve H₂O when assuming a closed system. A full description of the subsurface water scheme of Steele et al. (2017a) and the testing done on the scheme is described in Appendix B.3. Consequently, the MSSM has been designed so that it can be incorporated into the MGCM in the future and a description of this integration can be found in Appendix B.2. However, this thesis only uses the stand-alone MSSM and the MGCM is only used to provide surface atmospheric profiles.

3.7.1 Atmospheric Profiles from MGCM Simulations

The MGCM is used throughout this thesis to provide the surface conditions for all of the subsurface runs. Four MGCM runs were completed to be used as surface conditions, one at each of the four orbital obliquities considered in this thesis (15°, 25°, 35° and 45°). A different MGCM run was done for each obliquity because obliquity has a significant influence on the climate (see Section 2.7) and the change in surface conditions will impact the results.

The MGCM simulations were run for 4 martian years using the results from previous 20 martian year spin-up runs at each obliquity (15°, 25°, 35°, and 45°) and the present-day eccentricity and longitude of perihelion. The MGCM simulations were run at a T31 resolution (refers to a triangular truncation at a total wavenumber of 31), which relates to a physical grid with a resolution of 5° latitude x 5° longitude (72x36 grid points in total) and 25 vertical levels, extending to an altitude of 80 km at the top

of the model. The MGCM simulations were also run using the MGS dust profile for MY 24, timesteps of 1.5 minutes (960 timesteps per day) and no radiatively active dust or ice. For a detailed description of the parameters used for the MGCM simulations see Appendix B.1.

Surface annual cycles for each latitude (averaged over longitude) and for 12 individual locations (Section 4.1.1) were determined from the final year of these MGCM simulations by averaging out the diurnal cycle. These annual cycles are then used as the surface condition for the MSSM in all of the simulations discussed in this thesis. While MGCM simulations were run for all four obliquities, only the 25° obliquity atmospheric profiles are discussed here. The atmospheric profiles for the other obliquities (15° , 35° , and 45°) can be found in Section 6.1 before the obliquity simulations are discussed.

Annual temperature, pressure, CO_2 vapour density and H_2O vapour density cycles at each latitude are shown in Figure 3.16. The CO_2 vapour and H_2O vapour concentrations are output as mass mixing ratios in the MGCM, so vapour density values have been calculated by multiplying the mass mixing ratio by atmospheric density, which follows the same patterns as surface pressure. Therefore, any variations in surface pressure are replicated in the CO_2 vapour density and H_2O vapour density cycles. This will have the largest influence in the northern polar region (55° – 80°N), where the longitudinally averaged surface pressure values are highest during northern winter, which is also seen in the CO_2 vapour density cycle. At this time of year, it would be expected that CO_2 vapour density is lowest (due to the formation of the seasonal polar cap). However, the higher surface pressures will mean that CO_2 ice forms at both higher temperature and with a higher saturation vapour density (Figure 3.14), resulting in higher CO_2 vapour densities.

Overall, each of the four cycles shows the expected annual atmospheric patterns (see Section 2.6) and the results have been compared with observations and the MCD (e.g., Lewis et al., 1999; Smith, 2002, 2004). The main patterns that can be seen are large variations in the polar regions from the formation of seasonal polar caps (Figure 3.17) during the winter of each hemisphere and smaller variations in the equatorial

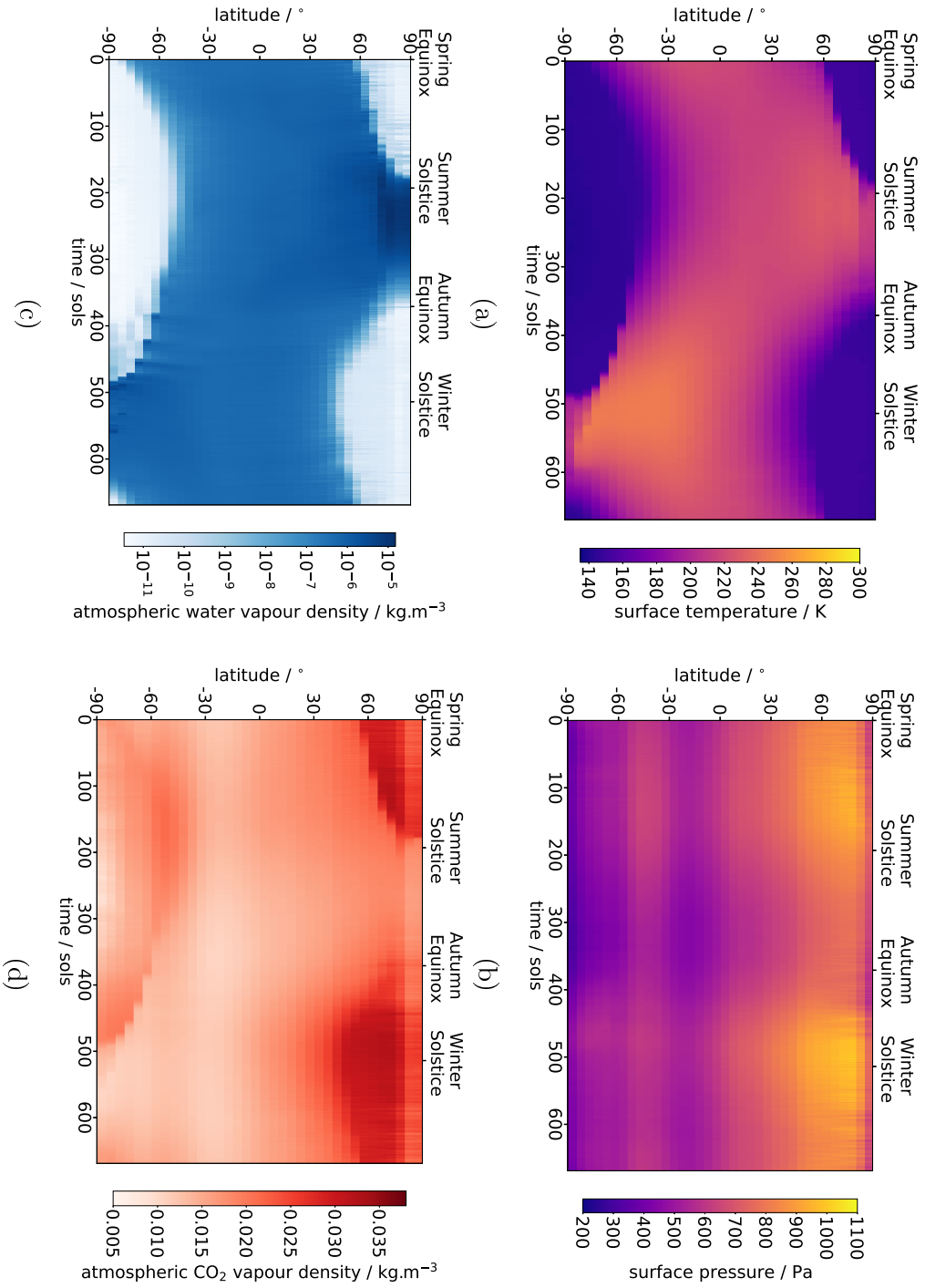
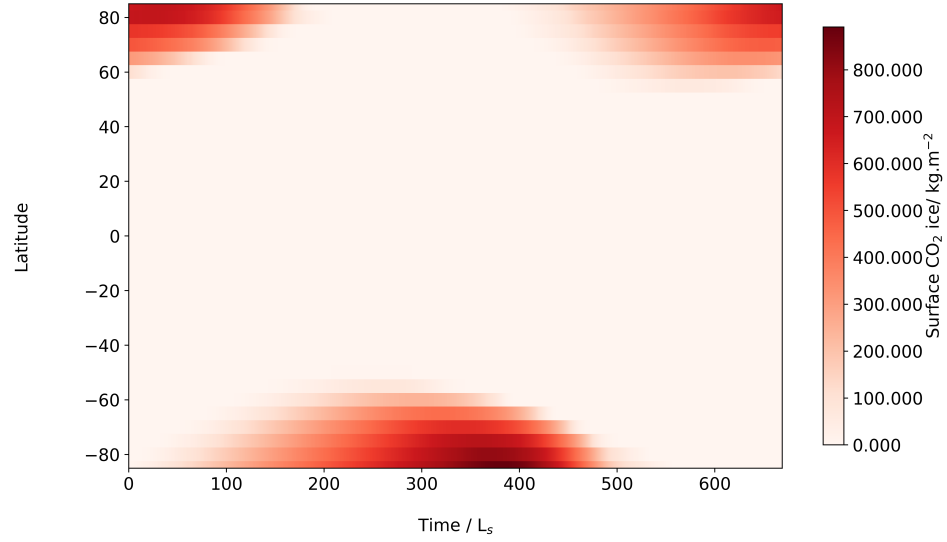
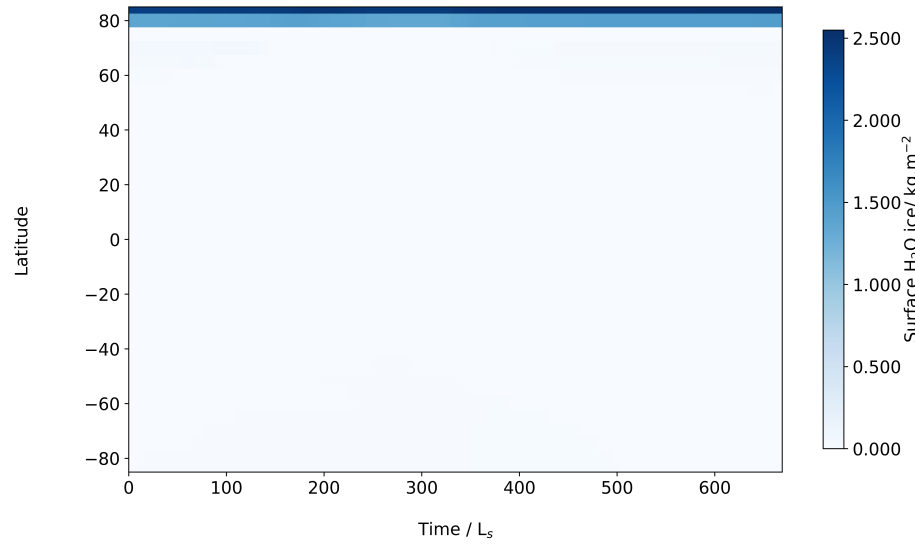


Figure 3.16: Longitudinal averages as a function of latitude over time for the surface (a) temperature, (b) pressure, (c) H_2O vapour and (d) CO_2 vapour cycles in the present-day (Obliquity = 25°). The values are taken from the lowest atmospheric layer in the MGCM to represent the near-surface atmospheric values.

regions. These small equatorial variations will influence the long term ice stability in this region. Figure 3.18 shows the variations between 40°N and 40°S, demonstrating that the annual cycle is more pronounced at these latitudes than it appears to be in Figure 3.16.



(a)



(b)

Figure 3.17: Annual surface (a) CO₂ ice and (b) H₂O ice cycles with zonal latitude for the present-day (Obliquity = 25°).

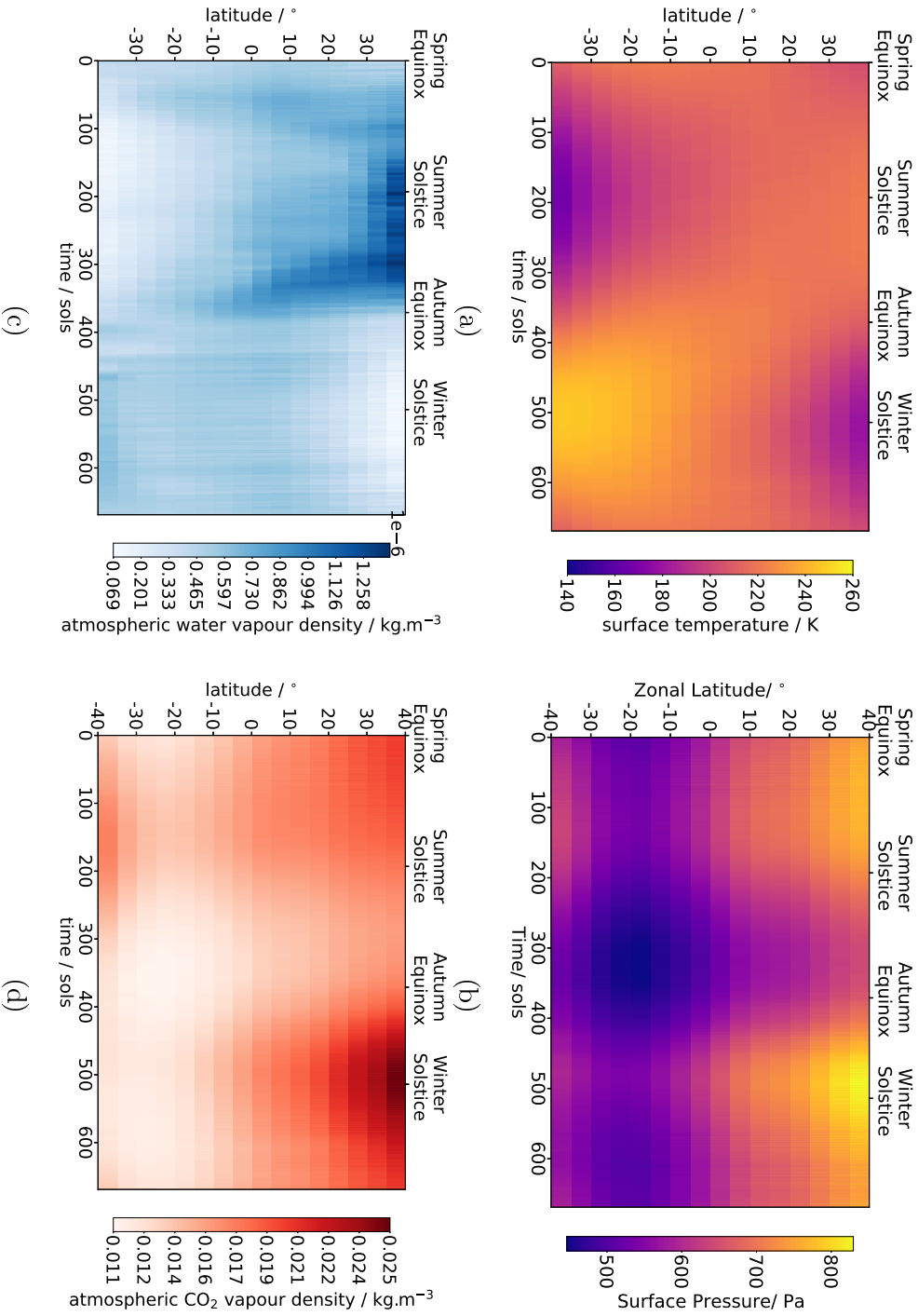


Figure 3.18: Longitudinal averages as a function of latitude over time for the surface (a) temperature and (b) pressure (c) H_2O vapour and (d) CO_2 vapour cycles across the equatorial region (40°N to 40°S) for the present-day (Obliquity = 25°). The values are taken from the lowest atmospheric layer in the MGCN to represent the near-surface atmospheric values.

3.8 Summary

The MSSM is a thermal and vapour diffusion subsurface model that simulates the partitioning of H_2O and CO_2 into vapour, ice and adsorbate (and liquid H_2O). This chapter describes the equations and methods used to develop the MSSM and the justifications for the equations chosen over other available equations.

The thermal scheme uses a thermal conductivity that varies with depth and ice content, ensuring subsurface temperatures reflect the changes expected for a regolith with variable ice content. The vapour diffusion scheme is consistent for both H_2O and CO_2 vapour, with diffusion coefficients calculated for each vapour separately. Saturation vapour densities for H_2O ice and CO_2 ice are calculated for the updated surface temperature, then used to determine whether ice is deposited or sublimated in each timestep.

Both the thermal scheme and the vapour diffusion schemes require a surface boundary condition which is taken from the MGCM. The thermal scheme uses a fixed daily average surface temperature, while the vapour diffusion schemes use a surface flux condition. In this thesis, the stand-alone version of the MSSM is used, so a prescribed annual atmospheric cycle (i.e. a fixed value for each sol) is used as the surface condition for each property. These annual atmospheric cycles are taken from the results of a MGCM simulation that has been diurnally averaged.

4 | How do CO₂ ice and H₂O ice interact within the regolith?

Until recently, carbon dioxide (CO₂) ice has been assumed to mainly exist at the surface in the polar caps and as CO₂ frost at lower latitudes. This idea relates to studies of surface CO₂ ice which show that, in the present-day, surface CO₂ ice is seasonal at nearly all latitudes and persists throughout the year only at the highest southern latitudes (e.g., Ingersoll, 1974; Lambert and Chamberlain, 1978). This has been shown through both observational, theoretical and numerical studies (e.g., Aharonson et al., 2004; Blackburn et al., 2010; Leighton and Murray, 1966; Piqueux et al., 2016; Smith et al., 2001a) as discussed in Sections 2.2 and 2.4. The recent discovery of metre-scale CO₂ ice deposits within the South Polar Layered Deposits (SPLD) demonstrates the existence of subsurface CO₂ ice in a large enough quantity to significantly impact atmospheric pressure if released (~ 6 mbar; Bierson et al., 2016; Phillips et al., 2011).

Previous studies of the martian subsurface have focused on water (H₂O) ice and the conditions that control its formation and stability over time (e.g., Aharonson and Schorghofer, 2006; Bandfield and Feldman, 2008; Mellon et al., 2004; Schorghofer, 2010). In these studies, the impact of subsurface CO₂ ice on the formation and stability of H₂O ice has not been considered. The amount of time that CO₂ ice can survive in the subsurface with H₂O ice has also not yet been explored. This chapter explores several scenarios with one and two ice-layers within the subsurface to investigate whether subsurface CO₂ ice can survive longer at depth within a regolith matrix than at the surface and whether its presence has an impact on the distribution of H₂O ice and vice versa. The results presented here suggest that while CO₂ ice is unstable when there is no overlying protective layer, a metre-scale overlying layer of H₂O ice-filled regolith is sufficient for CO₂ ice to survive for long periods of time. The presence of subsurface CO₂ ice also has a complex effect on the behaviour of H₂O ice, due to variations in

temperature and diffusion coefficient caused by the presence of both ices. When interpreting the results in this chapter it is important to keep in mind that the initial amounts of CO₂ ice and H₂O ice used are probably higher than the amounts expected within the subsurface across the low and mid-latitude regions. The high values are used to simplify the initial conditions and to investigate overall effects that may not be as noticeable for small amounts of either ice.

Section 4.1 outlines the methods specific to the simulations described in this chapter, including an overview of the initial subsurface conditions used. The results from the simulations with only one type of ice present are discussed in Section 4.2 and those with two ices present are discussed in Section 4.3. A series of simulations where fixed model parameters, such as the maximum sublimation rate, are changed to reflect the range expected on Mars are described in Section 4.4 and all of the results are summarised in Section 4.5.

4.1 Initial Conditions

The Martian Subsurface Model (MSSM) simulations discussed in this chapter were initialised with a subsurface containing either one or two ice-layers. Ice layers refer to the regions in the subsurface that contain either completely ice-free pore space or pore space filled with either H₂O or CO₂ ice. These ice layers are different from the model layers discussed in Section 3.1, which refer to the regions between the numerical grid points that the equations in the MSSM are discretised onto. In the scenarios used, the different ice layers are either an ice-free regolith, a regolith with the pore space filled with H₂O ice, or a regolith with pore space filled with CO₂ ice. In the rest of this thesis when the pore space is filled with H₂O ice, or when the pore space is filled with CO₂ ice, the ice layers will be referred to as a H₂O ice-filled regolith layer or a CO₂ ice-filled regolith layer, respectively.

The amount of ice in the pore space is assumed to fill all available space when ice is present. This assumption has been used because this is an initial study to investigate how CO₂ ice and H₂O ice affect each other within the subsurface. Previous work has only investigated H₂O ice distribution within the subsurface, both as pore ice and as

excess ice (where the volume of ice is greater than the pore volume; Bramson et al., 2015; Schorghofer and Forget, 2012), and there is no previous work on CO₂ ice in the subsurface to use as an indicator of the amount of CO₂ ice that is expected to be present. For this initial study, it is assumed that only pore ice can exist, as excess ice can only form by vapour diffusion when there are fractures within the subsurface geology (Fisher, 2005) and is generally assumed to form by the burial of ice sheets (Section 2.3). Similar to the design of early models of subsurface H₂O ice (e.g., Mellon, 1996; Schorghofer and Aharonson, 2005), an understanding of the behaviour of pore ice is useful before the additional complexities of the inclusion of excess ice are investigated (Schorghofer and Forget, 2012). Future studies could, therefore, include the presence of excess CO₂ ice into the MSSM after the impact of the inclusion of CO₂ pore ice has been investigated further. In this chapter it is also assumed that the pore space is entirely filled with only one ice when ice is present. This is generally expected when both ices exist in the same location since the frost point temperatures of both ices are different (~ 195 K for water and ~ 145 K for CO₂; Hardy, 1998; Kasting, 1991). Alongside this, it has been suggested that CO₂ clathrate hydrates might form between layers of pure H₂O ice and pure CO₂ ice (Section 2.1.4; e.g., Hoffman, 2001; Lambert and Chamberlain, 1978; Miller and Smythe, 1970).

The amounts of H₂O ice and CO₂ ice used (see Table 4.1 for column density values) are likely to be greater than the amount that would be deposited on Mars. Especially in some latitudes where, in the present-day, CO₂ and H₂O ice are not stable and there is not enough of either vapour in the atmosphere to form such ice deposits. However, higher atmospheric pressures in previous martian epochs (during the Noachian and Hesperian; see Section 2.8) and the different atmospheric conditions during different obliquities (see Section 2.7.1) are expected to have caused deposition in locations where ices are not expected in the present-day. This is due to the increased frost point temperature of both ices with increased pressure (see Figures 3.10 and 3.14) and to different climatic conditions that occur at higher atmospheric pressures and different obliquities. Alongside the change in climatic conditions and frost point temperatures, higher amounts of ice will also be expected to be deposited under higher atmospheric pressures (>0.5 bar) than at present due to the increase in vapour concentration of

both volatiles that occurs with the increased pressures, which is how features such as glaciers would have formed (Souness and Hubbard, 2012). Therefore, a large initial amount of ice can be used to investigate how long any of these larger ice deposits could have survived.

Table 4.1: The column density of ice within the subsurface if the ice fills the pore space between 2 depths within the subsurface. The volume of the pore space decreases with depth as compaction increases according to Equation 3.9b (see Section 3.2 for more details) and the volume of ice within the pore space is adjusted accordingly. H_2O ice density = 927 kg m^{-3} and CO_2 ice density is calculated at 145 K. The equivalent thickness of ice in each model layer is calculated by multiplying the porosity by the thickness of the model layer. The column density of ice is calculated by multiplying the thickness of the ice layer by the density of ice.

Depth (m)	Column density of ice (kg m^{-2})	
	H_2O	CO_2
0 to 0.5	9.70	17.03
0 to 1	19.09	33.51
0 to 2	26.56	46.62
0.5 to 38	355.03	623.08
1 to 38	345.64	606.60
2 to 38	338.17	593.49

All configurations of the three ice layer types have been run with the depth of the boundary between the ice layers varying between 0.5 m, 1 m and 2 m. Table 4.1 shows how the amount of ice in the two ice-layers varies according to the type of ice, the depth of the boundary and which ice is in the upper or lower region. The different initial ice layer scenarios are referred to using an acronym defined in Chapter VII and simulations are referred to using a short code which includes the run number and a prefix corresponding to the version of the MSSM used (e.g. S01 for run 1 with the baseline version). This can be used to find the details of the scenarios in Tables VII.III and VII.IV. Table VII.III is the list of the scenarios that used the present-day obliquity and the baseline version of the MSSM described in Chapter 3, while Table VII.IV is the list of scenarios that use different parameters in the MSSM to investigate the effect of assumptions included in the baseline. The details of the different versions of the MSSM can be found in Table VII.I and the results of these simulations in

Section 4.4 and Chapter 5. CO₂ and H₂O sublimation rates have been calculated for all simulations and are only discussed in the text where relevant. The sublimation rates for all simulations discussed in this thesis have therefore been included in Appendix C for reference.

The combinations of ice layers used in this chapter are either observed on Mars at present or are expected to occur under different obliquities, although the amounts of each ice are likely to be smaller than in the scenarios presented here or as pure ice rather than ice-filled regolith. Schematics for each scenario can be found in Section VII.IV. Table 4.2 summarises some of the potential locations where the two-ice-layer configurations investigated could be found across Mars. All of the scenarios discussed in this chapter only consider the present-day solar luminosity and obliquity (25°). Under these conditions CO₂ ice is only expected to form in the polar regions or as frost at lower latitudes (see Section 2.2; e.g., Bibring et al., 2004; Forget et al., 1998; Schorghofer and Edgett, 2006). Any subsurface CO₂ ice in the present-day outside of these regions is unlikely. However, during the Hesperian (when atmospheric pressures were decreasing), remnants of CO₂ ice deposits that formed under high atmospheric pressures may have persisted for a few thousand years after atmospheric conditions changed (discussed in Sections 2.7 and 2.8; e.g., Forget et al., 2013; Nakamura and Tajika, 2003).

The MSSM simulations in this chapter use a fixed annual cycle, with the diurnal cycle smoothed out, taken from the present-day LMD-UK Mars global circulation model (MGCM) run discussed in Section 3.7.1. The annual cycle for H₂O and CO₂ vapour is used to calculate the surface flux into the regolith (Section 3.5) and one of the limitations of this model is that it assumes the atmosphere acts as both an infinite supply and an infinite sink for both H₂O vapour and CO₂ vapour. The assumption that the atmosphere is an infinite source is unlikely to have a large effect on the results shown here because the initial amount of both ices used in these scenarios are greater than the atmospheric vapour content and sublimation of each ice is more likely. Simulations with no supply of vapour from the atmosphere (i.e. the atmosphere is an infinite sink only) have been run in order to test the impact of an atmospheric source in Section

Table 4.2: Potential locations on Mars where the two-ice-layer configurations could occur.

Ice-layer configuration	Potential Locations on Mars
Ice-free Regolith over CO ₂ Ice-filled Regolith	This scenario occurs while the CO ₂ polar caps are sublimating away at high obliquities, leaving behind an overlying dust lag layer.
	This scenario could also occur in regions where surface temperatures are around the CO ₂ frost point and no surface CO ₂ ice forms, but the subsurface is cold enough (~ 145 K) for CO ₂ pore ice to form.
Ice-free Regolith over H ₂ O Ice-filled Regolith	This scenario is observed in the mid-latitudes, where features such as the Latitude Dependent Mantle (LDM) and debris covered glaciers are found under a metre-scale debris cover (e.g., Brough et al., 2019; Kreslavsky and Head, 2002; Souness et al., 2012).
CO ₂ Ice-filled Regolith Over H ₂ O Ice-filled Regolith	This scenario is observed with the formation of the northern CO ₂ seasonal polar cap over the permanent H ₂ O ice cap (e.g., Kieffer and Titus, 2001; Langevin et al., 2007; Schmidt et al., 2009)
	This scenario may also occur when CO ₂ frost (Piqueux et al., 2019) forms in a location with buried subsurface H ₂ O ice (e.g., over the latitude dependent mantle or buried glaciers; Conway and Balme, 2014; Kreslavsky and Head, 2002)
H ₂ O Ice-filled Regolith Over CO ₂ Ice-filled Regolith	This scenario has been observed at the polar caps, within the SPLD, where H ₂ O ice layers have been found to cap buried CO ₂ ice deposits (Bierson et al., 2016; Phillips et al., 2011).
	This scenario could potentially have occurred in the mid-latitudes during the Noachian. In general it is assumed that the mid latitudes only contain subsurface H ₂ O ice, although Nakamura and Tajika (2003) found that under the Noachian solar luminosity, a band of CO ₂ surface ice forms in the mid-latitudes. If this CO ₂ ice-filled regolith layer was then covered in H ₂ O ice and dust before it could fully sublimate, then there could be some CO ₂ ice trapped deep in the subsurface. Several studies have shown that mid-latitude H ₂ O ice deposits form only at high obliquity (e.g., Mischna et al., 2003) and take a long time to sublimate away. Consequently, they may have insulated some CO ₂ ice in the subsurface for long periods of time.
	Another possibility is that a CO ₂ ice deposit that forms above a H ₂ O ice deposit would act as a diapir due to the density difference between the two ices and would eventually sink below the H ₂ O ice deposit (Turbet et al., 2017). In their study, Turbet et al. (2017) suggest that a 100 m diapir of CO ₂ ice would take around 10^4 years to sink to the base of a 1 km thick water ice layer.

4.4.2. The opposite case of the atmosphere acting only as an infinite source has not been simulated because without the potential for vapour to be lost to the atmosphere, the subsurface becomes a closed system, since there is no flux at the base of the MSSM and the amount of ice will not change over time.

4.1.1 Zonal Latitudes and Individual Locations

For every initial scenario considered, the MSSM was run at every 5 degrees of latitude and at 12 locations on the surface (see Figure 4.1), using the corresponding atmospheric data from the present-day MGCM run described in Section 3.7.1. Of the 12 individual locations in Figure 4.1, 9 locations are landing sites, 2 are key features (Olympus Mons and Hellas Basin), and one is a ‘typical’ location on Mars. The locations of all of the features used for the atmospheric profiles are from the grid point that site falls within rather than the actual location, since the 3D MGCM was run with a spatial resolution of 5° latitude and longitude.

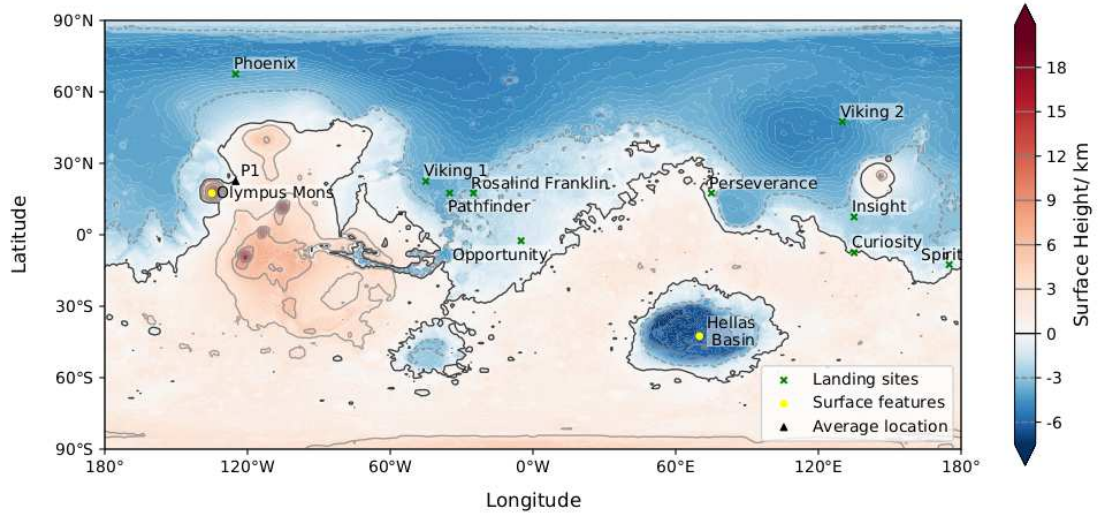


Figure 4.1: Map of the individual locations at which the MSSM is run. Landing sites, features on the surface, and the ‘typical’ location are shown with different symbols.

The ‘typical’ location was chosen using annual surface pressure, albedo and thermal inertia data. The thermal inertia and albedo maps used were derived from TES observations by Wilson et al. (2007) and Christensen et al. (2001) respectively. The surface pressure values are from the final year of a 4 martian year run of the MGCM which was initialised using a restart file from the end of a 20 martian year spin up run (see Section 3.7.1 for details). The criteria used to select this typical point were an annual average

surface pressure within ± 10 Pa of the global average (636 Pa), an albedo within ± 0.05 of the global average (0.206) and a thermal inertia within $\pm 20 \text{ J m}^{-2} \text{ K}^{-1} \text{ s}^{-\frac{1}{2}}$ of the global average ($258 \text{ J m}^{-2} \text{ K}^{-1} \text{ s}^{-\frac{1}{2}}$), resulting in only one location on the MGCM grid (at 5° resolution): 22.5°N - 125°E (P1 on Figure 4.1). At this location, the annual average surface pressure is 632 Pa, albedo is 0.22 and thermal inertia is $244 \text{ J m}^{-2} \text{ K}^{-1} \text{ s}^{-\frac{1}{2}}$.

The majority of the results discussed in this chapter are from the simulations at each latitude (where the atmosphere is averaged over longitude) since these simulations capture the general patterns observed at each latitude that are also seen in the individual location results. However, the individual location results are discussed when they differ from the corresponding latitude simulation. An important note for the figures shown is that, unless stated, the results are from 200 martian year simulations, which output only one time step per year at spring equinox ($L_S = 0^\circ$ or sol 0) to reduce the run time of each simulation. This means that all of the results shown reflect the state of the volatile reservoirs during northern hemisphere spring (see Figure 3.17b), when the northern polar cap has started to recede and the southern polar cap is at its smallest extent. Simulations spanning 50 martian years that output every sol were also run to show the seasonal cycle of all properties. The results from simulations spanning 50 martian years have been used to show either annual averages or to explain specific features within the results of the simulations spanning 200 martian years and it is stated when a figure shows results from simulations spanning 50 martian years instead of 200 martian years.

4.2 Simulations with Only One Ice Present

The simulations with one ice present assume that each ice (H_2O or CO_2) either fills the pore space of the entire subsurface (S29 and S30), fills the pore space below the boundary between ice layers (S08 to S13) or fills the pore space above the boundary at a depth of 1 m (S31). For scenarios where ice fills the pore space below a boundary depth, three different boundary depths were used: 0.5 m (S08, S11), 1 m (S09, S12) and 2 m (S10, S13). The scenario with ice filling the pore space above 1 m was only run for H_2O ice because all of the scenarios with CO_2 ice in the upper region showed the same general distribution over time. This decision was made because the individual ice

scenarios were performed to examine how each ice behaves individually and as baselines to be compared with when both ices are present.

A completely ice-free regolith across the entire subsurface (*IF*) simulation was also run as a baseline that the rest of the simulations can be compared with. The *IF* simulation shows no accumulation of CO₂ ice and accumulation of very small amounts of H₂O ice ($<1\text{e}^{-6} \text{ kg m}^{-3}$) at some latitudes. This is because the atmospheric vapour density profiles that are used as the atmospheric boundary for all simulations are taken from a complete MGCM simulation (see Section 3.7.1 for details) which deposits both H₂O and CO₂ ice when the temperature reaches the frost point for each ice. When the frost point is reached in the MGCM, any vapour above the saturation vapour density is condensed into ice, reducing the vapour density to the saturation vapour density. This means that the value from the MGCM that is used as the atmospheric condition in the MSSM is the saturation vapour density (in locations where ice is present in the MGCM) rather than the supersaturated vapour density value which would be the case before deposition. Therefore, the value used as the atmospheric condition in the MSSM is unlikely to exceed the saturation vapour density. Ice deposition in the MSSM can only occur within the subsurface where vapour densities are increased (or decreased) due to vapour exchange between the atmosphere and subsurface, or due to diffusion throughout the subsurface. The results from this *IF* simulation therefore show that if the atmosphere acts as an infinite source for the subsurface, this has a negligible impact due to the way the MSSM has been set up. Ideally, a full three dimensional (3-D) global circulation model (GCM) would be used to accurately simulate the vapour exchange and formation of both ices at the surface and in the subsurface. However, as mentioned in Section 1.1, this work is an initial investigation into subsurface CO₂ ice that can be used as a baseline for future work using a full GCM.

The *IF* simulation (S01) can be used to show the expected pattern of average annual surface flux at each latitude when both ices are either fully sublimated away or are in equilibrium with the atmosphere. The annual average surface flux over each martian year can then be used to investigate inter-annual variations. However, it can only be calculated for the 50 martian year simulations because it requires a surface flux value

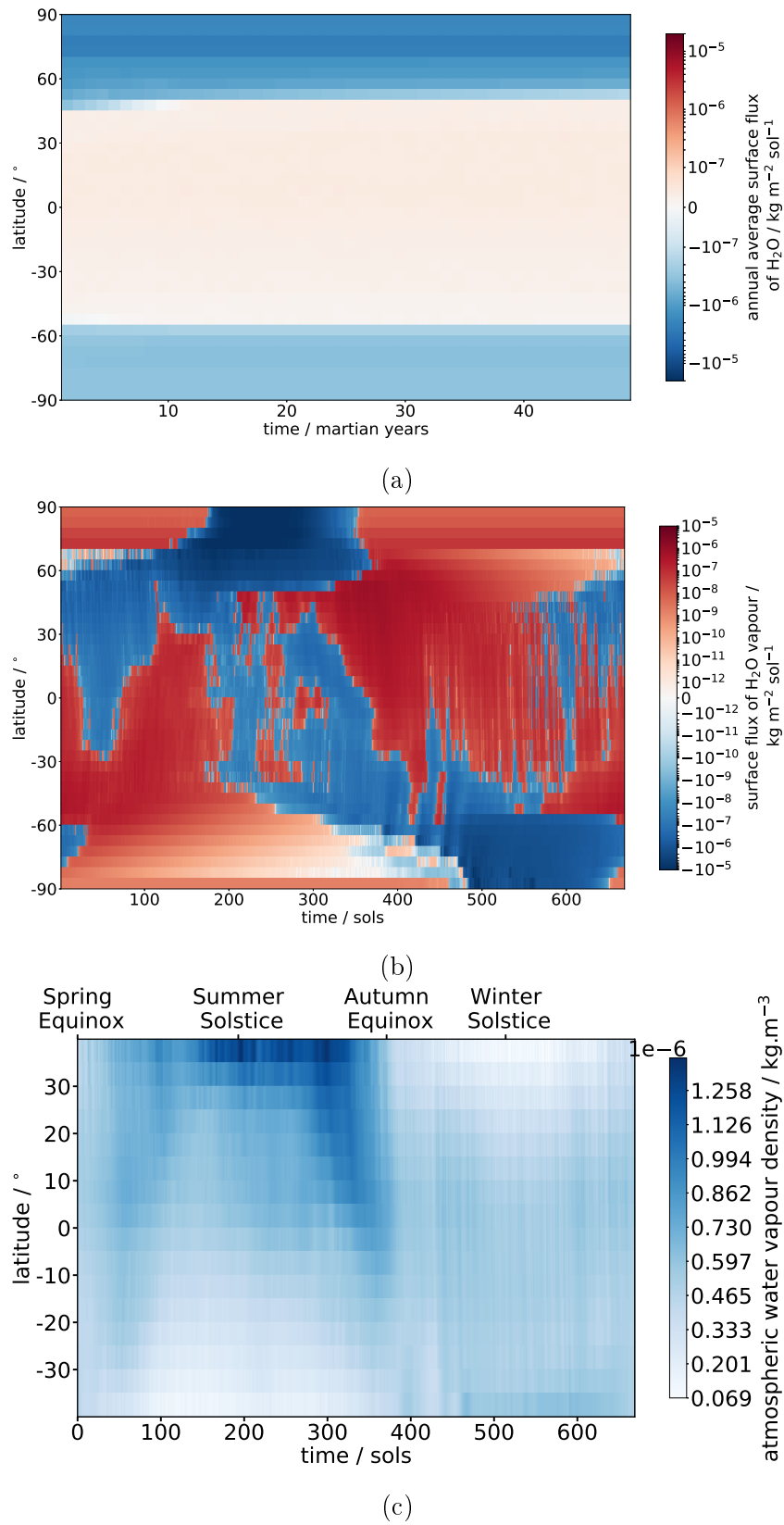
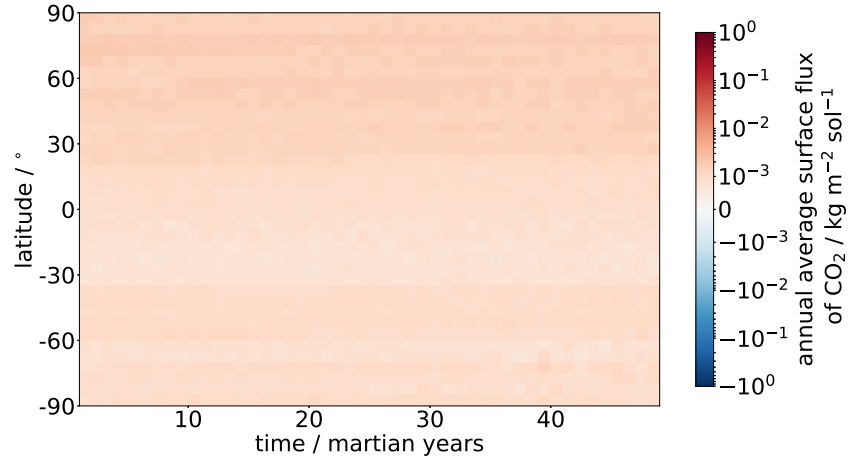
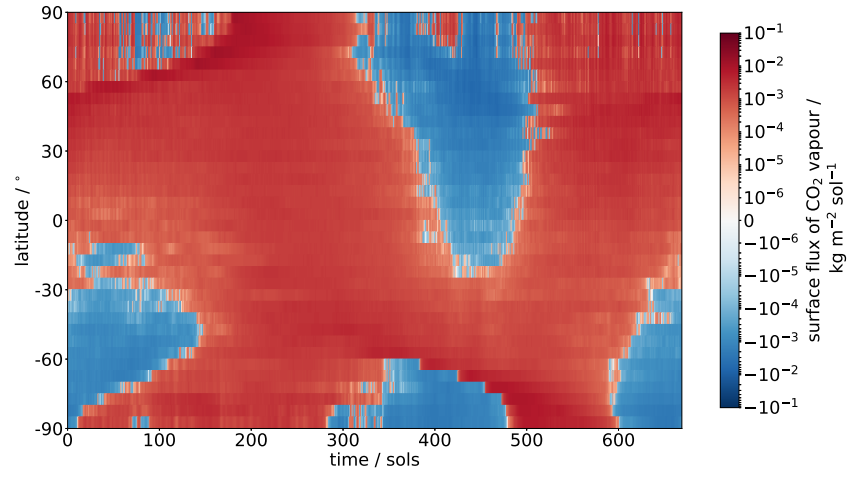


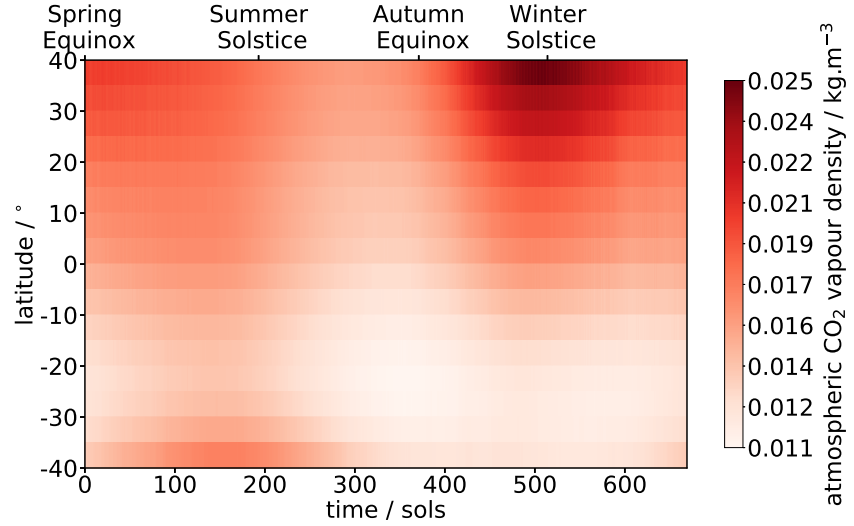
Figure 4.2: Results from the 50 martian year completely *IF* set of simulations (S01): (a) annual average H_2O vapour surface flux, (b) surface flux over simulated martian year 50 (c) is the atmospheric H_2O vapour density for 1 martian year between 40°N and 40°S .



(a)



(b)



(c)

Figure 4.3: Results from the 50 martian year completely *IF* set of simulations (S01): (a) annual average CO_2 vapour surface flux, (b) CO_2 vapour surface flux over simulated martian year 50 (c) is the atmospheric CO_2 vapour density for 1 martian year between 40°N and 40°S .

for each sol, rather than just the one value per year (at $L_S = 0^\circ$) that is output in the 200 martian year simulations. When the annual average surface flux in scenarios that are initialised with ice have the same patterns over time as in the *IF* simulation (see Figures 4.2a and 4.3a) the subsurface vapour in the simulation has reached equilibrium with the atmosphere. This equilibrium can be seen in Figures 4.2a and 4.3a, as the annual average surface flux remains fairly constant within each latitude over the 50 martian years. On average, H_2O vapour flows out of the subsurface (positive flux) within the equatorial and mid-latitude regions and into the subsurface (negative flux) in the polar regions, whereas CO_2 vapour flows out of the subsurface on average at all latitudes. These values show CO_2 vapour flows out of the subsurface for more of the year than into it, rather than CO_2 vapour always flowing out of the subsurface, which would eventually deplete the subsurface of CO_2 vapour. This is because the annual average surface flux summarises the general behaviour of vapour over a year (i.e. whether more vapour flows out of the subsurface than in, or vice versa) rather than showing the detailed seasonal variations.

The seasonal cycles of H_2O and CO_2 surface flux from the final year of the 50 martian year simulations are shown in Figures 4.2b and 4.3b. In these figures, vapour fluctuates between flowing into (negative flux) or out of (positive flux) the subsurface throughout the year and the patterns within the cycles directly correspond to the variations in atmospheric vapour density (see Figure 3.16 for the annual atmospheric vapour cycles). Atmospheric vapour density fluctuations are largest at the poles, which can also be seen in the seasonal surface flux cycles. This is most obvious for H_2O vapour density which varies by around 6 orders of magnitude (between 10^{-11} and $10^{-5} \text{ kg m}^{-3}$) in the polar regions over the course of a martian year. This large amplitude is partially due to the deposition and removal of the seasonal caps, which cover the H_2O ice cap during winter. The large amplitude is also the result of the atmospheric H_2O vapour density being limited by the H_2O saturation vapour density, which varies drastically with the seasonal surface temperature cycle (see Figure 3.16a). Surface temperatures are both higher and less variable in the mid- to low latitudes, resulting in H_2O saturation vapour densities higher than atmospheric H_2O vapour densities. Consequently, H_2O vapour density variations in these regions are dominated by the atmospheric cir-

culatation rather than ice formation and have a much smaller amplitude throughout the year. Figures 4.2c and 4.3c show the atmospheric vapour density (for H_2O and CO_2 respectively) between 40°N and 40°S , showcasing the small-scale annual variations that are not visible at the scale of Figure 3.16. Comparing the small-scale variations in these figures with the surface flux, it can be seen that the surface flux variations in Figures 4.2b and 4.3b directly correspond to these small-scale variations.

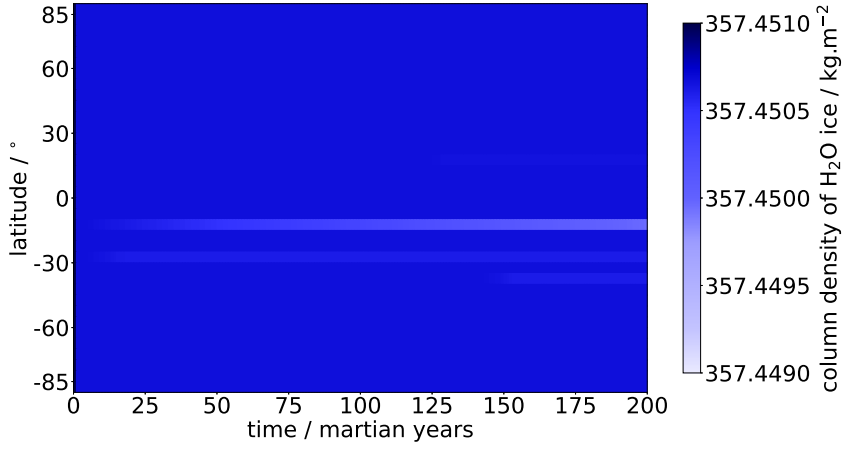
In the rest of this section, the results from the individual ice simulations are discussed in detail and compared with the *IF* simulations described above.

4.2.1 H_2O Ice

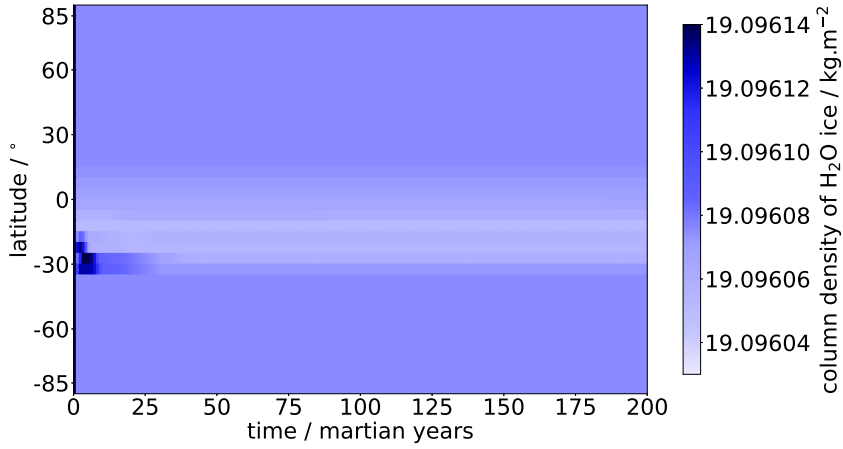
A series of H_2O ice-filled regolith simulations were run to investigate the behaviour of H_2O ice within the MSSM when it is the only ice initially present. Three scenarios have been run: H_2O Ice-filled Regolith across the entire subsurface (*‘W’*, S29); Ice-free Regolith over H_2O Ice-filled Regolith below a boundary depth of 0.5 m, 1 m or 2 m (*‘IF-W’*, S11, S12 and S13, respectively); and H_2O Ice-filled Regolith over Ice-free Regolith with the boundary at 1 m (*‘W-IF’*, S31). In the rest of this section, the results for the *IF-W* scenario will be from the simulations with a boundary depth at 1 m (S12) since the results from the *W-IF* scenario (S31) also assume a boundary depth at 1 m.

The results from all three scenarios are shown in Figure 4.4 and each scenario is plotted over a different scale due to differences in the initial column density of H_2O ice and the amount that sublimates away over 200 martian years in each scenario. While there are clear differences in the behaviour of H_2O ice between the scenarios, there are a few general trends which will be discussed first.

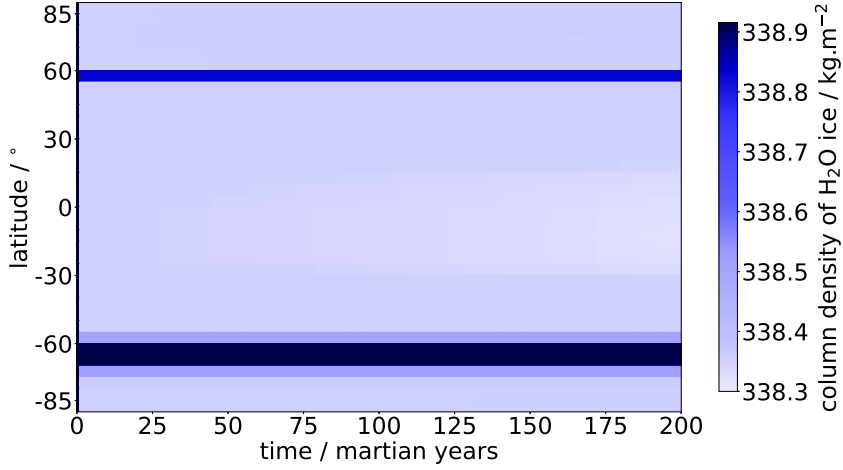
Over the first martian year, there is an initial rapid decrease in the column density of H_2O ice (decrease of $\sim 212 \text{ kg m}^{-2}$ in S12 and S29, $\sim 0.88 \text{ kg m}^{-2}$ in S31), as H_2O ice sublimates within the pore space until the H_2O vapour density reaches H_2O saturation vapour density. Once the H_2O vapour density has reached H_2O saturation vapour density in the model layers where H_2O ice is present, the rate of sublimation becomes more strongly latitudinally dependent and is limited by the rate of diffusion through the subsurface into the ice-free region and out into the atmosphere by surface flux. For



(a) W (S29)



(b) $W-IF$ (S31)



(c) $IF-W$ (S12)

Figure 4.4: Column density of H_2O ice at each latitude over time for the (a) H_2O ice only (S29), (b) $W-IF$ (S31) and (c) $IF-W$ (S12) sets of simulations. Each figure is plotted using a different scale due to the differences in the initial column density of H_2O ice between the scenarios. Grey represents where the H_2O ice column density is less than 0.0001 kg m^{-2} .

the *W* (S29) and *IF-W* (S12) scenarios, only sublimation occurs as the H₂O vapour density is highest in the lowest portion of the subsurface and will, therefore, always diffuse upward and out of the subsurface. In the *W-IF* regolith scenario (S31) on the other hand, small amounts of H₂O ice ($\sim 1\text{e}^{-5} \text{ kg m}^{-3}$) form initially at some latitudes as the subsurface region below the H₂O ice-filled regolith layer has a lower H₂O vapour density than the H₂O vapour density in the H₂O ice-filled regolith layer, leading to H₂O vapour flowing further into the subsurface as well as out into the atmosphere. This increases the H₂O vapour density in the model layers below the H₂O ice-filled regolith layer, which can lead to a slight increase in H₂O ice column density if this increase in H₂O vapour density raises H₂O vapour density to above the saturation vapour density. This is the case between latitudes 20° to 30°S during the first few martian years in Figure 4.4b.

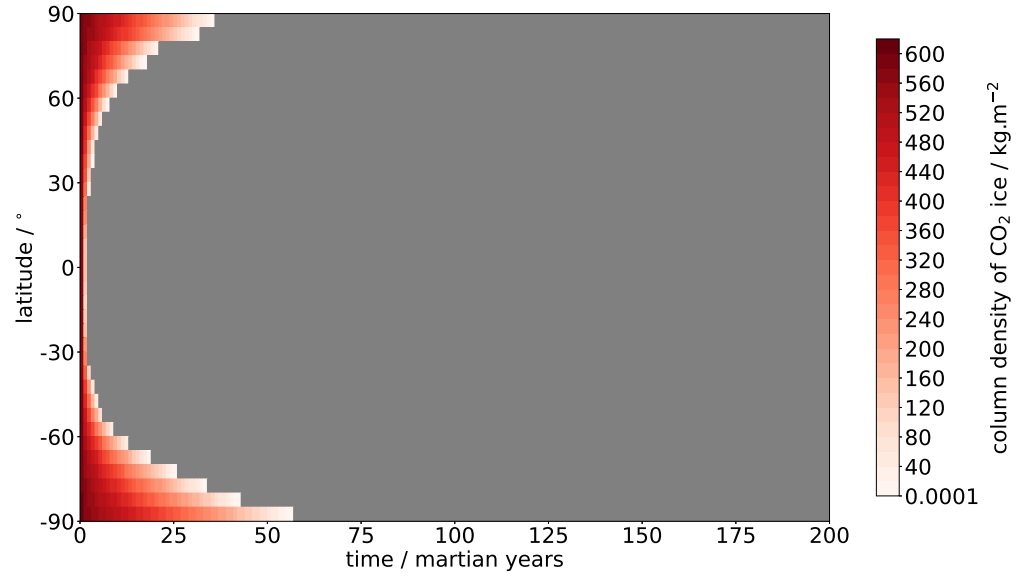
After the initial rapid decrease in H₂O ice column density, the column density remains mostly consistent over time within the polar and mid-latitude regions for all three scenarios and the sublimation rate drops from 228 mm MY⁻¹ to <0.0004 mm MY⁻¹ (in S12 and S29). The column density of H₂O ice with latitude after the first year is slightly different between the three scenarios due to the slight subsurface temperature differences caused by the different subsurface thermal conductivities. In the *IF-W* scenario (S12), there are also a few latitudes (55°N and 55°-70°S) with slightly higher H₂O ice column densities than the rest of the polar and mid-latitude regions. At these latitudes, a small amount of H₂O ice formed in the model layer above the initial H₂O ice-filled regolith layer within the first martian year as H₂O vapour density in the model layer increased above the H₂O saturation vapour density. This small amount of H₂O ice persists once formed, resulting in the slightly higher H₂O ice column densities observed at these latitudes. In the equatorial regions (15°N to 35°S) there is a steady decrease in the column density of H₂O ice over time in all three scenarios. At these latitudes, H₂O ice is not expected to be stable due to the high surface and subsurface temperatures. The rate of this decline is limited by the rate of diffusion of H₂O vapour through the subsurface and out into the atmosphere.

4.2.2 CO₂ Ice

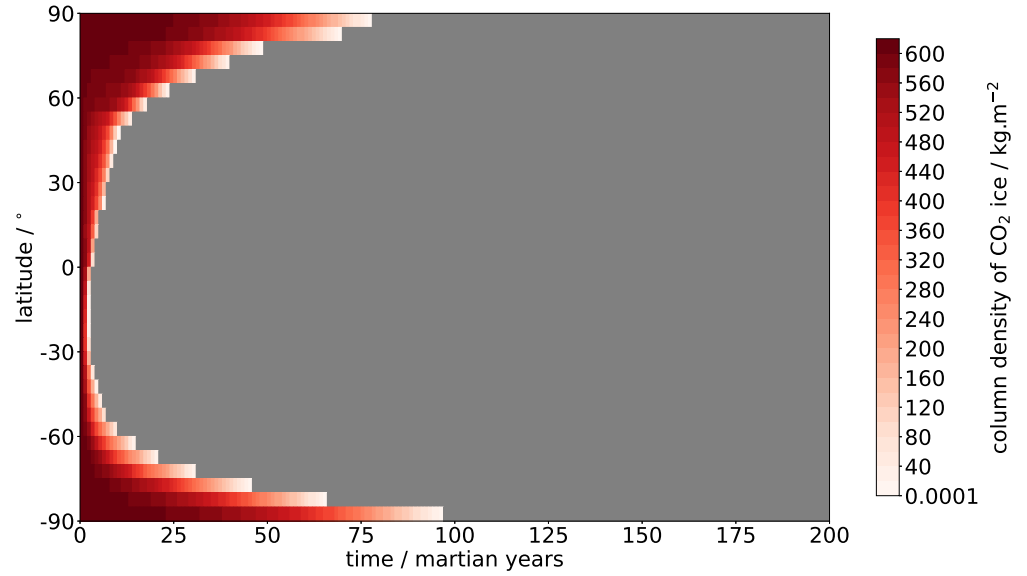
A series of CO₂ ice-filled regolith simulations were run to investigate the behaviour of CO₂ ice within the MSSM when it is the only ice initially present. Two scenarios were run: CO₂ Ice-filled Regolith across the entire subsurface ('*C*', S30) and Ice-free Regolith over CO₂ Ice-filled Regolith (*IF-C*) with boundary depths of 0.5 m, 1 m and 2 m (S08, S09 and S10 respectively). In all of these scenarios, CO₂ ice fully sublimated within the 200 martian years at all latitudes, with global average sublimation rates ranging from 1220 mm MY⁻¹ (S30) to 1795 mm MY⁻¹ (S10). CO₂ ice survived around twice as long when CO₂ ice filled the entire subsurface pore space compared with when there was an overlying ice-free layer, as shown in Figure 4.5.

Another interesting feature of these results is that CO₂ ice takes longer to sublimate in the southern polar region (average sublimation rate of ~ 367 mm MY⁻¹ in S09) than in the northern polar region (average sublimation rate of ~ 512 mm MY⁻¹ in S09). This matches present-day observations, as any CO₂ ice that would have been deposited in the northern polar region during a previous epoch (and would now be exposed at the surface) has fully sublimated, whereas in the south polar region, a thin CO₂ ice cap is still in the process of sublimating away after its formation during a previous epoch (e.g., Aharonson et al., 2004; Kelly et al., 2006).

The slower sublimation of CO₂ ice in the southern polar region can be understood by looking at the annual average surface flux from the 50 martian year simulation of the entire subsurface pore space filled with CO₂ ice (S30; Figure 4.6a). The annual average surface flux is highest in the mid- to low latitudes, where CO₂ ice sublimates away the fastest and once CO₂ ice has fully sublimated the annual average surface flux follows the same pattern as when there is no ice present in the subsurface (the *IF* scenario; Figure 4.3a). In the polar regions, however, the rate of sublimation is more variable. Initially CO₂ ice sublimates at a faster rate in the southern polar region than in the northern polar region, due to the higher annual average surface flux of CO₂ vapour out of the atmosphere in the southern polar region. Annual average surface flux is higher in the southern region because of the lower atmospheric CO₂ vapour density throughout the year (Figure 4.3c). However, in the northern region,



(a) *IF-C* (S09)



(b) *C* (S30)

Figure 4.5: Column density of CO₂ ice at each latitude over time for the (a) *IF-C* with a boundary at 1 m (S09) and (b) the *C* (S30) set of simulations. Grey represents where the CO₂ ice column density is less than 0.0001 kg m⁻².

the annual average surface flux increases over time, due to the deposition of H₂O ice as CO₂ ice sublimates away (see Figure 4.6b). The increase in the column density of H₂O ice over time increases subsurface temperatures during summer, which in turn increases the diffusion coefficient of CO₂ ice (Equation 3.39). The higher diffusion coefficient increases the surface flux rate, leading to more CO₂ ice loss over time and the pattern that can be seen in Figure 4.6a. In the southern polar region, however, the annual average surface flux remains consistent over time, leading to CO₂ ice surviving less time overall in the northern polar region. This scenario is consistent with previous observations of surface CO₂ ice and previous modelling studies of the behaviour of surface CO₂ ice (e.g., Aharonson et al., 2004; Kelly et al., 2006).

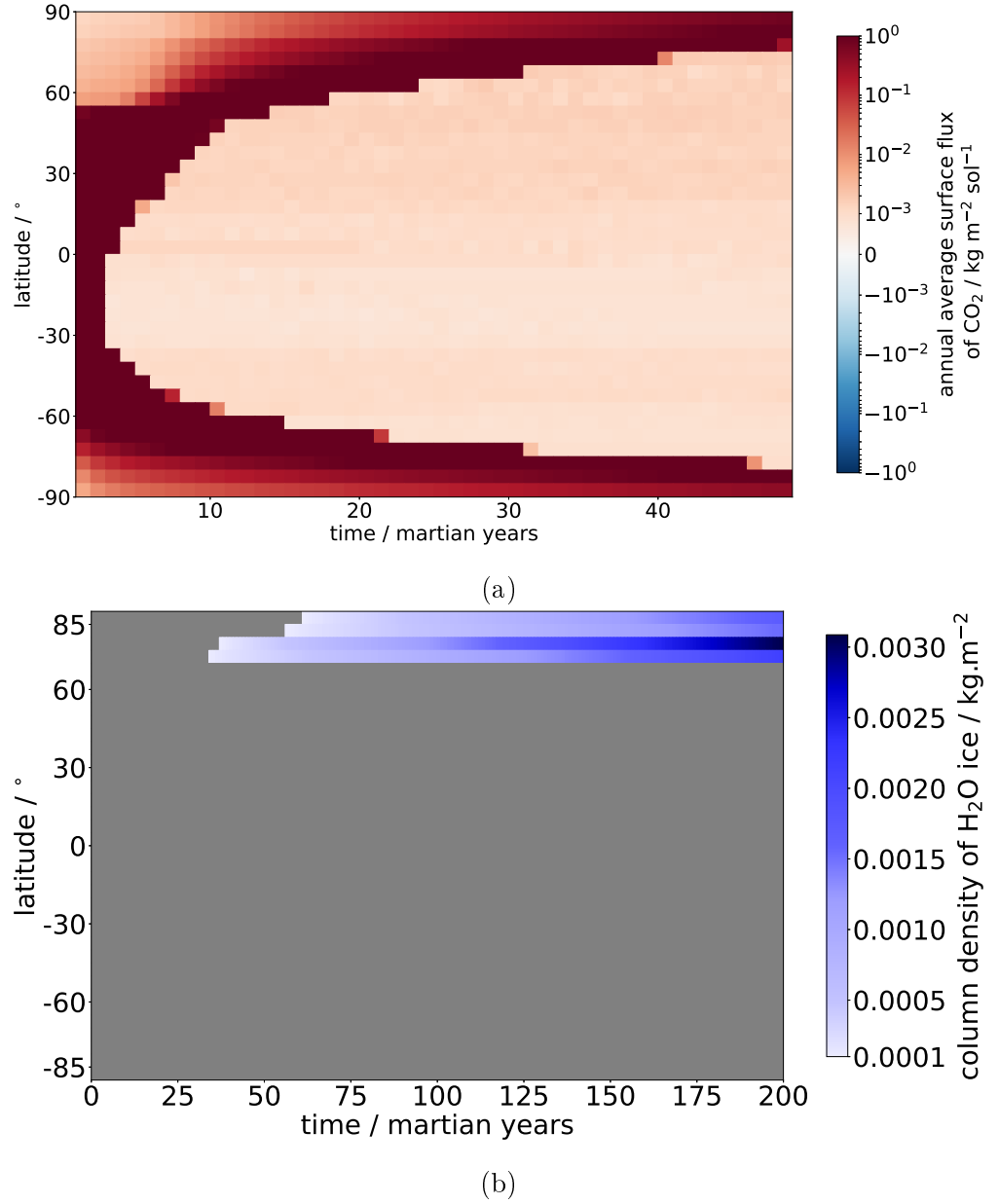


Figure 4.6: (a) Annual average CO_2 surface flux over time for the 50 martian year simulation and (b) the column density of H_2O ice over the 200 martian year simulation for the *C* set of simulations (S30). A positive surface flux means CO_2 vapour is flowing out of the subsurface and into the atmosphere. Grey on the H_2O ice column density figure represents where the H_2O ice density is less than 0.0001 kg m^{-2} .

4.3 Simulations with Both Ices

The simulations with both ices present have two ice-layers and assume that all of the pore space within each layer is filled with one of the two ices. There are two ice-layer configurations, one with CO₂ Ice-filled Regolith Over H₂O Ice-filled Regolith ('*C-W*'; S02, S03, S04) and vice versa ('*W-C*'; S05, S06 and S07). For each of the two configurations, three different boundary depths were used (0.5 m, 1 m and 2 m) and the results from the six scenarios are summarised in this section.

4.3.1 CO₂ Ice Filled Regolith over H₂O Ice Filled Regolith

In the scenarios with CO₂ Ice-filled Regolith Over H₂O Ice-filled Regolith ('*C-W*'; S02, S03, S04), all of the CO₂ ice within the subsurface has sublimated away within a maximum of 20 martian years, which can be seen in Figure 4.7. The initial amount of H₂O ice also sublimates slightly in the first year (as discussed in Section 4.2.1) and then remains mostly stable for the remainder of the 200 year simulation due to the repeatable surface flux replenishing the amount of H₂O vapour each year. Small amounts of H₂O ice form after CO₂ ice has fully sublimated away, following the same pattern described for the *IF* scenario (Section 4.2).

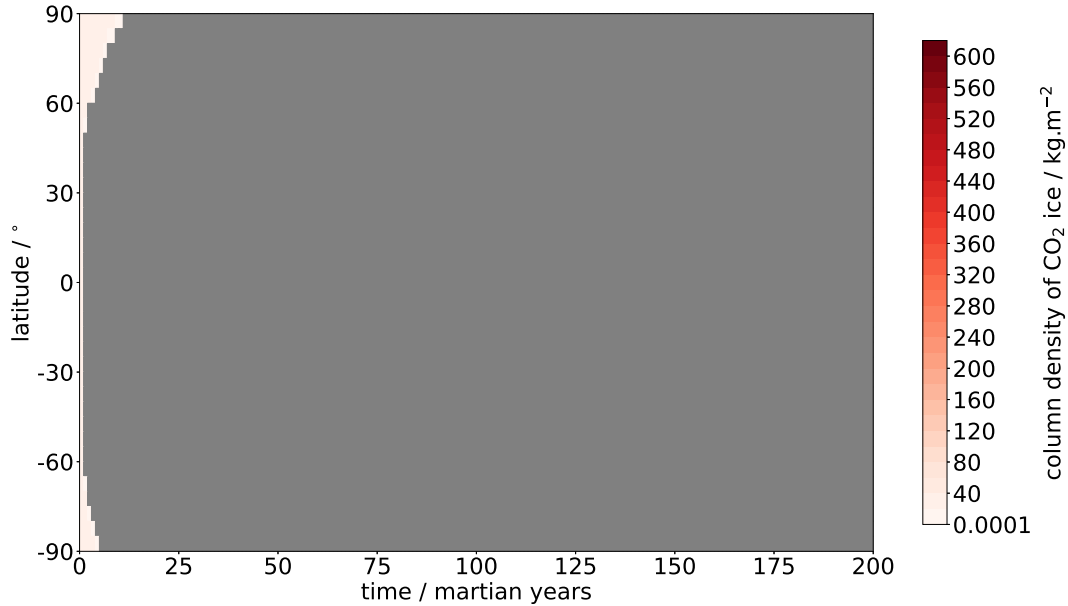


Figure 4.7: Column density of CO₂ ice at each latitude over time for the *C-W* with the boundary at 1 m set of simulations (S03). Grey represents where the CO₂ ice column density is less than 0.0001 kg m⁻².

Figure 4.7 shows that CO₂ ice survives longer in the northern polar region than in the southern polar region. This is opposite to the results from the CO₂ Ice-filled Regolith across the entire subsurface (*C*) scenario (Section 4.2.2) and observed for the polar caps at present, where there is both a seasonal and perennial CO₂ ice cap in the south and only a seasonal CO₂ ice cap in the north (e.g., Blackburn et al., 2010; Pollack et al., 1990). This is because atmospheric CO₂ vapour density is higher over the northern polar region during northern summer than over the southern polar region during southern summer (Figure 3.16d). This means that the southern polar region will have a larger difference between the atmospheric CO₂ vapour density and the subsurface CO₂ vapour density, which is held at CO₂ saturation vapour density while CO₂ ice is still present. To account for the larger difference, more CO₂ vapour diffuses out of the subsurface in each time step and, consequently, more CO₂ ice will sublime in each time step to keep CO₂ vapour density at CO₂ saturation vapour density within the pore space of each model layer after diffusion has occurred. This is shown in the annual average CO₂ surface flux which is higher in the southern polar region than in the northern polar region for the first few years (Figure 4.8). However, the annual average surface flux in the northern polar region increases over time. This increase occurs due to the increase in the diffusion coefficient and temperature within each model layer as the amount of CO₂ ice within the subsurface of the northern region decreases and the column density of H₂O ice increases. This in turn causes the surface flux to increase.

The annual average surface flux (Figure 4.8) remains high for a few years after all of the CO₂ ice within the subsurface has sublimated away because the CO₂ saturation vapour density is higher than the atmospheric CO₂ vapour density across the planet. This means that when all of the CO₂ ice has sublimated, the CO₂ vapour density within the pore space is still greater than the atmospheric CO₂ vapour density and it takes a few years before the subsurface CO₂ vapour density reaches equilibrium with the atmospheric CO₂ vapour density. Once all of the excess CO₂ vapour has been removed from the subsurface, the annual average surface flux returns to the same values as for the *IF* scenario (S01; Figure 4.3a).

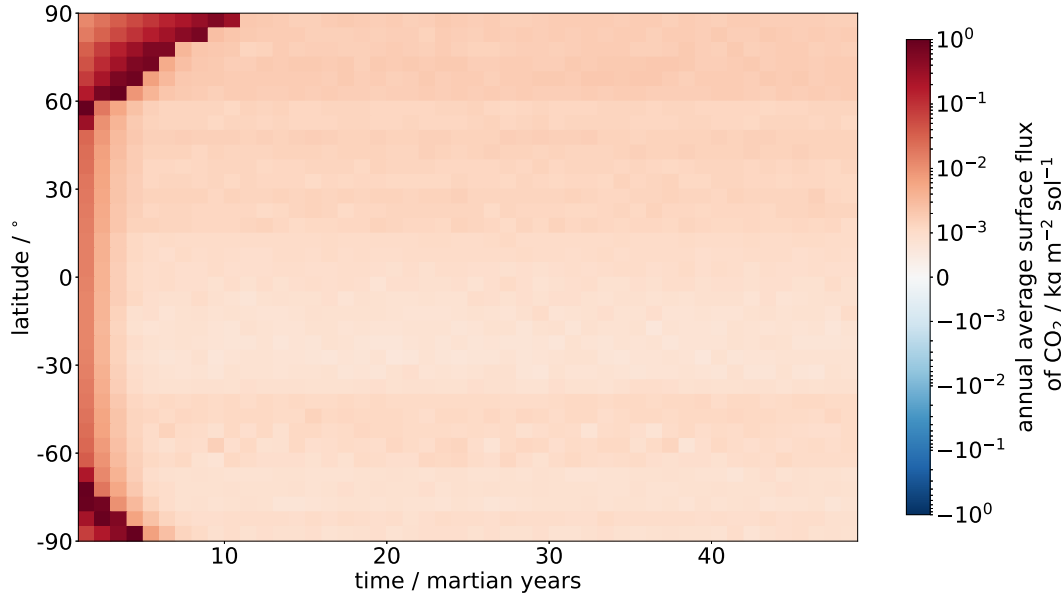
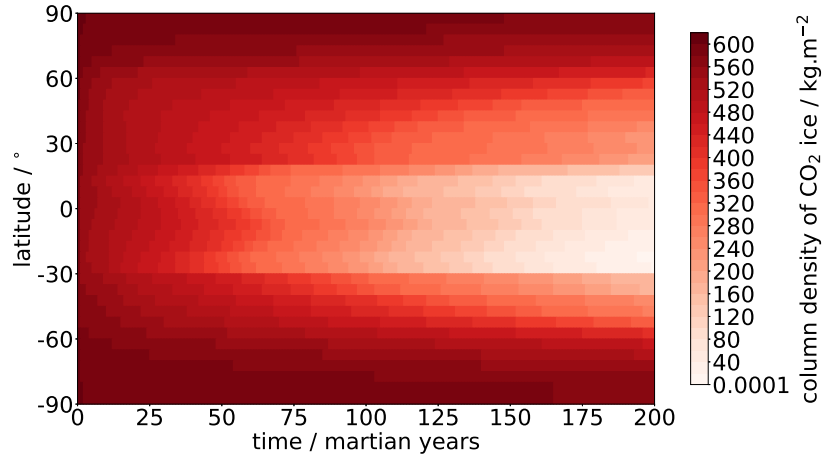


Figure 4.8: Annual average CO₂ surface flux for the *C-W* (S03) set of simulations.

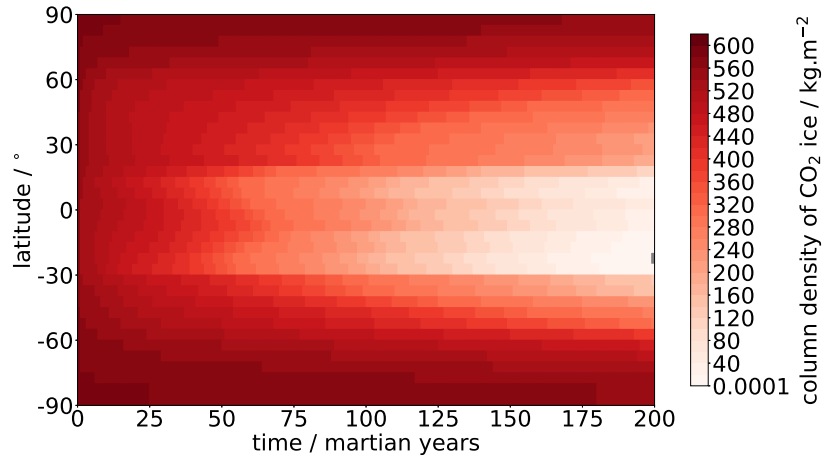
4.3.2 H₂O Ice Filled Regolith over CO₂ Ice Filled Regolith

The results from the H₂O Ice-filled Regolith Over CO₂ Ice-filled Regolith (*W-C*) simulations at all three boundary depths (0.5, 1 and 2 m) are shown in Figure 4.9, showing significantly different results from those shown previously in this chapter. In all three figures, CO₂ ice takes at least 200 martian years to fully sublimate at nearly all latitudes and the final column density of CO₂ ice decreases with decreasing latitude. The behaviour of CO₂ ice with latitude can be understood by splitting the planet into three broad regions: polar (>60° latitude), mid-latitude (15°N to 60°N and 30°S to 60°S) and equatorial (15°N to 30°S) regions, with latitude ranges that differ slightly from their purely geographical definition. To understand the differences between these regions the scenario with the boundary between the H₂O ice-filled regolith layer and the CO₂ ice-filled regolith layer at 1 m (S06) is looked at in more detail.

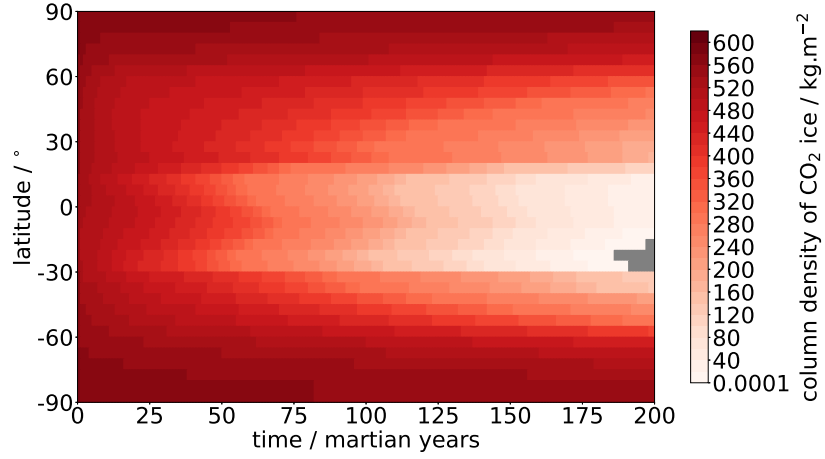
In the polar regions (of scenario S06), CO₂ ice sublimates at a very similar rate in both the northern and southern polar regions, with CO₂ ice taking slightly longer to sublimate away in the southern hemisphere compared with the northern. This difference is reflected in the slightly lower annual average surface flux in the southern hemisphere over the first 50 martian years compared with the northern hemisphere (see Figure 4.10). In Figure 4.10, this difference looks insignificant, but over the hundreds to thousands of martian years that it will take for the CO₂ ice to fully sublimate, these



(a) Boundary at 0.5 m (S05)



(b) Boundary at 1 m (S06)



(c) Boundary at 2 m (S07)

Figure 4.9: Column density of CO₂ ice at each latitude over time for the *W-C* with a boundary at (a) 0.5 m (S05) (b) 1 m (S06) and (c) 2 m (S07) sets of simulations. Grey represents where the CO₂ ice column density is less than 0.0001 kg m⁻².

small differences have a significant impact that is discussed in more detail in Section 4.3.2.3. The other important aspect of the annual average surface flux figure is that, at all latitudes, CO₂ ice is sublimating away for more of the year than it is accumulating, implying there is net depletion of near surface polar CO₂ ice reservoirs, which matches observations.

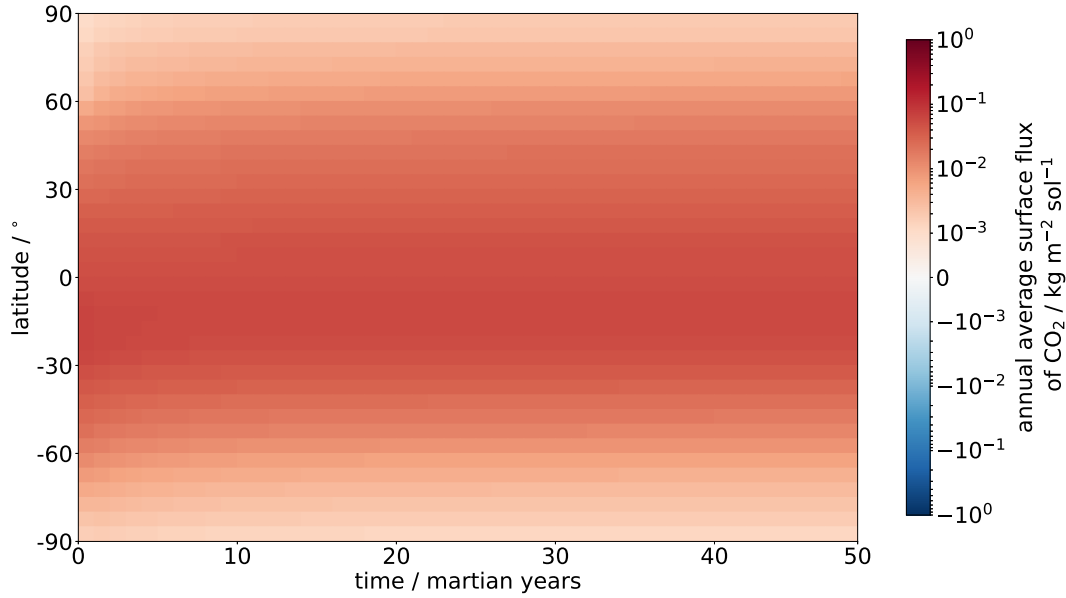


Figure 4.10: Annual average CO₂ surface flux over time for the 50 martian year *W-C* set of simulations (S06).

In the mid-latitudes, a hemispherical difference also exists in the behaviour of CO₂ ice. In the northern hemisphere, the rate of sublimation of CO₂ ice increases only slightly with decreasing latitude: from 19.5 mm MY⁻¹ at 58°N to 28.6 mm MY⁻¹ at 38°N in S06. Whereas in the southern mid-latitude region, there is a more pronounced latitudinal difference in the rate that the column density of CO₂ ice changes over time, with sublimation rates increasing from 16.2 mm MY⁻¹ at 57°S to 35.8 mm MY⁻¹ at 37°S in S06. This relates to the change in the average subsurface temperature with latitude, which can be seen in Figure 4.11. From this figure, it can be seen that temperatures increase from around 180 K (at the base of the polar region) to 225 K (at the top of the equatorial region) occurs over 45° of latitude in the northern hemisphere and only over 30° of latitude in the southern hemisphere. The more drastic change in temperature with decreasing latitude in the southern hemisphere is therefore the cause of the sharper increase in rate of sublimation of CO₂ ice with decreasing latitude.

The influence of the more gradual change in temperature in the northern mid-

latitude region compared with the southern mid-latitude region can also be seen in the annual average surface flux (Figure 4.10), which increases over a smaller latitude range in the southern mid-latitudes than in the northern mid-latitudes. In the northern mid-latitudes, the region of gradually increasing surface flux actually extends down to between 10° and 15°N in the northern hemisphere, rather than to 30° as in the southern hemisphere. This is due to the 1 to 3 km variations in topography with longitude between $\sim 20^\circ\text{N}$ and the equator: these latitudes cover the transition region between the northern lowlands and southern highlands for most longitudes. This latitude region also includes Olympus Mons, the Tharsis volcanic province and the Elysium volcanic province, all of which are substantial enough to impact the surrounding climate. Longitudinal variations in climate within this region are, therefore, substantial enough to affect the atmospheric zonal averages used and result in values that are artificially higher or lower than would be expected at individual longitudes. The impact of using the zonally averaged atmosphere rather than the individual latitude/longitude values is discussed in more detail in Section 4.3.2.2. The mid-latitudes of the southern hemisphere have a much stronger variation in surface flux across each martian year, and the rate of sublimation of CO_2 ice decreases steadily with increasing latitude from around 30°S (36.8 mm MY^{-1}) to the southern pole (2.66 mm MY^{-1}).

Throughout the equatorial region ($\sim 15^\circ\text{N}$ to 30°S in these simulations), CO_2 ice sublimates rapidly and has almost fully sublimated at every latitude within the region over the 200 martian years. This is expected due to the higher temperatures in this region compared with the mid-latitudes and polar regions (see Figure 4.11). Alongside the higher temperatures, the atmospheric CO_2 vapour density (0.011 to 0.017 kg m^{-3} ; Figure 3.18d) is several orders of magnitude lower than the CO_2 saturation vapour density (10 to 16 kg m^{-3}) at equatorial temperatures. Since the regolith is initialised with a CO_2 vapour density equal to the atmospheric CO_2 vapour density, the initial CO_2 ice in the subsurface is unstable and CO_2 ice will sublimate until the CO_2 vapour density in the pore space is equal to the CO_2 saturation vapour density. After the CO_2 vapour density within the pore space has reached CO_2 saturation vapour density, the rate of sublimation is then limited by the rate of diffusion of CO_2 vapour out of the subsurface.

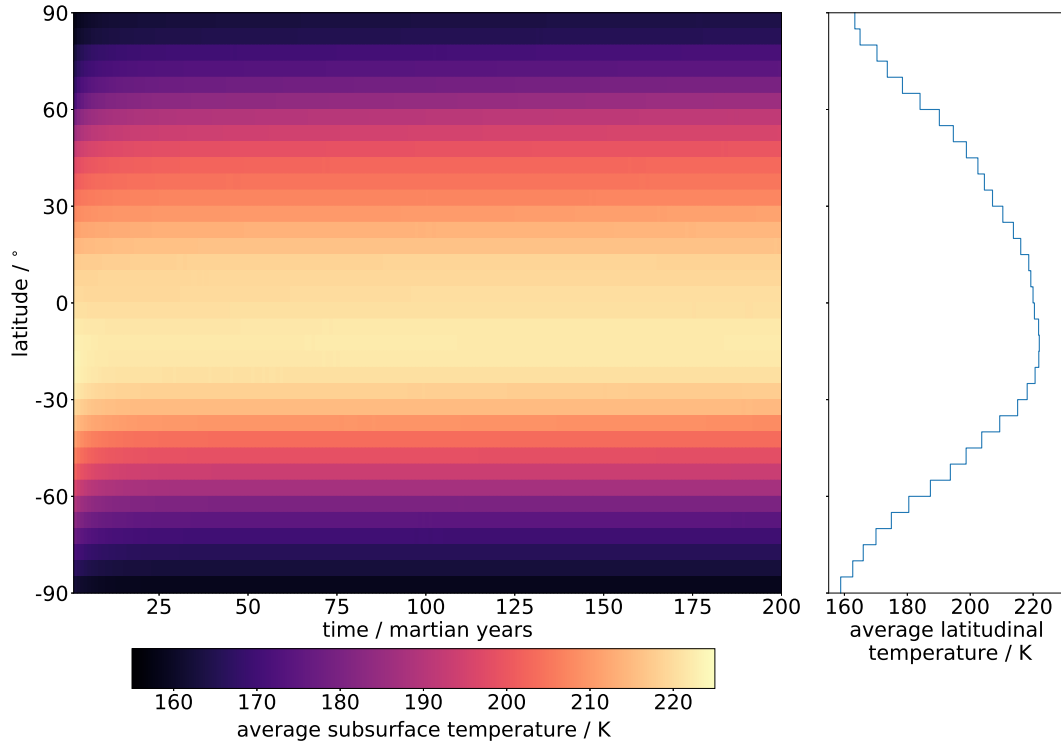


Figure 4.11: Average subsurface temperature over 200 martian years (left) and the latitudinally averaged temperature (right) for the *W-C* set of simulations (S06).

Between 5°N and 10°S , the column density of CO_2 ice takes around 5 martian years longer to sublimate away than the surrounding latitudes (20°N to 5°N and 10°S to 30°S). Based on the gradual increase in temperature from 20°N to 30°S (Figure 4.11), a gradual increase in sublimation rate is expected across the region. This means the gradual decrease in the annual average CO_2 sublimation rate from 46.1 mm MY^{-1} at 5°S to 36.8 mm MY^{-1} at 30°S is the expected variation with latitude from subsurface temperature variations. The faster sublimation of CO_2 ice with latitude between 20°N and the equator (annual average sublimation rates of $30.6\text{--}45.0 \text{ mm MY}^{-1}$), on the other hand, is not explained by the increase in subsurface temperatures from 20°N to 30°S , since the CO_2 ice column density is expected to be higher at 20°N than at the equator. The observed faster sublimation rate in this region is a consequence of the higher H_2O ice density, higher atmospheric H_2O vapour density and the smaller annual variations in surface temperature between 20°N and the equator than between the equator and 10°S . The variations in surface temperature throughout the year from 20°N to 10°S (Figure 3.18a) influence the saturation vapour density of each ice, as saturation vapour density increases at higher temperatures. This in turn influences the annual sublimation rate, which is dependent on the difference between saturation vapour density and vapour

density. Between 20°N and the equator, surface temperatures vary by less than 10 K throughout the year, whereas between the equator and 10°S, surface temperatures vary by 20-30 K throughout the year. The more consistent surface temperatures between 20°N and the equator result in a more continuous high sublimation rate of CO₂ ice, that in the long term results in a faster loss of CO₂ ice over time. Alongside the effect of surface temperature, the slightly larger (by $\sim 3 \times 10^{-6} \text{ kg m}^{-2}$) subsurface column density of H₂O ice at these latitudes compared with that found between the equator and 10°S (Figure 4.12) also results in a faster sublimation rate. This slightly higher column density of H₂O ice is a consequence of a smaller amount of sublimation occurring within the first year due to the higher initial subsurface H₂O vapour density used at these latitudes from the higher atmospheric H₂O vapour densities. The subsurface H₂O vapour density is initialised with atmospheric H₂O vapour density values which are generally lower than the H₂O saturation vapour density, particularly in the equatorial region where temperatures are above the average frost point on Mars (195 K; Mellon and Jakosky, 1993). Therefore, in the first year H₂O ice sublimates rapidly until the H₂O vapour density within the pore space equals the H₂O saturation vapour density. Since atmospheric H₂O vapour density is on average higher in the northern equatorial region than in the southern equatorial region throughout the year (see Figure 4.2c), less sublimation is required for the subsurface H₂O vapour density to increase to the H₂O saturation vapour density value in the northern equatorial region. This results in the H₂O ice column density remaining slightly higher than in the southern equatorial regions and this small amount of extra H₂O ice has a long term impact through its effect on subsurface thermal properties.

H₂O ice has a significantly larger thermal conductivity ($\sim 2.5 \text{ W m}^{-1} \text{ K}^{-1}$) than both the empty regolith (0.01 to 0.1 $\text{W m}^{-1} \text{ K}^{-1}$) and CO₂ ice ($\sim 0.7 \text{ W m}^{-1} \text{ K}^{-1}$). Therefore, the presence of small amounts of H₂O ice can have a large impact on the effective thermal conductivity of the regolith. The small amount extra at latitudes 20°N to 5°N result in a thermal conductivity that is $\sim 0.01\text{-}0.02 \text{ W m}^{-1} \text{ K}^{-1}$ greater than in the latitudes below the equator. The difference in thermal conductivity seems small, but it is a $\sim 100\%$ increase in thermal conductivity from that of an empty regolith at the surface and results in a slight increase in subsurface temperatures over time ($< 1 \text{ K}$)

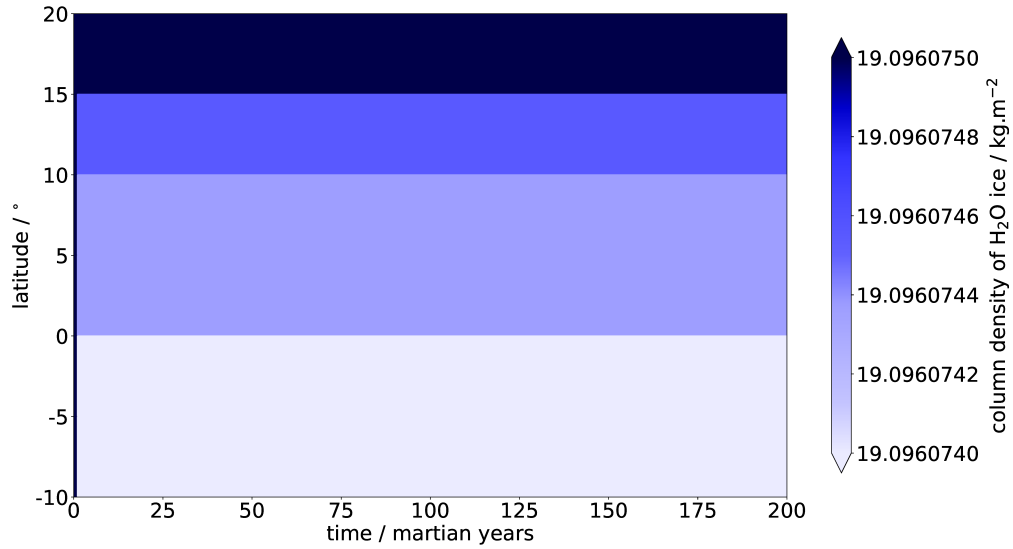


Figure 4.12: Column density of H₂O ice between 20°N and 10°S over time, for the *W-C* set of simulations (S06). A difference of $1 \times 10^{-6} \text{ kg m}^{-2}$ is within same order of magnitude as atmospheric H₂O vapour density. Grey represents where the H₂O ice column density is less than 0.0001 kg m^{-2} .

at the latitudes containing extra H₂O ice. This is due to the greater amount of heat conducted and stored throughout the year. The slightly higher temperatures at these latitudes result in an increase in the CO₂ saturation vapour density, resulting in the observed faster rate of CO₂ ice sublimation.

Alongside latitudinal differences already discussed, the sublimation of CO₂ ice in these simulations is highly dependent on the depth of the boundary. In the equatorial region of Figure 4.9, it can be seen that the deeper the boundary, the less time it takes for CO₂ ice to fully sublimate away. However, through estimating the number of years that CO₂ ice takes to sublimate using the average sublimation rate over the 200 martian year period, shown in Figure 4.13, it can be seen that this is only the case in parts of the equatorial region. At higher latitudes, the reverse is true, as CO₂ ice survives longer when buried deeper in the subsurface.

In the equatorial region, the faster sublimation as CO₂ ice is buried deeper is due to both the decrease in the initial column density of CO₂ ice and the corresponding increase in the amount of H₂O ice. As the depth of the boundary increases, the initial amount of CO₂ ice decreases, resulting in a decrease in the time taken for the CO₂ to fully sublimate. Alongside this, the increase in the amount of H₂O ice results in higher

equatorial temperatures due to the higher thermal conductivity between depths of 0.5 m to 2 m, which has a larger effect than the rate of sublimation and diffusion of CO₂ vapour at these latitudes. Across the equatorial region, these increased temperatures result in higher CO₂ and H₂O saturation vapour densities, causing more of both ices to sublimate. This increases the porosity and the diffusion coefficient across the regolith, resulting in a more rapid loss of vapour to the atmosphere over each sol. Consequently, the initial amount of CO₂ ice in this region sublimates rapidly for all boundary depths.

At latitudes higher than 55°N and 55°S, on the other hand, surface temperatures are lower than 190 K (the frost point of H₂O on Mars; Mellon and Jakosky, 1993), which means that the initial H₂O vapour density will be close to the H₂O saturation vapour density in all model layers within the subsurface. This means that only a small initial decrease in the column density of H₂O ice will occur during the first year and the porosity of the overlying H₂O ice-filled regolith layer will be small for all three boundary depths (0.5, 1 and 2 m). The small porosity in the overlying H₂O ice-filled regolith layer reduces the diffusion coefficient enough that the rate of CO₂ ice sublimation is dominated by the rate of diffusion out of the subsurface rather than the difference between subsurface CO₂ vapour density and CO₂ saturation vapour density.

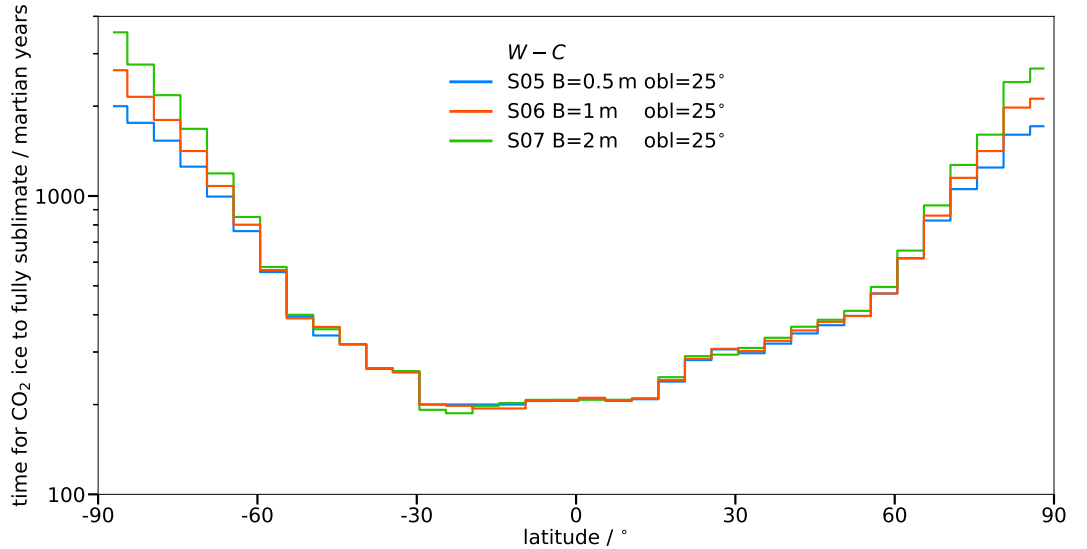


Figure 4.13: Comparison of the estimated number of years that CO₂ ice survives in the *W-C* set of simulations with the boundary depth at (a) 0.5 m (S05), (b) 1 m (S06) and (c) 2 m (S07)

4.3.2.1 Time Taken To Fully Sublimate CO₂ Ice When Under H₂O Ice

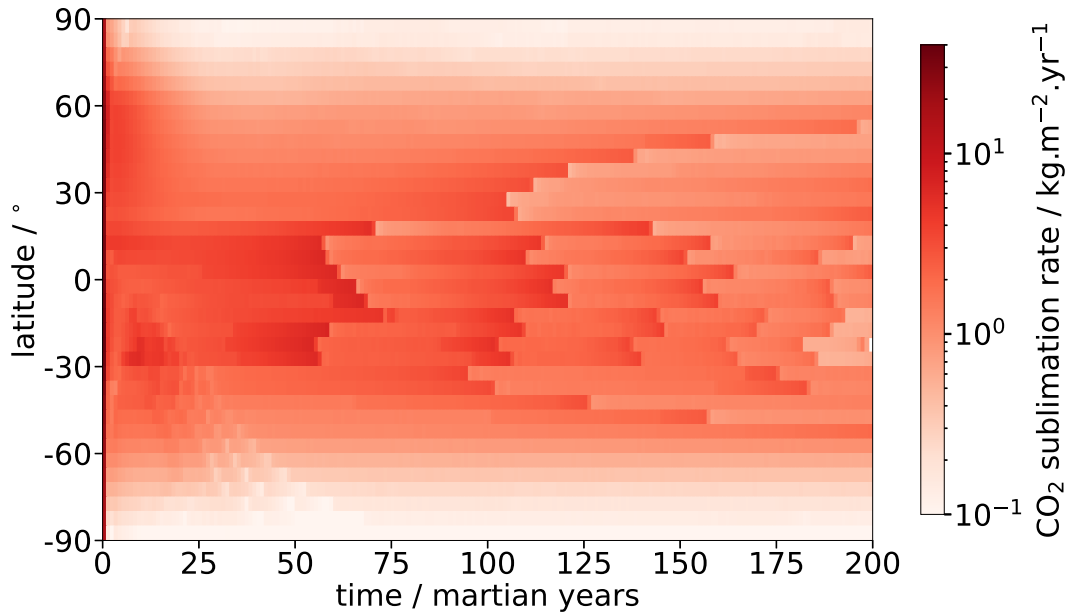
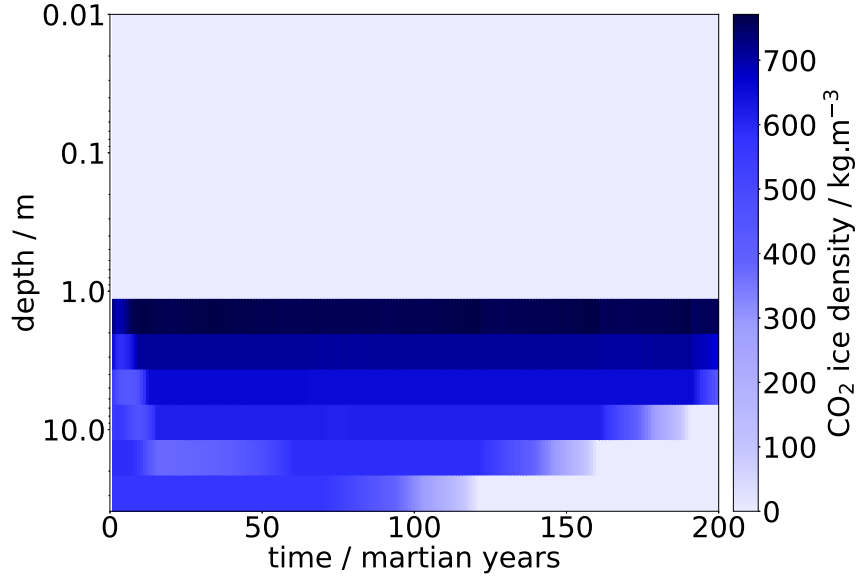


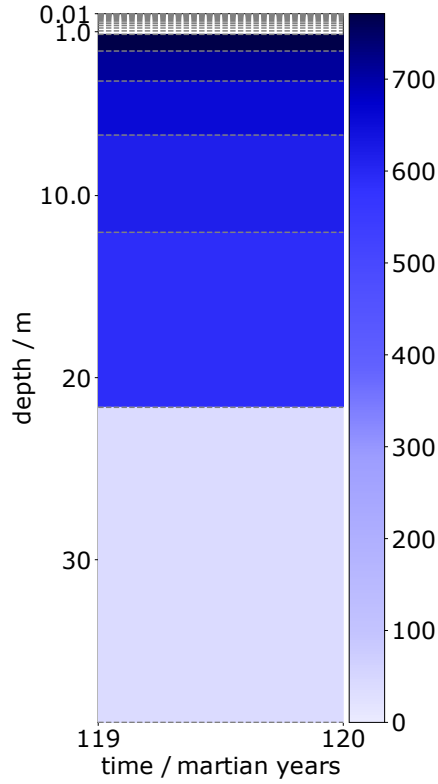
Figure 4.14: Annual sublimation rate of CO₂ ice in the 200 martian year set of simulations for the *W-C* scenario (S06). The sublimation rate is calculated using the difference in column density of CO₂ ice between each year at $L_S = 0^\circ$, when the model data are output.

The number of years that CO₂ ice could survive in the subsurface can be estimated using the average annual sublimation rate (the change in CO₂ ice column density over time) to calculate how long it would take for the initial amount of CO₂ ice to fully sublimate. The annual sublimation rate changes with both time and latitude, as shown in Figure 4.14 for the 200 martian year *W-C* scenario (S06). In the polar regions (and across most of the mid-latitudes), the sublimation rate is fairly consistent after the first few years when a large amount of CO₂ ice initially sublimates to increase the CO₂ vapour density within the pore space to that of the CO₂ saturation vapour density at all latitudes. Once CO₂ vapour density has reached CO₂ saturation vapour density (for the temperatures at each latitude) the sublimation rate decreases rapidly until a repeatable pattern of sublimation rate is reached, limited by the rate of diffusion.

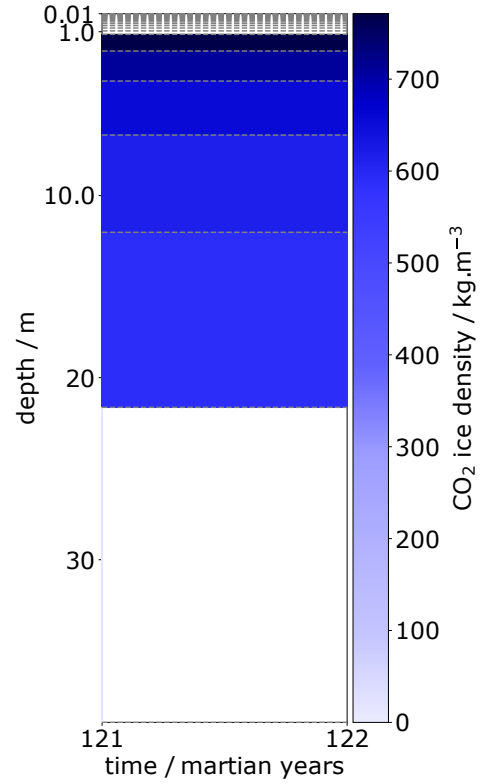
Within the low to mid-latitudes (40°N to 40°S), the sublimation rate is more variable. This variability is a consequence of the way CO₂ ice column density is calculated using the model layers: in each time step, the density of CO₂ ice is calculated separately for each model layer, which represents a percentage of the total column. The



(a)



(b) Column density = 172 kg m^{-3}



(c) Column density = 166 kg m^{-3}

Figure 4.15: CO_2 ice density with depth at latitude 7°S (a) over the entire 200 MY period and at (b) 119 MY and, (c) 121 MY for the *W-C* scenario (S06). The dashed grey lines on the panels (b) and (c) represent depths of the boundaries between the model layers.

CO₂ ice density is multiplied by this percentage and the sum of this across all model layers is the total column density. The sublimation rate is then calculated using the change in this total column density. Therefore, the sublimation rate is representative of changes across all model layers, and when one model layer becomes fully depleted of CO₂ ice, this layer no longer contributes to the sublimation rate and causes the drop in sublimation rate seen in Figure 4.14. Figure 4.15 shows an example of the CO₂ ice density at 7°S for two individual years (119 and 121 MY) and across the entire 200 MY period. Looking at the entire time period, it can be seen that the timing of the drops in CO₂ sublimation rate in Figure 4.14 corresponds with the timing of model layer depletion in Figure 4.15a. The two individual years (Figure 4.15b-c) demonstrate how the depletion of one model layer can also have a significant impact on total column density, which will further impact the sublimation rate.

The high variability of sublimation rate in the mid- to low latitudes means that estimates of the number of years that it will take for CO₂ ice to sublimate based on the average sublimation rate over the entire 200 martian year period will likely be slightly lower than the actual number of years it will take for the initial amount CO₂ ice to fully sublimate. This also implies that the estimates for the polar (and parts of the mid-latitude) regions will also be slightly lower than the actual number of years for CO₂ ice to fully sublimate away. This is because the estimate of the number of years for CO₂ ice to fully sublimate away uses the annual average sublimation rate calculated when there are larger column densities of CO₂ ice remaining within the subsurface. This is equivalent to the situation in the first 50 martian years in the equatorial regions, which implies that as the column density of CO₂ ice falls and the model layers become depleted in CO₂ ice, so will the sublimation rate. Despite this, the average annual sublimation rate is a useful way to estimate the number of years CO₂ ice can be expected to survive based on the results shown here. Figure 4.16 compares the estimated survival time from the *W-C* scenario with the estimated survival time from the scenarios with only CO₂ ice present, showing the significant impact the overlying H₂O ice-filled regolith layer has on the number of martian years that CO₂ ice can survive at all latitudes.

While CO₂ ice was still present after 200 martian years at nearly all latitudes of

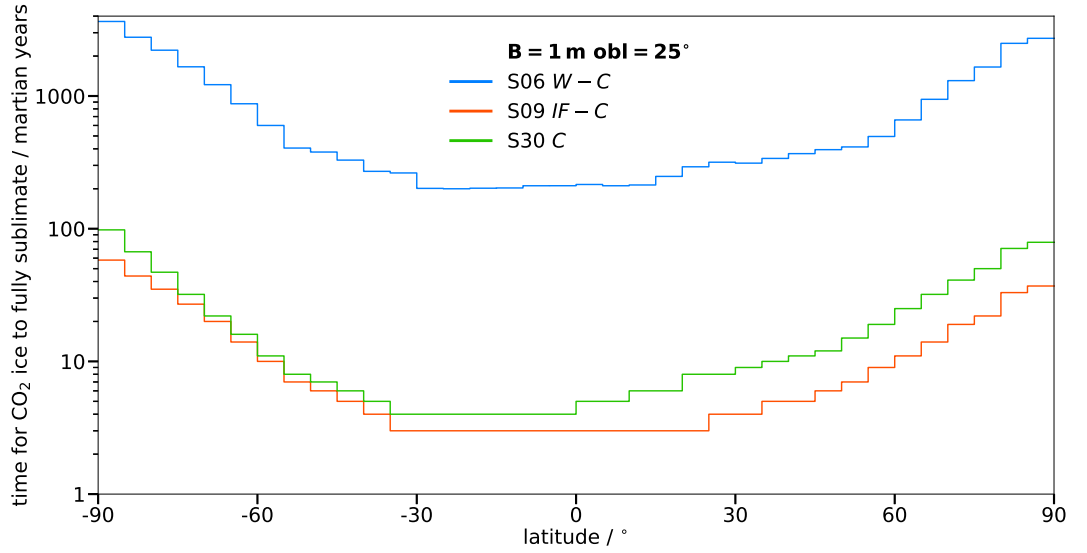


Figure 4.16: Comparison of the estimated number of years that CO_2 ice survives of the $W-C$ set of simulations (S06) with the estimated number of years from both C sets of simulations (S09, S30)

the $W-C$ simulations (Figure 4.9), the estimated survival times in Figure 4.16 suggest that CO_2 ice is expected to fully sublimate within 1000 martian years across the mid-latitude and equatorial regions. Therefore, a 1000 martian year set of simulations with the $W-C$ ice layer scenario were run to investigate whether this is the case. Ideally a several thousand year simulation would be done to compare all of the estimated values. However, a simulation of that length would take several months to run making it infeasible in the timescale of this work. Figure 4.17 shows the results of this 1000 martian year simulation for the $W-C$ with the boundary at 1m scenario. The 1000 martian year results show the expected distribution based on Figure 4.16 and is similar to the C simulations described in Section 4.2.2. CO_2 ice entirely sublimates within the equatorial region (15°N to 30°S) first and is fully sublimated in the mid-latitudes of both hemispheres after 1000 martian years. The polar regions of both hemispheres also show a decrease in the column density of CO_2 ice, with a smaller amount remaining in the northern polar region than in the southern polar region. This is the expected pattern based on present-day observations of the perennial polar caps (e.g., Hansen, 1999), as a small CO_2 ice cap remains at the southern pole, while any surface CO_2 ice that was deposited during a previous epoch at the northern pole has fully sublimated away.

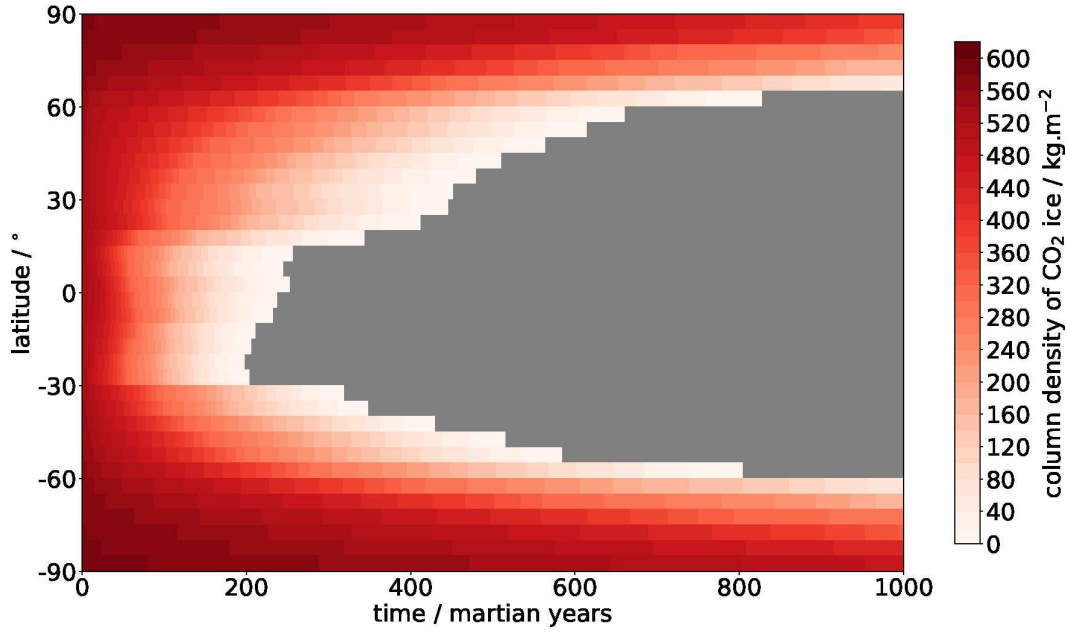


Figure 4.17: Column density of CO₂ ice over time for *W-C* (boundary at 1 m) scenario (S06) over 1000 martian years. Grey represents where the CO₂ ice column density is less than 0.0001 kg m⁻².

In Figure 4.18, the number of years it takes for CO₂ ice to fully sublimate within the 1000 martian year simulation is compared with the estimates made from the 200 martian year simulation in Figure 4.16, along with estimates from the 50 martian year simulation, to test the accuracy of the estimates. I have truncated the line for the actual number of years to fully sublimate CO₂ ice in the 1000 martian year simulation at 1000 Mars Year (MY) if sublimation takes longer than 1000 MY. From Figure 4.16 it can be seen that the shorter length (50 and 200 martian year) simulations tend to underestimate the number of years it would take for CO₂ ice to fully sublimate in the equatorial and mid-latitude regions, although the estimated number of years is within the right order of magnitude. This means that the estimates for the number of years it would take to fully sublimate CO₂ ice within the polar regions are likely to be within the right order of magnitude, but are unlikely to represent the exact number of years CO₂ could survive.

The average sublimation rates used for these estimates, therefore, do not give an accurate estimate of the number of years for CO₂ ice to fully sublimate away when the number of years the simulation is run for is significantly shorter than the estimated number of years it takes for CO₂ ice to sublimate. For example, the estimated time

for CO₂ ice to fully sublimate at 30°S in the 50 martian year simulation was ~ 130 martian years, whereas the actual time in the 1000 martian year simulation was ~ 220 martian years. This is because sublimation rate is highly variable over time (see Figure 4.14). The sublimation rate is dependent on factors such as thermal conductivity, temperature, porosity of the overlying model layer and surface flux, all of which have been shown to vary considerably with ice content. The calculated number of years for CO₂ ice to fully sublimate can, therefore, be used to compare how the behaviour of CO₂ ice might change under different scenarios, even though the actual number of years might be an underestimate if CO₂ ice becomes stable at a certain depth or an overestimate if CO₂ ice fully sublimates at a faster rate.

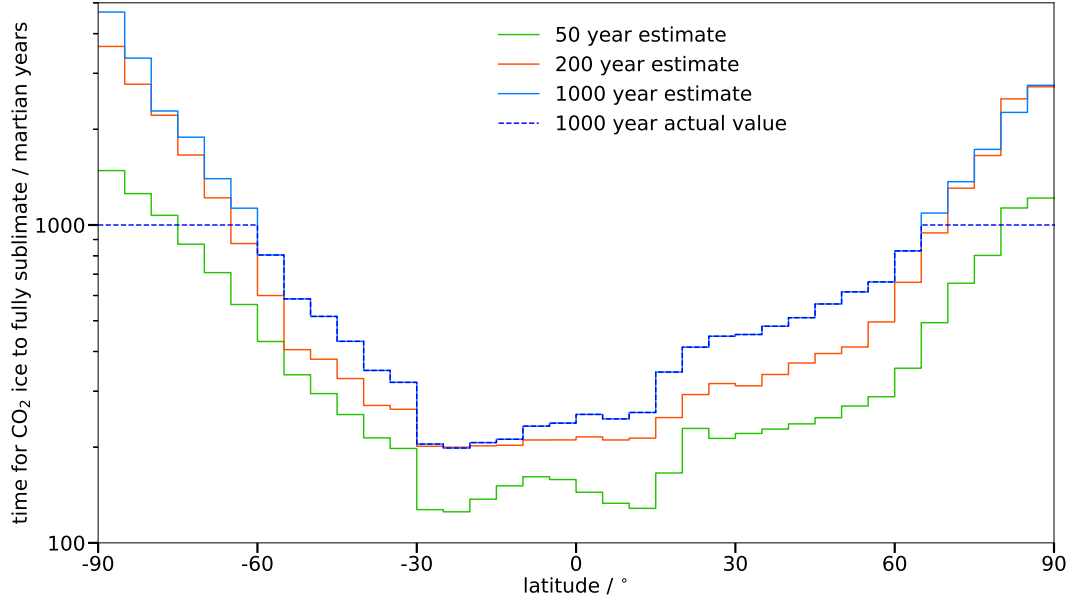


Figure 4.18: Comparison of the estimated number of years that CO₂ ice survives in the 50, 200 and 1000 martian year simulations of the *W-C* (boundary at 1 m) scenario (S06). The actual number of years taken for CO₂ ice to fully sublimate in the 1000 martian year simulation is also included, with a limit of 1000 martian years at latitudes where CO₂ ice survives longer than the 1000 martian years of the simulation.

4.3.2.2 Zonal Latitudes vs Longitudes

In the *W-C* simulations, there is a sharp boundary in the behaviour of CO₂ ice at $\sim 15^\circ\text{N}$, as shown in all three examples in Figure 4.9. This boundary corresponds partially with the topographic boundary between the northern lowland and the southern highlands. However, as mentioned earlier, the topographic boundary extends across

multiple latitudes and is therefore not likely to be the main cause of the shift in CO₂ ice behaviour. Alongside the topographic boundary, the zonal latitude simulation at 15°N corresponds with the zonal latitude into which Olympus Mons falls. Olympus Mons will significantly affect surface atmospheric properties since the atmospheric values are zonally averaged across all longitudes and the presence of Olympus Mons will affect the surrounding climate. The effect of Olympus Mons can be investigated using the individual location simulations, since three of the other individual locations fall within the same 5° latitude band as Olympus Mons: the landing sites of Pathfinder, Rosalind Franklin and Perseverance.

A comparison of the results at these four locations for the set of simulations with the boundary between H₂O ice-filled regolith and the underlying CO₂ ice-filled regolith at 1 m (S06; Figure 4.19), shows that the presence of Olympus Mons drastically impacts the survival of CO₂ ice within the subsurface. In the three lander locations, the amount of CO₂ ice decreases at the same rate across the sites and is nearly fully sublimated by the end of the 200 martian years. At Olympus Mons however, the amount of CO₂ ice after 200 martian years is equivalent to the amount remaining after 50 martian years at the landing sites and CO₂ ice remains in the subsurface for around four times longer. This implies that a longitude region with significantly different atmospheric conditions caused by surface topographical features, such as Olympus Mons, can drastically change the zonal latitude results, since the atmospheric conditions used are an average of the values at all longitudes. This is clearly shown in Figure 4.19, where the amount of CO₂ ice over time for the zonally averaged atmosphere simulation decreases at a rate between that of the Olympus Mons and the three lander simulations. Therefore, the zonal latitude results for this latitude region (latitudes 15° to 20°N) do not represent the scenario at any specific point on Mars, and a more detailed study that takes into account latitude and longitude topographic and climate variations is needed for this.

The difference between the results using zonally averaged atmospheric profiles and atmospheric profiles at individual locations is smaller across the rest of the planet, where topographic variations with longitude are much smaller. This can be seen when comparing the results from the simulation that uses the atmospheric profiles at the

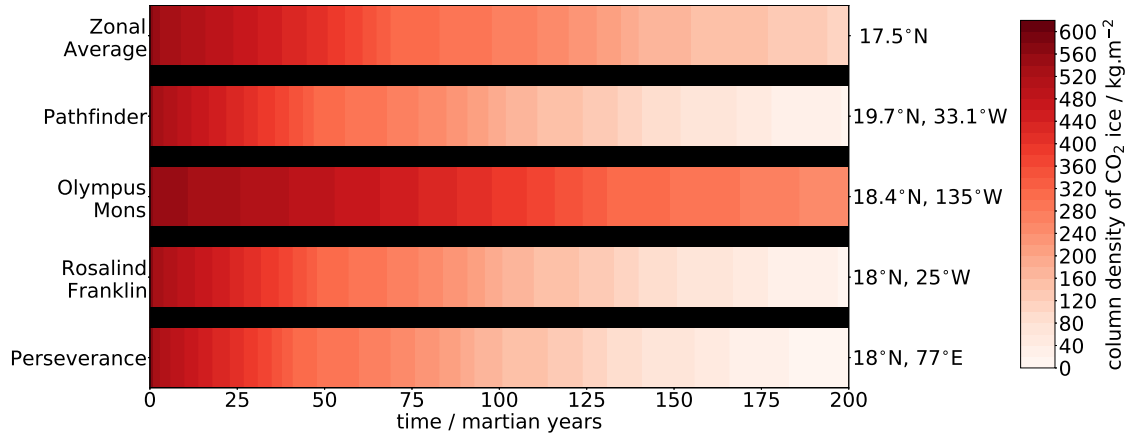


Figure 4.19: Variation in the column density of CO₂ ice over time for the latitude (17°N), Pathfinder, Olympus Mons, Rosalind Franklin and Perseverance locations for the *W-C* with the boundary at 1 m set of simulations (S06).

location of Hellas Basin with the corresponding results that use the zonally averaged atmospheric profiles for the same latitude (-42.5°S). A third location at the same latitude was chosen at random since Hellas Basin is a topographic low and may not be representative of the average behaviour at that latitude. Figure 4.20 shows the column density of CO₂ ice over time for these three simulations and the results are very similar. There are slight differences in the rate of sublimation between the three, but the differences are small enough that they will not have a substantial impact on the overall results. Therefore, using zonally averaged atmospheric profiles for each latitude will probably provide a good indication of the expected behaviour of ice within the subsurface over time as long as any topographic variations with longitude only have a small influence on global scale circulations.

4.3.2.3 Effect on the Behaviour of H₂O Ice

The presence of CO₂ ice impacts subsurface temperatures and the diffusion of H₂O vapour, both of which will impact the survival of H₂O ice. In order to investigate the impact of CO₂ ice on H₂O ice when both exist within the subsurface, the behaviour of H₂O ice in the three scenarios that contain H₂O ice-filled regolith in the upper metre can be compared. In the rest of the subsurface, these scenarios contain either no ice (*W-IF*; S31), H₂O ice-filled regolith (*W*; S29) or CO₂ ice-filled regolith (*W-C*; S06). Figure 4.21 shows the column density of H₂O ice in the upper metre for

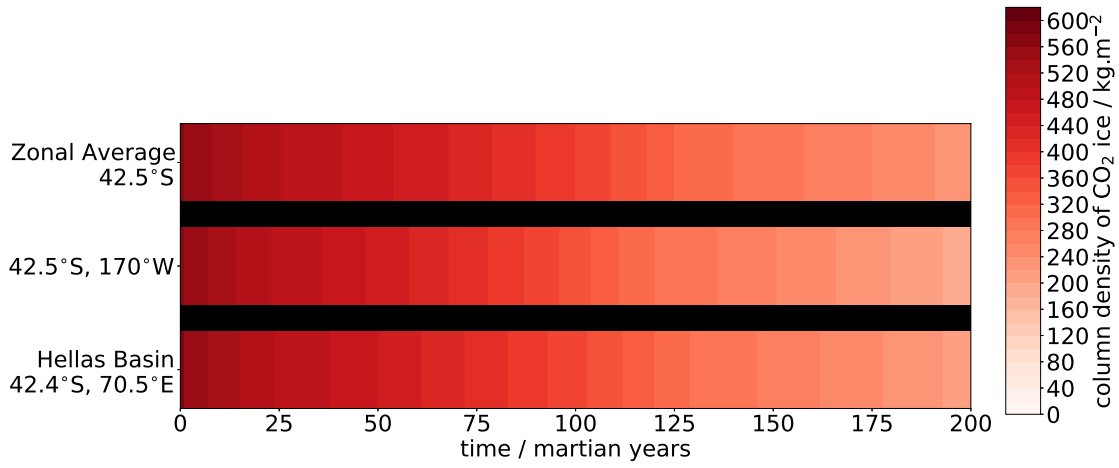
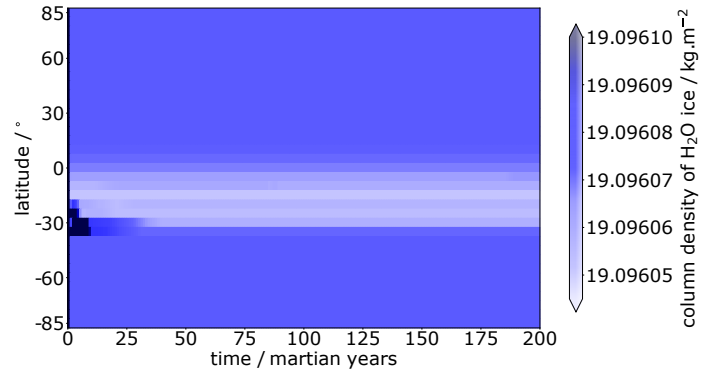


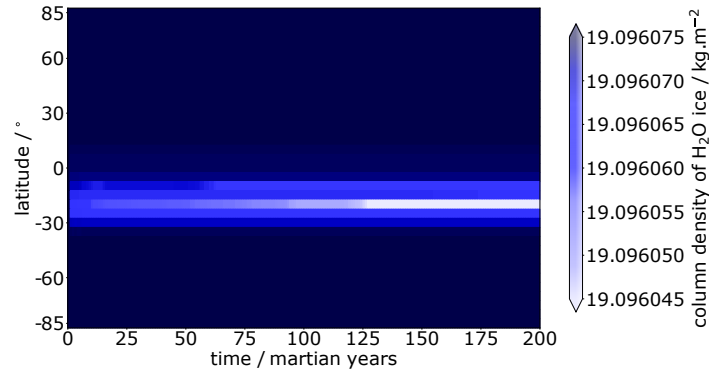
Figure 4.20: Variation in the column density of CO₂ ice over time for the zonal average simulation at 42.5°S simulation compared with the results at Hellas Basin and at 42°S, 170°W for the *W-C* with the boundary at 1 m set of simulations (S06).

each of these scenarios. The column density is only calculated for the upper metre to allow for comparisons between the scenarios, since the scenario with H₂O ice-filled regolith throughout the subsurface has a higher overall column density, due to the larger amounts of H₂O ice that are stored below 1 m (Table 4.1). The three scenarios produce a similar rate of H₂O ice sublimation poleward of 15°N and 35°S in the figure. However, within the equatorial region (15°N to 35°S) the column density of H₂O ice is more variable between the scenarios, showing the impact of the three different lower ice layers.

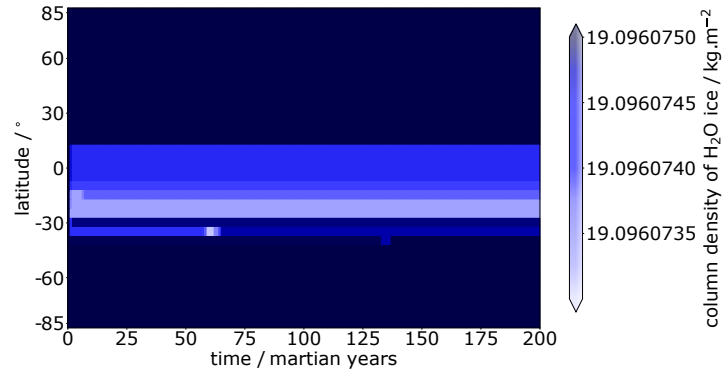
In the scenarios with H₂O ice-filled regolith (S29) or CO₂ ice-filled regolith (S06) in the lower ice layer (Figures 4.21b and 4.21c), the amount of H₂O ice in the equatorial region decreases slowly over time, as only sublimation can occur due to the lack of available pore space throughout the subsurface for any ice to form. In the scenario with an ice-free lower ice layer (S31), on the other hand, H₂O ice can form within the pore space of this lower ice-free layer. The formation of H₂O ice within this ice-free region occurs between 20° to 35°S in Figure 4.21a. H₂O ice forms in the lower ice layer because the higher H₂O vapour density in the H₂O ice-filled regolith layer is diffused to the lower ice-free layer at a faster rate than out of the subsurface (into the atmosphere) due to the higher diffusion coefficient in the uppermost ice-free model layer compared with the surface model layer (Figure 4.22 shows an example of the change in diffusion coefficient with depth at 17°S). This results in a faster increase in



(a) *W-IF* (S31)



(b) *W-C* (S06)



(c) *W* (S29)

Figure 4.21: Column density of H₂O ice in the upper metre of the subsurface at each latitude over time. For the (a) *W-IF* (S31), (b) *W-C* (S06) and (c) *W* (S29) sets of simulations. Simulations S06 and S31 only contain H₂O ice-filled regolith between the surface and a depth of 1 m, so the results for S29 only show the column density of the upper metre so the values can be compared. Grey represents where the H₂O ice column density is less than 0.0001 kg m⁻².

the H_2O vapour density across the ice-free layer than is lost to the atmosphere. In the region between 20° and 35°S , this increase in H_2O vapour density is enough for H_2O ice to form within the ice-free layer, whereas at all other latitudes the increase in H_2O vapour density is either insufficient for H_2O ice formation or the amount that forms in the ice-free region is less than the amount sublimated in the upper H_2O ice layer. Once H_2O vapour equilibrium is reached across the subsurface, the exchange of H_2O vapour to or from the atmosphere becomes the dominant process affecting H_2O ice deposition or sublimation. From this point, H_2O vapour tends to flow out of the subsurface for more of the year resulting in H_2O ice sublimation, which occurs after around 10 martian years at 20° to 35°S in Figure 4.21a.

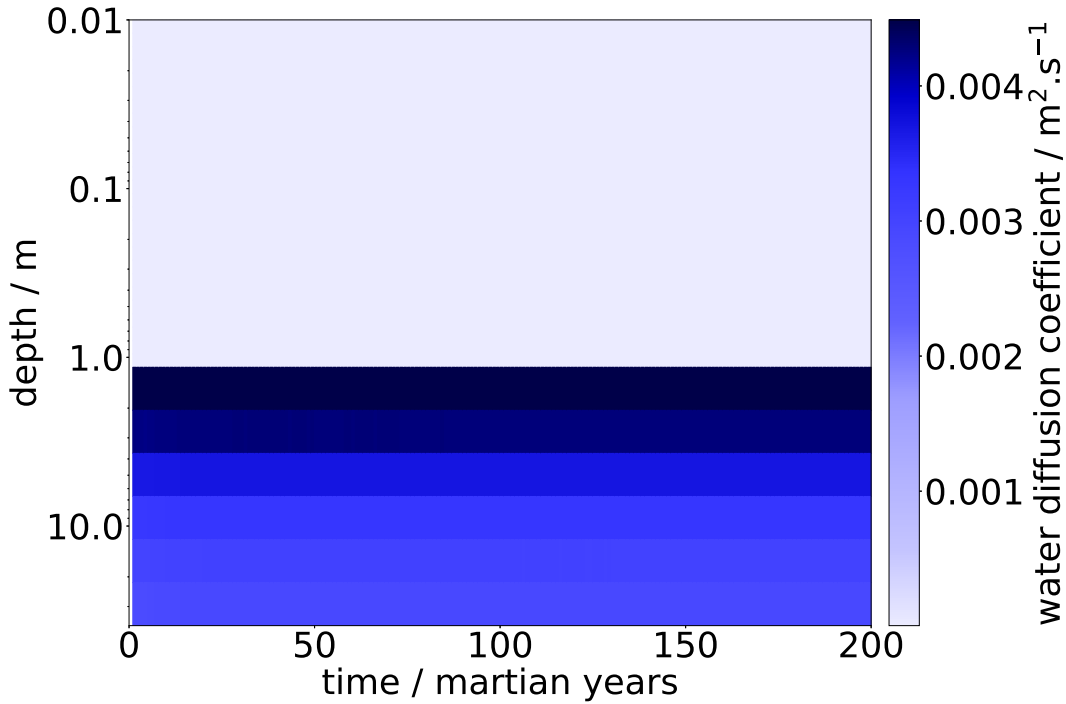


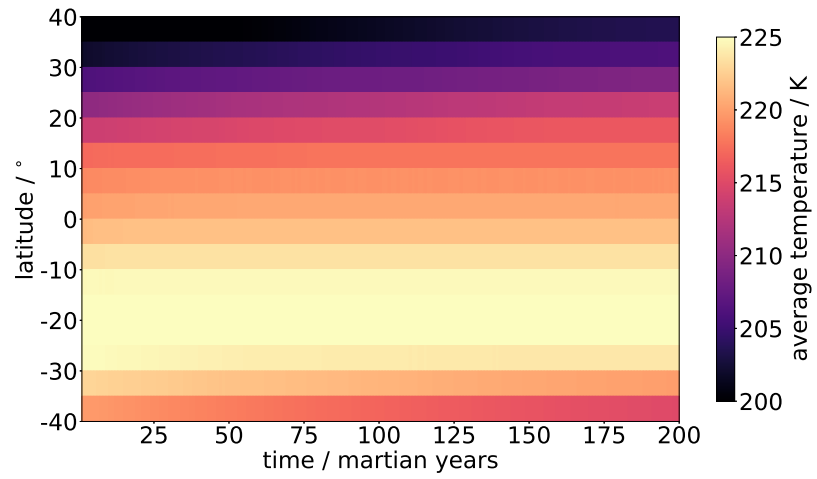
Figure 4.22: The diffusion coefficient at 17°S for the *W-IF* (S31) set of simulations.

Another difference between the three scenarios that impacts H_2O ice deposition or sublimation is the thermal conductivity of the subsurface. Both H_2O ice and CO_2 ice have higher thermal conductivities than the empty regolith (0.01 to $0.1 \text{ W m}^{-1} \text{ K}^{-1}$), but the thermal conductivity of CO_2 ice ($0.7 \text{ W m}^{-1} \text{ K}^{-1}$) is still significantly lower than that of H_2O ice ($2.5 \text{ W m}^{-1} \text{ K}^{-1}$). A high thermal conductivity throughout the subsurface, as in S29, causes more heat to be conducted deeper into the subsurface during summer and this heat is gradually released during winter. Since H_2O ice has a much higher thermal conductivity, when all of the pore space is filled with H_2O

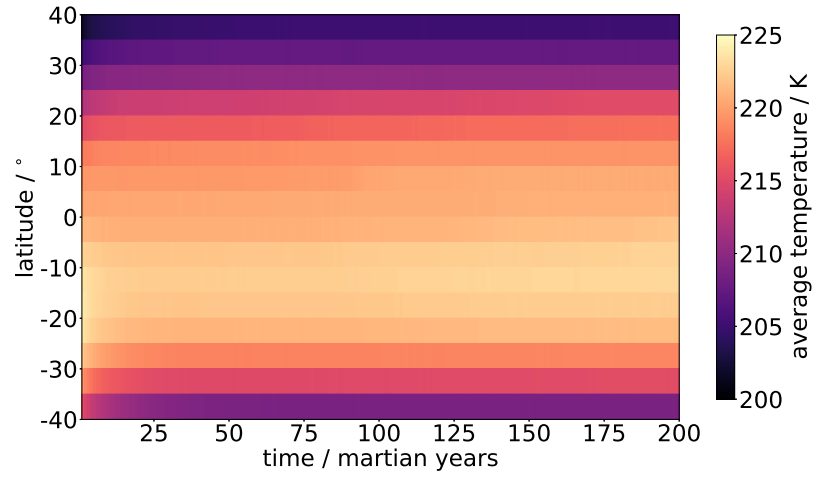
ice (S29) subsurface temperatures are expected to be higher than when the lower ice layer (below 1 m) is either completely ice-free (S31) or filled with CO₂ ice (S06). This can be clearly seen when comparing average subsurface temperatures across the equatorial region for the *W* scenario (S29; Figure 4.23a) with that of the *W-IF* (S31; Figure 4.23b) and the *W-C* scenarios (S06; Figure 4.23c). It can also be seen that average subsurface temperatures are similar in both the *W-IF* (S31) and *W-C* (S06) scenarios despite the slight differences in thermal conductivity of the lower ice layer: 0.1 and 0.7 W m⁻¹ K⁻¹, respectively. This is because in both scenarios, roughly the same amount of heat is stored and released by the subsurface throughout the year as the abrupt change in thermal conductivity at the 1 m boundary acts to insulate the H₂O ice-filled regolith layer, reducing heat conduction further into the subsurface compared with the *W* scenario (S29).

Since subsurface temperatures are highest when H₂O ice fills the entire pore space, it might be expected that H₂O ice sublimates away the fastest in this scenario. However, H₂O ice actually sublimates fastest in the *W-C* scenario (see Figure 4.21), due to a combination of different effects. The first is a process that occurs in all scenarios initialised with H₂O ice. In the initial profiles, H₂O vapour in all model layers is set to the atmospheric vapour density, which is generally lower than the H₂O saturation vapour density. Therefore where H₂O ice is present, it will sublime until the H₂O vapour density in the model reaches the H₂O saturation vapour density. When this occurs, the H₂O vapour density in these model layers is higher than in the surrounding model layers that contain no H₂O ice. As a result, the excess H₂O vapour is either redistributed vertically within the subsurface by diffusion (into the ice-free model layers) or flows out of the subsurface and into the atmosphere, which is most likely to have a lower H₂O vapour density. This process occurs until an equilibrium is reached between the H₂O vapour density in the pore space within the entire subsurface and the atmospheric H₂O vapour density. The rate of vertical redistribution is heavily dependent on the number of model layers that do not contain H₂O ice and the diffusion coefficient between the subsurface model layers containing H₂O ice and those that do not. In the *W* scenario (S29), the region below 1 m is also H₂O ice-filled regolith, which means that the H₂O vapour density in all model layers will be at H₂O saturation vapour density after the

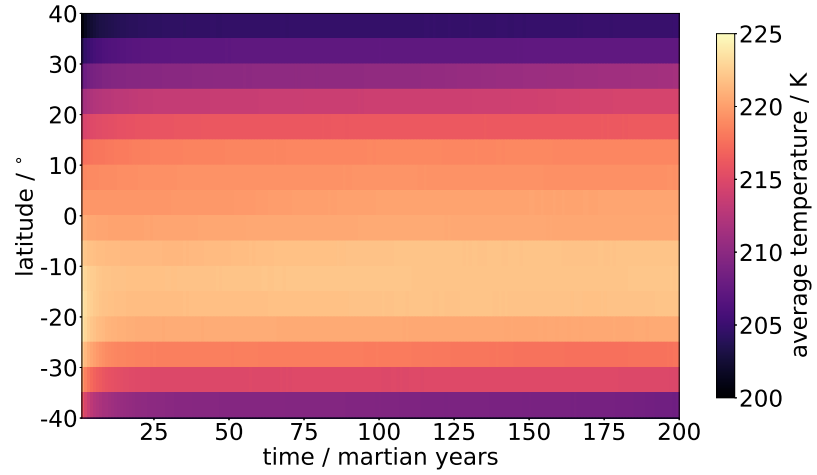
initial period of H₂O ice sublimation. This means the H₂O vapour gradient within the subsurface will be small and vapour loss will only occur from H₂O vapour exchange with the atmosphere, which is expected to have a smaller H₂O vapour density than H₂O saturation vapour density. In the *W-C* scenario (S06), on the other hand, the lower region is filled with CO₂ ice and H₂O vapour density in these model layers remains at the initial atmospheric H₂O vapour density until diffusion occurs. This causes a large H₂O vapour gradient between the upper region that contains H₂O ice-filled regolith and the lower region that contains CO₂ ice-filled regolith. As H₂O vapour is redistributed into the lower model layers, the H₂O vapour density in the model layers containing H₂O ice will fall below H₂O vapour saturation vapour density, leading to further sublimation of the subsurface H₂O ice. At the same time as H₂O vapour is redistributed into the lower model layers, H₂O vapour also flows out of the subsurface into the atmosphere, due to the strong vapour gradient between the uppermost model layer (which contains H₂O ice) and the atmosphere. The combination of both of these processes cause H₂O ice to sublimate away faster in the *W-C* scenario (S06), than the *W* scenario (S29; where only H₂O vapour loss to the atmosphere occurs) even though subsurface temperatures are higher in the *W* scenario and H₂O saturation vapour density is higher.



(a) W (S29)



(b) $W-IF$ (S31)



(c) $W-C$ (S06)

Figure 4.23: Average subsurface temperature for the equatorial region of the (a) W (S29), (b) $W-IF$ (S31), and (c) $W-C$ (S06) set of simulations.

4.4 Alternate Assumptions within the MSSM

The results described in the sections above assume that all of the parameters of the MSSM are set as described in Chapter 3 and this version of the model is referred to as the baseline version (see Table VII.I). There are several assumptions made for the baseline version which may impact the results discussed so far and to account for these assumptions, a series of simulations has been run to test how they have affected the results. To make comparison simpler, all of the different versions were run using the same initial condition of $W-C$ with the boundary at 1 m. For the baseline version of the MSSM, the comparative results are from simulation S06, which are shown in Figure 4.9b. A summary of the different versions of the MSSM used in this section is given in Table VII.I and a list of the simulations run with these versions can be found in Table VII.IV.

4.4.1 Maximum Sublimation Rate

In the baseline simulations, the rate of sublimation per year is limited by a maximum sublimation rate value based on previous studies (Section 3.6). While there have been many studies on the sublimation of H_2O ice under a regolith layer (e.g., Chevrier et al., 2007; Hudson et al., 2007), there have been no previous studies on the effect of an overlying regolith on the sublimation rate of CO_2 ice. Therefore, since the maximum sublimation rate values used in the MSSM are for CO_2 ice exposed at the surface, a simulation was run without a limit for the maximum amount of sublimation per timestep. This limit was calculated depending on the depth of the ice for H_2O ice (Equation 3.45) and was the measured surface CO_2 sublimation rate for CO_2 ice (see Section 3.6). The results of this simulation (Figure 4.24) showed very little difference to the baseline results (Figure 4.9b), which proves that the use of a maximum sublimation rate is not drastically altering the result. This is as expected because an overlying regolith will lower the sublimation rate, rather than increase it, based on previous experimental studies of H_2O ice under an ice-free regolith layer (e.g., Chevrier et al., 2007; Hudson et al., 2007).

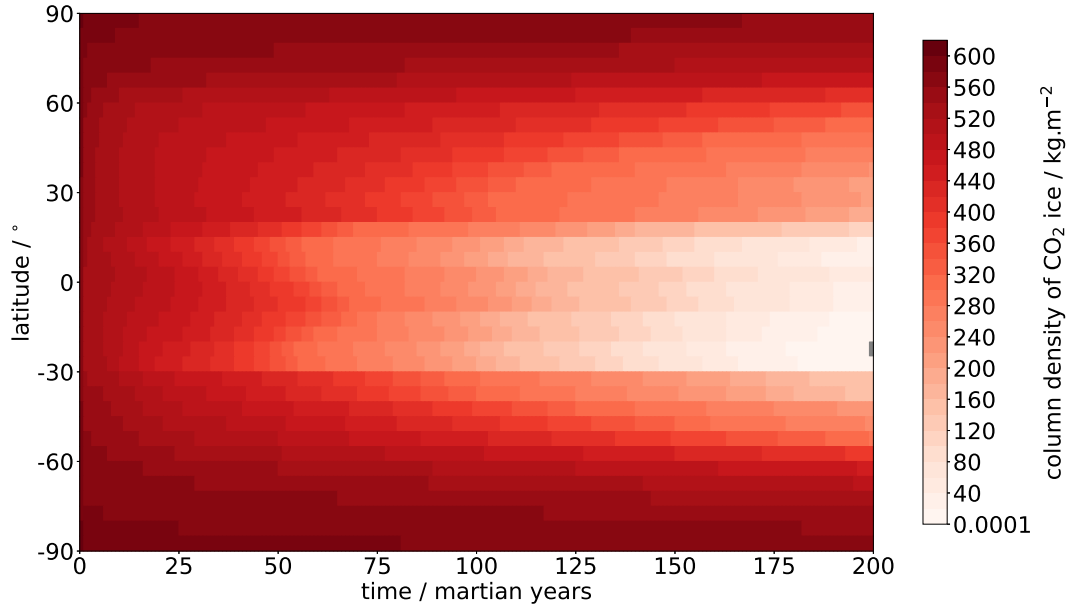


Figure 4.24: Column density of CO₂ ice at each latitude over time. For the simulations using the version of the model with the sublimation routine turned off (NS01). Grey represents where the CO₂ ice column density is less than 0.0001 kg m⁻².

4.4.2 Atmospheric Source

Another assumption in the baseline version of the MSSM is that the atmosphere can act as a constant source for H₂O and CO₂ vapour. In reality, the atmosphere is not an unlimited resource and to test how this assumption has impacted the results, several simulations were run assuming there is no flux into the regolith from the atmosphere, but vapour could still diffuse out of the regolith. This represents the other extreme to an atmosphere that is a never ending supply of vapour. To test this, three scenarios were run: *C-W* with a boundary at 1 m (NF01); *W-C* with a boundary at 1 m (NF02); and *W* (NF03) were chosen in order to investigate the effect on both H₂O and CO₂ ice sublimation.

In the case of H₂O ice sublimation, both the *W-C* scenario (NF02) and the H₂O ice-filled regolith scenario (NF03) show the same rate of sublimation as the baseline simulations with the same initial scenarios, S06 and S29 respectively. The rate of H₂O ice sublimation in three all scenarios is limited by the H₂O vapour surface flux and rate of H₂O vapour diffusion through the subsurface, showing that any replenishment of H₂O vapour from the atmosphere throughout a martian year is not enough to prevent H₂O ice sublimation. This is also seen for CO₂ ice in all three scenarios, as CO₂ also

sublimates away at the same rate in both the *C-W* (NF01) and the *W-C* (NF02) scenarios.

4.5 Discussion and Summary

The scenarios discussed in this chapter show that the presence of both CO₂ ice and H₂O ice can impact the behaviour of each ice by altering the subsurface thermal structure and by reducing the porosity, thus slowing the rate of diffusion. When only CO₂ ice is present, it is unstable at nearly all latitudes and survives, at most, 90 years (Figure 4.5). This is the scenario that is expected based on previous studies, which have only considered surface CO₂ ice and assume there is no overlying H₂O ice-filled regolith layer to trap the CO₂ ice (e.g., Aharonson et al., 2004; Schmidt et al., 2009). However, the recent discovery of subsurface CO₂ ice in the southern polar layered deposits (PLD) (Phillips et al., 2011) showed that CO₂ ice could survive underneath H₂O ice-filled regolith for longer and in larger quantities than previously thought. The simulations of *W-C* shown here confirm these observations and from them, it can be estimated that CO₂ ice could persist under a porous H₂O ice layer for thousands of years in the polar regions.

The porosity of the overlying subsurface model layer is shown to have a significant influence on the number of years it takes to fully sublimate CO₂ ice. When the CO₂ ice-filled regolith layer is at the top of the subsurface or there is an overlying ice-free regolith, CO₂ ice survives less than 100 years at most latitudes (Figure 4.16). However, when a H₂O ice-filled regolith layer overlies the CO₂ ice-filled regolith layer, CO₂ ice can survive hundreds to thousands of years depending on the latitude (Figure 4.9).

The porosity in the upper region of the subsurface also affects the rate of surface flux, which is dependent on the diffusion coefficient which, in turn, is dependent on the porosity. A low outward surface flux limits the amount of vapour that will diffuse out of the subsurface within a time step, which will limit the amount of ice that sublimates. This is because the amount sublimated will only be enough to replenish the vapour lost from each model layer by diffusion either throughout the subsurface or into the atmosphere.

After porosity, the change in thermal properties caused by the presence of either ice has the next largest influence on the behaviour of each ice. When H₂O ice fills the pore space of the entire subsurface and is the only ice present, average subsurface temperatures are higher than when the pore space in the regolith is empty (Figure 4.23). This is due to the increased thermal conductivity, which increases conduction and storage of heat deeper in the subsurface throughout the martian year. When CO₂ ice is also present, the rise in average subsurface temperature is smaller than when only H₂O ice fills the pore space. This smaller rise in temperature means that the saturation vapour density for both H₂O and CO₂ remains lower compared with when only H₂O ice is present, which will make H₂O ice stable for longer. When this H₂O ice-filled regolith is overlying the CO₂ ice-filled regolith layer, the slower sublimation of the H₂O ice keeps the porosity in the upper regolith layers low which limits the rate of CO₂ vapour diffusion out into the atmosphere. This in turn limits the CO₂ sublimation rate and keeps CO₂ ice stable for longer.

The *W-C* simulations show that CO₂ ice in the pore space of a regolith, below a 1 m H₂O ice filled pore space regolith layer, can survive thousands of martian years in the polar regions and several hundred martian years in the equatorial and mid-latitude regions, as shown in Figure 4.18. This is considerably longer than is expected from previous surface CO₂ ice studies, especially in the equatorial and mid-latitude regions, where CO₂ ice is assumed to not exist at present since temperatures are too high for CO₂ ice to form. This can be used to provide an estimate for the age of the CO₂ ice layers buried within the PLD since the thinnest layers in the PLD are 1.6 m (Hvidberg et al., 2012). These results can also be used to infer that, provided a layer of H₂O ice formed over the CO₂ ice before it could fully sublimate, some CO₂ ice could have remained underneath the LDM or under the mid-latitude glaciers for many years after atmospheric conditions became unsuitable for CO₂ ice formation in these regions. However, it is unlikely that these deposits survived to the present-day. The CO₂ ice would have needed to be deposited during the Noachian (or early Hesperian), when CO₂ partial pressures are assumed to have been higher (estimates range from 0.1 bar to 10 bar; e.g., Forget et al., 2013; Haberle et al., 1994; Nakamura and Tajika, 2001) and CO₂ ice could have formed at higher temperatures as a result (~ 195 K; see

Figure 4.25). CO₂ ice is also only likely to form outside of the polar region at very low obliquities ($<15^\circ$), when the polar caps extend further equatorward, or at very high obliquities ($>45^\circ$), when temperatures in the northern mid-latitudes (Figure 6.2a) are around the frost point of CO₂ at the high pressures expected during the Noachian (e.g., Nakamura and Tajika, 2003). However, any CO₂ ice deposits formed in the Noachian (or in other periods of Mars' history) are unlikely to have survived to the present-day and subsurface CO₂ ice is therefore not expected outside of the polar regions in the present-day.

During the late Noachian and early Hesperian, when surface pressures remained higher than 600 mbar (estimates are up to 1 bar; e.g., Kite et al., 2014; Manning et al., 2006), previous work has suggested that permanent surface CO₂ ice deposits would form on Olympus Mons (after its formation) at an obliquity of 15° and the current solar luminosity (Soto et al., 2015). Soto et al. (2015) also showed that at even higher pressures, surface CO₂ ice forms at the latitude of Olympus Mons for higher obliquities as well. Nakamura and Tajika (2003) found that at the low solar luminosities expected during the Noachian (70% of the current solar constant) and high obliquity ($>45^\circ$), a permanent CO₂ ice reservoir forms a belt around the mid-latitudes as well as the extensive seasonal polar CO₂ caps that have been shown to form in other studies. If a permanent CO₂ ice reservoir formed in the mid-latitudes, as suggested by Nakamura and Tajika (2003), then the formation of H₂O ice glaciers (similar to those observed in the present-day) or other H₂O ice deposits could have overlain remnants of these CO₂ ice deposits allowing them to persist for several thousand martian years longer than they would have. However, none of these CO₂ ice deposits would survive to the present-day.

In the scenarios shown here, the thickness of the overlying H₂O ice-filled regolith layer is at most 2m and the underlying CO₂ ice is estimated to survive thousands of years. However, the number of years it would take for the initial amount of CO₂ ice to fully sublimate cannot be directly compared between the scenarios with different boundary depths since it is partially dependent on the initial column density of CO₂ ice, which differs between scenarios (see Table 4.1). Therefore, the number of years it

would take for CO₂ ice to fully sublimate has been recalculated for the initial amount of CO₂ ice below 2 m in all scenarios so a comparison can be made. When the boundary between the H₂O ice-filled regolith layer and the CO₂ ice-filled regolith layer is at 0.5 m, the maximum number of years that CO₂ ice can survive (for the CO₂ ice below 2 m) is estimated to be 2000 martian years, whereas when the boundary is at 1 m, it is estimated to take 2640 martian years and when the boundary is at 2 m, it is estimated to take 3530 martian years. This can be extrapolated to suggest that a further increase in burial depth of 0.5 m will result in the same initial amount of CO₂ ice taking around 500 martian years longer to fully sublimate. For an overlying H₂O ice-filled regolith layer of 130 m (the average thickness of the mid-latitude glaciers; Brough et al., 2019), CO₂ ice can be estimated to take around 130,000 martian years to fully sublimate away in the polar regions. However, this assumes that the estimation that it takes 500 martian years longer to sublimate away the same amount of CO₂ ice for each subsequent 0.5 m of H₂O ice continues to apply to a depth of 130 m. Further work would be needed to demonstrate that this extrapolation can be used for H₂O ice thicknesses equivalent to H₂O ice glaciers.

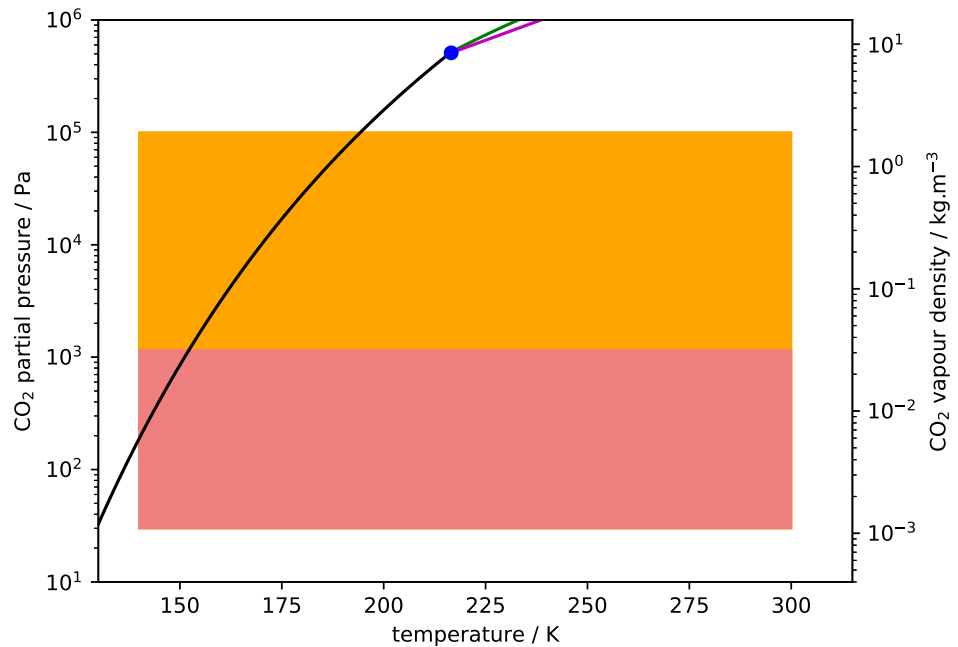


Figure 4.25: CO₂ phase diagram using the phase equations in the MSSM. The red box is the partial pressure conditions from present-day Mars, yellow box is the partial pressure conditions expected during the Noachian and early Hesperian (e.g., Kasting, 1991; Kite et al., 2014; Wordsworth et al., 2013).

In summary, a H₂O ice-filled regolith layer overlying CO₂ ice-filled regolith results in CO₂ ice surviving for longer than without the overlying H₂O ice-filled regolith. The overlying H₂O ice-filled regolith in this scenario is also likely to be more stable near the surface, than when only H₂O ice in the upper region is present due to the lower temperatures and rates of diffusion caused by the presence of CO₂ ice instead of empty regolith.

5 | What role do subsurface properties and ice layer configurations play in the stability of CO₂ ice?

The surface and subsurface of Mars are heterogeneous and a variety of geological materials have been observed and are expected (see Section 2.1; e.g., Bandfield, 2007; Bibring et al., 2005; Putzig et al., 2005). Alongside the diverse geological materials, ice formation can occur in multiple ways and over varying timescales, leading to a range of layered configurations and porosities. In the previous chapter, simple two-ice-layer configurations were discussed to investigate the general behaviour of both water (H₂O) ice and carbon dioxide (CO₂) ice when both ices are present using the baseline version of the Martian Subsurface Model (MSSM) and all of the assumptions included within it (see Chapter 3). In this chapter I investigate how CO₂ ice sublimation is impacted by changes to the assumptions incorporated into the MSSM and by multiple small ice-layers compared with the simple two-ice-layer configuration previously used. The sublimation rates from all scenarios discussed in this chapter can be found in Appendix C.

One of the assumptions incorporated into the MSSM is that of a fixed initial ice porosity ($\phi_{\text{ice ini}}$) of 0.001, which is also the minimum possible value within that simulation. This initial ice porosity ensures that the vapour in the deepest model layers are in contact with the atmosphere from the beginning and vapour exchanges can always occur. Vapour exchange is necessary for sublimation to occur as the vapour density within a model layer can only be reduced (to below the saturation vapour density) by the removal of vapour into either the surrounding subsurface model layers or into the atmosphere. However, across Mars the porosity of ice-filled regolith is likely to vary considerably. Therefore, a series of simulations with initial ice porosities ranging from

0 to 0.1 have been run to encompass the range of porosities that would be expected. The results of these simulations are discussed in detail in Section 5.1, showing that when the porosity is smaller, CO₂ ice takes longer to sublimate away.

In the scenarios discussed in the previous chapter, the geological composition of the subsurface with depth has been assumed to be homogeneous across the entire planet, which is not the case. Mars' surface is diverse and geological materials vary from very fine dust to solid bedrock or ice (described in Section 2.1.1). The thickness of the surface geological unit is also expected to vary across the planet. Across much of the planet the surface material is expected to be a fine dust cover of varying thicknesses (Ruff and Christensen, 2002). In many places, rather than an abrupt boundary between this surface dust layer and the underlying geological unit, there is likely to be a gradual compaction of the surface dust deposited by winds, into a denser dry sand layer that will be further compacted with depth (and time) into a sandstone. The baseline version of the MSSM that is used throughout most of Chapter 4 assumes a subsurface structure of a single regolith unit composed of an unconsolidated regolith (with similar properties to a surface dust layer) that is gradually compacted with depth into a coarse dry sand. While this subsurface structure will occur across parts of the martian surface, many other subsurface structures are also expected. Consequently, simulations using an initial ice-layer configuration of H₂O Ice-filled Regolith Over CO₂ Ice-filled Regolith (*W-C*) have been run for a few different subsurface structures that encompass some of the diversity in subsurface structures on Mars. These simulations are discussed in detail in Section 5.2 and show that, while the different subsurface structures alter thermal properties, the largest influence on the stability of CO₂ ice is the initial column density of CO₂ ice that can be stored within the pore space.

The two-ice-layer configurations discussed in the previous chapter are likely to occur in some places, but the actual configuration of ices with depth is likely to be more complex in many locations. To investigate the impact of the chosen ice-layer configurations, a series of simulations with different combinations of ice-free regolith, H₂O ice-filled regolith and CO₂ ice-filled regolith layers have been run and the results of these simulations are discussed in detail in Section 5.3. The main impact of the differ-

ent combinations of ice-layers is on the thermal properties of the subsurface, showing that higher subsurface thermal conductivities can increase the stability of CO₂ ice.

5.1 Initial Ice Porosity

Across the regions of Mars containing either CO₂ ice or H₂O ice, the porosity of the ice is likely to vary with location and depth depending on the compaction of the ice (from snow to compacted ice) and on the presence of fractures within the ice. On Earth, snow porosity has been found to range between ~60 and 80% (Clifton et al., 2007). However, these porosity values are for pure ice, whereas in the MSSM, ice forms within the regolith matrix which has a fixed porosity profile (see Section 3.2) across all simulations discussed in this section. Therefore, two types of porosity are referred to across this work: the regolith matrix porosity and ice porosity. The regolith matrix porosity, ϕ_r , is the porosity of the ice-free regolith matrix and ranges from 0.63 to 0.37 in the baseline version of the MSSM (Table VII.I). The ice porosity, ϕ_{ice} , refers to the proportion of the empty pore space within the regolith that is filled with ice. Combining the regolith matrix porosity with the ice porosity produces the total porosity, ϕ_{tot} , in each model layer. For example, if there is no ice within the pore space in the uppermost model layer, $\phi_{ice}=1$ and $\phi_{tot} = 0.63$. Whereas if 10% of the pore space in the uppermost model layer is filled with ice, ϕ_{ice} is now 0.9 and $\phi_{tot} = 0.567$. Throughout this section, porosity refers to the ice porosity since the regolith matrix porosity is constant over time and between the simulations discussed in this section. All of the simulations in this section also assume a fixed permeability that is defined by a tortuosity value of 1 (see Section 3.3.1.2) to ensure that vapour can always travel through the pore space when porosity is greater than zero.

The initial ice porosity, ϕ_{iceini} , used in the MSSM is an important factor for the sublimation rate of both ices, since the presence of any porosity ensures that vapour exchange can occur across the entire subsurface. In the baseline version, the initial ice porosity is fixed at 0.001, but this assumption is unlikely to hold across the entirety of Mars. There are many scenarios when the ice porosity will be higher or lower than 0.001, such as when ice is deposited, sublimating away or when fractures form. In these scenarios, the rate of ice deposition and sublimation at depth will be drastically

different as the porosity is one of the main controls on the rate of diffusion and a large porosity (>0.1) will allow vapour to diffuse through the subsurface rapidly, whereas, when ice fills the entire pore space (when $\phi_{\text{ice ini}} = 0$ in the MSSM), the ice at the base of the model is completely isolated from the atmosphere until the overlying ice has started to sublimate away and porosity increases. Variations in the porosity of ice will also occur with location as compaction and fracturing of ice can vary on much smaller scales ($<1\text{ m}$) than the 5° latitude resolution used for the MSSM. Within that 5° latitude region, porosity could have a range of 0 to 0.9 across the different longitudes and this is a limitation of using fixed zonally averaged atmospheric values.

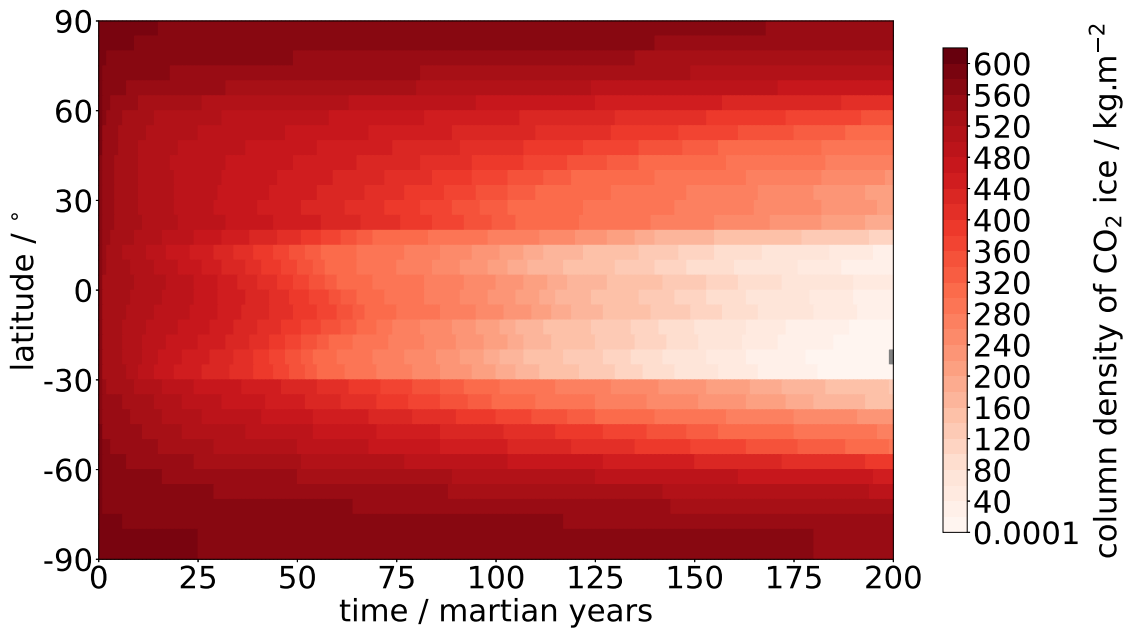
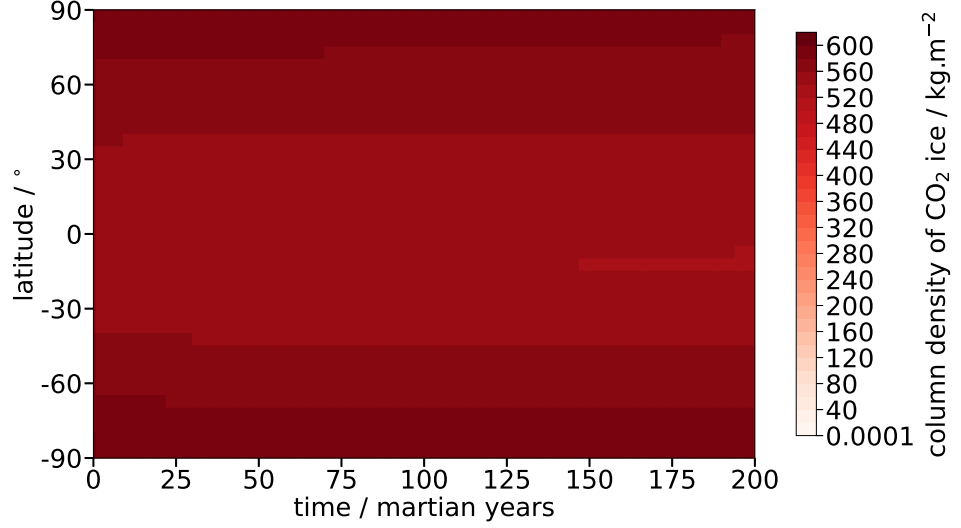


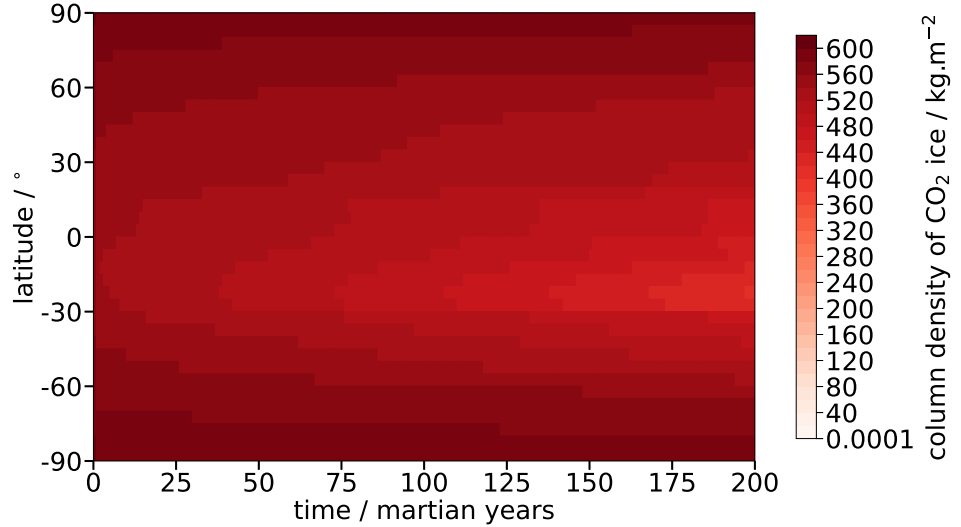
Figure 5.1: Column density of CO_2 ice at each latitude over time for the *W-C* with a boundary at 1 m (S06) using the baseline version of the MSSM. Grey represents where the CO_2 ice column density is less than 0.0001 kg m^{-2} .

A series of simulations have been run to investigate how the chosen $\phi_{\text{ice ini}}$ value (0.001 in the baseline version) impacts the sublimation rate of CO_2 ice with time and latitude, using the *W-C* scenario from Chapter 4 (boundary at 1 m; S06) as the initial ice-layer configuration. Initial ice porosities of 0, 0.0001, 0.01, and 0.1 (PM01, PM02, PM03 and PM04, respectively) were chosen to encompass the wide range of porosities that could occur in the scenarios mentioned previously. Figure 5.1 shows the column density of CO_2 ice over time from the initial baseline simulation with $\phi_{\text{ice ini}} = 0.001$ (S06) while Figures 5.2 and 5.4 show results for each of the simulations with different

initial ice porosities. The results all show a similar pattern in CO₂ ice sublimation, as CO₂ ice sublimates fastest in the equatorial region and slowest in the polar regions. The smaller latitudinal variations are also consistent across all of the simulations and show that the porosity is a dominant factor controlling the rate of sublimation through limiting the amount of CO₂ vapour that can diffuse out of the subsurface within a sol.



(a) $\phi_{\text{ice ini}} = 0$ (PM01)



(b) $\phi_{\text{ice ini}} = 0.0001$ (PM02)

Figure 5.2: Column density of CO₂ ice at each latitude over time for the variable initial ice porosity sets of simulations and the initial ice porosity ($\phi_{\text{ice ini}}$) used is (a) 0 and (b) 0.0001, which correspond to simulations PM01 and PM02, respectively. Grey represents where the CO₂ ice column density is less than 0.0001 kg m⁻².

In the simulations with a smaller initial ice porosity than in the baseline version ($\phi_{\text{ice ini}} < 0.001$; Figure 5.2), CO₂ ice sublimates at a slower rate (global average is 5.66 mm MY⁻¹ in PM02) than when initial ice porosity is 0.001 (global average is

25.7 mm MY⁻¹ in S06; Figure 5.1). This is expected as smaller porosities will result in smaller diffusion coefficients (Equation 3.22d) and slower vapour transport between the atmosphere and the CO₂ ice-filled regolith layer. In the simulations shown here (Figure 5.2), the column density of CO₂ ice decreases over time at all latitudes. The rate of this decrease shows the same three latitudinal zones as would be expected from surface temperature observations as well as in the results in Section 4.3.2: polar, mid-latitude and equatorial.

In the results from the $\phi_{\text{ice ini}} = 0$ set of simulations (PM01), the column density of CO₂ ice changes at a nearly constant rate within each of the three zones. The average sublimation rate in each region across both hemispheres is 1.37 mm MY⁻¹ in the polar regions, 1.81 mm MY⁻¹ in the mid-latitudes, and 2.29 mm MY⁻¹ in the equatorial region. Whereas in the results from the $\phi_{\text{ice ini}} = 0.001$ set of simulations (PM02), the CO₂ ice sublimation rate increases steadily with decreasing latitude, with average sublimation rates of 2.16 mm MY⁻¹ in the polar regions; 5.53 mm MY⁻¹ in the mid-latitudes and 9.28 mm MY⁻¹ in the equatorial region. This gradual increase makes the three latitudinal zones harder to distinguish in Figure 5.2a. This is because when the initial ice porosity is 0, vapour diffusion, and therefore sublimation, can only occur when some of the H₂O ice within the overlying H₂O ice-filled regolith layer has sublimated away. This creates a pathway for the CO₂ vapour to travel from the top of the CO₂ ice-filled regolith layer to the surface. If no H₂O ice sublimates, the underlying CO₂ ice remains trapped and cannot sublimate even if it is out of equilibrium with the atmosphere. Figure 5.3a shows the column density of H₂O ice over time for the $\phi_{\text{ice ini}} = 0$ set of simulations (PM01). In this figure, it can be seen that there is a small decrease in the column density of H₂O ice at most latitudes ($\sim 0.1 - 1 \times 10^{-5}$ kg m⁻²) within the first martian year, which is the result of H₂O ice sublimating to increase the vapour density in the pore space to saturation vapour density. Around the mid-latitudes (65-50°N and 65-75°S), there appears to be no change in the column density of H₂O ice in the figure, but this is because the initial drop in column density is an order of magnitude smaller at these latitudes ($\sim 0.1 - 1 \times 10^{-6}$ kg m⁻²) and is not visible at the scale of the figure. At these latitudes, the atmospheric H₂O vapour density is closest to the saturation vapour density and the smallest amount of H₂O ice sublimates

as a result ($<1 \times 10^{-6} \text{ kg m}^{-2}$). From this, it would be expected that CO_2 ice sublimates the slowest at the latitudes where the least amount of H_2O ice sublimates. However, temperatures in the mid-latitudes remain higher than the CO_2 frost point for a larger portion of the year than in the polar regions, resulting in more sublimation of CO_2 ice overall in the mid-latitudes (average sublimation rates of 5.53 mm MY^{-1} in the mid-latitudes rather than 2.16 mm MY^{-1} in the polar regions), despite the lower porosity. The increase in the column density of H_2O ice over time in the equatorial region of Figure 5.3a, is due to H_2O ice forming where CO_2 ice has already sublimated and the H_2O vapour density has increased to above the saturation vapour density. This was discussed previously in Section 4.3.2.3 and while the increase in H_2O ice will result in a slight increase in subsurface temperatures, it will not impact the porosity of the overlying H_2O ice-layer and therefore only has a small impact on the rate of sublimation of CO_2 ice.

The simulations with a higher porosity than in the baseline version ($\phi_{\text{ice ini}} > 0.001$; Figure 5.4) show the expected, opposite, results to the simulations with a lower porosity in the baseline, as CO_2 ice sublimates away at a much faster rate. In these simulations ($\phi_{\text{ice ini}} = 0.01$ and $\phi_{\text{ice ini}} = 0.1$; PM03 and PM04, respectively), CO_2 ice fully sublimates away within 200 martian years across the mid- and equatorial latitudes and when $\phi_{\text{ice ini}} = 0.1$, at all polar latitudes as well. The porosity in these simulations is lower than that of snow (~ 0.6 - 0.8) implying that any H_2O snow that forms on top of surface CO_2 ice would need to be compacted enough that the porosity was reduced to around 0.01 or lower within the first 20 martian years for this amount of CO_2 ice to survive longer. If the overlying H_2O ice had not compacted enough within that time, the underlying CO_2 ice would have mostly sublimated away. However, if the total column density of CO_2 ice ($\sim 640 \text{ kg m}^{-2}$) within the regolith matrix was compressed into a single solid CO_2 ice-layer, the layer would only be 40 cm, which is drastically smaller than the smallest CO_2 ice-layer discovered within the SPLD (Bierson et al., 2016). This implies that while CO_2 ice will sublimate more rapidly at higher porosities, at the sublimation rate at 88°S (49.01 mm MY^{-1}) in the time it would take for the overlying H_2O snow to compact into a low-porosity (<0.001) H_2O ice (14 kyr; Manning et al., 2019), 686 m of pure CO_2 ice would have sublimated away which is small enough

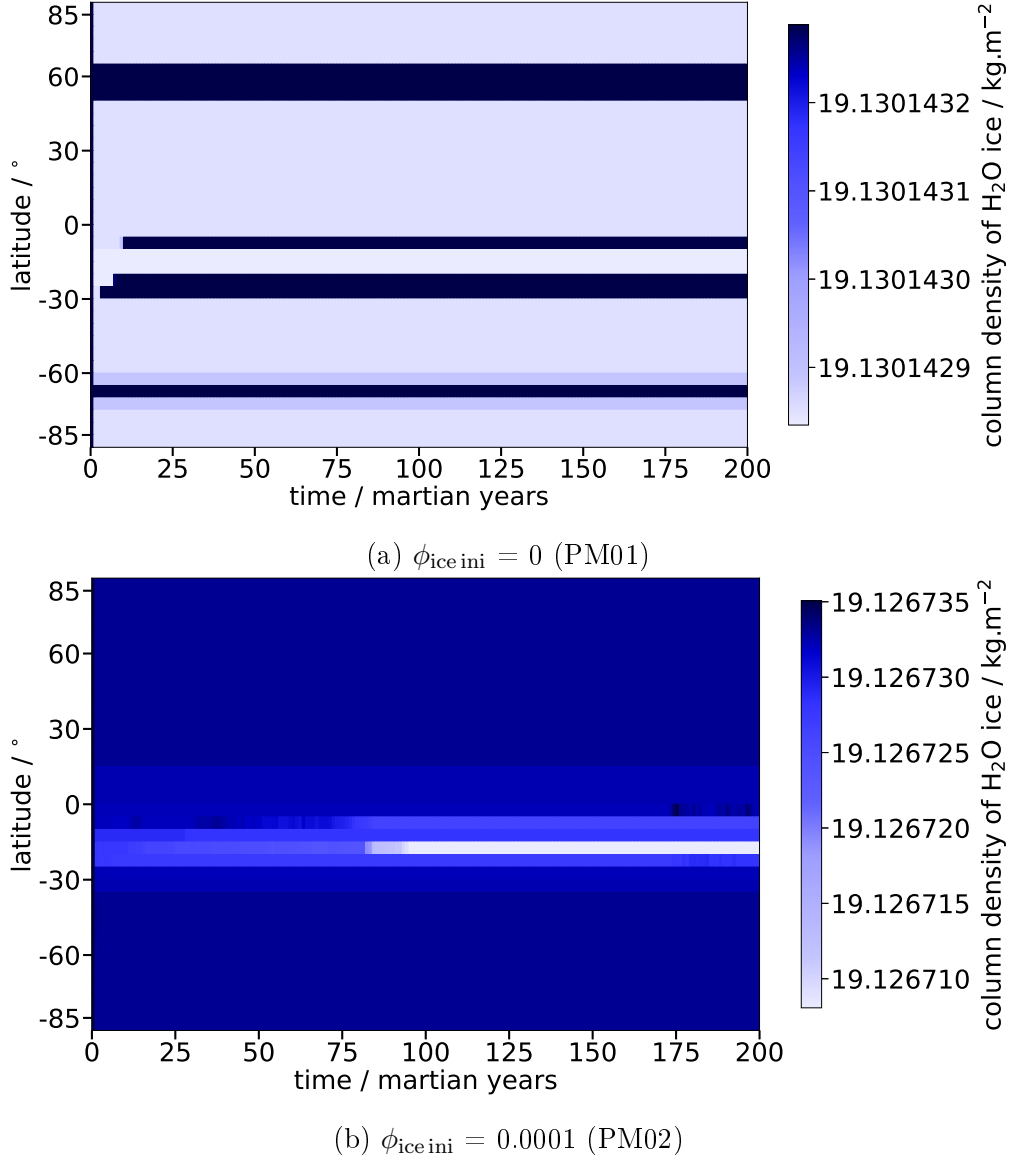


Figure 5.3: Column density of H₂O ice at each latitude over time for the (a) $\phi_{\text{ice ini}} = 0$ (PM01) and (b) $\phi_{\text{ice ini}} = 0.0001$ (PM02) sets of simulations. Grey represents where the H₂O ice column density is less than 0.0001 kg m⁻².

that it is plausible for some CO₂ ice to remain after this amount of CO₂ ice has sublimated away. This assumes the sublimation rate would be the same for both pure CO₂ ice and CO₂ ice within a regolith matrix, which is plausible because the thermal conductivities of CO₂ ice ($\sim 0.7 \text{ W m}^{-1} \text{ K}^{-1}$) and the regolith at the base of the model where CO₂ ice exists in this scenario ($\sim 0.1 \text{ W m}^{-1} \text{ K}^{-1}$), will have a similar influence on subsurface temperatures and therefore on sublimation rates. Once the overlying H₂O ice has compacted to 0.001, CO₂ ice sublimation rate has been reduced by an order of magnitude (2.66 mm MY^{-1} at 88°S in S06) and any remaining CO₂ ice will take even longer to sublimate away.

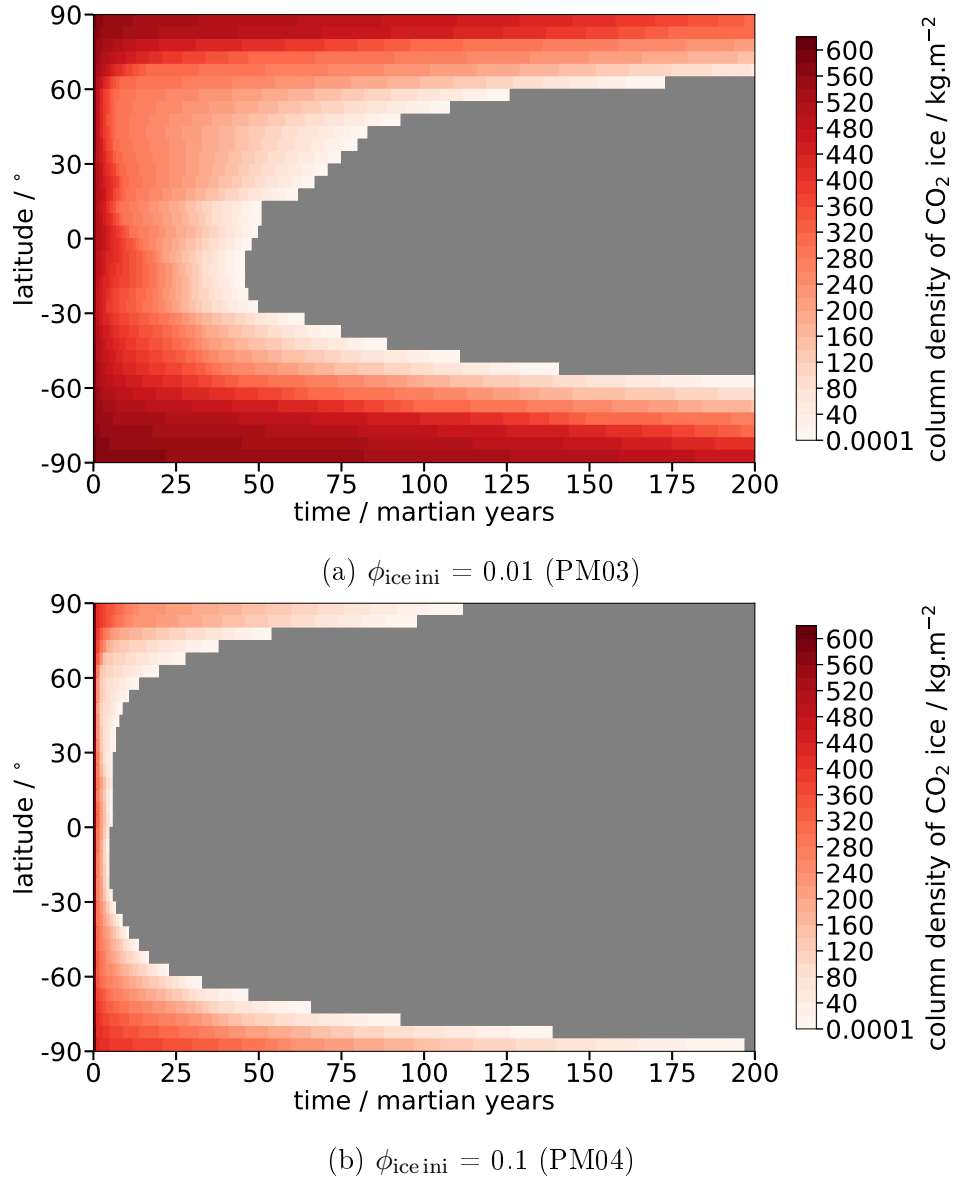


Figure 5.4: Column density of CO₂ ice at each latitude over time for the variable initial ice porosity sets of simulations and the initial ice porosity ($\phi_{\text{ice ini}}$) used is (a) 0.01 and (b) 0.1, which correspond to simulations PM03 and PM04, respectively. Grey represents where the CO₂ ice column density is less than 0.0001 kg m⁻².

The presence of fractures and pathways within the overlying ice therefore has a considerable influence on the amount of time that CO₂ ice takes to sublimate when overlain by a H₂O ice-filled regolith layer. Figure 5.5 shows the estimated number of years it would take for this underlying CO₂ ice to fully sublimate for the range of initial ice porosities discussed (0.1 to 0). As expected, CO₂ ice survives longest when the overlying H₂O ice-layer is initially impermeable and survives the least amount of time when the initial ice porosity is largest (0.1 in this case). In general, CO₂ ice survives the longest at the poles, following a similar pattern with latitude for each initial

ice porosity value. The main exception is within the equatorial region for the $\phi_{\text{ice ini}} = 0.0001$ (FM02) set of simulations. In this region, CO₂ ice takes longer to fully sublimate at 30°N than at 30°S. This reflects the gradual increase in temperature from 30°N to 30°S (Figure 4.11) which was discussed in detail in Section 4.3.2. As temperatures increase over this latitude range, the amount of H₂O ice that sublimates away increases (Figure 5.3b), increasing the porosity, and therefore diffusion coefficient, in the upper model layers. This in turn allows CO₂ vapour to diffuse out of the subsurface faster and consequently, sublimation of CO₂ ice occurs at a faster rate.

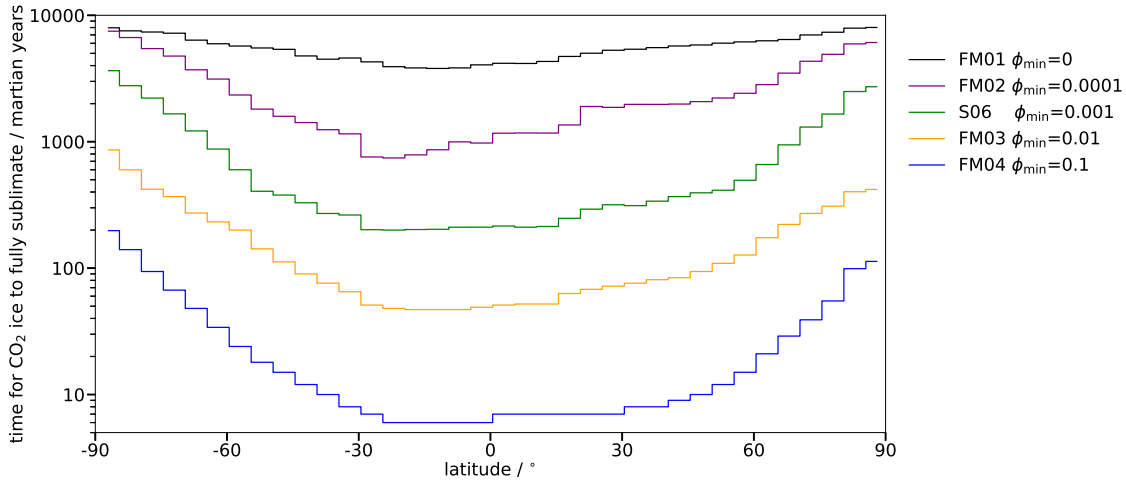


Figure 5.5: Comparison of the number of years that CO₂ ice survives for the varying initial ice porosity simulations and the baseline simulation (S06). $\phi_{\text{ice ini}}$ is the initial ice porosity value used in each version of the MSSM.

5.2 Geological Properties

Observations by the Thermal Emission Spectrometer (TES) on the Mars Global Surveyor (MGS) have shown that the surface material is highly variable across the planet (Putzig et al., 2005, see Section 2.1.1 for more details on variations in surface geology). This diversity extends into the subsurface where geological units of varying thickness and composition are expected. The exact thickness and composition of these geological units remain unknown as most observations can only be used to infer the geological material at the surface and even this remains uncertain in many locations due to the non-uniqueness of thermal inertia and albedo values for different geological materials. Therefore, the assumption of a homogeneous subsurface structure at all latitudes used in the MSSM does not fully represent the diversity in both surface and subsurface

geological materials that is expected across Mars. In the MSSM, the fixed subsurface structure is that of a single regolith unit composed of an unconsolidated regolith at the surface that is compacted with depth into a coarse dry sand. The thermal conductivity value measured by the Heat Flow and Physical Properties Package (HP³) on the InSight lander ($0.039 \text{ W m}^{-1} \text{ K}^{-1}$; Grott et al., 2021) falls within the range of thermal conductivities used for this regolith unit (0.01 to $0.1 \text{ W m}^{-1} \text{ K}^{-1}$), confirming the likelihood of regions with geological properties similar to those used for the baseline subsurface structure. However, many other combinations of geological materials and unit thicknesses are also likely. There are also areas where the subsurface contains layers that are composed of mainly H_2O ice (excess ice or a buried ice sheet) rather than an ice-filled regolith. All of these different scenarios will impact the formation and stability of both ices. Therefore, simulations with a few different subsurface structures have been run to investigate the effect of subsurface structure on the stability of H_2O ice and CO_2 ice at different latitudes.

The subsurface properties (density, porosity and thermal conductivity) for the regolith unit used in the MSSM are all calculated using equations from Grott et al. (2007, Equations 3.9a, 3.9b and 3.11) that were developed, based on measurements of lunar regolith, to simulate the martian regolith and the expected compaction of surface regolith material with depth. These equations require two bounding values, one for the surface geological material and one for the final compacted geological material deeper within the subsurface (i.e. resulting from compaction of the surface material). In the baseline version of the model, the surface values used are for an unconsolidated regolith and the compacted values are for a coarse dry sand, the values for which are also taken from Grott et al. (2007). These equations for density, porosity and thermal conductivity (Equations 3.9a, 3.9b and 3.11; Grott et al., 2007) assume that the regolith unit is composed of a material that is initially unconsolidated and is then compacted to 95% of a constant geological material (referred to as the compacted material) at 10 m. This assumption, while developed for lunar regolith, is plausible in the near surface at locations where the surface is covered in atmospheric dust, making this equation appropriate for large portions of the martian surface. However, there are also large areas where either the surface is not covered in atmospheric dust or the unconsolidated

dust layer is thin and overlies another geological material rather than consolidated dust (coarse dry sand in the Grott et al., 2007, model). In these cases, the assumption of an unconsolidated regolith that is then compacted into a consolidated dust unit is no longer valid. Consequently some of the subsurface structures investigated assumed a surface material other than unconsolidated regolith.

While the subsurface of Mars is likely to be composed of a diverse mixture of geological materials, only five materials are considered here for simplicity: an unconsolidated regolith (UR); coarse dry sand (CDS); fine dry sand (FDS); sandstone (SS); and basalt (B). These geological materials were also chosen because their properties correspond to those expected across the surface of Mars based on the thermophysical units determined by Putzig et al. (2005, discussed in Section 2.1.1). These units split the surface according to thermal inertia and albedo (Figure 2.3 and Table 2.1), covering the entire range of surface geological materials. The thermal inertias of unconsolidated regolith (UR) and fine dry sand (FDS) correspond to those used for units A and D, the thermal inertia of coarse dry sand (CDS) corresponds to units B and E, while sandstone and basalt correspond to the thermal inertias of unit F. This covers the entire thermal inertia range used for the Putzig et al. (2005) thermophysical units and, therefore, is likely to cover the majority of the expected range in geological material.

In these simulations, different subsurface structures are defined using a combination of these five materials. Thermal conductivity, density and specific heat capacity values are needed to define the subsurface structure and values for all of the geological materials are given in Table 5.1. Four of the five geological materials (UR, FDS, CDS and SS) are used to define the subsurface structure within the regolith unit. The values for the regolith unit are then input into the same equations (from Grott et al., 2007) as for the baseline version of the MSSM, with the material used for the surface and compacted geological material changing according to the subsurface structure being investigated. The final geological material considered here (basalt) cannot be formed by compaction of atmospheric dust and therefore can not be used as one of the two bounding materials for the regolith unit. Instead, basalt is used as a basement unit that does not have enough pore space to store large quantities of H₂O ice or CO₂ ice,

Table 5.1: Properties of the geological materials used across the different subsurface structures.

Material	Thermal Conductivity $\text{W m}^{-1} \text{K}^{-1}$	Density kg m^{-3}	Specific Heat Capacity $\text{J K}^{-1} \text{kg}^{-1}$	Thermal Inertia $\text{J m}^{-2} \text{K}^{-1} \text{s}^{-\frac{1}{2}}$	Reference
Unconsolidated Regolith (UR)	0.01	1000	830	91	Grott et al. (2007)
Coarse Dry Sand (CDS)	0.1	1750	830	381	Grott et al. (2007)
Fine Dry Sand (FDS)	0.02	1750	830	170	Grott et al. (2007)
Sandstone (SS)	2.97	2310	850	2414	Mellon et al. (2008)
Basalt (B)	1.75	2900	865	2095	Mellon et al. (2008)

but will impact the thermal properties of the subsurface and consequently the stability of both ices. The subsurface structures containing only a regolith unit are discussed first, followed by a discussion on the subsurface structures which also contain a basalt basement unit below a depth of 10 m.

5.2.1 Varying the Regolith Unit Materials

Three different combinations of surface and compacted geological material for the regolith unit were tested to investigate the effect of the chosen regolith properties on results (the geological materials used are summarised in Table 5.1). The first two combinations tested were chosen based on the materials used by Grott et al. (2007) to represent the regolith that is expected to cover large portions of the martian surface. In Grott et al. (2007), an unconsolidated regolith was used as the surface geological material and either a fine dry sand or a coarse dry sand (equivalent to consolidated dust layers) were used as the compacted geological material. The unconsolidated regolith properties represent surface dust cover from wind driven redistribution of dust across the majority of the planet, whereas, fine dry sand and coarse dry sand represent the material at depth from compaction of the unconsolidated regolith. Since the subsurface structure of the baseline version of the MSSM assumes an unconsolidated regolith at the surface that gets compacted to a coarse dry sand (S06), a complimentary simulation with an unconsolidated regolith that is compacted to a fine dry sand (UR-FDS) is investigated. Alongside this, a simulation with fine dry sand to coarse dry sand (FDS-CDS) was also run to investigate the other plausible structure that could occur from the three geological materials. The final subsurface structure tested was from a coarse dry sand to a sandstone (CDS-SS), which is another stage of compaction that would be expected. The two subsurface structures with no unconsolidated regolith at the surface, represent locations where dust has been removed from the surface, rather than deposited, and the more compacted geological layers are exposed at the surface. The final common subsurface structure that is expected is a small unconsolidated regolith dust layer (<10 m) over basalt, however, in locations where this occurs, the dust layer is expected to be thin and since basalt has a very small porosity (<0.01), only small amounts of ice are expected in the pore space of these regions, which will sublime

away rapidly. As a result, this subsurface structure is not considered in this work.

Figure 5.6 shows a comparison of the density, porosity and thermal conductivity profiles of the baseline subsurface structure with the different subsurface structures investigated, including the profiles for the subsurface structures that include a basalt basement unit below 10 m that are discussed in the next section. The profiles show the gradual change in values as the surface material becomes compacted into the final compacted material, with the steps in the figures showing the layering caused by the numerical grid (i.e. the model layers). In the profiles for the subsurface structures with a basalt basement unit, the values instantaneously change from the compacted material's value to that of basalt and remain constant with depth from this point.

The results from the three different regolith units (UR-FDS, FDS-CDS and CDS-SS) are shown in Figure 5.7 and the column density of CO₂ ice from all the three subsurface structures show a similar latitudinal pattern to the results from the baseline structure (S06; Figure 5.1). The latitudes that sublimated fastest in the simulation with the baseline structure, 5°S to 25°S, still sublimate fastest for all three subsurface structures and the polar regions take the longest to sublimate. However, there are differences between the scenarios that are the result of the differing thermal properties and column densities of both ices within the subsurface. The initial column density of CO₂ ice is limited by the maximum amount of CO₂ ice that can fit within the pore space (see porosity profiles in Figure 5.6b). The three subsurface structures each have a different porosity profile with depth and therefore each is initialised with a different amount of CO₂ ice (see Table 5.2).

The UR-FDS results are the closest to those from the baseline subsurface structure because the density and porosity profiles of the subsurface with depth are the same between the two models, which means the initial column density of each ice is the same and only the thermal conductivity differs. The thermal conductivity of fine dry sand is significantly lower than that of coarse dry sand (see Table 5.1), which means that the skin depth is significantly shallower (0.5 m instead of 1.14 m). Since the CO₂ ice is mostly deeper in the subsurface than the depth at which the surface thermal cycle is damped (below 2.5 m) in the UR-FDS scenario, temperatures will be stable at the

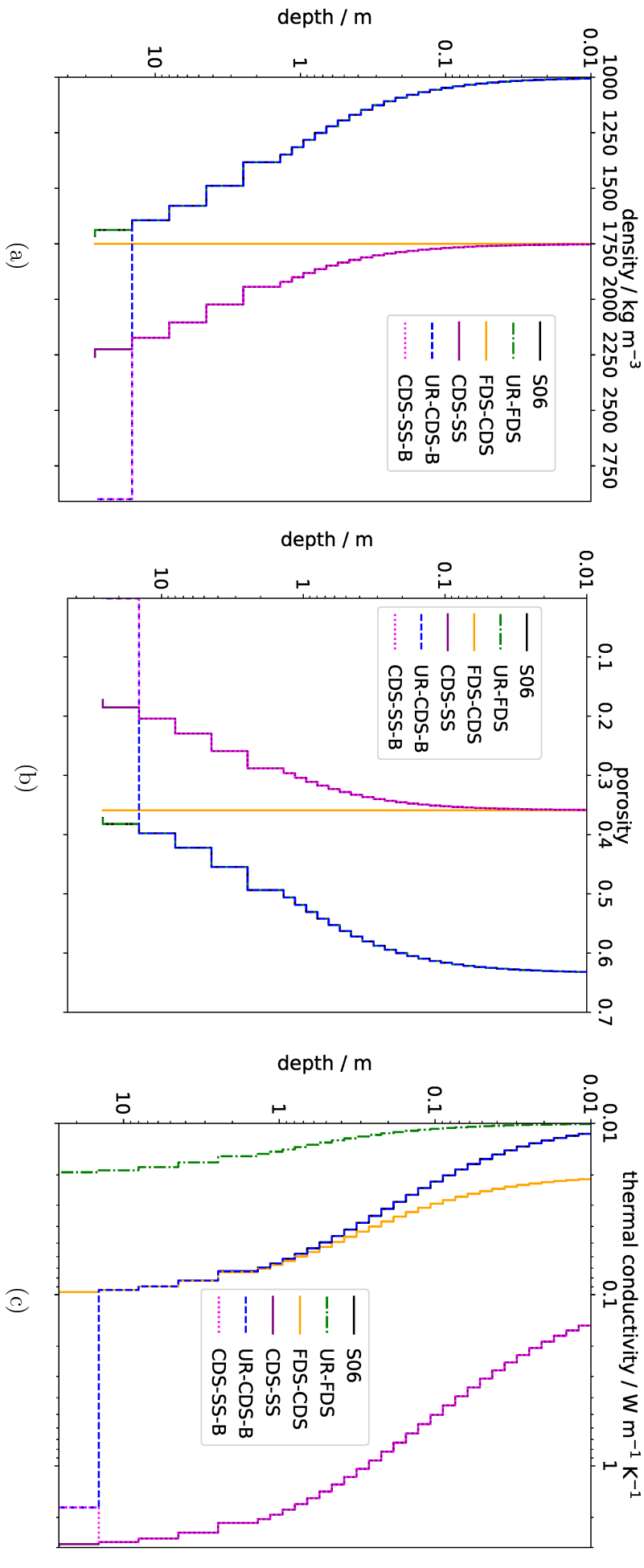
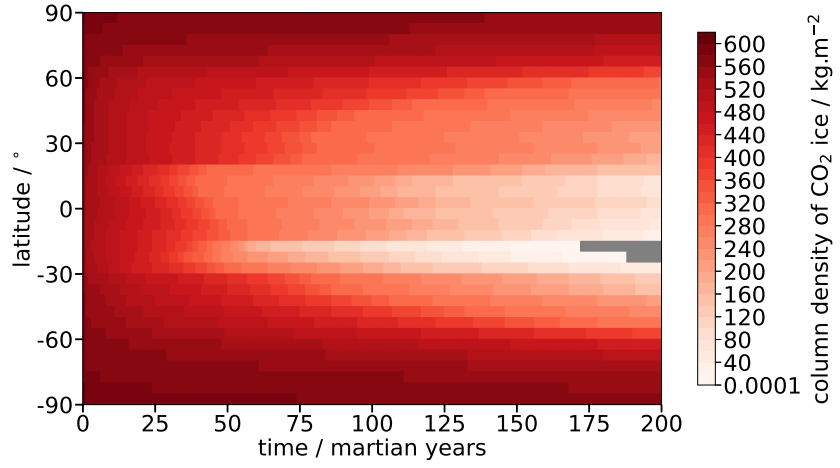
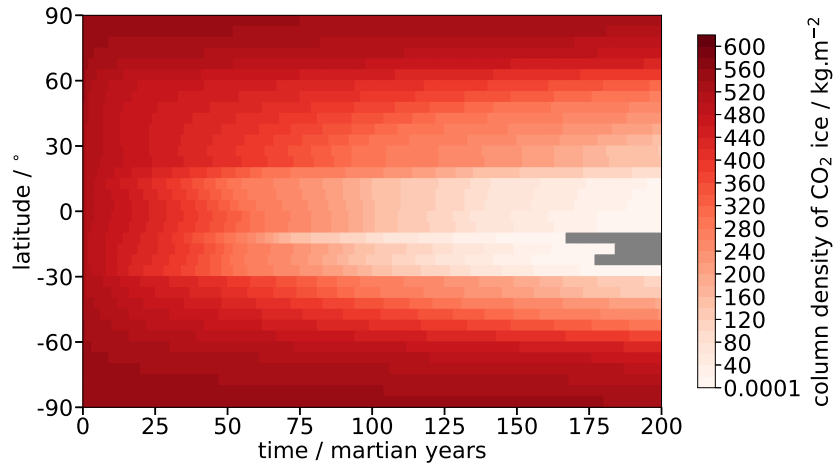


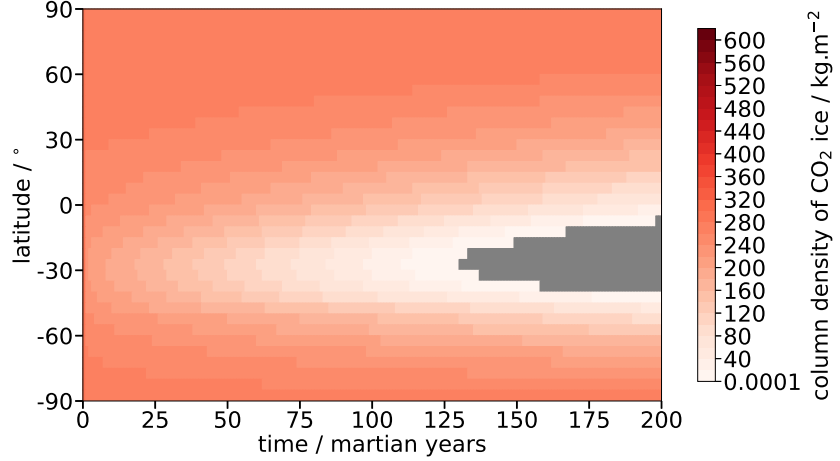
Figure 5.6: Comparison of (a) density [kg m^{-3}], (b) porosity and (c) thermal conductivity [$\text{W m}^{-1} \text{K}^{-1}$] profiles for the different subsurface structures. The labels on the figure refer to the subsurface structure: S06 is the baseline subsurface structure (unconsolidated regolith to coarse dry sand), CDS-SS is coarse dry sand to sandstone, FDS-CDS is fine dry sand to coarse dry sand, UR-FDS is unconsolidated regolith to fine dry sand, UR-CDS-B is unconsolidated regolith to coarse dry sand with a basalt basement layer below 10 m and CDS-SS-B is coarse dry sand to sandstone with a basalt basement layer below 10 m. The steps in these figures represent the layering caused by the discretisation onto the numerical grid rather than distinct geological layers, since a single value is used within each model layer.



(a) UR-FDS



(b) FDS-CDS



(c) CDS-SS

Figure 5.7: Column density of CO₂ ice over time for the scenarios with different sub-surface structures: (a) unconsolidated regolith to fine dry sand (UR-FDS), (b) fine dry sand to coarse dry sand (FDS-CDS) and (c) coarse dry sand to sandstone (CDS-SS). Grey represents where the CO₂ ice column density is less than 0.0001 kg.m⁻².

Table 5.2: The column density of ice for the upper H₂O ice-filled regolith layer and the lower CO₂ ice-filled regolith layer for all subsurface structures. Column densities are calculated using a H₂O ice density of 927 kg m⁻³ and the CO₂ ice density is calculated at 145 K. The equivalent thickness of ice in each model layer is calculated by multiplying the porosity by the thickness of the model layer. The total column density of ice is then calculated by multiplying the thickness of the ice-layer by the density of ice.

Subsurface structure (m)	Column density of ice (kg m ⁻²)	
	H ₂ O	CO ₂
S06	19.09	606.60
UR-FDS	19.09	606.6
FDS-CDS	12.19	560.97
CDS-SS	11.08	297.05
UR-CDS-B	19.09	186.21
CDS-SS-B	11.08	100.18

depths of the CO₂ ice-filled regolith layer and CO₂ ice will tend to survive slightly longer, as is shown in the results.

The FDS-CDS results are also very similar to those from the baseline structure (S06; Figure 5.1) and the rate of sublimation is actually closer in the simulation with the baseline structure than for the UR-FDS simulation at some latitudes. The main difference is in the amount of CO₂ ice that is initially present in the subsurface. In this scenario (FDS-CDS), the porosity is constant throughout the subsurface as fine dry sand and coarse dry sand are assumed to have the same density but different thermal conductivities, as shown in Figure 5.6. Since the amount of CO₂ ice that can fill the pore space is controlled by the regolith porosity, the larger density of the surface material means that less ice is required to fill the pore space. The smaller initial column density will also mean that CO₂ ice will generally sublimate away faster than in the baseline structure, even if the sublimation rate is the same.

The final subsurface structure (CDS-SS) results in a distribution over time that looks very different at a first glance. This is due to the 2-3 times smaller capacity of the pore space, depending on depth, in this subsurface structure, which results in an initial column density that is drastically smaller than the others. Despite this large difference in initial column density, the overall behaviour of CO₂ ice in the equatorial

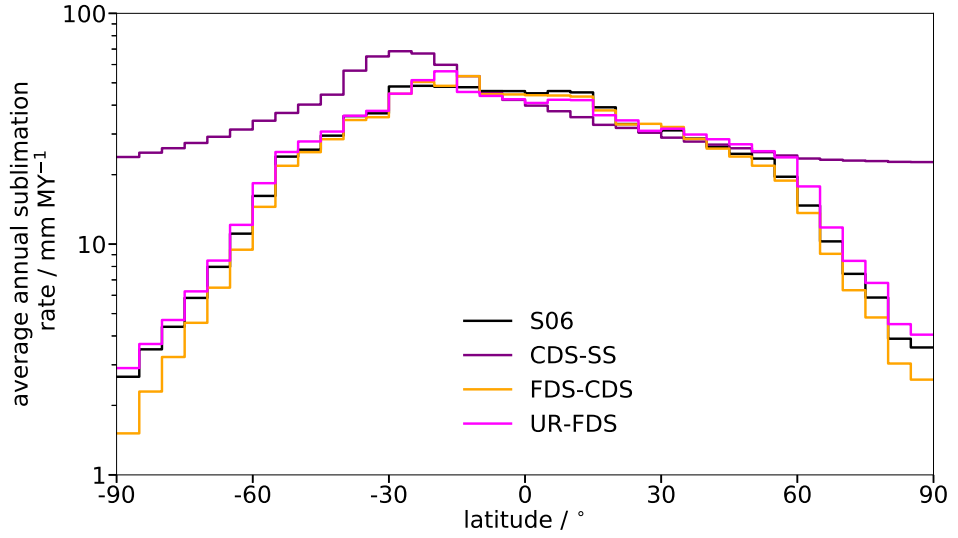


Figure 5.8: Comparison of the average annual CO_2 ice sublimation rate [mm MY^{-1}] for the different regolith unit subsurface structures and the baseline simulation (S06).

region and northern mid-latitudes is similar to the other simulations with CO_2 ice sublimating away the fastest at these latitudes. In the polar and southern mid-latitude regions, on the other hand, the sublimation rate follows a different trend from the other scenarios. This can be seen in Figure 5.8 which shows the annual average sublimation rate for each subsurface structure. As already mentioned, CO_2 ice sublimation rate in the equatorial region and northern mid-latitudes (20°S to 50°N) follows the same trend as in the other subsurface structures, but across the rest of the latitudes, CO_2 ice sublimation rate is much higher. This difference is due to the higher thermal conductivity throughout the subsurface structure (Figure 5.6c) which results in more heat being conducted (and stored) deeper into the subsurface (to the depths of the CO_2 ice-filled regolith layer) during summer and more being released during winter. This in turn causes warmer winter temperatures, which result in more sublimation during that time and increase the annual sublimation rate of CO_2 ice. Figure 5.9 shows the difference in average subsurface temperature between the baseline simulation (S06) and the CDS-SS simulation at $L_S = 0^\circ$, when the northern hemisphere is at the beginning of spring. In the figure, temperatures are warmer in the northern hemisphere and cooler in the southern hemisphere, following what is expected from the higher thermal conductivity. The latitudes with the largest changes in temperature correspond to those with the higher sublimation rates in Figure 5.8, showcasing the large effect that subsurface thermal conductivity can have on CO_2 ice stability.

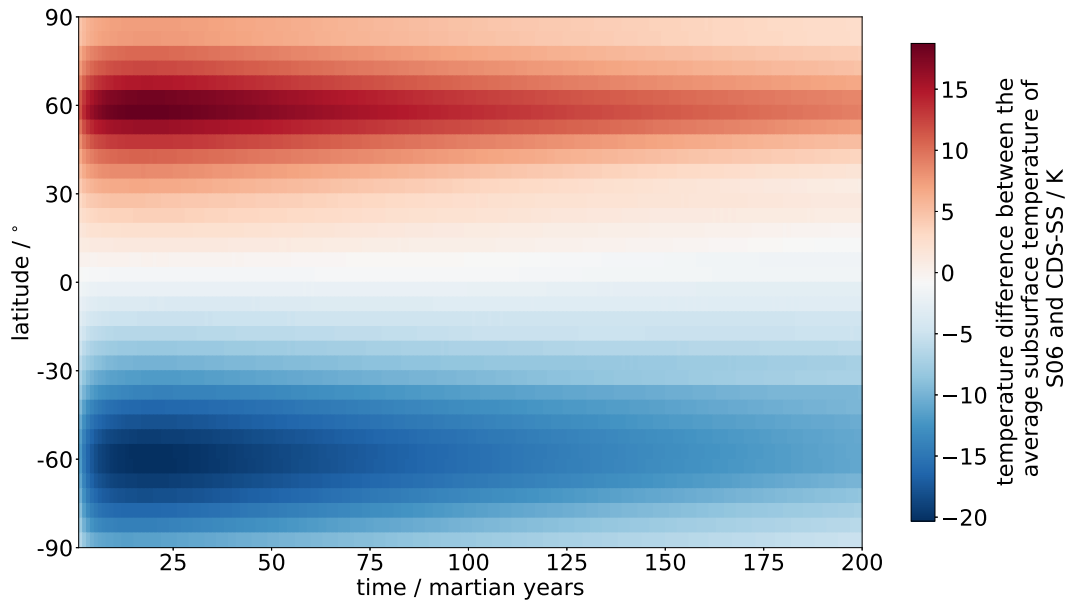


Figure 5.9: Difference in average temperature across the subsurface between the baseline simulation (S06) and the CDS-SS simulation.

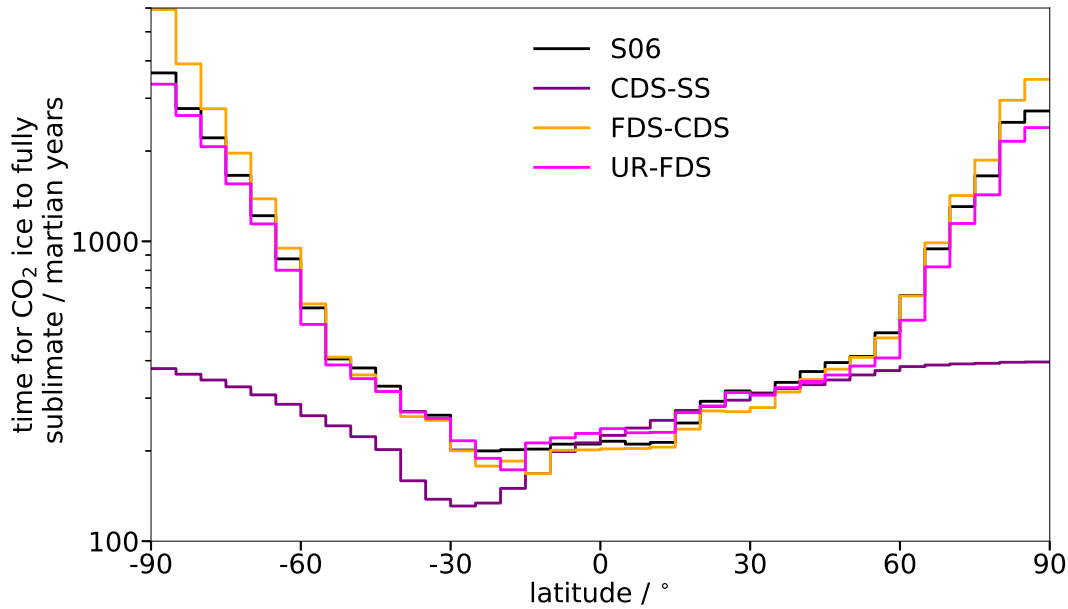


Figure 5.10: Comparison of the number of years it takes to fully sublimate CO_2 ice for the different regolith unit subsurface structures and the baseline simulation (S06).

The subsurface structure of the regolith unit used in the simulations, therefore, can have a large impact on the number of martian years it would take to fully sublimate an initial amount of CO₂ ice when overlain by an H₂O ice-filled regolith layer, as shown in Figure 5.10. In the equatorial region, the length of time that CO₂ ice takes to fully sublimate is similar across all subsurface structures, even if the initial amount of ice differs. However, as latitude increases, the amount of time that CO₂ ice can survive becomes more dependent on the initial amount of CO₂ ice that is present and the thermal conductivity of the subsurface. This is especially noticeable for the CDS-SS simulation, since CO₂ ice takes between 200 and 400 martian years to fully sublimate at all latitudes, whereas for the other three scenarios, the CO₂ ice takes an order of magnitude longer to fully sublimate in the polar regions than in the equatorial region. These differences caused by the different subsurface structures are important to remember since the surface of Mars is not homogeneous and the locations where subsurface CO₂ ice could survive will be highly dependent on the subsurface structure and the thermal properties of the region.

5.2.2 Inclusion of a Basalt Basement Unit

In many locations with a regolith at the surface, the regolith is expected to be overlying a basement unit (Ruff and Christensen, 2002). The starting depth of this basement unit is unknown and it is expected to be composed of basalt based on surface geology observations (see Section 2.1.1). Therefore, two simulations have been run with a compacting regolith unit overlying a basalt basement unit from 10 m. In one scenario, the regolith unit has a surface material of unconsolidated regolith and the compacted material is coarse dry sand (UR-CDS-B), in the other the surface material is coarse dry sand and the compacted material is sandstone (CDS-SS-B). These subsurface structures cover the main differences discussed in the previous section and Figure 5.11 shows the results from these scenarios. It is important to note that the initial amount of CO₂ ice is significantly less than in all of the previous scenarios because the basalt basement unit occurs from a depth of 10 m and very little CO₂ ice is stored in this region, since below this depth the regolith porosity is less than 0.01. In all previous simulations, a large portion of the total CO₂ ice column density is stored below 10 m because of the

uneven grid, as shown in Table 4.1 and consequently, the simulations with a basement layer are initialised with less than a third of the initial CO₂ ice than for the baseline structure (S06). Therefore, a different scale has been used in Figure 5.11 compared with all other figures of CO₂ ice column density.

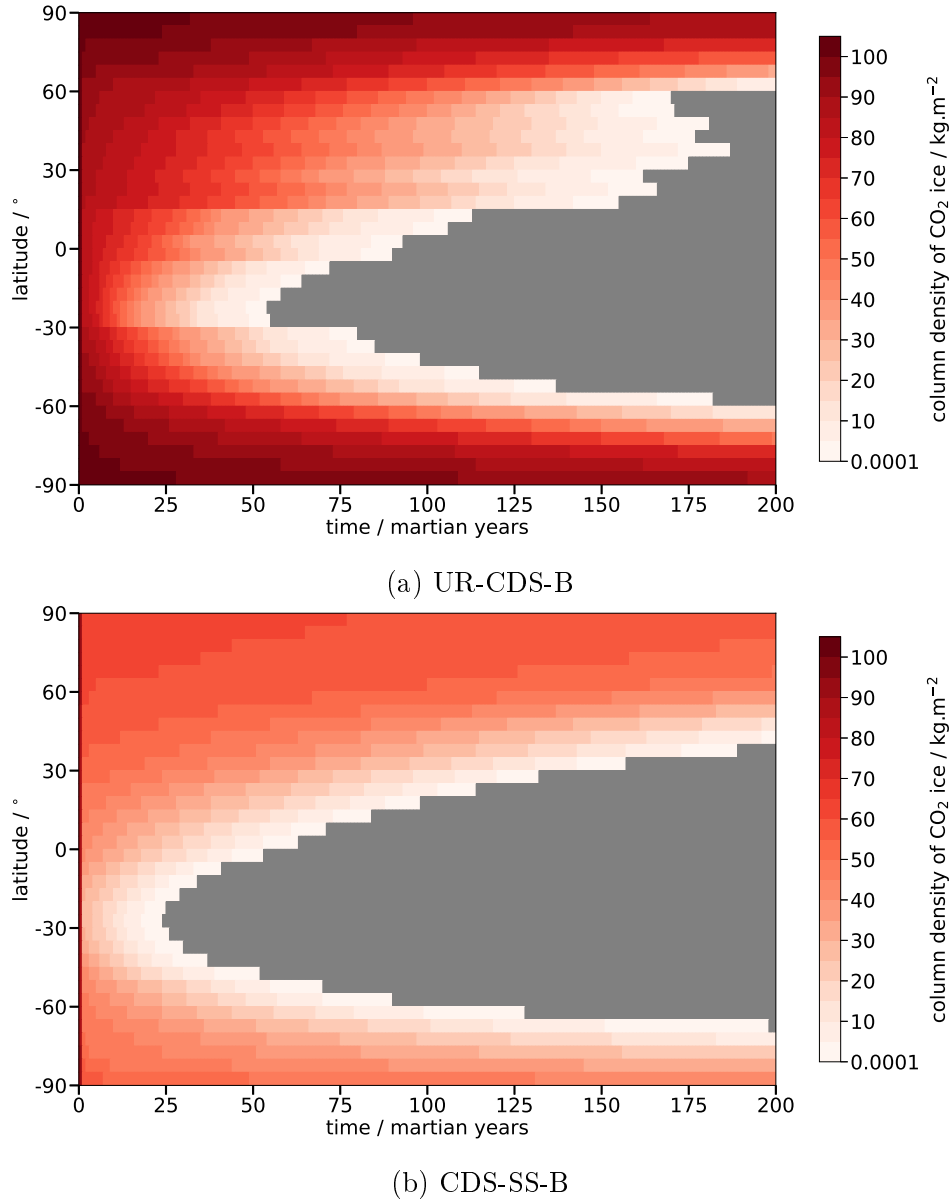


Figure 5.11: Column density of CO₂ ice over time for the scenarios with different subsurface structures with a basalt basement unit below 10 m: (a) unconsolidated regolith to coarse dry sand with a basalt basement (UR-CDS-B), (b) coarse dry sand to sandstone with a basalt basement (CDS-SS-B). Grey represents where the CO₂ ice column density is less than 0.0001 kg m⁻².

CO₂ ice in both simulations with a basement unit fully sublimates away within 200 martian years at more latitudes than in the simulations without a basement unit, which is expected due to the smaller initial amount of CO₂ ice and higher subsurface

thermal conductivities. Out of the two subsurface structures with a basement layer, the CDS-SS-B structure has a smaller initial column density of CO₂ ice because the porosity of the entire subsurface structure is smaller (Figure 5.6b) than in the UR-CDS-B structure. This will contribute to CO₂ ice fully sublimating away in less time in the CDS-SS-B structure, which is seen in Figure 5.11.

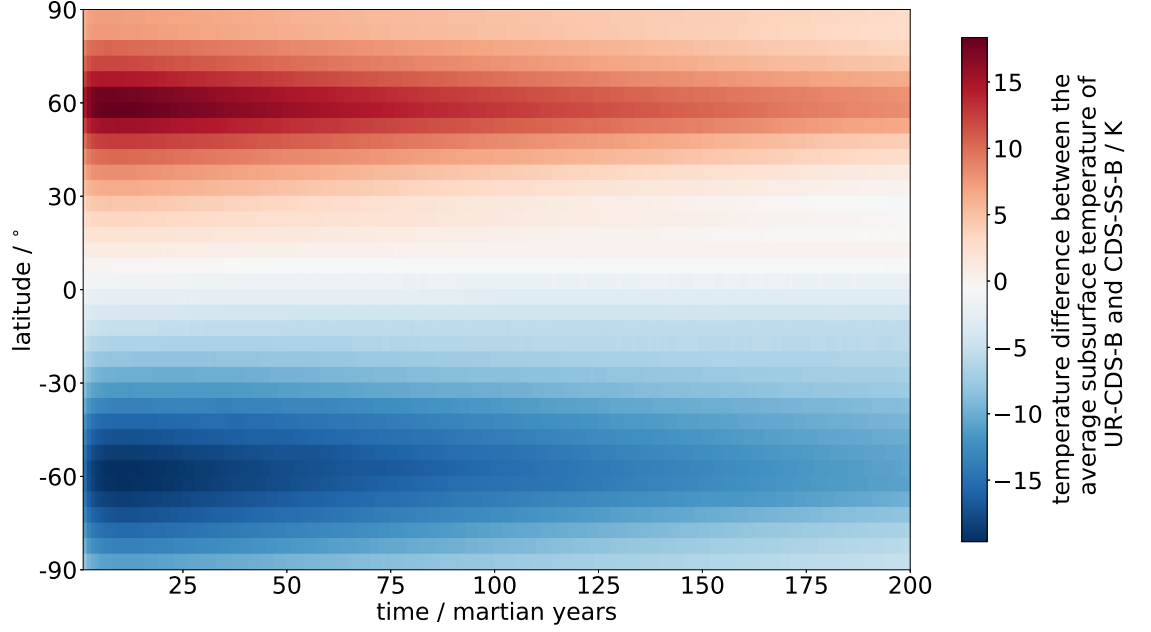
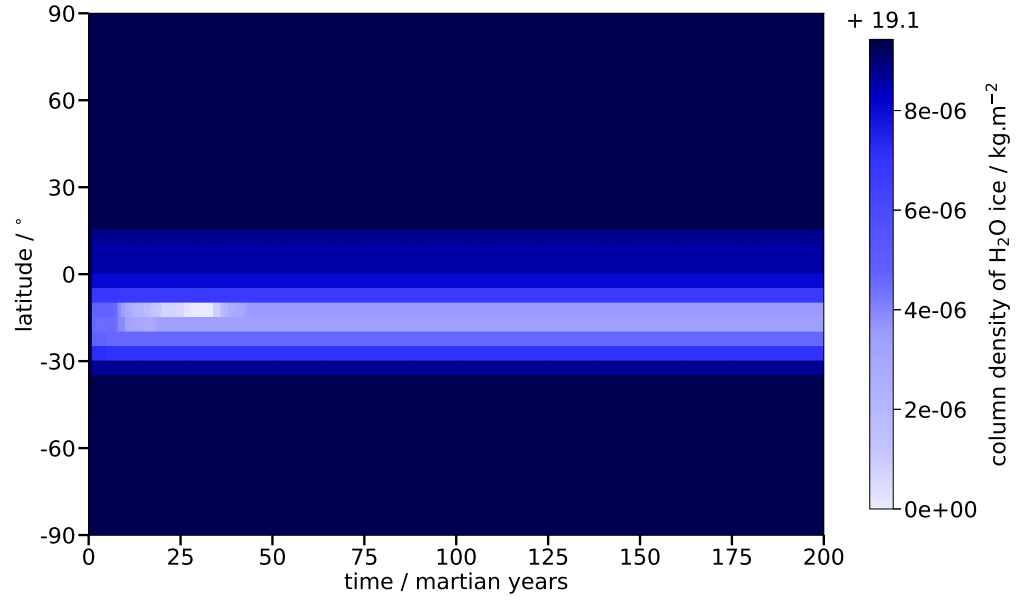


Figure 5.12: Difference in the average temperature across the entire subsurface between the UR-CDS-B structure and the CDS-SS-B structure sets of simulations. Positive values mean average subsurface temperature is higher in the UR-CDS-B simulations, while negative values mean average subsurface temperatures are higher in the CDS-SS-B simulations.

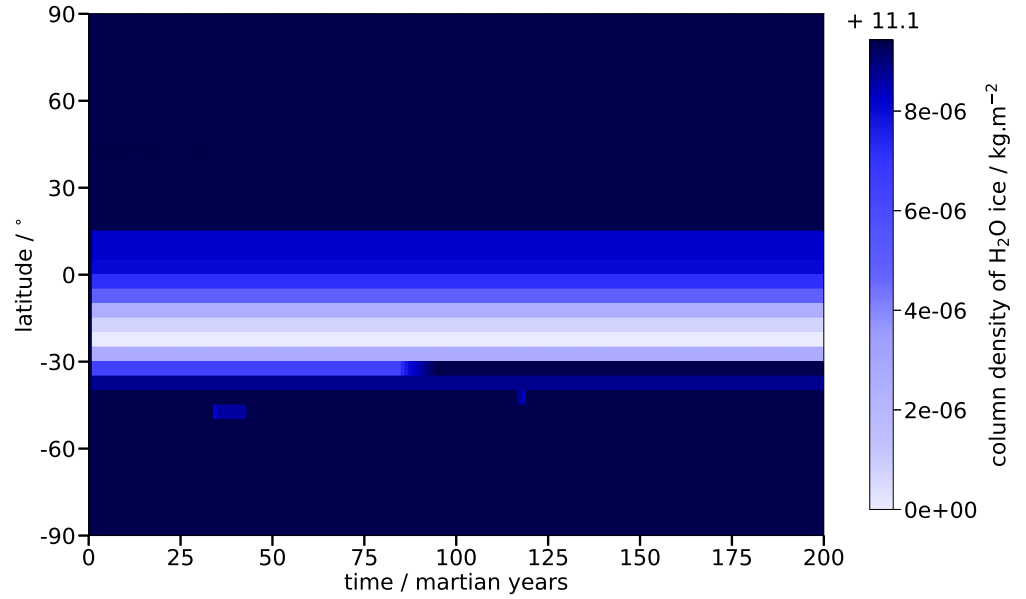
The CO₂ ice column density pattern over time also differs between the two scenarios with a basement unit. The CDS-SS-B structure produces a column density pattern that is symmetric around 25°S, correlating with the surface temperature distribution at $L_S = 0^\circ$ (the date of output in the 200 martian year simulations; Figure 3.16a). In these results, there is no clear distinction between the different latitude zones: polar, mid-latitude, and equatorial. In the simulations using the UR-CDS-B structure, on the other hand, these latitude zones can be clearly picked out in the northern region (Figure 5.11a). This is due to the influence of the thermal conductivities of the two subsurface structures (Figure 5.6c). While the higher thermal conductivity of CDS-SS-B regolith unit will result in faster sublimation rates (as discussed in the previous section), the change in thermal conductivity at the top of the basement unit will have a larger ef-

fect. In the CDS-SS-B structure, thermal conductivity drops from the sandstone value ($2.97 \text{ W m}^{-1} \text{ K}^{-1}$) to the basalt value ($1.75 \text{ W m}^{-1} \text{ K}^{-1}$) at 10 m, whereas in the UR-CDS-B, the thermal conductivity actually increases from $\sim 0.1 \text{ W m}^{-1} \text{ K}^{-1}$ (CDS) to $1.75 \text{ W m}^{-1} \text{ K}^{-1}$ (B) at this depth. Since thermal conductivity increases at the boundary in one subsurface structure, but decreases at the boundary in the other, the effect of the basement unit on temperature will be different. Figure 5.12 shows the difference in the average subsurface temperature between the simulation with the UR-CDS-B structure and the simulation with the CDS-SS-B structure. The differences between the two scenarios are also dependent on the hemisphere being considered, which is expected as the northern hemisphere is experiencing spring conditions, whereas in the southern hemisphere it is autumn. As the thermal conductivity of the subsurface increases, more heat is conducted deeper (and stored) during summer and then is released out of the subsurface during winter. Therefore, in the UR-CDS-B scenario, the large increase in thermal conductivity at the basement boundary causes an increase in conduction and storage of heat during summer and a corresponding release of heat in winter, resulting in cooler surface temperatures during summer and warmer temperatures during winter than when there is no basement unit. In the CDS-SS-B scenario, the opposite occurs and temperatures are warmer in summer and cooler in winter than when there is no basement unit. This in turn means that the UR-CDS-B scenario is expected to be warmer than the CDS-SS-B scenario during spring due to the extra heat released by the subsurface over winter, which causes the positive values that can be seen in the northern hemisphere (Figure 5.12). During autumn the reverse is expected with the average subsurface temperature being colder in the UR-CDS-B scenario due to the increased conduction and deeper storage of heat than in the CDS-SS-B scenario, which results in the negative values seen in the southern hemisphere (Figure 5.12).

The opposite effect of the basement unit on the two subsurface structure scenarios also impacts the behaviour of H_2O ice in the upper H_2O ice-filled regolith layer (Figure 5.13). While H_2O ice sublimates the most around 20° to 30°S in both scenarios, more sublimates away in the CDS-SS-B scenario than in the UR-CDS-B scenario. This is a consequence of the warmer summer subsurface temperatures in the CDS-SS-B scenario at these latitudes due to the thermal conductivity differences already discussed. These



(a) UR-CDS-B



(b) CDS-SS-B

Figure 5.13: Column density of H₂O ice at each latitude over time. For the (a) unconsolidated regolith to coarse dry sand with a basalt basement (UR-CDS-B) and (b) coarse dry sand to sandstone with a basalt basement (CDS-SS-B) sets of simulations. Grey represents where the H₂O ice column density is less than 0.0001 kg m⁻².

differences in the column densities of H₂O ice at these latitudes will impact the rate of sublimation of the underlying CO₂ ice and the bulk thermal conductivity of the upper subsurface. This in turn, will have contributed to the more distinct latitudinal zones that can be observed in the column density of CO₂ ice in the UR-CDS-B scenario (Figure 5.11a) compared with the CDS-SS-B scenario (Figure 5.11b). Another effect that can be seen in Figure 5.13a is the decrease then increase in H₂O ice column density in the first 50 martian years at 10°-20°S, which is due to the gradual decrease in temperature that occurs while the system reaches equilibrium in the first 50 martian years. In this time, subsurface temperatures decrease by ~2K in the upper few metres (Figure 5.14) which causes a gradual decrease in H₂O saturation vapour density. At the start of the simulation, the H₂O saturation vapour density is $3.5 \times 10^{-5} \text{ kg m}^{-3}$ which is reduced to $2.9 \times 10^{-5} \text{ kg m}^{-3}$ in the first 50 martian years. As a result, in the first 40-50 martian years (while temperatures are ~222 K), H₂O ice sublimates away rapidly based on the higher saturation vapour pressure, but when temperature drops to ~221 K, the corresponding drop in saturation vapour density is enough that the H₂O vapour density is now higher than saturation vapour density. This causes H₂O ice deposition until an equilibrium value is reached and is the cause of the increasing H₂O ice column density between 40 and 50 martian years at 12°S.

The distinct latitudinal zones in the UR-CDS-B scenario can be clearly seen in the estimates of the number of years it would take for CO₂ ice to fully sublimate away (Figure 5.15a). The estimates in this figure also show that, in general, CO₂ ice takes less time to fully sublimate away when the subsurface structure contains a coarse dry sand to sandstone (CDS-SS) regolith unit than for an unconsolidated regolith to coarse dry sand (UR-CDS) regolith unit, regardless of the presence of the basement unit below 10 m (UR-CDS-B and CDS-SS-B scenarios). This difference is due to both the smaller initial amount of CO₂ ice that the CDS-SS regolith unit can hold and the faster sublimation rate caused by the higher total thermal conductivity (and therefore higher temperatures in the lowest model layers) of the CDS-SS-B subsurface structure. However, this difference is not the case at all latitudes for the scenarios with a basement unit. Between 30° and 80°N, CO₂ ice sublimates away slower in the CDS-SS-B scenario than in the UR-CDS-B scenario, which is unexpected based on the higher

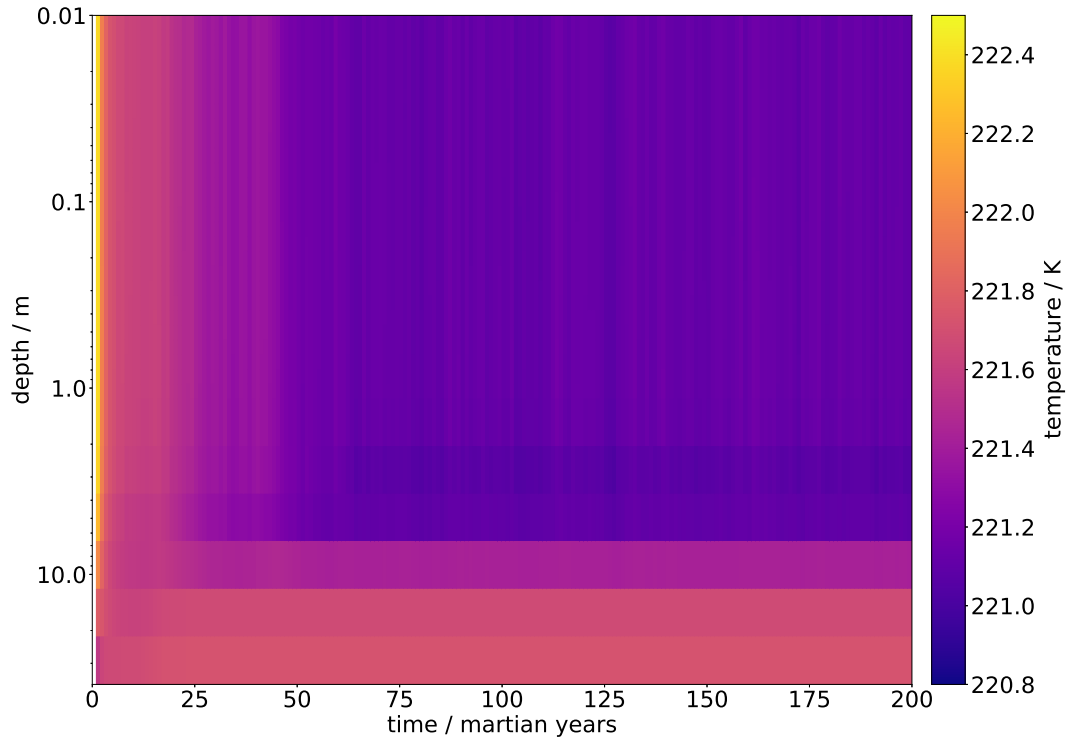
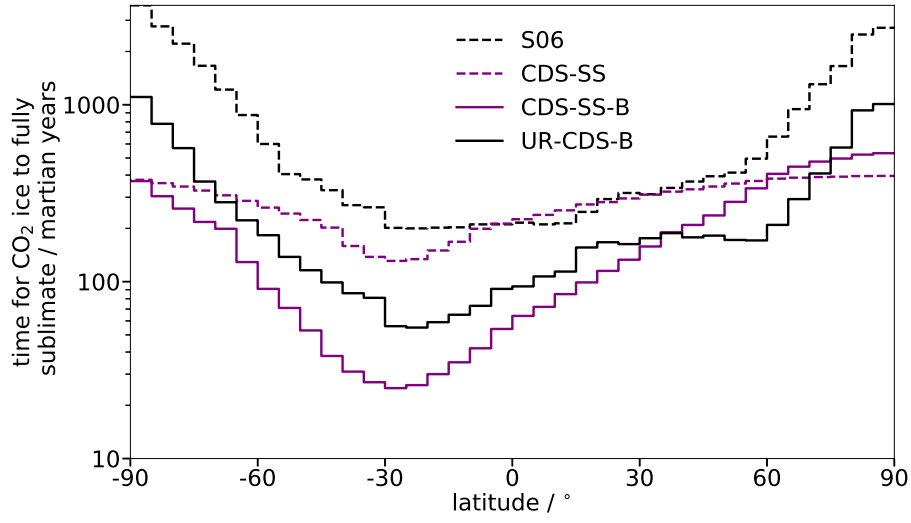
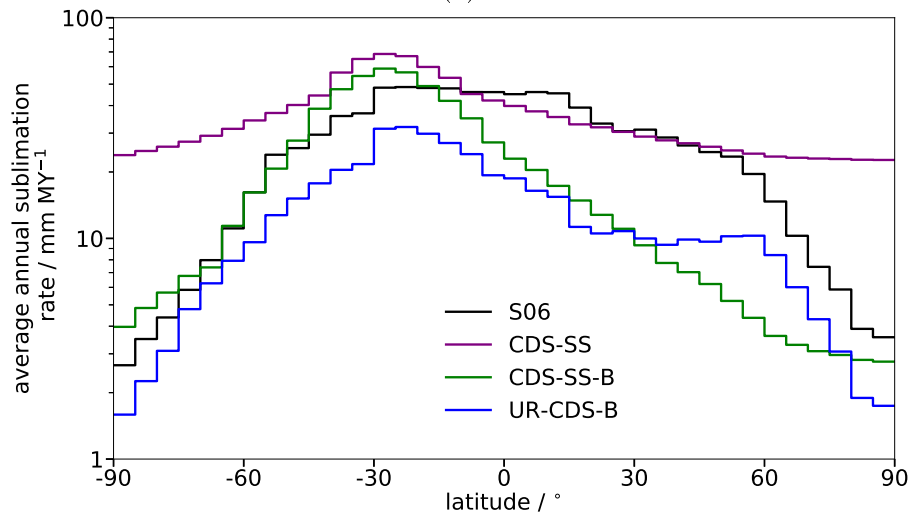


Figure 5.14: Subsurface temperature with depth over time at 12°S for the UR-CDS-B scenario.

thermal conductivities. At these latitudes, surface temperatures are warmer in the UR-CDS-B scenario (Figure 5.12), due to the differing thermal properties discussed earlier, which leads to CO₂ ice sublimating at a faster rate in the UR-CDS-B scenario (Figure 5.15a). This effect emphasises the importance of considering different subsurface structures with differing thermal properties, as the different thermal properties have a large influence on the number of years either ice can survive in the subsurface.



(a)



(b)

Figure 5.15: Comparison of (a) the number of years it takes to fully sublimate CO_2 ice and (b) the annual average sublimation rate for the different subsurface structures with a basement unit (UR-CDS-B and CDS-SS-B) and the same subsurface structures without a basement unit (S06 and CDS-SS). The different subsurface structures are: unconsolidated regolith to coarse dry sand with a basalt basement (UR-CDS-B) and coarse dry sand to sandstone with a basalt basement (CDS-SS-B).

5.3 Simulations with Multiple Ice-Layers

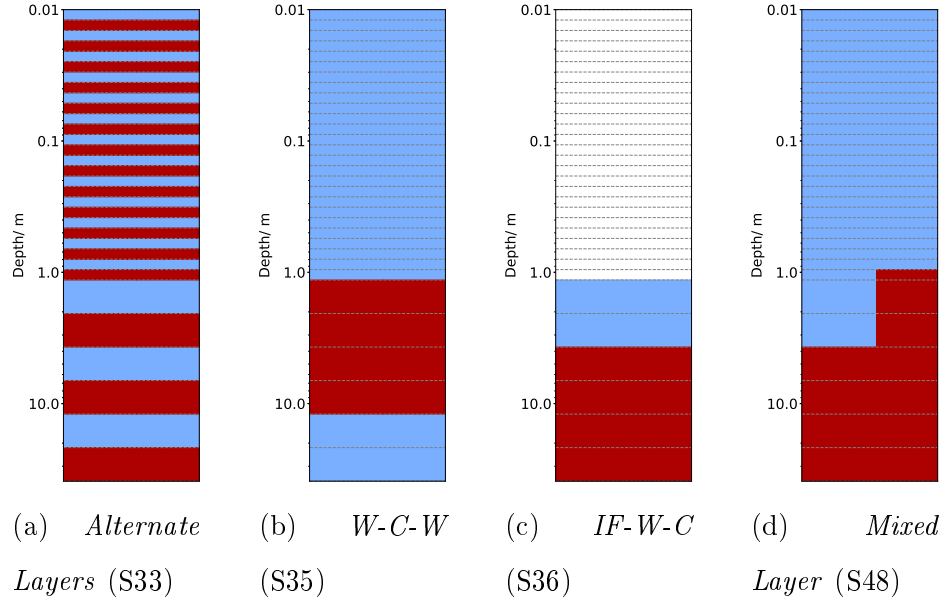


Figure 5.16: Initial subsurface profiles showing the distribution of H_2O ice and CO_2 ice for the (a) *Alternate Layers* (S33), (b) *W-C-W* (S35), (c) *IF-W-C* (S36) and (d) *Mixed Layer* (S48) scenarios. White represents an ice-free regolith, blue represents a H_2O ice-filled regolith and red represents a CO_2 ice-filled regolith. The dashed grey lines represent the boundary between model layers.

In the scenarios discussed so far, there are at most two ice-layers within the subsurface. This two-ice-layer structure is the simplest combination of the three different ice-layer types (ice-free regolith, H_2O ice-filled regolith, and CO_2 ice-filled regolith) that can be created. However, on Mars, a simple two-ice-layer structure is unlikely in many locations due to the cyclical nature of H_2O ice and CO_2 ice deposition caused by cycles in the orbital parameters. Particularly in the polar regions, where obliquity cycles have been demonstrated to produce layers of H_2O ice, CO_2 ice and dust, known as the polar layered deposits (PLD; e.g., Hvidberg et al., 2012; Phillips et al., 2011). Therefore, several more combinations of the three-ice-layer types have been run to investigate the effect of a more complex ice-layer combination on the rate of sublimation of each ice. Four different combinations were chosen: (i) Alternate Model layers of H_2O ice and CO_2 ice-filled regolith (*‘Alternate Layers’*; S33); (ii) H_2O Ice-filled Regolith Over CO_2 Ice-filled Regolith Over H_2O Ice-filled Regolith (*‘W-C-W’*; boundaries at 1 m and 10 m; S35); (iii) Ice-free Regolith Over H_2O Ice-filled Regolith Over CO_2 Ice-filled Regolith

(‘*IF-W-C*’; boundaries at 1 m and 4 m; S36); and (iv) H₂O Ice-filled Regolith Over CO₂ Ice-filled Regolith With A Mixed Layer between 1 and 4 m (‘*Mixed Layer*’; 50% of each ice in the mixed layer; S48). The initial H₂O ice (blue) and CO₂ ice (red) subsurface profiles for these scenarios are shown in Figure 5.16 and a summary of where these scenarios could be found on Mars is in Table 5.3.

Table 5.3: Locations on Mars where the multiple ice-layer configurations could be found.

Ice-layer configuration	Location on Mars
Alternate Model Layers of H ₂ O Ice and CO ₂ Ice-filled Regolith	This scenario could occur throughout the year at low obliquity, when the seasonal deposition and sublimation of H ₂ O ice and CO ₂ ice occurs. H ₂ O ice will be deposited first due to its higher frost point temperature, followed by CO ₂ ice later in the year. Each year the deposition of H ₂ O ice will occur before CO ₂ ice forming alternating layers of varying thickness depending on the amount of sublimation that occurs during summer. These alternating layers will be smaller than the layers observed within the SPLD which are 10s-100s m thick (Phillips et al., 2011).
H ₂ O Ice-filled Regolith Over CO ₂ Ice-filled Regolith over H ₂ O Ice-filled Regolith	This scenario has been observed within the SPLD, where there are multiple alternating layers of H ₂ O ice capping a CO ₂ ice-layer which also overlies another H ₂ O ice-layer (Bierson et al., 2016; Phillips et al., 2011). The formation of these alternating layers is caused by variations in the orbital parameters. It has been suggested that H ₂ O ice forms over CO ₂ ice either as obliquity cycles between high and low obliquity (Buhler et al., 2019) or from the longitude of perihelion shifting from northern winter to northern summer during a low obliquity period (Manning et al., 2019).

Continuation of table 5.3	
Ice-layer configuration	Location on Mars
Ice-free Regolith Over H ₂ O Ice-filled Regolith over CO ₂ Ice-filled Regolith	This scenario could have occurred within the PLD, after an H ₂ O ice-layer formed over the CO ₂ ice-layer. During the summer season, the overlying H ₂ O ice-layer would sublimate away leaving a lag deposit of dust which protects the underlying H ₂ O ice.
	This scenario could also have occurred in the mid-latitudes during the Noachian. At this time, atmospheric pressures were higher and CO ₂ ice could have deposited in the mid-latitudes due to the higher frost point temperature (~ 195 K). This CO ₂ ice-layer could have then been covered by a H ₂ O ice-layer that remained stable for longer as atmospheric pressures decreased. When H ₂ O ice became unstable at the surface and started to sublimate away, a lag layer would form, protecting the H ₂ O ice from rapid sublimation as observed today. This may have protected the underlying CO ₂ ice for a few hundred to thousand years, but not enough that CO ₂ ice would survive to the present-day.
H ₂ O Ice-filled Regolith Over CO ₂ Ice-filled Regolith With A Mixed Layer	This scenario could occur when a period of H ₂ O ice deposition follows CO ₂ ice deposition, as has been proposed by Buhler et al. (2019) and Manning et al. (2019) when the orbital parameters change. There may be a period of co-deposition of H ₂ O ice and CO ₂ ice forming a mixed layer of both H ₂ O ice and CO ₂ ice.

Continuation of table 5.3	
Ice-layer configuration	Location on Mars
	<p>This scenario can also be used as a proxy for the existence of CO₂ clathrate hydrates (Section 2.1.4) between a layer of pure H₂O ice and a layer of pure CO₂ ice which has been suggested by Hoffman (2000). This theory suggests that H₂O ice and CO₂ ice will not be deposited directly after each other, instead suggesting that a layer of CO₂ clathrate hydrates would form in between. Since the MSSM does not have the equations for CO₂ clathrate hydrates included, this acts as an initial exploration into what the effects of a mixed layer would be.</p>

The column density of CO₂ ice results for the four multi-layer scenarios are shown in Figure 5.17. An important thing to note when comparing these results is the large differences in initial column densities of CO₂ ice, which have led to the different scales used for each figure. In all four scenarios, the three latitudinal zones (polar, mid-latitude and equatorial), and the behaviours within each latitudinal zone, follow the same pattern as surface temperature (Figures 3.16a and 4.23c). This latitudinal pattern can be seen in all scenarios where CO₂ ice takes longer than 20 martian years to fully sublimate in the equatorial region and has already been discussed in detail for the two layer scenarios in Chapter 4 so will not be discussed here.

In the *Alternate Layers* scenario (S33), there is one third less CO₂ ice at the beginning of the scenario than in the *W-C* scenario (S06), which suggests that the CO₂ ice would take less time to fully sublimate. However, between the two scenarios, the global average annual sublimation rate is reduced from 25.75 mm MY⁻¹ in S06 to 14.57 mm MY⁻¹ in S33, showing that CO₂ ice in the *Alternate Layers* scenario (S33) will actually take longer to sublimate away than in the *W-C* (S06) scenario. This is partially due to the low porosity of the entire subsurface which results in low CO₂ diffusion coefficients throughout the subsurface (Figure 5.18a). While the CO₂

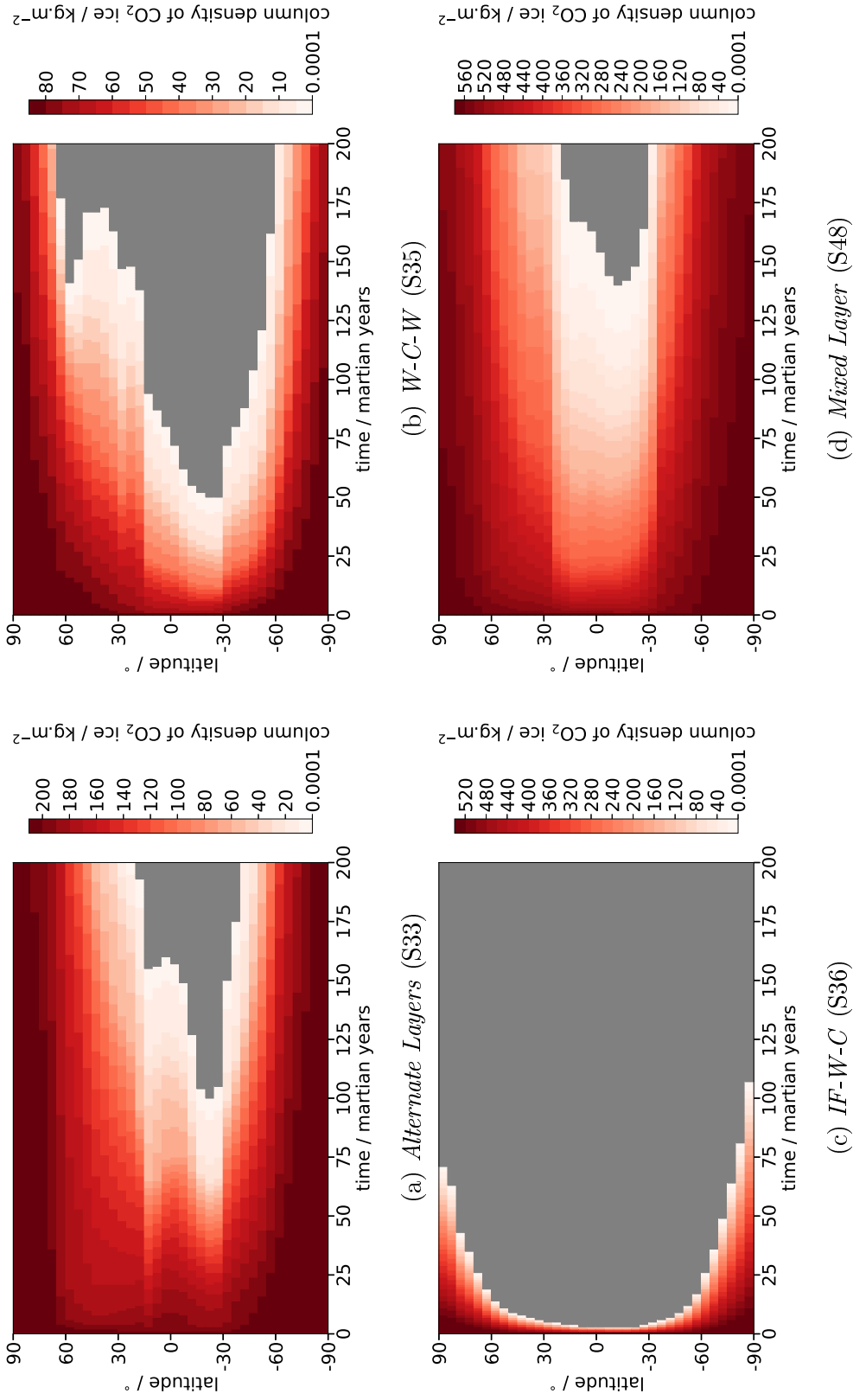


Figure 5.17: Column density of CO₂ ice over time for the (a) *Alternate Layers* (S33), (b) *W-C-W* (S35), (c) *IF-W-C* (S36) and (d) *Mixed Layer* (S48) scenarios. The colour scales for each figure are different due to the large differences in the initial column density of CO₂ ice. Grey represents where the CO₂ ice column density is less than 0.0001 kg m⁻².

diffusion coefficient increases as CO₂ ice sublimates away, the consistently low CO₂ diffusion coefficient at every other model layer (where H₂O ice fills the pore space) inhibits vapour diffusion, limiting the amount of CO₂ ice sublimation that can occur. Another factor that will slow the rate of sublimation is the large swings in thermal conductivity at each model layer (Figure 5.19) due to the large difference in thermal conductivity between H₂O ice-filled regolith ($\sim 3.5 \text{ W m}^{-1} \text{ K}^{-1}$ at 160 K and $\phi_r = 0.63$) and CO₂ ice-filled regolith ($\sim 0.6 \text{ W m}^{-1} \text{ K}^{-1}$ at 160 K and $\phi_r = 0.63$). The alternating ice-layers cause the average thermal conductivity of the upper metre of the subsurface to be lower than it would be if the pore space was only filled by H₂O ice (as in S06), resulting in a smaller warming effect from the presence of ice and reducing the amount of both ices that needs to sublimate for vapour density to reach saturation vapour density in each time step. The combination of these factors all increase the stability of CO₂ ice implying that having many thin layers of both H₂O ice and CO₂ ice (as in S33) increases the stability of the CO₂ ice more than a single H₂O ice-filled regolith layer over a CO₂ ice-filled regolith layer (S06). Especially considering the significantly smaller initial column density of CO₂ ice in the *Alternate Layers* scenario.

The *W-C-W* scenario (S35) is initialised with the smallest CO₂ ice column density ($\sim 80 \text{ kg m}^{-2}$), but a large portion of this initial amount remains after 200 martian years in both polar regions. This suggests that the CO₂ ice-filled regolith layer being surrounded by H₂O ice-filled regolith layers does increase the stability of CO₂ ice. The rate of vapour diffusion does not appear to be the cause of the increased stability of CO₂ ice in the *W-C-W* scenario (S35) compared with the *Alternate Layers* scenario (S33). This is because the CO₂ diffusion coefficient is similar between the two scenarios (Figures 5.18a and 5.18b; S33 and S35) as both are initialised with ice filling the entire pore space and have very low porosities. This increased stability is more likely to be due to the thermal conductivity differences between the scenarios (Figure 5.19), since the average initial thermal conductivity is $3.21 \text{ W m}^{-1} \text{ K}^{-1}$ for S35, whereas it is only $2.17 \text{ W m}^{-1} \text{ K}^{-1}$ for S33. The higher average thermal conductivity results in cooler temperatures during summer and warmer temperatures during winter (as discussed previously), which reduces the seasonal fluctuations in the rate of sublimation. Overall, this has the effect of reducing the global average annual sublimation

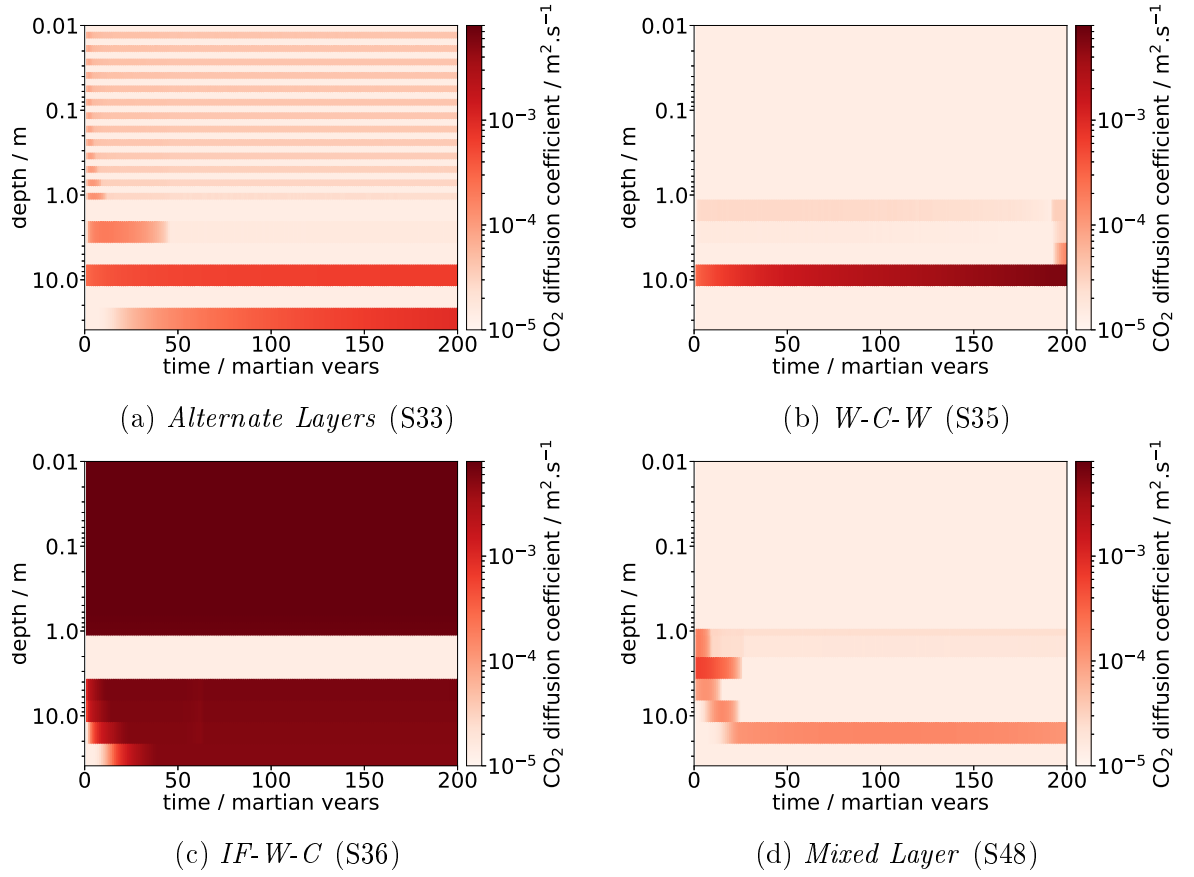


Figure 5.18: CO₂ diffusion coefficient at 77°S for the (a) *Alternate Layers* (S33), (b) *W-C-W* (S35), (c) *IF-W-C* (S36) and (d) *Mixed Layer* (S48) scenarios.

rate (averaged across all latitudes when CO₂ ice is present) from 25.75 mm MY⁻¹ (S06) to 12.57 mm MY⁻¹ (S35). This sublimation rate is significantly smaller and since this scenario (S35) is close to that observed within the SPLD where CO₂ ice-layers have been detected between H₂O ice-layers (see Section 2.4.1; Phillips et al., 2011), it could explain the large volumes of CO₂ ice that have survived within the SPLD.

The *IF-W-C* scenario (S36) is the only multi-layer scenario that has no CO₂ ice remaining by the end of the 200 martian years simulation (Figure 5.17c), despite the fact this scenario contains over double the initial column density of CO₂ ice ($\sim 520 \text{ kg m}^{-2}$) compared with the previous two scenarios discussed ($\sim 200 \text{ kg m}^{-2}$ and $\sim 80 \text{ kg m}^{-2}$ in S33 and S35, respectively). The rapid sublimation of CO₂ ice in this scenario is due to the larger CO₂ diffusion coefficient across the entire ice-free regolith layer (Figure 5.18c). The CO₂ diffusion coefficient in the ice-free regolith layer is over two orders of magnitude larger than the diffusion coefficient at nearly all depths in the other scenarios (Figure 5.18). The large diffusion coefficient rapidly removes CO₂

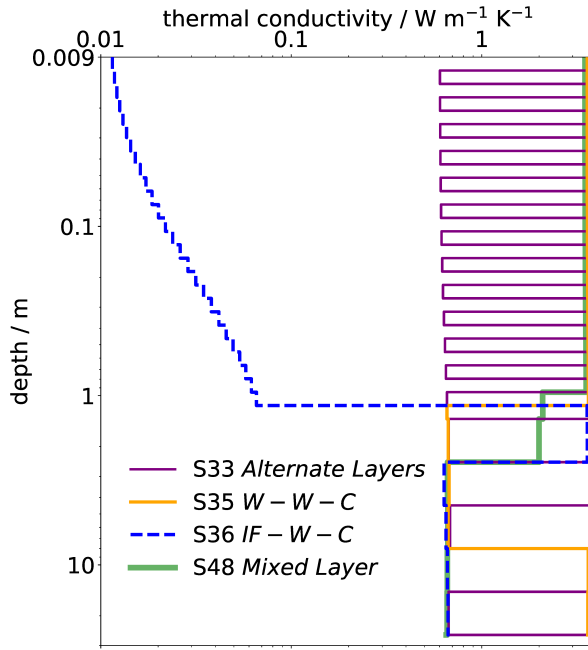


Figure 5.19: Thermal conductivity profiles for each of the multiple-ice-layer scenarios.

vapour from the model layers containing CO₂ ice into the ice-free regolith layers and out into the atmosphere. Since CO₂ saturation vapour density can be up to two orders of magnitude higher than the atmospheric vapour density in the equatorial region of Mars, large amounts of CO₂ vapour will be removed from the CO₂ ice-filled regolith model layers into the ice-free model layers by diffusion, causing a similarly large amount of sublimation to occur in the CO₂ ice-filled regolith model layers in response. This process is reflected in the global average annual sublimation rate which is 1125.36 mm MY⁻¹ in this scenario (S36), significantly higher than the 25.75 mm MY⁻¹ global average annual sublimation rate of the *W-C* scenario (S06). However, the global average annual sublimation rate is still lower than that of the Ice-free Regolith over CO₂ Ice-filled Regolith (*IF-C*) scenario (1812 mm MY⁻¹; S09), showing that the presence of the overlying H₂O ice-filled regolith does increase the stability of the CO₂ ice. The results from this scenario show that the presence of an overlying porous layer will cause the rapid loss of CO₂ ice and that even the presence of an overlying H₂O ice-filled regolith layer to cap the CO₂ ice-filled regolith layer will not stabilise CO₂ ice enough for it to survive 200 martian years.

The final multiple layer scenario is similar to the *W-C* scenario (S06) discussed previously, but the boundary between the model layers with only H₂O ice filling the pore space and those with CO₂ ice filling the pore space is more diffuse. Instead of a

sharp boundary, there is a 4 m region that contains 50% H₂O ice and 50% CO₂ ice within the pore space (Figure 5.16d). While it is unlikely that CO₂ ice and H₂O ice will be deposited in equal amounts at the same time, it has been suggested that an intermediate zone of CO₂ clathrate hydrates would form between a pure H₂O ice and a pure CO₂ ice-layer (e.g., Hoffman, 2000, see Section 2.1.4 for details on CO₂ clathrate hydrates). The mixed layer used in this scenario is a proxy for a CO₂ clathrate hydrate layer as the equations for CO₂ clathrate hydrates are not included in the MSSM. The CO₂ ice column density results from this scenario (Figure 5.17d) have the largest portion of the initial CO₂ ice column density remaining after 200 martian years in the multiple-ice-layer scenarios. However, part of this is caused by the larger initial column density of CO₂ ice ($\sim 560 \text{ kg m}^{-2}$), since the initial column density of this scenario is the closest to that of the *W-C* scenario (S06) and the largest of the four multiple-ice-layer scenarios. Therefore, looking at the annual average sublimation rate is needed to see if CO₂ ice is more or less stable in this scenario (S48). The annual average sublimation rate of S48 (32.25 mm MY^{-1}) is actually higher than that of the other multiple layer scenarios with CO₂ ice remaining after 200 martian years (14.57 mm MY^{-1} and 12.57 mm MY^{-1} for S33 and S35, respectively) implying that CO₂ ice is less stable in this scenario. The rate of vapour diffusion through the subsurface is not the cause of the higher sublimation rate, since the porosity of the subsurface remains relatively low throughout the subsurface until CO₂ ice has begun to sublimate away, as in both the *Alternate Layers* (S33) and *W-C-W* (S35) scenarios. The higher sublimation rate is instead due to the lower thermal conductivity caused by the presence of the mixed layer instead of a H₂O ice-filled regolith as in S06. This results in warmer temperatures in summer and cooler temperatures in winter. The warmer summer temperatures result in higher saturation vapour densities and more sublimation, which can be seen in Figure 5.17d. Therefore, the presence of the mixed H₂O ice and CO₂ ice filled regolith layer actually acts to reduce the stability of CO₂ ice within the subsurface.

Estimates of the number of years it would take for each initial column density of CO₂ ice to fully sublimate for each of the multiple layer scenarios can be seen in Figure 5.20, showcasing the importance of layering on the amount of time CO₂ ice can survive within the subsurface. The estimates shown in this figure are calculated using the

average annual sublimation rate for each latitude and the initial CO₂ column density for the scenario, rather than the number of years to fully sublimate a fixed quantity of CO₂ ice. Based on the column density of CO₂ ice results (Figure 5.17), it would be expected that CO₂ ice survives the longest in the *Mixed Layer* scenario (S48). However, the estimates in Figure 5.20 show that while CO₂ ice takes longer to sublimate away in the *Mixed Layer* scenario (S48) for the southern hemisphere, CO₂ ice actually takes slightly longer to sublimate away in the *Alternate Layers* scenario (S33) for the northern hemisphere. This is especially interesting because the *Mixed Layer* scenario (S48) is initialised with over double the CO₂ column density that the *Alternate Layers* scenario (S33) is initialised with. This suggests that small alternating layers of pore space filled with each ice increases the stability of CO₂ ice more than a single large H₂O ice-filled regolith layer overlying the CO₂ ice-filled regolith layer. This is supported by the decrease in global average sublimation rate between the two scenarios: 25.8 mm MY⁻¹ in the *W-C* scenario (S06) and 14.5 mm MY⁻¹ in the *Alternate Layers* scenario (S33).

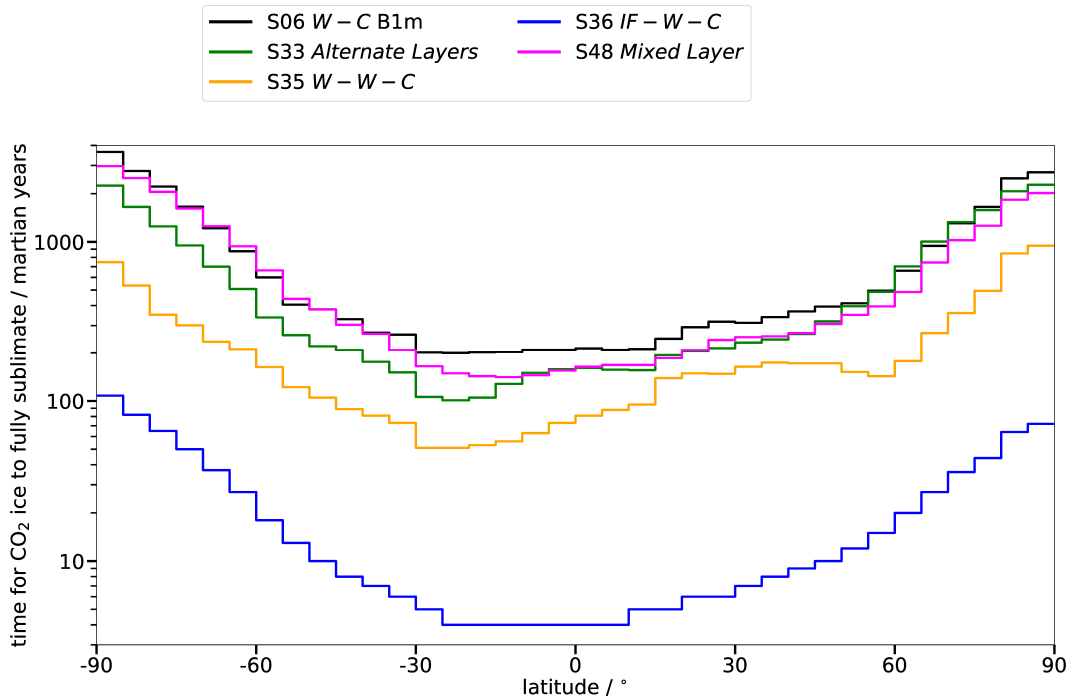


Figure 5.20: Comparison of the number of years that CO₂ ice survives for the multi-layer scenarios and the baseline simulation (S06).

From the annual average sublimation rates discussed earlier, CO₂ ice would also be expected to take a similar number of years to fully sublimate in the *W-C-W* scenario (S35) as in the *Alternate Layers* (S33) and *Mixed Layer* scenarios (S48). However,

the drastically smaller initial column density of CO₂ ice ($\sim 80 \text{ kg m}^{-2}$ compared with 200 kg m^{-2} and 560 kg m^{-2}) means the estimated number of years is not entirely comparable. Since the annual average sublimation rate is lowest for the *W-C-W* scenario (12.57 mm MY^{-1}), for the same initial column density as the other multi-layer scenarios, it would be expected for CO₂ ice to survive the longest in the *W-C-W* scenario (S35). However, this may not be the case due to the change in thermal properties that would occur with the increased column density of CO₂ ice.

CO₂ ice sublimates away the fastest in the final scenario (*IF-W-C* scenario; S36) as is expected from the earlier discussion and this configuration of ice-layers would therefore not allow any buried CO₂ ice to survive for long at the present obliquity. These results suggest that subsurface ice layering is one of the most important factors for CO₂ ice stability. They also imply that there needs to be no ice-free regolith and the presence of at least one H₂O ice-filled regolith layer for CO₂ ice to survive more than 100 martian years in the mid-latitude and polar regions, for the column densities considered.

5.4 Summary

The simulations that use different initial ice porosities, subsurface structures, and ice-layer configurations all have a considerable influence on the rate of CO₂ ice sublimation. This influence is largest in the polar regions, where the number of years it takes for an initial column density to fully sublimate varies from 100 to 7000 martian years across the scenarios. The simulations using different subsurface structures and initial ice porosities were run using an initial ice-layer configuration of a *W-C* (boundary at 1 m) so the simulations could be compared directly with S06 from Chapter 4.

The scenarios with different initial ice porosities (ranging from 0 to 0.1) test the assumption that there is always a small amount of porosity remaining within the subsurface. This assumption is required for vapour equilibrium with the atmosphere to be maintained when the pore space of each model layer is filled with ice. Since the main effect of initial ice porosity is to limit the rate of vapour diffusion, which in turn limits the rate of sublimation, smaller initial ice porosities are expected to increase the

amount of time CO_2 ice can survive in the subsurface. The results show this expected outcome of CO_2 ice taking longer to fully sublimate away at all latitudes when the initial ice porosity is smaller (Figure 5.5). They also show that the porosity of the overlying ice-layer needs to be lower than 0.01 for CO_2 ice to survive longer than 1000 martian years in the polar regions.

Five different subsurface structures were also investigated to test the impact of the geological materials chosen for the baseline version of the MSSM on CO_2 ice sublimation. Each subsurface structure has a different porosity profile (Figure 5.6b) and the subsurface structures with larger porosities can hold more ice within their pore space. This leads to CO_2 ice surviving longer in the subsurface structures that can hold more CO_2 ice initially, as expected. The differing thermal properties of each subsurface structure (Figure 5.6c) also impact the rate of CO_2 ice sublimation, but are a secondary influence compared with the initial column density of CO_2 ice. However, the effect of the differing thermal conductivities cannot be easily separated from the effect of the differing initial CO_2 ice column densities in these simulations, so the thermal properties may have a larger influence than can be seen in these results.

The multiple-ice-layer scenarios were run to investigate how the layering of H_2O ice-filled regolith, CO_2 ice-filled regolith, and ice-free regolith impacts the stability of CO_2 ice in the subsurface. The results show that the presence of an ice-free regolith layer causes CO_2 ice to sublimate faster than if the pore space of the entire subsurface is initially filled with ice (Figure 5.20) due to higher diffusion coefficients. This is consistent with the results from two layer scenarios with an ice-free regolith layer in Chapter 4. When all of the pore space is filled with one of the two ices, the diffusion coefficient remains consistently low across the entire subsurface, limiting the amount of sublimation by the rate of vapour removal from the subsurface. In these scenarios, the thermal conductivity of the subsurface is instead a greater influence on the sublimation rate. In the scenarios with higher thermal conductivities, sublimation rates are slower and CO_2 ice takes longer to sublimate away.

In summary, the number of years that CO_2 ice takes to fully sublimate away within the subsurface is highly dependent on the porosity, amount of each ice present, and

the thermal properties of the subsurface. All of these factors will be highly variable across the surface of Mars and a single scenario cannot be used to represent the expected behaviour at each latitude and longitude. Despite this, the simulations run can be used to indicate different locations where CO₂ ice is expected to remain stable for longer, provided deposition of CO₂ ice occurs in these locations under different atmospheric conditions (higher atmospheric pressure or different obliquity).

6 | How does Mars' orbital obliquity change the stability of CO₂ ice and H₂O ice within the subsurface?

The orbital obliquity of Mars has a large control on the distribution of subsurface ices, because it impacts the latitudinal distribution of solar insolation, which in turn affects temperatures and atmospheric circulation (discussed in Sections 2.7.1 and 2.8; e.g., Laskar et al., 2004; Levrard et al., 2004; Toon et al., 1980). As obliquity increases, solar insolation on the polar regions increases, while solar insolation on the equatorial region decreases. Figure 6.1 shows the position of the polar region (60-90°N/S) at each obliquity investigated in this thesis (15°, 25°, 35°, and 45°). The effect of this change on the distribution of surface carbon dioxide (CO₂) ice and water (H₂O) ice has been studied (e.g. Levrard et al., 2004; Mischna et al., 2003), alongside studies of the effect of obliquity on subsurface H₂O ice (e.g., Richardson et al., 2003; Schorghofer and Aharonson, 2005).

At low obliquities (<20°), the equatorial regions receive the largest proportion of annual solar insolation and the polar regions are at their coldest. Under these conditions, large permanent CO₂ polar caps form that extend further equatorward than under present-day conditions (25° obliquity; Forget et al., 2017; Toon et al., 1980). Seasonal variations are also smaller than at moderate obliquities (~25°) and atmospheric circulation is weaker (Newman et al., 2005). At high obliquities, on the other hand, the polar regions experience the largest temperature variations and permanent polar caps are no longer stable (e.g. Mischna et al., 2003; Toon et al., 1980). Instead, large seasonal CO₂ polar caps form that extend even further equatorward than the permanent CO₂ polar caps that form at low obliquity (Jakosky and Carr, 1984). During the summer season, H₂O ice is exposed at the poles and sublimates away, migrating

towards the mid-latitudes at high obliquities ($\sim 35^\circ$) and building up large deposits of H_2O ice, such as the Latitude Dependent Mantle (LDM) and the Lobate Debris Aprons (LDAs) that have been observed in the present-day (Holt et al., 2008; Mischna et al., 2003; Mustard et al., 2001). Under present-day atmospheric pressures, the stability of subsurface CO_2 ice is expected to follow a similar pattern to surface CO_2 ice: stable throughout the year at low obliquity and only seasonally stable at high obliquities. This chapter aims to investigate how the sublimation rate of CO_2 ice is impacted by each obliquity for the scenarios already discussed across the previous chapters.

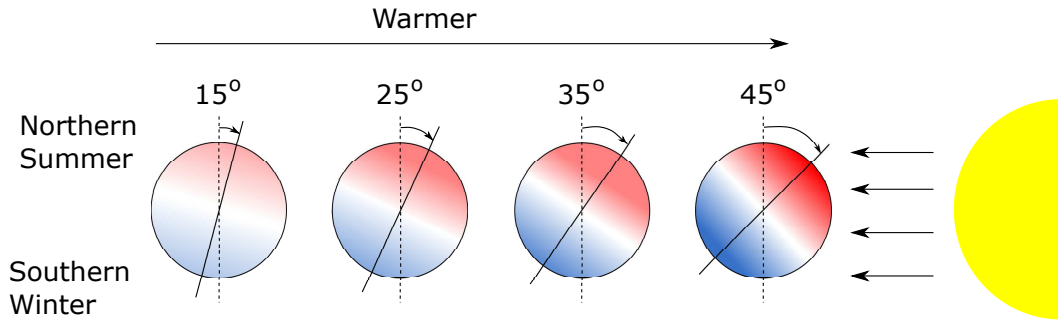


Figure 6.1: The effect of the tilt of Mars on northern summer and southern winter temperatures relative to 0° obliquity for four obliquities: 15° , 25° , 35° , and 45° . The red colour represents warmer temperatures and the blue colour represents colder temperatures than for the corresponding season at 0° obliquity, with the strength of the colour representing the magnitude of this difference.

Section 6.1 summarises the initial atmospheric profiles for each obliquity (15° , 35° and 45°) and Section 6.2 summarises initial subsurface profiles used for the scenarios that are discussed for each obliquity in this chapter. The results for each obliquity (15° , 35° , and 45°) are then discussed separately (Sections 6.3, 6.4, and 6.5, respectively). These results are then all compared with each other and the previous present-day results in Section 6.6, alongside a discussion of the implications of these results.

6.1 Atmospheric Profiles

To investigate the role of obliquity, the atmospheric annual cycles that are used for the surface condition in the Martian Subsurface Model (MSSM) have to be updated to reflect the change in atmospheric conditions that occurs with obliquity. This was done using the same method as for the 25° obliquity atmospheric profiles (see Section

3.7.1), by taking the outputs from the final year of a 4 martian year LMD-UK Mars global circulation model (MGCM) simulation that was initialised using the restart files from a 20 martian year spin up run for each obliquity (15° , 35° , and 45°). The annual surface temperature, pressure, H_2O vapour density and CO_2 vapour density profiles for the three obliquities were then taken from the final year of their respective obliquity MGCM simulation. The MGCM outputs were zonally averaged and diurnally averaged to produce the final profiles. The profiles for each property show the expected annual patterns at each obliquity and these cycles are briefly summarised here. As discussed for the atmospheric profiles for the 25° obliquity (Section 3.7.1), the higher CO_2 vapour density values in northern winter at latitudes 55° – 80°N are due to the higher surface pressures, which will have increased both the CO_2 frost point temperature and the saturation vapour density.

In the 15° obliquity atmospheric profiles (Figure 6.2), polar conditions (temperature and vapour densities) remain low enough for permanent CO_2 polar caps to persist throughout the year. Although there is a portion of the year (~ 550 to ~ 650 sols) when surface temperatures rise to above the CO_2 frost point ($\sim 145\text{ K}$; Kasting, 1991), which will impact the survival of CO_2 ice in the subsurface. This can be seen in Figure 6.3a which shows the annual surface CO_2 ice cycle from the final year of the 15° obliquity simulation. In this figure, the surface CO_2 ice that remains throughout the year has built up over the 24 martian years of simulation rather than representing the thickness of the total CO_2 ice reservoir that would form over an obliquity cycle. CO_2 ice remains at the surface throughout the year at the highest northern polar latitudes, with a decrease in the column density over northern summer, reaching a minimum seasonal thickness of 1.6 m (assuming no porosity). In the southern polar region, surface CO_2 ice also persists throughout the year, but the amount that exists from sol 500 to sol 100 is significantly less than in the northern hemisphere. The minimum thickness of CO_2 ice at the southern pole is only 30 cm if the CO_2 ice exists as a solid slab with no porosity. However, this CO_2 ice is likely to contain some porosity and is unlikely to completely seal the underlying subsurface. The CO_2 ice thicknesses in both hemispheres are built up over the 24 martian years of the MGCM simulation and these thicknesses will therefore be smaller than would be expected on Mars since obliquity varies over

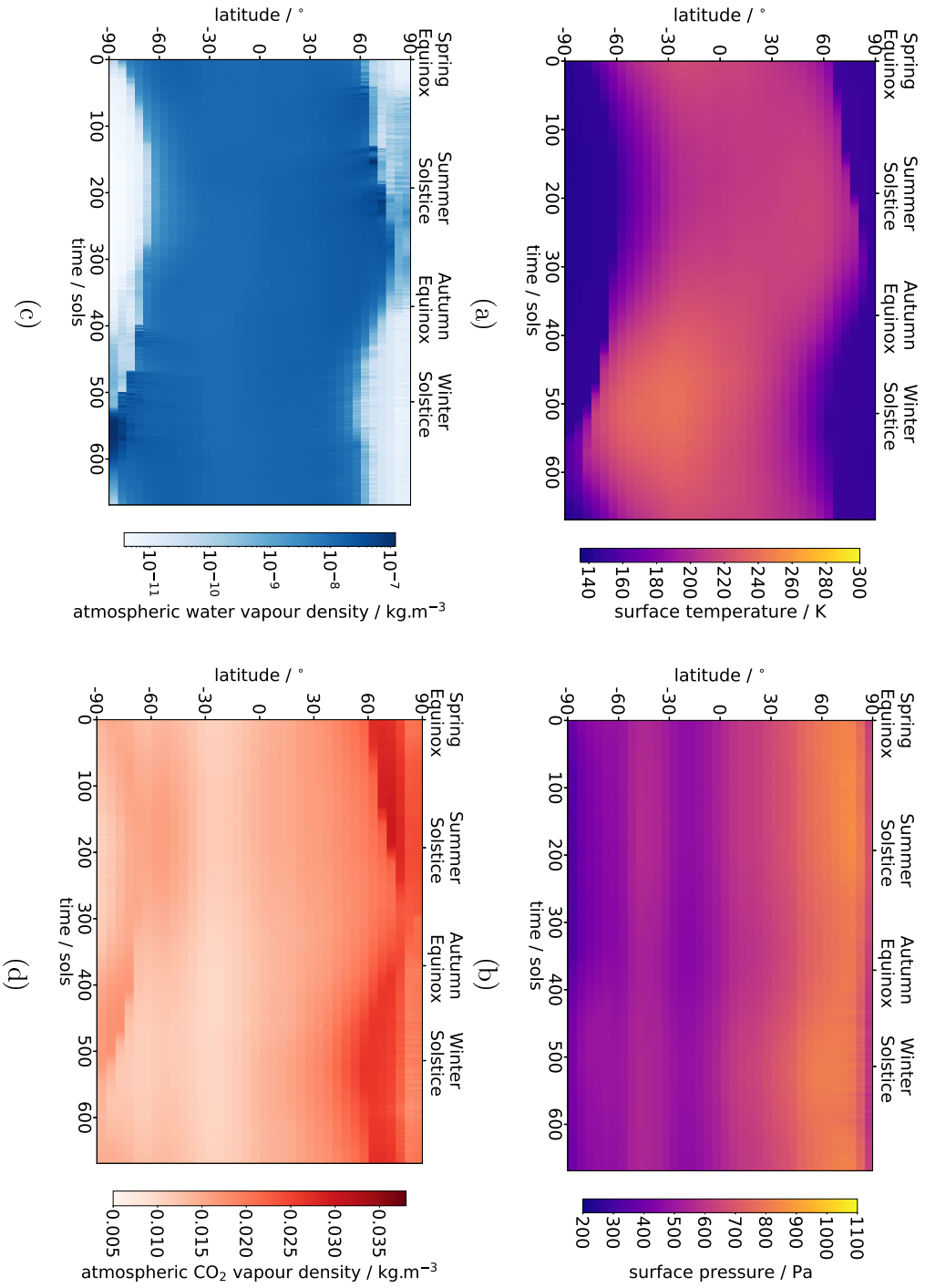


Figure 6.2: Longitudinal averages as a function of latitude over time for the surface (a) temperature, (b) pressure, (c) H_2O vapour and (d) CO_2 vapour cycles from the MGCM simulation at an obliquity of 15° . The values are taken from the lowest atmospheric layer in the MGCM to represent the near-surface atmospheric values.

tens of thousands of years, so more CO₂ ice would have built up over that time.

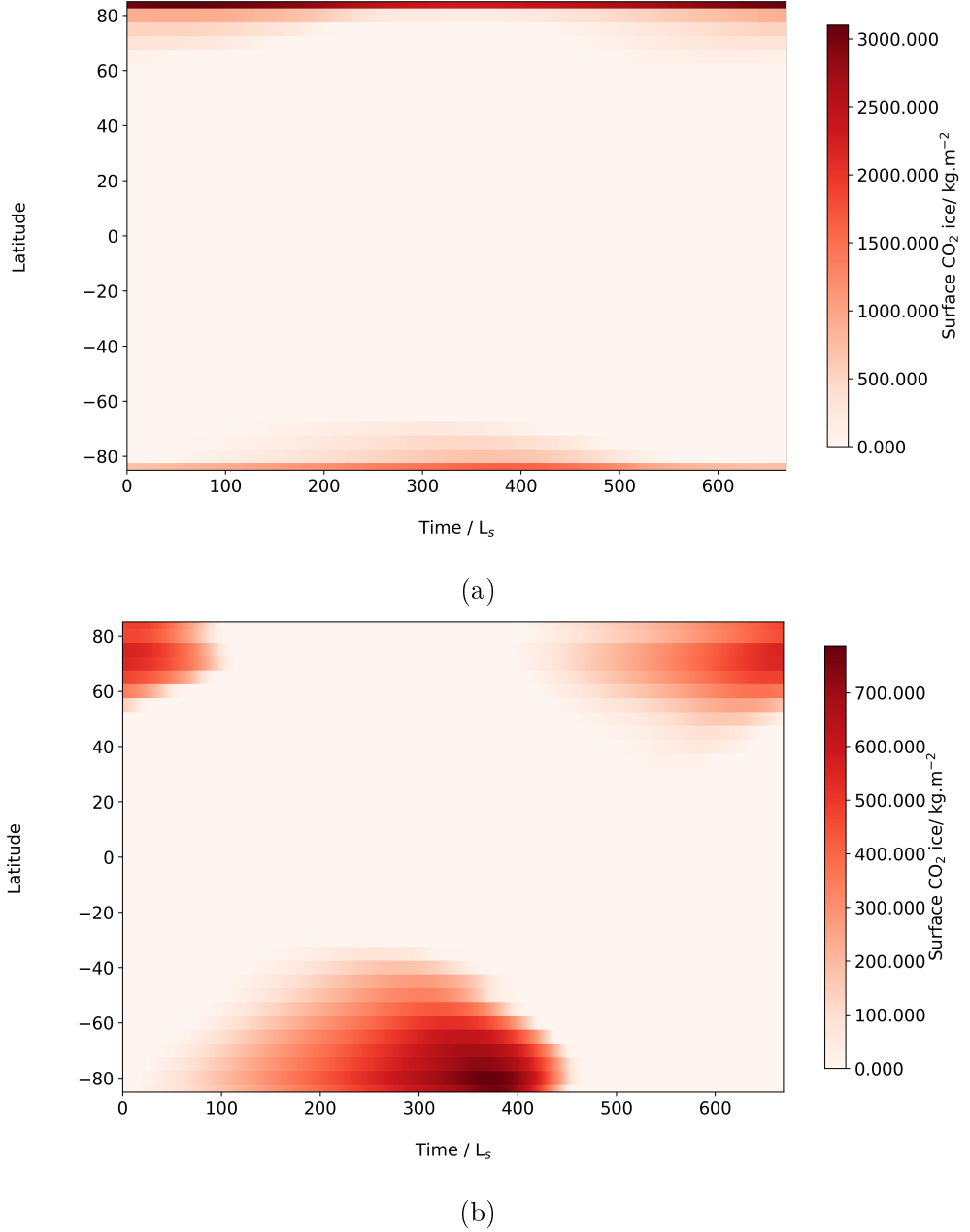


Figure 6.3: Longitudinal averages as a function of latitude over time for the surface CO₂ ice and H₂O ice cycles from the obliquity = (a) 15° and (b) 45° MGCM simulations.

In both the 35° (Figure 6.4) and 45° (Figure 6.5) obliquity atmospheric profiles, polar conditions (temperature and vapour densities) are too high during the summer seasons for permanent CO₂ ice caps to be stable. Instead, large seasonal CO₂ ice caps that can extend down to $\sim 45^\circ$ N/S form during winter, as shown in Figure 6.3b (from the 45° obliquity MGCM simulation). The formation of large seasonal polar caps is consistent with the findings of previous high obliquity studies (see Section 2.7.1.1; e.g., Jakosky, 1985a; Richardson and Wilson, 2002) and will mean that any initial

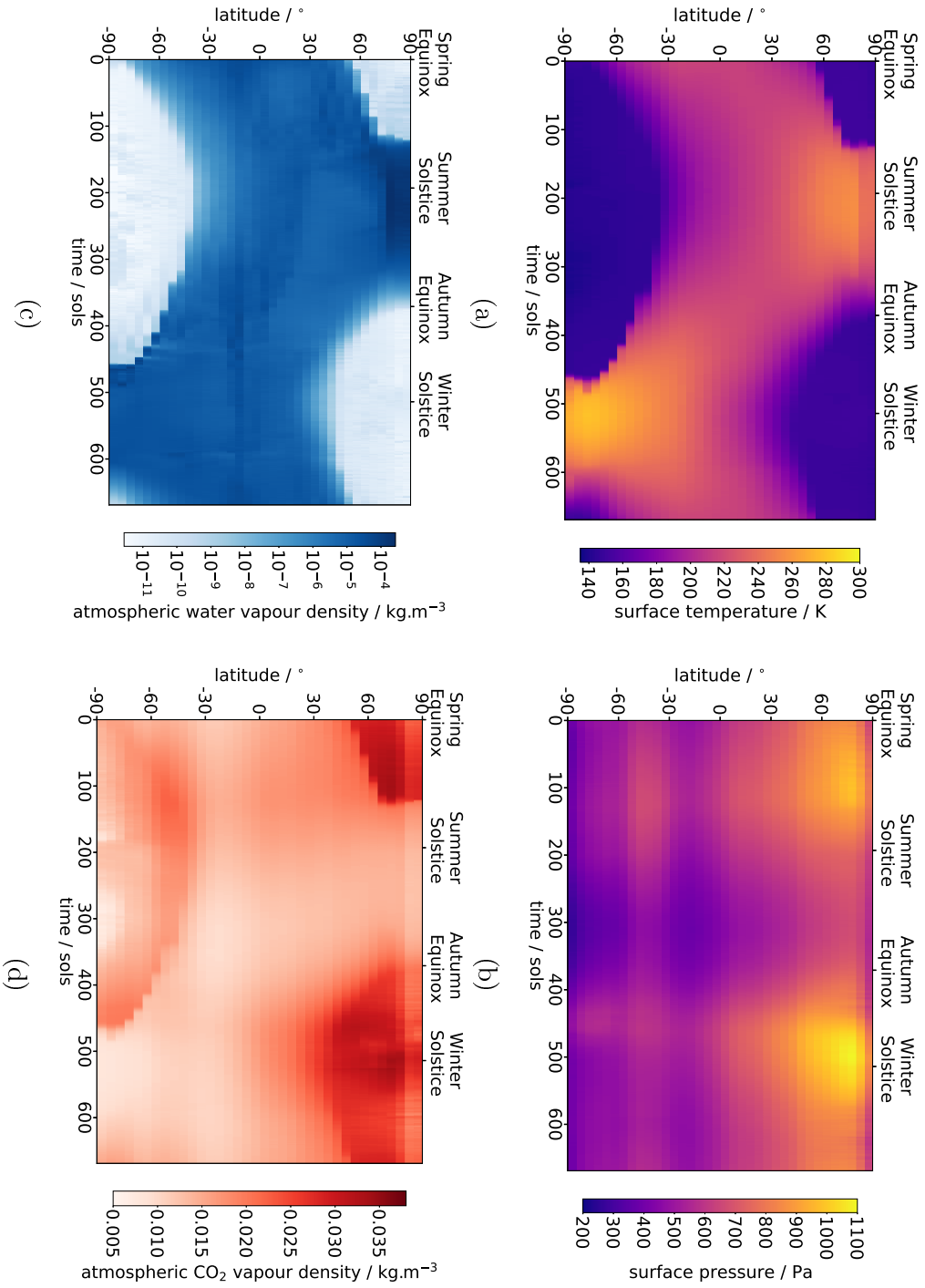


Figure 6.4: Longitudinal averages as a function of latitude over time for the surface (a) temperature, (b) pressure, (c) H_2O vapour and (d) CO_2 vapour cycles from the MGCM simulation at an obliquity of 35°. The values are taken from the lowest atmospheric layer in the MGCM to represent the near-surface atmospheric values.

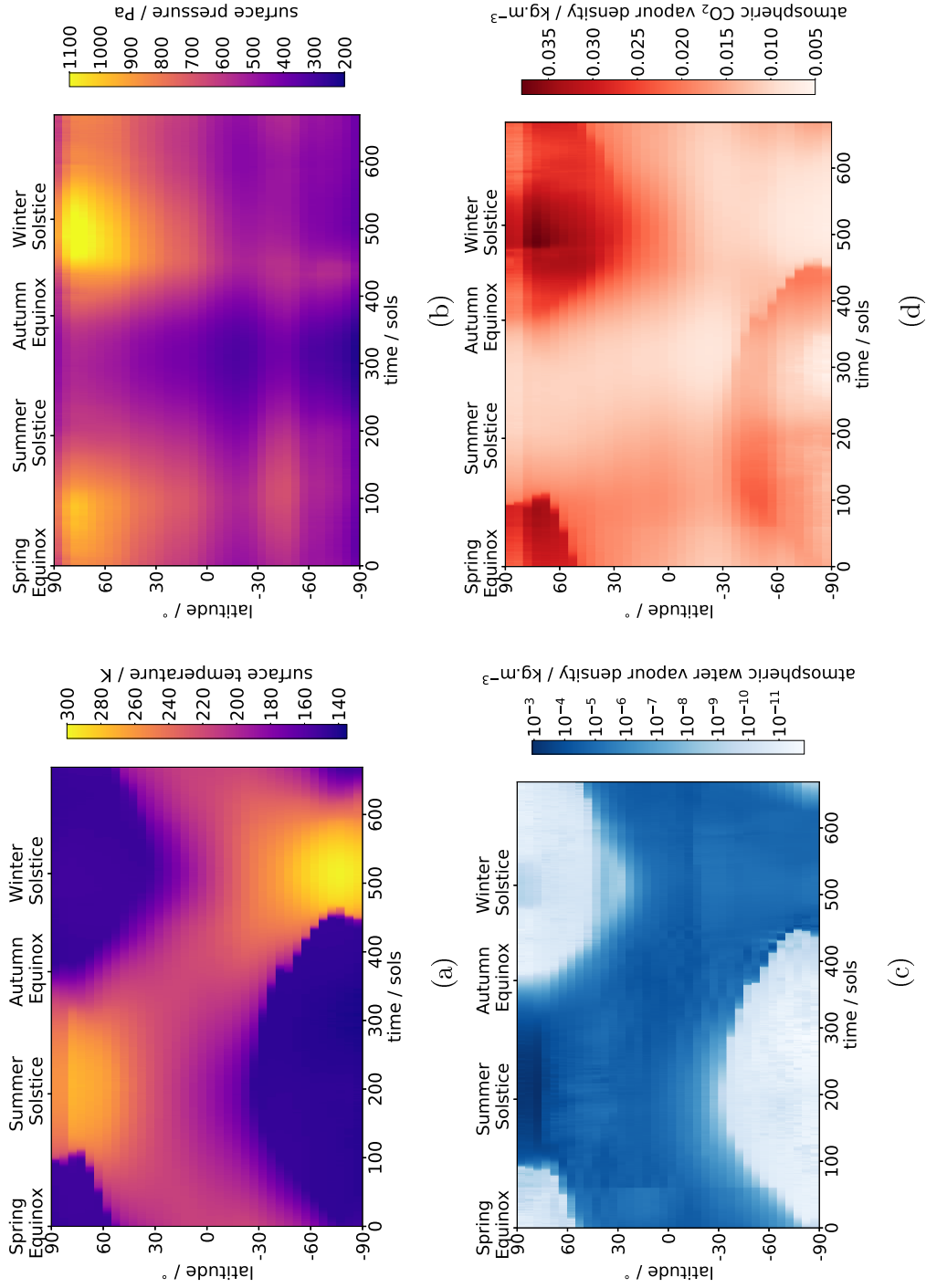


Figure 6.5: Longitudinal averages as a function of latitude over time for the surface (a) temperature, (b) pressure, (c) H_2O vapour and (d) CO_2 vapour cycles from the MGCM simulation at an obliquity of 45° . The values are taken from the lowest atmospheric layer in the MGCM to represent the near-surface atmospheric values.

subsurface CO₂ ice should be expected to sublimate away over time. Since CO₂ ice is unstable at both poles, rather than only at the northern pole as is the case when obliquity is 25°, CO₂ ice is expected to take less time to fully sublimate away in the polar regions for all scenarios when obliquity is high (35° or 45°). In the mid-latitude and equatorial regions, however, the changes in atmospheric conditions with increased obliquity are expected to increase the stability of CO₂ ice compared with when obliquity is 25°, such as the lower winter temperatures (which remain at or below the H₂O frost point temperature) and pressures (since lower pressure reduces the difference between saturation vapour pressure and atmospheric pressure). This is based on the increased stability of H₂O ice in these regions with increasing obliquity (see Section 2.7.1.1; e.g., Mischna et al., 2003). However, the increased stability with increasing obliquity is expected to be insufficient for subsurface CO₂ ice deposits to persist permanently, since surface temperatures remain above the CO₂ frost point for most of the year in the equatorial and mid-latitude regions (Figures 6.4a and 6.5a).

6.2 Subsurface Ice Profiles

The scenarios discussed throughout Chapters 4 and 5 were investigated using the atmospheric profiles for each of the three obliquities (15°, 35°, and 45°). These results can then be compared with the previously discussed results for the same scenarios run with the atmospheric profiles for the present-day obliquity (25°). Explanations for why each scenario is relevant to Mars can be found in Tables 4.2 and 5.3. As in the previous chapters, the scenarios are referred to by an acronym (a list of these acronyms can be found in Chapter VII) and each simulation has a short code (e.g. S01) with a prefix referring to the version of the MSSM used and the run number. This code can be used to look up the details of the simulation in Table VII.III (for the 25° obliquity simulations) and Table VII.V for all of the simulations at the other three obliquities (15°, 35°, and 45°). Sublimation rates from all scenarios can be found in Appendix C.

The influence of obliquity on the stability of CO₂ ice can be seen across all scenarios, with the expected higher CO₂ ice stability at low obliquity and lower CO₂ ice stability at high obliquity in the polar region. In the scenarios that are initialised with similar ice-layer configurations, the impact of the different obliquities is consistent between them.

An example is the H₂O Ice-filled Regolith Over CO₂ Ice-filled Regolith (*W-C*) and H₂O Ice-filled Regolith Over CO₂ Ice-filled Regolith With A Mixed Layer (*Mixed Layer*) scenarios, which are both initialised with a H₂O ice-filled regolith layer over a CO₂ ice-filled regolith layer. The influence of the H₂O ice-filled regolith layer on temperature and porosity is similar for both scenarios at an obliquity of 25°, as discussed in Section 5.3. In the simulations with these initial scenarios at each obliquity, the influence of the different atmospheric conditions shows the same effects across both scenarios and, therefore, the simulations initialised with the *W-C* scenario for each obliquity can be used to represent the effect of obliquity on the *Mixed Layer* scenario as well. The same principle has been applied to the Ice-free Regolith over CO₂ Ice-filled Regolith (*IF-C*), Ice-free Regolith Over H₂O Ice-filled Regolith Over CO₂ Ice-filled Regolith (*IF-W-C*) and CO₂ Ice-filled Regolith Over H₂O Ice-filled Regolith (*C-W*) scenarios, since all show rapid CO₂ ice loss at a 25° obliquity due to the lack of a protective ice-filled layer directly below the surface to reduce the rate of vapour diffusion. The *IF-W-C* scenario is, therefore, used to represent all three of these scenarios in this chapter, since CO₂ ice takes the longest to sublimate in this scenario (*IF-W-C*) out of the three. The final two initial ice-layer scenarios (H₂O Ice-filled Regolith Over CO₂ Ice-filled Regolith Over H₂O Ice-filled Regolith, ‘*W-C-W*’, and Alternate Model layers of H₂O ice and CO₂ ice-filled regolith, ‘*Alternate Layers*’) are also discussed for all obliquities, due to the differences in the stability of CO₂ ice across these and the *W-C* and *IF-W-C* scenarios. Figure 6.6 shows a schematic diagram of the four ice-layer scenarios discussed in this chapter: the *W-C*, *IF-W-C*, *W-C-W*, and *Alternate Layers* scenarios.

A simulation with ice-free regolith across the entire subsurface (*IF*) was also run for all obliquities to use as a baseline simulation for comparison, which was also done for the 25° obliquity atmospheric profiles. Similar to the results from the 25° *IF* simulation, at an obliquity of 15°, no H₂O or CO₂ ice forms at any latitude. At obliquities of 35° and 45°, CO₂ ice still does not form, but H₂O ice forms at nearly every latitude (see Figure 6.7). This is because of the fixed atmospheric cycle used as the surface condition of the MSSM. The atmospheric cycle (for all obliquities) is taken from one of the MGCM simulations (see Sections 3.7.1 and 6.1 for details). The surface H₂O and CO₂ vapour

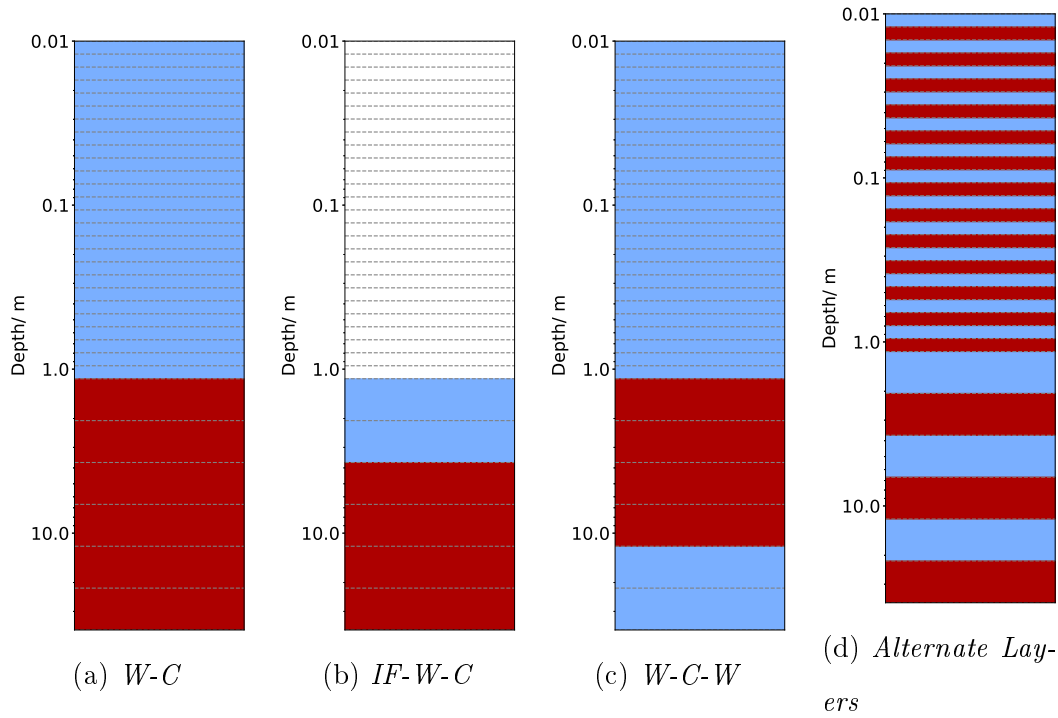
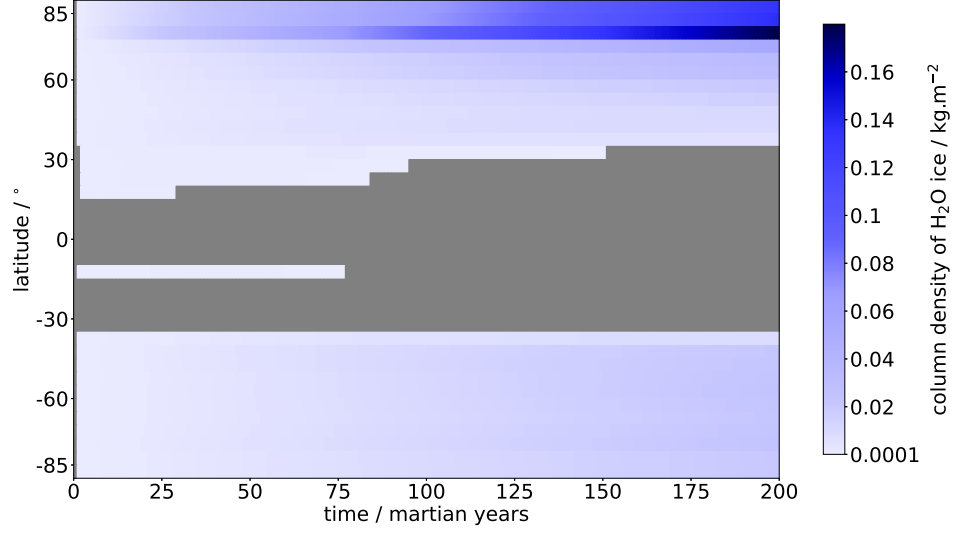


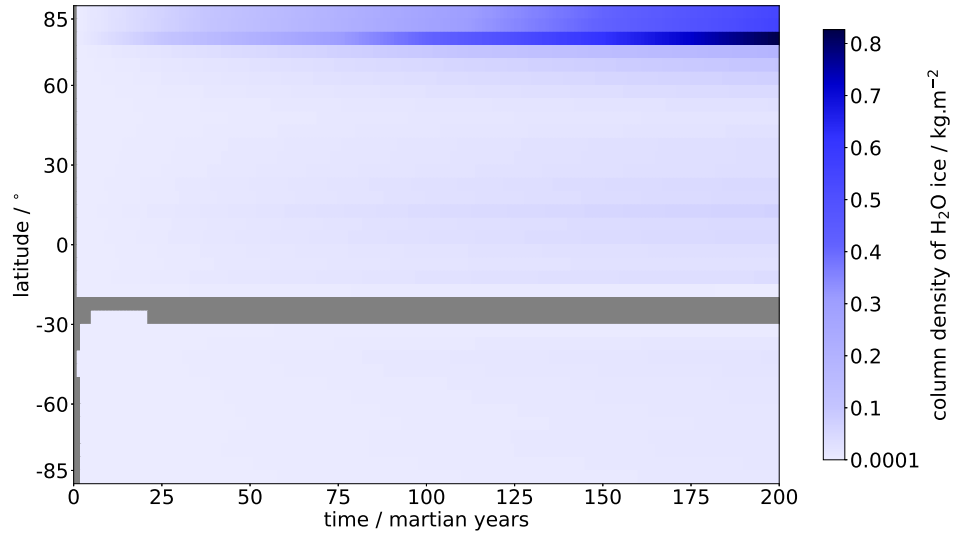
Figure 6.6: Initial subsurface profile schematics showing the distribution of H₂O ice and CO₂ ice for the four scenarios: (a) *W-C*, (b) *IF-W-C*, (c) *W-C-W*, and (d) *Alternate Layers*. White represents an ice-free regolith, blue represents a H₂O ice-filled regolith and red represents a CO₂ ice-filled regolith.

densities taken from these runs, are the vapour densities after deposition has occurred. This means that in places where either ice is deposited, the vapour density will be at the saturation vapour density and when used as the surface boundary for the MSSM, there is no excess vapour for any ice to form. The small amounts of H₂O ice ($<0.2 \text{ kg m}^{-3}$) that form in the high obliquity *IF* MSSM simulations are a consequence of the atmosphere behaving as a constant source when the H₂O vapour density in the uppermost subsurface layer is lower than the atmospheric vapour density. In the *IF* scenarios, the H₂O vapour density in the uppermost subsurface layer is likely to be lower than the atmospheric value since the vapour that is diffused from the surface into this uppermost layer is further diffused into the subsurface. This can increase the vapour density in the lower subsurface layers to above the saturation vapour density, while the vapour density in the uppermost layer remains close to the atmospheric vapour density.

The lack of deposition of CO₂ ice and the small amounts of H₂O ice deposition will likely reduce the survival time of both CO₂ ice and H₂O ice over time. Further work



(a) 35° obliquity (S27)



(b) 45° obliquity (S28)

Figure 6.7: Column density of H₂O ice at each latitude over time for the *IF* set of simulations at (a) 35° obliquity (S27) and (b) 45° obliquity (S28). Grey represents where the H₂O ice column density is less than 0.0001 kg m⁻².

will be needed using a full global circulation model (GCM) with the MSSM integrated into it to determine the extent of this impact.

6.3 Obliquity = 15°

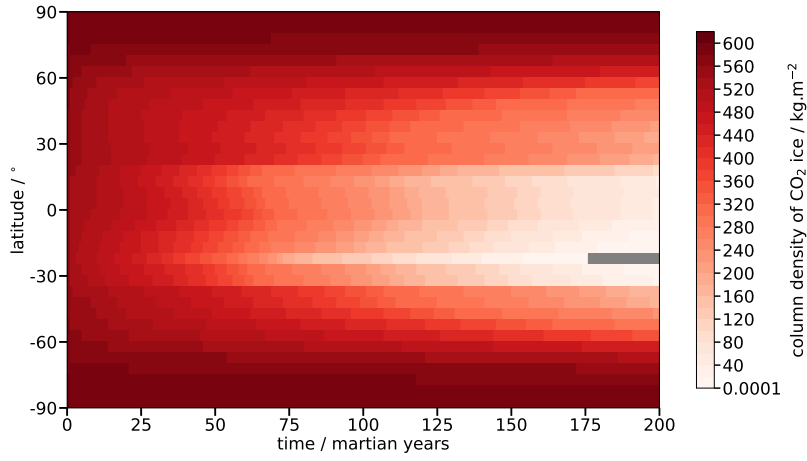
Simulations using the four chosen initial subsurface scenarios (discussed in the previous section) were run using the 15° obliquity atmospheric profiles shown in Figure 6.2 and the results from these simulations are shown across Figures 6.8 and 6.9, alongside the results for the *IF-C* scenario. The differences in the column density of CO₂ ice over time for these scenarios compared with those discussed in previous chapters for a 25° obliquity follow the expected patterns based on the differences in the atmospheric profiles. Sublimation in the equatorial regions occurs at roughly the same rate (or slightly faster), while in the polar regions, CO₂ ice sublimates at a slower rate than in the equivalent 25° obliquity simulations for all scenarios. CO₂ ice within the equatorial region is expected to sublimate at a similar rate because surface temperatures and pressures within this region are almost the same between the two obliquity scenarios throughout the year, whereas in the polar regions, surface temperatures are cold enough for CO₂ ice to be stable for most of the year and, based on previous studies of surface CO₂ ice, permanent polar caps are expected to build up.

The similar sublimation rate in the equatorial region (15°N to 35°S) can be seen in the *W-C* scenario results (S15; Figure 6.8a), with an equatorial sublimation rate of 43.7mm MY⁻¹ at 25° obliquity (S06) and 44.4mm MY⁻¹ at 15° obliquity (S15). Across this region, the column density of CO₂ ice remaining after 200 martian years is nearly the same as from the 25° obliquity simulation (Figure 4.9b). The main difference between the two scenarios is that CO₂ ice fully sublimates in 175 martian years at 25°S when the obliquity is 15° rather than in 199 martian years when obliquity is 25°. This difference is due to the redistribution of solar insolation that occurs as obliquity decreases (see Section 2.7.1.2), which causes minimum winter temperatures (Figure 6.2a) to be ~20 K higher than they are when obliquity is 25° (Figure 3.16a). The higher winter temperatures result in more sublimation throughout the year and are the cause of CO₂ ice fully sublimating away faster at 20°S when obliquity is 15°.

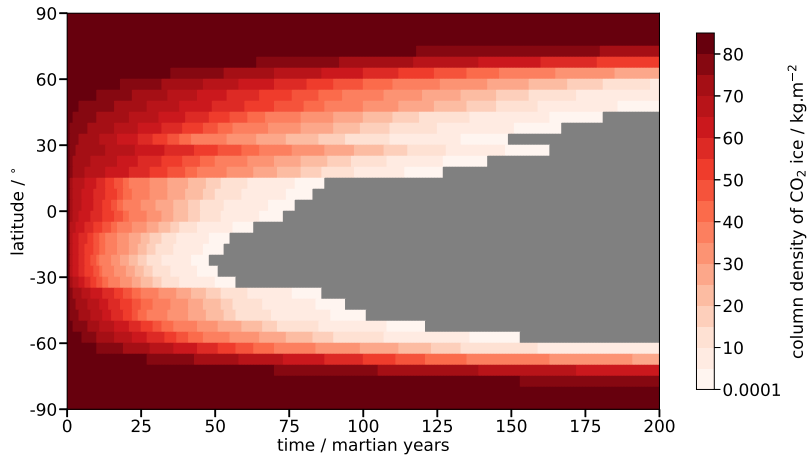
The greater stability of CO₂ ice in the polar regions when obliquity is 15° can also be seen in the *W-C* (S15), *Alternate Layers* (S37), and *Mixed Layer* (S40) scenario results (Figure 6.8). In these scenarios, nearly all of the initial column density of CO₂ ice remains after 200 martian years in the polar regions. This is due to the very low annual sublimation rate ($\sim 3.26 \text{ mm MY}^{-1}$ on average) in the polar regions caused by the presence of H₂O ice within the subsurface. In the model layers containing H₂O ice, the pore space is low which results in a small diffusion coefficient and since any layers containing CO₂ ice are overlain by a H₂O ice-filled regolith layer in these scenarios, CO₂ ice sublimation is then limited by the rate of diffusion through the H₂O ice-filled regolith layers (as previously discussed in Sections 4.3.2 and 5.3).

The increased stability of CO₂ ice in the polar regions can also be seen when comparing the results from the *IF-C* (S16) and *IF-W-C* (S43) simulations (Figure 6.9) with their equivalent 25° obliquity simulations (S09 and S36, respectively). In the *IF-C* simulation at an obliquity of 15°, CO₂ ice sublimation rate (81.5 mm MY^{-1} at 88°N) is an order of magnitude smaller than when obliquity is 25° (262 mm MY^{-1} at 88°N), resulting in CO₂ ice taking nearly three times as long to fully sublimate away in the polar regions (Figure 4.5a). While in the *IF-W-C* scenario, some CO₂ ice remains after 200 martian years when obliquity is 15°, whereas CO₂ ice fully sublimates within 110 martian years at an obliquity of 25° (S36; Figure 5.17c). This is due to the slower sublimation rate when obliquity is 15° (44.2 mm MY^{-1} at 88°N) than when obliquity is 25° (131 mm MY^{-1} at 88°N). While the increased stability of CO₂ ice as obliquity decreases can be observed in these results, CO₂ ice still sublimates at a faster rate in these scenarios than in those with a H₂O ice-filled regolith layer near the surface (Figure 6.8). This is due to the ice-free regolith layer having a higher porosity (and therefore diffusion coefficient) than the layers containing ice. This allows CO₂ vapour from the model layers containing CO₂ ice to be transported away at a faster rate than if the ice-free regolith layers contained ice, therefore increasing the sublimation rate of CO₂ ice.

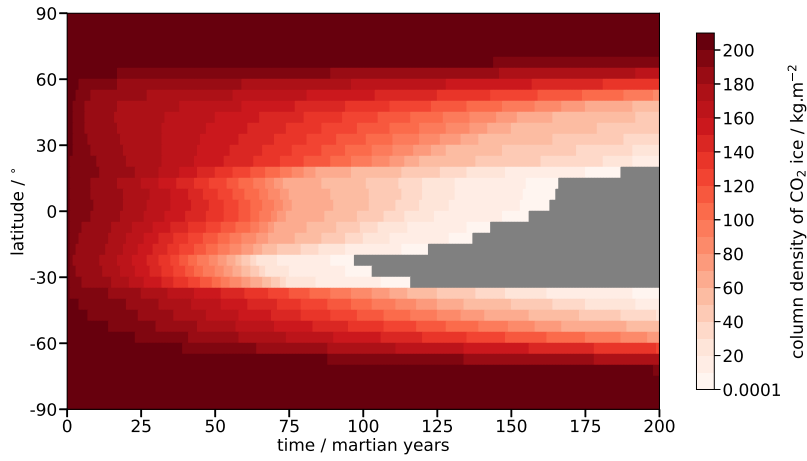
The average annual sublimation rate can be used to estimate the number of years that it will take for the initial amount of CO₂ ice to fully sublimate (Figure 6.10). As



(a) *W-C* (S15)

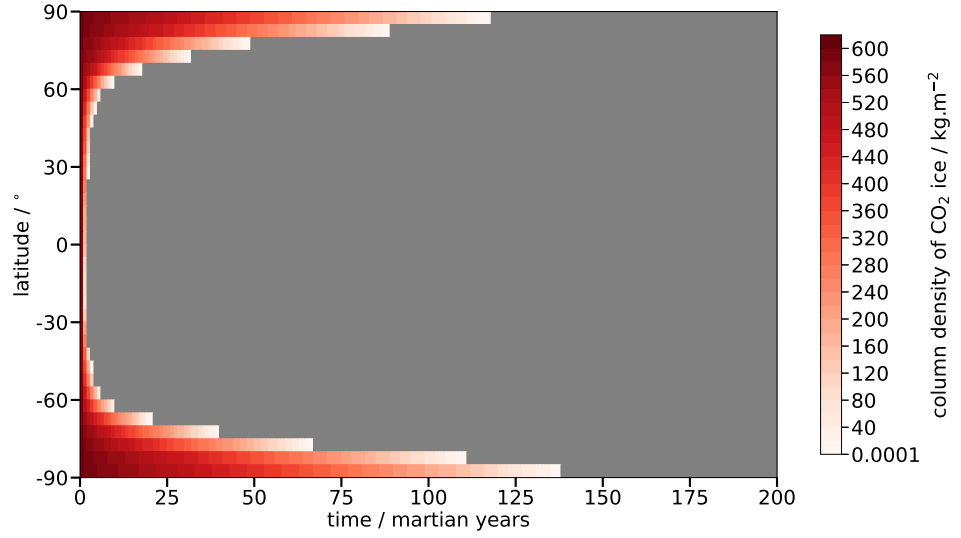


(b) *W-C-W* (S40)

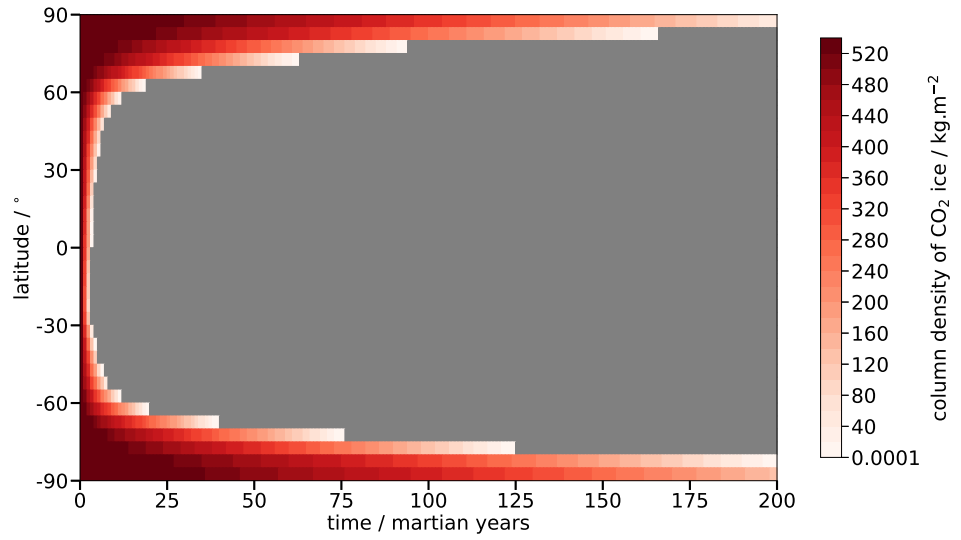


(c) *Alternate Layers* (S37)

Figure 6.8: Column density of CO₂ ice at each latitude over time for the (a) *W-C* (S15), (b) *W-C-W* (S40) and (c) *Alternate Layers* (S37) scenarios at an obliquity of 15°. Grey represents where the CO₂ ice column density is less than 0.0001 kg m⁻².



(a) *IF-C* (S16)



(b) *IF-W-C* (S43)

Figure 6.9: Column density of CO₂ ice at each latitude over time for the (a) *IF-C* (S16) and (b) *IF-W-C* (S43) scenarios at an obliquity of 15°. Grey represents where the CO₂ ice column density is less than 0.0001 kg m⁻².

expected from the 25° obliquity results (discussed in Chapters 4 and 5), CO_2 ice takes the longest to sublimate away when covered by a H_2O ice-filled regolith layer than in any other scenario. In that scenario (*W-C*; S15), CO_2 ice takes over two thousand years longer to fully sublimate away than in the equivalent 25° obliquity simulation (S06), showing the increased stability of CO_2 ice at lower obliquities. Despite the longer timescales for CO_2 ice to fully sublimate, these results still suggest that CO_2 ice is unstable and any initial amount of CO_2 ice will be expected to continue sublimating until it has all sublimated away. However, all previous low obliquity studies indicate that CO_2 ice is stable at the highest latitudes and will form permanent polar caps over time (see Section 2.7.1.2; e.g., Forget et al., 2017; Toon et al., 1980). This means that the results discussed here do not accurately represent the behaviour of CO_2 ice when obliquity is 15° , since they show continuous annual sublimation at all latitudes.

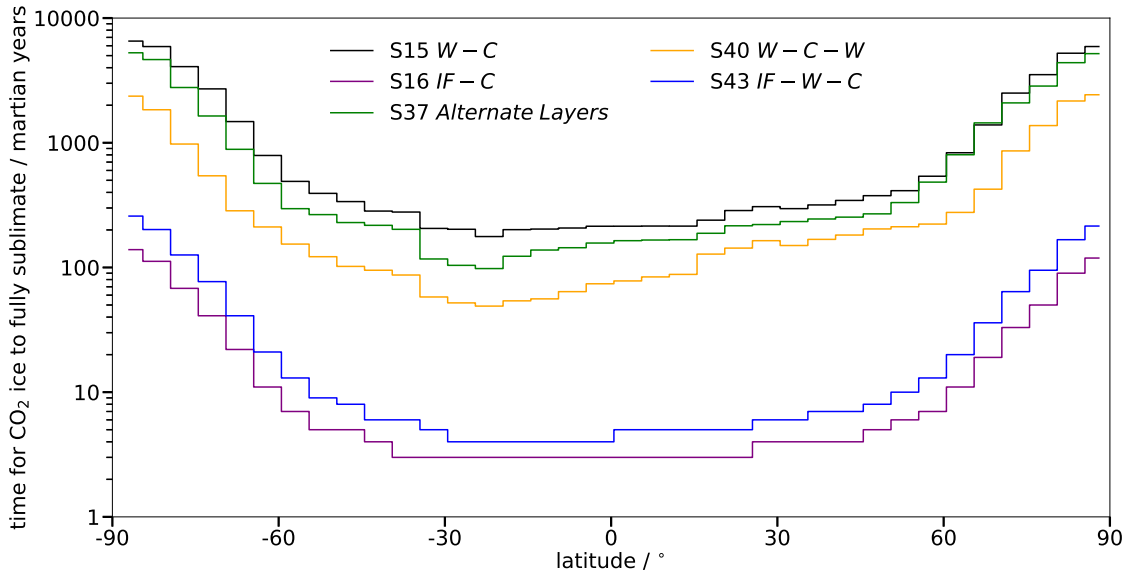


Figure 6.10: Comparison of the number of years that CO_2 ice takes to fully sublimate away for the 15° obliquity simulations (S15, S16, S37, S40 and S43).

The continuous annual sublimation seen in these simulations is a consequence of using a one dimensional (1-D) model with a fixed atmospheric cycle for CO_2 and H_2O vapour rather than a full three dimensional (3-D) GCM. In the fixed atmospheric cycles used for the 15° obliquity scenarios (Figure 6.2), there is a period of nearly 200 sols when temperatures are above the CO_2 frost point and CO_2 ice will sublimate away. In a 3-D GCM simulation, surface CO_2 ice that was deposited from the atmosphere throughout the rest of the year will seal off the subsurface and would need to sublimate

away before any subsurface CO₂ ice can begin to sublimate. Therefore, the surface CO₂ ice would sublimate first and since CO₂ ice deposition occurs for more of the year than sublimation, a net increase in surface CO₂ ice is expected (if sublimation and deposition rates are similar). In the MSSM, however, the fixed representation of the atmosphere means that no CO₂ ice deposition occurs when surface temperatures are low enough for CO₂ ice to form (as discussed in Section 6.1). This in turn means that during the 200 sols of higher surface temperatures, the initial amount of CO₂ ice will be slowly sublimated away until it has all sublimated rather than the seasonal surface CO₂ ice sublimating away as is simulated in previous GCM studies (e.g., Kreslavsky and Head, 2005). Therefore, in order to properly simulate the stability of CO₂ ice when obliquity is 15°, a full GCM simulation is needed, which will be the next steps for this work (Section 7.2.2).

6.4 Obliquity = 35°

The results from the scenarios run with the 35° obliquity atmospheric profiles (S19, S38, S41, and S44; Figure 6.11) have distinct differences to those run with the 15° and 25° obliquity atmospheric profiles (see Section 6.3 and Chapters 4 and 5). In all of the 35° obliquity results, the behaviour of CO₂ ice can still be split into the broad latitudinal regions previously used: polar, mid-latitude and equatorial. However, the latitudinal ranges of these regions are different and the hemispherical differences are more extreme, due to the higher obliquity. The effect of a higher obliquity in all scenarios will therefore be discussed using these broad latitude ranges to cover the full range of changes that can be seen in the results.

The polar regions behave similarly in both the 25° and 35° obliquity simulations. The main difference between them is the increase in sublimation rate as obliquity increases. For example, at 88°N in the *W-C* scenario, sublimation rate increases from 3.56 mm MY⁻¹ at 25° obliquity to 8.95 mm MY⁻¹ at 35° obliquity. This is due to the increased amount of solar insolation received by the poles during summer as obliquity increases (see Figure 6.1). The increase in solar insolation results in warmer summer temperatures (by >40 K; Figure 6.4a), which makes CO₂ ice unstable for more of the year and causes the permanent polar caps to become unstable. The large swings in

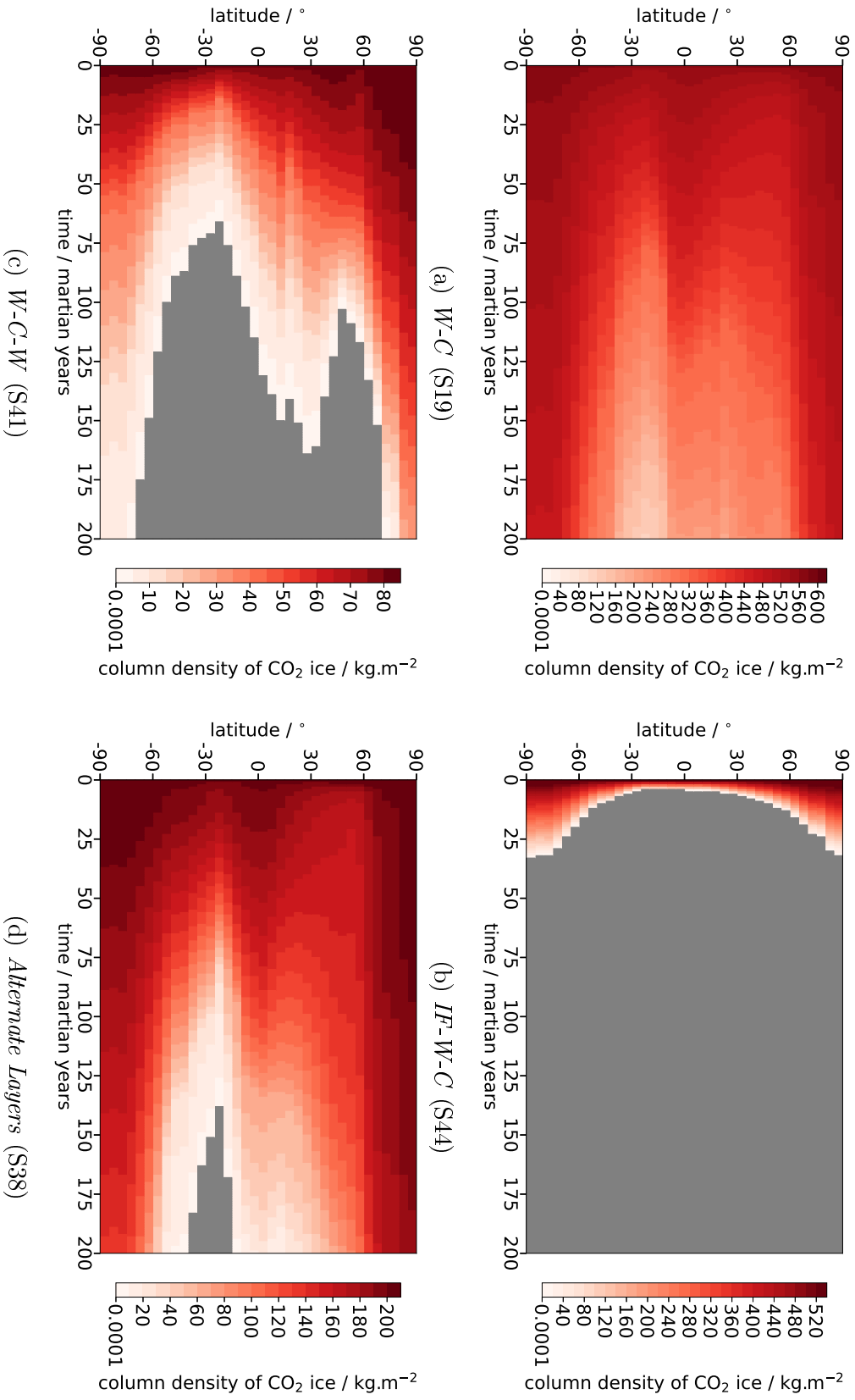


Figure 6.11: Column density of CO_2 ice at each latitude over time for the (a) *W-C* (S19), (b) *IF-W-C* (S44), (c) *W-C-W* (S41) and (d) *Alternate Layers* (S38) scenarios at an obliquity of 35° . Grey represents where the CO_2 ice column density is less than 0.0001 kg m^{-2} .

temperature throughout the year result in periods when subsurface CO₂ ice is stable and periods when it is unstable. Since CO₂ ice is unstable for more of the year in these simulations than when obliquity is 25°, the annual sublimation rate increases and a smaller column density of CO₂ ice remains after 200 martian years. This can be seen by comparing the final column density of CO₂ ice in the northern polar region for the *W-C* scenario for both obliquities. In the 25° obliquity simulation (S06; Figure 4.9b), $\sim 560 \text{ kg m}^{-2}$ remained after the 200 martian years, whereas only $\sim 500 \text{ kg m}^{-2}$ of CO₂ ice remains after 200 martian years in the 35° obliquity simulation (S19; Figure 6.11a). A similar difference in the final column density of CO₂ ice is seen between the 25° obliquity and 35° obliquity simulations for the northern polar region of the other three scenarios (S38, S41 and S44; Figure 6.11). The southern polar regions of all four scenarios also show the same increase in sublimation rate, but with even less CO₂ ice remaining after 200 martian years. This is due to the higher summer temperatures ($\sim 40 \text{ K}$ higher) in the southern polar region than in the northern polar region at 35° obliquity (Figure 6.4a).

Alongside the higher annual sublimation rate, the higher obliquity increases the latitudinal extent of the seasonal polar caps, since the larger axial tilt means that more of the surface has winter temperatures around the CO₂ frost point temperature (Figure 6.4a). Using surface temperature profiles, it can be seen that the latitudes that experience temperatures around the CO₂ frost point temperature during winter extend from the pole to $\sim 50^\circ\text{N}$ in the northern hemisphere and from the pole to $\sim 45^\circ\text{S}$ in the southern hemisphere when obliquity is 25° (Figure 3.16a). Whereas, when obliquity is 35°, this region extends to $\sim 35^\circ\text{N}$ in the north and to $\sim 30^\circ\text{S}$ in the south (Figure 6.4a). This increased latitudinal limit of the seasonal polar caps has been simulated in previous high obliquity studies (discussed in Section 2.7.1.1; e.g., Greve, 2000; Mischna et al., 2003). The extended latitudinal region of CO₂ ice stability during winter results in a decreased CO₂ ice sublimation rate between $\sim 60^\circ$ to 30° N/S during winter compared with in the lower obliquity runs. This decreased sublimation rate is counteracted during summer by the increase in surface temperature caused by the higher obliquity (Figure 6.12), which increases both the saturation vapour densities and the rate of sublimation. This is shown by the similar annual sublimation rates at 52°S in the *W-C* scenario for

the 25° obliquity simulation (23.9 mm MY^{-1}) and the 35° simulation (24.1 mm MY^{-1}). The increase in temperature during summer is greater than the decrease during winter, leading to higher annual sublimation rates in the mid-latitudes ($\sim 60^\circ$ to 30° N/S) of both hemispheres in all scenarios.

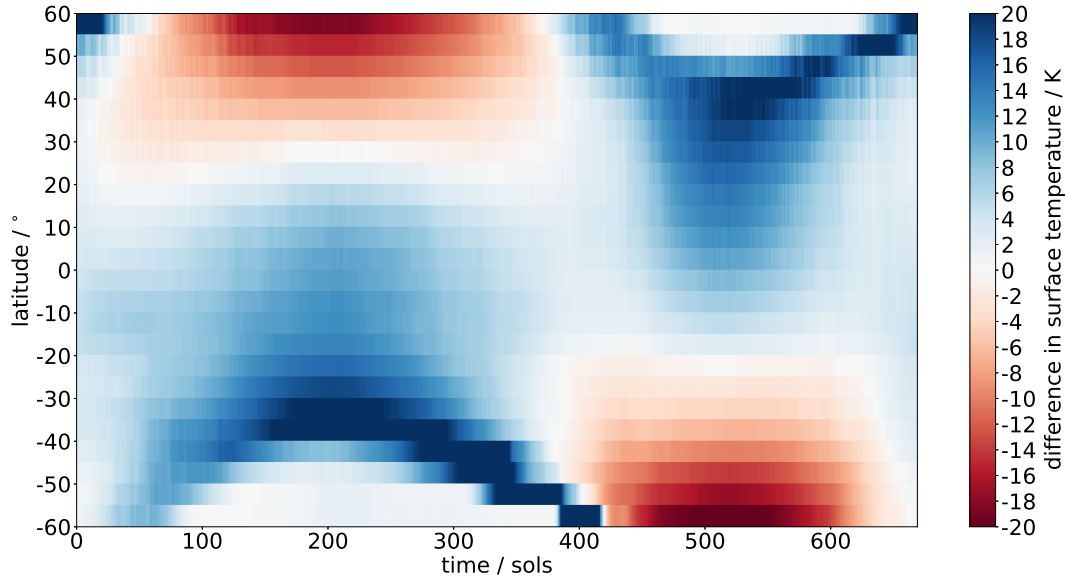


Figure 6.12: Difference in diurnal average surface temperature between the 25° and 35° obliquity atmospheric profiles. Positive values mean that surface temperatures are higher at the 25° obliquity, while negative values mean surface temperatures are higher at 35° obliquity.

In the equatorial regions (30° N/S), the stability of CO_2 ice increases when obliquity is higher. This is due to the reduction in the amount of solar insolation that reaches the surface around the equator, which in turn results in colder temperatures throughout the year (Figure 6.12). The colder temperatures mean that the CO_2 saturation vapour density is lower and less CO_2 ice needs to sublime during each sol for the vapour density in each model layer (containing CO_2 ice) to be kept at CO_2 saturation vapour density after CO_2 vapour has diffused through the subsurface. This increased stability is most obvious in the *Alternate Layers* scenario results (S38; Figure 6.11d), since $\sim 20 \text{ kg m}^{-2}$ of CO_2 ice remains after 200 martian years between 10°N and 15°S when obliquity is 35° , whereas when obliquity is 25° , all of the initial column density of CO_2 ice had sublimated away within 160 martian years (Figure 5.17b).

For many latitudes in these scenarios, particularly in the polar regions, some CO_2 ice remains after 200 martian years. Therefore, the average annual sublimation rate

is used to estimate the number of years that it will take to fully sublime the initial amount of CO₂ ice for each of the scenarios and the estimates are shown in Figure 6.13. These estimates show the same general pattern as when the obliquity is 25°, but the number of years it would take for an initial column density of CO₂ ice to fully sublime away is shorter in the polar regions and longer in the equatorial regions, which is as expected based on the discussion above. The most unstable scenario for CO₂ ice at an obliquity of 35° is the *IF-W-C* scenario, since all CO₂ ice has sublimated away within 40 martian years. The most stable scenario is the *W-C* scenario: CO₂ ice survives ~1000 martian years in this ice-layer configuration. While 1000 martian years is a long time for CO₂ ice to survive when it is unstable, it takes 3000 martian years longer to fully sublime at an obliquity of 25° for the same scenario. This is consistent with the expectation of no permanent surface CO₂ ice in the polar regions at high obliquities. However, as in the 15° obliquity scenarios discussed earlier (Section 6.3), the lack of CO₂ ice deposition during the winter seasons will impact the results shown here. At an obliquity of 35°, the formation of large seasonal caps (see Section 2.7.1.1; e.g., Greve, 2000) will mean that any sublimation during the spring/summer seasons would first remove the seasonal caps before any subsurface CO₂ ice would begin to sublime. In the MSSM simulations shown here, no overlying seasonal CO₂ ice cover forms during winter, which will result in a higher annual sublimation rate for the subsurface CO₂ ice than if the seasonal CO₂ ice cover was simulated. Therefore, the amount of CO₂ ice loss during the simulated 200 martian year period represents the maximum annual sublimation rate and further work with a full 3-D GCM is needed to constrain this value further (see Section 7.2.2).

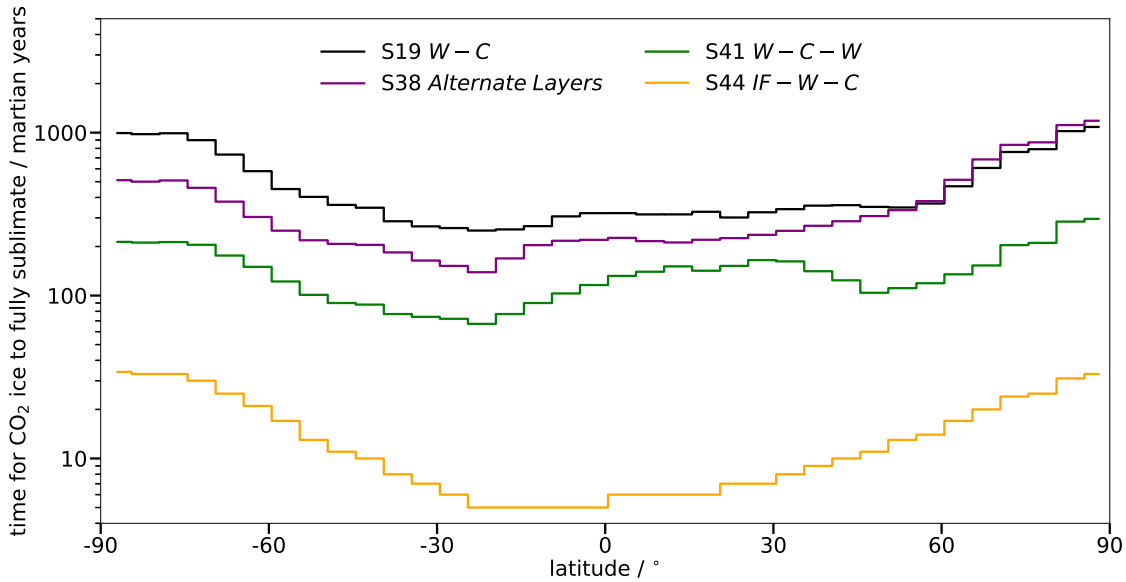


Figure 6.13: Comparison of the number of years that CO₂ ice takes to fully sublimate away for the 35° obliquity simulations (S19, S38, S41 and S44).

6.5 Obliquity = 45°

The final obliquity value investigated was 45°, which is often used as an upper limit for obliquity studies since this is expected to be the upper limit of obliquity in the last 10 million years (Myr). However, 45° is also the value found for the average obliquity across Mars' entire history by Laskar et al. (2004) so this is the scenario that would have been most likely across much of martian history.

The results from the scenarios run with the 45° obliquity atmospheric profiles are similar to those run with the 35° obliquity atmospheric profiles. This is because the changes that occur when obliquity increases from 25° to 35°, become more pronounced as obliquity is increased further (e.g., Forget et al., 2017; Jakosky et al., 1995).

At 45° obliquity (Figure 6.1), the annual solar insolation received by the polar regions increases and the amount received by the equatorial region decreases. This is reflected by the increase in annual average surface temperature in the polar regions, which increases from 162K to 185K in the northern polar region and from 155K to 180K in the southern polar region when obliquity increases from 25° to 45°. The increase in annual average temperature is due to the increase in the summer maximum temperature, since the winter minimum temperature is fixed at the frost point of CO₂ ice (Figure 6.5a). Higher summer temperatures result in higher annual sublimation

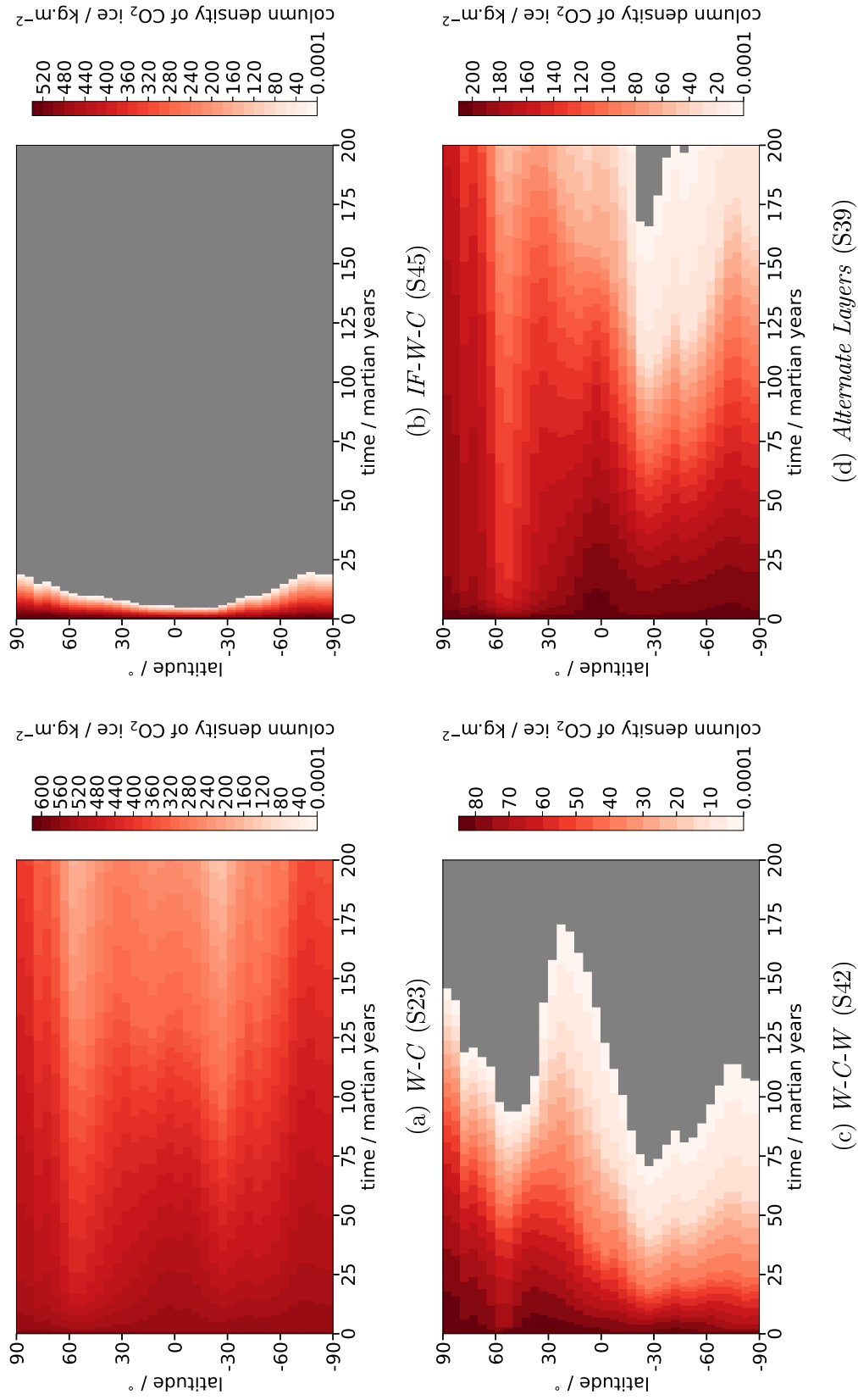


Figure 6.14: Column density of CO_2 ice at each latitude over time for the (a) *W-C* (S23), (b) *IF-W-C* (S45), (c) *W-C-W* (S42) and (d) *Alternate Layers* (S39) scenarios at an obliquity of 45° . Grey represents where the CO_2 ice column density is less than 0.0001 kg m^{-2} .

rates, which can be seen in the results of all four scenarios shown in Figure 6.14: the *W-C* (S23), *IF-W-C* (S45), *W-C-W* (S42) and *Alternate Layers* (S39) scenarios. The smaller increase in annual average temperature in the northern polar region means that CO₂ ice generally takes longer to sublimate away there than in the southern polar region. This is particularly clear in the *Alternate Layers* scenario (S39; Figure 6.14d), since around half of the initial column density of CO₂ ice remains after 200 martian years in the northern hemisphere, while it has almost entirely sublimated away within the same period of time in the southern hemisphere. This is due to the sublimation rate in the northern polar region (5.52 mm MY⁻¹ at 88°N in S39) being an order of magnitude smaller than in the southern polar region (16.7 mm MY⁻¹ at 88°S in S39). Comparing the final column density from this 45° obliquity simulation (S39) with the final column density of the equivalent 25° obliquity simulation (S33; Figure 5.17a) shows that this hemispherical difference is enhanced by the increased obliquity, since CO₂ ice sublimates at almost the same rate between the two hemispheres when obliquity is 25° (at ~1.63 mm MY⁻¹ at 88°N/S in S33). This drastic hemispherical difference in the stability of CO₂ ice as obliquity increases will influence which hemisphere retains polar CO₂ ice deposits for longer (Laskar et al., 2004).

The increased obliquity also influences the stability of CO₂ ice in the equatorial and mid-latitude regions. As discussed for the 35° obliquity simulation results (Section 6.4), the mid-latitude regions experience larger seasonal temperature variations due to the seasonal polar caps extending further equatorward. However, while the seasonal temperature variations are larger, the effect of the lower winter temperatures is still mostly counteracted by the warmer summer temperatures, as is the case for the 35° obliquity. The final column density of CO₂ ice in the mid-latitudes is similar in the equivalent simulations for obliquities of 35° and 45°. The equatorial region, on the other hand, shows a further decrease in the annual CO₂ ice sublimation rate as obliquity increases from 35° (16.8 mm MY⁻¹ at 2°S in S38) to 45° (14.8 mm MY⁻¹ at 2°S in S39). This is due to the decrease in surface temperature mentioned earlier, since annual average surface temperature decreases from 218 K at the equator when obliquity is 25° to 207 K at 45° obliquity.

The combination of the increased sublimation rate at the poles and the decreased sublimation rate in the equatorial region causes the variation in CO₂ ice sublimation rate with latitude to decrease. This less pronounced latitudinal variation is clearly visible in Figure 6.15, which shows the estimated number of years it would take for the initial column density of CO₂ ice to fully sublimate away for the 45° obliquity simulations. The latitudinal variation in the number of years for CO₂ ice to fully sublimate is at most 300 martian years (for the *W-C* scenario; S23) when obliquity is 45°, whereas when obliquity is 35°, the latitudinal variation for the same scenario (S19) is 700 martian years. This corresponds to the reduction in CO₂ ice stability in the polar regions due to the polar regions receiving more solar insolation with increasing obliquity, and the increased stability in the equatorial region, which receives less solar insolation.

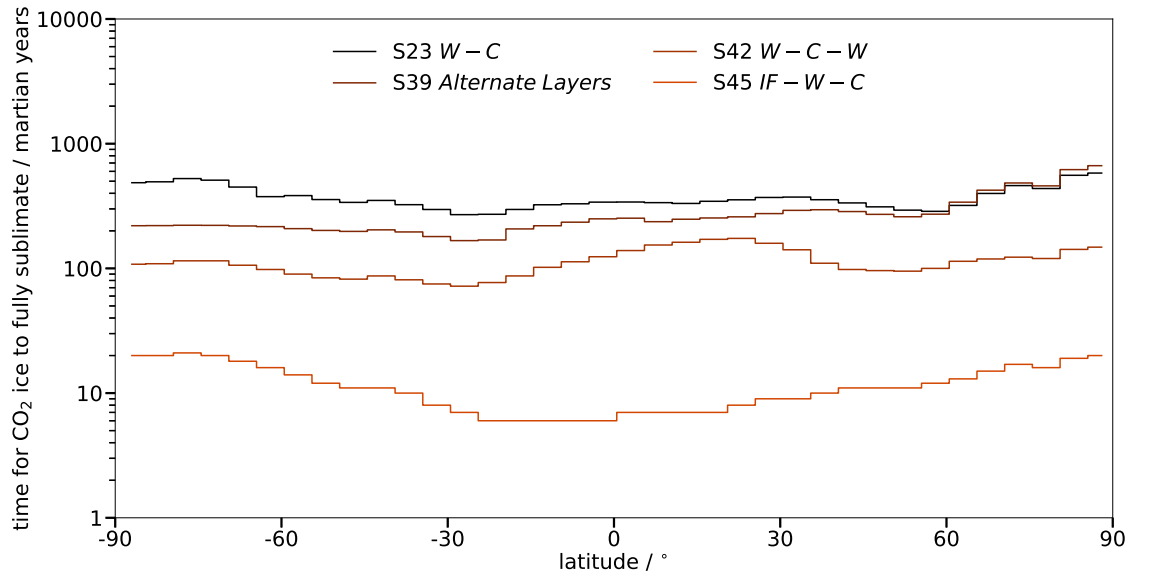


Figure 6.15: Comparison of the number of years that CO₂ ice takes to fully sublimate away for the 45° obliquity simulations: the *W-C* (S23), *IF-W-C* (S45), *W-C-W* (S42) and *Alternate Layers* (S39) scenarios.

6.6 Discussion

The effect of obliquity on subsurface CO₂ ice can be clearly seen when comparing the estimated number of years that CO₂ ice will take to fully sublimate for the *W-C* scenario at each obliquity (Figure 6.16). The estimates for the *W-C* scenario are used because CO₂ ice is more stable in this ice-layer configuration than in any other ice-layer

configuration investigated, so these estimates are the maximum values for all of the results. From these estimates, it can be seen that the largest differences in CO₂ ice stability as obliquity increases occur in the polar regions, while the smallest variations in stability are found in the mid-latitudes.

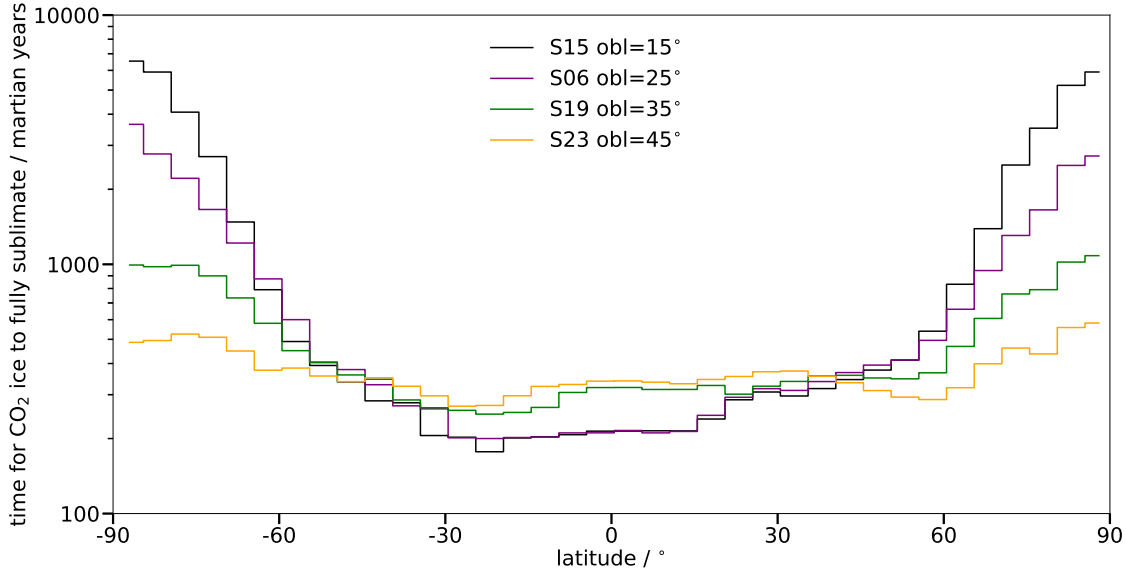


Figure 6.16: Comparison of the number of years that CO₂ ice takes to fully sublimate away for the *W-C* scenario at each obliquity: 15°, 25°, 35° and 45°.

Across the mid-latitudes ($\sim 50\text{--}20^\circ\text{N}$ and $50\text{--}30^\circ\text{S}$), the stability of CO₂ ice appears to be independent of obliquity, since the fixed initial amount of CO₂ ice sublimates away at nearly the same rate ($\sim 0.019 \text{ mm MY}^{-1}$) and takes roughly the same amount of time to fully sublimate (300–400 martian years) for all obliquities (Figure 6.16). As mentioned earlier, this is different from the behaviour of H₂O ice, as the region of H₂O ice stability moves further equatorward as obliquity increases due to the decrease in equatorial temperatures (see Figure 6.12; e.g., Jakosky and Carr, 1984; Levrard et al., 2004; Mischna et al., 2003). The lower equatorial temperatures at higher obliquity also act to increase the stability of CO₂ ice, which takes around 100 martian years longer to sublimate away at high obliquities (at a rate of $\sim 0.028 \text{ mm MY}^{-1}$ for both 35° and 45° obliquity) than at low or moderate obliquities (at a rate of $\sim 0.018 \text{ mm MY}^{-1}$ for both 15° and 25° obliquity; Figure 6.16). This timescale is similar to the timescale for CO₂ ice sublimation in the mid-latitudes at all obliquities and overall, CO₂ ice is not expected to survive longer than 500 martian years between 50° N/S at all obliquities. This matches the current understanding of surface CO₂ ice which shows that permanent

surface CO₂ ice is unstable outside of the polar regions for all obliquities. However, this only considers stability under current atmospheric conditions and under the current obliquity range.

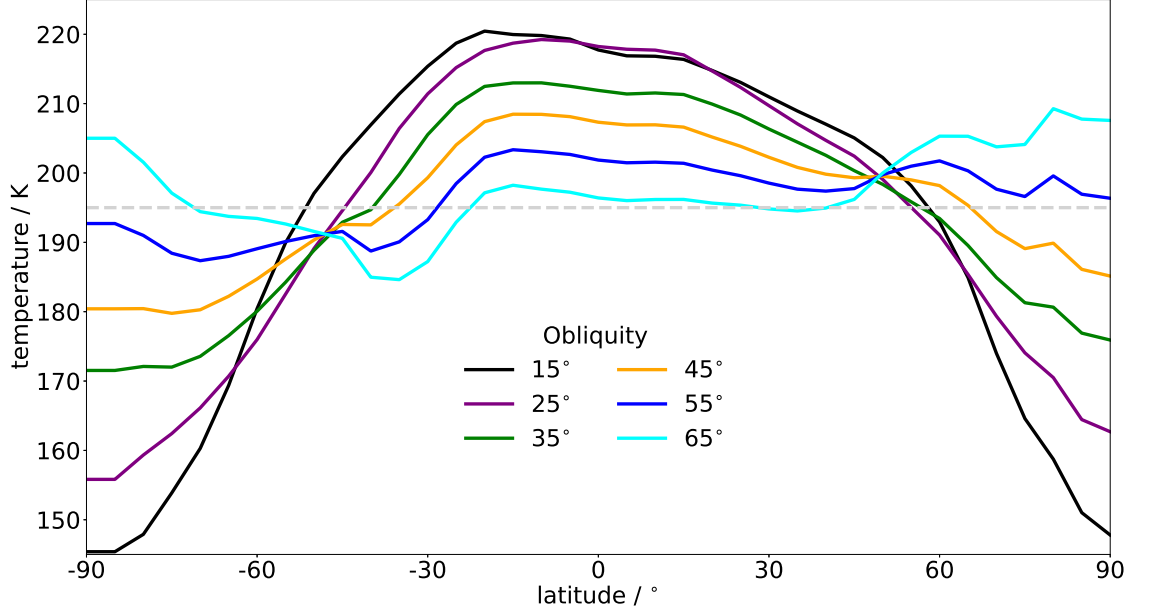


Figure 6.17: Annual average surface temperature with latitude from the MGCM simulations at each obliquity (15°, 25°, 35° and 45°) and estimates of annual average surface temperature for obliquities 55° and 65°. The grey dashed line represents the CO₂ frost point temperature at 1 bar (195 K).

During the Noachian and early Hesperian, surface pressures are estimated to have been between 0.1 and 1 bar (Section 2.8; e.g., Forget et al., 2013; Haberle et al., 1994; Manning et al., 2006) and obliquity is estimated to have a higher maximum of around 60° (Figure 2.12; Laskar et al., 2004). At a 60° obliquity, the latitudes receiving the lowest amount of solar insolation shift even further equatorward (Mischna et al., 2003) and, similar to the behaviour of H₂O ice discussed, the regions of CO₂ ice deposition may shift to the mid-latitudes. Using the surface temperatures at each obliquity from the MGCM simulations (Sections 3.7.1 and 6.1), the change in average annual surface temperature as obliquity increases can be estimated. Figure 6.17 shows the annual average surface temperature with latitude from each MGCM obliquity simulation (15°, 25°, 35°, and 45°) and the estimated surface temperature with latitude for a 55° and 65° obliquity. Estimated surface temperatures at 55° obliquity were calculated by changing the surface temperatures at a 45° obliquity by the average change in surface temperature as obliquity increases by 10° across all four obliquities investigated (15°, 25°, 35°, 45°).

and 45°). The same change in surface temperature was applied to the 55° obliquity estimated temperatures to produce the 65° obliquity estimated surface temperatures. The pattern of increasing temperature at the poles and decreasing temperature in the equatorial and mid-latitude regions can be clearly seen in this figure. Although temperatures in the equatorial and mid-latitude regions do not fall to below 145 K (the CO_2 frost point in the present-day), temperatures in the southern mid-latitudes do fall below 195 K, which is the CO_2 frost point temperature at 1 bar. This suggests that at high obliquities and pressures, the regions of stability for CO_2 ice will shift towards the mid-latitudes. This has been simulated by Nakamura and Tajika (2003) using a 70% solar constant and pressures greater than 0.1 bar to represent the Noachian solar luminosity and pressure. Their results found that a ring of permanent CO_2 ice formed around the mid-latitudes. However, the simulations were done using a 1-D energy balance climate model, which cannot fully simulate the details of the martian climate. Another issue is that the state of the early martian climate is still largely unknown and is still heavily debated (see Section 2.8; Kahre et al., 2012; Wordsworth et al., 2015). This means that while there is a potential for CO_2 ice to have formed in the mid-latitudes at very high obliquity under high atmospheric pressures, it is an area that requires further research.

If a CO_2 ice-layer did form in the mid-latitudes during the Noachian under periods of high obliquity, it is unlikely that any remains in the present-day, especially under a shallow H_2O ice-layer (<2 m) where it would survive for a time period shorter than one modern-day obliquity cycle (~ 120 kyr; Laskar et al., 2002). Under thicker H_2O ice-layers, such as beneath LDAs, which are estimated to be 130 m thick (Section 2.3.3; Brough et al., 2019; Holt et al., 2008), an underlying CO_2 ice deposit might persist for far longer periods of time, particularly if the LDA porosity was low (discussed in Section 5.1). Again, further work would be needed to confirm this. The formation of CO_2 ice deposits during the Noachian could have implications for the formation of some geological features observed in the mid-latitudes of Noachian age, since CO_2 ice has been shown to flow more easily than H_2O ice at martian temperatures and pressure (Clark and Mullin, 1976; Smith et al., 2016). Sublimation of near-surface CO_2 ice has also been suggested as a potential formation mechanism for gullies in the present-day

(e.g., Conway et al., 2018) and a similar mechanism could have occurred throughout Mars’ history when subsurface CO₂ ice distribution was more extensive. However, more research would be needed to determine the likelihood of these features being formed from CO₂ ice processes rather than H₂O ice processes.

The polar regions show the largest variation of CO₂ ice persistence with obliquity: CO₂ ice can survive several thousands years longer at low obliquities than at high obliquities (Figure 6.16). This is as expected based on previous studies of surface CO₂ ice distribution with obliquity (e.g., Mischna et al., 2003; Soto et al., 2015), although the number of years for CO₂ ice to sublime at low obliquity is probably underestimated in these results, as discussed earlier (Section 6.3). At high obliquities, on the other hand, the more rapid loss of CO₂ ice follows the expected scenario of ‘seasonal CO₂ polar caps and the continual loss of any permanent CO₂ ice over time’. Despite the differences in the plausibility of the low and high obliquity results, it is interesting to note that there is an order of magnitude difference in the rate of CO₂ ice sublimation between the low obliquity scenario (1.48 mm MY⁻¹ at 88°S at 15°; S15) and the high obliquity scenarios (19.9 mm MY⁻¹ at 88°S at 45°; S23) in the southern polar regions. This means that a 1 km CO₂ ice-layer that forms during a period of low obliquity would take between ~180 Myr (35° obliquity) and ~100 Myr (45° obliquity) to fully sublime away when obliquity increases, if under a 1 m layer of H₂O ice-filled regolith. This mechanism forms one of the main processes that might have influenced the survival of the CO₂ ice deposits within the South Polar Layered Deposits (SPLD), and which will be discussed further in the next section.

6.6.1 Insights into the CO₂ Deposits within the SPLD

Recent observations of the SPLD led to the discovery of three layers of CO₂ ice deposits, each covered by an overlying H₂O ice-layer (Bierson et al., 2016; Phillips et al., 2011). These CO₂ ice-layers were determined to be between 10 and 1000 m thick and the bounding H₂O ice-layers were determined to be between 10 and 60 m thick (Bierson et al., 2016). This scenario of H₂O ice overlying CO₂ ice is similar to the *W-C* scenario which was run for the full range of obliquities, porosities and geological subsurface configurations discussed in this work. It is also similar to the *W-C-W* scenario, although

only the *W-C* scenario was run under all conditions (different obliquities, initial ice porosities and subsurface structures), so the results from that scenario allow for a more complete analysis to be made. While all of the results shown here are for ice-filled regolith rather than pure ice, the results from the simulations discussed throughout this thesis can be combined to form new insights into the presence of the CO₂ ice deposits within the SPLD (Bierson et al., 2016; Phillips et al., 2011). This is because the effects of an overlying porous layer on the rate of diffusion, and consequently on the sublimation rate are expected to be similar in magnitude whether the overlying layer is pure ice or an ice-filled regolith. The porosity of the overlying layer will be similar for both pure ice and ice-filled regolith which reduces the rate of diffusion by the same amount since the diffusion coefficient is dependent on the total porosity rather than the composition of the overlying layer. Another factor that will likely have an influence on the insights presented here is the fact that pure ice (H₂O or CO₂) will have a higher thermal conductivity than an ice-filled regolith, which will have an influence on subsurface temperature variations.

There are two main hypotheses for the presence of CO₂ ice deposits within the SPLD, both of which rely on different assumptions: (i) assumes that the H₂O ice is deposited in isolated events (Manning et al., 2019), while (ii) assumes that H₂O ice is continuously deposited onto the polar regions (Buhler et al., 2019).

The Manning et al. (2019) hypothesis suggests that during a period of low obliquity, there is a period of CO₂ ice deposition that is followed by a period of low-porosity H₂O ice deposition as the longitude of perihelion shifts to occur during northern summer. This low-porosity H₂O ice insulates the CO₂ ice deposits and seals the CO₂ ice from sublimation during the high obliquity periods that follow. This hypothesis requires the H₂O ice-layer to be thick enough to completely seal the underlying CO₂ ice, which will depend on both the accumulation rate and the densification rate of the deposited snow into low porosity ice. While the overlying H₂O ice-layer forms, CO₂ ice will be sublimating away and the results from the simulations in this thesis can be used to estimate the thickness of the CO₂ ice-layer that would sublimate in the time taken to form a 1 m thick H₂O ice-layer. The estimates are discussed in the following paragraphs

and summarised in Table 6.1

The Manning et al. (2019) model uses an estimated deposition rate of $\sim 5 \text{ mm MY}^{-1}$ for H_2O ice in the south when perihelion occurs during northern winter. This implies that it would take only 200 martian years to accumulate 1 m of H_2O ice. Over this time period, only $\sim 1.4 \text{ m}$ of CO_2 ice would have sublimated away if the H_2O ice was deposited with a low porosity (~ 0.01) and sublimates away at the average polar sublimation rate calculated for the 25° obliquity *W-C* scenario (S06; 6.76 mm MY^{-1}). This deposition rate is an order of magnitude faster than the present-day deposition rate, which has been estimated to be between 0.13 and 0.39 mm MY^{-1} (Becerra et al., 2019). This higher deposition rate means that a CO_2 ice deposit is more likely to survive an obliquity cycle since 50 m of zero-porosity ice could accumulate in the $\sim 10 \text{ kyr}$ period that perihelion is expected to occur during northern summer.

The estimate for the amount of CO_2 ice that sublimates away while H_2O ice is accumulating assumes H_2O ice is deposited as low-porosity slab ice. However, H_2O ice is more likely to initially be deposited as snow that then compacts and becomes denser over time. Therefore, the thickness of the layer that sublimates away in the time it would take for a high porosity snow to compact into low-porosity H_2O ice can be estimated and combined with the accumulation estimate to give a total estimate. In their study, Manning et al. (2019) use a timescale of 14 thousand years (kyr) for the densification of a 70% porosity snow into a low porosity ice, which will be used as a minimum timescale in this work. While this initial porosity of snow is higher than the highest porosity used for the variable minimum porosity simulations (Section 5.1), the sublimation rate from the ' $\phi_{\text{ice ini}} = 0.1$ ' simulation (PM04) can be used to estimate the thickness of a CO_2 ice-layer that would have sublimated away during the time taken for this compaction to occur (14 kyr), assuming there was at least 1 m of porous H_2O ice overlying the CO_2 ice already. The CO_2 ice sublimation rate in the PM04 simulation ($\phi_{\text{ice ini}} = 0.1$) in the south polar region (latitude 88°S) was found to be 49.0 mm MY^{-1} , so over 14 kyr, 686 m of CO_2 ice would sublime away. However, this timescale is an order of magnitude smaller than the densification rate calculated by Arthern (2000), who calculated timescales of 300-550 kyr depending on

Table 6.1: The estimated thickness of CO₂ ice sublimated during the time taken for each process involved in the formation of a 1 m H₂O ice-layer, including the different estimated timescales from different studies.

Process	Timescale [martian years]	Timescale Reference	Sublimation rate from this thesis [mm MY ⁻¹]	Simulation code	Thickness of CO ₂ ice sublimated [m]
Accumulation of 1 m of low-porosity H ₂ O ice	200	Manning et al. (2019)	6.76	S06	1.3
Densification of snow to low- porosity H ₂ O ice	14,000	Manning et al. (2019)	49.0	PM04	690
Densification of snow to low-porosity H ₂ O ice	300,000	lower end of range in Arthern (2000)	49.0	PM04	14,700
Densification of snow to low-porosity H ₂ O ice	550,000	upper end of range in Arthern (2000)	49.0	PM04	27,000

the accumulation rate and temperature of the northern polar region. At the upper end of this range (550 kyr; the maximum densification timescale), ~ 27 km of CO₂ ice would sublimate away before the overlying H₂O ice-layer porosity had reduced to 0.001.

Of course, both the accumulation and densification process will occur simultaneously, acting to further reduce the sublimation rate of the underlying CO₂ ice over time, so the maximum thickness of CO₂ ice that would sublimate away would be a combination of the values calculated for accumulation and densification, and therefore, ~ 0.7 –27 km of CO₂ ice (depending on the densification timescale) is suggested to have sublimated away while the 1 m layer of H₂O ice was forming. This could explain why many CO₂ ice deposits have not survived an obliquity cycle.

Once the low-porosity H₂O ice-layer has formed, CO₂ sublimation rate drops to 2.66 mm MY^{-1} , which is small enough that during the time it would take to build up the remaining 10–60 m of low-porosity H₂O ice that forms the observed bounding layers (140 kyr to 33 Myr, using the minimum and maximum timescales for accumulation and densification), another 372 m to 87 km more of CO₂ ice would sublimate away, depending on the densification timescale used. If the smaller timescale is used (densification takes 14 kyr), around 1 km of CO₂ ice would sublimate away while a 10 m H₂O ice-layer forms and before the remaining CO₂ ice is protected from sublimation. This is a small enough amount that it is plausible that some CO₂ ice could remain in the subsurface, whereas if the longer densification timescale is used, no CO₂ ice could survive an obliquity cycle and the deposits observed within the SPLD could not exist.

The estimates provided so far assume present-day atmospheric conditions (obliquity of 25°) in order to assess the impact of a variable ice porosity on the thickness of a CO₂ ice-layer that would sublimate away, since the initial ice porosity simulations were only run at a 25° obliquity. However, the hypothesis of Manning et al. (2019) assumes the H₂O ice-layer forms during a period of low obliquity. The low obliquity simulations discussed in this chapter (15° ; Section 6.3) show that the CO₂ sublimation rate for the *W-C* scenario (S15) is even smaller than for the present obliquity, being only 1.48 mm MY^{-1} for the baseline ice porosity (0.001). At this sublimation rate, a maximum of 824 m of CO₂ ice would have sublimated away in the upper limit of the

time taken for a 1 m low-porosity H₂O ice-layer to form (557 kyr). However, the results from the low obliquity simulations do not account for the accumulation of CO₂ ice that occurs throughout the year in all previous studies (e.g., Forget et al., 2017; Mischna et al., 2003) and, therefore, the amount of CO₂ ice lost at low obliquity is likely to be even less. This implies that, alongside the GCM simulations of subsurface CO₂ ice at low obliquity, further work is also needed on the accumulation and densification rates under low obliquity conditions before the Manning et al. (2019) hypothesis can be used to develop a full accumulation and sublimation history of the SPLD.

The other hypothesis for the origin of the CO₂ ice deposits within the SPLD was proposed by Buhler et al. (2019), which assumes that H₂O ice is continuously deposited onto the polar regions at the same accumulation rate as observed at present ($\sim 0.1 \text{ mm MY}^{-1}$) and that any H₂O ice that overlies CO₂ ice is permeable. In their model, a H₂O ice deposition rate of 0.1 mm MY^{-1} is used (from Byrne et al., 2008), which is a similar rate to the estimates of Becerra et al. (2019). Using this deposition rate, Buhler et al. (2019) estimate that 10 m equivalent of H₂O ice would take 100 kyr to deposit, which would occur as obliquity decreases from its maximum to its minimum value within an obliquity cycle. Over this time, they also estimate that CO₂ ice is deposited at a rate of \sim a few mm MY^{-1} . In the opposite scenario, when obliquity is increasing from its minimum to maximum value, their model predicts that CO₂ ice sublimates at the same rate (\sim a few mm MY^{-1}), while the H₂O ice deposits concentrate into a lag layer that overlies the remaining CO₂ ice. Over this time they estimate that a few hundred metres of CO₂ ice will sublimate away. When obliquity decreases again, this H₂O ice lag layer is buried by depositing CO₂ ice and then as obliquity increases again, the CO₂ ice sublimates away. If the entire CO₂ ice deposit sublimates away during a period of increasing obliquity, the H₂O ice lag deposit that forms will combine with the previous H₂O ice lag deposit and if some of the CO₂ ice deposit remains after a period of increasing obliquity, this becomes buried by the H₂O ice lag deposit and the newly depositing CO₂ ice. Buhler et al. (2019) suggest that the reason several CO₂ ice-layers have survived periods of increasing obliquity is due to the gradually decreasing obliquity maxima that have occurred over the last 510 kyr (Figure 2.12; Laskar et al., 2004). While this is a plausible explanation for why CO₂

ice deposits have been discovered within 2 km of the surface of the SPLD, their estimates for the rate of CO₂ ice sublimation are likely to be underestimates based on the simulations presented in this chapter.

The Buhler et al. (2019) model predicts CO₂ ice sublimation according to changes in saturation vapour pressure as surface temperatures respond to changes in insolation with obliquity. From this, their model estimates a CO₂ ice sublimation rate of \sim a few mm MY⁻¹ for the period when obliquity increases. However, there are two issues with the sublimation rate used in the Buhler et al. (2019) model: (i) the sublimation rate does not change as obliquity increases and (ii) the sublimation rate is unaffected by the variable thickness of the overlying layer (H₂O ice lag deposit formation and sublimation), both of which would occur in reality.

From the simulations presented in this chapter, it is clear that the sublimation rate is highly dependent on the obliquity since this controls the time throughout the martian year that CO₂ ice is unstable. For the *W-C* scenario, sublimation rates at 88°S (latitude of the SPLD) vary from 1.48 mm MY⁻¹ at 15° obliquity (S15) to 19.9 mm MY⁻¹ at 45° obliquity (S23). At 15° obliquity, the sublimation rate is similar to that predicted by Buhler et al. (2019) and the estimated thickness of CO₂ ice that would sublimate away during an obliquity cycle (100 kyr) is also similar (148 m). However, at 45° obliquity, the higher sublimation rate means that \sim 1.9 km of CO₂ ice would sublimate away, making it more likely for the entire CO₂ ice deposit to sublimate away. This supports the Buhler et al. (2019) hypothesis that the gradually decreasing obliquity maxima is the reason why more CO₂ ice has survived recent obliquity cycles, even though their lower estimated sublimation rate at high obliquities is likely to have underestimated the amount of CO₂ ice that sublimated away during periods of high obliquity.

The other factor that might impact the results of Buhler et al. (2019) is the change in sublimation rate that would occur as the thickness of the H₂O ice lag deposit increases. The increased burial of the CO₂ ice-layer is expected to reduce the CO₂ ice sublimation rate, while the presence of a thicker overlying H₂O ice-layer is expected to increase subsurface temperatures and therefore increase sublimation rates. The presence of the overlying H₂O ice-filled regolith layer decreases the CO₂ sublimation rate

at 88°S from $\sim 167 \text{ mm MY}^{-1}$ when the CO₂ ice-filled regolith layer is overlain by only regolith to 2.66 mm MY^{-1} . This demonstrates the large influence the overlying H₂O ice-filled regolith layer has on the survival of the CO₂ ice and the further decrease to 1.63 mm MY^{-1} (in S33) when there are multiple small alternating layers of H₂O ice-filled regolith and CO₂ ice-filled regolith also supports this. The other factor that needs to be considered is the reduced sublimation rate that occurs as the thickness of the overlying layer increases. In the MSSM, the CO₂ sublimation rate is purely calculated from the difference between the CO₂ vapour density and CO₂ saturation vapour density, with a maximum sublimation rate that was experimentally determined for surface CO₂ ice (Blackburn et al., 2010). It is expected that the sublimation rate in the MSSM will therefore be limited by the CO₂ vapour diffusion rate, which is not well constrained in the literature (see Section 3.4.2). The results from the *W-C* simulations with boundary depths varying from 0.5 m (S05) to 2 m (S07) found that CO₂ ice sublimation rate at 88°S increases from 2.65 mm MY^{-1} (S05) to 2.68 mm MY^{-1} (S07). These simulations demonstrate that while the sublimation rate is impacted by the rate of diffusion of CO₂ vapour out of the subsurface, the faster diffusion rate implies that this effect is smaller than for H₂O ice. However, as mentioned earlier, the diffusion coefficient of CO₂ vapour is not well constrained and further experimental work is needed to constrain this value further before the full influence of an overlying layer on CO₂ sublimation rate can be confirmed. Future simulations with H₂O ice-layers closer to the thicknesses of the observed H₂O ice boundary layers in the SPLD (10-60 m) are also needed before the extent of impact of an overlying H₂O ice-filled regolith on CO₂ ice persistence can be fully understood.

Both hypotheses (Buhler et al., 2019; Manning et al., 2019) are plausible explanations for how the CO₂ ice deposits within the SPLD formed. However, more work is needed before either can be determined to be the more likely formation mechanism. Both hypotheses do not yet account for the effect of an overlying H₂O ice-layer or of the orbital obliquity on the CO₂ ice sublimation rate. The work in this thesis shows that both of these factors have a driving influence on the survival of CO₂ ice within the SPLD and need to be accounted for in models of the formation of the SPLD.

6.7 Summary

Obliquity has a strong influence on the stability of CO₂ ice, which can be seen in all of the results discussed in this chapter. The lower the obliquity, the greater the stability of CO₂ ice and the longer it can remain in the subsurface of the polar regions. At the highest obliquities in the present-day obliquity cycle (35-45°; Laskar et al., 2004), CO₂ ice is not stable throughout the year at any latitude and sublimates continuously throughout the year. While this sublimation rate is dependent on latitude, the latitudinal dependence decreases as obliquity increases and at an obliquity of 45°, CO₂ ice sublimates at a similar rate across all latitudes. The sublimation rates determined from the simulations in this chapter are likely to be overestimates, since one of the limitations of the MSSM is that the seasonal deposition of CO₂ ice cannot be simulated, leading to sublimation rates higher than would be expected.

At the lowest obliquities in the present-day obliquity cycle (15°; Laskar et al., 2004), CO₂ ice sublimates up to an order of magnitude slower than at the present-day obliquity, and in the polar regions can take several thousand years longer to sublimate away than at high obliquities. However, previous studies have shown that CO₂ ice should form permanent polar caps at low obliquities (e.g., Jakosky et al., 1995; Mischna et al., 2003), disagreeing with the continual loss of CO₂ ice found in the results in this chapter. This is again due to the inability of the stand-alone MSSM to form seasonal CO₂ ice deposits and a full GCM simulation with the MSSM integrated into it is needed to simulate the behaviour of CO₂ ice at low obliquity fully.

Even with the limitations of the MSSM, the results presented here can be used to provide an insight into the two formation hypotheses that have been suggested for the CO₂ ice deposits that have been observed within the SPLD. The Manning et al. (2019) hypothesis assumes an overlying H₂O ice-layer is deposited directly after the CO₂ ice-layer due to changes in the orbital parameters. This H₂O ice-layer is likely to be deposited as snow that becomes compacted over time into low-porosity H₂O ice. The timescale of this compaction is critical for the survival of any underlying CO₂ ice deposits. If H₂O ice formation and compaction takes ~14 kyr as suggested by Manning et al. (2019), an estimated 750 m of CO₂ ice would sublimate away in the time it would

take for 1 m of compact H₂O ice to form. Whereas if H₂O ice formation and compaction takes 550 kyr as suggested by Arthern (2000), the thickness of CO₂ ice deposits that would sublimate away increases to 27 km and it is unlikely that any will survive an obliquity cycle.

In the other hypothesis, the overlying H₂O ice-layer is instead assumed to form as a lag deposit when CO₂ ice sublimates away at high obliquity (Buhler et al., 2019). The thickness of this lag layer will therefore increase over time, gradually reducing the sublimation rate as the H₂O ice lag layer thickness increases. The results from the simulations in this chapter show that while the sublimation rate is expected to be influenced by the thickness of the H₂O ice lag layer, the obliquity has a larger influence on the sublimation rate. The Buhler et al. (2019) model uses the same sublimation rate for all obliquities, which is likely to have underestimated the thickness of CO₂ ice deposits that would have sublimated away during each obliquity cycle. The Buhler et al. (2019) hypothesis also does not account for the influence of the thickness of the H₂O ice lag layer on CO₂ ice sublimation rate, since the increase in H₂O ice will increase subsurface temperatures and the thicker overlying layer will decrease sublimation rate. Further work is needed on the influence of subsurface properties on subsurface CO₂ ice sublimation for both of the scenarios presented for the formation of CO₂ ice deposits within the SPLD before either can be confirmed.

7 | Conclusions and Future Work

7.1 Summary and Conclusions

This thesis presents the development of a new subsurface model (the Martian Subsurface Model, ‘MSSM’; Chapter 3) that accounts for the deposition and sublimation of both water (H_2O) ice and carbon dioxide (CO_2) ice within the subsurface for the first time. Previous martian subsurface models have only modelled the behaviour of H_2O ice in detail and CO_2 ice has not been included in subsurface models (e.g., Leighton and Murray, 1966; Schorghofer and Aharonson, 2005). The MSSM includes a thermal scheme that accounts for changes in thermal properties with depth (within a compacting regolith unit) and ice content (for both ices). Both H_2O and CO_2 vapour are diffused through the pore space and the partition of each volatile (between vapour and ice) is recalculated at every time step using a saturation vapour density that is recalculated using the temperature in the current time step.

The MSSM is used to simulate different ice-layer configurations of ice-free regolith, H_2O ice filled regolith and CO_2 ice filled regolith. These simulations were run to investigate the factors that influence subsurface CO_2 ice distribution, since previous research focused on subsurface H_2O ice and since understanding the conditions required for CO_2 ice deposits to survive in the South Polar Layered Deposits (SPLD) for long time periods has been identified as a priority area for research (Banfield, 2020; Diniega and Putzig, 2019). The results of these simulations (discussed in Chapters 4, 5 and 6) suggest that the main factors influencing the stability of subsurface CO_2 ice across Mars are: the layering of H_2O ice-filled regolith and CO_2 ice-filled regolith; the porosity; the geological properties of the regolith unit that ice forms within; and the obliquity.

CO_2 ice is unstable when exposed directly to the atmosphere, either at the surface or with only an ice-free regolith cover. However, the model outputs show that when there is an overlying H_2O ice-filled regolith layer, the stability of CO_2 ice increases.

When this H₂O ice-filled regolith layer extends to the surface, CO₂ ice can take several thousand years to sublimate away in the polar regions. In the equatorial region, on the other hand, CO₂ ice is unlikely to survive more than a few hundred years. The thickness of these H₂O ice-filled regolith and CO₂ ice-filled regolith layers is also an important factor, which was demonstrated by the Alternate Model layers of H₂O ice and CO₂ ice-filled regolith (*Alternate Layers*) and H₂O Ice-filled Regolith Over CO₂ Ice-filled Regolith Over H₂O Ice-filled Regolith (*W-C-W*) scenarios which have global average sublimation rates of 14.6 mm MY⁻¹ and 12.6 mm MY⁻¹, respectively. The results from these scenarios suggest that the stability of CO₂ ice increases as the thickness of the CO₂ ice-filled regolith and H₂O ice-filled regolith layers increases. The increased stability with the thickness of the ice-layers can be used to infer that for the CO₂ ice deposits within the SPLD that have survived periods of high obliquity, they would have needed to be covered relatively quickly by a H₂O ice-layer thick enough to drastically reduce the CO₂ ice sublimation rate.

Another factor that has a large influence on stability is the initial porosity of the overlying H₂O ice-filled regolith layer. If the initial porosity in the H₂O ice-filled regolith layer is high (~ 0.1), CO₂ ice sublimates away rapidly at a global average rate of 848.93 mm MY⁻¹. Whereas when the overlying H₂O ice-filled regolith layer has a lower initial porosity (~ 0.001), the average global sublimation rate drops by an order of magnitude to 25.75 mm MY⁻¹. When the overlying H₂O ice-filled regolith layer has no initial porosity, sublimation of CO₂ ice is limited by the rate of H₂O ice sublimation and the global CO₂ ice sublimation rate falls by another order of magnitude to 1.82 mm MY⁻¹. This implies that the method of H₂O ice deposition (particularly for surface H₂O ice) will have a large influence on the stability of any CO₂ ice. If the H₂O ice-layer deposited onto the CO₂ ice deposits in the SPLD was deposited as snow, the layer's high porosity would mean that the CO₂ ice deposit would rapidly sublimate away and remnant deposits are unlikely.

The geological properties of the regolith unit within which both ices form will also influence the stability of CO₂ ice deposits through changes in subsurface thermal conductivity. If the ice forms within a high thermal conductivity material, heat is con-

ducted faster to deeper regions, which causes any ice at these depths to become more unstable than when the thermal conductivity is lower. Six different subsurface structures were used in this thesis to explore this parameter space, including five different geological materials. The geological materials covered the range of thermal inertias expected on Mars, based on surface thermal inertia observations (Putzig et al., 2005), and the results matched those found in subsurface H₂O ice studies (e.g., Bandfield, 2007; Paige, 1992). In the H₂O Ice-filled Regolith Over CO₂ Ice-filled Regolith (*W-C*) scenario, CO₂ ice fills the pore space in the regolith below 1 m, which means that an increase in subsurface thermal conductivity is expected to reduce the stability of this CO₂ ice because subsurface temperatures in winter are warmer, resulting in more sublimation. This is demonstrated by the increase in global average sublimation rate from 25.8 mm MY⁻¹ (S06) to 35.6 mm MY⁻¹ (CDS-SS) when the average subsurface thermal conductivity is increased from 0.04 W m⁻¹ K⁻¹ to 1.12 W m⁻¹ K⁻¹. This will have a small influence on which regions are more likely to contain buried CO₂ ice over long timescales.

The obliquity has the largest influence on subsurface CO₂ ice of all the tested input parameters, due to its influence on surface solar insolation distribution. In the polar regions, the time needed for subsurface CO₂ ice to sublimate away is longest at the lowest obliquity (~ 7000 martian years at 15°; Figure 6.16) and shortest at the highest obliquity (400 martian years at 45°). Whereas in the equatorial regions the reverse is seen, since CO₂ ice stability is lowest at low obliquity (takes ~ 200 martian years to sublimate at 15° obliquity) and highest at high obliquities (~ 300 martian years at 45° obliquity). These variations are as expected because they follow the change in insolation as obliquity increases: polar regions become warmer and the equatorial region becomes cooler (Mischna et al., 2003). Since the obliquity results follow the expected distribution from previous work on surface CO₂ ice, they can then be used to provide insights into the formation of the CO₂ ice deposits in the SPLD. The sublimation rates calculated for the *W-C* scenario at each obliquity are of a similar order of magnitude to those from Buhler et al. (2019) for the net CO₂ loss/gain rate of the SPLD, showing that the results presented here can be used to provide further insights into CO₂ ice in the SPLD. I combined the estimated accumulation rates (Manning et al., 2019) and the

time it would take for H₂O snow to compact into a low porosity ice (Arthern, 2000; Manning et al., 2019) with the results from the simulations presented in this thesis to estimate the thickness of the CO₂ ice-layer that sublimates away during the formation of the bounding H₂O ice-layers in the SPLD. As H₂O snow, the porosity is high (~ 0.7) and sublimation rates would be closer to those calculated for a high initial porosity (0.1; PM04), whereas when the snow has compacted into low porosity H₂O ice, the results from the baseline simulations (with a porosity of 0.001) can be used. From these results, 0.7–27 km of CO₂ ice could sublimate away during the time it would take for H₂O snow to compact and form a 1 m thick H₂O ice-layer, depending on the densification timescale used. However, these estimates are based on values for an icy regolith and use estimated ice compaction timescales that vary drastically. Therefore, further work with dust proportions closer to those in the SPLD using the detailed schemes for vapour diffusion and phase partitioning of CO₂ and H₂O that are used in the MSSM are needed before more accurate estimates can be made.

7.1.1 Responses to Research Questions

1. **What is the impact of adding CO₂ ice physics on the H₂O ice distribution predicted by models that previously only took H₂O physics into account?**

The distribution of subsurface H₂O ice is well understood from previous studies using observational (e.g., Feldman et al., 2004) and numerical methods (e.g., Boynton et al., 2002; Mellon and Jakosky, 1993). In general, subsurface H₂O ice is expected to be stable across the polar regions and below a metre-scale regolith cover in the mid-latitudes (e.g., Feldman et al., 2004). Any H₂O ice within the equatorial regions is expected to be unstable and to sublimate away over time. These regions of stability are replicated in the MSSM simulations that are initialised with only H₂O ice, after the model has equilibrated in the first martian year. In these simulations, the H₂O ice sublimation rate is highest in the equatorial regions between 10°N/S, with sublimation rates of around 1.7×10^{-5} mm MY⁻¹ (S29). The only exception is in the H₂O Ice-filled Regolith over Ice-free Regolith (*W-IF*) scenario, where H₂O ice starts to form in the lowest layers of the subsurface. However, this is a consequence of using a fixed annual

atmospheric cycle and a no-flux base boundary, and after 25 martian years, the H₂O ice column density starts to decrease as expected. In the polar and mid-latitude regions, sublimation rate drops to zero apart from at the highest latitudes, where small amounts of H₂O ice accumulate ($\sim 0.0004 \text{ mm MY}^{-1}$ in the polar regions of S12) when there is an ice-free regolith layer. The same accumulation rates were also found in the CO₂ Ice-filled Regolith Over H₂O Ice-filled Regolith (*C-W*) scenario (S03) after the CO₂ ice had sublimated away within the first few martian years and in the Ice-free Regolith Over H₂O Ice-filled Regolith Over CO₂ Ice-filled Regolith (*IF-W-C*) scenario (S36) within the ice-free regolith layer.

The H₂O ice accumulation at the highest latitudes is due to the way the seasonal H₂O cycle is simulated by the MSSM. In the seasonal cycle, H₂O ice sublimates from the northern pole during northern summer, when the overlying CO₂ ice cover has sublimated away and vapour is transported away from the pole (e.g., Titov, 2002). Then, during northern winter, H₂O vapour is transported back to the northern pole and re-deposited at the surface, creating a closed system. This closed system is mostly simulated in the ice-free regolith across the entire subsurface (*IF*) scenario results, with the exception of a small build-up of H₂O ice ($<< 1 \text{ mm}$) in the northern polar region over time. This build up occurs because the atmosphere acts as a constant source of H₂O vapour in the MSSM, due to the fixed annual atmospheric cycles that are used. This small build up will not occur when the MSSM is integrated into the full three dimensional (3-D) LMD-UK Mars global circulation model (MGCM) and the atmospheric vapour pressure can respond to changes in subsurface vapour pressure. The integration of the MSSM into the MGCM is part of the next steps for this work and is discussed further in Section 7.2.2. To summarise, the addition of CO₂ ice physics into subsurface modelling of H₂O ice does not influence the distribution of H₂O ice when no CO₂ ice is initially present and the results produced match the distributions produced by previous models and observations.

2. How do CO₂ ice and H₂O ice interact in the subsurface of Mars?

The interactions of the CO₂ and H₂O cycles during condensation and sublimation is an area of research that was identified by Diniega and Putzig (2019) and Banfield (2020) as

needing in depth examination, so that the factors controlling the mass balance of both ices can be understood. The results presented here contribute to this understanding: when only CO₂ ice is present within the regolith, CO₂ ice sublimates away rapidly (in <100 martian years) at all latitudes. Whereas when covered by a H₂O ice-filled regolith layer, CO₂ ice stability increases drastically and the global average sublimation rate decreases by two orders of magnitude from 1810 mm MY⁻¹ in S09 to 25.8 mm MY⁻¹ in S06. This stability increases further when the CO₂ ice-filled regolith layer lies between two H₂O ice-filled regolith layers, as in the *W-C-W* scenario (S35), where the global average sublimation rate is 12.6 mm MY⁻¹.

The effect of subsurface CO₂ ice on the stability of H₂O ice, on the other hand, is much smaller. From the simulations presented here, it can be seen that the presence of CO₂ ice instead of H₂O ice under a 1 m H₂O ice-filled regolith layer causes a decrease in average subsurface temperatures (by ~3 K; Figure 4.23) due to the lower thermal conductivity. CO₂ ice also keeps the diffusion coefficient low in the model layers containing no H₂O ice, which acts to limit the H₂O ice sublimation rate. This can be seen in the order of magnitude difference in H₂O ice sublimation rate between the *W-IF* scenario (4.41×10^{-06} mm MY⁻¹ in S31) and the *W-C* scenario (2.98×10^{-07} mm MY⁻¹ in S06). The presence of a CO₂ ice-filled regolith layer between two H₂O ice-filled regolith layers also reduces the H₂O ice sublimation rate further (3.92×10^{-08} mm MY⁻¹ in S35) through limiting diffusion of H₂O vapour out of the lowest H₂O ice-filled regolith layer into the overlying CO₂ ice-filled regolith layer.

To summarise, the presence of subsurface CO₂ ice only has a small influence on H₂O ice stability and this influence is mostly due to changes in the thermal conductivity and porosity of the model layers that do not contain H₂O ice, whereas, an overlying H₂O ice-layer has a large influence on subsurface CO₂ ice and can reduce CO₂ ice sublimation enough that CO₂ ice takes thousands of martian years to sublimate away.

3. What impact does layering have on the stability of both H₂O and CO₂ ice?

Based on my simulation results, the stability of subsurface H₂O ice remains mostly

unaffected by the order in which ice-layers are arranged, whereas CO₂ ice is heavily dependent on the order of the ice-layers. An upper CO₂ ice-layer rapidly sublimates away and a slower sublimation rate of CO₂ ice is dependent on the presence of H₂O ice within the upper subsurface. The presence of an ice-free regolith layer causes rapid sublimation of CO₂ ice due to the faster rate of CO₂ vapour diffusion throughout the subsurface and into the atmosphere. The presence of an overlying H₂O ice-filled regolith layer is shown to be required for CO₂ ice to survive hundreds to thousands of martian years in the polar regions. However, this overlying H₂O ice-filled regolith layer is still not sufficient to prevent rapid CO₂ ice loss (<100 martian years to fully sublimate) if there is an overlying ice-free regolith layer, such as a debris cover. For a subsurface containing multiple layers of H₂O ice-filled regolith and CO₂ ice-filled regolith, the scenarios explored demonstrated that the thicknesses of these layers also influence their stability. In the *Alternate Layers* scenario, the ice within the regolith was alternated for every model layer, resulting in an global average sublimation rate of 14.6 mm MY⁻¹, whereas when there were only three larger layers (*W-C-W* scenario), the global average sublimation rate decreased to 12.6 mm MY⁻¹, demonstrating the increased stability that occurs with thicker ice-layers. This has obvious implications for the SPLD since their thinnest CO₂ ice-layers are thought to be ~10 m thick. These results can be used to infer that thinner CO₂ ice-layers (<2 m) are unlikely to be preserved over long timescales (>5 kyr). This investigation into the impact of layering has contributed to the aim of understanding the CO₂ ice deposits within the SPLD (identified as an area for future research by Diniega and Putzig, 2019) by demonstrating that the presence of H₂O ice-layers on either side of the CO₂ ice deposits in the SPLD are a key factor for allowing these CO₂ deposits to survive recent obliquity cycles.

4. How important are subsurface properties for the distribution of ices?

The results from the series of simulations run with different subsurface structures (Section 5.2) demonstrate the importance of the subsurface properties used. A series of four different regolith unit structures were investigated and the results showed that the thermal conductivity is the subsurface property that has the largest influence on CO₂ ice sublimation rate. The global average sublimation rate increases as average

subsurface thermal conductivity increases, which means that CO₂ ice is more likely to form and survive in regions of low thermal conductivity and therefore, low thermal inertia. However, the increase in thermal conductivity required to slightly increase the sublimation rate is large and the dependence of the distribution of CO₂ ice on thermal inertia, therefore, is likely to be smaller than the dependence of H₂O ice distribution on thermal inertia.

The porosity of the subsurface also influences the sublimation rate of each ice, but this is dependent on total porosity (regolith plus ice) rather than the intrinsic porosity of the regolith unit. This was also investigated through a series of initial ice porosity simulations (Section 5.1) that represented different initial total porosities. These results show the expected behaviour of CO₂ ice sublimating at a faster rate when initial porosity is higher: global average sublimation rate increases from 1.82 mm MY⁻¹ when the initial ice porosity is 0 (PM01) to 849 mm MY⁻¹ when the initial ice porosity is 0.1 (PM04).

In summary, variations in the total porosity are important to consider for the survival of CO₂ ice, whereas different subsurface structures will only have a small influence and do not need to be considered in detail. The total porosities used in this thesis assume a fixed permeability, which will also influence the time it takes for subsurface CO₂ ice to sublimate away and is an area for future investigation.

5. How do changes in the orbital obliquity of Mars change the stability of subsurface CO₂ ice?

The orbital obliquity has a large influence on subsurface CO₂ ice stability, with stability in the polar regions increasing as obliquity decreases and polar annual average sublimation rate decreases from 21.4 mm MY⁻¹ at 45° obliquity (S23) to 4.72 mm MY⁻¹ at 15° obliquity (S15) for the *W-C* scenario. In the equatorial regions, the opposite is the case as subsurface CO₂ ice stability decreases with decreasing obliquity and annual average sublimation rate increases from 30.1 mm MY⁻¹ at 45° obliquity (S23) to 44.4 mm MY⁻¹ at 15° obliquity (S15). Across the mid-latitudes, CO₂ ice stability appears to be mostly insensitive to the obliquity, with annual average sublimation rates remaining around

28 mm MY⁻¹ at all obliquities. Under present-day atmospheric conditions, these results suggest that CO₂ ice is only expected in the polar regions, confirming previous work on surface CO₂ ice. However, these results also suggest that as obliquity increases further, CO₂ ice in the equatorial region will become more stable and under the higher atmospheric pressures expected during the Noachian, the regions of CO₂ ice stability may have shifted towards the equator. This means that surface features on Noachian age terrains could also have formed due to CO₂ ice processes as well as H₂O ice processes and future investigations should explore this possibility further. In summary, the orbital obliquity is the most important of parameter of the ones explored in this thesis for the stability of CO₂ ice under present-day atmospheric conditions.

7.2 Future Work

The results presented in this thesis provide an initial investigation into the stability and behaviour of CO₂ ice within the subsurface using the MSSM. The ice-layer configurations, initial ice porosities and subsurface structures used only represent a small portion of the potential scenarios. Further work with the stand-alone MSSM should therefore focus on these other scenarios as well as on different features that would be useful to incorporate into the MSSM (Section 7.2.1).

Alongside further development of the MSSM, future work should include investigations using a version of the MGCM with the MSSM integrated into it. This is needed because the stand-alone MSSM uses fixed annual atmospheric cycles which do not fully capture the complexities of the surface-atmosphere boundary. The main way that this limitation causes issues is for CO₂ ice deposition. In the MSSM, the atmospheric CO₂ vapour density values are always at or below the CO₂ saturation vapour density, since the atmospheric CO₂ vapour density cycles are the final values after deposition has occurred in the initial MGCM simulations (see Section 3.7.1). This causes CO₂ ice to sublimate away over more of the year in the polar regions of the MSSM scenarios than would be expected for a full MGCM simulation because there is no seasonal CO₂ ice to protect the underlying CO₂ ice during spring when this seasonal cover would be sublimated away. Therefore, using the full MGCM for the atmospheric boundary will improve the accuracy of the results. Initial work has been done to integrate the

MSSM into the MGCM, which is discussed in Section 7.2.2 alongside potential scenarios that can be investigated with this combined model. A detailed description of this integration can be found in Appendix B.2.

The MSSM (both as a stand-alone and combined with the MGCM) will also be a useful tool for interpreting future observational data. Future missions, such as the international Mars Ice Mapper (i-MIM), are aiming to characterise the subsurface in more detail and models such as the MSSM are useful for investigating seasonal changes across the surface at times when observations are not taken. This is discussed in more detail in Section 7.2.3.

The final avenue for future work is experimental, rather than using the MSSM. During development of the MSSM it became clear that many of the equations for CO₂ properties, such as CO₂ adsorption and CO₂ sublimation under a regolith cover, have limited experimental results that are often contradictory. Future experiments would therefore be useful to clarify the current understanding and these are discussed in Section 7.2.4.

7.2.1 Future Work with the MSSM

Future work with the MSSM will include further investigations into what possible ice-layer configurations are required such that CO₂ ice could remain stable at different obliquities. In particular this should focus on obliquities higher than 45°, which is the limit used in this thesis, since CO₂ ice is expected to be stable at different locations as obliquity increases. The current version can also be integrated into either the 3-D MGCM to investigate global effects (discussed in Section 7.2.2) or into the one dimensional (1-D) version of the MGCM to investigate local effects. Integrating the MSSM into the 1-D MGCM would be particularly useful for investigating the formation of frost on slopes and for detailed modelling at individual locations, such as at the landing sites of rovers and landers. The MSSM could also be used alongside models of the formation of CO₂ ice deposits within the SPLD (Buhler et al., 2019; Manning et al., 2019) to estimate how the sublimation rates of CO₂ ice would be affected by the overlying H₂O ice-layer over time while the H₂O ice-layer increases in thickness. The MSSM can also be used to investigate the behaviour of H₂O ice and CO₂ ice under

Noachian conditions if the atmospheric profiles were taken from the outputs of an early-Mars global circulation model (GCM), which takes into account the climatic changes that would occur under higher atmospheric pressures and lower solar luminosities.

The MSSM can also be adapted easily for a variety of different martian investigations by either altering the subsurface properties already incorporated or adding in new properties. One way to adapt the MSSM is to alter the subsurface structure (defined by thermal conductivity, density and porosity), which was shown in Section 5.2 for six potential subsurface structures. Mars is expected to host terrains with a wide variety of subsurface structures based on the diversity seen in surface thermal inertia (Putzig et al., 2005). New investigations using a wider variety of subsurface structures (including varying properties such as porosity, permeability, thermal conductivity) or under a variety of deposition scenarios (such as an advancing glacier or frozen water from outflow channels covering already deposited CO₂ ice) would further our understanding of the influence of the subsurface on both subsurface H₂O ice and CO₂ ice.

One feature that would be useful to update is the adsorption of H₂O and CO₂. In the MSSM, a fixed value is used for both due to the conflicting measurements for both properties in the literature, where measurements using similar minerals have a wide range and a clear adsorption isotherm is hard to define (Figures 3.12 and 3.15). However, this fixed value is only appropriate for long time-scale studies (>30 martian years; Schorghofer and Aharonson, 2005) and investigations of annual variations in the subsurface will require full adsorption isotherms for each volatile to be incorporated (Böttger et al., 2004). This will require experimental work to determine these isotherms, which is discussed further in Section 7.2.4.

The value of tortuosity used in the subsurface is another feature that would be useful to update in the future, since a constant value is only applicable for a limited number of subsurfaces. Ideally, a depth and ice-content dependent equation for tortuosity would be incorporated. In order for this to be added, experimental work constraining the relationship between tortuosity and porosity for a variety of materials and ice contents would be required.

A further feature that could be useful to add in is the ability to simulate excess ice

and clathrates. Excess ice will influence the stability of both ices, as well as the H_2O and CO_2 diffusion rates. The influence of excess H_2O ice has been modelled in several studies (e.g. Fisher, 2005; Schorghofer, 2010) and the methods used to incorporate excess H_2O ice can be adapted to be appropriate for excess CO_2 ice. The equations for the formation of clathrates would also be useful to include since it has been suggested that clathrates could form between a pure H_2O ice and pure CO_2 ice-layer (Hoffman, 2000). The impact of their presence on the stability of CO_2 ice and H_2O ice-layers is an area that needs further exploration, and the MSSM could be used for this.

7.2.2 Future Work with the Combined MGCM and MSSM Model

The MSSM has been designed to be easily integrated into the MGCM to allow for runs with a complex atmosphere. However, in this thesis, all of the simulations were run using the stand-alone version of the MSSM that uses a fixed annual atmospheric cycle for the surface boundary. This was done because of the computational time required and the fact that the integration of the MSSM into the MGCM is still in progress (a detailed description of this integration process can be found in Appendix B.2). One of the main features of the MSSM that needs updating before the combined version of the MGCM and MSSM can be used is the subsurface structure. In the combined version, the subsurface structure of the MSSM needs to be defined at every location to correspond with the surface thermal inertia values. This will ensure that surface temperature calculations are minimally affected by the addition of the MSSM. In the current combined version, a fixed subsurface structure is used at all locations, which creates mismatches with the surface temperature calculations already used in the MGCM. Future work will, therefore, involve improving the integration between the two schemes.

The use of a detailed climate model is expected to have a large impact on the stability of CO_2 ice in the mid-latitude and equatorial regions, where diurnal temperature cycles are the largest, and a smaller impact on the stability of CO_2 ice in the polar regions, where diurnal temperature changes are smaller. Therefore, future simulations with the combined model are necessary to more accurately investigate the stability of

subsurface CO₂ ice in different ice-layer configurations across Mars. However, the subsurface structure at each location needs to be updated to correspond with the surface thermal inertia and albedo before this can be done. Testing will also be required to ensure that the addition of the MSSM does not completely change the climate results of the MGCM when no ice is included. Alongside the stability of carbon dioxide ice under different ice-layer and obliquity configurations, the combined model can also be used in several other investigations to answer questions such as:

- Does the presence of subsurface CO₂ ice have an impact on climate dynamics?
- How do simulations of early Mars change with the inclusion of subsurface CO₂ ice?
- Could subsurface CO₂ ice deposits provide an explanation for some of the excess CO₂ from the Noachian that is unaccounted for by current CO₂ reservoirs?

7.2.3 Future Mars Missions and Observations

The results from this thesis and future work with the MSSM can also be used to inform and interpret future observations and missions of subsurface properties. The MSSM has been designed so that the subsurface structure is customisable and it can be initialised with any amounts of H₂O ice and CO₂ ice. This makes it an invaluable tool for interpreting observations of the subsurface, particularly for interpreting orbital observations, which can measure hydrogen content within the shallow subsurface (such as with Mars Odyssey Neutron Spectrometer (MONS) on Mars Odyssey) or the properties of subsurface layers (such as with Shallow Radar (SHARAD) on Mars Reconnaissance Orbiter (MRO) and the planned radar instrument on the i-MIM mission) and are spatially variable over time. The MSSM can therefore be used to model the behaviour of ice within the subsurface between times of observation.

The i-MIM orbital mission is a spacecraft concept that includes a radar-carrying orbiter that will map the distribution of H₂O ice within the upper 10 m of the subsurface and characterise the subsurface materials with depth (Ianson et al., 2021; Watzin and Haltigin, 2020). The eventual aim of these observations is to determine the furthest equatorward region of H₂O ice stability to inform future work towards human exploration. An accurate characterisation of these regions of H₂O ice stability, and

all of the factors that influence this stability, is therefore important to ensure that future human exploration missions are focused on areas containing accessible H_2O ice. The results in this thesis and future work with the MSSM can be used to investigate the plausibility of the different subsurface structures found by the radar observations. Future work with the MSSM can also be used to characterise seasonal variations in H_2O ice within these subsurface structures throughout the year; orbital observations are spatially variable due to the tracking of the spacecraft and year-long observations at individual locations are not possible. The MSSM can therefore be used to assimilate these low cadence observations into a coherent model of the subsurface.

7.2.4 Future Experimental Work

During development of the MSSM it became clear that several material properties needed for the model are not yet well constrained. Future work to constrain these values and relationships would, therefore, be worthwhile. One such property is H_2O adsorption onto martian regolith. There have been many studies into H_2O adsorption (e.g., Fanale and Cannon, 1971; Jänchen et al., 2009; Zent et al., 1993), although the results of these studies show a wide range of results (Figure 3.12). This range is expected for different geological materials, since different materials have different adsorption capacities. However, some of the range that can be seen in Figure 3.12 occurs for the same materials, or those that are expected to have similar adsorption capacities (e.g. basalt and palagonite) depending on the study. Therefore, further work to determine the adsorption of H_2O onto regolith grains for a variety of geological materials would be useful to constrain the adsorption isotherms appropriate for martian regolith. Alongside H_2O adsorption, CO_2 adsorption under martian conditions is another area that would benefit from further experimental work. The experimental work to date has produced diverse results (Figure 3.15) and the relationship between CO_2 adsorption, temperature and pressure is not clear when all of the studies are compared with each other.

The final two areas that would benefit from further experimental work are other CO_2 properties. The first is the diffusion coefficient of CO_2 vapour in martian regolith. The equation used for this relationship in the MSSM (Equation 3.38) is the only equa-

tion available in the literature, but is derived from an Earth-based theoretical study (Barrer, 1967) and robust experimental confirmation that this equation is appropriate for CO₂ vapour diffusion under martian conditions is needed. The second property is the sublimation rate of CO₂ ice when under a regolith layer. Previous studies of CO₂ ice sublimation rate have only investigated the surface sublimation rate (e.g. Aylward et al., 2019; Blackburn et al., 2010; Cedillo-Flores et al., 2011). However, this sublimation rate is likely to be higher than the true CO₂ ice sublimation rate if the CO₂ ice is under a porous layer (of regolith, debris or H₂O ice). This has been proven in experimental studies of the sublimation rate of buried H₂O ice, which have shown that sublimation rate is inversely proportional to the depth of the layer (e.g., Bryson et al., 2008; Chevrier et al., 2007, 2008; Soare et al., 2008). Therefore, an experimental study of the effect of an overlying regolith or porous H₂O ice-layer on the CO₂ ice sublimation rate would be beneficial for both the MSSM and for future studies investigating the buried CO₂ ice within the SPLD.

8 | References

- Aharonson, O. and Schorghofer, N. Subsurface Ice on Mars with Rough Topography. *Journal of Geophysical Research: Planets*, vol. 111(E11), 2006. ISSN 2156-2202. doi: 10.1029/2005je002636.
- Aharonson, O., Zuber, M. T., Smith, D. E., Neumann, G. A., Feldman, W. C., and Prettyman, T. H. Depth, Distribution, and Density of CO₂ Deposition on Mars. *Journal of Geophysical Research: Planets*, vol. 109(E5), 2004. ISSN 2156-2202. doi: 10.1029/2003JE002223.
- Anderson, D. M., Gaffney, E. S., and Low, P. F. Frost Phenomena on Mars. *Science*, 155(3760):319–322, 1967. doi: 10.1126/science.155.3760.319.
- Armstrong, J. C., Leovy, C. B., and Quinn, T. A 1 Gyr Climate Model for Mars: New orbital statistics and the importance of seasonally resolved polar processes. *Icarus*, vol. 171(2):pp. 255–271, 2004. ISSN 0019-1035. doi: 10.1016/j.icarus.2004.05.007.
- Arthern, R. Densification of Water Ice Deposits on the Residual North Polar Cap of Mars. *Icarus*, 144(2):367–381, apr 2000. doi: 10.1006/icar.1999.6308.
- Aylward, D. S., Schmidt, L. M., and Levy, J. S. Formation of Coarse Sediment Lags in Ice-sediment Mixtures: A geomorphic signature of sublimation on regolith surfaces. *Planetary and Space Science*, May 2019. doi: 10.1016/j.pss.2019.05.006. URL <https://doi.org/10.1016/j.pss.2019.05.006>.
- Ballou, E. V., Wood, P. C., Wydeven, T., Lehwalt, M. E., and Mack, R. E. Chemical Interpretation of Viking Lander 1 Life Detection Experiment. *Nature*, 271(5646): 644–645, February 1978. doi: 10.1038/271644a0. URL <https://doi.org/10.1038/271644a0>.
- Bandfield, J. L. Spectroscopic Identification of Carbonate Minerals in the Martian Dust. *Science*, 301(5636):1084–1087, aug 2003. doi: 10.1126/science.1088054.
- Bandfield, J. L. High-resolution Subsurface Water-Ice Distributions on Mars. *Nature*, vol. 447(7140):pp. 64–67, 2007. ISSN 0028-0836. doi: 10.1038/nature05781.
- Bandfield, J. L. and Feldman, W. C. Martian High Latitude Permafrost Depth and Surface Cover Thermal Inertia Distributions. *Journal of Geophysical Research: Planets*, vol. 113(E8), 2008. ISSN 2156-2202. doi: 10.1029/2007je003007.
- Banfield, D. Mars Scientific Goals, Objectives, Investigations, and Priorities. white paper posted March, 2020 by the Mars Exploration Program Analysis Group (MEPAG), 2020. URL <https://mepag.jpl.nasa.gov/reports.cfm>, 2020.
- Banin, A. The enigma of the martian soil. *Science*, 309(5736):888–890, 2005. doi: 10.1126/science.1112794.
- Banks, M. E., Byrne, S., Galla, K., McEwen, A. S., Bray, V. J., Dundas, C. M., Fishbaugh, K. E., Herkenhoff, K. E., and Murray, B. C. Crater Population and Resurfacing of the Martian North Polar Layered Deposits. *Journal of Geophysical*

- Research*, 115(E8), August 2010. doi: 10.1029/2009je003523. URL <https://doi.org/10.1029/2009je003523>.
- Barnes, J. R., Haberle, R. M., Wilson, R. J., Lewis, S. R., Murphy, J. R., and Read, P. L. The Global Circulation. In Haberle, R. M., Clancy, R. T., Forget, F., Smith, M. D., and Zurek, R. W., editors, *The Atmosphere and Climate of Mars*, pages 229–294. Cambridge University Press, 2017. doi: 10.1017/9781139060172.009.
- Barrer, R. M. Surface and volume flow in porous media. *The solid-gas interface*, 2: 557–609, 1967.
- Beardsmore, G. R. and Cull, J. P. *Crustal Heat Flow: A guide to measurement and modelling*. Cambridge University Press, 2001.
- Becerra, P., Sori, M. M., Thomas, N., Pommerol, A., Simioni, E., Sutton, S. S., Tulyakov, S., and Cremonese, G. Timescales of the Climate Record in the South Polar Ice Cap of Mars. *Geophysical Research Letters*, 46(13):7268–7277, jul 2019. doi: 10.1029/2019gl083588.
- Bell, J. F., McSween, H. Y., Crisp, J. A., Morris, R. V., Murchie, S. L., Bridges, N. T., Johnson, J. R., Britt, D. T., Golombek, M. P., Moore, H. J., et al. Mineralogic and compositional properties of Martian soil and dust: Results from Mars Pathfinder. *Journal of Geophysical Research: Planets*, 105(E1):1721–1755, 2000. doi: 10.1029/1999je001060.
- Bibring, J.-P., Langevin, Y., Poulet, F., Gendrin, A., Gondet, B., Berthé, M., Soufflot, A., Drossart, P., Combes, M., Bellucci, G., et al. Perennial Water Ice Identified in the South Polar Cap of Mars. *Nature*, 428(6983):627, 2004. doi: 10.1038/nature02461.
- Bibring, J.-P., Langevin, Y., Gendrin, A., Gondet, B., Poulet, F., Berthé, M., Soufflot, A., Arvidson, R., Mangold, N., Mustard, J., et al. Mars Surface Diversity as Revealed by the OMEGA/Mars Express Observations. *Science*, 307(5715):pp. 1576–1581, 2005. doi: 10.1126/science.1108806.
- Bierson, C. J., Phillips, R. J., Smith, I. B., Wood, S. E., Putzig, N. E., Nunes, D., and Byrne, S. Stratigraphy and Evolution of the Buried CO₂ Deposit in the Martian South Polar Cap. *Geophysical Research Letters*, 43(9):4172–4179, 2016. doi: 10.1002/2016gl068457.
- Bills, B. G. The Rigid Body Obliquity History of Mars. *Journal of Geophysical Research: Solid Earth*, 95(B9):14137–14153, 1990. doi: 10.1029/jb095ib09p14137.
- Bills, B. G. and Keane, J. T. Mars Obliquity Variations are Both Non-chaotic and Possibly Fully Damped. In *The 50th Lunar and Planetary Science Conference 2019*, 2019.
- Bish, D. L., Vaniman, D. T., Fialips, C. I., Carey, J. W., and Feldman, W. C. Can Hydrous Minerals Account for the Observed Mid-latitude Water on Mars? In *Sixth International Conference on Mars*, 2003. URL <https://www.osti.gov/biblio/976616>.
- Blackburn, D. G., Bryson, K. L., Chevrier, V. F., Roe, L. A., and White, K. F. Sublimation Kinetics of CO₂ Ice on Mars. *Planetary and Space Science*, vol. 58(5): pp. 780–791, 2010. ISSN 0032-0633. doi: 10.1016/j.pss.2009.12.004.

- Böttger, H. M., Lewis, S. R., Read, P. L., and Forget, F. The Effect of a Global Dust Storm on Simulations of the Martian Water Cycle. *Geophysical Research Letters*, 31 (22), 2004. ISSN 1944-8007. doi: 10.1029/2004GL021137.
- Böttger, H. M., Foing, B. H., Read, P. L., and Lewis, S. R. Diurnal Variability in Martian Atmospheric Water Vapour: Near surface ice out of equilibrium as a source. In *36th Annual Lunar and Planetary Science Conference*, volume 36, page p. 1647, 2005.
- Böttger, H. M., Lewis, S. R., Read, P. L., and Forget, F. The Effects of the Martian Regolith on GCM Water Cycle Simulations. *Icarus*, vol. 177(1):pp. 174–189, 2005b. ISSN 0019-1035. doi: 10.1016/j.icarus.2005.02.024.
- Boynton, W. V., Feldman, W. C., Squyres, S. W., Prettyman, T. H., Brückner, J., Evans, L. G., Reedy, R. C., Starr, R., Arnold, J. R., and Drake, D. M. Distribution of Hydrogen in the Near Surface of Mars: Evidence for subsurface ice deposits. *Science*, vol. 297(5578):pp. 81–85, 2002. ISSN 0036-8075. doi: 10.1126/science.1073722.
- Bramson, A. M., Byrne, S., Putzig, N. E., Sutton, S., Plaut, J. J., Brothers, T. C., and Holt, J. W. Widespread Excess Ice in Arcadia Planitia, Mars. *Geophysical Research Letters*, 42(16):6566–6574, 2015. doi: 10.1002/2015gl064844.
- Brough, S., Hubbard, B., and Hubbard, A. Area and Volume of Mid-latitude Glacier-like Forms on Mars. *Earth and Planetary Science Letters*, 507:10–20, February 2019. doi: 10.1016/j.epsl.2018.11.031. URL <https://doi.org/10.1016/j.epsl.2018.11.031>.
- Bryson, K. L., Chevrier, V., Sears, D. W. G., and Ulrich, R. Stability of Ice on Mars and the Water Vapor Diurnal Cycle: Experimental study of the sublimation of ice through a fine-grained basaltic regolith. *Icarus*, 196(2):pp. 446–458, 2008. doi: 10.1016/j.icarus.2008.02.011.
- Buffett, B. A. Clathrate Hydrates. *Annual Review of Earth and Planetary Sciences*, 28(1):477–507, may 2000. doi: 10.1146/annurev.earth.28.1.477.
- Buhler, P. B., Ingersoll, A. P., Piqueux, S., Ehlmann, B. L., and Hayne, P. O. Co-evolution of Mars’s atmosphere and massive south polar CO₂ ice deposit. *Nature Astronomy*, 4(4):364–371, dec 2019. doi: 10.1038/s41550-019-0976-8.
- Buntebarth, G. *Geothermics: An introduction*. Springer Science & Business Media, 1984. doi: 10.1007/978-3-642-69323-6.
- Byrne, S., Zuber, M. T., and Neumann, G. A. Interannual and seasonal behavior of Martian residual ice-cap albedo. *Planetary and Space Science*, 56(2):194–211, feb 2008. doi: 10.1016/j.pss.2006.03.018.
- Byrne, S., Dundas, C. M., Kennedy, M. R., Mellon, M. T., McEwen, A. S., Cull, S. C., Daubar, I. J., Shean, D. E., Seelos, K. D., Murchie, S. L., Cantor, B. A., Arvidson, R. E., Edgett, K. S., Reufer, A., Thomas, N., Harrison, T. N., Posiolova, L. V., and Seelos, F. P. Distribution of Mid-Latitude Ground Ice on Mars from New Impact Craters. *Science*, 325(5948):1674–1676, sep 2009. doi: 10.1126/science.1175307.
- Carr, M. H. *Overview*, pages 1–22. Cambridge Planetary Science. Cambridge University Press, 2007a. doi: 10.1017/CBO9780511536007.003.

- Carr, M. H. *Global structure and tectonics*, page 77–94. Cambridge Planetary Science. Cambridge University Press, 2007b. doi: 10.1017/CBO9780511536007.006.
- Carr, M. H. and Head, J. W. Geologic History of Mars. *Earth and Planetary Science Letters*, 294(3–4):pp. 185–203, 2010. doi: 10.1016/j.epsl.2009.06.042.
- Carrozzo, F. G., Bellucci, G., Altieri, F., D’aversa, E., and Bibring, J. P. Mapping of Water Frost and Ice at Low Latitudes on Mars. *Icarus*, vol. 203(2):pp. 406–420, 2009. ISSN 0019-1035. doi: 10.1016/j.icarus.2009.05.020.
- Carslaw, H. S. and Jaeger, J. C. *Conduction of Heat in Solids. Oxford: Clarendon Press, 1959, 2nd ed.*, 1959.
- Cedillo-Flores, Y., Treiman, A. H., Lasue, J., and Clifford, S. M. CO₂ Gas Fluidization in the Initiation and Formation of Martian Polar Gullies. *Geophysical Research Letters*, vol. 38(21), 2011. ISSN 1944-8007. doi: 10.1029/2011GL049403.
- Chamberlain, M. A. and Boynton, W. V. Response of Martian Ground Ice to Orbit-induced Climate Change. *Journal of Geophysical Research: Planets*, 112(E6), 2007. doi: 10.1029/2006je002801.
- Chevrier, V., Sears, D. W. G., Chittenden, J. D., Roe, L. A., Ulrich, R., Bryson, K., Billingsley, L., and Hanley, J. Sublimation Rate of Ice Under Simulated Mars Conditions and The Effect of Layers of Mock Regolith JSC Mars-1. *Geophysical Research Letters*, 34(2), 2007. doi: 10.1029/2006gl028401.
- Chevrier, V., Ostrowski, D. R., and Sears, D. W. G. Experimental Study of the Sublimation of Ice Through an Unconsolidated Clay Layer: Implications for the stability of ice on Mars and the possible diurnal variations in atmospheric water. *Icarus*, 196(2):pp. 459–476, 2008. doi: 10.1016/j.icarus.2008.03.009.
- Christensen, P. R. and Zurek, R. W. Martian north polar hazes and surface ice: Results from the Viking Survey/Completion Mission. *Journal of Geophysical Research: Solid Earth*, 89(B6):4587–4596, jun 1984. doi: 10.1029/jb089ib06p04587.
- Christensen, P. R., Bandfield, J. L., Hamilton, V. E., Ruff, S. W., Kieffer, H. H., Titus, T. N., Malin, M. C., Morris, R. V., Lane, M. D., and Clark, R. L. Mars Global Surveyor Thermal Emission Spectrometer Experiment: Investigation description and surface science results. *Journal of Geophysical Research: Planets*, vol. 106(E10):pp. 23823–23871, 2001. ISSN 2156-2202. doi: 10.1029/2000JE001370.
- Christensen, P. R., Jakosky, B. M., Kieffer, H. H., Malin, M. C., McSween, H. Y., Nealson, K., Mehall, G. L., Silverman, S. H., Ferry, S., Caplinger, M., and Ravine, M. The Thermal Emission Imaging System (THEMIS) for the Mars 2001 Odyssey Mission. *Space Science Reviews*, 110(1):85–130, Jan 2004. ISSN 1572-9672. doi: 10.1023/B:SPAC.0000021008.16305.94. URL <https://doi.org/10.1023/B:SPAC.0000021008.16305.94>.
- Clancy, R. T., Grossman, A. W., Wolff, M. J., James, P. B., Rudy, D. J., Billawala, Y. N., Sandor, B. J., Lee, S. W., and Muhleman, D. O. Water Vapor Saturation at Low Altitudes around Mars Aphelion: A Key to Mars Climate? *Icarus*, 122(1): 36–62, July 1996. doi: 10.1006/icar.1996.0108. URL <https://doi.org/10.1006/icar.1996.0108>.
- Clapeyron, É. Mémoire Sur la Puissance Motrice de la Chaleur. *Journal de l’École polytechnique*, 14:153–190, 1834.

- Clark, B. R. and Mullin, R. P. Martian Glaciation and the Flow of Solid CO₂. *Icarus*, 27(2):215–228, 1976.
- Clark, R. N. The surface condensates on Mars observed by Viking: Frost layers several tenths of a millimeter thick. In *Lunar and Planetary Science Conference*, volume 11, pages 160–161, 1980.
- Clennell, M. B. Tortuosity: A guide through the maze. *Geological Society, London, Special Publications*, 122(1):299–344, 1997. doi: 10.1144/gsl.sp.1997.122.01.18.
- Clifford, S. M. and Parker, T. J. The Evolution of the Martian Hydrosphere: Implications for the fate of a primordial ocean and the current state of the northern plains. *Icarus*, 154(1):pp. 40–79, 2001. doi: 10.1006/icar.2001.6671.
- Clifton, A., Manes, C., Rüedi, J.-D., Guala, M., and Lehning, M. On Shear-Driven Ventilation of Snow. *Boundary-Layer Meteorology*, 126(2):249–261, nov 2007. doi: 10.1007/s10546-007-9235-0.
- Colaïtis, A., Spiga, A., Hourdin, F., Rio, C., Forget, F., and Millour, E. A Thermal Plume Model for the Martian Convective Boundary Layer. *Journal of Geophysical Research: Planets*, 118(7):1468–1487, jul 2013. doi: 10.1002/jgre.20104.
- Conway, S. J. and Balme, M. R. Decameter Thick Remnant Glacial Ice Deposits on Mars. *Geophysical Research Letters*, 41(15):5402–5409, August 2014. doi: 10.1002/2014gl060314. URL <https://doi.org/10.1002/2014gl060314>.
- Conway, S. J., de Haas, T., and Harrison, T. N. Martian gullies: a comprehensive review of observations, mechanisms and insights from Earth analogues. *Geological Society, London, Special Publications*, 467(1):7–66, October 2018. doi: 10.1144/sp467.14. URL <https://doi.org/10.1144/sp467.14>.
- Cornwall, M. *Estimated Planetary Heat Flow from a Shallow Subsurface Heat Flow Measurement*. Thesis, The Open University, 2014.
- Cross, A. J., Goldsby, D. L., Hager, T. F., and Smith, I. B. The Rheological Behavior of CO₂ Ice: Application to glacial flow on Mars. *Geophysical Research Letters*, 47(22), nov 2020. doi: 10.1029/2020gl090431.
- Cuffey, K. M. and Paterson, W. S. B. *The Physics of Glaciers*. Academic Press, 2010.
- Cull, S., Arvidson, R. E., Mellon, M. T., Skemer, P., Shaw, A., and Morris, R. V. Compositions of Subsurface Ices at the Mars Phoenix Landing Site. *Geophysical Research Letters*, vol. 37(24), 2010. ISSN 1944-8007. doi: 10.1029/2010GL045372.
- Currie, J. A. Gaseous Diffusion in Porous Media. Part 2.-Dry granular materials. *British Journal of Applied Physics*, 11(8):pp. 318, 1960. doi: 10.1088/0508-3443/11/8/303.
- Dehant, V., Banerdt, B., Lognonne, P., Grott, M., Asmar, S., Biele, J., Breuer, D., Forget, F., Jaumann, R., Johnson, C., et al. Future Mars Geophysical Observatories for Understanding its Internal Structure, Rotation, and Evolution. *Planetary and Space Science*, 68(1):pp. 123–145, 2012. doi: 10.1016/j.pss.2011.10.016.
- Demidov, N. E., Bazilevskii, A. T., and Kuz'min, R. O. Martian soils: Varieties, structure, composition, physical properties, drillability, and risks for landers. *Solar System Research*, 49(4):pp. 209–225, 2015. doi: 10.1134/s0038094615040024.

- Devkota, B. H. and Imberger, J. Lagrangian Modeling of Advection-Diffusion Transport in Open Channel Flow. *Water Resources Research*, 45(12), dec 2009. doi: 10.1029/2009wr008364.
- Di Achille, G. and Hynek, B. M. Ancient ocean on Mars supported by global distribution of deltas and valleys. *Nature Geoscience*, 3(7):pp. 459, 2010. doi: 10.1038/ngeo891.
- Dickson, J. L., Head, J. W., and Marchant, D. R. Late Amazonian Glaciation at the Dichotomy Boundary on Mars: Evidence for glacial thickness maxima and multiple glacial phases. *Geology*, 36(5):411, 2008. doi: 10.1130/g24382a.1. URL <https://doi.org/10.1130/g24382a.1>.
- Diniega, S. and Putzig, N. E. MEPAG ICE-SAG Final Report. Report from the Ice and Climate Evolution Science Analysis group (ICE-SAG), 2019. URL <http://mepag.nasa.gov/reports.cfm>, 2019.
- Dobrovolskis, A. and Ingersoll, A. P. Carbon Dioxide-Water Clathrate as a Reservoir of CO₂ on Mars. *Icarus*, vol. 26(3):pp. 353–357, 1975. ISSN 0019-1035. doi: 10.1016/0019-1035(75)90178-5.
- Dundas, C. M. and Byrne, S. Modeling Sublimation of Ice Exposed by New Impacts in the Martian Mid-latitudes. *Icarus*, 206(2):716–728, apr 2010. doi: 10.1016/j.icarus.2009.09.007.
- Dundas, C. M., Bramson, A. M., Ojha, L., Wray, J. J., Mellon, M. T., Byrne, S., McEwen, A. S., Putzig, N. E., Viola, D., Sutton, S., Clark, E., and Holt, J. W. Exposed Subsurface Ice Sheets in the Martian Mid-latitudes. *Science*, 359(6372):pp. 199–201, 2018. ISSN 0036-8075. doi: 10.1126/science.aao1619.
- Ehlmann, B. L., Mustard, J. F., Murchie, S. L., Poulet, F., Bishop, J. L., Brown, A. J., Calvin, W. M., Clark, R. N., Marais, D. J. D., Milliken, R. E., Roach, L. H., Roush, T. L., Swayze, G. A., and Wray, J. J. Orbital Identification of Carbonate-Bearing Rocks on Mars. *Science*, 322(5909):1828–1832, December 2008. doi: 10.1126/science.1164759. URL <https://doi.org/10.1126/science.1164759>.
- Ehlmann, B. L., Mustard, J. F., Murchie, S. L., Bibring, J.-P., Meunier, A., Fraeman, A. A., and Langevin, Y. Subsurface Water and Clay Mineral Formation During the Early History of Mars. *Nature*, 479(7371):pp. 53, 2011. doi: 10.1038/nature10582.
- Fanale, F. P. and Cannon, W. A. Adsorption on the Martian regolith. *Nature*, 230(5295):pp. 502, 1971. doi: 10.1038/230502a0.
- Fanale, F. P. and Cannon, W. A. Exchange of Adsorbed H₂O and CO₂ Between the Regolith and Atmosphere of Mars Caused by Changes in Surface Insolation. *Journal of Geophysical Research*, 79(24):pp. 3397–3402, 1974. doi: 10.1029/jc079i024p03397.
- Fanale, F. P. and Cannon, W. A. Mars: CO₂ adsorption and capillary condensation on clays—significance for volatile storage and atmospheric history. *Journal of Geophysical Research: Solid Earth*, vol. 84(B14):pp. 8404–8414, 1979. ISSN 2156-2202. doi: 10.1029/JB084iB14p08404.
- Fanale, F. P. and Jakosky, B. M. Regolith-Atmosphere Exchange of Water and Carbon Dioxide on Mars: Effects on atmospheric history and climate change. *Planetary and Space Science*, 30(8):pp. 819–831, 1982b. doi: 10.1016/0032-0633(82)90114-3.

- Fanale, F. P. and Salvail, J. R. Quasi-periodic Atmosphere-Regolith-Cap CO₂ Redistribution in the Martian Past. *Icarus*, 111(2):305–316, oct 1994. doi: 10.1006/icar.1994.1147.
- Fanale, F. P., Banerdt, B. W., Saunders, S. R., Johansen, L. A., and Salvail, J. R. Seasonal Carbon Dioxide Exchange Between the Regolith and Atmosphere of Mars: Experimental and theoretical studies. *Journal of Geophysical Research: Solid Earth*, vol. 87(B12):pp. 10215–10225, 1982a. ISSN 2156-2202. doi: 10.1029/jb087ib12p10215.
- Fanale, F. P., Salvail, J. R., Banerdt, B. W., and Saunders, S. R. Mars: The regolith-atmosphere-cap system and climate change. *Icarus*, vol. 50(2):pp. 381–407, 1982c. ISSN 0019-1035. doi: 10.1016/0019-1035(82)90131-2.
- Fanale, F. P., Salvail, J. R., Zent, A. P., and Postawko, S. E. Global Distribution and Migration of Subsurface Ice on Mars. *Icarus*, vol. 67(1):pp. 1–18, 1986. ISSN 0019-1035. doi: 10.1016/0019-1035(86)90170-3.
- Farris, H. N., Conner, M. B., Chevrier, V. F., and Rivera-Valentin, E. G. Adsorption Driven Regolith-Atmospheric Water Vapor Transfer on Mars: An analysis of Phoenix TECP data. *Icarus*, 308:pp. 71 – 75, 2018. ISSN 0019-1035. doi: 10.1016/j.icarus.2017.08.002. Mars Polar Science VI.
- Fassett, C. I. and Head, J. W. Valley network-fed, open-basin lakes on Mars: Distribution and implications for Noachian surface and subsurface hydrology. *Icarus*, 198(1):37–56, November 2008. doi: 10.1016/j.icarus.2008.06.016. URL <https://doi.org/10.1016/j.icarus.2008.06.016>.
- Fastook, J. L., Head, J. W., Marchant, D. R., and Forget, F. Tropical Mountain Glaciers on Mars: Altitude-dependence of ice accumulation, accumulation conditions, formation times, glacier dynamics, and implications for planetary spin-axis/orbital history. *Icarus*, 198(2):pp. 305–317, 2008. doi: 10.1016/j.icarus.2008.08.008.
- Feldman, W. C., Prettyman, T. H., Maurice, S., Plaut, J. J., Bish, D. L., Vaniman, D. T., Mellon, M. T., Metzger, A. E., Squyres, S. W., Karunatillake, S., et al. Global Distribution of Near-Surface Hydrogen on Mars. *Journal of Geophysical Research: Planets*, 109(E9), 2004. doi: 10.1029/2003je002160.
- Fischer, E., Martínez, G. M., Elliott, H. M., and Rennó, N. O. Experimental Evidence for the Formation of Liquid Saline Water on Mars. *Geophysical Research Letters*, vol. 41(13):pp. 4456–4462, 2014. ISSN 1944-8007. doi: 10.1002/2014GL060302.
- Fisher, D. A. A Process to Make Massive Ice in the Martian Regolith using Long-term Diffusion and Thermal Cracking. *Icarus*, vol. 179(2):pp. 387–397, 2005. ISSN 0019-1035. doi: 10.1016/j.icarus.2005.07.024.
- Forget, F., Hourdin, F., and Talagrand, O. CO₂ Snowfall on Mars: Simulation with a General Circulation Model. *Icarus*, vol. 131(2):pp. 302–316, 1998. ISSN 0019-1035. doi: 10.1006/icar.1997.5874.
- Forget, F., Hourdin, F., Fournier, R., Hourdin, C., Talagrand, O., Collins, M., Lewis, S. R., Read, P. L., and Huot, J.-P. Improved General Circulation Models of the Martian Atmosphere from the Surface to Above 80 km. *Journal of Geophysical Research: Planets*, vol. 104(E10):pp. 24155–24175, 1999. ISSN 2156-2202. doi: 10.1029/1999JE001025.

- Forget, F., Haberle, R. M., Montmessin, F., Levrard, B., and Head, J. W. Formation of Glaciers on Mars by Atmospheric Precipitation at High Obliquity. *Science*, vol. 311(5759):pp. 368–371, 2006. doi: 10.1126/science.1120335.
- Forget, F., Wordsworth, R., Millour, E., Madeleine, J. B., Kerber, L., Leconte, J., Marcq, E., and Haberle, R. M. 3D Modelling of the Early Martian Climate Under a Denser CO₂ Atmosphere: Temperatures and CO₂ ice clouds. *Icarus*, vol. 222(1):pp. 81–99, 2013. ISSN 0019-1035. doi: 10.1016/j.icarus.2012.10.019.
- Forget, F., Byrne, S., Head, J. W., Mischna, M. A., and Schörghofer, N. Recent Climate Variations. In Haberle, R. M., Clancy, R. T., Forget, F., Smith, M. D., and Zurek, R. W., editors, *The Atmosphere and Climate of Mars*, Cambridge Planetary Science, pages 497 – 525. Cambridge University Press, 2017. doi: 10.1017/9781139060172.016.
- François, L. M., Walker, J. C. G., and Kuhn, W. R. A Numerical Simulation of Climate Changes During the Obliquity Cycle on Mars. *Journal of Geophysical Research: Solid Earth*, 95(B9):pp. 14761–14778, 1990. doi: 10.1029/jb095ib09p14761.
- Gallagher, C. and Balme, M. Eskers in a Complete, Wet-based Glacial System in the Phlegra Montes Region, Mars. *Earth and Planetary Science Letters*, 431:96–109, 2015. doi: 10.1016/j.epsl.2015.09.023.
- Golombek, M. P. and Bridges, N. T. Erosion rates on Mars and implications for climate change: Constraints from the Pathfinder landing site. *Journal of Geophysical Research: Planets*, 105(E1):1841–1853, jan 2000. doi: 10.1029/1999je001043.
- Gooding, J. L. Martian Dust Particles as Condensation Nuclei: A preliminary assessment of mineralogical factors. *Icarus*, 66(1):56–74, April 1986. doi: 10.1016/0019-1035(86)90006-0. URL [https://doi.org/10.1016/0019-1035\(86\)90006-0](https://doi.org/10.1016/0019-1035(86)90006-0).
- Gooding, J. L. Soil Mineralogy and Chemistry on Mars: Possible clues from salts and clays in SNC meteorites. *Icarus*, 99(1):28–41, sep 1992. doi: 10.1016/0019-1035(92)90168-7.
- Greve, R. Waxing and Waning of the Perennial North Polar H₂O Ice Cap of Mars over Obliquity Cycles. *Icarus*, vol. 144(2):pp. 419–431, 2000. ISSN 0019-1035. doi: 10.1006/icar.1999.6291.
- Grindrod, P. and NASA/JPL-Caltech/University of Arizona/USGS). Glacier on Mars (HiRISE), Jan 2018. URL https://twitter.com/peter_grindrod/status/955476910573785088, Jan 2018. Date Accessed: 06-12-2021.
- Grott, M. and Breuer, D. On the Spatial Variability of the Martian Elastic Lithosphere Thickness: Evidence for mantle plumes? *Journal of Geophysical Research: Planets*, 115(E3), 2010. doi: 10.1029/2009je003456.
- Grott, M., Helbert, J., and Nadalini, R. Thermal Structure of Martian Soil and the Measurability of the Planetary Heat Flow. *Journal of Geophysical Research: Planets*, vol. 112(E9), 2007. ISSN 2156-2202. doi: 10.1029/2007je002905.
- Grott, M., Spohn, T., Smrekar, S. E., Banerdt, W. B., Hudson, T. L., Morgan, P., van Zoest, T., Kargl, G., and Wieczorek, M. A. InSight: constraining the Martian heat flow from a single measurement. In *43rd Lunar and Planetary Science Conference*, 2012.

- Grott, M., Spohn, T., Knollenberg, J., Krause, C., Hudson, T. L., Piqueux, S., Müller, N., Golombek, M., Vrettos, C., Marteau, E., Nagihara, S., Morgan, P., Murphy, J. P., Siegler, M., King, S. D., Smrekar, S. E., and Banerdt, W. B. Thermal Conductivity of the Martian Soil at the InSight Landing Site From HP 3 Active Heating Experiments. *Journal of Geophysical Research: Planets*, 126(7), jul 2021. doi: 10.1029/2021je006861.
- Guo, X., Lawson, W. G., Richardson, M. I., and Toigo, A. Fitting the Viking Lander Surface Pressure Cycle with a Mars General Circulation Model. *Journal of Geophysical Research: Planets*, 114(E7), 2009. doi: 10.1029/2008je003302.
- Haberle, R. M., Pollack, J. B., Barnes, J. R., Zurek, R. W., Leovy, C. B., Murphy, J. R., Lee, H., and Schaeffer, J. Mars Atmospheric Dynamics as Simulated by the NASA Ames General Circulation Model: 1. The zonal-mean circulation. *Journal of Geophysical Research: Planets*, 98(E2):3093–3123, 1993. doi: 10.1029/92je02946.
- Haberle, R. M., Tyler, D., McKay, C. P., and Davis, W. L. A Model for the Evolution of CO₂ on Mars. *Icarus*, vol. 109(1):pp. 102–120, 1994. ISSN 0019-1035. doi: 10.1006/icar.1994.1079.
- Haberle, R. M., Forget, F., Colaprete, A., Schaeffer, J., Boynton, W. V., Kelly, N. J., and Chamberlain, M. A. The Effect of Ground Ice on the Martian Seasonal CO₂ Cycle. *Planetary and Space Science*, vol. 56(2):pp. 251–255, 2008. ISSN 0032-0633. doi: 10.1016/j.pss.2007.08.006.
- Hansen, G. B. Control of the Radiative Behavior of the Martian Polar Caps by Surface CO₂ Ice: Evidence from Mars Global Surveyor measurements. *Journal of Geophysical Research: Planets*, vol. 104(E7):pp. 16471–16486, 1999. ISSN 2156-2202. doi: 10.1029/1998je000626.
- Hapke, B. Applications of an Energy Transfer Model to Three Problems in Planetary Regoliths: The solid-state greenhouse, thermal beaming, and emittance spectra. *Journal of Geophysical Research: Planets*, vol. 101(E7):pp. 16833–16840, 1996. ISSN 2156-2202. doi: 10.1029/96JE00918.
- Hardy, B. ITS-90 Formulations for Vapor Pressure, Frostpoint Temperature, Dewpoint Temperature, and Enhancement Factors in the Range -100 to +100 C. In *Proceedings of the third international symposium on humidity and moisture, Teddington, London, England*, 1998.
- Hayne, P. O., Paige, D. A., Schofield, J. T., Kass, D. M., Kleinböhl, A., Heavens, N. G., and McCleese, D. J. Carbon Dioxide Snow Clouds on Mars: South polar winter observations by the Mars Climate Sounder. *Journal of Geophysical Research: Planets*, 117(E8), 2012. doi: 10.1029/2011je004040.
- Head, J. W. and Marchant, D. R. Cold-based Mountain Glaciers on Mars: Western Arisia Mons. *Geology*, 31(7):pp. 641–644, 2003. doi: 10.1130/0091-7613(2003)031<0641:cmgomw>2.0.co;2.
- Head, J. W. and Pratt, S. Extensive Hesperian-aged south polar ice sheet on Mars: Evidence for massive melting and retreat, and lateral flow and ponding of meltwater. *Journal of Geophysical Research: Planets*, 106(E6):12275–12299, June 2001. doi: 10.1029/2000je001359. URL <https://doi.org/10.1029/2000je001359>.

- Head, J. W., Mustard, J. F., Kreslavsky, M. A., Milliken, R. E., and Marchant, D. R. Recent Ice Ages on Mars. *Nature*, vol. 426(6968):pp. 797–802, 2003. ISSN 0028-0836. doi: 10.1063/pt.5.021479.
- Heiken, G., Vaniman, D., and French, B. M. *Lunar Sourcebook: A user's guide to the Moon*. CUP Archive, 1991. doi: 10.1016/0160-9327(92)90014-g.
- Heldmann, J. L. and Mellon, M. T. Observations of Martian Gullies and Constraints on Potential Formation Mechanisms. *Icarus*, 168(2):285–304, 2004. doi: 10.1016/j.icarus.2003.11.024.
- Herkenhoff, K. Surface Ages and Resurfacing Rates of the Polar Layered Deposits on Mars. *Icarus*, 144(2):243–253, apr 2000. doi: 10.1006/icar.1999.6287.
- Hess, S. L., Henry, R. M., Leovy, C. B., Ryan, J. A., and Tillman, J. E. Meteorological results from the surface of Mars: Viking 1 and 2. *Journal of Geophysical Research*, 82(28):pp. 4559–4574, 1977. doi: 10.1029/js082i028p04559.
- Hess, S. L., Ryan, J. A., Tillman, J. E., Henry, R. M., and Leovy, C. B. The annual cycle of pressure on Mars measured by Viking Landers 1 and 2. *Geophysical Research Letters*, 7(3):197–200, mar 1980. doi: 10.1029/gl007i003p00197.
- Hobbs, P. V. *Ice Physics*. Oxford University press, 1974. doi: 10.1063/1.3069211.
- Hoffman, N. White Mars: A new model for Mars' surface and atmosphere based on CO₂. *Icarus*, 146(2):326–342, 2000. doi: 10.1006/icar.2000.6398.
- Hoffman, N. Modern Geothermal Gradients on Mars and Implications for Subsurface Liquids. *Conference on the Geophysical Detection of Subsurface Water on Mars*, page 7044, 2001.
- Holmes, J. A., Lewis, S. R., Patel, M. R., and Lefèvre, F. A reanalysis of ozone on Mars from assimilation of SPICAM observations. *Icarus*, 302:308–318, mar 2018. doi: 10.1016/j.icarus.2017.11.026.
- Holt, J. W., Safaeinili, A., Plaut, J. J., Head, J. W., Phillips, R. J., Seu, R., Kempf, S. D., Choudhary, P., Young, D. A., Putzig, N. E., et al. Radar Sounding Evidence for Buried Glaciers in the Southern Mid-latitudes of Mars. *Science*, 322(5905):pp. 1235–1238, 2008. doi: 10.1126/science.1164246.
- Hourdin, F., Le Van, P., Forget, F., and Talagrand, O. Meteorological Variability and the Annual Surface Pressure Cycle on Mars. *Journal of the atmospheric sciences*, 50(21):pp. 3625–3640, 1993. doi: 10.1175/1520-0469(1993)050<3625:mvatas>2.0.co;2.
- Hourdin, F., Forget, F., and Talagrand, O. The sensitivity of the Martian surface pressure and atmospheric mass budget to various parameters: A comparison between numerical simulations and Viking observations. *Journal of Geophysical Research*, 100(E3):5501, 1995. doi: 10.1029/94je03079.
- Howard, A. D. Etched plains and braided ridges of the south polar region of Mars: Features produced by basal melting of ground ice? *Reports of Planetary Geology Program*, pages 286–288, 1981.
- Hu, R., Cahoy, K., and Zuber, M. T. Mars Atmospheric CO₂ Condensation Above the North and South Poles as Revealed by Radio Occultation, Climate Sounder, and Laser Ranging Observations. *Journal of Geophysical Research: Planets*, 117(E7), 2012. doi: 10.1029/2012je004087.

- Hu, R., Kass, D. M., Ehlmann, B. L., and Yung, Y. L. Tracing the Fate of Carbon and the Atmospheric Evolution of Mars. *Nature Communications*, 6(1), nov 2015. doi: 10.1038/ncomms10003.
- Hudson, T. L. and Aharonson, O. Diffusion Barriers at Mars Surface Conditions: Salt crusts, particle size mixtures, and dust. *Journal of Geophysical Research: Planets*, 113(E9), 2008. doi: 10.1029/2007je003026.
- Hudson, T. L., Aharonson, O., Schorghofer, N., Farmer, C. B., Hecht, M. H., and Bridges, N. T. Water Vapor Diffusion in Mars Subsurface Environments. *Journal of Geophysical Research: Planets*, 112(E5), 2007. doi: 10.1029/2006je002815.
- Hütter, E. S., Kömle, N. I., Kargl, G., and Kaufmann, E. Determination of the Effective Thermal Conductivity of Granular Materials under Varying Pressure Conditions. *Journal of Geophysical Research: Planets*, 113(E12), 2008. doi: 10.1029/2008je003085.
- Hvidberg, C. S., Fishbaugh, K. E., Winstrup, M., Svensson, A., Byrne, S., and Herkenhoff, K. E. Reading the Climate Record of the Martian Polar Layered Deposits. *Icarus*, 221(1):405–419, September 2012. doi: 10.1016/j.icarus.2012.08.009. URL <https://doi.org/10.1016/j.icarus.2012.08.009>.
- Ianson, E., Davis, R., Meyer, M., and Haltigin, T. International Mars Ice Mapper Mission: Update and Participation Opportunity. Presented to MEPAG, June 2021. URL https://mepag.jpl.nasa.gov/meeting/2021-06/03_MIM_MEPAG_Presentation_%2021_JUN_2021.pdf, June 2021.
- Ingersoll, A. P. Mars: The case against permanent CO₂ frost caps. *Journal of Geophysical Research*, 79(24):3403–3410, aug 1974. doi: 10.1029/jc079i024p03403.
- Jakosky, B. M. The Role of Seasonal Reservoirs in the Mars Water Cycle: I. Seasonal exchange of water with the regolith. *Icarus*, 55(1):1–18, 1983. doi: 10.1016/0019-1035(83)90046-5.
- Jakosky, B. M. The Seasonal Cycle of Water on Mars. *Space Science Reviews*, vol. 41: pp. 131–200, 1985a. ISSN 0038-6308. doi: 10.1007/BF00241348.
- Jakosky, B. M. and Carr, M. H. Mars at High Obliquity: Possible Precipitation of Ice at Low Latitudes. *Bulletin of the American Astronomical Society*, vol. 16:pp. 673, 1984.
- Jakosky, B. M. and Carr, M. H. Possible Precipitation of Ice at Low Latitudes of Mars During Periods of High Obliquity. *Nature*, 315(6020):pp. 559–561, 1985b. doi: 10.1038/315559a0.
- Jakosky, B. M., Henderson, B. G., and Mellon, M. T. Chaotic Obliquity and the Nature of the Martian Climate. *Journal of Geophysical Research: Planets*, vol. 100(E1):pp. 1579–1584, 1995. ISSN 2156-2202. doi: 10.1029/94JE02801.
- Jakosky, B. M., Zent, A. P., and Zurek, R. W. The Mars Water Cycle: Determining the Role of Exchange with the Regolith. *Icarus*, 130(1):87–95, November 1997. doi: 10.1006/icar.1997.5799. URL <https://doi.org/10.1006/icar.1997.5799>.
- Jakosky, B. M., Mellon, M. T., Varnes, E. S., Feldman, W. C., Boynton, W. V., and Haberle, R. M. Mars Low-Latitude Neutron Distribution: Possible remnant near-surface water ice and a mechanism for its recent emplacement. *Icarus*, vol. 175(1): pp. 58–67, 2005. ISSN 0019-1035. doi: 10.1016/j.icarus.2004.11.014.

- Jakosky, B. M., Slipski, M., Benna, M., Mahaffy, P., Elrod, M., Yelle, R., Stone, S., and Alsaed, N. Mars' Atmospheric History Derived from Upper-atmosphere Measurements of $^{38}\text{Ar}/^{36}\text{Ar}$. *Science*, 355(6332):1408–1410, mar 2017. doi: 10.1126/science.aai7721.
- Jänchen, J., Bish, D. L., Möhlmann, D. T. F., and Stach, H. Investigation of the Water Sorption Properties of Mars-relevant Micro-and Mesoporous Minerals. *Icarus*, 180(2):353–358, 2006. doi: 10.1016/j.icarus.2005.10.010.
- Jänchen, J., Morris, R. V., Bish, D. L., Janssen, M., and Hellwig, U. The H_2O and CO_2 Adsorption Properties of Phyllosilicate-poor Palagonitic Dust and Smectites under Martian Environmental Conditions. *Icarus*, 200(2):463–467, 2009. doi: 10.1016/j.icarus.2008.12.006.
- JPL/NASA/STScI. Seasonal Changes in Mars' North Polar Ice Cap, May 1998. URL <https://www.jpl.nasa.gov/images/seasonal-changes-in-mars-north-polar-ice-cap>, May 1998. Date Accessed: 06-12-2021.
- Kadish, S. J., Head, J. W., Fastook, J. L., and Marchant, D. R. Middle to Late Amazonian Tropical Mountain Glaciers on Mars: The ages of the Tharsis Montes fan-shaped deposits. *Planetary and Space Science*, 91:52–59, feb 2014. doi: 10.1016/j.pss.2013.12.005.
- Kahn, R. The Evolution of CO_2 on Mars. *Icarus*, vol. 62(2):pp. 175–190, 1985. ISSN 0019-1035. doi: 10.1016/0019-1035(85)90116-2.
- Kahre, M. A., Haberle, R. M., Hollingsworth, J. L., Vines, S. K., and Leovy, C. The Early Martian Climate: Effects of Airborne Dust, CO_2 Ice Cap Albedo, and Orbital Obliquity on Atmospheric Collapse. In *Hydrologic, and Climatic Evolution and the Implications for Life*, volume 1680, 2012. ISBN 0161-5297.
- Kahre, M. A., Vines, S. K., Haberle, R. M., and Hollingsworth, J. L. The Early Martian Atmosphere: Investigating the role of the dust cycle in the possible maintenance of two stable climate states. *Journal of Geophysical Research E: Planets*, vol. 118(6): pp. 1388–1396, 2013. doi: 10.1002/jgre.20099.
- Kahre, M. A., Murphy, J. R., Newman, C. E., Wilson, R. J., Cantor, B. A., Lemmon, M. T., and Wolff, M. J. The Mars Dust Cycle. In Haberle, R. M., Clancy, R. T., Forget, F., Smith, M. D., and Zurek, R. W., editors, *The Atmosphere and Climate of Mars*, Cambridge Planetary Science, page 295–337. Cambridge University Press, 2017. doi: 10.1017/9781139060172.010.
- Kargel, J. S. and Strom, R. G. Ancient glaciation on Mars. *Geology*, 20(1):3, 1992. doi: 10.1130/0091-7613(1992)020<0003:agom>2.3.co;2.
- Kargel, J. S., Tanaka, K. L., Baker, V. R., Komatsu, G., and MacAyeal, D. R. Formation and Dissociation of Clathrate Hydrates on Mars: Polar caps, northern plains and highlands. In *Lunar and Planetary Science Conference*, volume 31, 2000.
- Karlsson, N. B., Schmidt, L. S., and Hvidberg, C. S. Volume of Martian Midlatitude Glaciers from Radar Observations and Ice Flow Modeling. *Geophysical Research Letters*, 42(8):2627–2633, April 2015. doi: 10.1002/2015gl063219. URL <https://doi.org/10.1002/2015gl063219>.

- Kasting, J. CO₂ Condensation and the Climate of Early Mars. *Icarus*, vol. 94(1), 1991. doi: 10.1016/0019-1035(91)90137-I.
- Kelly, N. J., Boynton, W. V., Kerry, K., Hamara, D., Janes, D., Reedy, R. C., Kim, K. J., and Haberle, R. M. Seasonal Polar Carbon Dioxide Frost on Mars: CO₂ mass and columnar thickness distribution. *Journal of Geophysical Research: Planets*, 111 (E3), 2006. doi: 10.1029/2006je002678.
- Kieffer, H. Interpretation of the Martian polar cap spectra. *Journal of Geophysical Research*, 75(3):510–514, jan 1970. doi: 10.1029/jc075i003p00510.
- Kieffer, H. and Titus, T. N. TES Mapping of Mars' North Seasonal Cap. *Icarus*, 154 (1):162–180, nov 2001. doi: 10.1006/icar.2001.6670.
- Kieffer, H. H., Christensen, P. R., and Titus, T. N. CO₂ Jets Formed by Sublimation Beneath Translucent Slab Ice in Mars' Seasonal South Polar Ice Cap. *Nature*, vol. 442(7104):pp. 793–796, 2006. ISSN 0028-0836. doi: 10.1038/nature04945.
- Kite, E. S., Williams, J.-P., Lucas, A., and Aharonson, O. Low Palaeopressure of the Martian Atmosphere Estimated from the Size Distribution of Ancient Craters. *Nature Geoscience*, 7(5):335–339, apr 2014. doi: 10.1038/ngeo2137.
- Klinger, J. Some Consequences of a Phase Transition of Water Ice on the Heat Balance of Comet Nuclei. *Icarus*, 47(3):pp. 320–324, 1981. doi: 10.1016/0019-1035(81)90179-2.
- Konstantinov, V. A., Manzhelii, V. G., Smirnov, S. A., and Tolkachev, A. M. Heat-transfer in Solid CO₂ and N₂O-dependence on Temperature and Volume. *FIZIKA NIZKIKH TEMPERATUR*, 14(2):189–196, 1988.
- Kossacki, K. J., Kömle, N. I., Kargl, G., and Steiner, G. The Influence of Grain Sintering on the Thermoconductivity of Porous Ice. *Planetary and Space Science*, 42(5):pp. 383–389, 1994. doi: 10.1016/0032-0633(94)90127-9.
- Kravchenko, Y. and Krupskii, I. Thermal Conductivity of Solid N₂O and CO₂. *Sov. J. Low Temp. Phys*, 12:46–48, 1986.
- Kreslavsky, M. A. and Head, J. W. Kilometer-scale Roughness of Mars: Results from MOLA data analysis. *Journal of Geophysical Research: Planets*, 105(E11):26695–26711, November 2000. doi: 10.1029/2000je001259. URL <https://doi.org/10.1029/2000je001259>.
- Kreslavsky, M. A. and Head, J. W. Mars: Nature and evolution of young latitude-dependent water-ice-rich mantle. *Geophysical Research Letters*, 29(15):14–1–14–4, August 2002. doi: 10.1029/2002gl015392. URL <https://doi.org/10.1029/2002gl015392>.
- Kreslavsky, M. A. and Head, J. W. Mars at Very Low Obliquity: Atmospheric collapse and the fate of volatiles. *Geophysical Research Letters*, vol. 32(12), 2005. ISSN 1944-8007. doi: 10.1029/2005GL022645.
- Kreslavsky, M. A. and Head, J. W. Carbon Dioxide Glaciers In The Recent Geological History Of Mars. *Icarus*, 170:343–364, 2010.
- Kreslavsky, M. A. and Head, J. W. Carbon Dioxide Glaciers on Mars: Products of recent low obliquity epochs (?). *Icarus*, 216(1):111–115, nov 2011. doi: 10.1016/j.icarus.2011.08.020.

- Labus, M. and Labus, K. Thermal conductivity and diffusivity of fine-grained sedimentary rocks. *Journal of Thermal Analysis and Calorimetry*, 132(3):1669–1676, feb 2018. doi: 10.1007/s10973-018-7090-5.
- Lambert, R. S. J. and Chamberlain, V. E. CO₂ Permafrost and Martian Topography. *Icarus*, 34(3):568–580, 1978. doi: 10.1016/0019-1035(78)90046-5.
- Langevin, Y., Bibring, J., Montmessin, F., Forget, F., Vincendon, M., Douté, S., Poulet, F., and Gondet, B. Observations of the South Seasonal Cap of Mars During Recession in 2004–2006 by the OMEGA Visible/Near-infrared Imaging Spectrometer on board Mars Express. *Journal of Geophysical Research: Planets*, vol. 112(E8), 2007. ISSN 2156-2202. doi: 10.1029/2006JE002841.
- Laskar, J., Levrard, B., and Mustard, J. F. Orbital Forcing of the Martian Polar Layered Deposits. *Nature*, 419(6905):375–377, September 2002. doi: 10.1038/nature01066. URL <https://doi.org/10.1038/nature01066>.
- Laskar, J., Correia, A. C. M., Gastineau, M., Joutel, F., Levrard, B., and Robutel, P. Long Term Evolution and Chaotic Diffusion of the Insolation Quantities of Mars. *Icarus*, 170(2):pp. 343–364, 2004. doi: 10.1016/j.icarus.2004.04.005.
- Lasue, J., Mangold, N., Hauber, E., Clifford, S., Feldman, W., Gasnault, O., Grima, C., Maurice, S., and Mosis, O. Quantitative Assessments of the Martian Hydrosphere. *Space Science Reviews*, 174(1-4):155–212, nov 2012. doi: 10.1007/s11214-012-9946-5.
- Lauro, S. E., Pettinelli, E., Caprarelli, G., Guallini, L., Rossi, A. P., Mattei, E., Cosciotti, B., Cicchetti, A., Soldovieri, F., Cartacci, M., Di Paolo, F., Noschese, R., and Orosei, R. Multiple Subglacial Water Bodies Below the South Pole of Mars Unveiled by New MARSIS Data. *Nature Astronomy*, sep 2020. doi: 10.1038/s41550-020-1200-6.
- Leighton, R. B. and Murray, B. C. Behavior of Carbon Dioxide and Other Volatiles on Mars. *Science*, vol. 153(3732):pp. 136–144, 1966. ISSN 0036-8075. doi: 10.1126/science.153.3732.136.
- Leovy, C. Mars Ice Caps. *Science*, 154(3753):1178–1179, dec 1966. doi: 10.1126/science.154.3753.1178.
- Levitz, P. Knudsen Diffusion and Excitation Transfer in Random Porous Media. *The Journal of Physical Chemistry*, 97(15):pp. 3813–3818, 1993. doi: 10.1021/j100117a030.
- Levrard, B., Forget, F., Montmessin, F., and Laskar, J. Recent Ice-rich Deposits Formed at High Latitudes on Mars by Sublimation of Unstable Equatorial Ice During Low Obliquity. *Nature*, vol. 431(7012):pp. 1072–1075, 2004. ISSN 0028-0836. doi: 10.1038/nature03055.
- Levrard, B., Forget, F., Montmessin, F., and Laskar, J. Recent Formation and Evolution of Northern Martian Polar Layered Deposits as Inferred from a Global Climate Model. *Journal of Geophysical Research: Planets*, 112(E6), 2007. doi: 10.1029/2006je002772.
- Levy, J. S., Fassett, C. I., Head, J. W., Schwartz, C., and Watters, J. L. Sequestered Glacial Ice Contribution to the Global Martian Water Budget: Geometric constraints on the volume of remnant, midlatitude debris-covered glaciers. *Journal of Geophysical Research: Planets*, 119(10):pp. 2188–2196, 2014. doi: 10.1002/2014je004685.

- Lewis, S. R. Modelling the Martian Atmosphere. *Astronomy and Geophysics*, 44(4): 406–414, aug 2003. doi: 10.1046/j.1468-4004.2003.44406.x.
- Lewis, S. R., Collins, M., Read, P. L., Forget, F., Hourdin, F., Fournier, R., Hourdin, C., Talagrand, O., and Huot, J.-P. A Climate Database for Mars. *Journal of Geophysical Research: Planets*, 104(E10):24177–24194, 1999. doi: 10.1029/1999JE001024.
- Maass, O. and Barnes, W. H. Some Thermal Constants of Solid and Liquid Carbon Dioxide. *Proceedings of the Royal Society of London. Series A, Containing Papers of a Mathematical and Physical Character*, 111(757):224–244, may 1926. doi: 10.1098/rspa.1926.0065.
- Madeleine, J.-B., Forget, F., Head, J. W., Levrard, B., Montmessin, F., and Millour, E. Amazonian Northern Mid-latitude Glaciation on Mars: A proposed climate scenario. *Icarus*, 203(2):pp. 390–405, 2009. doi: 10.1016/j.icarus.2009.04.037.
- Mangan, T. P., Salzmann, C. G., Plane, J. M. C., and Murray, B. J. CO₂ Ice Structure and Density Under Martian Atmospheric Conditions. *Icarus*, vol. 294(Supplement C):pp. 201–208, 2017. ISSN 0019-1035. doi: 10.1016/j.icarus.2017.03.012.
- Manning, C. V., McKay, C. P., and Zahnle, K. J. Thick and Thin Models of the Evolution of Carbon Dioxide on Mars. *Icarus*, vol. 180(1):pp. 38–59, 2006. ISSN 0019-1035. doi: 10.1016/j.icarus.2005.08.014.
- Manning, C. V., Bierson, C., Putzig, N. E., and McKay, C. P. The Formation and Stability of Buried Polar CO₂ Deposits on Mars. *Icarus*, 317:509–517, 2019. doi: 10.1016/j.icarus.2018.07.021.
- Martín-Torres, F. J., Zorzano, M.-P., P.Valentín-Serrano, Harri, A.-M., Genzer, M., Kemppinen, O., Rivera-Valentin, E. G., Jun, I., Wray, J., Madsen, M. B., Goetz, W., McEwen, A. S., Hardgrove, C., Renno, N., Chevrier, V. F., Mischna, M., Navarro-González, R., Martínez-Frías, J., Conrad, P., McConnochie, T., Cockell, C., Berger, G., Vasavada, A. R., Sumner, D., and Vaniman, D. Transient Liquid Water and Water Activity at Gale Crater on Mars. *Nature Geoscience*, 8(5):357–361, apr 2015. doi: 10.1038/ngeo2412.
- Mellon, M. T. Limits on the CO₂ Content of the Martian Polar Deposits. *Icarus*, vol. 124:pp. 268–274, 1996. doi: 10.1006/icar.1996.0203.
- Mellon, M. T. and Feldman, W. C. The Global Distribution of Martian Subsurface Ice and Regional Ice Stability. In *37th Annual Lunar and Planetary Science Conference*, volume 37, 2006.
- Mellon, M. T. and Jakosky, B. M. Geographic Variations in the Thermal and Diffusive Stability of Ground Ice on Mars. *Journal of Geophysical Research: Planets*, vol. 98(E2):pp. 3345–3364, 1993. ISSN 2156-2202. doi: 10.1029/92JE02355.
- Mellon, M. T., Feldman, W. C., and Prettyman, T. H. The Presence and Stability of Ground Ice in the Southern Hemisphere of Mars. *Icarus*, vol. 169(2):pp. 324–340, 2004. ISSN 0019-1035. doi: 10.1016/j.icarus.2003.10.022.
- Mellon, M. T., Fergason, R. L., and Putzig, N. E. The Thermal Inertia of the Surface of Mars. In Bell, J., editor, *The Martian Surface*, pages 399–427. Cambridge University Press, 2008. doi: 10.1017/cbo9780511536076.019. URL <https://doi.org/10.1017/cbo9780511536076.019>.

- Mellon, M. T., Arvidson, R. E., Sizemore, H. G., Searls, M. L., Blaney, D. L., Cull, S., Hecht, M. H., Heet, T. L., Keller, H. U., Lemmon, M. T., Markiewicz, W. J., Ming, D. W., Morris, R. V., Pike, W. T., and Zent, A. P. Ground Ice at the Phoenix Landing Site: Stability state and origin. *Journal of Geophysical Research: Planets*, vol. 114(E1), 2009. ISSN 2156-2202. doi: 10.1029/2009JE003417.
- Meslin, P.-Y., Forget, F., and Millour, E. An Improved Model of Regolith-Atmosphere Exchange of Water Vapor in the LMD Global Climate Model. In *Third International Workshop on The Mars Atmosphere: Modeling and Observations*, volume 1447, 2008.
- Mikhail, R. S. and Robens, E. *Microstructure and Thermal Analysis of Solid Surface*. John Wiley & Sons Inc, 01 1983. ISBN 0 471 26230 7. doi: 10.1002/sia.740060109.
- Milkovich, S. M. North Polar Cap of Mars: Polar layered deposit characterization and identification of a fundamental climate signal. *Journal of Geophysical Research*, 110(E1), 2005. doi: 10.1029/2004je002349. URL <https://doi.org/10.1029/2004je002349>.
- Miller, S. L. and Smythe, W. D. Carbon Dioxide Clathrate in the Martian Ice Cap. *Science*, 170(3957):pp. 531–533, 1970. doi: 10.1126/science.170.3957.531.
- Mischna, M. A., Richardson, M. I., Wilson, R. J., and McCleese, D. J. On the Orbital Forcing of Martian Water and CO₂ Cycles: A general circulation model study with simplified volatile schemes. *Journal of Geophysical Research: Planets*, vol. 108(E6), 2003. ISSN 2156-2202. doi: 10.1029/2003JE002051.
- Mitrofanov, I. G., Zuber, M. T., Litvak, M. L., Boynton, W. V., Smith, D. E., Drake, D., Hamara, D., Kozyrev, A. S., Sanin, A. B., Shinohara, C., Saunders, R. S., and Tretyakov, V. CO₂ Snow Depth and Subsurface Water-Ice Abundance in the Northern Hemisphere of Mars. *Science*, vol. 300(5628):pp. 2081–2084, 2003. ISSN 00368075, 10959203. doi: 10.1126/science.1084350.
- Möhlmann, D. T. F. Adsorption Water in Mid-and Low Latitude Martian Soil. In *Exo-Astrobiology*, volume 518, pages 169–172, 2002.
- Möhlmann, D. T. F. Unfrozen Subsurface Water on Mars: Presence and implications. *International Journal of Astrobiology*, 2(3):213–216, 2003. doi: 10.1017/s1473550403001617.
- Möhlmann, D. T. F. Water in the Upper Martian Surface at Mid-and Low-latitudes: Presence, state, and consequences. *Icarus*, 168(2):318–323, 2004. doi: 10.1016/j.icarus.2003.11.008.
- Möhlmann, D. T. F. Adsorption Water-related Potential Chemical and Biological Processes in the Upper Martian Surface. *Astrobiology*, 5(6):770–777, 2005. doi: 10.1089/ast.2005.5.770.
- Montabone, L., Forget, F., Millour, E., Wilson, R. J., Lewis, S. R., Cantor, B., Kass, D., Kleinböhl, A., Lemmon, M. T., Smith, M. D., et al. Eight-year Climatology of Dust Optical Depth on Mars. *Icarus*, 251:65–95, 2015. doi: 10.1016/j.icarus.2014.12.034.
- Montmessin, F. and Lefèvre, F. Transport-driven Formation of a Polar Ozone Layer on Mars. *Nature Geoscience*, 6(11):930–933, sep 2013. doi: 10.1038/ngeo1957.

- Montmessin, F., Forget, F., Rannou, P., Cabane, M., and Haberle, R. M. Origin and Role of Water Ice Clouds in the Martian Water Cycle as Inferred from a General Circulation Model. *Journal of Geophysical Research: Planets*, 109(E10), 2004. doi: 10.1029/2004je002284.
- Montmessin, F., Smith, M. D., Langevin, Y., Mellon, M. T., and Fedorova, A. The Water Cycle. In Haberle, R. M., Clancy, R. T., Forget, F., Smith, M. D., and Zurek, R. W., editors, *The Atmosphere and Climate of Mars*, pages 338–373. Cambridge University Press, 2017. doi: 10.1017/9781139060172.011.
- Moore, H. J., Clow, G. D., and Hutton, R. E. A summary of Viking sample-trench analyses for angles of internal friction and cohesions. *Journal of Geophysical Research*, 87(B12):10043, 1982. doi: 10.1029/jb087ib12p10043.
- Mustard, J. F., Cooper, C. D., and Rifkin, M. K. Evidence for Recent Climate Change on Mars from the Identification of Youthful Near-surface Ground Ice. *Nature*, 412(6845):411–414, July 2001. doi: 10.1038/35086515. URL <https://doi.org/10.1038/35086515>.
- Nakamura, T. and Tajika, E. Stability and evolution of the climate system of Mars. *Earth, Planets and Space*, 53(8):851–859, aug 2001. doi: 10.1186/bf03351682.
- Nakamura, T. and Tajika, E. Climate Change of Mars-like Planets Due to Obliquity Variations: Implications for Mars. *Geophysical Research Letters*, vol. 30(13), 2003. ISSN 1944-8007. doi: 10.1029/2002GL016725.
- NASA/JPL - Caltech/University of Arizona/Texas A&M University. Phoenix Mars Lander: Disappearing ice in color, Jun 2008. URL https://www.nasa.gov/mission_pages/phoenix/images/press/sol_020_024_change_dodo_v3.html, Jun 2008. Date Accessed: 06-12-2021.
- NASA/JPL-Caltech). Mars south polar layered deposits - December 8, 2003, Dec 2003. URL <https://mars.nasa.gov/resources/1258/mars-south-polar-layered-deposits-december-8-2003/>, Dec 2003. Date Accessed: 06-12-2021.
- NASA/JPL-Caltech/University of Arizona. Frosty Slopes on Mars (HiRISE), Nov 2014. URL <https://www.nasa.gov/content/frosty-slopes-on-mars>, Nov 2014. Date Accessed: 06-12-2021.
- NASA/JPL-Caltech/University of Arizona). Blockfall on the North Polar Layered Deposits (HiRISE), June 2014. URL <https://www.jpl.nasa.gov/images/blockfall-on-the-north-polar-layered-deposits>, June 2014. Date Accessed: 06-12-2021.
- NASA/JPL-Caltech/University of Arizona. Frosty Sand Dunes of Mars (HiRISE), March 2021. URL <https://www.nasa.gov/image-feature/frosty-sand-dunes-of-mars>, March 2021. Date Accessed: 06-12-2021.
- Navarro, T., Madeleine, J.-B., Forget, F., Spiga, A., Millour, E., Montmessin, F., and Määttänen, A. Global Climate Modeling of the Martian Water Cycle with Improved Microphysics and Radiatively Active Water Ice Clouds. *Journal of Geophysical Research: Planets*, 119(7):pp. 1479–1495, 2014. doi: 10.1002/2013je004550.

- Neumann, G. A., Zuber, M. T., Wieczorek, M. A., McGovern, P. J., Lemoine, F. G., and Smith, D. E. Crustal Structure of Mars from Gravity and Topography. *Journal of Geophysical Research: Planets*, 109(E8), 2004. doi: 10.1029/2004je002262.
- Newman, C. E., Lewis, S. R., Read, P. L., and Forget, F. Modeling the Martian Dust Cycle: 1. Representations of dust transport processes. *Journal of Geophysical Research: Planets*, 107(E12), 2002. doi: 10.1029/2002je001910.
- Newman, C. E., Lewis, S. R., and Read, P. L. The Atmospheric Circulation and Dust Activity in Different Orbital Epochs on Mars. *Icarus*, 174(1):pp. 135–160, 2005. doi: 10.1016/j.icarus.2004.10.023.
- Nikolakakos, G. and Whiteway, J. A. Laboratory Study of Adsorption and Deliquescence on the Surface of Mars. *Icarus*, 308:pp. 221 – 229, 2018. ISSN 0019-1035. doi: 10.1016/j.icarus.2017.05.006. Mars Polar Science VI.
- Nye, J., Durham, W. B., Schenk, P. M., and Moore, J. M. The Instability of a South Polar Cap on Mars Composed of Carbon Dioxide. *Icarus*, 144(2):449–455, apr 2000. doi: 10.1006/icar.1999.6306.
- Orosei, R., Lauro, S. E., Pettinelli, E., Cicchetti, A., Coradini, M., Cosciotti, B., Di Paolo, F., Flamini, E., Mattei, E., Pajola, M., et al. Radar Evidence of Subglacial Liquid Water on Mars. *Science*, 361(6401):490–493, 2018. doi: 10.1126/science.aar7268.
- Paige, D. A. The Thermal Stability of Near-Surface Ground Ice on Mars. *Nature*, vol. 356(6364):pp. 356043a0, 1992. ISSN 1476-4687/1476-4687. doi: 10.1038/356043a0.
- Pál, B. and Kereszturi, Á. Annual and Daily Ideal Periods for Deliquescence at the Landing Site of InSight Based on GCM Model Calculations. *Icarus*, 340:113639, apr 2020. doi: 10.1016/j.icarus.2020.113639.
- Palluconi, F. D. and Kieffer, H. H. Thermal Inertia Mapping of Mars from 60°S to 60°N. *Icarus*, vol. 45(2):pp. 415–426, 1981. ISSN 0019-1035. doi: 10.1016/0019-1035(81)90044-0.
- Parker, T. J., Gorsline, D. S., Saunders, R. S., Pieri, D. C., and Schneeberger, D. M. Coastal geomorphology of the Martian northern plains. *Journal of Geophysical Research*, 98(E6):11061, 1993. doi: 10.1029/93je00618.
- Patankar, S. *Numerical Heat Transfer and Fluid Flow: CRC press*. Taylor & Francis Group, LLC. Florida, United States, 1980.
- Phillips, R. J., Zuber, M. T., Smrekar, S. E., Mellon, M. T., Head, J. W., Tanaka, K. L., Putzig, N. E., Milkovich, S. M., Campbell, B. A., Plaut, J. J., et al. Mars North Polar Deposits: Stratigraphy, age, and geodynamical response. *Science*, 320(5880):pp. 1182–1185, 2008. doi: 10.1126/science.1157546.
- Phillips, R. J., Davis, B. J., Tanaka, K. L., Byrne, S., Mellon, M. T., Putzig, N. E., Haberle, R. M., Kahre, M. A., Campbell, B. A., Carter, L. M., Smith, I. B., Holt, J. W., Smrekar, S. E., Nunes, D. C., Plaut, J. J., Egan, A. F., Titus, T. N., and Seu, R. Massive CO₂ Ice Deposits Sequestered in the South Polar Layered Deposits of Mars. *Science*, 332(6031):838–841, 2011. doi: 10.1126/science.1203091.

- Pilorget, C. and Forget, F. Formation of Gullies on Mars by Debris Flows Triggered by CO₂ Sublimation. *Nature Geoscience*, vol. 9:pp. 65–69, 2015. ISSN 1752-0894. doi: 10.1038/ngeo2619.
- Pilorget, C., Forget, F., Millour, E., Vincendon, M., and Madeleine, J. B. Dark Spots and Cold Jets in the Polar Regions of Mars: New clues from a thermal model of surface CO₂ ice. *Icarus*, vol. 213(1):pp. 131–149, 2011. ISSN 0019-1035. doi: 10.1016/j.icarus.2011.01.031.
- Piqueux, S. and Christensen, P. R. A Model of Thermal Conductivity for Planetary Soils: 1. Theory for unconsolidated soils. *Journal of Geophysical Research: Planets*, 114(E9), 2009. ISSN 2156-2202. doi: 10.1029/2008JE003308.
- Piqueux, S., Byrne, S., and Richardson, M. I. Sublimation of Mars’s Southern Seasonal CO₂ Ice Cap and the Formation of Spiders. *Journal of Geophysical Research: Planets*, vol. 108(E8), 2003. ISSN 2156-2202. doi: 10.1029/2002je002007.
- Piqueux, S., Kleinböhl, A., Hayne, P. O., Heavens, N. G., Kass, D. M., McCleese, D. J., Schofield, J. T., and Shirley, J. H. Discovery of a Widespread Low Latitude Diurnal CO₂ Frost Cycle on Mars. *Journal of Geophysical Research: Planets*, vol. 121(7):pp. 1174–1189, 2016. ISSN 2169-9100. doi: 10.1002/2016JE005034.
- Piqueux, S., Buz, J., Edwards, C. S., Bandfield, J. L., Kleinböhl, A., Kass, D. M., Hayne, P. O., The MCS, and THEMIS Teams. Widespread Shallow Water Ice on Mars at High Latitudes and Midlatitudes. *Geophysical Research Letters*, 46(24): 14290–14298, dec 2019. doi: 10.1029/2019gl083947.
- Plaut, J. J., Safaeinili, A., Holt, J. W., Phillips, R. J., Head, J. W., Seu, R., Putzig, N. E., and Frigeri, A. Radar Evidence for Ice in Lobate Debris Aprons in the Mid-Northern Latitudes of Mars. *Geophysical research letters*, 36(2), 2009. doi: 10.1029/2008gl036379.
- Plesa, A.-C., Grott, M., Tosi, N., Breuer, D., Spohn, T., and Wieczorek, M. A. How Large are Present-Day Heat Flux Variations Across the Surface of Mars? *Journal of Geophysical Research: Planets*, vol. 121(12):pp. 2386–2403, 2016. ISSN 2169-9100. doi: 10.1002/2016JE005126. jgre20611.
- Pollack, J. B. and Toon, O. B. Quasi-Periodic Climate Changes on Mars: A review. *Icarus*, vol. 50(2):pp. 259–287, 1982. ISSN 0019-1035. doi: 10.1016/0019-1035(82)90126-9.
- Pollack, J. B., Haberle, R. M., Schaeffer, J., and Lee, H. Simulations of the General Circulation of the Martian Atmosphere: 1. Polar processes. *Journal of Geophysical Research: Solid Earth*, vol. 95(B2):pp. 1447–1473, 1990. ISSN 2156-2202. doi: 10.1029/JB095iB02p01447.
- Pommerol, A., Schmitt, B., Beck, P., and Brissaud, O. Water Sorption on Martian Regolith Analogs: Thermodynamics and near-infrared reflectance spectroscopy. *Icarus*, 204(1):114–136, 2009. doi: 10.1016/j.icarus.2009.06.013.
- Presley, M. A. and Christensen, P. R. Thermal Conductivity Measurements of Particulate Materials 1. A review. *Journal of Geophysical Research: Planets*, vol. 102(E3): pp. 6535–6549, 1997a. ISSN 2156-2202. doi: 10.1029/96JE03302.

- Presley, M. A. and Christensen, P. R. Thermal Conductivity Measurements of Particulate Materials 2. Results. *Journal of Geophysical Research: Planets*, vol. 102(E3): pp. 6551–6566, 1997b. ISSN 2156-2202. doi: 10.1029/96JE03303.
- Presley, M. A. and Christensen, P. R. The Effect of Bulk Density and Particle Size Sorting on the Thermal Conductivity of Particulate Materials under Martian Atmospheric Pressures. *Journal of Geophysical Research: Planets*, 102(E4):pp. 9221–9229, 1997c. doi: 10.1029/97je00271.
- Presley, M. A. and Christensen, P. R. Thermal Conductivity Measurements of Particulate Materials: 4. Effect of bulk density for granular particles. *Journal of Geophysical Research: Planets*, vol. 115(E7), 2010. ISSN 2156-2202. doi: 10.1029/2009JE003482.
- Presley, M. A. and Craddock, R. A. Thermal Conductivity Measurements of Particulate Materials: 3. Natural samples and mixtures of particle sizes. *Journal of Geophysical Research: Planets*, vol. 111(E9), 2006. ISSN 2156-2202. doi: 10.1029/2006JE002706.
- Putzig, N. E., Mellon, M. T., Kretke, K. A., and Arvidson, R. E. Global Thermal Inertia and Surface Properties of Mars from the MGS Mapping Mission. *Icarus*, vol. 173(2):pp. 325–341, 2005. ISSN 0019-1035. doi: 10.1016/j.icarus.2004.08.017.
- Read, P. L. and Lewis, S. R. *The Martian Climate Revisited: Atmosphere and environment of a desert planet*. Springer Science & Business Media, 2004.
- Read, P. L., Lewis, S. R., and Mulholland, D. P. The Physics of Martian Weather and Climate: A review. *Reports on Progress in Physics*, 2015. doi: 10.1088/0034-4885/78/12/125901.
- Read, P. L., Galperin, B., Larsen, S. E., Lewis, S. R., Määttänen, A., Petrosyan, A., Rennó, N., Savijärvi, H., Siili, T., Spiga, A., and et al. The Martian Planetary Boundary Layer. In Haberle, R. M., Clancy, R. T., Forget, F., Smith, M. D., and Zurek, R. W., editors, *The Atmosphere and Climate of Mars*, Cambridge Planetary Science, page 172–202. Cambridge University Press, 2017. doi: 10.1017/9781139060172.007.
- Richardson, M. I. and Wilson, R. J. Investigation of the Nature and Stability of the Martian Seasonal Water Cycle with a General Circulation Model. *Journal of Geophysical Research: Planets*, 107(E5):pp. 7–1, 2002. doi: 10.1029/2001je001536.
- Richardson, M. I., Mischna, M. A., McCleese, D. J., Wilson, R. J., and Vasavada, A. R. Formation of Obliquity-driven Subsurface Ice Deposits on Mars: Study with a general circulation model. In *AGU Fall Meeting Abstracts*, volume 2003, pages C12C–01, 2003.
- Ross, R. G. and Kargel, J. S. Thermal Conductivity of Solar System Ices, with Special Reference to Martian Polar Caps. In *Solar system ices*, pages 33–62. Springer, 1998.
- Ruff, S. W. and Christensen, P. R. Bright and Dark Regions on Mars: Particle size and mineralogical characteristics based on Thermal Emission Spectrometer data. *Journal of Geophysical Research: Planets*, 107(E12), 2002. doi: 10.1029/2001je001580.
- Sanz, E., Vega, C., Abascal, J. L. F., and MacDowell, L. G. Phase Diagram of Water from Computer Simulation. *Physical review letters*, 92(25):255701, 2004. doi: 10.1103/physrevlett.92.255701.
- Satterfield, C. N. *Mass Transfer in Heterogeneous Catalysis*. MIT Press, Cambridge, 1970.

- Scheepbouwer, E., Davidson, M. J., and Nokes, R. I. Tracer Distributions of Line Advected Thermals. *Environmental Fluid Mechanics*, 8(5-6):561–568, sep 2008. doi: 10.1007/s10652-008-9100-9.
- Scheller, E. L., Ehlmann, B. L., Hu, R., Adams, D. J., and Yung, Y. L. Long-term drying of Mars by sequestration of ocean-scale volumes of water in the crust. *Science*, 372(6537):56–62, mar 2021. doi: 10.1126/science.abc7717.
- Schmidt, F., Douté, S., Schmitt, B., Vincendon, M., Bibring, J.-P., and Langevin, Y. Albedo Control of Seasonal South Polar Cap Recession on Mars. *Icarus*, 200(2): 374–394, April 2009. doi: 10.1016/j.icarus.2008.12.014. URL <https://doi.org/10.1016/j.icarus.2008.12.014>.
- Schon, S. C., Head, J. W., and Milliken, R. E. A Recent Ice Age on Mars: Evidence for climate oscillations from regional layering in mid-latitude mantling deposits. *Geophysical Research Letters*, 36(15):n/a–n/a, August 2009. doi: 10.1029/2009gl038554. URL <https://doi.org/10.1029/2009gl038554>.
- Schorghofer, N. Dynamics of Ice Ages on Mars. *Nature*, 449(7159):pp. 192, 2007. doi: 10.1038/nature06082.
- Schorghofer, N. Temperature Response of Mars to Milankovitch cycles. *Geophysical Research Letters*, 35(18), September 2008. doi:10.1029/2008gl034954. URL <https://doi.org/10.1029/2008gl034954>.
- Schorghofer, N. Fast Numerical Method for Growth and Retreat of Subsurface Ice on Mars. *Icarus*, 208(2):598–607, 2010. doi: 10.1016/j.icarus.2010.03.022.
- Schorghofer, N. and Aharonson, O. Stability and Exchange of Subsurface Ice on Mars. *Journal of Geophysical Research: Planets*, vol. 110(E5), 2005. ISSN 2156-2202. doi: 10.1029/2004JE002350.
- Schorghofer, N. and Edgett, K. S. Seasonal Surface Frost at Low Latitudes on Mars. *Icarus*, vol. 180(2):pp. 321–334, 2006. ISSN 0019-1035. doi: 10.1016/j.icarus.2005.08.022.
- Schorghofer, N. and Forget, F. History and Anatomy of Subsurface Ice on Mars. *Icarus*, vol. 220(2):pp. 1112–1120, 2012. ISSN 0019-1035. doi: 10.1016/j.icarus.2012.07.003.
- Seiferlin, K., Kömle, N. I., Kargl, G., and Spohn, T. Line Heat-source Measurements of the Thermal Conductivity of Porous H₂O Ice, CO₂ Ice and Mineral Powders Under Space Conditions. *Planetary and Space Science*, 44(7):pp. 691–704, 1996. doi: 10.1016/0032-0633(96)00068-2.
- Shean, D. E., Head, J. W., Fastook, J. L., and Marchant, D. R. Recent Glaciation at High Elevations on Arsia Mons, Mars: Implications for the formation and evolution of large tropical mountain glaciers. *Journal of Geophysical Research*, 112(E3), March 2007. doi: 10.1029/2006je002761. URL <https://doi.org/10.1029/2006je002761>.
- Shorthill, R. W., Moore, H. J., Scott, R. F., Hutton, R. E., Liebes, S., and Spitzer, C. R. The "Soil" of Mars (Viking 1). *Science*, 194(4260):91–97, 1976. doi: 10.1126/science.194.4260.91.
- Shoshany, Y., Prialnik, D., and Podolak, M. Monte Carlo Modeling of the Thermal Conductivity of Porous Cometary Ice. *Icarus*, 157(1):pp. 219–227, 2002. doi: 10.1006/icar.2002.6815.

- Siegler, M., Aharonson, O., Carey, E., Choukroun, M., Hudson, T., Schorghofer, N., and Xu, S. Measurements of Thermal Properties of Icy Mars Regolith Analogs. *Journal of Geophysical Research: Planets*, 117(E3), 2012. ISSN 2156-2202. doi: 10.1029/2011JE003938.
- Sizemore, H. G. and Mellon, M. T. Effects of Soil Heterogeneity on Martian Ground-ice Stability and Orbital Estimates of Ice Table Depth. *Icarus*, 185(2):pp. 358 – 369, 2006. ISSN 0019-1035. doi: 10.1016/j.icarus.2006.07.018.
- Sizemore, H. G. and Mellon, M. T. Laboratory Characterization of the Structural Properties Controlling Dynamical Gas Transport in Mars-analog Soils. *Icarus*, 197 (2):pp. 606 – 620, 2008. ISSN 0019-1035. doi: 10.1016/j.icarus.2008.05.013.
- Smith, D. E., Zuber, M. T., Solomon, S. C., Phillips, R. J., Head, J. W., Garvin, J. B., Banerdt, W. B., Muhleman, D. O., Pettengill, G. H., Neumann, G. A., et al. The Global Topography of Mars and Implications for Surface Evolution. *Science*, 284 (5419):pp. 1495–1503, 1999. doi: 10.1126/science.284.5419.1495.
- Smith, D. E., Zuber, M. T., and Neumann, G. A. Seasonal Variations of Snow Depth on Mars. *Science*, vol. 294(5549):pp. 2141–2146, 2001a. ISSN 0036-8075. doi: 10.1126/science.1066556.
- Smith, D. E., Zuber, M. T., Frey, H. V., Garvin, J. B., Head, J. W., Muhleman, D. O., Pettengill, G. H., Phillips, R. J., Solomon, S. C., Zwally, H. J., Banerdt, W. B., Duxbury, T. C., Golombek, M. P., Lemoine, F. G., Neumann, G. A., Rowlands, D. D., Aharonson, O., Ford, P. G., Ivanov, A. B., Johnson, C. L., McGovern, P. J., Abshire, J. B., Afzal, R. S., and Sun, X. Mars Orbiter Laser Altimeter: Experiment summary after the first year of global mapping of Mars. *Journal of Geophysical Research: Planets*, 106(E10):23689–23722, oct 2001b. doi: 10.1029/2000je001364.
- Smith, I. B., Larour, E., Putzig, N. E., Greve, R., and Schlegel, N. J. CO₂ Glaciers on the South Polar Layered Deposits of Mars. In *Sixth International Conference on Mars Polar Science and Exploration*, volume 1926, 2016.
- Smith, M. D. The annual cycle of water vapor on Mars as observed by the Thermal Emission Spectrometer. *Journal of Geophysical Research: Planets*, 107(E11):25–1–25–19, November 2002. doi: 10.1029/2001je001522. URL <https://doi.org/10.1029/2001je001522>.
- Smith, M. D., Bougher, S. W., Encrenaz, T., Forget, F., and Kleinböhl, A. Thermal Structure and Composition. In Haberle, R. M., Clancy, R. T., Forget, F., Smith, M. D., and Zurek, R. W., editors, *The Atmosphere and Climate of Mars*, Cambridge Planetary Science, page 42–75. Cambridge University Press, 2017. doi: 10.1017/9781139060172.004.
- Smith, M. D. Interannual variability in TES atmospheric observations of Mars during 1999–2003. *Icarus*, 167(1):148–165, jan 2004. doi: 10.1016/j.icarus.2003.09.010.
- Smith, P. H., Tamppari, L. K., Arvidson, R. E., Bass, D., Blaney, D., Boynton, W. V., Carswell, A., Catling, D. C., Clark, B. C., Duck, T., DeJong, E., Fisher, D., Goetz, W., Gunnlaugsson, H. P., Hecht, M. H., Hipkin, V., Hoffman, J., Hviid, S. F., Keller, H. U., Kounaves, S. P., Lange, C. F., Lemmon, M. T., Madsen, M. B., Markiewicz, W. J., Marshall, J., McKay, C. P., Mellon, M. T., Ming, D. W., Morris, R. V., Pike, W. T., Renno, N., Stauffer, U., Stoker, C., Taylor, P., Whiteway, J. A., and Zent,

- A. P. H₂O at the Phoenix Landing Site. *Science*, vol. 325(5936):pp. 58–61, 2009. ISSN 00368075, 10959203. doi: 10.1126/science.1172339.
- Smoluchowski, R. Mars: Retention of Ice. *Science*, 159(3821):pp. 1348–1350, 1968. doi: 10.1126/science.159.3821.1348.
- Soare, R. J., Osinski, G. R., and Roehm, C. L. Thermokarst Lakes and Ponds on Mars in the Very Recent (Late Amazonian) Past. *Earth and Planetary Science Letters*, 272(1-2):382–393, jul 2008. doi: 10.1016/j.epsl.2008.05.010.
- Soto, A., Mischna, M. A., and Richardson, M. I. Ancient Mars and Atmospheric Collapse. *Mars Atmosphere: Modelling and observation*, pages pp. 449–452, 2011.
- Soto, A., Mischna, M., Schneider, T., Lee, C., and Richardson, M. Martian Atmospheric Collapse: Idealized GCM studies. *Icarus*, vol. 250(Supplement C):pp. 553–569, 2015. ISSN 0019-1035. doi: 10.1016/j.icarus.2014.11.028.
- Souness, C. and Hubbard, B. Mid-latitude Glaciation on Mars. *Progress in Physical Geography: Earth and Environment*, 36(2):238–261, February 2012. doi: 10.1177/0309133312436570. URL <https://doi.org/10.1177/0309133312436570>.
- Souness, C., Hubbard, B., Milliken, R. E., and Quincey, D. An Inventory and Population-scale Analysis of Martian Glacier-like Forms. *Icarus*, 217(1):pp. 243–255, 2012. doi: 10.1016/j.icarus.2011.10.020.
- Span, R. and Wagner, W. A New Equation of State for Carbon Dioxide Covering the Fluid Region from the Triple-point Temperature to 1100 K at Pressures up to 800 MPa. *Journal of physical and chemical reference data*, 25(6):1509–1596, 1996. doi: 10.1063/1.555991.
- Squyres, S. W. and Carr, M. H. Geomorphic Evidence for the Distribution of Ground Ice on Mars. *Science*, vol. 231(4735):pp. 249–252, 1986. ISSN 0036-8075. doi: 10.1126/science.231.4735.249.
- Squyres, S. W., Clifford, S. M., Kuzmin, R. O., Zimbelman, J. R., and Costard, F. M. Ice in the Martian Regolith. In *Mars*, pages 523–554. University of Arizona Press, 1992. doi: 10.2307/j.ctt207g59v.20.
- Steele, L. J., Balme, M. R., and Lewis, S. R. Regolith-Atmosphere Exchange of Water in Mars’ Recent Past. *Icarus*, 284(Supplement C):pp. 233–248, 2017a. ISSN 0019-1035. doi: 10.1016/j.icarus.2016.11.023.
- Steele, L. J., Balme, M. R., and Lewis, S. R. Using a GCM to Track Mars’ Surface Water Ice Deposits Over >100 Obliquity Cycles from 20 Mya to Present. In *Mars Workshop on Amazonian and Present Day Climate*, volume 2086, page 4014, 2018.
- Steiner, G., Kömle, N. I., and Kührt, E. Thermal Modelling of Comet Simulation Experiments. In Kömle, N. I., Bauer, S. J., and Spohn, T., editors, *Theoretical Modelling of Comet Simulation Experiments*, page 11, January 1991.
- Stevens, M. H., Conway, R. R., Englert, C. R., Summers, M. E., Grossmann, K. U., and Gusev, O. A. PMCs and the Water Frost Point in the Arctic Summer Mesosphere. *Geophysical research letters*, 28(23):4449–4452, 2001. doi: 10.1029/2001gl013598.
- Stewart, S. T. and Nimmo, F. Surface Runoff Features on Mars: Testing the carbon dioxide formation hypothesis. *Journal of Geophysical Research: Planets*, 107(E9), 2002. doi: 10.1029/2000je001465.

- Tanaka, K. L. The stratigraphy of Mars. *Journal of Geophysical Research*, 91(B13): E139, 1986. doi: 10.1029/jb091ib13p0e139.
- Tanaka, K. L. and Kolb, E. J. Geologic history of the polar regions of Mars based on Mars Global Surveyor Data: I. Noachian and Hesperian Periods. *Icarus*, 154(1): 3–21, 2001. doi: 10.1006/icar.2001.6675.
- Tanaka, K. L., Banerdt, W. B., Kargel, J. S., and Hoffman, N. Huge, CO₂-charged Debris-flow Deposit and Tectonic Sagging in the Northern Plains of Mars. *Geology*, 29(5):427, 2001. doi: 10.1130/0091-7613(2001)029<0427:hccdfd>2.0.co;2. URL [https://doi.org/10.1130/0091-7613\(2001\)029<0427:hccdfd>2.0.co;2](https://doi.org/10.1130/0091-7613(2001)029<0427:hccdfd>2.0.co;2).
- Taylor, G. J., Boynton, W., Brückner, J., Wänke, H., Dreibus, G., Kerry, K., Keller, J., Reedy, R., Evans, L., Starr, R., Squyres, S., Karunatillake, S., Gasnault, O., Maurice, S., d’Uston, C., Englert, P., Dohm, J., Baker, V., Hamara, D., Janes, D., Sprague, A., Kim, K., and Drake, D. Bulk Composition and Early Differentiation of Mars. *Journal of Geophysical Research: Planets*, 111(E3), 2006. doi: 10.1029/2005JE002645.
- Thomas, P. C., Malin, M. C., Edgett, K. S., Carr, M. H., Hartmann, W. K., Ingersoll, A. P., James, P. B., Soderblom, L. A., Veverka, J., and Sullivan, R. North–South Geological Differences Between the Residual Polar Caps on Mars. *Nature*, 404(6774): 161–164, March 2000. doi: 10.1038/35004528. URL <https://doi.org/10.1038/35004528>.
- Tillman, J. E., Landberg, L., and Larsen, S. E. The Boundary Layer of Mars: Fluxes, Stability, Turbulent Spectra, and Growth of the Mixed Layer. *Journal of the Atmospheric Sciences*, 51(12):1709–1727, jun 1994. doi: 10.1175/1520-0469(1994)051<1709:tblomf>2.0.co;2.
- Titov, D. V. Water Vapour in the Atmosphere of Mars. *Advances in Space Research*, 29(2):183–191, January 2002. doi: 10.1016/s0273-1177(01)00568-3. URL [https://doi.org/10.1016/s0273-1177\(01\)00568-3](https://doi.org/10.1016/s0273-1177(01)00568-3).
- Titus, T. N., Byrne, S., Colaprete, A., Forget, F., Michaels, T. I., and Prettyman, T. H. The CO₂ Cycle. In Haberle, R. M., Clancy, R. T., Forget, F., Smith, M. D., and Zurek, R. W., editors, *The Atmosphere and Climate of Mars*, Cambridge Planetary Science, page 374–404. Cambridge University Press, 2017. doi: 10.1017/9781139060172.012.
- Toon, O. B., Pollack, J. B., Ward, W., Burns, J. A., and Bilski, K. The Astronomical Theory of Climatic Change on Mars. *Icarus*, 44(3):pp. 552–607, 1980. ISSN 0019-1035. doi: 10.1016/0019-1035(80)90130-X.
- Touma, J. and Wisdom, J. The Chaotic Obliquity of Mars. *Science*, 259(5099):pp. 1294–1297, 1993. doi: 10.1126/science.259.5099.1294.
- Turbet, M., Forget, F., Leconte, J., Charnay, B., and Tobie, G. CO₂ condensation is a serious limit to the deglaciation of Earth-like planets. *Earth and Planetary Science Letters*, 476:11–21, oct 2017. doi: 10.1016/j.epsl.2017.07.050.
- Turcotte, D. L. and Schubert, G. *Geodynamics*. Cambridge University press, 2002.
- Van Olphen, H. and Fripiat, J.-J. *Data Handbook for Clay Materials and Other Non-metallic Minerals*. Pergamon Press, Oxford and Elmsford, New York, 1979. doi: 10.1346/ccmn.1980.0280215.

- Versteeg, H. K. and Malalasekera, W. *An Introduction to Computational Fluid Dynamics: The finite volume method*. Pearson education, 2007.
- Vincendon, M., Mustard, J. F., Forget, F., Kreslavsky, M. A., Spiga, A., Murchie, S. L., and Bibring, J. Seasonal CO₂ Ice at Mid-Latitudes on Mars: Implications for subsurface water ice. In *AGU Fall Meeting Abstracts*, 2009.
- Vincendon, M., Mustard, J., Forget, F., Kreslavsky, M., Spiga, A., Murchie, S., and Bibring, J. Near Tropical Subsurface Ice on Mars. *Geophysical Research Letters*, vol. 37(1), 2010. ISSN 1944-8007. doi: 10.1029/2009gl041426.
- Viola, D., McEwen, A. S., Dundas, C. M., and Byrne, S. Expanded Secondary Craters in the Arcadia Planitia Region, Mars: Evidence for tens of Myr-old shallow subsurface ice. *Icarus*, 248:190–204, mar 2015. doi: 10.1016/j.icarus.2014.10.032.
- Ward, W. R. Climatic Variations on Mars: 1. Astronomical theory of insolation. *Journal of Geophysical Research*, 79(24):pp. 3375–3386, 1974a. doi: 10.1029/jc079i024p03375.
- Ward, W. R., Murray, B. C., and Malin, M. C. Climatic Variations on Mars: 2. Evolution of carbon dioxide atmosphere and polar caps. *Journal of Geophysical Research*, 79(24):pp. 3387–3395, 1974b. doi: 10.1029/jc079i024p03387.
- Ward, W. R., Burns, J. A., and Toon, O. B. Past Obliquity Oscillations of Mars: The role of the Tharsis Uplift. *Journal of Geophysical Research: Solid Earth*, 84(B1): 243–259, jan 1979. doi: 10.1029/jb084ib01p00243.
- Warren, S. G., Wiscombe, W. J., and Firestone, J. F. Spectral Albedo and Emissivity of CO₂ in Martian Polar Caps: Model results. *Journal of Geophysical Research: Solid Earth*, vol. 95(B9):pp. 14717–14741, 1990. ISSN 2156-2202. doi: 10.1029/JB095iB09p14717.
- Watzin, J. and Haltigin, T. Mars Exploration Ice Mapper. Presented to MEPAG Spring Meeting, 2020. URL https://mepag.jpl.nasa.gov/meeting/2020-04/Day1/16_WATZIN-HALTIGIN-Ice%20Mapper_MEPAG_%20April%20152020_Final%20v2_post.pdf, 2020.
- Whiteway, J. A., Komguem, L., Dickinson, C., Cook, C., Illnicki, M., Seabrook, J., Popovici, V., Duck, T. J., Davy, R., Taylor, P. A., et al. Mars Water-ice Clouds and Precipitation. *Science*, 325(5936):pp. 68–70, 2009. doi: 10.1126/science.1172344.
- Wieczorek, M. A. Constraints on the Composition of the Martian South Polar Cap from Gravity and Topography. *Icarus*, 196(2):506–517, 2008. doi: 10.1016/j.icarus.2007.10.026.
- Williams, K. E., McKay, C. P., and Heldmann, J. L. Modeling the Effects of Martian Surface Frost on Ice Table Depth. *Icarus*, 261:pp. 58–65, 2015. doi: 10.1016/j.icarus.2015.08.005.
- Wilson, R. J. and Smith, M. D. The Effects of Atmospheric Dust on the Seasonal Variation of Martian Surface Temperature. In *Second International Workshop on the Mars Atmosphere: Modelling and Observation*, CNES, volume 27, 2006.
- Wilson, R. J., Neumann, G. A., and Smith, M. D. Diurnal Variation and Radiative Influence of Martian Water Ice Clouds. *Geophysical Research Letters*, 34, 2007.

- Witkowski, A., Majkut, M., and Rulik, S. Analysis of Pipeline Transportation Systems for Carbon Dioxide Sequestration. *Archives of Thermodynamics*, 35:s. 117–140, 03 2014. doi: 10.2478/aoter-2014-0008.
- Wood, S. E. A General Analytic Model for the Thermal Conductivity of Loose, Indurated or Icy Planetary Regolith. In *Lunar and Planetary Science Conference*, volume 42, page 2795, 2011.
- Wood, S. E. and Griffiths, S. D. A Mechanism for Mars Subsurface Warming at Low Obliquity: Its effects on the state and distribution of volatiles. pages pp. P41A–10, may 2007a.
- Wood, S. E. and Griffiths, S. D. Mars Subsurface Warming at Low Obliquity. In *Seventh International Conference on Mars*, volume 1353, page 3387, 2007b.
- Wood, S. E. and Griffiths, S. D. Epochal Seasonal Thermal Modeling of Mars’ Polar Surface Energy Balance: Perennial CO₂ ice and atmospheric collapse. In *Third International Workshop on Mars Polar Energy Balance and the CO₂ Cycle*, volume 1494, pages 65–66, 2009.
- Wood, S. E. and Paige, D. A. Modeling Interannual Variability in the Martian Seasonal CO₂ Cycle. In *Polar Regions of Mars: Geology, Glaciology, and Climate History*, 1992. URL <https://adsabs.harvard.edu/pdf/1992prmg.work...26W>.
- Wordsworth, R., Forget, F., Millour, E., Head, J. W., Madeleine, J. B., and Charnay, B. Global Modelling of the Early Martian Climate Under a Denser CO₂ Atmosphere: Water cycle and ice evolution. *Icarus*, vol. 222(1):pp. 1–19, 2013. ISSN 0019-1035. doi: 10.1016/j.icarus.2012.09.036.
- Wordsworth, R. D. The Climate of Early Mars. *Annual Review of Earth and Planetary Sciences*, 44(1):381–408, June 2016. doi: 10.1146/annurev-earth-060115-012355. URL <https://doi.org/10.1146/annurev-earth-060115-012355>.
- Wordsworth, R. D., Kerber, L., Pierrehumbert, R. T., Forget, F., and Head, J. W. Comparison of “warm and wet” and “cold and icy” scenarios for early Mars in a 3-D climate model. *Journal of Geophysical Research: Planets*, 120(6):pp. 1201–1219, 2015. doi: 10.1002/2015je004787.
- Zalc, J. M., Reyes, S. C., and Iglesia, E. The Effects of Diffusion Mechanism and Void Structure on Transport Rates and Tortuosity Factors in Complex Porous Structures. *Chemical Engineering Science*, 59(14):pp. 2947–2960, 2004. doi: 10.1016/j.ces.2004.04.028.
- Zent, A. P. and Quinn, R. C. Simultaneous Adsorption of CO₂ and H₂O Under Mars-like Conditions and Application to the Evolution of the Martian Climate. *Journal of Geophysical Research: Planets*, 100(E3):5341–5349, 1995. doi: 10.1029/94je01899.
- Zent, A. P. and Quinn, R. C. Measurement of H₂O Adsorption under Mars-like Conditions: Effects of adsorbent heterogeneity. *Journal of Geophysical Research: Planets*, 102(E4):pp. 9085–9095, 1997. doi: 10.1029/96je03420.
- Zent, A. P., Fanale, F. P., and Postawko, S. E. Carbon Dioxide: Adsorption on palagonite and partitioning in the Martian regolith. *Icarus*, 71(2):241–249, 1987. doi: 10.1016/0019-1035(87)90149-7.

- Zent, A. P., Haberle, R. M., Houben, H. C., and Jakosky, B. M. A Coupled Subsurface-boundary Layer Model of Water on Mars. *Journal of Geophysical Research: Planets*, 98(E2):pp. 3319–3337, 1993. doi: 10.1029/92je02805.
- Zuber, M. T., Solomon, S. C., Phillips, R. J., Smith, D. E., Tyler, L. G., Aharonson, O., Balmino, G., Banerdt, B. W., Head, J. W., Johnson, C. L., et al. Internal Structure and Early Thermal Evolution of Mars from Mars Global Surveyor Topography and Gravity. *Science*, 287(5459):pp. 1788–1793, 2000. doi: 10.1126/science.287.5459.1788.
- Zurek, R. W., Tolson, R. A., Bougher, S. W., Lugo, R. A., Baird, D. T., Bell, J. M., and Jakosky, B. M. Mars Thermosphere as seen in MAVEN Accelerometer Data. *Journal of Geophysical Research: Space Physics*, 122(3):3798–3814, mar 2017. doi: 10.1002/2016ja023641.

A | Detailed Description of Diffusion Methods

A.1 Derivation of the Discretisation of the Heat Conduction Equation

The one dimensional (1-D) heat conduction equation is:

$$\rho(z)c_p \frac{\partial T}{\partial t} = \frac{\partial}{\partial z} \left(k(z) \frac{\partial T}{\partial z} \right), \quad (\text{A.1})$$

where T is the temperature [K] at a depth z [m] and time t [s], k is the thermal conductivity [$\text{W m}^{-1} \text{K}^{-1}$], ρ is the density [kg m^{-3}] and c_p is the specific heat capacity [$\text{J K}^{-1} \text{kg}^{-1}$].

This is discretised using the finite control volume method, by integrating over the control volume, cv , and over the time interval from t to $t + \delta t$:

$$\rho c_p \int_{cv} \int_t^{t+\delta t} \frac{\partial T}{\partial t} dt dz = \int_t^{t+\delta t} \int_{cv} \frac{\partial}{\partial z} \left(k \frac{\partial n}{\partial z} \right) dz dt \quad (\text{A.2})$$

$$\rho c_p \int_{i-1}^{i+1} \int_t^{t+\delta t} \frac{\partial T}{\partial t} dt dz = \int_t^{t+\delta t} \int_{i-1}^{i+1} \frac{\partial}{\partial z} \left(k \frac{\partial n}{\partial z} \right) dz dt \quad (\text{A.3})$$

where $i-1$ and $i+1$ represent the midpoint of the previous and next layers, with $i-0.5$ and $i+0.5$ being the interface between the layers and i is the midpoint of the current layer. Figure A.1 shows the relationships between the grid points. In the following equations, when the variable is for the current timestep, there is either a superscript of t or no superscript, and for the previous timestep, the superscript is 0.

The discretised form can then be written as:

$$\rho c_p \Delta z (T_i - T_i^0) = \int_t^{t+\delta t} \left[\frac{k_{i+0.5} (T_{i+1} - T_i)}{(\delta z)_{i+0.5}} - \frac{k_{i-0.5} (T_i - T_{i-0.5})}{(\delta z)_{i-0.5}} \right] \quad (\text{A.4})$$

where the superscript 0 represents the previous timestep. As we are assuming an implicit scheme, this can then be written as:

$$\rho c_p \frac{\Delta z}{\Delta t} (T_i^1 - T_i^0) = \left[\frac{k_{i+0.5} (T_{i+1} - T_i)}{(\delta z)_{i+0.5}} - \frac{k_{i-0.5} (T_i - T_{i-1})}{(\delta z)_{i-0.5}} \right] \quad (\text{A.5})$$

This can be rearranged into a form that can be used for a tri-diagonal matrix algorithm (TDMA) as follows

$$a_i^t T_i = b_i^t T_{i+1} + c_i^t T_{i-1} + d_i^t \quad (\text{A.6a})$$

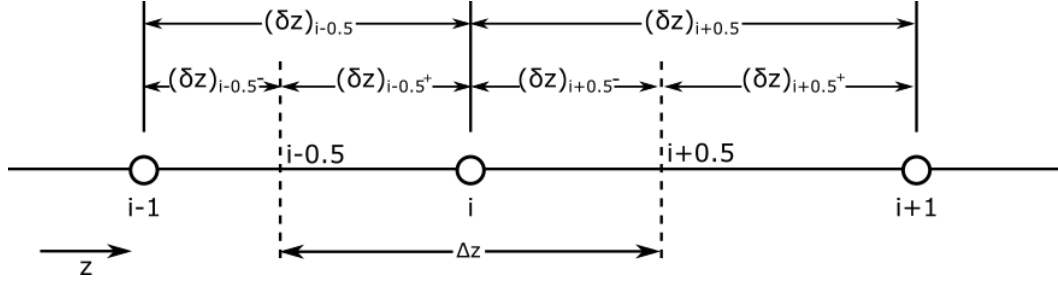


Figure A.1: Grid used for the discretisation, where i is the midpoint of the layer at which the value is currently being calculated, $i - 1$ is the midpoint of the layer before and $i + 1$ is the midpoint of the layer after. $\delta z_{i-0.5}$ and $\delta z_{i+0.5}$ represent the distance between the midpoints of the layers before and after the current layer with the current layer's midpoint, i . Δz is the distance between the interface of layer $i - 1$ (interface $i - 0.5$) and layer $i + 1$ (interface $i + 0.5$), i.e. the thickness of layer i . Figure is adapted from Patankar (1980).

where

$$a_i^t = \frac{\rho c_p \Delta z}{\Delta t} + \frac{k_{i+0.5}}{(\delta z)_{i+0.5}} + \frac{k_{i-0.5}}{(\delta z)_{i-0.5}} \quad (\text{A.6b})$$

$$b_i^t = \frac{k_{i+0.5}}{(\delta z)_{i+0.5}} \quad (\text{A.6c})$$

$$c_i^t = \frac{k_{i-0.5}}{(\delta z)_{i-0.5}} \quad (\text{A.6d})$$

$$d_i^t = \frac{\rho c_p \Delta z}{\Delta t} T_i^0 \quad (\text{A.6e})$$

The TDMA method is then numerically solved by substituting Equation A.7 into Equation A.6a.

$$T_{i-1}^t = P_{i-1} n_i^t + Q_{i-1} \quad (\text{A.7})$$

$$a_i T_i^t = b_i T_{i+1}^t + c_i (P_{i-1} T_i^t + Q_{i-1}) + d_i \quad (\text{A.8})$$

$$a_i T_i^t = b_i T_{i+1}^t + c_i P_{i-1} T_i^t + c_i Q_{i-1} + d_i \quad (\text{A.9})$$

$$T_i^t (a_i - c_i P_{i-1}) = b_i T_{i+1}^t + c_i Q_{i-1} + d_i \quad (\text{A.10})$$

$$T_i^t = \frac{b_i}{a_i - c_i P_{i-1}} T_{i+1}^t + \frac{c_i Q_{i-1} + d_i}{a_i - c_i P_{i-1}} \quad (\text{A.11})$$

This can then be solved using Equations A.12a-c. Equations A.12d-e are the initial conditions for this system.

$$T_i^t = P_i T_{i+1}^t + Q_i \quad (\text{A.12a})$$

where

$$P_i = \frac{b_i}{a_i - c_i P_{i-1}} \quad (\text{A.12b})$$

$$Q_i = \frac{c_i Q_{i-1} + d_i}{a_i - c_i P_{i-1}} \quad (\text{A.12c})$$

$$P_1 = \frac{b_1}{a_1} \quad (\text{A.12d})$$

$$Q_1 = \frac{d_1}{a_1} \quad (\text{A.12e})$$

A.1.1 Boundary Conditions

A.1.1.1 Surface

For the surface condition, the temperature in the atmosphere, T_{surf} , is the 'fixed' temperature that is used, and the discretised equation for the first grid point, 1, is:

$$\rho c_p \frac{\Delta z}{\Delta t} (T_1 - T_1^0) = \frac{k_{1.5} (T_2 - T_1)}{(\delta z)_{1.5}} - \frac{k_1 (T_1 - T_{surf})}{(\delta z)_{0.5}} \quad (\text{A.13})$$

This can be rearranged into the form for a TDMA as follows

$$a_1^t T_1 = b_1^t T_2 + c_1^t T_0 + d_1^t \quad (\text{A.14a})$$

where

$$a_1^t = \frac{\rho c_p \Delta z}{\Delta t} + \frac{k_{1.5}}{(\delta z)_{1.5}} + \frac{k_1}{(\delta z)_{0.5}} \quad (\text{A.14b})$$

$$b_1^t = \frac{k_{1.5}}{(\delta z)_{1.5}} \quad (\text{A.14c})$$

$$c_1^t = 0. \quad (\text{A.14d})$$

$$d_1^t = \frac{\rho c_p \Delta z}{\Delta t} T_1^0 + \frac{k_1}{(\delta z)_{0.5}} T_{surf} \quad (\text{A.14e})$$

A.1.1.2 Base

The base boundary has a fixed temperature flux, B_{flux} , and the final grid point is 33. The discretisation equation for the base boundary is:

$$\rho c_p \frac{\Delta z}{\Delta t} (T_{33} - T_{33}^0) = B_{flux} - \frac{k_{32.5} (T_{33} - T_{32})}{(\delta z)_{32.5}} \quad (\text{A.15})$$

This can be rearranged into the form for a TDMA as follows

$$a_{33}^t T_{33} = b_{33}^t T_{34} + c_{33}^t T_{32} + d_{33}^t \quad (\text{A.16a})$$

where

$$a_{33}^t = \frac{\rho c_p \Delta z}{\Delta t} + \frac{k_{32.5}}{(\delta z)_{32.5}} \quad (\text{A.16b})$$

$$b_{33}^t = 0. \quad (\text{A.16c})$$

$$c_{33}^t = \frac{k_{32.5}}{(\delta z)_{32.5}} \quad (\text{A.16d})$$

$$d_{33}^t = B_{flux} + \frac{\rho c_p \Delta z}{\Delta t} T_{33}^0 \quad (\text{A.16e})$$

A.2 Derivation of the Finite Volume Method for Diffusion of Vapour

Vapour is transported through the regolith by the unsteady diffusion equation (Fick's 1st law), which is expressed as follows in 1-D:

$$f_{\text{H}_2\text{O}} = D_{\text{H}_2\text{O}} \frac{\partial n_{\text{H}_2\text{O}}}{\partial z}, \quad (\text{A.17})$$

$$J = -D \frac{\partial n}{\partial z} \quad (\text{A.18})$$

where J is the vapour flux [$\text{kg m}^{-1}\text{s}^{-1}$], D is the diffusion coefficient [m^2s^{-1}], and n the vapour concentration [kg m^{-3}]. This is combined with the relation $\frac{\partial n}{\partial t} = \frac{\partial J}{\partial z}$ to form Equation A.19, which is the diffusion equation that needs to be solved.

$$\frac{\partial n}{\partial t} = \frac{\partial}{\partial z} \left(D \frac{\partial n}{\partial z} \right) \quad (\text{A.19})$$

The finite control volume discretisation of Equation A.19 is then carried out over a control volume, cv and over a finite time step δt in the following equations, where V is the volume of the control volume and A is the area. In the following equations $i - 1$ and $i + 1$ represent the midpoint of the previous and next layers, with $i - 0.5$ and $i + 0.5$ being the interface between the layers and i is the midpoint of the current layer. Figure A.1 shows the relationships between the grid points. When the variable is for the current timestep, there is either a superscript of t or no superscript, and for the previous timestep, the superscript is 0.

$$\int_{cv} \int_t^{t-\delta t} \left(\frac{\partial n}{\partial t} dt \right) dV = \int_t^{t-\delta t} \int_{cv} \left(\frac{\partial D \frac{\partial n}{\partial z}}{\partial z} dV \right) dt \quad (\text{A.20})$$

$$\int_{i+1}^{i-1} \int_t^{t-\delta t} \left(\frac{\partial n}{\partial t} dt \right) dV = \int_t^{t-\delta t} \left[\left(DA \frac{\partial n}{\partial z} \right)_{i+1} - \left(DA \frac{\partial n}{\partial z} \right)_{i-1} \right] dt \quad (\text{A.21})$$

$$(n_i^t - n_i^{t-\delta t}) \Delta V = \int_t^{t-\delta t} \left[\left(DA \frac{\partial n}{\partial z} \right)_{i+1} - \left(DA \frac{\partial n}{\partial z} \right)_{i-1} \right] dt \quad (\text{A.22})$$

$$(n_i^t - n_i^{t-\delta t})\Delta V = \int_t^{t-\delta t} \left[D_{i+0.5}^t A_i \frac{n_{i+1}^t - n_i^t}{\delta z_i} - D_{i-0.5}^t A_{i-1} \frac{n_i^t - n_{i-1}^t}{\delta z_{i-1}} \right] dt \quad (\text{A.23})$$

$$(n_i^t - n_i^{t-\delta t})\Delta V = D_{i+0.5}^t A_i \frac{(n_{i+1}^t - n_i^t)\delta t}{\delta z_i} - \quad (\text{A.24})$$

$$D_{i-0.5}^t A_{i-1} \frac{(n_i^t - n_{i-1}^t)\delta t}{\delta z_{i-1}} \quad (\text{A.25})$$

Then divide by $A\Delta t$:

$$(\text{A.26})$$

$$(n_i^t - n_i^{t-\delta t}) \frac{\Delta z}{\Delta t} = D_{i+0.5}^t \frac{(n_{i+1}^t - n_i^t)}{\delta z_i} - D_{i-0.5}^t \frac{(n_i^t - n_{i-1}^t)}{\delta z_{i-1}} \quad (\text{A.27})$$

$$\Delta V n_i^t - \Delta V n_i^{t-\delta t} = \frac{D_{i+0.5}^t A_i \Delta t}{\delta z_i} n_{i+1}^t - \frac{D_{i+0.5}^t A_i \Delta t}{\delta z_i} n_i^t - \frac{D_{i-0.5}^t A_{i-1} \Delta t}{\delta z_{i-1}} n_i^t + \frac{D_{i-0.5}^t A_{i-1} \Delta t}{\delta z_{i-1}} n_{i-1}^t \quad (\text{A.28})$$

$$\left(\Delta V + \frac{D_{i+0.5}^t A_i \delta t}{\delta z_i} + \frac{D_{i-0.5}^t A_{i-1} \delta t}{\delta z_{i-1}} \right) n_i^t = \frac{D_{i+0.5}^t A_i \delta t}{\delta z_i} n_{i+1}^t + \frac{D_{i-0.5}^t A_{i-1} \delta t}{\delta z_{i-1}} n_{i-1}^t \quad (\text{A.29})$$

$$+ \Delta V n_i^{t-\delta t} \quad (\text{A.30})$$

This can be rearranged into the correct form for a TDMA to be used:

$$a_i n_i = b_i n_{i+1} + c_i n_{i-1} + d_i \quad (\text{A.31a})$$

where

$$a_i^t = \Delta V + \frac{D_{i+0.5}^t A_i \delta t}{\delta z_i} + \frac{D_{i-0.5}^t A_{i-1} \delta t}{\delta z_{i-1}} \quad (\text{A.31b})$$

$$b_i^t = \frac{D_{i+0.5}^t A_i \delta t}{\delta z_i} \quad (\text{A.31c})$$

$$c_i^t = \frac{D_{i-0.5}^t A_{i-1} \delta t}{\delta z_{i-1}} \quad (\text{A.31d})$$

$$d_i^t = \Delta V n_i^{t-\delta t} \quad (\text{A.31e})$$

The TDMA is achieved by substituting Equation A.32 into Equation A.31a.

$$n_{i-1}^t = P_{i-1} n_i^t + Q_{i-1} \quad (\text{A.32})$$

This substitution gives:

$$a_i n_i^t = b_i n_{i+1}^t + c_i (P_{i-1} n_i^t + Q_{i-1}) + d_i \quad (\text{A.33})$$

$$a_i n_i^t = b_i n_{i+1}^t + c_i P_{i-1} n_i^t + c_i Q_{i-1} + d_i \quad (\text{A.34})$$

$$n_i^t (a_i - c_i P_{i-1}) = b_i n_{i+1}^t + c_i Q_{i-1} + d_i \quad (\text{A.35})$$

$$n_i^t = \frac{b_i}{a_i - c_i P_{i-1}} n_{i+1}^t + \frac{c_i Q_{i-1} + d_i}{a_i - c_i P_{i-1}} \quad (\text{A.36})$$

The final form of the TDMA is solved using Equations A.37a-c. Equations A.37d-e are the initial conditions for this system.

$$n_i^t = P_i n_{i+1}^t + Q_i \quad (\text{A.37a})$$

where:

$$P_i = \frac{b_i}{a_i - c_i P_{i-1}} \quad (\text{A.37b})$$

$$Q_i = \frac{c_i Q_{i-1} + d_i}{a_i - c_i P_{i-1}} \quad (\text{A.37c})$$

and the surface condition is:

$$P_1 = \frac{b_1}{a_1} \quad (\text{A.37d})$$

$$Q_1 = \frac{d_1}{a_1} \quad (\text{A.37e})$$

A.2.1 Boundary Conditions

A.2.1.1 Surface

The surface boundary is a vapour flux, S_{flux} , that is calculated in Section 3.5, and the discretisation equation for the first grid point with a flux boundary is:

$$\frac{\Delta z}{\Delta t} (n_1 - n_1^0) = \frac{D_{1.5} (n_2 - n_1)}{(\delta z)_{1.5}} - S_{flux} \quad (\text{A.38})$$

This can be rearranged into the form for a TDMA as follows

$$a_1^t n_1 = b_1^t n_2 + c_1^t n_0 + d_1^t \quad (\text{A.39a})$$

where

$$a_1^t = \frac{\Delta z}{\Delta t} + \frac{D_{1.5}}{(\delta z)_{1.5}} \quad (\text{A.39b})$$

$$b_1^t = \frac{D_{1.5}}{(\delta z)_{1.5}} \quad (\text{A.39c})$$

$$c_1^t = 0. \quad (\text{A.39d})$$

$$d_1^t = \frac{\Delta z}{\Delta t} n_1^0 - S_{flux} \quad (\text{A.39e})$$

A.2.1.2 Base

The base boundary has a fixed vapour flux, B_{flux} , and the final grid point is 33. In the Martian Subsurface Model (MSSM), the base flux is $0 \text{ kg m}^{-1}\text{s}^{-1}$, but it has been set up to be able to handle other base fluxes if required. The discretisation equation for the last grid point, 33, with a flux boundary is:

$$\frac{\Delta z}{\Delta t} (n_{33} - n_{33}^0) = B_{flux} - \frac{D_{32.5} (n_{33} - n_{32})}{(\delta z)_{32.5}} \quad (\text{A.40})$$

This can be rearranged into the form for a TDMA as follows

$$a_{33}^t n_{33} = b_{33}^t n_{34} + c_{33}^t n_{32} + d_{33}^t \quad (\text{A.41a})$$

where

$$a_{33}^t = \frac{\Delta z}{\Delta t} + \frac{D_{32.5}}{(\delta z)_{32.5}} \quad (\text{A.41b})$$

$$b_{33}^t = 0. \quad (\text{A.41c})$$

$$c_{33}^t = \frac{D_{32.5}}{(\delta z)_{32.5}} \quad (\text{A.41d})$$

$$d_{33}^t = B_{flux} + \frac{\Delta z}{\Delta t} n_{33}^0 \quad (\text{A.41e})$$

B | The LMD-UK Mars global circulation model

B.1 Input Files

Once compiled the LMD-UK Mars global circulation model (MGCM) uses two input files to set the parameters for the simulation. The `model.input` file sets many of the input variables and `callphys.def` sets the physics schemes to be used in the simulation. This section provides an explanation of both files and the reasoning behind the variables used for them in the four MGCM simulations discussed in this thesis.

B.1.1 `model.input`

An example `model.input` file is shown in Figure B.1 and Tables B.1 and B.2 give an explanation of the variables, the range of values and the reasoning behind these values used for this thesis.

```
1  &INPB
2    RNTAPE=3351.300D0
3    ,KSTART=starttime
4    ,KTOTAL=endtime
5    ,TSPD=timestep.0D0
6    ,KOUNTP=0
7    ,KOUNTH=40
8    ,KOUNTR=0
9    ,BIDISS=0.1,0.2,0.5,1.0,2.0,20*0.0
10   ,TDISS=0.1D0,NDEL=6
11   ,LTOPOG=.TRUE.,LBINTP=.FALSE.,LSPONGE=.TRUE.,LTVEC=.FALSE.
12   ,LSPINUP=.FALSE.
13   &END
14   &PHYSIC
15     KPHYSIC = 10
16     ,KVIKING = 10
17     ,KMASBUD = 96
18     ,LMASBUD = .TRUE.
19     ,LMASCOR = .TRUE.
20     ,LVIKING = .FALSE.
21     ,LMARSNET = .FALSE.
22     ,LPMIRR = .FALSE.
23     ,PTOTAL = 732.0
24     ,RELIEF = 'MOL'
25     ,IECRI = -1
26     ,ECRITPHY = 0.08333333D0
27   &END
```

Figure B.1: An example of the `model.input` file

Table B.1: Description of the dynamics parameters in the model.input file for the MGCM and the range of values used.

Parameter	Description	Values	Reason
KSTART	Starting timestep number	0	Starts at northern spring equinox
KTOTAL	Final timestep number	642240	If running for 1 year with TSPD=960, KTOTAL = 642240
TSPD	Number of timesteps per sol	960	Horizontal resolution needs to be considered when choosing TSPD. This often ranges from 48–960
KOUNTP	Number of timesteps between printed output for the spectral and gridded fields	0	No output is produced for any of the runs presented here
KOUNTH	Number of timesteps between the output of history records	40	
KOUNTR	Number of timesteps between restart records	0	Default value is 0 which means no output is produced
BIDISS	Controls the timescale of diffusion in the atmosphere to prevent large accelerations in the upper atmosphere (>80km)	>80km: 0.1, 0.2, 0.5, 1.0, 2.0, 20*0. <80km: 0.	For these simulations, the height of the top of the atmosphere has been limited to <80km for most runs (apart from the very initial) so BIDISS is not needed
TDISS	Controls the timescales for biharmonic diffusion of shorter wavelengths	0.1	These values are chosen because generally
NDEL	The exponent used to apply diffusion to remove small scale build up of energy and entropy at the resolution limit of the model	6	TDISS=1/6 and NDEL = 6 prevent build up for a moderate resolution. TDISS=1/8 and NDEL=8 works better because they do not affect large scales but can cause more issues
LTOPOG	Sets whether topography is used	.true.	Always use Mars Orbiter Laser Altimeter (MOLA) topography because the near surface atmosphere is sensitive the topography used
LBINTP	Applies a diffusive smoothing to the atmospheric pressure levels (instead of sigma levels)	.false.	Should be false simulations focusing on the lower atmosphere

Continuation of table B.1			
Parameter	Description	Values	Reason
LSPONGE	Sets a sponge layer so the Rayleigh friction acts only on eddies. Stops reflections from the upper two atmospheric layers reflecting back into the lower atmosphere due to the fixed upper boundary in the model, whereas in the atmosphere, a wave would continue travelling to space rather than reflecting back	<code>.true.</code>	Interested in the near surface atmosphere so the upper limit of the atmosphere for most simulations has been limited to ~ 40 km
LTVEC	Controls which method is used to calculate Legendre transforms depending on the machine used	<code>.false.</code>	The method used when LTVEC is set to False is more efficient on a serial processor which has been used in this thesis
LSPINUP	Is the run a spin up?	<code>.false.</code>	A spin up run resets the atmosphere and is only used in an initial simulation with no start files

Table B.2: Description of the physics parameters in the model.input file and the range of values used.

Parameter	Description	Values	Reason
KPHYSIC	Number of dynamics timesteps before the physics schemes are run	5 - 10	Dependent on the resolution used for the model. For example, a value of 6 means the physics scheme is run once every 6 dynamics timesteps, so for a tspd 96, the physics scheme is run 16 times each day (every 1 and a half hours)
KVIKING	Number of timesteps between phoney Viking observations of the physics schem	5-10	Set as the same value as KPHYSIC because it is calculated in the same way. Only used if LVIKING=True
KMASBUD	Number of timesteps before the mass budget is checked against PTOTAL		Ensures the total mass is conserved and if it differs from PTOTAL, a correction is applied
LMASBUD	Output the mass budget	<code>.true.</code>	Allows one to keep track of how the mass budget changes

Continuation of table B.2			
Parameter	Description	Values	Reason
LMASCOR	Perform a mass conservation correction if the mass budget is vastly different from PTO-TAL?	<code>.true.</code>	This ensures the total mass of the atmosphere and surface ice remains reasonable
LVIKING	Controls whether phoney observations as if from the Viking lander locations are output	<code>.false.</code>	This is only used if data that can be compared with Viking observations are needed
LMARSNET	Controls whether phoney observations as if from the MARSNET stations are output	<code>.false.</code>	This is only used if data that can be compared with MARSNET observations are needed
LPMIRR	Controls whether phoney observations as if from the PMIRR instrument on Mars Orbiter are output	<code>.false.</code>	This is only used if data that can be compared with PMIRR observations are needed
PTOTAL	Total CO2 equivalent pressure for the atmosphere and polar caps referenced at mola zero datum	732.0	A value of 732.0 is used for the present day atmosphere based on the best fit of the mass budget between the output of the MGCM and Viking lander data
RELIEF	Sets which topography data are used	'MOL'	The topography used in all simulations is based on MOLA data
IECRI ECRITPHY	Period of output to the diagfi record files in terms of number of times per day	0.0833 - 50.	A value of 0.0833 means that output is recorded every two hours which is frequent enough to show diurnal changes. For the low resolution runs (T10), a larger value is used because the simulation is run for 10s-100s martian years rather than a few martian years.

B.1.2 callphys.def

The callphys.def file (Figure B.2) is used to define which physics schemes should be used in a specific run. These parameters remain the same between the runs shown in this thesis because the majority of parameters control changes in the atmosphere and the atmosphere has been kept consistent across runs so that comparisons can be easily made.

A brief description for each parameter is given in the script and they have all been grouped in smaller categories. In the General Options section, `tracer`, `diurnal` and `season` are set to `.true.` to run the model with tracers, a diurnal cycle and a seasonal cycle. The other general options control how often various values are output and are

all set to `.false.` for the purpose of the runs in this thesis.

The dust scenario parameters are also kept consistent between runs, using the Mars Year 26 (MY26) dust scenario (`iaervar=26`) because MY26 was the first martian year (without a dust storm) with Thermal Emission Spectrometer (TES) data for the entire martian year. MY24, which was the first year of TES data, only has data from $L_S = 100^\circ$, the rest of the year uses an estimate for the dust scenario from Montabone et al. (2015). `tauvis` is only used if `iaervar = 1`, therefore the value in the script will not be used in the model for these runs. The Mars Global Surveyor (MGS) scenario (`iddist=3`) is used for the vertical dust profile because this is the most detailed vertical dust profile that has been implemented into the MGCM. The `topdustref` is another unused parameter because it only has an effect if `iddist=1`.

The physical parametrisations cover the radiative schemes as well as the thermal schemes for the atmosphere. The thermal schemes are all `.true.` because Colaïtis et al. (2013) demonstrated that turning these schemes off introduces a cooling bias to the planetary boundary layer (PBL). Since the largest effect of turning off the thermal schemes is shown to be in the PBL, which is the region of interest for this study, these parameters have all been turned on to ensure that the simulations are representative of the present day atmosphere. The radiative transfer is set to be computed for every physical timestep (`iradia=1`) because the physics and radiative schemes will affect each other.

When simulating the water (H_2O) cycle, the majority of tracer options are set to `.true.` to allow radiatively active H_2O ice and dust to work (apart from `callddevil` which is only used when investigating dust). Using radiatively active H_2O ice and dust improves the thermal structure so it is preferable that both are turned on. However, at low resolution (T10,10) both need to be turned off to keep the atmosphere stable. To turn radiatively active dust and H_2O ice off, only `sedimentation`, `water` and `caps` are `.true.` and the rest of the tracer true/false variables are set to `.false..` The values used for the H_2O variables were all chosen based on the work of Navarro et al. (2014), who showed that these values produce the best representation of the present day atmosphere.

The photochemistry is turned off because this scheme adds a complexity to the H_2O simulation (as well as more chemical species) that are not required for these runs. The thermospheric options are all set to `.false.` because this work focuses on the lower atmosphere and the PBL and uses an upper atmospheric limit of 80 km which is much lower than the base of the thermospheric layer of the martian atmosphere (~ 120 km; Zurek et al., 2017). The assimilation options have also all been turned off because this study is not assimilating any data into the MGCM. The regolith scheme is turned on because the focus of this thesis is on the distribution of subsurface ice and this flag turns on the integrated Martian Subsurface Model (MSSM) with the features described in Chapter 3.

```

1  ##General options
2  ##~~~~~
3  #Run with or without tracer transport ?
4  tracer=.true.
5
6  #Directory where external input files are:
7  datadir=/STEM/scratch.san/laf87/mgcm/datafile
8
9  #Diurnal cycle ? if diurnal=False, diurnal averaged solar heating
10 diurnal=.true.
11
12 #Seasonal cycle ? if season=False, Ls stays constant, to value set in "start"
13 season = .true.
14
15 #write some more output on the screen ?
16 lwrite = .false.
17
18 #Save statistics in file "stats.nc" ?
19 callstats =.false.
20
21 #Save EOF profiles in file "profiles" for Climate Database?
22 calleofdump = .false.
23
24 ## Dust scenario. Used if the dust is prescribed (i.e. if tracer=F or
25 active=F)
26 ## ~~~~~
27 # =1 Dust opt.deph read in startfi; =2 Viking scenario; =3 MGS scenario,
28 # =4 Mars Year 24 from TES assimilation (old version of MY24; dust_tes.nc
29 # file)
30 # =6 "cold" (low dust) scenario ; =7 "warm" (high dust) scenario
31 # =24 Mars Year 24 ; =25 Mars Year 25 (year with a global dust storm) ; ...
32 # =30 Mars Year 30
33 iaervar = 26
34 # Dust opacity at 610 Pa (when constant, i.e. for the iaervar=1 case)
35 tauvis=0.1
36 # Dust vertical distribution:
37 # (=0: old distrib. (Pollack90), =1: top set by "topdustref",
38 # =2: Viking scenario; =3 MGS scenario)
39 iddist = 3
40 # Dust top altitude (km). (Matters only if iddist=1)
41 topdustref = 55.
42
43 ## Physical Parameterizations :
44 ## ~~~~~
45 # call radiative transfer ?
46 callrad = .true.
47 # call NLTE radiative schemes ? matters only if callrad=T
48 callnlte = .true.
49 # call CO2 NIR absorption ? matters only if callrad=T
50 callnirco2 = .true.
51 # NIR NLTE correction ? matters only if callnirco2=T
52 nircorr=0
53 # call turbulent vertical diffusion ?
54 calldifv = .true.
55 # call convective adjustment ?
56 calladj = .true.
57 # Thermals
58 calltherm = .true.
59 callrichs1 = .true.
60 # call CO2 condensation ?
61 callcond = .true.
62 # call thermal conduction in the soil ?
63 callsoil = .true.
64 # call Lott's gravity wave/subgrid topography scheme ?
65 calllott = .true.
66 # Impose polar cap surface albedos as observed by TES?
67 TESicealbedo = .true.
68 ## Coefficient for Northern cap albedoes
69 TESice_Ncoef=1.6

```

```

1  ##General options
2  ##~~~~~
3  #Run with or without tracer transport ?
4  tracer=.true.
5
6  #Directory where external input files are:
7  datadir=/STEM/scratch.san/laf87/mgcm/datafile
8
9  #Diurnal cycle ? if diurnal=False, diurnal averaged solar heating
10 diurnal=.true.
11
12 #Seasonal cycle ? if season=False, Ls stays constant, to value set in "start"
13 season = .true.
14
15 #write some more output on the screen ?
16 lwrite = .false.
17
18 #Save statistics in file "stats.nc" ?
19 callstats =.false.
20
21 #Save EOF profiles in file "profiles" for Climate Database?
22 calleofdump = .false.
23
24 ## Dust scenario. Used if the dust is prescribed (i.e. if tracer=F or
25 active=F)
26 ## ~~~~~
27 # =1 Dust opt.deph read in startfi; =2 Viking scenario; =3 MGS scenario,
28 # =4 Mars Year 24 from TES assimilation (old version of MY24; dust_tes.nc
29 # =6 "cold" (low dust) scenario ; =7 "warm" (high dust) scenario
30 # =24 Mars Year 24 ; =25 Mars Year 25 (year with a global dust storm) ; ...
31 # =30 Mars Year 30
32 iaervar = 26
33 # Dust opacity at 610 Pa (when constant, i.e. for the iaervar=1 case)
34 tauvis=0.1
35 # Dust vertical distribution:
36 # (=0: old distrib. (Pollack90), =1: top set by "topdustref",
37 # =2: Viking scenario; =3 MGS scenario)
38 iddist = 3
39 # Dust top altitude (km). (Matters only if iddist=1)
40 topdustref = 55.
41
42 ## Physical Parameterizations :
43 ## ~~~~~
44 # call radiative transfer ?
45 callrad = .true.
46 # call NLTE radiative schemes ? matters only if callrad=T
47 callnlte = .true.
48 # call CO2 NIR absorption ? matters only if callrad=T
49 callnirco2 = .true.
50 # NIR NLTE correction ? matters only if callnirco2=T
51 nircorr=0
52 # call turbulent vertical diffusion ?
53 calldifv = .true.
54 # call convective adjustment ?
55 calladj = .true.
56 # Thermals
57 calltherm = .true.
58 callrichs1 = .true.
59 # call CO2 condensation ?
60 callcond =.true.
61 # call thermal conduction in the soil ?
62 callsoil = .true.
63 # call Lott's gravity wave/subgrid topography scheme ?
64 calllott = .true.
65 # Impose polar cap surface albedos as observed by TES?
66 TESicealbedo = .true.
67 ## Coefficient for Northern cap albedoes
68 TESice_Ncoef=1.6

```

```

1  ##General options
2  ##~~~~~
3  #Run with or without tracer transport ?
4  tracer=.true.
5
6  #Directory where external input files are:
7  datadir=/STEM/scratch.san/laf87/mgcm/datafile
8
9  #Diurnal cycle ? if diurnal=False, diurnal averaged solar heating
10 diurnal=.true.
11
12 #Seasonal cycle ? if season=False, Ls stays constant, to value set in "start"
13 season = .true.
14
15 #write some more output on the screen ?
16 lwrite = .false.
17
18 #Save statistics in file "stats.nc" ?
19 callstats =.false.
20
21 #Save EOF profiles in file "profiles" for Climate Database?
22 calleofdump = .false.
23
24 ## Dust scenario. Used if the dust is prescribed (i.e. if tracer=F or
    active=F)
25 ## ~~~~~
26 # =1 Dust opt.deph read in startfi; =2 Viking scenario; =3 MGS scenario,
27 # =4 Mars Year 24 from TES assimilation (old version of MY24; dust_tes.nc
    file)
28 # =6 "cold" (low dust) scenario ; =7 "warm" (high dust) scenario
29 # =24 Mars Year 24 ; =25 Mars Year 25 (year with a global dust storm) ; ...
30 # =30 Mars Year 30
31 iaervar = 26
32 # Dust opacity at 610 Pa (when constant, i.e. for the iaervar=1 case)
33 tauvis=0.1
34 # Dust vertical distribution:
35 # (=0: old distrib. (Pollack90), =1: top set by "topdustref",
36 # =2: Viking scenario; =3 MGS scenario)
37 iddist = 3
38 # Dust top altitude (km). (Matters only if iddist=1)
39 topdustref = 55.
40
41 ## Physical Parameterizations :
42 ## ~~~~~
43 # call radiative transfer ?
44 callrad = .true.
45 # call NLTE radiative schemes ? matters only if callrad=T
46 callnlte = .true.
47 # call CO2 NIR absorption ? matters only if callrad=T
48 callnirco2 = .true.
49 # NIR NLTE correction ? matters only if callnirco2=T
50 nircorr=0
51 # call turbulent vertical diffusion ?
52 calldifv = .true.
53 # call convective adjustment ?
54 calladj = .true.
55 # Thermals
56 calltherm = .true.
57 callrichsl = .true.
58 # call CO2 condensation ?
59 callcond =.true.
60 # call thermal conduction in the soil ?
61 callsoil = .true.
62 # call Lott's gravity wave/subgrid topography scheme ?
63 calllott = .true.
64 # Impose polar cap surface albedos as observed by TES?
65 TESicealbedo = .true.
66 ## Coefficient for Northern cap albedoes
67 TESice_Ncoef=1.6

```

Figure B.2: An example of a callphys.def file

B.2 Integration of the MSSM into the MGCM

The MSSM, described in Chapter 3, is a stand-alone model that can be used to investigate the annual cycle at individual locations. It has been designed so that simulations of >100 martian years can be run in a few hours, which is useful for the investigations into long term ice stability that are done in this thesis. To allow for future investigations using diurnal timescales or into global distribution, the MSSM has been integrated into version 6 of the MGCM.

To integrate the MSSM, the subsurface grid layering, subsurface temperature and volatile routine, and surface flux calculations had to be updated from the methods currently used (developed by Steele et al., 2017a, and described in Section B.3) to those described in this appendix. The calculation for surface flux was the only equation that could not be directly integrated into the MGCM and the equation used is described in Section B.2.1. Figure B.3 shows an overview of the files that were changed to fully integrate the MSSM. Although the MSSM has been integrated into the MGCM, the stand-alone MSSM was used for results presented in this thesis. Using the stand-alone MSSM allows for an initial detailed investigation into how carbon dioxide (CO_2) ice will behave at zonal latitudes and individual locations, which has not yet been investigated, without the complexities added by the use of a full climate on that behaviour.

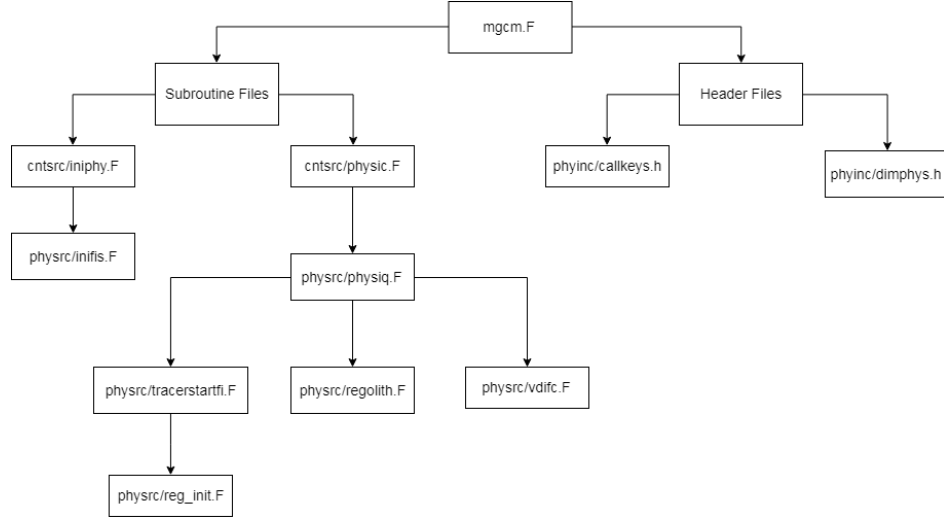


Figure B.3: Flowchart showing the links between the files edited to integrate the MSSM into the MGCM.

B.2.1 Surface Flux in the MGCM

The atmosphere-to-regolith flux for H_2O and CO_2 vapour used in the MSSM is not appropriate for the MGCM because the method designed for the MSSM assumes the atmospheric variables at the surface have a prescribed annual cycle, which is not the case for the MGCM. To account for the more complex, and more accurate, description of the atmosphere in the MGCM, I decided to use the surface flux calculation that is already used in the MGCM for the Steele et al. (2017a) subsurface model. The flux from the atmosphere to the surface (Equation B.1a) is taken from Forget et al. (1999).

$$F_{atm} = \rho_{1a} k_{atm} (q_{1a} - q_b), \quad (\text{B.1a})$$

$$k_{atm} = C_d |\mathbf{u}|, \quad (\text{B.1b})$$

where ρ is the density of the atmosphere [kg m^{-3}], k_{atm} is the coefficient for the atmosphere, q is the mass mixing ratio, C_d is the drag coefficient and $|\mathbf{u}|$ is the magnitude of the near-surface wind. The subscripts 1a and b represent the lowest atmospheric layer and the boundary layer values respectively. The mass mixing ratio, q can be converted to a vapour concentration, n , using $q = n/\rho$.

The equation for the flux from the surface to the regolith (Equation B.2a) is taken from Steele et al. (2017a) and follows a similar format to the atmospheric flux.

$$F_{reg} = k_{reg}(n_b - n_{1r}), \quad (\text{B.2a})$$

$$k_{reg} = \frac{D}{z_{0.5}}, \quad (\text{B.2b})$$

where n is the vapour concentration, D is the diffusion coefficient and $z_{0.5}$ is the depth to the midpoint of the first regolith layer. The fluxes are assumed to be equal at the boundary and rearranging $F_{atm} = F_{reg}$ gives the value at the boundary between the atmosphere and the regolith (Equation B.3). This value is calculated using the values from the previous time step.

$$n_b = \frac{k_{atm} \rho_{1a} q_{1a} + k_{reg} n_{1r}}{k_{reg} + k_{atm}} \quad (\text{B.3})$$

Then the vapour concentration in the boundary layer, n_b , is divided by the density of the atmosphere, ρ_{1a} to convert it back into a mass mixing ratio. This value is then input into Equation B.1a to calculate the atmospheric flux in the current time step.

B.3 The Steele et al. (2017a) subsurface water scheme in the MGCM

The subsurface water scheme within the MGCM is based on the subsurface model of Zent et al. (1993), which was incorporated into the MGCM and updated by Böttger et al. (2005b) and Steele et al. (2017a). This water scheme was incorporated into the MSSM during the early development stages, since the initial aim was to develop and test the MSSM separately from the MGCM before re-integrating it back into the MGCM. This was done so the MSSM could be tested without some of the additional complexities added by using the detailed climate in the MGCM, as fixed annual or diurnal atmospheric profiles could be used. However, while testing the water scheme several issues were found with the method used for diffusion of H_2O , which resulted in the development of a new scheme to mitigate these issues (described in Section 3.3). The following sections provide a description of the Steele et al. (2017a) water scheme and the testing results that led to the development of a new water scheme for the MSSM.

B.3.1 Water Scheme Description

In the Steele et al. (2017a) scheme, H_2O is assumed to exist in one of three states: vapour (n), adsorbed H_2O (α) and pore ice (ζ). The method to determine the distribution between these phases is based on the models of Zent et al. (1993) and Böttger et al. (2005b). These models determine the total H_2O content using Equation B.4:

$$\sigma = \phi n + \alpha + \zeta, \quad (\text{B.4})$$

where σ is the total amount of H_2O , ϕ is the regolith porosity, n is the mass of H_2O vapour per unit volume of regolith [kg m^{-3} ; or density], α is the density of adsorbed H_2O [kg m^{-3}], and ζ is the density of subsurface H_2O ice [kg m^{-3}] (Böttger et al., 2005b; Zent et al., 1993). In the scheme, H_2O vapour and adsorbed H_2O are diffused through the subsurface in each time step before the density of H_2O pore ice is calculated. A summary of the method used to develop the discretised diffusion equation used by Steele et al. (2017a) is provided here and for a more detailed derivation of the maths used in the Steele et al. (2017a) diffusion scheme, see Appendix B.3.3.

Vapour diffusion is calculated using a combination of the diffusion equation (Fick's 1st law; Equation 3.17) and an adsorption isotherm. The adsorption isotherm was incorporated into the vapour diffusion scheme to account for the suggestion that adsorbed H_2O will diffuse and equilibrate across time scales less than the time steps used in the MGCM (lower limit of 5 minutes) based on the results of Zent and Quinn (1995). However, adsorption lifetimes have since been estimated to be longer than those suggested by Zent and Quinn (1995) and adsorbed H_2O may take longer than vapour to diffuse and equilibrate (Möhlmann, 2005).

The density of adsorbed H_2O was incorporated into the vapour diffusion equation by using a combined mass of H_2O vapour and adsorbed H_2O , $m = \phi n + \alpha$, instead of only H_2O vapour, n . The density of adsorbed H_2O was calculated using the experimental adsorption isotherm (Equation B.5) developed by Zent et al. (1993) from the results of Fanale and Cannon (1974):

$$\alpha = \rho_s \frac{\beta P^{\gamma_w}}{e^{\delta/T}}, \quad (\text{B.5})$$

where ρ_s is the density of the regolith [kg m^{-3}], $\beta = 2.043 \times 10^{-8} \text{ Pa}^{-1}$, $\gamma_w = 0.51$, $\delta = -2679.8 \text{ K}$, P is the partial vapour pressure [Pa] and T is the soil temperature [K]. This isotherm was simplified using the ideal gas equation to:

$$\alpha = F \sqrt{n}, \quad (\text{B.6})$$

where $F = \frac{\rho_s \beta}{e^{\delta/T}} \left(\frac{k_B T}{m_w} \right)^{0.51}$, where k_B is the Boltzmann constant [$\text{m}^2 \text{ kg s}^{-2} \text{ K}^{-1}$] and m_w is the mass of a H_2O molecule [kg]. Then using Equation B.6, the combined equation for H_2O vapour and adsorbed H_2O becomes:

$$m = \phi n + F \sqrt{n}, \quad (\text{B.7})$$

which can be rearranged and solved for n to form:

$$n = \frac{m^2}{F^2} \left(1 - \frac{2m\phi}{F^2} \right) \quad (\text{B.8})$$

and to form the relation:

$$\frac{\delta m_i^t}{\delta t} = \frac{\delta n_i^t - B_i^t}{A_i^t \delta t}, \quad (\text{B.9})$$

where the superscript t represents the current time step, the subscript i represents the

grid point, the superscript dt represents the time between time steps and:

$$A_i^t = \frac{2 m_i^{t-dt}}{F_i^{t/2}} - \frac{6 m_i^{t-dt/2} \phi_i^t}{F_i^{t/4}} \quad (\text{B.10})$$

$$B_i^t = m_i^{t-dt/2} \left(\frac{1}{F_i^{t/2}} - \frac{1}{F_i^{t-dt/2}} \right) - 2 \phi_i^{t-dt} m_i^{t-dt/3} \left(\frac{1}{F_i^{t/4}} - \frac{1}{F_i^{t-dt/4}} \right) \quad (\text{B.11})$$

This relation can then be substituted into Equation B.12 (the diffusion equation) to form Equation B.13, which can then be numerically solved using the tri-diagonal matrix algorithm (TDMA) method. The detailed derivation is described in Appendix B.3.3.

$$\phi \frac{\partial n}{\partial t} = \frac{\partial}{\partial z} \left(D \frac{\partial n}{\partial z} \right) \quad (\text{B.12})$$

$$\square_i^t n_i^t - d_{i+0.5}^t n_{i+1}^t - d_{i-0.5}^t n_{i-1}^t = C_i^t (n_i^{t-dt} + B_i^t) \quad (\text{B.13})$$

where

$$C_i^t = \frac{z_{i+0.5} - z_{i-0.5}}{A_i^t \delta t} \quad (\text{B.14})$$

$$d_{i+0.5}^t = \frac{D_{i+0.5}^t}{z_{i+1} - z_i} \quad (\text{B.15})$$

$$d_{i-0.5}^t = \frac{D_{i-0.5}^t}{z_i - z_{i-1}} \quad (\text{B.16})$$

where D_i^t is the diffusion coefficient [$\text{m}^2 \text{s}^{-1}$], calculated using the method of Hudson et al. (2007). This equation can then be numerically solved with a TDMA, using the method of Böttger et al. (2005b), by setting a zero flux boundary at the base and a positive flux towards the surface (see Appendix B.3.3). Once vapour has diffused through the regolith using Equation B.13, the density of adsorbed H_2O is recalculated using Equation B.6 and the density of H_2O ice is calculated with Equation B.4, assuming the total amount of H_2O is the same as for the previous time step.

B.3.2 Testing of the Steele et al. (2017a) model

During development and testing of the MSSM after a replica of the Steele et al. (2017a) water scheme had been incorporated, several issues with the Steele et al. (2017a) water scheme were noticed. The main issue was the non-conservative nature of the Steele et al. (2017a) diffusion scheme (see Section B.3.2.2 for details). This would have caused issues when the MSSM was integrated into the MGCM because the MGCM has been designed to physically conserve all atmospheric components and, consequently, the subsurface also needs to conserve all of its components.

Another issue with the Steele et al. (2017a) water scheme was that the assumptions made to simplify the adsorption equation did not produce adsorption values similar to the original equation (see Section B.3.2.1 for details). The errors produced by this assumption propagate through the subsurface model, reducing the accuracy of the overall model. Therefore, a method for diffusion vapour through the subsurface without the inclusion of adsorbed H_2O would produce more accurate results than the method used by Steele et al. (2017a). Alongside this, the theory that H_2O adsorption would slow vapour diffusion through the regolith (Zent et al., 1993) has been shown by other studies to have an insignificant effect on ice formation over more than 30 martian years

(e.g. Fanale and Jakosky, 1982b; Schorghofer and Aharonson, 2005; Toon et al., 1980), especially in basalts, which are common across the surface of Mars and are the material used for the adsorption experiments on which the adsorption isotherm is based. All of the reasons described above led to the decision to develop a new water scheme for the MSSM that is described in detail in Section 3.3.

B.3.2.1 Vapour Diffusion Assumptions

The method for H₂O vapour diffusion used in the Steele et al. (2017a) water scheme uses an adapted version of the adsorption equation (Equation B.6) as one of the starting points for the derivation. However, the adapted version requires the use of several assumptions.

The first of these assumptions is that Equation B.17 can substitute for pressure, P , in Equation B.5.

$$P = \frac{k_B T n}{m_w}, \quad (\text{B.17})$$

where k_B is the Boltzmann constant [$\text{m}^2 \text{kg s}^{-2} \text{K}^{-1}$], T is the temperature [K], n is the amount of H₂O vapour [kg m^{-3}] and m_w is the mass of a H₂O molecule [kg]. This is a reasonable assumption to make because Equation B.17 is derived from the ideal gas equation (Clapeyron, 1834). However, the next step is to approximate γ_w for the vapour term, n , in Equation B.5 as 0.5 instead of 0.51 (Equation B.18a). This approximation makes it simpler to derive the final form of the diffusion equation (Equation B.13) that can be solved with a TDMA, but will impact the accuracy of the results.

$$\alpha = \frac{\rho_s \beta}{e^{\delta/T}} \left(\frac{k_B T}{m_w} \right)^{\gamma_w} \sqrt{n} \quad (\text{B.18a})$$

$$= F_w \sqrt{n} \quad (\text{B.18b})$$

where

$$F_w = \frac{\rho_s \beta}{e^{\delta/T}} \left(\frac{k_B T}{m_w} \right)^{0.51} \quad (\text{B.18c})$$

To test the effect of this assumption, the results of Equations B.5 and B.18a were compared (Table B.3) across the conditions expected within the model. In order to cover the entire range of conditions, the effects across all independent variables used in this equation are tested and these are: temperature, density and vapour concentration. On Mars, the expected temperature range is between 148 K and 315 K (Presley and Craddock, 2006) and density is expected to range between 1000 kg m^{-3} and 1750 kg m^{-3} within the model. The amount of H₂O vapour, n , is not well defined as this depends on a variety of conditions, but we can assume that the absolute minimum pressure is 0 and the maximum pressure is 10 MPa. The maximum assumption is from the region over which the equations of state for H₂O above the triple point are valid (Sanz et al., 2004). These maximum and minimum values are for pressure and must first be converted into vapour densities before being used in Equation B.5 or Equation B.18a. The vapour pressure is converted to vapour concentration using Equation B.19, which has been derived from the ideal gas equation (Clapeyron, 1834):

$$n = \frac{P m_w}{k_B T}, \quad (\text{B.19})$$

where P is the pressure [Pa], T is the temperature [K], m_w is the mass of a H_2O molecule ($m_w = 2.993e - 26$ kg) and k_B is the Boltzmann constant [$\text{m}^2 \text{kg s}^{-2} \text{K}^{-1}$]. The results show a large variation between the two equations and this led to a further investigation into the adsorption equation used, which is discussed in detail in Section 3.3.2.3.

Table B.3: Testing the effect of using \sqrt{n} instead of $n^{0.51}$ in Equation B.18a for the expected range of conditions

T	ρ_s	P	n	α	
				$\gamma_w=0.51$	$\gamma_w = 0.5$
148	1000	0.0001	1.46e-9	13.61	16.68
148	1000	1e7	146.39	5.545e6	5.275e6
148	1750	0.0001	1.46e-9	23.82	29.19
148	1750	1e7	146.39	9.704e6	9.232e6
315	1000	0.0001	6.88e-10	0.0009	0.0011
315	1000	1e7	68.78	375.78	360.22
315	1750	0.0001	6.88e-10	0.0016	0.0020
315	1750	1e7	68.78	657.620	630.38

Another key assumption used in the diffusion scheme is that $\frac{4m\phi}{F_w^4}$ is much smaller than unity. This was tested using different values for m , ϕ and F_w , in the expected range for the model, as well as for extreme cases. F_w is determined by Equation B.18c, which is dependent on temperature, T , and density, ρ_s . The ranges for temperature, density and the amount diffused, m , are the same as those used for testing the adsorption assumptions earlier in this section. The range for ϕ is well defined as this can only range between 0 and 1. The results from these tests (Table B.4) show that across the majority of the expected conditions, $\frac{4m\phi}{F_w^4}$ is less than 1 and the assumption is valid.

B.3.2.2 Conservation Properties

The degree of conservation of the diffusion scheme was tested using a series of closed system top-hat tests which assume no flux at each boundary. These are the same tests that are used to test different grid structures and the details of the tests can be found in Section 3.1. The conservation was tested using the same top-hat experiment in Section 3.1 because it is important for the water scheme in the MGCM to conserve H_2O during a run. The results of these tests (See Table B.5) showed that this method is not conservative and as around half of the total amount of H_2O is destroyed during a run of the scheme in a closed system. This was an issue because the total amount of H_2O in the entire system (atmosphere and regolith) should not change throughout a single simulation. From both the tests on the assumptions used in the vapour diffusion method and the conservation tests, it was clear that another methods for calculating H_2O vapour diffusion was necessary and a new method was developed that is described in Section 3.3.1.

Table B.4: Checking whether $\frac{4m\phi}{F^4}$ is smaller than 1 for the expected range of conditions

T	ρ_s	P	n	ϕ	$\frac{4m\phi}{F_w^4}$
148	1000	0.0001	1.46e-9	0.0001	1.62e-35
148	1000	0.0001	1.46e-9	1	1.62e-31
148	1000	1e7	146.39	0.0001	1.62e-24
148	1000	1e7	146.39	1	1.62e-20
148	1750	0.0001	1.46e-9	0.0001	1.72e-36
148	1750	0.0001	1.46e-9	1	1.72e-32
148	1750	1e7	146.39	0.0001	1.72e-25
148	1750	1e7	146.39	1	1.72e-21
315	1000	0.0001	6.88e-10	0.0001	7.73e-20
315	1000	0.0001	6.88e-10	1	7.73e-16
315	1000	1e7	68.78	0.0001	7.73e-9
315	1000	1e7	68.78	1	7.73e-5
315	1750	0.0001	6.88e-10	0.0001	8.24e-21
315	1750	0.0001	6.88e-10	1	8.24e-17
315	1750	1e7	68.78	0.0001	8.24e-10
315	1750	1e7	68.78	1	8.24e-6

Table B.5: Checking whether the scheme is conservative on the grid structures investigated in Section 3.1.

	Constant	Variable	Steele et al. (2017)
Initial total	0.079	0.055	0.067
Final total	0.024	0.024	0.034

B.3.3 Derivation of the Finite Difference Method for Vapour Diffusion used in Steele et al. (2017a)

The Steele et al. (2017a) H₂O vapour diffusion scheme starts from the same equations as vapour diffusion in the MSSM:

$$\frac{\partial m}{\partial t} = \frac{\partial J}{\partial z}, \quad (\text{B.20})$$

where

$$J = D \frac{\partial n}{\partial z} \quad (\text{B.21})$$

Combining these equations produces the diffusion equation:

$$\frac{\partial m}{\partial t} = \frac{\partial}{\partial z} \left(D \frac{\partial n}{\partial z} \right) \quad (\text{B.22})$$

where J is the H₂O vapour flux [kg m⁻¹s⁻¹], m is the concentration of H₂O [kg m⁻³] that can be diffused at time t [s] and depth z [m], and D is the diffusion coefficient [m²s⁻¹]. In the following equations $i-1$ and $i+1$ represent the midpoint of the previous and next layers, with $i-0.5$ and $i+0.5$ being the interface between the layers and i is

the midpoint of the current layer. Figure A.1 shows the relationships between the grid points. When the variable is for the current timestep, there is either a superscript of t or no superscript, and for the previous timestep, the superscript is 0. In the Steele et al. (2017a) scheme, adsorbed H_2O , α [kg m^{-3}], is diffused alongside the H_2O vapour, n :

$$m_i^t = \phi_i^t n_i^t + \alpha, \quad (\text{B.23})$$

where ϕ is the porosity and α is calculated using :

$$\alpha(n, T) = \rho_s \frac{\beta P^{0.51}}{e^{\delta/T}} \quad (\text{B.24})$$

$$= \rho_s \frac{\beta \left(\frac{k_B T n}{m_w} \right)^{0.51}}{e^{\delta/T}} \quad (\text{B.25})$$

$$= \rho_s \frac{\beta \left(\frac{k_B T}{m_w} \right)^{0.51}}{e^{\delta/T}} n^{0.51} \quad (\text{B.26})$$

$$= F(T) \sqrt{n} \quad (\text{B.27})$$

This differs from the scheme used in the MSSM which diffuses only H_2O vapour. Equation B.27 can be inserted into Equation B.23 to form:

$$m_i^t = \phi_i^t n_i^t + F_i^t \sqrt{n_i^t} \quad (\text{B.28})$$

This equation is then rearranged and solved to form an equation for H_2O vapour that can be substituted into Equation B.20.

$$F_i^t \sqrt{n_i^t} = m_i^t - \phi_i^t n_i^t \quad (\text{B.29})$$

$$F_i^{t^2} n_i^t = m_i^{t^2} - 2m_i^t \phi_i^t n_i^t + \phi_i^{t^2} n_i^{t^2} \quad (\text{B.30})$$

$$0 = \phi_i^{t^2} n_i^{t^2} - (F_i^{t^2} + 2m_i^t \phi_i^t) n_i^t + m_i^{t^2} \quad (\text{B.31})$$

This is of the same form as $a n^2 + b n + c = 0$, so can be solved using the quadratic formula

$$n = \frac{-b \pm \sqrt{b^2 - 4 a c}}{2 a}, \quad (\text{B.32})$$

where $a = \phi_i^{t^2}$, $b = -(F_i^{t^2} + 2m_i^t \phi_i^t)$ and $c = m_i^{t^2}$. To solve this, the most complex part is the square root, so considering that part only, we have:

$$b^2 - 4ac = F_i^{t^4} + 4m_i^{t^2} \phi_i^{t^2} + 4F_i^{t^2} m_i^t \phi_i^t - 4\phi_i^{t^2} m_i^{t^2} \quad (\text{B.33a})$$

$$= F_i^{t^4} + 4F_i^{t^2} m_i^t \phi_i^t \quad (\text{B.33b})$$

$$= F_i^{t^4} + \frac{4F_i^{t^4} m_i^t \phi_i^t}{F_i^{t^2}} \quad (\text{B.33c})$$

$$= F_i^{t^4} \left(1 + \frac{4m_i^t \phi_i^t}{F_i^{t^2}} \right) \quad (\text{B.33d})$$

Therefore, $\sqrt{b^2 - 4ac} = F_i^{t^2} \sqrt{1 + \frac{4m_i^t \phi_i^t}{F_i^{t^2}}}$, and the quadratic formula can be written as:

$$n = \frac{F_i^{t^2} + 2m_i^t \phi_i^t \pm F_i^{t^2} \sqrt{1 + \frac{4m_i^t \phi_i^t}{F_i^{t^2}}}}{2\phi_i^{t^2}} \quad (\text{B.34})$$

$$= \frac{2m_i^t \phi_i^t + F_i^{t^2} \left(1 \pm \sqrt{1 + \frac{4m_i^t \phi_i^t}{F_i^{t^2}}}\right)}{2\phi_i^{t^2}} \quad (\text{B.35})$$

$$= \frac{m_i^t}{\phi_i^t} + \frac{F_i^{t^2}}{2\phi_i^{t^2}} \left(1 \pm \sqrt{1 + \frac{4m_i^t \phi_i^t}{F_i^{t^2}}}\right) \quad (\text{B.36})$$

$$(\text{B.37})$$

The next step is to decide what is taken from the \pm term in Equation B.36. First, we rearrange Equation B.29 to give:

$$\frac{F_i^t \sqrt{n_i^t}}{\phi_i^t} = \frac{m_i^t}{\phi_i^t} - n_i^t \quad (\text{B.38})$$

$$n_i^t = \frac{m_i^t}{\phi_i^t} - \frac{F_i^t \sqrt{n_i^t}}{\phi_i^t} \quad (\text{B.39})$$

Since F_i^t , n_i^t and ϕ_i^t are all > 0 , and are subtracted from $\frac{m_i^t}{\phi_i^t}$, we must have $n_i^t < \frac{m_i^t}{\phi_i^t}$. Thus, in equation B.36 we need the last term to be negative, so we take the negative of the square root term, giving:

$$n_i^t = \frac{m_i^t}{\phi_i^t} + \frac{F_i^{t^2}}{2\phi_i^{t^2}} \left(1 - \sqrt{1 + \frac{4m_i^t \phi_i^t}{F_i^{t^2}}}\right) \quad (\text{B.40})$$

Evaluating a square root numerically will require a series of iterations to solve exactly. Therefore, approximating the square root term will reduce the number of operations that are needed to solve Equation B.40. This can be done by taking the binomial expansion of $\sqrt{1+x}$ (Equation B.41), where $x = -\frac{4m\phi}{F^2}$

$$\sqrt{1+x} \approx 1 + \frac{x}{2} - \frac{x^2}{8} + \frac{x^3}{16} + \dots \quad (\text{B.41})$$

From this expansion, if we only use the first four terms, and substitute these into Equation B.40, we can produce:

$$n_i^t = \frac{m_i^t}{\phi_i^t} + \frac{F_i^{t^2}}{2\phi_i^{t^2}} \left(1 - 1 - \frac{x}{2} + \frac{x^2}{8} - \frac{x^3}{16}\right) \quad (\text{B.42})$$

$$= \frac{m_i^t}{\phi_i^t} + \frac{F_i^{t^2}}{2\phi_i^{t^2}} \left(-\frac{2m_i^t \phi_i^t}{F_i^{t^2}} + \frac{2m_i^{t^2} \phi_i^{t^2}}{F_i^{t^4}} - \frac{4m_i^{t^3} \phi_i^{t^3}}{F_i^{t^6}}\right) \quad (\text{B.43})$$

$$= \frac{m_i^t}{\phi_i^t} - \frac{m_i^t}{\phi_i^t} + \frac{m_i^{t^2}}{F_i^{t^2}} - \frac{2m_i^{t^3} \phi_i^t}{F_i^{t^4}} \quad (\text{B.44})$$

$$(\text{B.45})$$

The final form of this equation is:

$$n_i^t = \frac{m_i^{t\,2}}{F_i^{t\,2}} \left(1 - \frac{2 m_i^t \phi_i^t}{F_i^{t\,2}} \right) \quad (\text{B.46})$$

Then as

$$\delta n_i^t = n_i^t - n_i^{t-dt} \quad (\text{B.47})$$

$$\delta n_i^t = \left[\frac{m_i^{t\,2}}{F_i^{t\,2}} \left(1 - \frac{2 m_i^t \phi_i^t}{F_i^{t\,2}} \right) \right] - \left[\frac{m_i^{t-dt\,2}}{F_i^{t-dt\,2}} \left(1 - \frac{2 m_i^{t-dt} \phi_i^{t-dt}}{F_i^{t-dt\,2}} \right) \right] \quad (\text{B.48})$$

The next step is to remove the dependence on m_i^t by substituting in $m_i^t = m_i^{t-dt} + \delta m_i^t$

$$\delta n_i^t = \left[\frac{(m_i^{t-dt} + \delta m_i^t)^2}{F_i^{t\,2}} \left(1 - \frac{2 (m_i^{t-dt} + \delta m_i^t) \phi_i^t}{F_i^{t\,2}} \right) \right] - \left[\frac{m_i^{t-dt\,2}}{F_i^{t-dt\,2}} \left(1 - \frac{2 m_i^{t-dt} \phi_i^{t-dt}}{F_i^{t-dt\,2}} \right) \right] \quad (\text{B.49})$$

$$\begin{aligned} \delta n_i^t = & \left[\frac{m_i^{t-dt\,2} + 2 m_i^{t-dt} \delta m_i^t + \delta m_i^{t\,2}}{F_i^{t\,2}} \left(1 - \frac{2 (m_i^{t-dt} + \delta m_i^t) \phi_i^t}{F_i^{t\,2}} \right) \right] \\ & - \left[\frac{m_i^{t-dt\,2}}{F_i^{t-dt\,2}} \left(1 - \frac{2 m_i^{t-dt} \phi_i^{t-dt}}{F_i^{t-dt\,2}} \right) \right] \end{aligned} \quad (\text{B.50})$$

Then assume $\delta m_i^{t\,2}$ is small enough that any terms including this can be ignored

$$\delta n_i^t = \left[\frac{m_i^{t-dt\,2}}{F_i^{t\,2}} \left(1 - \frac{2 (m_i^{t-dt} + \delta m_i^t) \phi_i^t}{F_i^{t\,2}} \right) \right] + \left[\frac{2 m_i^{t-dt} \delta m_i^t}{F_i^{t\,2}} \left(1 - \frac{2 (m_i^{t-dt} + \delta m_i^t) \phi_i^t}{F_i^{t\,2}} \right) \right] \quad (\text{B.51})$$

$$\begin{aligned} & - \left[\frac{m_i^{t-dt\,2}}{F_i^{t-dt\,2}} \left(1 - \frac{2 m_i^{t-dt} \phi_i^{t-dt}}{F_i^{t-dt\,2}} \right) \right] \\ \delta n_i^t = & \frac{m_i^{t-dt\,2}}{F_i^{t\,2}} - \frac{2 m_i^{t-dt\,3} \phi_i^t}{F_i^{t\,4}} - \frac{2 m_i^{t-dt\,2} \delta m_i^t \phi_i^t}{F_i^{t\,4}} + \frac{2 m_i^{t-dt} \delta m_i^t}{F_i^{t\,2}} \\ & - \frac{4 m_i^{t-dt\,2} \delta m_i^t \phi_i^t}{F_i^{t\,4}} - \frac{4 m_i^{t-dt\,2} \delta m_i^{t\,2} \phi_i^t}{F_i^{t\,4}} - \frac{m_i^{t-dt\,2}}{F_i^{t-dt\,2}} + \frac{2 m_i^{t-dt\,3} \phi_i^{t-dt}}{F_i^{t-dt\,4}} \end{aligned} \quad (\text{B.52})$$

Again need to assume $\delta m_i^{t\,2}$ is small enough that any terms including this can be ignored

$$\delta n_i^t = \frac{2 m_i^{t-dt} \delta m_i^t}{F_i^{t^2}} + \frac{m_i^{t-dt^2}}{F_i^{t^2}} - \frac{2 m_i^{t-dt^2} \delta m_i^t \phi_i^t}{F_i^{t^4}} - \frac{4 m_i^{t-dt^2} \delta m_i^t \phi_i^t}{F_i^{t^4}} - \frac{m_i^{t-dt^2}}{F_i^{t-dt^2}} - \frac{2 m_i^{t-dt^3} \phi_i^t}{F_i^{t^4}} \quad (\text{B.53})$$

$$+ \frac{2 m_i^{t-dt^3} \phi_i^{t-dt}}{F_i^{t-dt^4}}$$

$$\delta n_i^t = \frac{2 m_i^{t-dt} \delta m_i^t}{F_i^{t^2}} + \frac{m_i^{t-dt^2}}{F_i^{t^2}} - \frac{6 m_i^{t-dt^2} \delta m_i^t \phi_i^t}{F_i^{t^4}} - \frac{m_i^{t-dt^2}}{F_i^{t-dt^2}} - \frac{2 m_i^{t-dt^3} \phi_i^t}{F_i^{t^4}} + \frac{2 m_i^{t-dt^3} \phi_i^{t-dt}}{F_i^{t-dt^4}} \quad (\text{B.54})$$

This is then rearranged into the form $\delta n_i^t = A \delta m_i^t + B$

$$\delta n_i^t = \left(\frac{2 m_i^{t-dt}}{F_i^{t^2}} - \frac{6 m_i^{t-dt^2} \phi_i^t}{F_i^{t^4}} \right) \delta m_i^t + m_i^{t-dt^2} \left(\frac{1}{F_i^{t^2}} - \frac{1}{F_i^{t-dt^2}} \right) - 2 \phi_i^{t-dt} m_i^{t-dt^3} \left(\frac{1}{F_i^{t^4}} - \frac{1}{F_i^{t-dt^4}} \right) \quad (\text{B.55})$$

Therefore

$$\delta n_i^t = A \delta m_i^t + B, i \quad (\text{B.56})$$

where:

$$A = \frac{2 m_i^{t-dt}}{F_i^{t^2}} - \frac{6 m_i^{t-dt^2} \phi_i^t}{F_i^{t^4}} \quad (\text{B.57})$$

$$B = m_i^{t-dt^2} \left(\frac{1}{F_i^{t^2}} - \frac{1}{F_i^{t-dt^2}} \right) - 2 \phi_i^{t-dt} m_i^{t-dt^3} \left(\frac{1}{F_i^{t^4}} - \frac{1}{F_i^{t-dt^4}} \right) \quad (\text{B.58})$$

Therefore, we have

$$\frac{\delta m_i^t}{\delta t} = \frac{\delta n_i^t - B_i^t}{A_i^t \delta t} \quad (\text{B.59})$$

This can be substituted into Equation B.20 to give

$$\frac{\delta n_i^t - B_i^t}{A_i^t \delta t} = \frac{\delta J}{\delta z} \frac{n_i^t - n_i^{t-dt} - B_i^t}{A_i^t \delta t} = \frac{J_{i+0.5}^t - J_{i-0.5}^t}{z_{i+0.5} - z_{i-0.5}} \quad (\text{B.60})$$

where

$$J_{i+0.5}^t = D_{i+0.5}^t \frac{n_{i+1}^t - n_i^t}{z_{i+1} - z_i} \quad (\text{B.61})$$

$i \pm 1$ subscript denotes terms evaluated at the midpoints of the layers either side of the

layer being considered, and $i \pm 0.5$ denotes terms evaluated at the boundaries of layers. Equation B.60 can then be simplified as follows:

$$\frac{n_i^t - n_i^{t-dt} - B_i^t}{A_i^t \delta t} = \frac{\left(D_{i+0.5}^t \frac{n_{i+1}^t - n_i^t}{z_{i+1} - z_i}\right) - \left(D_{i-0.5}^t \frac{n_i^t - n_{i-1}^t}{z_i - z_{i-1}}\right)}{z_{i+0.5} - z_{i-0.5}} \quad (\text{B.62})$$

If we set:

$$g_{i+0.5}^t = \frac{D_{i+0.5}^t}{z_{i+1} - z_i} \quad (\text{B.63})$$

and

$$g_{i-0.5}^t = \frac{D_{i-0.5}^t}{z_i - z_{i-1}} \quad (\text{B.64})$$

then, this further simplifies to:

$$\frac{n_i^t - n_i^{t-dt} - B_i^t}{A_i^t \delta t} = \frac{g_{i+0.5}^t (n_{i+1}^t - n_i^t) - g_{i-0.5}^t (n_i^t - n_{i-1}^t)}{z_{i+0.5} - z_{i-0.5}} \quad (\text{B.65})$$

$$\frac{z_{i+0.5} - z_{i-0.5}}{A_i^t \delta t} (n_i^t - n_i^{t-dt} - B_i^t) = g_{i+0.5}^t (n_{i+1}^t - n_i^t) - g_{i-0.5}^t (n_i^t - n_{i-1}^t) \quad (\text{B.66})$$

Then if:

$$C_i^t = \frac{z_{i+0.5} - z_{i-0.5}}{A_i^t \delta t} \quad (\text{B.67})$$

$$C_i^t (n_i^t - n_i^{t-dt} - B_i^t) = g_{i+0.5}^t (n_{i+1}^t - n_i^t) - g_{i-0.5}^t (n_i^t - n_{i-1}^t) \quad (\text{B.68})$$

$$C_i^t n_i^t - C_i^t n_i^{t-dt} - C_i^t B_i^t = g_{i+0.5}^t n_{i+1}^t - g_{i+0.5}^t n_i^t - g_{i-0.5}^t n_i^t + g_{i-0.5}^t n_{i-1}^t \quad (\text{B.69})$$

$$(C_i^t + g_{i+0.5}^t + g_{i-0.5}^t) n_i^t = g_{i+0.5}^t n_{i+1}^t + g_{i-0.5}^t n_{i-1}^t + C_i^t (n_i^{t-dt} + B_i^t) \quad (\text{B.70})$$

Then if

$$\square_i^t = C_i^t + g_{i+0.5}^t + g_{i-0.5}^t \quad (\text{B.71})$$

$$\square_i^t n_i^t - g_{i+0.5}^t n_{i+1}^t - g_{i-0.5}^t n_{i-1}^t = C_i^t (n_i^{t-dt} + B_i^t) \quad (\text{B.72})$$

Equation B.72 can finally be solved using a TDMA, because it is in the right form ($a_i n_i - b_i n_{i+1} - c_i n_{i-1} = d_i$). This is achieved by substituting in Equations B.73a-e.

$$n_{i-1}^t = P_{i-1} n_i^t + Q_{i-1} \quad (\text{B.73a})$$

$$a_i^t = \square_i^t \quad (\text{B.73b})$$

$$b_i^t = g_{i+0.5}^t \quad (\text{B.73c})$$

$$c_i^t = g_{i-0.5}^t \quad (\text{B.73d})$$

$$d_i^t = C_i^t (n_i^{t-dt} + B_i^t) \quad (\text{B.73e})$$

The substitution gives:

$$a_i n_i^t = b_i n_{i+1}^t + c_i (P_{i-1} n_i^t + Q_{i-1}) + d_i \quad (\text{B.74})$$

$$a_i n_i^t = b_i n_{i+1}^t + c_i P_{i-1} n_i^t + c_i Q_{i-1} + d_i \quad (\text{B.75})$$

$$n_i^t (a_i - c_i P_{i-1}) = b_i n_{i+1}^t + c_i Q_{i-1} + d_i \quad (\text{B.76})$$

$$n_i^t = \frac{b_i}{a_i - c_i P_{i-1}} n_{i+1}^t + \frac{c_i Q_{i-1} + d_i}{a_i - c_i P_{i-1}} \quad (\text{B.77})$$

$$(\text{B.78})$$

This is in the right form to be numerically solved using Equations B.79a-c. Equations B.79d-e are the initial conditions for this system.

$$n_i^t = P_i n_{i+1}^t + Q_i \quad (\text{B.79a})$$

$$P_i = \frac{b_i}{a_i - c_i P_{i-1}} \quad (\text{B.79b})$$

$$Q_i = \frac{c_i Q_{i-1} + d_i}{a_i - c_i P_{i-1}} \quad (\text{B.79c})$$

$$P_1 = \frac{b_1}{a_1} \quad (\text{B.79d})$$

$$Q_1 = \frac{d_1}{a_1} \quad (\text{B.79e})$$

C | Sublimation Rates

C.1 CO₂ Sublimation Rate at all latitudes

Table C.1: Annual average carbon dioxide (CO₂) ice sublimation rate [mm MY⁻¹] at all latitudes for scenarios S02 to S19 (Tables VII.III and VII.V). Scenarios S01, S11, S12, and S13 have been excluded because they are initialised with no CO₂ ice and, therefore, CO₂ ice sublimation rate is 0 mm MY⁻¹ at all latitudes.

Latitude	Simulations													
	S02	S03	S04	S05	S06	S07	S08	S09	S10	S14	S15	S16	S18	S19
88	38.89	44.64	32.40	3.49	3.57	3.55	255.56	262.26	271.25	17.86	1.64	81.54	76.52	8.96
83	45.38	53.57	37.26	3.88	3.89	3.94	293.14	294.05	306.26	23.29	1.86	107.82	76.52	9.50
78	54.45	66.96	49.68	5.68	5.87	5.91	415.29	441.07	452.09	38.26	2.76	194.07	89.28	12.26
73	54.45	76.52	62.10	7.13	7.43	7.47	498.35	510.71	558.47	48.70	3.88	294.05	89.28	12.76
68	68.06	89.28	74.53	9.72	10.28	10.21	664.46	693.11	678.14	66.96	6.98	510.71	107.13	15.99
63	68.06	107.13	93.16	13.78	14.70	14.47	830.58	882.14	863.08	178.56	11.67	882.14	107.13	20.71
58	90.75	178.56	149.05	18.82	19.59	19.16	1107.44	1078.17	1186.74	267.83	18.00	1386.21	133.92	26.43
53	136.13	178.56	248.42	22.83	23.48	23.04	1423.85	1386.21	1356.27	267.83	23.50	1617.25	178.56	27.94
48	136.13	267.83	248.42	24.69	24.62	24.67	1661.15	1617.25	1582.32	267.83	25.78	1940.70	178.56	27.72
43	136.13	267.83	372.63	26.46	26.37	26.04	1993.38	1940.70	1898.78	267.83	28.14	2425.88	267.83	27.06
38	136.13	267.83	372.63	28.82	28.66	28.36	1993.38	1940.70	2373.48	267.83	30.58	2425.88	267.83	27.23
33	136.13	267.83	372.63	31.21	31.11	30.67	2491.73	2425.88	2373.48	267.83	32.74	2425.88	267.83	28.62
28	136.13	267.83	372.63	30.43	30.61	32.30	2491.73	2425.88	2373.48	267.83	31.56	2425.88	267.83	29.91
23	136.13	267.83	372.63	33.07	33.14	32.68	2491.73	3234.50	3164.64	267.83	33.92	3234.50	267.83	32.20

Continuation of table C.1														
Latitude	Simulations													
	S02	S03	S04	S05	S06	S07	S08	S09	S10	S14	S15	S16	S18	S19
18	136.13	267.83	372.63	39.47	39.15	38.44	3322.31	3234.50	3164.64	267.83	40.51	3234.50	267.83	29.71
13	136.13	267.83	372.63	45.51	45.44	45.23	3322.31	3234.50	3164.64	267.83	45.21	3234.50	267.83	30.82
8	136.13	267.83	372.63	46.12	46.05	45.76	3322.31	3234.50	3164.64	267.83	45.16	3234.50	267.83	30.83
3	136.13	267.83	372.63	45.21	45.04	45.77	3322.31	3234.50	3164.64	267.83	45.29	3234.50	267.83	30.27
-2	136.13	267.83	372.63	46.13	46.03	45.76	3322.31	3234.50	3164.64	267.83	45.31	3234.50	267.83	30.29
-7	136.13	267.83	372.63	46.24	46.05	45.79	3322.31	3234.50	3164.64	267.83	46.82	3234.50	267.83	31.70
-12	136.13	267.83	372.63	47.63	47.85	46.93	3322.31	3234.50	3164.64	267.83	47.75	3234.50	267.83	36.40
-17	136.13	267.83	372.63	48.15	48.06	47.95	3322.31	3234.50	3164.64	267.83	48.26	3234.50	267.83	38.12
-22	136.13	267.83	372.63	48.52	48.52	50.77	3322.31	3234.50	3164.64	267.83	54.82	3234.50	267.83	38.73
-27	136.13	267.83	372.63	48.21	48.20	49.45	3322.31	3234.50	3164.64	267.83	47.93	3234.50	267.83	37.39
-32	136.13	267.83	372.63	36.33	36.88	36.69	2491.73	3234.50	3164.64	267.83	47.19	3234.50	267.83	36.51
-37	136.13	267.83	372.63	35.33	35.86	35.94	2491.73	2425.88	2373.48	267.83	34.87	3234.50	267.83	33.97
-42	136.13	267.83	372.63	28.97	29.51	29.82	1993.38	1940.70	1898.78	267.83	34.25	2425.88	267.83	28.05
-47	136.13	267.83	372.63	26.93	25.66	26.55	1661.15	1617.25	1582.32	267.83	28.75	1940.70	267.83	26.95
-52	136.13	267.83	372.63	22.94	23.94	23.75	1245.86	1386.21	1356.27	267.83	24.70	1940.70	267.83	24.07
-57	136.13	267.83	248.42	15.62	16.18	16.42	996.69	970.35	949.39	267.83	19.80	1386.21	267.83	21.54
-62	136.13	267.83	186.31	10.75	11.10	11.16	664.46	693.11	678.14	267.83	12.27	882.14	267.83	16.73
-67	136.13	178.56	149.05	7.69	7.97	7.97	498.35	485.18	499.68	178.56	6.56	441.07	267.83	13.23
-72	136.13	178.56	124.21	5.62	5.85	5.65	369.15	359.39	365.15	133.92	3.59	236.67	267.83	10.79
-77	90.75	133.92	82.81	4.18	4.38	4.36	284.77	277.24	279.23	66.96	2.38	142.70	267.83	9.79
-82	90.75	107.13	62.10	3.34	3.50	3.44	226.52	220.53	226.05	28.19	1.64	86.64	267.83	9.92
-87	68.06	89.28	43.84	2.66	2.66	2.68	171.84	167.30	172.62	19.13	1.48	69.81	267.83	9.77

Table C.2: Annual average CO₂ ice sublimation rate [mm MY⁻¹] at all latitudes for scenarios S20 to S42 (Tables VII.III and VII.V) . Scenarios S26, S27, S28, S29 and S31 have been excluded because they are initialised with no CO₂ ice and, therefore, CO₂ ice sublimation rate is 0 mm MY⁻¹ at all latitudes.

Latitude	Simulations													
	S20	S22	S23	S24	S30	S33	S35	S36	S37	S38	S39	S40	S41	S42
88	570.79	89.28	16.69	882.14	129.61	1.62	1.63	131.86	0.71	3.12	5.53	0.64	5.22	10.43
83	606.47	107.13	17.39	882.14	144.21	1.78	1.82	148.34	0.84	3.31	5.95	0.71	5.43	10.87
78	693.11	107.13	22.20	1078.17	204.78	2.33	3.12	215.77	1.29	4.23	8.02	1.12	7.33	12.86
73	746.42	107.13	21.03	1078.17	249.74	2.77	4.30	263.72	1.76	4.38	7.61	1.79	7.57	12.55
68	882.14	107.13	24.32	1078.17	319.97	3.67	5.74	351.63	2.55	5.38	8.69	3.64	10.09	12.97
63	1078.17	133.92	30.34	1212.94	409.57	5.24	8.67	474.70	4.60	7.17	10.84	5.58	11.43	13.54
58	1212.94	133.92	33.84	1386.21	538.90	7.55	10.79	632.93	7.62	9.70	13.54	6.93	12.97	15.44
53	1386.21	178.56	33.10	1386.21	682.61	9.29	10.16	791.16	11.11	11.02	14.20	7.28	13.91	16.25
48	1617.25	178.56	31.14	1617.25	853.26	11.55	8.97	949.39	13.69	11.99	13.58	7.58	14.84	16.08
43	1617.25	267.83	28.97	1617.25	930.83	13.86	8.97	1054.88	14.54	12.89	12.90	8.48	12.45	15.75
38	1940.70	267.83	27.30	1617.25	1023.92	15.00	8.87	1186.74	15.05	13.75	12.47	9.19	10.95	14.03
33	1940.70	267.83	26.01	1617.25	1137.69	15.69	9.41	1356.27	15.78	14.76	12.61	10.29	9.53	10.95
28	2425.88	267.83	26.19	1940.70	1279.90	17.04	10.43	1582.32	16.67	15.62	13.39	9.41	9.36	9.71
23	2425.88	267.83	27.35	1940.70	1279.90	17.94	10.36	1582.32	17.06	16.36	14.22	10.79	10.16	8.87
18	2425.88	267.83	28.11	2425.88	1706.53	18.99	11.11	1898.78	19.59	16.75	14.51	12.06	10.87	9.03
13	2425.88	267.83	29.25	2425.88	1706.53	23.61	16.25	1898.78	22.05	17.40	14.86	17.54	10.22	9.53
8	3234.50	267.83	28.82	2425.88	2047.83	23.46	17.54	2373.48	22.19	17.07	15.55	18.38	11.03	10.02
3	2425.88	267.83	28.49	2425.88	2047.83	22.88	19.06	2373.48	22.46	16.30	14.58	19.79	11.69	11.11
-2	3234.50	267.83	28.55	2425.88	2559.79	23.31	21.15	2373.48	23.46	16.76	14.75	20.86	13.31	12.45
-7	3234.50	267.83	29.44	2425.88	2559.79	24.55	24.50	2373.48	25.58	16.98	15.69	24.12	14.99	13.66
-12	3234.50	267.83	29.97	2425.88	2559.79	28.77	27.57	2373.48	26.69	18.06	16.76	27.57	17.15	15.13
-17	3234.50	267.83	32.68	2425.88	2559.79	35.08	29.13	2373.48	29.94	21.79	17.77	28.59	20.05	17.74
-22	3234.50	267.83	35.73	2425.88	2559.79	36.47	30.27	2373.48	37.58	26.50	21.79	31.50	23.04	20.05

Continuation of table C.2														
Latitude	Simulations													
	S20	S22	S23	S24	S30	S33	S35	S36	S37	S38	S39	S40	S41	S42
-27	2425.88	267.83	35.97	2425.88	2559.79	34.75	30.27	1898.78	35.41	24.23	22.05	29.69	21.44	21.44
-32	2425.88	267.83	32.70	1940.70	2559.79	24.39	21.15	1582.32	31.48	22.46	20.46	26.61	20.86	20.58
-37	1940.70	267.83	29.92	1617.25	2047.83	20.93	19.06	1356.27	18.21	20.02	18.79	17.74	20.05	19.06
-42	1617.25	267.83	27.67	1617.25	1706.53	17.52	17.34	1186.74	16.92	18.00	18.08	16.25	17.54	17.74
-47	1617.25	267.83	28.68	1617.25	1462.74	16.57	14.70	949.39	16.07	17.75	18.60	15.13	17.15	18.83
-52	1386.21	267.83	27.22	1386.21	1279.90	14.11	12.65	730.30	13.88	16.87	18.27	12.65	15.28	18.38
-57	1078.17	267.83	25.30	1212.94	930.83	10.93	9.47	527.44	12.44	14.73	17.68	10.02	12.65	17.15
-62	882.14	267.83	25.80	1078.17	639.95	7.26	7.24	351.63	7.80	12.13	17.03	7.30	10.29	15.75
-67	693.11	267.83	21.61	970.35	465.42	5.26	6.50	256.59	4.16	9.77	16.83	5.42	8.77	14.56
-72	606.47	267.83	19.03	882.14	319.97	3.88	5.13	189.88	2.25	8.04	16.64	2.84	7.54	13.42
-77	539.08	267.83	18.48	808.63	217.85	2.95	4.40	146.06	1.33	7.24	16.61	1.58	7.25	13.42
-82	539.08	267.83	19.61	882.14	152.82	2.23	2.89	115.78	0.79	7.37	16.72	0.84	7.30	14.16
-87	510.71	267.83	19.95	882.14	104.48	1.64	2.07	87.91	0.70	7.22	16.75	0.65	7.23	14.29

Table C.3: Annual average CO₂ ice sublimation rate [mm MY⁻¹] at all latitudes for scenarios S43 to S51 (Tables VII.III and VII.V) .

Latitude	Simulations							
	S43	S44	S45	S45	S48	S49	S50	S51
88	44.18	287.69	474.70	474.70	4.77	1.50	7.80	14.10
83	56.85	306.26	499.68	499.68	5.25	1.72	8.22	14.79
78	99.94	379.76	593.37	593.37	7.62	2.58	10.54	19.36
73	148.34	395.58	558.47	558.47	9.39	3.67	10.98	18.32
68	263.72	474.70	632.93	632.93	12.94	6.31	13.62	21.26
63	474.70	558.47	730.30	730.30	19.77	11.16	17.93	26.43
58	730.30	678.14	791.16	791.16	24.32	17.96	23.60	28.60
53	949.39	730.30	863.08	863.08	27.48	23.66	24.41	28.42
48	1186.74	863.08	863.08	863.08	31.30	25.92	25.07	27.43

Continuation of table C.3								
Latitude	Simulations							
	S43	S44	S45	S45	S48	S49	S50	S51
43	1356.27	949.39	863.08	863.08	35.73	28.22	25.59	26.13
38	1356.27	1054.88	949.39	949.39	37.43	30.60	26.79	25.34
33	1582.32	1186.74	1054.88	1054.88	37.91	32.78	28.64	25.34
28	1582.32	1356.27	1054.88	1054.88	39.46	31.87	30.21	26.23
23	1898.78	1356.27	1186.74	1186.74	45.68	34.13	32.09	27.46
18	1898.78	1582.32	1356.27	1356.27	51.69	40.02	29.94	28.18
13	1898.78	1582.32	1356.27	1356.27	57.23	44.98	30.91	29.15
8	1898.78	1582.32	1356.27	1356.27	57.23	44.99	31.06	28.67
3	1898.78	1582.32	1356.27	1356.27	58.63	45.02	30.40	28.36
-2	2373.48	1898.78	1582.32	1582.32	62.03	44.98	30.48	28.47
-7	2373.48	1898.78	1582.32	1582.32	66.31	45.92	32.22	29.10
-12	2373.48	1898.78	1582.32	1582.32	68.19	47.06	36.33	29.76
-17	2373.48	1898.78	1582.32	1582.32	67.24	47.36	37.66	31.51
-22	2373.48	1898.78	1582.32	1582.32	64.53	52.83	38.12	34.52
-27	2373.48	1582.32	1356.27	1356.27	58.27	46.72	35.64	34.90
-32	1898.78	1356.27	1186.74	1186.74	45.66	45.90	35.59	30.12
-37	1582.32	1186.74	949.39	949.39	36.13	34.55	29.90	28.04
-42	1582.32	949.39	863.08	863.08	31.71	33.59	26.45	26.36
-47	1186.74	863.08	863.08	863.08	25.43	28.22	25.68	27.19
-52	1054.88	730.30	791.16	791.16	21.83	24.10	23.46	26.18
-57	730.30	558.47	678.14	678.14	14.50	18.52	18.68	24.56
-62	452.09	452.09	593.37	593.37	10.26	11.08	14.61	22.70
-67	231.56	379.76	527.44	527.44	7.68	6.06	11.25	18.90
-72	123.30	316.46	474.70	474.70	5.95	3.43	9.33	16.90
-77	75.35	287.69	452.09	452.09	4.69	2.24	8.51	16.48
-82	47.12	287.69	474.70	474.70	3.84	1.50	8.60	17.51
-87	36.76	279.23	474.70	474.70	3.23	1.34	8.48	17.63

Table C.4: Annual average CO₂ ice sublimation rate [mm MY⁻¹] at all latitudes for the different initial ice porosity simulations (Table VII.IV).

Latitude	Simulation				
	PM01	PM02	S06	PM03	PM04
88	1.21	1.59	3.57	23.16	85.87
83	1.23	1.63	3.89	24.14	98.02
78	1.32	1.98	5.87	31.40	176.43
73	1.39	2.24	7.43	35.85	248.81
68	1.51	2.78	10.28	43.78	334.60
63	1.54	3.43	14.70	55.77	462.07
58	1.58	4.02	19.59	76.41	646.90
53	1.61	4.38	23.48	89.02	808.63
48	1.67	4.68	24.62	103.23	970.35
43	1.70	4.89	26.37	115.52	1078.17
38	1.75	4.92	28.66	119.80	1212.94
33	1.80	4.91	31.11	127.68	1212.94
28	1.83	5.19	30.61	134.77	1386.21
23	1.94	5.11	33.14	142.70	1386.21
18	2.05	7.15	39.15	154.02	1386.21
13	2.25	8.29	45.44	186.61	1386.21
8	2.33	8.28	46.05	186.61	1386.21
3	2.33	8.31	45.04	190.26	1386.21
-2	2.39	9.94	46.03	198.03	1617.25
-7	2.53	9.73	46.05	206.46	1617.25
-12	2.56	11.24	47.85	206.46	1617.25
-17	2.53	12.34	48.06	206.46	1617.25
-22	2.47	13.05	48.52	202.16	1617.25
-27	2.27	12.82	48.20	190.26	1386.21
-32	2.11	8.41	36.88	149.28	1212.94
-37	2.16	7.80	35.86	127.68	970.35

Continuation of table C.4					
Latitude	Simulation				
	PM01	PM02	S06	PM03	PM04
-42	2.03	6.85	29.51	107.82	808.63
-47	1.80	6.11	25.66	86.64	646.90
-52	1.76	5.36	23.94	68.33	539.08
-57	1.70	4.14	16.18	48.51	404.31
-62	1.63	3.10	11.10	41.81	285.40
-67	1.53	2.62	7.97	35.59	202.16
-72	1.34	2.04	5.85	26.40	144.83
-77	1.32	1.78	4.38	23.08	103.23
-82	1.29	1.46	3.50	16.20	69.31
-87	1.22	1.30	2.66	11.27	49.01

Table C.5: Annual average CO₂ ice sublimation rate [mm MY⁻¹] at all latitudes for the different subsurface structure simulations (Table VII.IV).

Latitude	Simulation					
	S06	CDS-SS	CDS-SS-B	FDS-CDS	UR-CDS-B	UR-FDS
88	3.57	22.67	2.76	2.59	1.74	4.05
83	3.89	22.72	2.81	3.04	1.89	4.50
78	5.87	22.90	2.96	4.81	3.07	6.79
73	7.43	23.01	3.08	6.31	4.30	8.46
68	10.28	23.20	3.29	9.08	6.01	11.81
63	14.70	23.49	3.61	13.64	8.40	17.78
58	19.59	24.21	4.37	18.84	10.28	23.76
53	23.48	25.04	5.21	21.86	10.23	25.28
48	24.62	26.02	6.21	23.95	9.66	27.08
43	26.37	26.99	7.03	25.93	9.88	28.47
38	28.66	27.82	7.74	28.55	9.35	29.84
33	31.11	28.93	9.31	32.18	9.99	31.63

Continuation of table C.5						
Latitude	Simulation					
	S06	CDS-SS	CDS-SS-B	FDS-CDS	UR-CDS-B	UR-FDS
28	30.61	30.39	11.06	33.21	10.79	30.97
23	33.14	31.88	12.79	33.01	10.53	34.36
18	39.15	32.87	14.85	37.97	11.27	36.18
13	45.44	35.48	17.30	43.59	15.43	42.06
8	46.05	37.65	20.42	44.05	16.44	42.21
3	45.04	39.82	22.97	44.18	18.71	40.89
-2	46.03	42.17	27.23	44.53	19.33	42.42
-7	46.05	45.10	35.01	44.65	24.09	43.87
-12	47.85	53.43	42.01	53.43	27.06	45.63
-17	48.06	59.84	49.01	48.52	29.81	56.09
-22	48.52	66.98	56.55	50.42	31.98	51.34
-27	48.20	68.52	58.81	44.81	31.41	44.87
-32	36.88	65.04	54.46	35.48	21.71	37.79
-37	35.86	56.45	47.43	34.49	20.45	35.99
-42	29.51	44.42	38.69	28.48	17.76	30.75
-47	25.66	40.23	27.74	25.02	15.16	27.85
-52	23.94	37.01	20.71	21.85	12.74	25.07
-57	16.18	34.25	16.16	14.50	9.61	18.37
-62	11.10	31.37	11.40	9.46	7.92	12.12
-67	7.97	29.18	7.39	6.48	6.26	8.49
-72	5.85	27.43	6.76	4.56	4.78	6.24
-77	4.38	26.04	5.68	3.24	3.09	4.69
-82	3.50	24.90	4.84	2.30	2.26	3.69
-87	2.66	23.85	3.97	1.51	1.59	2.90

C.1.1 Regional Average CO₂ Sublimation Rates

Table C.6: Regional average CO₂ sublimation rates [mm MY⁻¹] for each baseline scenario (Tables VII.III and VII.V) across each latitude region (polar, mid-latitude and equatorial) in each hemisphere and averaged over both hemispheres. The final column is the global average sublimation rate for each scenario.

Run	North polar average	South polar average	Total polar average	Southern mid-latitude average	Northern mid-latitude average	Total mid-latitude average	Equatorial average	Global average
S01	0.00	0.00	0.00	0.00	0.00	0.00	0.00	0.00
S02	54.88	109.66	82.27	128.56	136.13	132.35	136.13	116.91
S03	73.02	159.21	116.11	238.07	267.83	252.95	267.83	212.30
S04	58.19	108.05	83.12	293.96	351.93	322.94	372.63	259.56
S05	7.28	5.71	6.49	25.47	27.69	26.58	43.72	25.60
S06	7.62	5.91	6.77	25.64	28.00	26.82	43.68	25.75
S07	7.59	5.88	6.74	25.32	28.20	26.76	43.90	25.80
S08	492.90	369.18	431.04	1778.49	1813.43	1795.96	3183.88	1803.62
S09	513.89	367.13	440.51	1731.49	1929.15	1830.32	3167.12	1812.65
S10	521.55	370.14	445.85	1795.18	1887.48	1841.33	3098.71	1795.30
S11	0.00	0.00	0.00	0.00	0.00	0.00	0.00	0.00
S12	0.00	0.00	0.00	0.00	0.00	0.00	0.00	0.00
S13	0.00	0.00	0.00	0.00	0.00	0.00	0.00	0.00
S14	62.27	115.76	89.02	267.83	267.83	267.83	267.83	208.23
S15	4.80	4.65	4.73	26.46	31.59	29.02	44.38	26.04
S16	345.05	309.84	327.45	2036.97	2360.42	2198.69	3167.12	1897.75
S17	0.00	0.00	0.00	0.00	0.00	0.00	0.00	0.00
S18	90.98	267.83	179.41	215.75	267.83	241.79	267.83	229.68
S19	13.36	11.71	12.54	27.50	28.51	28.01	33.03	24.52
S20	762.85	628.43	695.64	1619.18	1677.58	1648.38	2830.19	1724.74

Continuation of table C.6								
Run	North polar average	South polar average	Total polar average	Southern mid-latitude average	Northern mid-latitude average	Total mid-latitude average	Equatorial average	Global average
S21	0.00	0.00	0.00	0.00	0.00	0.00	0.00	0.00
S22	108.62	267.83	188.23	215.75	267.83	241.79	267.83	232.62
S23	22.00	20.75	21.37	30.06	28.58	29.32	30.05	26.91
S24	1035.29	917.26	976.27	1540.24	1565.27	1552.75	2345.01	1624.68
S25	0.00	0.00	0.00	0.00	0.00	0.00	0.00	0.00
S26	0.00	0.00	0.00	0.00	0.00	0.00	0.00	0.00
S27	0.00	0.00	0.00	0.00	0.00	0.00	0.00	0.00
S28	0.00	0.00	0.00	0.00	0.00	0.00	0.00	0.00
S29	0.00	0.00	0.00	0.00	0.00	0.00	0.00	0.00
S30	242.98	316.75	279.87	861.20	1664.60	1262.90	2118.94	1220.57
S31	0.00	0.00	0.00	0.00	0.00	0.00	0.00	0.00
S33	2.90	3.87	3.39	12.16	17.41	14.78	25.57	14.58
S35	4.21	4.71	4.46	9.53	15.73	12.63	20.63	12.57
S36	264.34	191.31	227.82	995.23	1055.41	1025.32	2122.95	1125.36
S37	1.96	2.84	2.40	12.96	18.17	15.56	24.89	14.28
S38	4.60	8.63	6.61	12.35	18.30	15.33	18.65	13.53
S39	7.77	16.76	12.27	13.22	18.65	15.93	16.33	14.84
S40	2.25	3.11	2.68	8.29	16.40	12.35	20.86	11.96
S41	7.85	8.06	7.95	12.44	17.26	14.85	14.44	12.42
S42	12.20	14.27	13.24	14.75	18.62	16.69	13.23	14.38
S43	181.29	161.03	171.16	1193.55	1339.22	1266.39	2109.76	1182.43
S44	400.41	333.82	367.12	910.42	940.71	925.57	1676.51	989.73
S45	581.57	499.50	540.54	897.45	888.60	893.02	1411.22	948.26
S48	9.96	5.94	7.95	32.36	29.21	30.79	58.04	32.26
S49	4.49	4.27	4.38	26.52	30.82	28.67	43.82	25.63
S50	11.52	10.13	10.82	25.68	26.63	26.16	32.92	23.30

Continuation of table C.6								
Run	North polar average	South polar average	Total polar average	Southern mid-latitude average	Northern mid-latitude average	Total mid-latitude average	Equatorial average	Global average
S51	19.04	18.35	18.70	26.88	27.08	26.98	29.69	25.12

Table C.7: Regional average CO₂ sublimation rates [mm MY⁻¹] for each scenario with a different initial ice porosity (Table VII.IV) across each latitude region (polar, mid-latitude and equatorial) in each hemisphere and averaged over both hemispheres. The final column is the global average sublimation rate for each scenario.

Run	North polar average	South polar average	Total polar average	Southern mid-latitude average	Northern mid-latitude average	Total mid-latitude average	Equatorial average	Global average
PM01	1.37	1.39	1.38	1.68	1.93	1.81	2.29	1.82
PM02	2.28	2.05	2.16	4.63	6.44	5.54	9.29	5.66
S06	7.62	5.91	6.77	25.64	28.00	26.82	43.68	25.75
PM03	35.68	25.73	30.70	105.27	98.04	101.66	183.73	105.37
PM04	234.30	142.32	188.31	988.32	763.70	876.01	1482.48	848.93

Table C.8: Regional average CO₂ sublimation rates [mm MY⁻¹] for each scenario with a different subsurface structure (Table VII.IV) across each latitude region (polar, mid-latitude and equatorial) in each hemisphere and averaged over both hemispheres. The final column is the global average sublimation rate for each scenario.

Run	North polar average	South polar average	Total polar average	Southern mid-latitude average	Northern mid-latitude average	Total mid-latitude average	Equatorial average	Global average
S06	7.62	5.91	6.77	25.64	28.00	26.82	43.68	25.75
CDS-SS	23.00	27.13	25.06	26.50	46.23	36.37	45.34	35.59
CDS-SS-B	3.09	6.67	4.88	6.64	34.20	20.42	30.67	18.66
FDS-CDS	6.58	4.59	5.58	25.22	26.64	25.93	43.53	25.01
UR-CDS-B	4.24	4.32	4.28	9.90	16.24	13.07	20.57	12.64
UR-FDS	8.90	6.35	7.63	27.68	29.30	28.49	42.58	26.23

C.2 H₂O Sublimation Rate

Table C.9: Annual average water (H₂O) ice sublimation rate [mm MY⁻¹] over the entire 200 martian year period at all latitudes for scenarios S01 to S14 (Tables VII.III and VII.V).

Latitude	Simulation													
	S01	S02	S03	S04	S05	S06	S07	S08	S09	S10	S11	S12	S13	S14
88	-0.00032	1.15	1.15	1.11	0.23	0.477	3.82	-0.00035	-0.00035	-0.00035	1.15	1.15	1.11	115
83	-0.00029	1.15	1.15	1.11	0.23	0.477	3.82	-0.00031	-0.00031	-0.00031	1.15	1.15	1.11	115
78	-0.00052	1.15	1.14	1.11	0.23	0.477	3.82	-0.00053	-0.00053	-0.00052	1.15	1.14	1.11	115
73	-0.00039	1.15	1.14	1.11	0.23	0.477	3.82	-0.00038	-0.00038	-0.00037	1.15	1.14	1.11	115
68	0	1.15	1.15	1.11	0.23	0.477	3.82	-7.6E-08	-8.2E-08	-8.7E-08	1.15	1.15	1.11	115
63	-4.6E-09	1.15	1.15	1.11	0.23	0.477	3.82	-1.4E-07	-1.5E-07	-6.6E-09	1.15	1.15	1.11	115
58	-2E-08	1.15	1.15	1.11	0.00231	0.00482	3.82	-4.8E-08	-5.6E-08	-4.6E-08	1.11	1.08	1.11	115
53	-4.9E-08	1.15	1.15	1.11	0.23	0.477	3.82	-1.3E-08	-1.1E-08	-6.2E-09	1.13	1.15	1.18	115
48	-1.2E-07	1.15	1.15	1.19	0.00648	0.0127	3.82	-6.3E-09	-1E-08	-3.1E-08	1.16	3.58	111	115
43	0	1.16	2.29	111	0.0115	0.477	3.82	0	0	0	12.8	115	111	115
38	0	115	115	111	0.0092	0.477	3.82	0	0	0	115	115	111	115
33	0	115	115	111	0.23	0.477	3.82	0	0	0	115	115	111	115
28	0	115	115	111	0.0023	0.477	3.82	0	0	0	115	115	111	115
23	0	115	115	111	0.00418	0.477	3.82	0	0	0	115	115	111	115
18	0	1.15	1.15	111	0.23	0.477	3.82	0	0	0	1.15	1.15	111	1.15
13	0	1.15	1.15	111	0.23	0.477	3.82	0	0	0	1.15	1.15	111	1.15
8	0	1.16	1.15	111	0.23	0.477	3.82	0	0	0	1.16	1.15	111	1.15
3	0	1.16	1.15	111	0.23	0.477	3.82	0	0	0	1.16	1.15	111	1.15
-2	0	1.16	1.15	111	0.23	0.159	3.82	0	0	0	1.16	1.15	111	1.15
-7	0	1.16	1.15	111	0.0078	0.0149	0.153	0	0	0	1.16	1.15	111	1.15
-12	0	1.16	1.15	111	0.0023	0.00545	1.91	0	0	0	1.16	1.15	111	1.15
-17	0	1.16	1.15	111	0.0023	0.0049	0.0384	0	0	0	1.16	1.15	111	1.15

Continuation of table C.9														
Latitude	Simulation													
	S01	S02	S03	S04	S05	S06	S07	S08	S09	S10	S11	S12	S13	S14
-22	0	1.16	1.15	111	0.0657	0.119	0.694	0	0	0	1.16	1.15	111	1.15
-27	0	1.16	1.15	111	0.0657	0.136	0.955	0	0	0	1.16	1.15	111	1.15
-32	0	1.16	1.15	111	0.0657	0.136	0.849	0	0	0	1.15	1.15	111	1.15
-37	0	1.15	1.15	111	0.092	0.119	1.27	0	0	0	115	115	111	1.15
-42	0	1.15	115	111	0.092	0.238	1.27	0	0	0	115	115	111	1.15
-47	0	115	115	111	0.0767	0.238	2.55	0	0	0	115	115	111	115
-52	0	115	115	111	0.23	0.318	1.91	0	0	0	115	115	111	115
-57	0	115	115	111	0.23	0.238	3.82	0	0	0	1.14	1.13	1.15	115
-62	0	1.53	2.79	1.92	0.23	0.477	3.82	0	0	0	1.11	1.07	1.03	115
-67	0	1.15	1.15	1.11	0.23	0.477	3.82	0	0	0	1.11	1.07	1.03	115
-72	0	1.15	1.15	1.11	0.23	0.477	3.82	-6.9E-09	-6.9E-09	-3.4E-09	1.15	1.12	1.08	115
-77	0	1.15	1.15	1.11	0.23	0.477	3.82	-7.7E-09	-7.7E-09	0	1.15	1.14	1.11	115
-82	0	1.15	1.15	1.11	0.23	0.477	3.82	-7.4E-07	-7E-07	-5.8E-07	1.15	1.15	1.11	115
-87	-8.9E-07	1.15	1.15	1.11	0.23	0.477	3.82	-3.1E-06	-3E-06	-2.7E-06	1.15	1.15	1.11	115

Table C.10: Annual average H₂O ice sublimation rate [mm MY⁻¹] over the entire 200 martian year period at all latitudes for scenarios S15 to S28 (Tables VII.III and VII.V).

Latitude	Simulation													
	S15	S16	S17	S18	S19	S20	S21	S22	S23	S24	S25	S26	S27	S28
88	0.477	0	115	1.13	0.477	-0.0188	1.12	1.06	0.477	-0.0765	1.06	0	-0.0188	-0.0767
83	0.477	0	115	1.12	0.477	-0.0193	1.12	1.06	0.477	-0.0782	1.06	0	-0.0193	-0.0783
78	0.477	0	115	1.12	0.477	-0.0252	1.12	1.02	0.477	-0.116	1.02	0	-0.0252	-0.116
73	0.477	0	115	1.14	0.477	-0.00802	1.14	1.12	0.477	-0.0271	1.11	0	-0.00781	-0.0267
68	0.477	0	115	1.14	0.477	-0.00502	1.14	1.13	0.00484	-0.0153	1.13	0	-0.00492	-0.0146
63	0.477	0	115	1.14	0.477	-0.00432	1.14	1.13	0.0265	-0.0104	1.13	0	-0.00445	-0.0103

Continuation of table C.10														
Latitude	Simulation													
	S15	S16	S17	S18	S19	S20	S21	S22	S23	S24	S25	S26	S27	S28
58	0.477	0	115	1.14	0.0111	-0.0033	1.14	1.14	0.477	-0.007	1.14	0	-0.00294	-0.00673
53	0.00964	0	115	1.14	0.477	-0.00255	1.08	1.14	0.00497	-0.00475	1.06	0	-0.00223	-0.00412
48	0.477	0	115	1.14	0.00489	-0.00212	1.06	1.14	0.00612	-0.00397	1.06	0	-0.00151	-0.00312
43	0.477	0	115	1.14	0.477	-0.00221	1.06	1.14	0.00677	-0.00448	1.06	0	-0.00146	-0.00382
38	0.477	0	115	1.14	0.0159	-0.00177	1.06	1.14	0.0177	-0.00595	1.06	0	-0.0008	-0.00521
33	0.477	0	115	1.14	0.00636	-0.00069	1.07	1.14	0.477	-0.00624	1.06	0	-2.2E-06	-0.00518
28	0.477	0	115	1.14	0.477	-0.00022	1.07	1.14	0.0217	-0.00693	1.06	0	-1.7E-06	-0.00526
23	0.477	0	1.15	1.14	0.318	-0.00013	1.07	1.13	0.00776	-0.00903	1.06	0	-2.1E-06	-0.00718
18	0.477	0	1.15	1.14	0.477	-2E-06	1.12	1.13	0.477	-0.00854	1.06	0	-1.6E-06	-0.00673
13	0.477	0	1.15	1.15	0.477	-7.8E-07	1.15	1.13	0.477	-0.012	1.05	0	-6.7E-07	-0.00962
8	0.477	0	1.15	1.17	0.477	-8.5E-07	1.15	1.14	0.477	-0.00897	1.06	0	-5.1E-07	-0.00664
3	0.477	0	1.15	1.15	0.318	-1.4E-06	1.12	1.14	0.106	-0.00938	1.06	0	-7.6E-07	-0.0071
-2	0.477	0	1.15	1.15	0.477	-9.8E-07	1.12	1.14	0.477	-0.00726	1.06	0	-5.2E-07	-0.0048
-7	0.159	0	1.15	1.15	0.191	-8.8E-07	1.07	1.14	0.238	-0.00664	1.06	0	-5.4E-07	-0.00388
-12	0.191	0	1.15	1.15	0.00555	-0.00063	1.07	1.14	0.238	-0.0084	1.06	0	-3.5E-06	-0.00547
-17	0.191	0	1.15	1.15	0.0561	-1.8E-06	1.07	1.15	0.159	-0.00298	1.06	0	-9.8E-07	-0.00014
-22	0.191	0	1.15	1.15	0.191	-3.5E-07	1.15	1.15	0.238	-4.8E-06	1.07	0	-8.4E-08	-1.6E-06
-27	0.00477	0	1.15	1.15	0.191	-5.3E-07	1.15	1.15	0.0954	-9.6E-05	1.07	0	-2.5E-07	-2.4E-06
-32	0.136	0	1.15	1.15	0.0867	-5E-06	1.11	1.15	0.238	-0.00162	1.07	0	-1.2E-06	-0.00073
-37	0.136	0	1.15	1.15	0.318	-0.00218	1.07	1.15	0.318	-0.00253	1.06	0	-0.00123	-0.00209
-42	0.477	0	115	1.15	0.119	-0.00342	1.06	1.15	0.477	-0.00346	1.06	0	-0.00301	-0.00323
-47	0.477	0	115	1.15	0.191	-0.00351	1.06	1.15	0.191	-0.0032	1.06	0	-0.00313	-0.0029
-52	0.477	0	115	1.14	0.191	-0.00334	1.06	1.15	0.238	-0.00261	1.06	0	-0.00327	-0.00245
-57	0.477	0	115	1.14	0.477	-0.00333	1.08	1.15	0.191	-0.00246	1.12	0	-0.00335	-0.00242
-62	0.477	0	115	1.14	0.477	-0.0032	1.12	1.15	0.318	-0.00217	1.14	0	-0.00322	-0.00226
-67	0.477	0	115	1.14	0.477	-0.0031	1.12	1.15	0.477	-0.00201	1.14	0	-0.00309	-0.00208
-72	0.477	0	107	1.14	0.477	-0.00329	1.14	1.15	0.238	-0.00219	1.14	0	-0.00326	-0.00225

Continuation of table C.10														
Latitude	Simulation													
	S15	S16	S17	S18	S19	S20	S21	S22	S23	S24	S25	S26	S27	S28
-77	0.477	0	107	1.14	0.477	-0.0034	1.14	1.15	0.477	-0.00218	1.14	0	-0.00335	-0.00221
-82	0.477	0	110	1.14	0.477	-0.00297	1.14	1.15	0.191	-0.00185	1.14	0	-0.00293	-0.00191
-87	0.477	0	107	1.14	0.477	-0.00295	1.14	1.15	0.477	-0.00165	1.14	0	-0.00292	-0.00173

Table C.11: Annual average H₂O ice sublimation rate [mm MY⁻¹] over the entire 200 martian year period at all latitudes for scenarios S29 to S43 (Tables VII.III and VII.V).

Latitude	Simulation														
	S29	S30	S31	S33	S34	S35	S36	S37	S38	S39	S40	S41	S42	S43	
88	115	-0.00024	0.477	66.9	102	80	0.0327	66.9	66.9	0.669	80	80	80	3.34	
83	115	-0.00022	0.477	66.9	102	80	0.0327	66.9	66.9	0.669	80	80	80	3.34	
78	115	-0.00043	0.477	66.9	102	80	0.0325	66.9	66.9	0.669	80	80	80	3.34	
73	115	-0.0003	0.477	66.9	102	80	0.0325	66.9	66.9	66.9	80	80	80	3.34	
68	115	0	0.477	66.9	102	80	0.033	66.9	66.9	0.801	80	80	80	3.34	
63	115	0	0.477	66.9	102	80	0.0331	66.9	66.9	1.17	80	80	1.04	3.34	
58	115	0	0.00645	0.672	102	80	0.0107	4.31	0.922	0.682	2.22	1.07	2.81	3.34	
53	115	0	0.106	8.91	3.91	3.72	0.0101	1.52	4.18	0.868	80	1.95	10.7	3.34	
48	115	0	0.0258	1.61	102	1.13	0.239	0.679	0.739	0.841	0.93	80	0.958	3.34	
43	115	0	0.0353	0.719	102	1.51	3.34	0.675	2.27	0.922	0.8	0.987	0.941	3.34	
38	115	0	0.0191	0.743	102	40	3.34	1.39	0.7	1.57	1.03	1.27	1.33	3.34	
33	115	0	0.00477	0.764	102	1.1	3.34	0.689	0.777	0.852	80	8.42	2.13	3.34	
28	115	0	0.00477	0.791	102	1.06	3.34	0.669	1.14	1.91	6.66	0.993	1.34	3.34	
23	115	0	0.00477	0.686	102	1.14	3.34	0.735	1.3	1.76	3.02	80	11.4	0.0339	
18	1.77	0	0.00477	0.669	102	0.808	0.0348	0.669	0.777	0.735	1.78	80	1.14	0.0351	
13	76.7	0	0.477	0.669	67.7	1.76	0.0364	0.669	0.669	1.11	80	80	1.86	0.0362	
8	76.7	0	0.318	0.669	67.7	3.14	0.0371	0.669	0.669	2.09	0.82	1.7	13.3	0.0366	

Continuation of table C.11														
Latitude	Simulation													
	S29	S30	S31	S33	S34	S35	S36	S37	S38	S39	S40	S41	S42	S43
3	76.7	0	0.318	0.669	67.7	0.808	0.0376	0.669	0.727	1.3	0.919	1.27	3.26	0.0367
-2	76.7	0	0.00502	0.669	67.7	1.23	0.038	0.669	0.735	2.35	1.6	4.57	80	0.0377
-7	76.7	0	0.0106	0.669	67.7	0.816	0.0387	0.669	0.715	1.67	0.8	1.82	1.55	0.0389
-12	1.15	0	0.318	0.669	67.7	0.8	0.0389	0.669	0.669	0.751	40	2.91	2.67	0.0393
-17	76.7	0	0.0318	0.669	67.7	0.8	0.0386	0.669	0.669	66.9	0.8	1.05	53.3	0.0394
-22	115	0	0.0434	0.669	20.3	1.4	0.0379	0.669	0.669	0.669	0.8	4.44	53.3	0.0399
-27	12.1	0	0.0233	0.669	67.7	1.01	0.0361	0.669	0.669	0.669	1.7	40	40	0.0386
-32	3.49	0	0.0298	0.669	67.7	5.71	0.0334	0.669	0.669	0.669	2.86	80	53.3	0.0361
-37	1.48	0	0.477	0.669	102	2.32	3.34	0.669	0.669	1.74	5.71	6.66	53.3	0.0334
-42	115	0	0.477	66.9	102	80	3.34	66.9	44.6	33.4	0.8	80	80	3.34
-47	115	0	0.477	44.6	102	80	3.34	66.9	44.6	44.6	4.44	80	53.3	3.34
-52	115	0	0.477	66.9	102	80	3.34	33.4	33.4	2.39	80	80	80	3.34
-57	115	0	0.477	66.9	102	80	0.0334	66.9	0.863	66.9	80	2.1	80	3.34
-62	115	0	0.477	66.9	102	80	0.0333	66.9	22.3	0.787	80	80	80	3.34
-67	115	0	0.477	66.9	102	80	0.00996	66.9	66.9	2.31	80	80	80	3.34
-72	115	0	0.477	66.9	102	80	0.00996	66.9	66.9	66.9	80	80	80	1.01
-77	115	0	0.477	66.9	102	80	0.0325	66.9	66.9	66.9	80	80	80	1.01
-82	115	-6.1E-10	0.477	66.9	102	80	0.0333	66.9	66.9	66.9	80	80	80	1.01
-87	115	-9.3E-07	0.477	66.9	102	80	0.0333	66.9	66.9	66.9	80	80	80	1.01

Table C.12: Annual average H₂O ice sublimation rate [mm MY⁻¹] over the entire 200 martian year period at all latitudes for scenarios S29 to S43 (Tables VII.III and VII.V).

Latitude	Simulation					
	S44	S45	S48	S49	S50	S51
88	0.0105	-0.06	0.895	3.13	3.13	3.13

Continuation of table C.12						
Latitude	Simulation					
	S44	S45	S48	S49	S50	S51
83	0.00985	-0.0619	1.25	0.0364	3.13	3.13
78	0.00197	-0.106	0.895	0.0331	3.13	3.13
73	0.0238	-0.00051	3.13	3.13	1.25	0.0346
68	0.027	0.0136	3.13	2.09	3.13	3.13
63	0.0281	0.0196	3.13	3.13	3.13	3.13
58	0.0297	0.0242	3.13	3.13	3.13	1.04
53	0.00712	0.00435	3.13	3.13	3.13	3.13
48	0.0076	0.00558	1.57	3.13	3.13	0.783
43	0.00715	0.00474	1.25	3.13	3.13	1.04
38	0.00748	0.00308	3.13	3.13	3.13	3.13
33	0.00887	0.00303	0.0333	3.13	3.13	3.13
28	0.0093	0.00238	3.13	3.13	3.13	3.13
23	0.00933	-0.00071	0.0559	3.13	0.626	1.25
18	0.0101	-0.00012	3.13	3.13	0.298	3.13
13	0.0329	-0.00439	3.13	3.13	0.0895	0.0994
8	0.0329	-0.00054	0.0522	3.13	0.232	2.09
3	0.0327	-0.00096	0.0497	3.13	2.09	0.241
-2	0.0328	0.00118	2.09	3.13	0.482	0.569
-7	0.0104	0.00133	0.0493	3.13	0.391	0.0704
-12	0.00777	-0.00085	0.0764	0.895	0.522	0.391
-17	0.0104	0.00522	0.118	0.783	0.272	0.33
-22	0.0336	0.032	0.0545	0.626	0.418	0.0318
-27	0.0334	0.0317	0.0608	0.12	0.313	0.391
-32	0.0331	0.00769	0.0591	0.569	0.348	0.391
-37	0.00729	0.00684	0.0335	1.25	0.33	1.57
-42	0.00582	0.00595	2.09	0.391	0.224	0.33
-47	0.00593	0.00617	0.285	0.0522	0.216	0.232

Latitude	Simulation					
	S44	S45	S48	S49	S50	S51
-52	0.0287	0.0296	0.125	0.391	0.224	0.0835
-57	0.0287	0.0305	0.0793	0.348	0.569	0.261
-62	0.0289	0.0306	0.202	0.313	1.25	0.368
-67	0.0289	0.0308	0.216	0.272	3.13	0.216
-72	0.0293	0.0306	0.522	3.13	3.13	1.57
-77	0.0292	0.0307	3.13	0.112	3.13	0.391
-82	0.0296	0.031	3.13	3.13	3.13	1.25
-87	0.0297	0.0312	0.157	3.13	3.13	3.13

Table C.13: Annual average H₂O ice sublimation rate [mm MY⁻¹] over a 199 martian year period (excluding the first year of simulation) at all latitudes for scenarios S01 to S11 (Tables VII.III and VII.V). The first year has been excluded from the annual averages because there is an initial rapid loss of H₂O ice as the system equilibrates and the annual changes after this year are orders of magnitude smaller.

[illegible]

Continuation of table C.13											
Latitude	Simulation										
	S01	S02	S03	S04	S05	S06	S07	S08	S09	S10	S11
33	0	0	0	0	0	0	0	0	0	0	0
28	0	0	0	0	-1.8E-10	0	0	0	0	0	0
23	0	0	0	0	0	0	0	0	0	0	0
18	0	4.36E-05	2.08E-05	0	0	0	0	0	0	0	0.000616
13	0	0.00344	0.00237	0	0	0	0	0	0	0	0.00469
8	0	0.00722	0.00343	0	0	0	0	0	0	0	0.00724
3	0	0.00968	0.00408	0	0	0	0	0	0	0	0.00842
-2	0	0.0121	0.00445	0	0	6.06E-07	0	0	0	0	0.01
-7	0	0.0139	0.00575	0	3.44E-06	2.04E-06	2.21E-06	0	0	0	0.012
-12	0	0.0146	0.00657	0	6.69E-07	1.4E-07	0	0	0	0	0.0127
-17	0	0.0153	0.00687	0	0.000002	5.62E-06	1.36E-06	0	0	0	0.0126
-22	0	0.0156	0.00687	0	1.07E-06	6.05E-07	3.67E-06	0	0	0	0.0117
-27	0	0.0144	0.00591	0	5.64E-07	8.44E-07	0	0	0	0	0.00762
-32	0	0.0126	0.00418	0	1.88E-07	-3.5E-07	-6.9E-07	0	0	0	0.00104
-37	0	0.00602	0.00202	0	5.48E-07	2.91E-07	4.07E-07	0	0	0	0
-42	0	5.51E-05	0	0	8.45E-07	0	4.07E-07	0	0	0	0
-47	0	0	0	0	0	3.77E-07	1.02E-06	0	0	0	0
-52	0	0	0	0	0	5.65E-07	6.78E-07	0	0	0	0
-57	0	0	0	0	0	0	0	0	0	0	2.45E-06
-62	0	-4.4E-09	-1.9E-08	0	0	0	0	0	0	0	-6.5E-05
-67	0	-5.2E-07	-2.9E-06	-1E-05	0	0	0	0	0	0	-7.9E-05
-72	0	-6.6E-05	-8.6E-05	-5.2E-05	0	0	0	1.97E-06	1.4E-06	7.01E-07	-9.1E-05
-77	0	-7.8E-05	-0.00012	-5.6E-05	0	0	0	1.13E-06	1.01E-06	0	-8.4E-05
-82	0	-8.6E-05	-0.00013	-8.1E-05	0	0	0	-5.8E-07	-5.4E-07	-4.3E-07	-8.7E-05
-87	-8.8E-07	-9.5E-05	-0.00014	-7.8E-05	0	0	0	-2.9E-06	-2.8E-06	-2.5E-06	-9.5E-05

Table C.14: Annual average H₂O ice sublimation rate [mm MY⁻¹] over a 199 martian year period (excluding the first year of simulation) at all latitudes for scenarios S12 to S22 (Tables VII.III and VII.V). The first year has been excluded from the annual averages because there is an initial rapid loss of H₂O ice as the system equilibrates and the annual changes after this year are orders of magnitude smaller.

Latitude	Simulation										
	S12	S13	S14	S15	S16	S17	S18	S19	S20	S21	S22
88	-0.00073	-0.00064	0	0	0	0	-0.0208	0	-0.0187	-0.0218	-0.0836
83	-0.00069	-0.0006	0	0	0	0	-0.0215	0	-0.0192	-0.0224	-0.0855
78	-0.00094	-0.00083	0	0	0	0	-0.0281	0	-0.0251	-0.0293	-0.125
73	-0.00091	-0.00078	0	0	0	0	-0.00911	0	-0.00798	-0.00948	-0.0306
68	-0.00046	-0.0004	0	0	0	0	-0.00617	0	-0.005	-0.0064	-0.018
63	-0.00038	-0.00029	0	0	0	0	-0.00526	0	-0.00429	-0.00537	-0.0131
58	-0.0002	-0.00014	0	0	0	0	-0.00406	0	-0.00328	-0.00392	-0.0094
53	-4.9E-07	3.99E-07	0	0	0	0	-0.00353	0	-0.00254	-0.00322	-0.00655
48	-1.1E-07	0	0	0	0	0	-0.00332	-1E-09	-0.00211	-0.00281	-0.00547
43	0	0	0	0	0	0	-0.00407	0	-0.00219	-0.00337	-0.00619
38	0	0	0	0	0	0	-0.004	0	-0.00175	-0.00291	-0.00783
33	0	0	0	0	0	0	-0.0028	0	-0.00067	-0.00156	-0.00822
28	0	0	0	0	0	0	-0.00245	0	-0.00021	-0.00106	-0.00928
23	0	0	0	0	0	0.000146	-0.00236	9.81E-08	-0.00011	-0.00108	-0.0121
18	0.00101	0	0.00145	0	0	0.0016	-0.00116	0	8.31E-06	-0.00012	-0.0114
13	0.00294	0	0.00302	0	0	0.0029	-1.3E-07	0	3.64E-06	0.000232	-0.0151
8	0.0036	0	0.00368	0	0	0.00331	5.78E-07	0	2.8E-06	0.000266	-0.0106
3	0.00385	0	0.00403	0	0	0.00345	-1.4E-06	4.37E-07	3.55E-06	3.32E-05	-0.0103
-2	0.00418	0	0.00438	0	0	0.00413	6.12E-07	0	2.84E-06	0.000239	-0.0074
-7	0.00455	0	0.00595	6.06E-07	0	0.00485	0.0004	0	1.5E-06	0.000426	-0.00582
-12	0.00495	0	0.00666	7.57E-07	0	0.00535	0.000736	6.61E-09	-0.00061	-0.0017	-0.00598
-17	0.00475	0	0.00712	1.67E-06	0	0.00559	0.0019	1.27E-07	7.64E-06	0.000577	0.000273
-22	0.00418	0	0.00843	0	0	0.00604	0.00301	8.48E-07	2.34E-06	0.00101	0.00121

Continuation of table C.14											
Latitude	Simulation										
	S12	S13	S14	S15	S16	S17	S18	S19	S20	S21	S22
-27	0.00313	0	0.00702	3.96E-06	0	0.00485	0.00288	2.83E-07	2.76E-06	0.000635	0.000789
-32	0.000605	0	0.00506	3.39E-07	0	0.0031	0.00135	1.13E-07	1.89E-06	0.00014	2.12E-07
-37	0	0	0.00325	3.39E-07	0	0.000225	2.5E-06	5.65E-07	-0.00217	-0.00244	-5.8E-06
-42	0	0	0.000585	0	0	0	-9.7E-06	0	-0.0034	-0.00413	-9.7E-06
-47	0	0	0	0	0	0	-3.6E-05	0	-0.00349	-0.00406	-5.7E-06
-52	0	0	0	0	0	0	-0.00091	0	-0.00332	-0.00396	-2.3E-06
-57	-1.8E-08	0	0	0	0	0	-0.00204	0	-0.00331	-0.00399	-3E-06
-62	-9.5E-05	-1.8E-05	0	0	0	0	-0.00269	0	-0.00318	-0.00392	-4.5E-06
-67	-0.00011	-5.3E-05	0	0	0	0	-0.00315	0	-0.00308	-0.00391	-6.3E-06
-72	-0.00011	-6.1E-05	0	0	0	0	-0.00394	0	-0.00327	-0.00437	-0.00053
-77	-0.00014	-6.6E-05	0	0	0	0	-0.00409	0	-0.00338	-0.00435	-0.00064
-82	-0.00014	-8.6E-05	0	0	0	0	-0.00364	0	-0.00295	-0.00392	-8.1E-05
-87	-0.00014	-8.2E-05	0	0	0	0	-0.00358	0	-0.00294	-0.00384	-6.4E-06

Table C.15: Annual average H₂O ice sublimation rate [mm MY⁻¹] over a 199 martian year period (excluding the first year of simulation) at all latitudes for scenarios S23 to S34 (Tables VII.III and VII.V). The first year has been excluded from the annual averages because there is an initial rapid loss of H₂O ice as the system equilibrates and the annual changes after this year are orders of magnitude smaller.

Latitude	Simulation									
	S23	S24	S25	S26	S27	S28	S29	S30	S31	S33
88	0	-0.0762	-0.0873	0	-0.0187	-0.0764	0	-0.00024	0	0
83	0	-0.0778	-0.0891	0	-0.0192	-0.0779	0	-0.00022	0	0
78	0	-0.115	-0.13	0	-0.0251	-0.115	0	-0.00043	0	0
73	0	-0.027	-0.0318	0	-0.00777	-0.0265	0	-0.0003	0	0
68	-1E-09	-0.0153	-0.0186	0	-0.0049	-0.0145	0	0	0	0
63	0	-0.0104	-0.0134	0	-0.00442	-0.0102	0	0	0	0

Continuation of table C.15										
Latitude	Simulation									
	S23	S24	S25	S26	S27	S28	S29	S30	S31	S33
58	0	-0.00696	-0.00909	0	-0.00292	-0.00669	0	0	0	0
53	-1E-09	-0.00473	-0.00603	0	-0.00222	-0.00409	0	0	0	0
48	0	-0.00395	-0.00485	0	-0.0015	-0.0031	0	0	0	0
43	0	-0.00445	-0.00562	0	-0.00144	-0.00379	0	0	0	0
38	0	-0.00592	-0.00713	0	-0.00078	-0.00517	0	0	0	0
33	0	-0.0062	-0.00738	0	1.15E-05	-0.00514	0	0	-1.9E-10	0
28	0	-0.00689	-0.00823	0	1.34E-05	-0.00522	0	0	-8.3E-10	0
23	0	-0.00898	-0.0107	0	1.58E-05	-0.00712	0	0	-3.5E-10	0
18	0	-0.00849	-0.0101	0	0.000019	-0.00667	3.88E-06	0	0	1.38E-06
13	0	-0.0119	-0.014	0	7.94E-06	-0.00955	1.82E-06	0	0	-1.9E-06
8	0	-0.00892	-0.0101	0	4.66E-06	-0.00659	1.82E-06	0	1.82E-06	-3.6E-06
3	0	-0.00933	-0.0105	0	4.1E-06	-0.00705	1.82E-06	0	1.51E-06	-5.9E-06
-2	0	-0.00722	-0.00836	0	4.83E-06	-0.00476	1.82E-06	0	-1.5E-07	-1.2E-05
-7	3.77E-07	-0.0066	-0.0081	0	1.68E-06	-0.00384	1.82E-06	0	-8.3E-07	-1.3E-05
-12	0	-0.00835	-0.0101	0	1.46E-05	-0.00543	9.99E-05	0	1.82E-06	-1.7E-05
-17	2.26E-07	-0.00296	-0.00421	0	5.84E-06	-0.00012	1.82E-06	0	1.69E-05	-2E-05
-22	1.13E-06	2.02E-06	-0.00015	0	2.33E-06	6.48E-06	0	0	0.000091	-2E-05
-27	3.77E-07	-8.9E-05	-0.00031	0	3.15E-06	5.31E-06	9.73E-05	0	1.58E-05	-1.6E-05
-32	7.54E-07	-0.00161	-0.00204	0	5.36E-06	-0.00072	-1.2E-07	0	3.08E-05	5.72E-06
-37	1.13E-06	-0.00252	-0.00306	0	-0.00121	-0.00207	1.25E-05	0	0	-6.3E-07
-42	0	-0.00344	-0.00407	0	-0.00299	-0.00322	0	0	0	0
-47	2.83E-07	-0.00318	-0.0038	0	-0.00311	-0.00288	0	0	0	1.02E-06
-52	0	-0.00259	-0.00293	0	-0.00325	-0.00244	0	0	0	0
-57	5.09E-07	-0.00244	-0.00291	0	-0.00334	-0.00241	0	0	0	0
-62	1.02E-06	-0.00216	-0.00274	0	-0.0032	-0.00225	0	0	0	0
-67	0	-0.002	-0.00259	0	-0.00307	-0.00207	0	0	0	0
-72	0	-0.00217	-0.00281	0	-0.00324	-0.00224	0	0	0	0

Continuation of table C.15										
Latitude	Simulation									
	S23	S24	S25	S26	S27	S28	S29	S30	S31	S33
-77	0	-0.00216	-0.00275	0	-0.00333	-0.0022	0	0	0	0
-82	0	-0.00184	-0.00241	0	-0.00292	-0.0019	0	-6.1E-10	0	0
-87	0	-0.00164	-0.00223	0	-0.0029	-0.00172	0	-9.3E-07	0	0

Table C.16: Annual average H₂O ice sublimation rate [mm MY⁻¹] over a 199 martian year period (excluding the first year of simulation) at all latitudes for scenarios S35 to S45 (Tables VII.III and VII.V). The first year has been excluded from the annual averages because there is an initial rapid loss of H₂O ice as the system equilibrates and the annual changes after this year are orders of magnitude smaller.

Latitude	Simulation										
	S35	S36	S37	S38	S39	S40	S41	S42	S43	S44	S45
88	0	-0.00072	0	0	-1E-07	0	0	0	0	-0.0228	-0.0929
83	0	-0.00067	0	0	-1.2E-07	0	0	0	0	-0.0234	-0.0948
78	0	-0.00092	0	0	-1.7E-06	0	0	0	0	-0.0313	-0.138
73	0	-0.00088	0	0	0	0	0	0	0	-0.0096	-0.0338
68	0	-0.00044	0	0	-3.2E-09	0	0	0	0	-0.00636	-0.0197
63	0	-0.00035	0	0	0	0	0	0	0	-0.00531	-0.0138
58	0	-0.00014	0	0	-2.7E-09	0	-1.3E-09	0	0	-0.00368	-0.00911
53	0	2.91E-05	0	0	-3.5E-09	0	0	0	0	-0.00294	-0.00569
48	0	2.33E-06	-8.4E-10	0	0	-1.2E-09	0	-1.2E-09	0	-0.00246	-0.00447
43	-1.9E-09	0	-8.3E-10	0	0	-6.9E-09	0	-1.2E-09	0	-0.0029	-0.00531
38	0	0	0	0	0	-1.3E-09	-1.6E-09	-1.7E-09	0	-0.00258	-0.00696
33	-1.4E-09	0	0	0	0	0	0	0	0	-0.00119	-0.007
28	-1.3E-09	0	0	0	0	0	0	-1.7E-09	0	-0.00077	-0.00765
23	-1.4E-09	0	1.3E-06	0	0	0	0	0	0.000529	-0.00073	-0.0107
18	0	0.00138	-1.9E-08	0	0	1.08E-07	0	-1.4E-09	0.00164	5.37E-05	-0.0101
13	-2.2E-09	0.00299	-3.1E-06	0	0	0	0	0	0.00277	0.000305	-0.0144

Table C.17: Annual average H₂O ice sublimation rate [mm MY⁻¹] over a 199 martian year period (excluding the first year of simulation) at all latitudes for scenarios S48 to S51 (Tables VII.III and VII.V). The first year has been excluded from the annual averages because there is an initial rapid loss of H₂O ice as the system equilibrates and the annual changes after this year are orders of magnitude smaller.

Latitude	Simulation			
	S48	S49	S50	S51
88	6.98E-07	0	0	0
83	2.88E-07	2.2E-08	0	0
78	1.45E-07	2.23E-08	0	0
73	0	0	6.54E-07	4.85E-09
68	0	1.88E-06	0	0
63	0	0	0	0
58	0	0	0	5.23E-07
53	0	0	0	0
48	1.74E-06	0	0	7.48E-07
43	2.18E-07	0	0	5.23E-07
38	0	0	0	0
33	-5.4E-09	0	0	0
28	0	0	0	0
23	-3.1E-08	0	7.56E-07	1.05E-06
18	0	0	-2.1E-07	0
13	0	0	4.55E-08	3.71E-08
8	6.93E-08	0	4.43E-08	1.7E-06
3	2.39E-06	0	5.65E-07	4.05E-07
-2	3.35E-06	0	2.42E-07	1.13E-07
-7	1.23E-06	0	6.87E-07	6.24E-06
-12	3.45E-06	1.91E-06	1.85E-07	5E-07
-17	-9.9E-07	3.14E-06	2.25E-07	7.03E-07
-22	1.4E-06	1.85E-06	1.92E-05	1.81E-06

Continuation of table C.17				
Latitude	Simulation			
	S48	S49	S50	S51
-27	1.57E-06	7.4E-06	2.41E-06	-4.4E-08
-32	-8.5E-08	-5.8E-07	3.59E-07	1.93E-07
-37	7.77E-07	-7.3E-08	5.09E-07	1.51E-06
-42	1.7E-06	4.76E-07	2.65E-07	4.41E-07
-47	4.15E-08	4.88E-08	1.77E-07	1.9E-07
-52	7.69E-08	2.51E-07	1.08E-07	6.29E-08
-57	2.57E-08	6.77E-08	0	3.79E-08
-62	1.69E-07	6.24E-07	0	1.27E-07
-67	4.11E-08	5.23E-08	0	3.12E-08
-72	2.86E-07	0	0	0
-77	0	2.09E-08	0	5.82E-08
-82	0	0	0	0
-87	2.82E-07	0	0	0

Table C.18: Annual average H₂O ice sublimation rate [mm MY⁻¹] over the entire 200 martian year period at all latitudes for the different initial ice porosity simulations (Table VII.IV).

Latitude	Simulation				
	PM01	PM02	S06	PM03	PM04
88	2.01E-05	0.0478	0.477	4.77	47.7
83	2.01E-05	0.0478	0.477	4.77	47.7
78	2.01E-05	0.0478	0.477	4.77	47.7
73	2.01E-05	0.0478	0.477	4.77	47.7
68	2.01E-05	0.0478	0.477	4.77	47.7
63	0.000014	0.0478	0.477	4.77	47.7
58	0.000014	0.0478	0.00482	0.0757	47.7

Continuation of table C.18					
Latitude	Simulation				
	PM01	PM02	S06	PM03	PM04
53	0.000014	0.0478	0.477	0.867	47.7
48	2.01E-05	0.000645	0.0127	0.0477	47.7
43	2.01E-05	0.00115	0.477	0.0681	47.7
38	2.01E-05	0.0478	0.477	0.0973	47.7
33	2.01E-05	0.0478	0.477	4.77	47.7
28	2.01E-05	0.0478	0.477	4.77	47.7
23	2.01E-05	0.000884	0.477	0.0575	47.7
18	2.01E-05	0.0478	0.477	4.77	47.7
13	2.01E-05	0.0478	0.477	4.77	47.7
8	2.01E-05	0.0478	0.477	4.77	47.7
3	2.01E-05	0.0478	0.477	0.0596	47.7
-2	2.01E-05	0.000478	0.159	0.0892	47.7
-7	2.55E-06	0.00113	0.0149	0.477	47.7
-12	2.04E-05	0.00309	0.00545	0.954	7.95
-17	2.04E-05	0.001	0.0049	0.183	4.34
-22	3.11E-06	0.000478	0.119	0.0615	3.41
-27	7.01E-06	0.0239	0.136	0.0802	3.29
-32	2.01E-05	0.0318	0.136	0.0575	4.34
-37	2.01E-05	0.0318	0.119	4.77	7.95
-42	2.01E-05	0.0239	0.238	1.59	47.7
-47	2.01E-05	0.0239	0.238	4.77	47.7
-52	2.01E-05	0.0318	0.318	4.77	47.7
-57	2.01E-05	0.0239	0.238	2.38	5.3
-62	1.96E-05	0.0478	0.477	4.77	5.61
-67	0.000014	0.0478	0.477	4.77	7.95
-72	1.96E-05	0.0478	0.477	4.77	47.7
-77	2.01E-05	0.0478	0.477	4.77	47.7

Continuation of table C.18					
Latitude	Simulation				
	PM01	PM02	S06	PM03	PM04
-82	2.01E-05	0.0478	0.477	4.77	47.7
-87	2.01E-05	0.0478	0.477	4.77	47.7

Table C.19: Annual average H₂O ice sublimation rate [mm MY⁻¹] over the entire 200 martian year period at all latitudes for the different subsurface structure simulations (Table VII.IV).

Latitude	Simulation					
	S06	CDS-SS	CDS-SS-B	FDS-CDS	UR-CDS-B	UR-FDS
88	0.000477	0.016	0.016	0.000477	0.000477	0.000477
83	0.000477	0.016	0.016	0.000477	0.000477	0.000477
78	0.000477	0.016	0.016	0.000477	0.000477	0.000477
73	0.000477	0.016	0.016	0.000477	0.000477	0.000477
68	0.000477	0.016	0.016	0.000477	0.000477	0.000477
63	0.000477	0.016	0.016	0.000477	0.000477	0.000477
58	4.82E-06	0.016	0.016	4.77E-06	0.000477	5.51E-06
53	0.000477	0.016	0.016	0.000477	8.67E-05	0.000477
48	1.27E-05	0.000241	0.00021	2.07E-05	0.000477	0.000477
43	0.000477	0.000181	0.001	0.000477	0.000477	5.61E-06
38	0.000477	0.000188	0.000324	0.000477	0.000477	0.000477
33	0.000477	0.000171	0.000207	0.000477	0.000477	0.000477
28	0.000477	0.000168	0.000174	0.000477	1.29E-05	0.000477
23	0.000477	0.000193	0.000169	0.000477	5.75E-06	0.000477
18	0.000477	0.000193	0.00016	2.73E-05	6.15E-06	0.000477
13	0.000477	0.016	0.016	0.000477	8.52E-06	0.000477
8	0.000477	0.016	0.016	0.000477	0.000477	0.000477
3	0.000477	0.016	0.016	0.000477	0.000477	0.000477

Continuation of table C.19						
Latitude	Simulation					
	S06	CDS-SS	CDS-SS-B	FDS-CDS	UR-CDS-B	UR-FDS
-2	0.000159	0.016	0.016	0.000477	0.000477	0.000159
-7	1.49E-05	0.016	0.016	0.000477	0.000106	7.34E-06
-12	5.45E-06	0.016	0.016	0.000318	2.12E-05	8.23E-06
-17	4.9E-06	0.016	0.016	0.000239	4.77E-05	3.29E-05
-22	0.000119	0.016	0.016	0.000159	0.000159	0.000136
-27	0.000136	0.00016	0.016	4.79E-06	0.000159	6.2E-06
-32	0.000136	0.000365	0.000338	0.000106	0.000318	0.000106
-37	0.000119	0.016	0.016	0.000238	0.000318	0.000191
-42	0.000238	0.000289	0.000267	0.000318	0.000238	0.000191
-47	0.000238	0.000782	0.000713	0.000238	0.000318	0.000238
-52	0.000318	0.016	0.016	0.000477	0.000477	0.000477
-57	0.000238	0.016	0.016	0.000191	0.000477	0.000477
-62	0.000477	0.016	0.016	0.000477	0.000477	0.000477
-67	0.000477	0.016	0.016	0.000477	0.000477	0.000477
-72	0.000477	0.016	0.016	0.000477	0.000477	0.000477
-77	0.000477	0.016	0.016	0.000477	0.000477	0.000477
-82	0.000477	0.016	0.016	0.000477	0.000477	0.000477
-87	0.000477	0.016	0.016	0.000477	0.000477	0.000477

[illegible]

Continuation of table C.20								
Run	North polar average	South polar average	Total polar average	Southern mid-latitude average	Northern mid-latitude average	Total mid-latitude average	Equatorial average	Global average
S17	1.146E+02	1.100E+02	1.123E+02	1.004E+02	7.677E+01	8.859E+01	1.150E+00	7.285E+01
S18	1.131E+00	1.142E+00	1.137E+00	1.143E+00	1.146E+00	1.144E+00	1.149E+00	1.143E+00
S19	4.770E-01	4.770E-01	4.770E-01	2.234E-01	2.304E-01	2.269E-01	2.679E-01	3.265E-01
S20	-1.344E- 02	-3.153E- 03	-8.295E- 03	-1.623E-03	-2.629E-03	-2.126E-03	-5.864E-05	-3.582E-03
S21	1.130E+00	1.134E+00	1.132E+00	1.076E+00	1.074E+00	1.075E+00	1.115E+00	1.105E+00
S22	1.087E+00	1.146E+00	1.116E+00	1.138E+00	1.146E+00	1.142E+00	1.140E+00	1.132E+00
S23	3.232E-01	3.630E-01	3.431E-01	1.274E-01	2.756E-01	2.015E-01	2.929E-01	2.715E-01
S24	-5.385E- 02	-2.009E- 03	-2.793E- 02	-6.045E-03	-2.645E-03	-4.345E-03	-5.988E-03	-1.288E-02
S25	1.084E+00	1.143E+00	1.114E+00	1.070E+00	1.074E+00	1.072E+00	1.060E+00	1.082E+00
S26	0.000E+00	0.000E+00	0.000E+00	0.000E+00	0.000E+00	0.000E+00	0.000E+00	0.000E+00
S27	-1.342E- 02	-3.127E- 03	-8.273E- 03	-1.120E-03	-2.331E-03	-1.725E-03	-9.727E-07	-3.395E-03
S28	-5.372E- 02	-2.072E- 03	-2.790E- 02	-5.078E-03	-2.305E-03	-3.691E-03	-4.099E-03	-1.204E-02
S29	1.151E+02	1.151E+02	1.151E+02	1.151E+02	7.754E+01	9.630E+01	5.399E+01	9.325E+01
S30	-1.988E- 04	-1.500E- 07	-9.947E- 05	0.000E+00	0.000E+00	0.000E+00	0.000E+00	-3.316E-05
S31	4.770E-01	4.770E-01	4.770E-01	2.587E-02	4.025E-01	2.142E-01	1.436E-01	2.749E-01
S33	6.686E+01	6.686E+01	6.686E+01	1.863E+00	4.108E+01	2.147E+01	6.686E-01	2.973E+01
S35	7.996E+01	7.996E+01	7.996E+01	1.620E+01	5.465E+01	3.542E+01	1.662E+00	3.971E+01
S36	3.275E-02	2.537E-02	2.906E-02	2.121E+00	2.239E+00	2.180E+00	3.704E-02	8.645E-01
S37	6.686E+01	6.686E+01	6.686E+01	1.334E+00	3.922E+01	2.028E+01	6.686E-01	2.931E+01
S38	6.686E+01	5.943E+01	6.314E+01	1.503E+00	2.080E+01	1.115E+01	6.940E-01	2.504E+01
S39	1.181E+01	4.509E+01	2.845E+01	1.176E+00	2.494E+01	1.306E+01	7.169E+00	1.607E+01

Continuation of table C.20								
Run	North polar average	South polar average	Total polar average	Southern mid-latitude average	Northern mid-latitude average	Total mid-latitude average	Equatorial average	Global average
S40	7.996E+01	7.996E+01	7.996E+01	2.182E+01	2.896E+01	2.539E+01	1.200E+01	3.992E+01
S41	7.996E+01	7.996E+01	7.996E+01	2.183E+01	5.477E+01	3.830E+01	2.706E+01	4.668E+01
S42	6.681E+01	7.996E+01	7.338E+01	3.950E+00	6.663E+01	3.529E+01	2.761E+01	4.340E+01
S43	3.341E+00	1.786E+00	2.563E+00	2.928E+00	2.239E+00	2.583E+00	3.768E-02	1.889E+00
S44	1.686E-02	2.925E-02	2.305E-02	1.082E-02	1.826E-02	1.454E-02	2.456E-02	1.972E-02
S45	-3.247E-02	3.084E-02	-8.166E-04	5.837E-03	1.446E-02	1.015E-02	6.572E-03	5.229E-03
S48	2.073E+00	1.227E+00	1.650E+00	1.929E+00	4.449E-01	1.187E+00	8.064E-01	1.297E+00
S49	1.925E+00	1.682E+00	1.804E+00	3.131E+00	5.008E-01	1.816E+00	1.980E+00	1.970E+00
S50	2.818E+00	2.818E+00	2.818E+00	2.818E+00	3.184E-01	1.568E+00	4.958E-01	1.761E+00
S51	2.615E+00	1.154E+00	1.885E+00	2.081E+00	4.772E-01	1.279E+00	7.032E-01	1.374E+00

Table C.21: Regional average H₂O sublimation rates [mm MY⁻¹] for each different initial ice porosity scenario (Table VII.IV) across each latitude region (polar, mid-latitude and equatorial) in each hemisphere and averaged over both hemispheres. The final column is the global average sublimation rate for each scenario.

Run	North polar average	South polar average	Total polar average	Southern mid-latitude average	Northern mid-latitude average	Total mid-latitude average	Equatorial average	Global average
FM01	1.91E-05	1.89E-05	0.000019	2.01E-05	1.81E-05	1.91E-05	1.62E-05	1.81E-05
FM02	0.0478	0.0478	0.0478	0.02785	0.032166	0.030008	0.022497	0.033435
S06	0.477	0.477	0.477	0.2145	0.32092	0.26771	0.275104	0.339938
FM03	4.77	4.77	4.77	3.05625	0.987633	2.021942	1.7535	2.848481
FM04	47.7	34.06	40.88	26.78167	47.7	37.24083	33.3825	37.16778

Table C.22: Regional average H₂O sublimation rates [mmMY⁻¹] for each different subsurface structure scenario (Table VII.IV) across each latitude region (polar, mid-latitude and equatorial) in each hemisphere and averaged over both hemispheres. The final column is the global average sublimation rate for each scenario.

Run	North polar average	South polar average	Total polar average	Southern mid-latitude average	Northern mid-latitude average	Total mid-latitude average	Equatorial average	Global average
S06	0.000477	0.000477	0.000477	0.000215	0.000321	0.000268	0.000275	0.00034
CDS-SS	0.016	0.016	0.016	0.008239	0.005464	0.006851	0.010726	0.011193
CDS-SS-B	0.016	0.016	0.016	0.00822	0.005624	0.006922	0.012042	0.011655
FDS-CDS	0.000477	0.000477	0.000477	0.000261	0.000322	0.000292	0.000341	0.00037
UR-CDS-B	0.000477	0.000477	0.000477	0.000358	0.000412	0.000385	0.000163	0.000342
UR-FDS	0.000477	0.000477	0.000477	0.00028	0.00032	0.0003	0.000268	0.000348